



# รายงานวิจัยฉบับสมบูรณ์

# โครงการ

สถาบันวิจัยเกี่ยวกับตัวเร่งปฏิกิริยาไทย Thai Catalysis Research Institute

โดย

ศาสตราจารย์ ดร. ปิยะสาร ประเสริฐธรรมและคณะ

ภาควิชาวิศวกรรมเคมี คณะวิศวกรรมศาสตร์ จุฬาลงกรณ์มหาวิทยาลัย

สิงหาคม 2555

# สัญญาเลขที่ DPG5280005

# รายงานวิจัยฉบับสมบูรณ์ โครงการ

# สถาบันวิจัยเกี่ยวกับตัวเร่งปฏิกิริยาไทย Thai Catalysis Research Institute

ผู้วิจัย สังกัด

ศ.คร. ปียะสาร ประเสริฐธรรม (หัวหน้าโครงการ) จุฬาลงกรณ์มหาวิทยาลัย จุฬาลงกรณ์มหาวิทยาลัย ศ.คร.สุทธิชัย อัสสะบำรุงรัตน์ จุฬาลงกรณ์มหาวิทยาลัย รศ.คร. ธราธร มงคลศรี จุฬาลงกรณ์มหาวิทยาลัย รศ.คร. บรรเจิด จงสมจิตร รศ.คร. จูงใจ ปั้นประณต จุฬาลงกรณ์มหาวิทยาลัย ผศ.คร. สุพจน์ พัฒนะศรี จุฬาลงกรณ์มหาวิทยาลัย คร. อัครวัต ศิริสุข จุฬาลงกรณ์มหาวิทยาลัย ผศ.คร. ชูวงศ์ ชัยสุข มหาวิทยาลัยศิลปากร ผศ.คร. โอกร เมฆาสุวรรณคำรง มหาวิทยาลัยศิลปากร เทคโนฯ ลาดกระบัง ผศ.คร. ควงกมล ณ ระนอง คร. สร้อยพัทธา สร้อยสุวรรณ มหาวิทยาลัยบูรพา

# สนับสนุนโดยสำนักงานคณะกรรมการการอุดมศึกษา และสำนักงานกองทุนสนับสนุนการวิจัย

(ความเห็นในรายงานนี้เป็นของผู้วิจัย สกอ.และสกว. ไม่จำเป็นต้องเห็นด้วยเสมอไป)

#### บทคัดย่อ

โครงการวิจัยนี้ได้ศึกษาตัวเร่งปฏิกิริยาหลากหลายชนิดสำหรับปฏิกิริยาต่าง ๆ กัน โดยทั่วไปได้ทำการสังเคราะห์ตัวเร่งปฏิกิริยาขึ้นมา ทดสอบคุณลักษณะต่างของ ตัวเร่งปฏิกิริยาดังกล่าว แล้วนำไปใช้ในปฏิกิริยาที่เหมาะสม ซึ่งจะเห็นว่ามีการ ประยุกต์ใช้ตัวเร่งปฏิกิริยาเหล่านี้มากมายในงานวิจัยดังกล่าวนี้ ได้แก่ ปฏิกิริยาการขจัด น้ำของเมทานอล การเร่งปฏิกิริยาโดยแสง ออกซิเดชันของโพรเพนและ การ์บอนมอนอกไซด์ เอสเทอริฟิเคชันและทรานส์เอสเทอริฟิเกชัน พอลิเมอร์ไรเซชัน ของเอทิลีนโดยตัวเร่งปฏิกิริยาซีเกลอร์-นัตตาและเมทัลโลซีน การผลิตไฮโดรเจน สำหรับเซลเชื้อเพลิง ปฏิกิริยาไอโซเมอร์ไรเซชันของบิวเทน ไฮโดรจิเนชันของ การ์บอนมอนอกไซด์ และปฏิกิริยาเมตาทีซิส ผลการวิจัยดังกล่าวทำให้สามารถผลิต บทความวิจัยที่ได้รับการตีพิมพ์ในระดับนานาชาติจำนวน 32 เรื่อง และสิทธิบัตรจำนวน 1 เรื่อง

คำสำคัญ ตัวเร่งปฏิกิริยาแบบวิวิธพันธุ์; ความว่องไว; วัฏภาคแก๊ส;วัฏภาคของเหลว; การ ทคสอบคุณลักษณะ **Abstract** 

In this present study, we investigated many kinds of catalysts used in various

reactions. In general, the catalysts were synthesized, characterized and tested under

specified reaction conditions. There are many applications of catalyst used in this

project such as methanol dehydration, photocatalysis, propane oxidation, CO

oxidation, esterification and transesterification, ethylene polymerization catalysts

(Ziegler-Natta and metallocene catalysts), hydrogen production for fuel cell

application, isomerization of butane, CO hydrogenation, and metathesis reaction. As

the results, we can produce 32 international research articles (JCR database) and 1

patent.

**Keywords:** Heterogeneous catalyst; Activity; Gas phase; Liquid phase;

Characterization

4

# สารบัญ

	หน้า
บทกัดย่อภาษาไทย	3
บทกัดย่อภาษาอังกฤษ	4
Executive Summary	6
เนื้อหางานวิจัย และ Output ที่ได้จากโครงการ	33
ภาคผนวก A Reprint บทความวิจัยต่างประเทศ (32 บทความ) และการของคสิทธิบัตร (1 เรื่อง)	)

#### หน้าสรุปโครงการ (Executive Summary)

#### **Executive Summary**

# 1. ความสำคัญและที่มาของปัญหา

จากการสำรวจกำลังคนเพื่อสนองตอบต่ออุตสาหกรรมน้ำมันและปีโตรเกมีของประเทศ ซึ่ง จัดทำโดยสำนักงานคณะกรรมการพัฒนาเศรษฐกิจและสังคมแห่งชาติพบว่า ศาสตร์เกี่ยวข้องกับ ตัวเร่งปฏิกิริยาเป็นองค์ความรู้หนึ่งที่อุตสาหกรรมน้ำมันและปีโตรเกมีของประเทศต้องการความ ช่วยเหลือจากรัฐ ในปัจจุบัน เฉพาะนิคมอุตสาหกรรมมาบตาพุด อำเภอเมือง จังหวัดระยอง มีโรงงานอุตสาหกรรมปีโตรเกมีและอุตสาหกรรมที่เกี่ยวข้องอยู่กว่า 40 โรงงาน เป็นเงินลงทุนทั้งสิ้น กว่า 1.3 ล้านล้านบาท (http://www.boi.go.th) สามารถส่งออกสินค้าสู่ตลาดต่างประเทศมากกว่า ร้อยละ 40 ของการผลิตทั้งหมด นำเงินรายได้เข้าสู่ประเทศเป็นจำนวนมหาศาล ดังนั้นรัฐน่าจะ ลงทุนสร้างสถาบันวิจัยเฉพาะทางเพื่อสนับสนุนอุตสาหกรรมน้ำมันและปิโตรเคมีในประเทศ งานวิจัยหนึ่งที่สำคัญที่เกี่ยวข้องกับอุตสาหกรรมเหล่านี้ได้แก่ การวิจัยทางด้านตัวเร่งปฏิกิริยา

จากรายงานการศึกษาเพื่อจัดทำยุทธศาสตร์การพัฒนาทรัพยากรมนุษย์เพื่อเพิ่มขีด ความสามารถของอุตสาหกรรม โดยสำนักงานคณะกรรมการพัฒนาการเสรษฐกิจและสังคม แห่งชาติ ที่นำเสนอเมื่อวันที่ 9 พฤษภาคม 2547 ได้ประมาณการไว้ว่าในส่วนของการผลิตพอลิเม อร์หลัก (Polyethylene, Polypropylene, Polyvinyl chloride, Polystyrene/EPS, ABS/SAN) มีทิศทาง และแนวโน้มที่จะเพิ่มกำลังการผลิตขึ้น โดยความต้องการรวมของปีพ.ศ. 2547 มีประมาณการที่ 3,757,000 ตัน และจะเพิ่มเป็น 5,265,000 ตัน (เพิ่มอีกประมาณร้อยละ 40) ในปีพ.ศ. 2552 และจาก การสำรวจความต้องการบุคลากรในบริษัทขนาดใหญ่จำนวน 13 บริษัทพบว่า ในด้านการวิจัยและ พัฒนาผลิตภัณฑ์ (Product Research & Development) นั้น ปัญหาความขาดแคลนบุคลากรทางด้าน การพัฒนาตัวเร่งปฏิกิริยา (Catalyst development) อยู่ในอันดับต้น โดยความต้องการที่แท้จริงอยู่ที่ ประมาณ 1 เท่าตัวของที่มีอยู่ในปัจจุบัน โดยเฉพาะอย่างยิ่งการขาดแคลนอาจารย์ที่เชี่ยวชาญเฉพาะ ด้าน เช่นด้านตัวเร่งปฏิกิริยา ทำให้เป็นปัญหาในการผลิตบุคลากรที่มีความรู้ความสามารถทางด้าน นี้ โดยความต้องการบุคลากรด้านวิทยาศาสตร์และเทคโนโลยีในปีพ.ศ. 2547 มีการประมาณการไว้ ที่ 5,383 คน และในอีก 2 ปีข้างหน้า (พ.ศ. 2549) จะเพิ่มเป็น 6,280 คน (เพิ่มอีกประมานร้อยละ 17)

จากการประชุมเพื่อระดมความคิดเพื่อสร้างงานวิจัยร่วมระหว่างศูนย์เชี่ยวชาญด้านคาตาไล ซีสและวิศวกรรมตัวเร่งปฏิกิริยาที่ใช้ตัวเร่งปฏิกิริยาและหน่วยงานภาคเอกชนที่จัด โดยสำนักงาน กองทุนสนับสนุนการวิจัย (สกว.) ณ สำนักงานกองทุนสนับสนุนการวิจัย เมื่อวันพุธที่ 4 สิงหาคม 2547 โดยมีผู้แทนจากภาคอุตสาหกรรมเข้าร่วมแสดงความคิดจาก 5 หน่วยงานดังนี้

- 1. สถาบันวิจัย บริษัท การปิโตรเลียมแห่งประเทศไทย จำกัด (มหาชน)
- 2. บริษัท ปีโตรเคมีแห่งชาติ จำกัด (มหาชน)
- 3. บริษัท คอนทีเนนทอลปีโตรเคมีคอล (ประเทศไทย) จำกัด
- 4. บริษัท ไทยโอเลฟินส์ จำกัด
- บริษัท ระยองโอเลฟินส์ จำกัด
   ผลจากการประชุมดังกล่าวได้ข้อสังเกต 2 ข้อดังนี้

ข้อสังเกตข้อที่ 1 : การจับกลุ่มบริษัทที่สนใจในตัวเร่งปฏิกิริยาที่ใกล้เคียงกัน

ในปัจจุบันการใช้ตัวเร่งปฏิกิริยาในประเทศไทยสามารถแบ่งออกได้เป็น 2 ส่วนหลักคือ ก) โรงกลั่นน้ำมัน และ ข) อุตสาหกรรมเคมีและปิโตรเคมี

โดยโรงกลั่นน้ำมันเป็นกลุ่มแรกที่มีการใช้ตัวเร่งปฏิกิริยาบางชนิดในปริมาณมากเพราะโรง กลั่นน้ำมันจะมีกำลังการผลิตที่สูง (ระดับ 1 ล้านบาร์เรลต่อวันขึ้นไป) จำนวนโรงกลั่นมีอยู่ไม่มาก ลักษณะของโรงกลั่นน้ำมันจะเป็นบรรษัทข้ามชาติที่มีบริษัทแม่อยู่ต่างประเทศ เทคโนโลยีการผลิต ต่าง ๆ รวมทั้งการแก้ปัญหาต่าง ๆ ที่เกิดขึ้นส่งตรงมาจากต่างประเทศ ในขณะที่กลุ่มอุตสาหกรรม เคมีและปิโตรเคมีนั้นบริษัทส่วนใหญ่จะมีฝ่ายไทยเป็นผู้ถือหุ้นรายใหญ่ในบริษัทโดยซื้อ เทคโนโลยีจากต่างประเทศ บริษัทส่วนใหญ่จะมีฝ่ายไทยเป็นผู้ถือหุ้นรายใหญ่ในบริษัทโดยซื้อ เทคโนโลยีจากต่างประเทศ บริษัทในกลุ่มอุตสาหกรรมเคมีและปิโตรเคมีมีการใช้ตัวเร่งปฏิกิริยาหลากหลายประเภทมากกว่าที่ใช้กันในโรงกลั่นน้ำมัน จำนวนบริษัท/โรงงานต่าง ๆ ที่อยู่ในส่วนอุตสาหกรรมเคมีและปิโตรเคมีมีมากกว่าส่วนโรงกลั่นน้ำมัน การจับคู่บริษัทที่มีความสนใจตัวเร่งปฏิกิริยาที่คล้ายคลึงกันและ/หรือมีแนวทางการทำวิจัยในหัวข้อที่ใกล้เคียงกันจึงทำได้ยาก

ข้อสังเกตข้อที่ 2 : การจัดตั้งหน่วยงานเพื่อแก้ปัญหาตัวเร่งปฏิกิริยาที่บริษัทประสบ ในปัจจุบัน ปัญหาที่สำคัญของอุตสาหกรรมที่ต้องเกี่ยวข้องกับตัวเร่งปฏิกิริยาคือ

- ก) การเลือกใช้ตัวเร่งปฏิกิริยาให้เหมาะสมกับกระบวนการผลิต
- ข) การใช้ตัวเร่งปฏิกิริยาที่มีอยู่ปัจจุบันได้ผลผลิตที่เป็นไปตามข้อกำหนด
- ค) การยืดอายุการทำงานของตัวเร่งปฏิกิริยา

ซึ่งปัญหาทั้ง 3 รูปแบบจะเน้นไปที่การเลือกใช้และการใช้งานอย่างกุ้มค่า ซึ่งโดยทั่วไป ตัวเร่งปฏิกิริยาเมื่อซื้อมาใช้แต่ละครั้งจะมีอายุการทำงานหลายปี ถ้าหากทางบริษัทลงทุนจัดตั้ง หน่วยงานเพื่อทำวิจัยเพื่อแก้ปัญหาที่ทางบริษัทประสบ และเมื่อแก้ปัญหาได้แล้วหน่วยงานที่จัดตั้ง ขึ้นมาใหม่นั้นจะเกิดการขาดช่วงการทำงาน ทำให้ทางบริษัทเองพึงพอใจที่จะจ้างหน่วยงานวิจัย ภายนอกให้ทำวิจัยแทนมากกว่า แต่จำนวนหน่วยงานภายนอกที่สามารถทำวิจัยแทนได้ก็มีจำนวน จำกัดมาก (หน่วยงานหนึ่งที่เป็นที่ยอมรับคือศูนย์เชี่ยวชาญด้านกาตาไลซิลและวิศวกรรมปฏิกิริยาที่ ใช้ตัวเร่งปฏิกิริยา ภาควิชาวิศวกรรมเคมี คณะวิศวกรรมศาสตร์ จุฬาลงกรณ์มหาวิทยาลัย) สถานการณ์ในปัจจุบันเองมีเพียงบางบริษัทเท่านั้นที่ได้เริ่มทำการศึกษาพัฒนาตัวเร่งปฏิกิริยาเพื่อใช้ งานเองโดยมีวัตถุประสงค์หลักเพื่อชดเชยการซื้อตัวเร่งปฏิกิริยาจากต่างประเทศ บริษัทเหล่านี้เป็น

บริษัทที่อยู่ในกลุ่มผลิตเม็ดพลาสติก (เช่น HDPE, LLDPE, PP) เพราะลักษณะกระบวนการผลิต พลาสติกในในกลุ่มนี้จะต้องสูญเสียตัวเร่งปฏิกิริยาโดยการติดผสมเข้าไปกับผลิตภัณฑ์เม็ดพลาสติก ที่ผลิต ได้ตลอดเวลา จึงจำเป็นต้องมีการนำเข้าตัวเร่งปฏิกิริยาอย่างต่อเนื่อง นอกจากนี้สมบัติ พลาสติกที่ได้ยังขึ้นอยู่กับตัวเร่งปฏิกิริยาที่ใช้ ทำให้เกิดความคุ้มค่าที่จะตั้งหน่วยงานเพื่อทำการวิจัย และผลิตตัวเร่งปฏิกิริยาที่ได้จากการวิจัยเพื่อนำมาใช้งานเองในบริษัท เพราะจะทำให้สามารถผลิต พลาสติกได้หลากหลายชนิดมากขึ้น และยังไม่ต้องกังวลว่าจะถูกจำกัดกำลังการผลิตด้วยการจำกัด ปริมาณตัวเร่งปฏิกิริยาที่เจ้าของเทคโนโลยีจะขายให้

ตัวเร่งปฏิกิริยาวิวิธพันธุ์ที่มีการใช้งานกันอยู่ในปัจจุบันสามารถแบ่งได้เป็น 3 ประเภท คือ 1) ตัวเร่งปฏิกิริยาที่ทำจากโลหะ 2) ตัวเร่งปฏิกิริยาที่ทำจากโลหะออกไซด์ และ 3) ตัวเร่งปฏิกิริยาใน ตระกูลซีโอไลต์ โดยที่ตัวเร่งปฏิกิริยาแต่ละประเภทจะมีลักษณะเฉพาะของมันเอง ซึ่งต้องการ การศึกษาที่เจาะลึกในทุกด้านซึ่งรวมถึง ความว่องไวในการทำปฏิกิริยาที่ต้องการ การเลือกเกิด เฉพาะผลิตภัณฑ์ที่ต้องการ อายุการใช้งาน และการเลื่อมสภาพของตัวเร่งปฏิกิริยา

จากสถิติของกรมศุลกากรในปีพ.ศ. 2544-2547 (ตารางที่ 1) จะเห็นว่าประเทศไทยนำเข้า ตัวเร่งปฏิกิริยาจากประเทศต่าง ๆ เป็นมูลค่าประมาณ 3,000 ล้านบาทในแต่ละปี แต่ราคาตัวเร่ง ปฏิกิริยายังไม่ใช่เป็นราคาส่วนใหญ่ของการผลิตสินค้า เพราะถ้าการทำงานของตัวเร่งปฏิกิริยาไม่ เป็นไปตามต้องการจะทำให้ไม่สามารถผลิตสินค้าได้ตามมาตรฐานที่กำหนด ทำให้ผู้ผลิตสูญเสีย โอกาส และสูญเสียวัสดุที่ใช้ในการผลิต ซึ่งเมื่อคิดเป็นมูลค่าแล้วจะพบว่าสูงกว่าราคาตัวเร่ง ปฏิกิริยาหลายเท่าตัว

**ตารางที่ 1** มูลค่าการนำเข้าตัวเร่งปฏิกิริยาของประเทศไทยในช่วงปีพ.ศ. 2544-2547 (ที่มา: เวปไซต์ ของกรมศุลกากร http://www.customs.go.th โดยตัวเร่งปฏิกิริยาอยู่ในกลุ่มรหัส HS code 3815)

ปีพ.ศ.	มูลค่าการนำเข้า CIF (บาท)
2545	2,755,654,105
2546	3,626,037,254
2547 (มกราคม - สิงหาคม)	2,312,783,834

ศูนย์เชี่ยวชาญเฉพาะทางด้านคาตาไลซิสและวิศวกรรมปฏิกิริยาที่ใช้ตัวเร่งปฏิกิริยา (Centre of excellence on catalysis and catalytic reaction engineering - ต่อไปจะเรียกอย่างสั้นว่า "ศูนย์ เชี่ยวชาญฯ") ภาควิชาวิศวกรรมเคมี คณะวิศวกรรมศาสตร์ จุฬาลงกรณ์มหาวิทยาลัย มีประสบการณ์ ทำงานวิจัยทางด้านตัวเร่งปฏิกิริยามานานกว่า 20 ปี ปัจจุบันมีคณาจารย์ 9 ท่าน และนิสิตระดับ ปริญญาเอกและปริญญาโทที่ทำวิจัยอยู่จำนวนเฉลี่ยไม่ต่ำกว่า 60 คนต่อปี มีอุปกรณ์วิจัยที่ทันสมัย

และสามารถผลิตผลงาน ตีพิมพ์ในวารสารนานาชาติได้อย่างต่อเนื่อง โดยงานวิจัยที่ได้รับการ ตีพิมพ์มีจุดเด่นหลักคือเป็นงานที่ผลิตขึ้นเองในห้องปฏิบัติการของสูนย์เชี่ยวชาญฯโดยไม่ จำเป็นต้องพึ่งพาห้องปฏิบัติการหรือบุคลากรจากต่างประเทศ

ศูนย์เชี่ยวชาญฯมีศักยภาพในการเป็นศูนย์กลาง (Hub) ทางด้านตัวเร่งปฏิกิริยา เพราะมี ความร่วมมือกับบุคลากรของมหาวิทยาลัยต่าง ๆ ในประเทศอย่างต่อเนื่อง อาทิเช่น มหาวิทยาลัยสงขลานครินทร์ มหาวิทยาลัยศิลปากร และ สถาบันเทคโนโลยีพระจอมเกล้า วิทยาเขต เจ้ากุณทหาร ลาดกระบัง เป็นต้น และยังมีความร่วมมือด้านการแลกเปลี่ยนนักวิจัยกับมหาวิทยาลัย ชั้นนำหลายแห่งในโลก อาทิเช่น University of Waterloo, University of Alberta ประเทศแคนาดา Tokyo Institute of Technology, Kyoto University, Nakoya University, Japan Advanced Institute of Science and Technology ประเทศญี่ปุ่น University of New South Wales ประเทศออสเตรเลีย เป็นต้น

อนึ่งศูนย์เชี่ยวชาญฯยังมีประสพการณ์ในการทำวิจัยร่วมกับบริษัทต่างๆ เช่น สถาบันวิจัย ของบริษัท การปีโตรเลียมแห่งประเทศไทย จำกัด (มหาชน) บริษัท คอนทิเนนทอล ปีโตรเคมีคอล (ประเทศไทย) จำกัด บริษัท บางกอกโพลิเอทิลีน จำกัด (มหาชน) และบริษัท ระยองโอลิฟิน จำกัด เป็นต้น นอกจากนี้ในปี พ.ศ. 2547 ศูนย์เชี่ยวชาญฯจะได้รับครุภัณฑ์จากโครงการเงินกู้จากธนาคาร JBIC ประเทศญี่ปุ่น ในวงเงินประมาณ 50 ล้านบาท โครงการวิจัยร่วมกับ บริษัท Mektec Manufacturing Cooperation (Thailand) จำกัด ในโครงการ Research and Development of Flexible Printed Circuit using Nanotechnology ในวงเงินมากกว่า 200 ล้านบาท

โครงการร่วมมือวิจัยเกี่ยวกับตัวเร่งปฏิกิริยากับ PTT Research and Technology Institute, PTT Chemical Public Company Limited, Siam Cement Group and UBE Group (Thailand) ในวงเงิน ประมาณ 100 ล้านบาท

# 2. วัตถุประสงค์

เพื่อเป็นศูนย์กลางสนับสนุนการวิจัยพัฒนาและการใช้ตัวเร่งปฏิกิริยาของอุตสาหกรรม ปีโตรเลียม อุตสาหกรรมปีโตรเคมี และตัวเร่งปฏิกิริยาที่ใช้ในการกำจัดมลพิษในประเทศ

# 3. ระเบียบวิธีวิจัยโดยสรุป

การวิจัยที่เกี่ยวข้องกับตัวเร่งปฏิกิริยาจะแบ่งออกเป็น 3 ส่วนคือ

- 1) วิธีการเตรียมตัวเร่งปฏิกิริยา
- 2) วิธีการทคสอบตัวเร่งปฏิกิริยา
- 3) วิธีการวัดคุณลักษณะของตัวเร่งปฏิกิริยาหรือผลิตภัณฑ์ที่เกิดขึ้น

โดยตัวเร่งปฏิกิริยาแต่ละประเภทจะมีวิธีการวิจัยที่แตกต่างกัน จึงจำเป็นต้องแยกวิธีวิจัยของ ตัวเร่งปฏิกิริยาประเภทต่าง ๆ ดังตัวอย่างที่ยกมาพอสังเขปดังนี้

## 3.1 ตัวเร่งปฏิกิริยาเมทัลโลซีนและซิกเกอร์-แนทตา

# 3.1.1 การเตรียมตัวเร่งปฏิกิริยา Ziegler Natta

- 1. ใส่ Anhydrous Chloride 0.476 g ลงใน Schlenk tube ขนาด 100 ml
- 2. ชั่ง Phathalic Anhydride 0.1089 g ลงในบวค
- 3. ฉีด Decane 2.5 ml ลงใน schlenk ปั่นกวนและเพิ่มอุณหภูมิช้า ๆ จนถึง  $130^{\circ}\mathrm{C}$
- 4. นิค 2-Ethyl-Hexanol 2.34 ml ที่อุณหภูมิ 130°C นาน 2 ชั่วโมง
- 5. เติม Phathalic Anhydride ที่อุณหภูมิ  $130^{\circ}$ C นาน 1 ชั่วโมง
- 6. ปิด heater และ stirrer ทิ้งไว้ 1 คืน
- 7. ปรับอุณหภูมิให้ได้ - $20^{\circ}$ C
- 8. ปั่นกวนช้า ๆ แล้วค่อย ๆ หยด TiCl, 20 ml ที่ -20°C นาน 1 ชั่วโมง
- 9. ปล่อยให้อุณหภูมิค่อย ๆ สูงขึ้นจนถึงอุณหภูมิห้อง
- 10. เพิ่มอุณหภูมิช้า ๆ จนถึง  $110^{\circ}$ C ในเวลา 4 ชั่วโมง
- 11. หยด Diethyl Phthalate 0.26 ml ที่อุณหภูมิ 110°C นาน 2 ชั่วโมง
- 12. ทิ้งให้ตกตะกอน (1.5 ชั่วโมง) แล้วคูคของเหลวออก
- 13. ค่อย ๆ หยด  ${
  m TiCl_4}$  20 ml ที่อุณหภูมิห้อง
- 14. เพิ่มอุณหภูมิจนถึง  $120^{\circ}$ C ในเวลา 4 ชั่วโมง ควบคุมอุณหภูมิที่  $120^{\circ}$ C นาน 2 ชั่วโมง
- 15. ทิ้งให้ตกตะกอนแล้วคูดของเหลวออก
- 16. ล้างตะกอนด้วย Dacane 10 ml 2 รอบ และ Hexane 10 ml 3 รอบ
- 17. ทำตะกอนให้แห้งโคยใช้ระบบ Vacuum

# 3.1.2 การเตรียมตัวเร่งปฏิกิริยา metallocene

# การเตรียม Catalyst Precusor

- 1. นำซิลิกาที่ทำการ calcine โดยให้ความร้อนที่  $400^{\circ}$ C นาน 6 ชั่วโมง ภายใต้ภาวะ สุญญากาสมา 940 mg ใส่ใน schlenk tube ขนาด 100 ml โดยชั่งใน glove box
- 2. เติม toluene 10 ml ภายใต้ภาวะอาร์กอน
- 3. เติม MAO 16 mmol ภายใต้ภาวะอาร์กอน
- 4. กวนให้เข้ากันนาน 30 นาที ที่อุณหภูมิห้อง

- 5. ดูคสารละลายใสออกและล้างของแข็งด้วย toluene 20 ml 5 ครั้งภายใต้บรรยากาศ อาร์กอน
- 6. ทำให้แห้งในสุญญากาศที่อุณหภูมิห้อง

## การเตรียมตัวเร่งปฏิกิริยา metallocene บนตัวรองรับ

- เติมสารละลายตัวเร่งปฏิกิริยา metallocene 8 μmol ภายใต้บรรยากาศอาร์กอนลงใน
   Catalyst precursor ที่อยู่ใน schlenk
- 2. กวนให้เข้ากันนาน 30 นาทีที่อุณหภูมิห้อง
- 3. ดูคสารละลายใสออกและล้างของแข็งด้วยโทลูอื่น 20 ml 2 ครั้ง ภายใต้บรรยากาศ อาร์กอน
- 4. ทำให้แห้งในสุญญากาศที่อุณหภูมิห้อง

#### 3.1.3 การทดสอบตัวเร่งปฏิกิริยา

นำตัวเร่งปฏิกิริยาไปทำปฏิกิริยา polypropylene polymerization

- 1. อบ autoclave reactor ขนาด 100 ml และ magnetic bar ให้แห้งที่อุณหภูมิ  $110^{\circ}$ C เป็นเวลา 30 นาที
- 2. ใส่ตัวเร่งปฏิกิริยาและตัวเร่งปฏิกิริยาร่วมลงใน reactor ที่อุณหภูมิห้องภายใน glove box แล้วทำการกวนทิ้งไว้ 5 นาที
- 3. ไล่แก๊สออกจาก reactor แล้วแช่ reactor ลงใน water bath เพื่อควบคุมอุณหภูมิตาม อุณหภูมิ polymerization
- 4. เริ่มปฏิกิริยา polymerization โดยป้อนแก๊ส propylene เข้าสู่ reactor แล้วทิ้งให้ เกิดปฏิกิริยาตาม polymerization time
- 5. หยุคปฏิกิริยาโดยระบายแก๊ส propylene ออก แล้วเติมกรดใน methanol
- 6. ล้างพอลิเมอร์ที่ได้ด้วยเมทานอลทันที แล้วทำให้แห้งที่อุณหภูมิห้อง
- 7. นำพอลิเมอร์ไปชั่งแล้วนำไปหาค่าความสามารถในการเร่งปฏิกิริยา (activity)

# 3.1.4 การวัดสมบัติของตัวเร่งปฏิกิริยาหรือผลิตภัณฑ์ที่ได้

#### 3.1.4.1. Small Angle Light Scattering (SALS)

เครื่อง static light scattering ที่ห้องทดลอง โพลิเมอร์ ภาควิชาวิศวกรรมเคมี จุฬาลงกรณ์ มหาวิทยาลัย ใช้ He/Ne laser ( $\lambda=632.8~\mathrm{nm}$ ) เป็นแหล่งกำเนิดแสง นำตัวอย่างใส่ใน holder ซึ่ง ตั้งอยู่ระหว่าง polarizer 2 อัน โดยทิศทางการเกิด polarization ของ polarizer ใกล้กับแหล่งกำเนิด

แสงอยู่ในแนวตั้งส่วนที่เหลืออยู่ในแนวนอน กราฟการกระเจิงของแสงถูกตรวจสอบด้วย CCD Camera ในเวลา 2 นาที ความสว่างของต้นกำเนิดแสงเลเซอร์ตั้งไว้ที่ตำแหน่ง 6 (gain 6) และ 10 (gain 10) โดยใช้คอมพิวเตอร์โปรแกรมซึ่งต่อเข้ากับเครื่องวิเคราะห์ กราฟที่ได้ถูกส่งเข้าวิเคราะห์ ด้วยคอมพิวเตอร์

#### 3.1.4.2. Scanning Electron Microscopy (SEM)

เครื่อง scanning electron microscope JSM-5410 ที่ Scientific and Technological Research Equipment Center จุฬาลงกรณ์มหาวิทยาลัย SEM ทำงานที่ 1.5 kV ซึ่งเป็นภาวะที่เหมาะสมเพราะ ถ้าค่าสูงเกินไปจะทำให้ตัวอย่างใหม้ ในเครื่อง scanning electron microscope ลำอิเล็คตรอนจะถูก สแกนผ่านพื้นผิวของตัวอย่างทีบแสง เมื่อลำอิเล็คตรอนกระทบพื้นผิวของตัวอย่าง ความแตกต่าง ของความหนาแน่นของอิเล็คตรอนในตัวอย่างจะทำให้เกิดการกระเจิงของอิเล็คตรอน และการแผ่ รังสีของอิเล็คตรอนแหล่านี้จะถูกวัด ปรับเปลี่ยน และใช้ลดความสว่างของลำแสงครั้งที่ 2 ใน cathode ray tube (CRT) ในเวลาเคียวกัน จุดที่มีการสะสมมากจะเกิดเป็นจุดสว่างในขณะที่จุดที่มี สัญญาณน้อยจะเป็นจุดที่สว่างน้อยกว่า

เนื่องจากวิธีการนี้ต้องใช้ตัวอย่างที่นำไฟฟ้าได้ดี ดังนั้นจึงต้องเตรียมตัวอย่างให้สภาพการ นำโดยเคลือบตัวอย่างด้วยชั้นโลหะบาง ๆ การทดลองนี้ใช้ทองคำมาเคลือบตัวอย่างเป็นฟิล์มบาง และเก็บใบที่ที่แห้งก่อบทำการทดลอง

## 3.1.4.3. Thermal Gravimetri Analysis (TGA)

การวิเคราะห์ทำด้วยเครื่อง SDT Q600 ตัวอย่างนำหนักประมาณ 10-20 มิลลิกรัมถูกบรรจุ ในถ้วยอะลูมิเนียมขนาด 90 ไมโครลิตร ตัวอย่างจะถูกให้ความร้อนจนถึงอุณหภูมิ 800°C ด้วยอัตรา 10°C/min โดยใช้ในโตรเจนใหลผ่าน

#### 3.1.4.4. X-Ray Diffraction (XRD)

เอ็กซเรย์คิฟแฟรก โตแกรมถูกวัคด้วยเครื่อง SIEMENS D5000 โดยใช้รังสี  $CuK \Box$  (ความ ยาวคลื่นเท่ากับ 1.54 อังสตรอม) ที่ 30 kV และ 30 mA และมีแผ่นกรองนิกเกิล ความเป็นผลึกของ ตัวอย่างจะถูกวัคในช่วง 2 $\theta$  = 20 $^{\circ}$  ถึง 2 $\theta$  = 80 $^{\circ}$  ที่ความละเอียด 0.04 $^{\circ}$ 

# 3.1.4.5. C-Nuclear Magnetic Resonance (<sup>13</sup>C-NMR)

เครื่อง  $^{13}$ C-NMR spectroscopy ถูกใช้ในการตรวจสอบโครงสร้างจุลภาคของพอลิเมอร์ ตัวอย่างถูกละลายใน 1,2,4-trichlorobenzene และ dichlorobenzene-d $_6$  (20 vol%) สำหรับ internal lock  $^{13}$ C-NMR spectra ทำที่  $110^{\circ}$ C ด้วยเครื่อง Bruker Avance II 400 ปฏิบัติการที่ 100 MHz โดย ใช้เวลาเก็บข้อมูล 1.5 วินาทีและเวลาถ่วง 4 วินาที

#### 3.1.4.6. Fourier Transformed Infrared Spectroscopy (FT-IR)

เครื่อง Nicolet FT-IR Impact 400 Spectrophotometer ที่ Center of Excellence on Catalysis and catalytic Reaction Engineering ภาควิชาวิศวกรรมเคมี คณะวิศวกรรมศาสตร์ จุฬาลงกรณ์

มหาวิทยาลัย เทคนิกการใช้ FT-IR ใช้กันกว้างขวางในการคูลักษณะ โครงสร้างของโพลิเมอร์ การ บันทึก IR spectrum จะทำการรวบรวม 32 ครั้ง ในช่วง 4000-400 cm<sup>-1</sup> โดยมีความละเอียด 4 cm<sup>-1</sup> การเปรียบเทียบตำแหน่งการคูดกลืน IR spectrum ของโพลิเมอร์ตัวอย่าง ลักษณะการคูดกลืนจะ สามารถหาค่า band และกลุ่มฟังก์ชันที่มีในโพลิเมอร์ IR spectrum ของพอลิเมอร์จะมีลักษณะ เฉพาะที่สามารถพิจารณาได้จาก fingerprint"

#### 3.1.4.7. Differential Scanning Calorimeter (DSC)

การวิเคราะห์ทำด้วยเครื่อง Perkin-Elmer DSC-7 เพื่อหาอุณหภูมิในการหลอมเหลวและ ความเป็นผลึกของพอลิเมอร์ ตัวอย่างถูกให้ความร้อนจนถึงอุณหภูมิ 200°C ด้วยอัตรา 10°C/min อุณหภูมินี้สูงกว่าอุณหภูมิในการหลอมเหลวของพอลิเมอร์พอควรและถูกคงไว้เป็นเวลานาน 10 นาที จากนั้นลดอุณหภูมิลงด้วยอัตรา 10°C/min จนถึงอุณหภูมิ 30°C เพื่อให้เกิดการตกผลึกขึ้น ตัวอย่างจะถูกให้ความร้อนอีกครั้งที่อัตราการเพิ่มอุณหภูมิ 10°C/min ผลการวิเคราะห์จะถูกบันทึก ในการให้ความร้อนครั้งที่สองเพื่อกำจัดความทรงจำทางความร้อนของพอลิเมอร์

## 3.2 ตัวเร่งปฏิกิริยาโลหะออกไซด์

- 3.2.1 เตรียมตัวเร่งปฏิกิริยาวาเนเดียมบนไททาเนีย
  - 1. เตรียมสารแขวนลอยไททาเนียมออกไซค์ โดยน้ำ  ${
    m TiO_2}$  ปริมาณ 4.65 g มา ละลายในน้ำ  ${
    m 50~ml}$
  - 2. นำสารแขวนลอย TiO, มาเพิ่มอุณหภูมิเป็น 70°C
  - 3. เตรียม  $\mathrm{NH_4VO_3}$  ปริมาณ 0.45 g และนำมาผสมในสารแขวนลอย  $\mathrm{TiO_2}$  ที่  $70^{\circ}\mathrm{C}$
  - 4. นำสารแขวนลอยที่ได้ไประเหยน้ำออกที่อุณหภูมิ  $80^{\circ}\mathrm{C}$  นาน 5 ชั่วโมง
  - 5. นำของแข็งที่ได้ไปอบในตู้อบที่อุณหภูมิ 110°C เป็นเวลา 24 ชั่วโมง
  - 6. นำของแข็งที่ผ่านการอบมา Calcine ด้วยอากาศที่มีอัตราการใหล 100 ml/min ที่ 550°C เป็นเวลา 6 ชั่วโมง จะได้วาเนเดียมบนไททาเนีย
- 3.2.2 การเติมโลหะทรานซิชันลงบนตัวเร่งปฏิกิริยา
  - 1. นำวานาเคียมบนไททาเนีย 5 g มาใส่ในน้ำ 50 ml
  - 2. นำสารแขวนลอยจากข้อ 1. มาเพิ่มอุณหภูมิเป็น  $70^{\circ}\mathrm{C}$
  - 3. เตรียมเกลือของโลหะที่ต้องการปริมาณตามตารางด้านล่าง และ  ${
    m MgNO_3}$  ปริมาณ 0.5791 g มาละลายในสารแขวนลอยข้อ 2.

#### ตารางที่ 2 การเติมโลหะตัวที่สอง

โลหะที่เติม	สารเคมี	ปริมาณ (g)
Mo	Ammonium molybdate ((NH <sub>4</sub> ) <sub>6</sub> Mo7O24.4H <sub>2</sub> O)	0.8
Cu	Cupric nitrate trihydrate (CuN <sub>2</sub> O <sub>6</sub> .3H <sub>2</sub> O)	1.6531
Fe	Ferric nitrate nonahydrate (FeN <sub>3</sub> O <sub>9</sub> ,9H <sub>2</sub> O)	3.1368
Zn	Zinc nitrate hexahydrate (ZnN <sub>2</sub> O <sub>6</sub> .6H <sub>2</sub> O)	1.9867

- 4. นำสารแขวนลอยที่ได้ไประเหยน้ำออกที่อุณหภูมิ 80°C เป็นเวลา 5 ชั่วโมง
- 5. นำของแข็งที่ได้ไปอบในตู้อบที่อุณหภูมิ  $110^{\circ}\mathrm{C}$  เป็นเวลา 24 ชั่วโมง
- 6. นำของแข็งที่ผ่านการอบมา Calcine ด้วยอากาศ 100 ml/min ที่ 550°C เป็นเวลา 6 ชั่วโมง จะได้ตัวเร่งปฏิกิริยาที่มีโลหะฝังอยู่

# 3.2.3 วัดสมบัติของตัวเร่งปฏิกิริยาด้วยเทคนิคต่อไปนี้

#### 3.2.3.1 การวัดพื้นที่ผิวสัมผัส

การวัดพื้นที่ผิวสัมผัสนั้นทำโดยใช้การคูดซับทางกายภาพของก๊าซไนโตรเจนด้วย เครื่อง Micromeritics ASAP 2000 ขั้นตอนการวัดแบ่งเป็น 2 ขั้น ดังนี้ ขั้นตอนการไล่ก๊าซ

- 1. นำตัวอย่างปริมาณ 0.3 กรัมใส่ในที่เก็บตัวอย่าง และนำที่เก็บตัวอย่าง ไปต่อกับแท่นไล่ก๊าซของเครื่องมือ
- 2. ในช่วงทำสูญญากาศ ที่เก็บตัวอย่างถูกให้ความร้อนจนถึง 90°C ด้วย อัตราการเพิ่มอุณหภูมิ 2°C/min และคงไว้เป็นเวลานาน 1 ชั่วโมง ภายใต้ การใหลของฮีเลียม
- 3. ในช่วงให้ความร้อน ที่เก็บตัวอย่างถูกให้ความร้อนจนถึง 200°C ด้วย อัตราการเพิ่มอุณหภูมิ 2°C/min และคงไว้เป็นเวลานาน 1 ชั่วโมง ภายใต้ การไหลของฮีเลียม

# ขั้นตอนการวิเคราะห์

- 1. ถอดที่เก็บตัวอย่างออกจากแท่นไล่ก๊าซที่เก็บตัวอย่างและนำไปต่อกับ แท่นวิเคราะห์ของเครื่องมือ
- 2. ทำการวิเคราะห์ด้วยการคูดซับในโตรเจนที่อุณหภูมิของ ในโตรเจนเหลว และบันทึกใอโซเทอร์มที่ได้

#### 3.2.3.2 X-Ray Diffraction (XRD)

เฟสของสารตัวอย่างวิเคราะห์ โดยใช้เครื่อง X-Ray Diffractometer ในที่นี้ใช้ เครื่อง Siemens รุ่น D5000 X-Ray Diffractometer โดยใช้ การแผ่รังสีของ CuKC ร่วมกับ Ni ซึ่งทำหน้าที่ตัวกรอง ใช้มุม  $2\theta$  ในช่วง 20 -  $80^\circ$  โดยมีความละเอียด  $0.04^\circ$ 

## 3.2.3.3 วัดค่าความเป็นกรดของพื้นผิว

ศึกษาความเป็นกรดของสารตัวอย่างจากการดูคซับ Pyridine โดยใช้เครื่อง GC9A แบบ FID โดยตั้งเครื่อง GC9A แบบ FID ที่ภาวะดังต่อไปนี้

อัตราการใหลของในโตรเจน	30 ml/mir
อุณหภูมิคอลัมน์	150°C
อุณหภูมิ Detector	180°C
อุณหภูมิ Injector	180°C
y y	

แล้วทำการวัดตามขั้นตอนต่อไปนี้

- 1. บรรจุตัวอย่าง 0.02 g ลงในคอลัมน์
- 2. ฉีด Pyridine 0.1 ml และวัด peak area อย่างต่อเนื่องจนกระทั่งตัวอย่าง ดูดซับ Pyridine จนอิ่มตัว
- 3. คำนวณความเป็นกรดของสารตัวอย่างจาก Total peak area ของการคูคซับ Pyridine

#### 3.2.3.4 วัดค่าความเป็นเบส

ศึกษาความเป็นเบสของสารตัวอย่างจากการดูดซับ Maleic Anhydride โดยใช้ เครื่อง GC9A แบบ FID โดยตั้งเครื่อง GC9A แบบ FID ที่ภาวะดังต่อไปนี้

อัตราการใหลของในโตรเจน	30 ml/min
อุณหภูมิคอลัมน์	250°C
อุณหภูมิ Detector	300°C
อุณหภูมิ Injector	300°C
าการวัดตามผับตองเตอใงใช้	

แล้วทำการวัดตามขั้นตอนต่อไปนี้

- 1. บรรจุสารตัวอย่าง 0.03 g ลงในคอลัมน์
- 2. ฉีด Maleic Anhydride เข้มข้น 0.104 g/ml ปริมาณ 0.3 μl และวัด peak area อย่างต่อเนื่องจนกระทั่งสารตัวอย่างดูดซับ Maleic Anhydride จนอิ่มตัว
- คำนวณความเป็นเบสของสารตัวอย่างจาก Total area peak ของการดูดซับ
   Maleic Anhydride

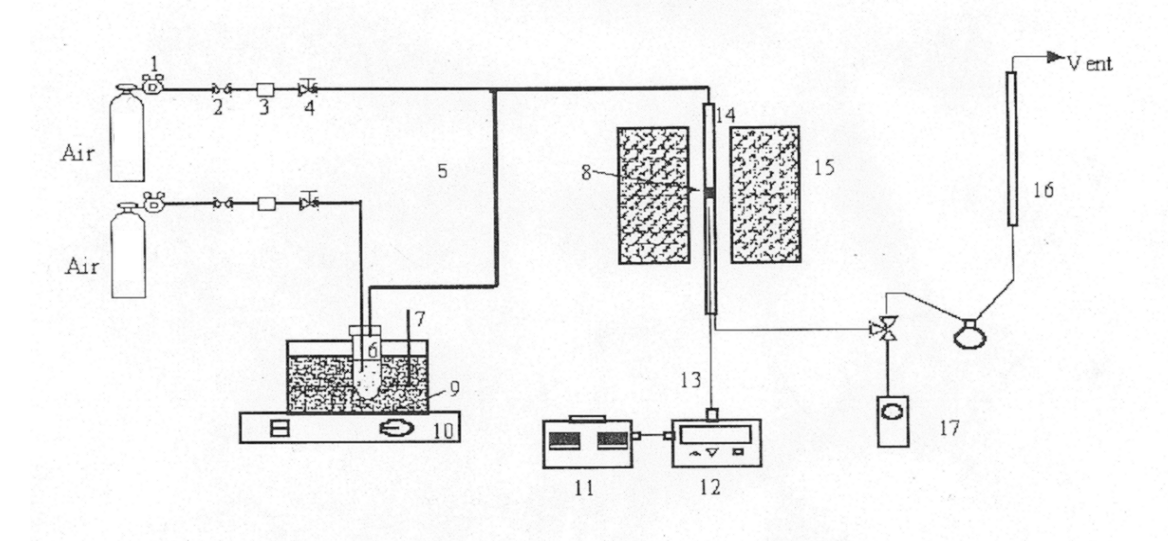
## 3.2.3.5 การหาองค์ประกอบโลหะของตัวเร่งปฏิกิริยา

การหาองค์ประกอบของโลหะต่างๆนตัวเร่งปฏิกิริยาทำโดยใช้เครื่อง Perkin-Elmer Optical Emission Optima 2100 DV ตัวอย่างจะถูกย่อยด้วยสารละลายกรดและพ่น ออกมาทางหัวฉีด จากนั้นทำการกระตุ้นอะตอมโลหะด้วยพลาสมา และบันทึก emission spectrum

# 3.2.4 การวัดความว่องไวในการทำปฏิกิริยาด้วยการทดลองในเครื่องปฏิกรณ์ชนิด fixed-

bed

ทำการวัดความว่องไวของตัวเร่งปฏิกิริยาด้วยระบบที่แสดงในรูปข้างล่าง



- 1. Pressure Regulator
- 2. On-Off valve
- 3. Gas Filter

- 4. Metering Valve
- 5. Heating Line
- 6. Saturator

- 7. Thermometer
- 8. Catalyst Bed
- 9. Sand Bath

- 10. Stirring Controller
- 13. Thermocouple

11. Variable Voltage Transformer

14. Reactor

15. Furnace

- 16. Flow Meter
- 17. Sampling Point

# **รูปที่ 1** ระบบเครื่องปฏิกรณ์

12. Temperature Controller

เครื่องปฏิกรณ์นี้ได้ทำมาจาก 3/8" stainless steel tube จุดที่เก็บสารตัวอย่างเพื่อนำมา ทดสอบวิเคราะห์อยู่บริเวณด้านบนและด้านล่างเบดตัวเร่งปฏิกิริยา ซึ่งตัวเร่งปฏิกิริยานี้จะ อยู่ระหว่างชั้นของ quartz wood อุณหภูมิของเครื่องปฏิกรณ์จะปรับได้ในช่วงระหว่าง 50-800°C การวิเคราะห์ Phthalic anhydride ในสารตั้งต้นและผลิตภัณฑ์ใช้ GC Shimadzu 9A

ติดตั้ง Detector แบบ FID และใช้ column Chromosorb W AW ใช้  $N_2$  (99.999%) เป็น carrier gas โดยตั้งค่าต่าง ๆ ดังนี้

อัตราการใหลของ $\mathbf{N}_{\!\scriptscriptstyle 2}$	30 ml/min
อุณหภูมิคอลัมน์	210°C
อุณหภูมิ Detector	250°C
อุณหภูมิ Injector	250°C

การวิเคราะห์ permanent gas ใช้เครื่อง GC Shimadzu 8A ติดตั้ง detector แบบ TCD โดยใช้คอลัมน์ molecular sieve 5A ในการแยก  ${\rm O}_2$  และ CO และ Porapak-Q ในการแยก  ${\rm CO}_2$ 

และน้ำ ใช้ He (99.999%) เป็น carrier gas โดยตั้งค่าต่าง ๆ ดังนี้

อัตราการใหลของ He	25 ml/min
อุณหภูมิคอลัมน์	100°C
อุณหภูมิ Detector	130°C
อุณหภูมิ Injector	130°C

## 3.3 ตัวเร่งปฏิกิริยาสำหรับปฏิกิริยาเลือกเติมไฮโดรเจน

- 3.3.1 การเตรียมตัวเร่งปฏิกิริยาแพลเลเดียม-ซิลเวอร์บนตัวรองรับอะลูมินา
- 3.3.1.1 เตรียมตัวรองรับอะลูมินา
  - 1. บดอะลูมินา (CS-303) แล้วร่อนผ่านตะแกรง 40/60 เมช
  - 2. ล้างอะลูมินาที่บดได้ด้วยน้ำกลั่นหลายๆ ครั้ง เพื่อกำจัดฝุ่น และสารปนเปื้อน
  - 3. อบแห้งเพื่อไล่น้ำ ที่อุณหภูมิ  $110^{\circ}$ C เป็นเวลา 12 ชั่วโมง
  - 4. เผาเหลือเถ้าในอากาศนิ่ง ที่  $300^{\circ}$ C เป็นเวลา 2 ชั่วโมง
  - 5. ร่อนผ่านตะแกรง 40/60 เมช อีกครั้ง แล้วเก็บใส่ขวดปิดผนึก
- 3.3.1.2 เตรียมสารละลายสต๊อกของแพลเลเคียม และซิลเวอร์ ละลาย  ${
  m Pd(NO_3)_2~0.1~g}$  ในน้ำ 25 ml และละลาย  ${
  m AgNO_3~0.5~g}$  ในน้ำ 25 ml แล้วเก็บใส่ขวดปิดผนึก
- 3.3.1.3 เตรียมตัวเร่งปฏิกิริยาแพลเลเคียม-ซิลเวอร์บนตัวรองรับอะลูมินา
  - 1. ชั่งอะลูมินา 2 g ใส่ในขวครูปชมพู่ขนาค 100 ml
  - 2. เตรียมสารละลายแพลเลเดียมจากสารละลายสต๊อก โดยคำนวณปริมาณ แพลเลเดียมที่ใช้ให้ได้เปอร์เซนต์ตามต้องการ เพื่อใช้กับอะลูมินา 2 g แล้ว เติมน้ำให้สารละลายแพลเลเดียมมีปริมาตรรวมเท่ากับ 1 ml

- 3. หยดสารละลายแพลเลเคียมที่ได้จากข้อ 2 ลงบนอะลูมินาเป็นหย่อมๆ ให้ทั่ว ถึง แล้วเขย่าเพื่อให้เกิดการกระจายตัวที่ดีของแพลเลเคียมบนอะลูมินา ทำซ้ำ จนกว่าสารละลายแพลเลเคียมจะหมด
- 4. ปล่อยให้ของผสมที่ได้จากข้อ 3 เกิดการกระจายตัว โดยทิ้งไว้ในอากาศนิ่งที่ อุณหภูมิห้อง เป็นเวลา 6 ชั่วโมง
- 5. อบแห้ง ที่  $110^{\circ}$ C เป็นเวลา 12 ชั่วโมง
- 6. เผาเหลือเถ้าในอากาศไหล ที่  $500^{\circ}$ C เป็นเวลา 2 ชั่วโมง ที่อัตราการไหล 100 ml/min และอัตราการเพิ่มอุณหภูมิ  $10^{\circ}$ C/min
- 7. นำของผสมที่ได้จากข้อ 6 มาทำซ้ำในข้อ 2 ถึง 5 แต่เปลี่ยนจากการใช้สาร ละลายแพลเลเคียม เป็นสารละลายซิลเวอร์
- 8. เผาเหลือเถ้าในอากาศไหล ที่ 370°C เป็นเวลา 1 ชั่วโมง ที่อัตราการไหล 100 ml/min และอัตราการให้ความร้อน 10°C/min
- 9. แล้วเก็บใส่ขวดปิดผนึก เพื่อนำไปใช้ต่อไป

## 3.3.2 ทดสอบความว่องไวของตัวเร่งปฏิกิริยา

- 1. บรรจุตัวเร่งปฏิกิริยาลงในเครื่องปฏิกรณ์โดยใช้ตัวเร่งปฏิกิริยา 0.5 g
- 2. ไล่อากาศที่เหลืออยู่ในเครื่องปฏิกรณ์ด้วยแก๊ส Ar เป็นเวลา 10 นาที
- 3. รีดิวซ์ด้วย  ${
  m H_2}$  100 ml/min ที่อุณหภูมิ 150  ${
  m ^{\circ}C}$  เป็นเวลา 2 ชั่วโมง และอัตราการ เพิ่มอุณหภูมิ 10  ${
  m ^{\circ}C/min}$
- 4. ไล่  $\mathbf{H}_{2}$  ที่เหลืออยู่ในเครื่องปฏิกรณ์ด้วยแก๊ส  $\mathbf{Ar}$  เป็นเวลา 10 นาที
- 5. ลดอุณหภูมิไปที่อุณหภูมิในการปรับสภาพ ซ่งอยู่ในช่วง 40-90°C โดยใช้แก๊ส ปรับสภาพเช่น CO CO $_2$  O $_2$  NO และ N $_2$ O เป็นต้น ฉีดเข้าไปในทางเข้าของเครื่อง ปฏิกรณ์ แล้วคงอุณหภูมิไว้เป็นเวลา 10 นาที จากนั้นลดอุณหภูมิลงไปที่ อุณหภูมิห้อง
- 6. ปรับอัตราการ ใหลเชิงปริมาตรของแก๊สตั้งต้นผสม ซึ่งมีส่วนประกอบของ  $C_2H_2$  0.716 vol%  $H_2$  0.823 vol%  $C_2H_6$  33.707 vol% และ  $C_2H_4$  ให้มีอัตราการ ใหลรวม 15 ml/min เพื่อทำการทดสอบความสามารถในการเกิดปฏิกิริยา
- กำการทดสอบก๊าซสารตั้งต้นที่อุณหภูมิ 40-90°C โดยแต่ละอุณหภูมิจะ
   ทำการศึกษาเมื่อระบบเข้าสู่ภาวะคงตัวแล้ว นั่นคือเมื่อเวลาผ่านไปแล้วประมาณ
   นาที

8. ทำการวิเคราะห์ก๊าซที่ไหลออกมาโดยการใช้ GC Shimadzu-9A ในการ วิเคราะห์แก็ส  $\mathrm{CH_4}\ \mathrm{C_2H_2}\ \mathrm{C_2H_4}$  และ  $\mathrm{C_2H_6}\ \mathrm{โดยใช้คอลัมน์}$  carbosieve S-II และใช้ GC Shimadzu-8A ในการวิเคราะห์ก๊าซ  $\mathrm{H_2}\ \mathrm{โดยใช้คอลัมน์}$  molecular sieve 5A

# 3.3.3 การวิเคราะห์สมบัติของตัวเร่งปฏิกิริยา

ทำการวัดสมบัติด้วยเครื่องมือต่าง ๆ ดังต่อไปนี้

# 3.3.3.1 การดูดซับก๊าซคาร์บอนมอนอกไซด์ (CO adsorption)

- 1. บรรจุตัวเร่งปฏิกิริยาในเครื่องปฏิกรณ์ขนาดเล็กจำนวน 0.3-0.5 g
- 2. ปรับก๊าซ He โดยให้ He ใหลผ่านเครื่องปฏิกรณ์ที่อัตราการใหล 30 ml/min เพื่อ เข้าไปในเครื่อง GC แบบ TCD โดยทำการวัดอัตราการใหลของก๊าซ He ทั้ง reference line และ line ที่ต้องการทดสอบ
- 3. ปรับก๊าซ H<sub>2</sub> ให้มีอัตราการใหล 100 ml/min
- 4. เปิดก๊าซ He ให้ใหลผ่านเครื่องปฏิกรณ์เพื่อไล่อากาศที่หลงเหลืออยู่ เป็นเวลา 10 นาที
- 5. เปลี่ยนจากก๊าซ He เป็นก๊าซ H<sub>2</sub> เพื่อทำการรีดิวส์ โดยเพิ่มความร้อนที่อัตราการ เพิ่มอุณหภูมิ 10°C/min จนอุณหภูมิถึง 150°C คงอุณหภูมิ 150°C เป็นเวลา 2 ชั่วโมง ทำการลดอุณหภูมิลงมาที่อุณหภูมิห้อง โดยใช้ก๊าซ He ใหลผ่านตลอดการ ลดอุณหภูมิ
- 6. ฉีดก๊าซ CO ทีละ 50  $\mu$ l พร้อมทั้งสังเกตสัญญาณจาก TCD
- 7. ฉีคซ้ำจนตัวเร่งปฏิกิริยาคูคซับปริมาณก๊าซ CO จนกระทั่งอิ่มตัว นำผลที่ได้มา คำนวณหาปริมาณก๊าซ CO ทั้งหมดที่ถูกคูคซับ

# 3.3.3.2 XPS (X-ray photoelectron spectroscopy)

- 1. นำตัวเร่งปฏิกิริยาที่ได้หลังจากการทำการทดสอบไปเตรียม  $\operatorname{grid}$  โดยการบด ตัวเร่งปฏิกิริยาในบรรยากาส  $\operatorname{N}_2$  เพื่อให้มีการกระจายตัวของผงตัวเร่งปฏิกิริยาอย่าง สม่ำเสมอ โดยใช้ double-side adhesive tape ติดทั้งสองข้าง
- 2. นำตัวอย่างที่เตรียมไปวางใน Kratos XSAM, XPS Spectrometer
- 3. สารตัวอย่างจะถูกส่งยังช่องที่ใช้ในการเตรียม ซึ่งเป็นระบบที่มีความคันต่ำกว่า  $10^{-7}$  Torr เป็นระบบสูญญากาศ
- 4. ในการวิเคราะห์ชาตุต่างๆที่อยู่ในสารตั้งต้น จะใช้ช่วงในการ scan ที่กว้าง โดย ใส่พลังงานมีค่าประมาณ160 eV และใช้เวลาในการเก็บอิเลคตรอนที่เคลื่อนออก จากผิว 300 วินาทีต่อ 1 eV

#### 3.3.3.3 TPR (Temperature-programmed reduction)

- 1. บรรจุตัวเร่งปฏิกิริยา 1 กรัม ใน TPR pyrex cell
- 2. ปรับก๊าซ Ar ให้มีอัตราไหล 20 ml/min โดยให้ใหลอยู่ในระบบ
- 3. ให้ความร้อนสารตัวอย่างโดยให้มีก๊าซ Ar ใหลตลอดเวลา โดยให้ความร้อนจน มีอุณหภูมิ 200°C และไว้เป็นเวลา 1 ชั่วโมงเพื่อไล่น้ำที่สารตัวอย่างดูดซับไว้
- 4. การทำ TPR ของ oxidized sample จะใช้  $10\% H_2/Ar$  เป็น reducing agent โดยมี อัตราการให้ความร้อน  $20^{\circ}C/min$  โดยจะให้ความร้อนไปจนถึงอุณหภูมิ  $500^{\circ}C$  และทำการคงอุณหภูมิไว้เป็นเวลา 10 นาที

#### 3.3.3.4 TPD (Temperature-programmed desorption)

- 1. ทำการรีดิวส์สารตัวอย่างที่อุณหภูมิ 150°C เป็นเวลา 2 ชั่วโมง
- 2. เปลี่ยนเป็นก๊าซ Ar เพื่อใช้ในการลดอุณหภูมิไปที่อุณหภูมิห้อง
- 3. ก๊าซ  $\mathbf{H}_2$  จะดูดซับบนสารตัวอย่างก่อนที่จะมีก๊าซ  $\mathbf{Ar}$  ใหลผ่าน
- 4. จะเกิด desorption spectra ระหว่างการเพิ่มอุณหภูมิที่อัตราการเพิ่ม 20°C/min

#### 3.3.3.5 Fourier transform infrared spectroscopy

- 1. อัดตัวเร่งปฏิกิริยาให้มีเส้นผ่านศูนย์กลาง 20 mm จากนั้นใส่เข้าไปในเซล สำหรับใส่สารตัวอย่าง โดยจะมีใช้การคูดซับรังสีอินฟาเรคในการวิเคราะห์ ที่ค่า ความละเอียดเท่ากับ 4 cm<sup>-1</sup>
- 2. ตัวเร่งปฏิกิริยาจะถูกรีดิวส์ในบรรยากาศ  ${
  m H_2}$  ณ อุณหภูมิ 150 $^{
  m O}$ C เป็นเวลา 2 ชั่วโมง หลังจากนั้นจะทำการลดอุณหภูมิไปที่อุณหภูมิห้อง โดยจะทำการเปลี่ยน ก๊าซจากก๊าซ  ${
  m H_2}$  เป็น  ${
  m Ar}$  ในการลดอุณหภูมิ
- 3. สำหรับตัวเร่งปฏิกิริยาที่มีการเตรียมพื้นที่ผิวของตัวเร่งปฏิกิริยาก่อนใช้ใน ปฏิกิริยา ในการลดอุณหภูมิหลังการรีดิวส์ จะทำการเปลี่ยนก๊าซจากก๊าซ  $\mathbf{H}_2$  เป็น  $\mathbf{Ar}$  ในขณะลดอุณหภูมิ จนกระทั่งมีอุณหภูมิถึงอุณหภูมิที่ต้องการใช้ในการเตรียม พื้นที่ผิว
- 4. ก๊าซที่ใช้ในการเตรียมพื้นที่ผิว ได้แก่ CO, CO2, NO, และ  $N_2$ O จะถูกฉีดเข้าไป ในระบบที่อุณหภูมิคงที่เป็นเวลา 10 นาที ก่อนทำการลดอุณหภูมิจนไปถึง อุณหภูมิห้อง
- 5. จากนั้นจึงทำการวัดค่าการคูดซับรังสีอินฟาเรด โมเลกุลของก๊าซต่างชนิดกันจะ ให้ตำแหน่งในการคูดซับรังสีอินฟาเรด ณ ตำแหน่งที่แตกต่างกัน

## 3.3.3.6 การวัดพื้นที่ผิวสัมผัส

การวัดพื้นที่ผิวสัมผัสนั้นทำโดยใช้การดูดซับทางกายภาพของก๊าซไนโตรเจนด้วย เครื่อง Micromeritics ASAP 2000 ขั้นตอนการวัดแบ่งเป็น 2 ขั้น ดังนี้

# ขั้นตอนการไล่ก๊าซ

- 1. นำตัวอย่างปริมาณ 0.3 กรัมใส่ในที่เก็บตัวอย่าง และนำที่เก็บตัวอย่าง ไปต่อกับแท่นไล่ก๊าซของเครื่องมือ
- 2. ในช่วงทำสูญญากาศ ที่เก็บตัวอย่างถูกให้ความร้อนจนถึง 90°C ด้วย อัตราการเพิ่มอุณหภูมิ 2°C/min และคงไว้เป็นเวลานาน 1 ชั่วโมง ภายใต้ การไหลของฮีเลียม
- 3. ในช่วงให้ความร้อน ที่เก็บตัวอย่างถูกให้ความร้อนจนถึง 200°C ด้วย อัตราการเพิ่มอุณหภูมิ 2°C/min และคงไว้เป็นเวลานาน 1 ชั่วโมง ภายใต้ การไหลของฮีเลียม

## ขั้นตอนการวิเคราะห์

- 1. ถอดที่เก็บตัวอย่างออกจากแท่นไล่ก๊าซที่เก็บตัวอย่างและนำไปต่อกับ แท่นวิเคราะห์ของเครื่องมือ
- 2. ทำการวิเคราะห์ด้วยการคูดซับในโตรเจนที่อุณหภูมิของ ในโตรเจนเหลว และบันทึกใอโซเทอร์มที่ได้

# 3.4 ตัวเร่งปฏิกิริยาเพื่อกำจัดมลพิษในอากาศ

# 3.4.1 การเตรียมตัวเร่งปฏิกิริยาโลหะ

- 8.4.1.1 ตัวอย่างการเตรียมตัวเร่งปฏิกิริยาแพลทินัมบนตัวรองรับอะลูมินา
- ก. เตรียมตัวรองรับอะลูมินา
  - 1. บดอะลูมินา (NKH-3) แล้วร่อนผ่านตะแกรง 40/60 เมช
  - 2. ล้างอะลูมินาที่บดได้ด้วยน้ำกลั่นหลายๆ ครั้ง เพื่อกำจัดฝุ่น และสารปนเปื้อน
  - 3. อบแห้งเพื่อไล่น้ำ ที่อุณหภูมิ 110°C เป็นเวลา 12 ชั่วโมง
  - 4. เผาเหลือเถ้าในอากาศนิ่ง ที่อุณหภูมิ  $300^{\circ}$ C เป็นเวลา 2 ชั่วโมง
  - 5. ร่อนผ่านตะแกรง 40/60 เมช อีกครั้ง แล้วเก็บใส่ขวดปิดผนึก
- ข. เตรียมสารละลายสต๊อก (Stock solution)

ละลาย H,PtCl<sub>6</sub>6H,O 1 กรัมในน้ำกลั่น 25 ml แล้วเก็บใส่ขวคปิดผนึก

ค. เตรียมตัวเร่งปฏิกิริยาแพลทินัมบนตัวรองรับอะลูมินา

เตรียมสารละลายแพลทินัมจากสารละลายสต๊อก โดยคำนวณปริมาณแพลทินัม
ที่ใช้ให้ได้เปอร์เซ็นต์ตามต้องการ เพื่อใช้กับอะลูมินา 2 g แล้วเติมน้ำกลั่นให้
สารละลาย

แพลทินัมมีปริมาตรรวมเท่ากับ 2 ml

- 2. ชั่งอะลูมินา 2 g ใส่ในขวครูปชมพู่ขนาค 100 ml
- 3. หยดสารละลายแพลทินัมที่ได้จากข้อ 1 ลงบนอะลูมินาเป็นหย่อมๆ ให้ทั่วถึง แล้วเขย่า เพื่อให้เกิดการกระจายตัวที่ดีของแพลทินัมบนอะลูมินา ทำซ้ำจนกว่า สารละลาย

แพลที่บัมจะหมด

- 4. ปล่อยให้ของผสมที่ได้จากข้อ 3 เกิดการกระจายตัว โดยทิ้งไว้ในอากาศนิ่ง ที่ อุณหภูมิห้อง เป็นเวลา 6 ชั่วโมง
- 5. อบแห้ง ที่อุณหภูมิ  $110^{\circ}$ C เป็นเวลา 12 ชั่วโมง
- 6. เผาเหลือเถ้าในอากาศไหล ที่อุณหภูมิ 500°C เป็นเวลา 3 ชั่วโมง ด้วยอัตราการ ใหล 100 ml/min และอัตราการให้ความร้อน 10°C/min
- 7. เก็บใส่ขวดปิดผนึก เพื่อนำไปใช้ต่อไป

## 3.4.1.2 ตัวอย่างการเตรียมตัวเร่งปฏิกิริยาวาเนเดียมบนตัวรองรับไทเทเนียมออกไซด์

- 1. เตรียมตัวรองรับ  $TiO_{2}$  โดยการเผาเหลือเถ้าในอากาศที่  $300^{\circ}$ C นาน 3 ชั่วโมง
- 2. เตรียมของผสมของตัวรองรับ  ${
  m TiO_2}$  และสารละลาย  ${
  m NH_4VO_3}$  ใส่ในขวครูปชมพู่ ขนาด 250 ml โดยคำนวณปริมาณวาเนเดียมที่ใช้ให้ได้เปอร์เซ็นต์ตามต้องการ แล้วเติมน้ำกลั่นลงไปให้มีปริมาตรรวมเท่ากับ 50 ml
- 3. กวนของผสมอย่างต่อเนื่อง ที่อุณหภูมิ 70°C จนกระทั่งน้ำระเหยหมด
- 4. อบแห้ง ที่อุณหภูมิ  $110^{\circ}$ C เป็นเวลา 12 ชั่วโมง
- 5. เผาเหลือเถ้าในอากาศไหล ที่อุณหภูมิ 380°C เป็นเวลา 3 ชั่วโมง ด้วยอัตราการ ใหล100 ml/min และอัตราการให้ความร้อน 10°C/min
- 6. เก็บใส่ขวดปิดผนึก เพื่อนำไปใช้ต่อไป

# 3.4.2 <u>ทดสอบประสิทธิภาพของตัวเร่งปฏิกิริยา</u>

# 3.4.2.1 การทดสอบความว่องไวของตัวเร่งปฏิกิริยา

- 1. บรรจุตัวเร่งปฏิกิริยาลงในเครื่องปฏิกรณ์ขนาดเล็ก 0.1 ถึง  $0.5~{
  m g}$
- 2.ปรับสภาพของตัวเร่งปฏิกิริยาให้พร้อมใช้งาน โดยขึ้นอยู่กับชนิดของตัวเร่ง ปฏิกิริยา

และวัตถุประสงค์ของการทคสอบ ตัวอย่างเช่น

- ตัวเร่งปฏิกิริยาแพลทินัมบนตัวรองรับอะลูมินา จะต้องปรับสภาพด้วยการรีดิวซ์ ในไฮโดรเจน ที่ 500°C เป็นเวลา 1 ชั่วโมง ด้วยอัตราการใหลเชิงปริมาตร 100 ml/min และอัตราการให้ความร้อน 10°C/min เพื่อเปิดไซส์ที่ว่องไวของตัวเร่ง ปฏิกิริยา แล้วตามด้วยการออกซิไดซ์ใน 10 เปอร์เซ็นต์ของออกซิเจนในฮีเลียม ที่ อุณหภูมิ 500°C เป็นเวลา 1 ชั่วโมง ด้วยอัตราการใหลเชิงปริมาตร 100 ml/min และอัตราการให้ความร้อน 10°C/min
- 3. ปรับอัตราการ ใหลเชิงปริมาตรของแก๊สตั้งต้นผสม ให้ได้ตามต้องการ ตัวอย่างเช่น
- การทคสอบตัวเร่งปฏิกิริยาแพลทินัมบนตัวรองรับอะลูมินา สำหรับปฏิกิริยา รีคักชั้นแบบเลือกเกิดของ NO ด้วย  $C_3H_6$  ในภาวะที่มีออกซิเจนมากเกินพอ จะใช้ แก๊สผสมของ NO 1000 ppm  $C_3H_6$  1000 ppm  $O_2$  5 mol% และส่วนที่เหลือเป็น He โดยมีอัตราการ ใหลรวมเป็น 200 ml/min
- การทคสอบตัวเร่งปฏิกิริยาแพลทินัมบนตัวรองรับอะลูมินา สำหรับปฏิกิริยาการ กำจัดแก๊สเสียที่ปล่อยออกมาจากเครื่องยนต์แก๊สโซลีน จะใช้แก๊สผสมของ NO 500 ppm CO 3000 ppm C3H8 2150 ppm O2 1.2 mol% และส่วนที่เหลือ He โดย มีอัตราการใหลเชิงปริมาตรรวมเป็น 141 ml/min
- 4. ทคสอบความว่องไวของตัวเร่งปฏิกิริยา ด้วยวิธีการทำปฏิกิริยาแบบโปรแกรม อุณหภูมิ กำหนดช่วงอุณหภูมิในการศึกษาอยู่ระหว่าง 50 ถึง 800°C โดยทำการให้ ความร้อน แบบขั้นบันได แต่ละอุณหภูมิ จะทำการเก็บแก๊สตัวอย่างเมื่อระบบเข้าสู่ สภาวะคงตัว
- 5. ทำการเก็บและวิเคราะห์แก๊สที่ปล่อยออกมาจากเครื่องปฏิกรณ์ โดยใช้เครื่อง GC แบบ TCD ร่วมกับคอลัมน์ชนิด MS-5A และ Porapak QS

# 3.4.2.2 การทดสอบความทนทานของตัวเร่งปฏิกิริยาต่อน้ำหรือ $\mathbf{SO}_2$

- การทคสอบแบบ Ex-situ
- 1. ทำการปรับสภาพตัวเร่งปฏิกิริยาก่อนการทดสอบความว่องไว ดังนี้

ด้องการทคสอบความทนทานของตัวเร่งปฏิกิริยาซีโอไลต์ต่อน้ำ จะต้อง ปรับสภาพด้วย 10% ของไอน้ำในฮีเลียม ที่อุณหภูมิ 600°C เป็นเวลา 24 ชั่วโมง ด้วยอัตราการใหล 170 ml/min และอัตราการให้ความร้อน 10°C/min (ช่วงการให้ ความร้อนทำในฮีเลียม)

ต้องการทดสอบความทนทานของตัวเร่งปฏิกิริยาแพลทินัมบนตัว รองรับอะลูมินาต่อ SO, จะต้องปรับสภาพด้วยแก๊สผสมของ SO, 500 ppm O, 5% และส่วนที่เหลือเป็นฮีเลียม ที่ 480°C เป็นเวลา 10 ชั่วโมง ด้วยอัตราการใหล 100 ml/min และอัตราการให้ความร้อน  $10^{\circ}$ C/min (ช่วงการให้ความร้อนทำใน  $O_2$  10% ในฮีเลียม)

2. หลังจากการปรับสภาพแล้ว ทำการทคสอบความว่องไวของตัวเร่งปฏิกิริยาตาม ขั้นตอนในข้อ 8.4.2.1 ต่อไป

#### - การทคสอบแบบ In-situ

ทำการทคลองเหมือนกับ การทคสอบความว่องไวของตัวเร่งปฏิกิริยาใน ข้อ 8.4.2.1 แต่เปลี่ยนแปลงในขั้นตอนที่ 4 และ 5 โคยทคสอบความว่องไวของ ตัวเร่งปฏิกิริยา ด้วยวิธีการทำปฏิกิริยาแบบสับเปลี่ยนวงจรดังนี้

- 1. เพิ่มอุณหภูมิด้วยฮีเลียมไปที่อุณหภูมิในการทดสอบ (ขึ้นอยู่กับชนิดของตัวเร่ง ปฏิกิริยา และสภาวะในการเกิดปฏิกิริยา)
- 2. เปลี่ยนแก๊สจาก He เป็นแก๊สตั้งต้นผสมที่ไม่มีน้ำหรือ  ${
  m SO_2}$  อยู่ แล้วคงอุณหภูมิ ไว้จนระบบเข้าสู่สภาวะคงตัว ทำการเก็บและวิเคราะห์แก๊สที่ปล่อยออกมาจาก เครื่องปฏิกรณ์โดยใช้เครื่อง GC แบบ TCD ร่วมกับคอลัมน์ชนิค MS-5A และ Porapak QS
- 3. ปล่อยน้ำและ/หรือ SO<sub>2</sub> ผสมกับแก๊สตั้งต้น คงอุณหภูมิไว้จนระบบเข้าสู่สภาวะ คงตัว ทำการเก็บ และวิเคราะห์แก๊สที่ปล่อยออกมาจากเครื่องปฏิกรณ์ โดยวิธี เดียวกับข้อ 2
- 4. ปิดน้ำและ/หรือ SO<sub>2</sub> ผสมกับแก๊สตั้งต้น คงอุณหภูมิไว้จนระบบเข้าสู่สภาวะคง ตัว ทำการเก็บ และวิเคราะห์แก๊สที่ปล่อยออกมาจากเครื่องปฏิกรณ์ โดยวิธีเดียวกับ ข้อ 2
- 5. ทำซ้ำในข้อ 3 และ 4 หลายๆ ครั้งตามต้องการ

# 3.4.2.3 การทดสอบความสามารถในการฟื้นฟูสภาพของตัวเร่งปฏิกิริยา

- 1. ทำการปรับสภาพตัวเร่งปฏิกิริยาด้วย 5%  ${
  m NH_3}$  ใน  ${
  m N_2}$  ที่อุณหภูมิห้อง เป็นเวลา 0.5 ถึง 2 ชั่ว โมง ด้วยอัตราการ ใหลเชิงปริมาตร 4  ${
  m ml/min}$
- นำตัวเร่งปฏิกิริยาที่ได้จากข้อ 1. มาทำคลอริเนชันแบบเปียก โดยผ่านอากาศชื้น ไปบนตัวเร่งปฏิกิริยา ในช่วงอุณหภูมิ 450 ถึง 550°C พร้อมด้วยการฉีดกรด อินทรีย์ของคลอรีน ปริมาณ 15 ถึง 50 μ1 แล้วทำการลดอุณหภูมิจนถึง อุณหภูมิห้อง
- 3. นำตัวเร่งปฏิกิริยาที่ได้จากข้อ 2. มาทำการรีคิวซ์ด้วย  ${
  m H_2}$  ที่  $500^{\circ}{
  m C}$  เป็นเวลา 1 ชั่วโมงด้วยอัตราการไหลเชิงปริมาตร 30 ml/min และอัตราการให้ความร้อน  $10^{\circ}{
  m C/min}$  แล้วทำการลดอุณหภูมิจนถึงอุณหภูมิห้อง

4. หลังจากการปรับฟื้นฟูสภาพของตัวเร่งปฏิกิริยาแล้ว ทำการทดสอบความว่องไว ของตัวเร่งปฏิกิริยาตามขั้นตอนในข้อ8.4.2.1 ต่อไป

# 3.4.2.4 การทดสอบเพื่อศึกษากลไกการเกิดปฏิกิริยา

1. การใช้เทคนิคทรานเชียนส์

สามารถแบ่งการทคลองออกได้เป็น 2 ขั้นตอน ได้แก่ ขั้นตอนที่ทคสอบ โดยไม่มีตัวเร่งปฏิกิริยา และขั้นตอนการทคสอบปฏิกิริยา ขั้นตอนที่ 1: การทคลองแบบไม่มีตัวเร่งปฏิกิริยา

ทดสอบการตอบสนองทางพลศาสตร์ของเครื่องปฏิกรณ์ขนาดเล็ก โดยไม่ ใส่ตัวเร่งปฏิกิริยา ด้วยการเปลี่ยนแก๊สขาเข้าจาก  $N_2$  เป็น NO 1.2 mol% ผ่านเครื่อง ปฏิกรณ์ โดยใช้อัตราการ ใหลรวม 50 ml/min ทำให้แก๊สมีเวลาในการ ใหลจาก วาล์วเข้าสู่เครื่องวิเคราะห์อินฟราเรด เป็นเวลาประมาณ 12 วินาที ที่อุณหภูมิห้อง หมายเหตุ : เครื่องสามารถวัดสัญญาณการดูดกลืนลำแสงอินฟราเรด ของ NO NO2 และ  $N_2$ O CO2 และ  $C_3H_8$  ในเวลาเคียวกัน แต่ไม่สามารถวัด  $N_2$  และ  $O_2$  ได้  $\frac{\tilde{v}_{u}}{\tilde{v}_{u}}$  2: การทดสอบปฏิกิริยา

1. บรรจุตัวเร่งปฏิกิริยาขนาด 10/20 เมช ประมาณ 1.2 g ลงไปในเครื่อง ปฏิกรณ์ สารตั้งต้นถูกปรับความเข้มข้นด้วยในโตรเจน เพื่อใช้เป็นสาร ป้อนเข้าเครื่องปฏิกรณ์ อัตราการใหลรวมเท่ากับ 50 ml/min ซึ่งมีค่า องค์ประกอบของแก๊สในการทดลอง คือ

- 2. ทคสอบปฏิกิริยา ในช่วงอุณหภูมิ 300 ถึง 400 $^{\circ}$ C โคยก่อนจะทำการ ทคลองทุกครั้งจะปล่อย  $N_2$  ที่อัตราการไหล 50 ml/min ที่อุณหภูมิ 450 $^{\circ}$ C เป็นเวลา 1 ชั่วโมง เพื่อจะกำจัดน้ำและองค์ประกอบที่เหลืออยู่บนพื้นผิว ของตัวเร่งปฏิกิริยา
- 3. ลดอุณหภูมิลงไปที่อุณหภูมิของปฏิกิริยา แก๊สตั้งต้นผสมจะป้อนเข้ามา แทน  $N_2$  หลังจากที่การคูดซับของแก๊สเริ่มคงที่ สารป้อนที่เข้าสู่เครื่อง ปฏิกรณ์จะเปลี่ยนไปเป็น  $N_2$  อีกครั้งอย่างทันทีทันใด เพื่อที่จะ ทำการศึกษาลักษณะพลศาสตร์ในส่วนของช่วงของการป้อนสารตั้งต้น เข้า และลดการป้อนสารตั้งต้นเข้าเครื่องปฏิกรณ์
- 2. การใช้เทคนิคแบบโปรแกรมอุณหภูมิ

สามารถแบ่งการทดลองแบบพื้นฐานออกได้เป็น 3 ขั้นตอน ได้แก่ ขั้นตอนการสร้างสปีชีส์บนพื้นผิวของตัวเร่งปฏิกิริยา ขั้นตอนการสลายตัว/หลุด ออกแบบโปรแกรมอุณหภูมิ และ ขั้นตอนการออกซิเดชันแบบโปรแกรมอุณหภูมิ ขั้นตอนที่ 1: การสร้างสปีชีส์บนพื้นผิวของตัวเร่งปฏิกิริยา

- 1. บรรจุตัวเร่งปฏิกิริยา ลงในเครื่องปฏิกรณ์ขนาดเล็ก โดยใช้ตัวเร่ง ปฏิกิริยา 0.1 ถึง 0.5 g ขึ้นอยู่กับการกำหนดภาวะของปฏิกิริยา
- 2. ปรับสภาพของตัวเร่งปฏิกิริยาให้พร้อมใช้งาน โดยขึ้นอยู่กับชนิดของ ตัวเร่งปฏิกิริยา และวัตถุประสงค์ของการทดสอบ
- 3. ปรับอัตราการใหลเชิงปริมาตรของแก๊สตั้งต้นผสม ให้ได้ตามต้องการ
- 4. สร้างสปีชีส์บนพื้นผิวของตัวเร่งปฏิกิริยา โดยปล่อยให้เกิดปฏิกิริยาที่ อุณหภูมิคงที่ตามต้องการ แต่กำหนดระยะเวลาของการเกิดปฏิกิริยาให้ แน่นอน โดยทั่วไปจะหยุดการสร้างสปีชีส์ หลังจากระบบเข้าสู่สภาวะคง ตัวแล้ว

# ขั้นตอนที่ 2: การสถายตัว/หถุดออกแบบ โปรแกรมอุณหภูมิ เพิ่มอุณหภูมิจากอุณหภูมิห้อง ถึง 800°C ด้วย He โดยใช้อัตราการใหล เชิงปริมาตร 50 ml/min และอัตราการให้ความร้อน 5°C/min ทำการเก็บ และวิเคราะห์แก๊สที่ปล่อยออกมาจากเครื่องปฏิกรณ์ ทุกๆ 5 หรือ 10 นาที

ทั้นตอนที่ 3: การออกซิเดชันแบบโปรแกรมอุณหภูมิ เพิ่มอุณหภูมิจากอุณหภูมิห้อง ถึง  $800^{\circ}$ C ด้วย  $1\%~O_{_2}$  ใน He โดยใช้อัตรา การใหลเชิงปริมาตร 50~ml/min และอัตราการให้ความร้อน  $5^{\circ}$ C/min ทำ การเก็บ และวิเคราะห์แก๊สที่ปล่อยออกมาจากเครื่องปฏิกรณ์ ทุกๆ 5~uni

# 3.4.3 ทำการวิเคราะห์สมบัติของตัวเร่งปฏิกิริยา

## 3.4.3.1 การวัดพื้นที่ผิวสัมผัส

การวัดพื้นที่ผิวสัมผัสนั้นทำโดยใช้การดูดซับทางกายภาพของก๊าซไนโตรเจนด้วย เครื่อง Micromeritics ASAP 2000 ขั้นตอนการวัดแบ่งเป็น 2 ขั้น ดังนี้ ขั้นตอนการไล่ก๊าซ

- 1. นำตัวอย่างปริมาณ 0.3 กรัมใส่ในที่เก็บตัวอย่าง และนำที่เก็บตัวอย่าง ไปต่อกับแท่นไล่ก๊าซของเครื่องมือ
- 2. ในช่วงทำสูญญากาศ ที่เก็บตัวอย่างถูกให้ความร้อนจนถึง 90°C ด้วย อัตราการเพิ่มอุณหภูมิ 2°C/min และคงไว้เป็นเวลานาน 1 ชั่วโมง ภายใต้ การไหลของฮีเลียม

3. ในช่วงให้ความร้อน ที่เก็บตัวอย่างถูกให้ความร้อนจนถึง 200°C ด้วย อัตราการเพิ่มอุณหภูมิ 2°C/min และคงไว้เป็นเวลานาน 1 ชั่วโมง ภายใต้ การไหลของฮีเลียม

#### ์ ขั้นตอนการวิเคราะห์

- 1. ถอดที่เก็บตัวอย่างออกจากแท่นไล่ก๊าซที่เก็บตัวอย่างและนำไปต่อกับ แท่นวิเคราะห์ของเครื่องมือ
- 2. ทำการวิเคราะห์ด้วยการดูดซับในโตรเจนที่อุณหภูมิของ ในโตรเจนเหลว และบันทึกใอโซเทอร์มที่ได้

# 3.4.3.2 การวิเคราะห์ตำแหน่งว่องไวและการกระจายตัวของโลหะบนตัวเร่งปฏิกิริยา

จำนวนตำแหน่งว่องไวและการกระจายตัวของโลหะบนตัวเร่งปฏิกิริยานั้นวัดด้วย เทคนิคการคูดซับทางเคมีแบบเป็นจังหวะของคาร์บอนมอนอกไซด์โดยใช้เครื่อง Micromeritics Chemisorb 2750 (pulse chemisorptions system) ปริมาณของการ์บอนมอน นอกไซด์ที่ทราบถูกฉีดเข้าสู่ระบบที่อุณหภูมิห้อง ปริมาณคาร์บอนมอนอกไซด์ที่ไม่โดน คูดซับจะถูกวัดด้วย TCD การฉีดคาร์บอนมอนอกไซด์เป็นจังหวะจะทำไปเรื่อยๆจนกระทั่ง พื้นผิวของตัวเร่งปฏิกิริยาเกิดการอิ่มตัว

ตัวเร่งปฏิกิริยาปริมาณ 0.2 กรัมถูกบรรจุในเซลล์ทำด้วย quartz และประกอบเข้า กับเตาอบที่ควบคุมอุณหภูมิได้และเชื่อมต่อกับ TCD ก๊าซฮีเลียมถูกป้อนเข้าสู้เซลล์ด้วย อัตราการไหล 30 ml/min เพื่อกำจัดอากาศที่เหลืออยู่ในเซลล์ ก่อนทำการดูดซับตัวอย่างจะ ถูกรีดิวซ์ด้วยไฮโดรเจนที่อัตราการไหล 50 ml/min ที่อุณหภูมิ 500°C เป็นเวลา 2 ชั่วโมงโดยอัตราการเพิ่มอุณหภูมิเท่ากับ 10°C/min หลังจากนั้นตัวอย่างถูกทำให้เย็นจนถึง อุณหภูมิห้องด้วยก๊าซฮีเลียม คาร์บอนมอนอกไซด์ถูกฉีดเข้าสู่เซลล์เป็นจังหวะ การ์บอนมอนอกไซด์ที่ไม่ถูกดูดซับจะถูกวัดด้วย TCD และจะฉีดการ์บอนมอนอกไซด์ไปจนกระทั่งไม่มีการดูดซับการ์บอนมอนอกไซด์เพิ่ม

# 3.4.3.3 การวิเคราะห์ค่าความเป็นกรดของตัวเร่งปฏิกิริยาด้วยใพริดีน เครื่องมือและอุปกรณ์

- 1. เครื่อง Fourier transform infrared spectroscopy (FT-IR) ใช้เป็นเครื่อง ตรวจสอบการดูดซับของไพริดีน ในการทดลองใช้รุ่น Nicolet moldel Impact 400 FT-IR ซึ่งมีตัวตรวจสอบแบบ deuterated triglycine sulfate (DTGS)
- 2. เซลสำหรับใช้ใส่สารในการทดลอง เซลทำจากควอทซ์และปิดหัวท้ายด้วย KBr ซึ่งมี O-ring เป็นตัวปิดกันอากาศเข้าสู่ระบบ
- 3. เครื่องมือที่ใช้ในการทดสอบทำจากเครื่องแก้ว มีหลอดทดลองสำหรับบรรจุไพ ริดีนเหลว หลอดทดลองสำหรับกักเก็บไอของไพริดีน และปั๊มสูญญากาศ

#### วิธีการทคลอง

การทดสอบแบ่งออกเป็น 2 ขั้นตอน คือ ขั้นตอนการเตรียมสารตัวอย่าง และ ขั้นตอนการทดสอบ

ขั้น<u>ตอนที่</u> 1: การเตรียมสารตัวอย่าง

นำสารตัวอย่างน้ำหนักประมาณ 0.06 g มาบดให้ละเอียด และขึ้นรูปด้วยแรงอัด 140-180 kg/cm² ให้เป็นแผ่นกลมและบาง แผ่นสารตัวอย่างมีความหนาแน่น 15 ถึง 20 mg/cm² ถูกบรรจุในเซล ซึ่งนำไปบรรจุในชุดอุปกรณ์ทดลองระบบปิด ขั้นตอนที่ 2: การทดสอบ

หลังจากบรรจุเซลในชุดอุปกรณ์ทคลอง ทคสอบสัญญาณอินฟราเรคก่อนมีการคูค ซับพริคีน พร้อมกับบันทึกค่าสัญญาณ หลังจากนั้นจะทำระบบให้เป็นสูญญากาส โดยใช้ ปั๊มสูญญากาสดึงอากาสภายในชุคอุปกรณ์ เป็นระยะเวลา 30 นาที ซึ่งไอของไพริคีนใน หลอดทคลอง จะกระจายในระบบสูญญากาส และคูคซับบริเวณพื้นผิวของสารตัวอย่าง ณ ตำแหน่งที่รับอิเลกตรอน การคูคซับจะใช้เวลาจนกระทั่งพบว่าสัญญานของไพริคีนไม่ เปลี่ยนแปลง เปิดปั๊มสูญญากาสอีกครั้งเพื่อดึงไอของไพริคีนในระบบและไพริคีนที่คูคซับ โดยแรงทางกายภาพจนพบว่าสัญญาณอินฟราเรคไม่เปลี่ยนแปลง ใช้เวลาประมาณ 1.5 ชั่วโมง จากนั้นเริ่มทำการทคสอบโดยเพิ่มอุณหภูมิให้กับระบบครั้งละ 25°C และทคสอบ สัญญานอินฟราเรค จนกระทั่งพบว่าสัญญาณอินฟราเรคของการคูคซับไพริคีนหมคไป จึง หยุคเพิ่มอุณหภูมิ และสิ้นสุคการทคลอง จากการทคลองจะพบอุณหภูมิสูงสุคที่สามารถดึง ไพริคีนหลุดออกจากพื้นผิวได้

# 3.4.3.4 วิเคราะห์ค่าความเป็นกรดของตัวเร่งปฏิกิริยาด้วยแก๊ส NH,

ความเป็นกรดบนพื้นผิวของตัวเร่งปฏิกิริยานั้นวัดด้วยเทคนิค temperature-programmed desorption โดยใช้ก๊าซแอมโมเนียด้วยเครื่อง Micromeritics Chemisorb 2750 (pulse chemisorption system) ตัวเร่งปฏิกิริยาปริมาณ 0.1 กรัมถูกบรรจุในเซลล์ทำด้วย quartz ตัวอย่างถูกให้ความร้อนที่อุณหภูมิ 450°C ภายใต้การ ใหลของก๊าซฮีเลียมเป็นเวลา 1 ชั่วโมงเพื่อกำจัดน้ำที่อยู่บนพื้นผิวของตัวเร่งปฏิกิริยา หลังจากตัวอย่างเย็นลงจนถึงอุณหภูมิ 100°C ก๊าซผสมของ 15% แอมโมเนียในฮีเลียมถูกป้อนเข้าสู่เซลล์เพื่อทำให้พื้นผิวอิ่มตัว ด้วยแอมโมเนีย ตัวเร่งปฏิกิริยาถูกเป่าด้วยฮีเลียมที่ 100°C เป็นเวลา 1 ชั่วโมงเพื่อกำจัด แอมโมเนียที่ดูดซับทางกายภาพออกไป จากนั้นตัวอย่างถูกให้ความร้อนจนถึงอุณหภูมิ 450°C ด้วยอัตราการเพิ่มอุณหภูมิเท่ากับ 20°C/min ภายใต้การ ใหลของฮีเลียมที่ 50 ml/min จำนวนตำแหน่งที่เป็นกรดบนพื้นผิวคำนวณได้จากปริมาณก๊าซแอมโมเนียที่คาย ออกมาที่วัดได้

# 3.4.3.5 การวิเคราะห์ค่าความเป็นเบสของตัวเร่งปฏิกิริยา

กวามเป็นเบสบนพื้นผิวของตัวเร่งปฏิกิริยานั้นวัคด้วยเทคนิค temperature-programmed desorption โดยใช้ก๊าซคาร์บอนไดออกไซด์ด้วยเครื่อง Micromeritics Chemisorb 2750 (pulse chemisorption system) ตัวเร่งปฏิกิริยาปริมาณ 0.1 กรัมถูกบรรจุใน เซลล์ทำด้วย quartz ตัวอย่างถูกให้ความร้อนที่อุณหภูมิ 450°C ภายใต้การไหลของก๊าซ ฮีเลียมเป็นเวลา 1 ชั่วโมงเพื่อกำจัดน้ำที่อยู่บนพื้นผิวของตัวเร่งปฏิกิริยา หลังจากตัวอย่าง เย็นลงจนถึงอุณหภูมิ 100°C ก๊าซคาร์บอนไดออกไซด์ถูกป้อนเข้าสู่เซลล์เพื่อทำให้พื้นผิว อิ่มตัวด้วยการ์บอนไดออกไซด์ ตัวเร่งปฏิกิริยาถูกเป่าด้วยฮีเลียมที่ 100°C เป็นเวลา 1 ชั่วโมงเพื่อกำจัดการ์บอนไดออกไซด์ที่คูดซับทางกายภาพออกไป จากนั้นตัวอย่างถูกให้ ความร้อนจนถึงอุณหภูมิ 450°C ด้วยอัตราการเพิ่มอุณหภูมิเท่ากับ 20°C/min ภายใต้การ ใหลของฮีเลียมที่ 50 ml/min จำนวนตำแหน่งที่เป็นเบสบนพื้นผิวคำนวณได้จากปริมาณ ก๊าซแอมโมเนียที่คายออกมาที่วัดได้

# 3.4.3.6 การวิเคราะห์ค่าความสามารถในการรีดิวซ์ของตัวเร่งปฏิกิริยา

ความสามารถในการรีดิวซ์ของตัวเร่งปฏิกิริยานั้นวัดด้วยเทคนิค temperature-programmed reduction โดยใช้ก๊าซไฮโครเจนด้วยเครื่อง Micromeritics Chemisorb 2750 (pulse chemisorption system) ตัวเร่งปฏิกิริยาปริมาณ 0.1 ถึง 0.2 กรัมถูกบรรจุในเซลล์ทำ ด้วย quartz ตัวอย่างถูกให้ความร้อนที่อุณหภูมิ 200°C ภายใต้การใหลของก๊าซฮีเลียมที่ 25 ml/min เป็นเวลา 1 ชั่วโมงเพื่อกำจัดน้ำที่อยู่บนพื้นผิวของตัวเร่งปฏิกิริยา หลังจากตัวอย่าง เย็นลงจนถึงอุณหภูมิ 100°C ก๊าซผสมของ 10% ไฮโครเจนในอาร์กอนถูกป้อนเข้าสู่เซลล์ ตัวเร่งปฏิกิริยาถูกให้ความร้อนจนถึงอุณหภูมิที่ต้องการในช่วง 100 ถึง 800°C ด้วยอัตรา การเพิ่มอุณหภูมิเท่ากับ 10°C/min ปริมาณไฮโครเจนที่ใช้ไปวัดด้วย TCD และนำไป คำนวณหาค่าความสามารถในการรีดิวซ์ของตัวเร่งปฏิกิริยา

# 3.4.4 การวิเคราะห์ลักษณะของโค้กที่เกิดขึ้นด้วยเทคนิคการออกซิเดชันแบบโปรแกรม อุณหภูมิ

การวิเคราะห์ลักษณะของโค้กที่เกิดขึ้นบนตัวเร่งปฏิกิริยานั้นใช้เทคนิค temperature-programmed oxidation ด้วยเครื่อง Micromeritics Chemisorb 2750 (pulse chemisorption system) ตัวเร่งปฏิกิริยาปริมาณ 0.1 ถึง 0.2 กรัมถูกบรรจุในเซลล์ทำด้วย quartz ตัวอย่างถูกให้ความร้อนที่อุณหภูมิ 200°C ภายใต้การ ใหลของก๊าซฮีเลียมที่ 25 ml/min เป็นเวลา 1 ชั่วโมงเพื่อกำจัดน้ำที่อยู่บนพื้นผิวของตัวเร่งปฏิกิริยา หลังจากตัวอย่าง

เย็นลงจนถึงอุณหภูมิ 100°C ก๊าซผสมของ 1% ออกซิเจนในไฮโครเจนถูกป้อนเข้าสู่เซลล์ ตัวเร่งปฏิกิริยาถูกให้ความร้อนจนถึงอุณหภูมิที่ต้องการในช่วง 100 ถึง 800°C ด้วยอัตรา การเพิ่มอุณหภูมิเท่ากับ 10°C/min ปริมาณการ์บอนไดออกไซด์ที่เกิดขึ้นวัดด้วย TCD และ นำไปหาลักษณะของโค้กที่เกิดขึ้นบนตัวเร่งปฏิกิริยา

## 4. แผนการดำเนินงานวิจัยในแต่ละช่วง 6 เดือนตลอดระยะเวลาโครงการ

- 4.1 รวบรวมฐานข้อมูลวิจัยที่เกี่ยวข้อง
- 4.2 ดำเนินการวิจัยตามเป้าหมาย
- 4.3 สรุปและผลวิจัย
- 4.4 เขียนบทความวิจัยต่างประเทศ
- 4.5 จัดทำรายงานความก้าวหน้า
- 4.6 จัดทำรายงานประจำปี
- 4.7 จัดเสนอผลงานวิจัยประจำปี

#### แผนการดำเนินโครงการตลอด 3 ปี

กิจกรรม/ เดือน	1-6	7-12	13-18	19-24	25-30	31-36
4.1						
4.2						
4.3						
4.4						
4.5						
4.6						
4.7						

#### 5. ผลที่คาดว่าจะได้จากโครงการ

- 5.1 ผลงานตีพิมพ์ในวารสารวิชาการนานาชาติ (ปีละ 10 เรื่อง)
- 5.2 ผลงานการจดสิทธิบัตร คาดว่าจะมี 1 เรื่อง เมื่อสิ้นสุดโครงการ
- 5.3 หนังสือคาดว่าจะมีหนังสือ 1 เล่ม เมื่อสิ้นสุดโครงการ
- 5.4 จำนวน นักวิจัยที่สร้างจากโครงการ จำนวนวิศวกร/นักวิจัยระดับปริญญาโท 35 คน จำนวนวิศวกร/นักวิจัย ระดับปริญญาเอก 6 คน
- 5.5 ประโยชน์ที่คาคว่าจะได้รับ
  - 1) สามารถมีบทความที่ตีพิมพ์ในวารสารระดับนานาชาติ ได้อย่างน้อย 30 เรื่อง
  - 2) สามารถผลิตจำนวนวิศวกร/นักวิจัยระดับปริญญาโท 35 คน
  - 3) สามารถผลิตจำนวนวิศวกร/นักวิจัย ระดับปริญญาเอก 6 คน
  - 4) เป็นศูนย์รวมในการทคสอบตัวเร่งปฏิกิริยาให้แก่อุตสาหกรรม

# 6. รายชื่อ สังกัด โทรศัพท์ และ e-mail ของผู้ร่วมวิจัย

6.1 หัวหน้าโครงการ ศาสตราจารย์ คร. ปิยะสาร ประเสริฐธรรม
ภาควิชาวิศวกรรมเคมี คณะวิศวกรรมศาสตร์ จุฬาลงกรณ์มหาวิทยาลัย
โทร. 02-218-6883; e-mail: piyasan.p@chula.ac.th

6.2 ผู้ร่วมวิจัย ผู้ช่วยศาสตราจารย์คร. สุพจน์ พัฒนะศรี
ภาควิชาวิศวกรรมเคมี คณะวิศวกรรมศาสตร์ จุฬาลงกรณ์มหาวิทยาลัย
โทร. 02-218-6890; e-mail: s\_phatanasri@yahoo.com

6.3 ผู้ร่วมวิจัย รองศาสตราจารย์ คร. ธราธร มงคลศรี
ภาควิชาวิศวกรรมเคมี คณะวิศวกรรมศาสตร์ จุฬาลงกรณ์มหาวิทยาลัย
โทร. 0-2218-6867; e-mail: Tharathon.m@eng.chula.ac.th

6.4 ผู้ร่วมวิจัย ศาสตราจารย์ คร. สุทธิชัย อัสสะบำรุงรัตน์
ภาควิชาวิศวกรรมเคมี คณะวิศวกรรมศาสตร์ จุฬาลงกรณ์มหาวิทยาลัย

โทร. 0-2218-6868; e-mail: Suttichai, A@eng, chula.ac.th รองศาสตราจารย์ คร. บรรเจิค จงสมจิตร 6.5 ผู้ร่วมวิจัย ภาควิชาวิศวกรรมเคมี คณะวิศวกรรมศาสตร์ จุฬาลงกรณ์มหาวิทยาลัย โทร. 0-2218-6869; e-mail: Bunjerd.j@chula.ac.th 6.6 ผู้ร่วมวิจัย คร. อัครวัต ศิริสุข ภาควิชาวิศวกรรมเคมี คณะวิศวกรรมศาสตร์ จุฬาลงกรณ์มหาวิทยาลัย โทร. 0-2218-6863; e-mail: akawat.s@chula.ac.th รองศาสตราจารย์ คร. จูงใจ ปั้นประณต 6.7 ผู้ร่วมวิจัย ภาควิชาวิศวกรรมเคมี คณะวิศวกรรมศาสตร์ จุฬาลงกรณ์มหาวิทยาลัย โทร. 0-2218-6869; e-mail: joonjai.j@chula.ac.th 6.8 ผู้ร่วมวิจัย ผู้ช่วยศาสตราจารย์ คร. ชูวงศ์ ชัยสุข ภาควิชาวิศวกรรมเคมี คณะวิศวกรรมศาสตร์และเทคโนโลยีอุตสาหกรรม มหาวิทยาลัยศิลปากร โทร. 034-219-364; e-mail: gnowoohc@hotmail.com ผู้ช่วยศาสตราจารย์ ดร.โอกร เมฆาสุวรรณดำรง 6.9 ผู้ร่วมวิจัย ภาควิชาวิศวกรรมเคมี คณะวิศวกรรมศาสตร์และเทคโนโลยีอุตสาหกรรม มหาวิทยาลัยศิลปากร โทร. 034-219-364; e-mail: <u>okornm@yahoo.com</u> ผู้ช่วยศาสตราจารย์ คร. ควงกมล ณ ระนอง 6.10 ผู้ร่วมวิจัย ภาควิชาวิศวกรรมเคมี คณะวิศวกรรมศาสตร์ สถาบับเทคโบโลยีพระจอม เกล้าเจ้าคุณทหารลาคกระบัง โทร. 02-739-2416 ต่อ 169; e-mail: knduangk@kmitl.ac.th 6.11 ผู้ร่วมวิจัย คร. สร้อยพัทธา สร้อยสุวรรณ ภาควิชาวิศวกรรมเคมี คณะวิศวกรรมศาสตร์ มหาวิทยาลัยบูรพา โทร. 038-102-222 ต่อ 3351; e-mail: soipatta@yahoo.com

# 7. สรุปเนื้อหางานวิจัยและผลที่ได้รับ

# ตารางที่ 3 แสดงผลที่คาดว่าจะได้รับจากโครงการวิจัยเทียบกับผลลัพธ์ที่ได้จริง

ลำดับ	ผลที่คาดว่าจะได้รับ	ผลลัพธ์ที่ได้จริง
1	ผลงานตีพิมพ์ในวารสารวิชาการนานาชาติ	ผลงานตีพิมพ์ในวารสารวิชาการนานาชาติ
	รวมทั้งสิ้น 30 เรื่อง	รวมทั้งสิ้น 32 เรื่อง (เอกสารแนบ 1-32)
2	การจดสิทธิบัตร 1 เรื่อง	ได้ยื่นจดสิทธิบัตร 1 เรื่อง (เอกสารแนบ 33)
3	หนังสือ 1 เรื่อง	หนังสือ 1 เรื่อง ความรู้พื้นฐานของตัวเร่ง
		ปฏิกิริยาวิวิธพันธุ์ โดย จูงใจ ปั้นประณต
		<u>ම</u> යීයීය
4	บัณฑิตระดับ ปริญญาโท 35 คน	บัณฑิตระดับ ปริญญาโท 40 คน*
	บัณฑิตระดับปริญญาเอก 6 คน	บัณฑิตระดับปริญญาเอก 10 คน**

# ้รายชื่อบัณฑิตระดับปริญญาโท จบปีการศึกษา 2552-54 จำนวน 40 คน

นาย สมจิตร พุคดี นาย ณัฐปคัลภ์ ศรีสวัสดิ์ น.ส.ธมลวรรณ อาจารีพิพัฒน์ นาย พิสิฐ ภักดี นาย วสุ ใชยตรี น.ส. นภาพร เที่ยงชัด น.ส.จิราภณณ์ ปุริวัฒน์ นาย กฤษณ์ เลิศเจียมรัตน์ น.ส.สุขุมาล สิงชัย น.ส.กมลวรรณ จันทร์มงคลทิพย์ น.ส.วนิดา ทัพหกิจ นส.พิมพ์ปฏิมา ปาณูปากรณ์ นส.ปิยะรัตน์ รอดผล นายฉัตรชัย ชาราวดี นส.จีรติ อบอาย นายกิตติพงศ์ ใพรศรี

นายวิทยา เหวรารักษ์ นายพุฒิพงศ์ สุวรรณ นายปรัชญา วารสิทธิ์ นายชวัช อินทร นส.ชมลวรรณ เจษฎานุรักษ์ นายอนิรุตติ๋ เล็กสมบูรณ์ นายเบญจพล นิธิเจริญวงศ์ นส.อรธิรา เย็นจิตต์รัตนวลี นส.แพร รถกิจ นายอภิวัตน์ โง้วธนะวัฒน์ นายสมชาติ อมรเลิศปรีชา นายวรวัฒน์ ชื่นชีพ นายจักรพันธ์ จันละมูล นายเอกรัตน์ บัวพัน นายวรวิทย์ ชื่นชีพ น.ส.มาถี วงค์เทพ นายวิทวัส ชูกิจธนสาร นายจิรวัฒน์ ภิญโญชีพ น.ส.ศิวนาถ ขุนทอง น.ส. แพรวพรรณ คันธะเนตร น.ส. บงกช ปิยานันทรักษ์ น.ส. เกียรติลดา วารินศิริรักษ์ น.ส. สุนันทา แก่นทอง น.ส. ฤดีมาส มโนศักดิ์

# \*\*รายชื่อบัณฑิตระดับปริญญาเอก จบปีการศึกษา 2552-54 จำนวน 10 คน

น.ส.กานคา ปัทมาคมสัน
นส.พัชราภรณ์ ใกวัลชัชวาล
นายเอกราชันย์ ใชยชนะ
น.ส.เพียงพิส วงศ์มณี
น.ส.ณัฐญา คุ้มทรัพย์
น.ส.กนกวรรณ จ้าวสุวรรณ

นายธงชัย กลิ่นหรั่น นายนิคม แซ่ม้า น.ส.ณิชาภัทร เซนโส น.ส. สุภนันท์ ปัทมะสังข์

## ภาคผนวก A

# Reprint บทความวิจัยต่างประเทศ จำนวน 32 เรื่อง

# 1<sup>st</sup> year

No	Title	Volume/Page/Year	Journal	IF (2011)	Acknowledgement (in paper)
1	"Modification of acid properties and catalytic properties of AlPO4 by hydrothermal pretreatment for methanol dehydration to dimethyl ether" [Krit Lertjiamrath, <b>Piyasan Praserthdam</b> , Masahiko Arai, Joongjai Panpranot*]	378, 119-123, <b>2010</b>	Applied Catalysis A: General	3.903	TRF&CHE
2	"Impact of Si and Zr addition on the surface defect and photocatalytic activity of the nanocrystalline TiO <sub>2</sub> synthesized by the solvothermal method" [Piyawat Supphasrirongjaroen, <b>Piyasan Praserthdam</b> , Okorn Mekasuwandumrong, Joongjai Panpranot*]	36, 1439-1446, <b>2010</b>	Ceramics International	1.751	TRF&CHE
3	"Effect of Milling on the formation of nanocrystalline χ-Al <sub>2</sub> O <sub>3</sub> from Gibbsite" [Wasu Chaitree, Sirithan Jiemsirilers, Okorn Mekasuwandumrong, <b>Piyasan Praserthdam</b> , Tawatchai Charinpanitkul, Joongjai Panpranot <sup>*</sup> ]	89, 2387-2392, <b>2010</b>	Journal of the American Ceramic Society	2.272	TRF&CHE
4	"Improvement of propane oxidation activity over $Pt/Al_2O_3$ by the use of mixed $\gamma$ - and $\chi$ - $Al_2O_3$ supports" [Thongchai Glinrun, Okorn Mekasuwandumrong, Joongjai Panpranot, Choowong Chaisuk, <b>Piyasan Praserthdam</b> *]	100, 441-448, <b>2010</b>	Reaction Kinetics Mechanisms and Catalysis	0.927	TRF&CHE

No	Title	Volume/Page/Year	Journal	IF (2011)	Acknowledgement (in paper)
5	"Solvent effect on synthesis of zirconia support for tungstated zirconia catalysts" [Peangpit Wongmaneenil, Bunjerd Jongsomjit*, <b>Piyasan Praserthdam</b> ]	16, 327-333, <b>2010</b>	Journal of Industrial and Engineering Chemistry	1.977	TRF&CHE
6	"The role of zirconia surface on catalytic activity of tungstated zirconia via two-phase eaterification of acetic acid and 1-heptanol" [Kanokwan Ngaosuwan, Bunjerd Jongsomjit, Piyasan Praserthdam*]	136, 134-140, <b>2010</b>	Catalysis Letters	2.242	TRF&CHE
7	"Ethylene-hexene copolymer derived fom [t-butylfluorenylsilyl-amido] dimethyl titanium complex" [Ekrachan Chaichana, Supaporn Khaubunsongserm, <b>Piyasan Praserthdam</b> , Bunjerd Jongsomjit*]	4, 94-100, <b>2010</b>	Express Polymer Letters	1.769	TRF&CHE
8	"Study on solvent/alkoxide molar ratios on synthesis zirconia nanoparticles for tungstated zirconia catalysts over esterification" [Peangpit Wongmaneenil, Bunjerd Jongsomjit*, <b>Piyasan Praserthdam</b> ]	139, 42-49, <b>2010</b>	Catalysis Letters	2.242	TRF&CHE

No	Title	Volume/Page/Year	Journal	IF (2011)	Acknowledgement (in paper)
9	"The influence of si-modified TiO <sub>2</sub> on the activity of Ag/TiO <sub>2</sub> in CO oxidation" [Nattaya Comsup, Joongjai Panpranot, <b>Piyasan Praserthdam</b> *]	16, 703-707, <b>2010</b>	Journal of Industrial and Engineering Chemistry	1.977	TRF&CHE
10	"Thermodynamic analysis of calcium oxide assisted hydrogen production from biogas" [S. Assabumrungrat*, P. Sonthisanga, W. Kiatkittipong, N. Laosiripojana, A. Arpornwichanop, A. Soottitantawat, W. Wiyaratn, <b>Piyasan Praserthdam</b> ]	16, 785-789, <b>2010</b>	Journal of Industrial and Engineering Chemistry	1.977	TRF&CHE

**Note:** No. 1-10 are the output for 1<sup>st</sup> year (including in the previous 12-month progress report).

# 2<sup>nd</sup> Year

No	Title	Volume/Page/Year	Journal	IF (2011)	Acknowledgement (in paper)
11	"Elucidation of the basicity dependence of 1- butene isomerization on MgO/Mg(OH) <sub>2</sub> catalysts" [Jiraporn Puriwat, Wasu Chaitree, Kongkiat Suriye, Siraprapa Dokjampa, <b>Piyasan Praserthdam</b> , Joongjai Panpranot <sup>*</sup> ]	12, 80-85, <b>2010</b>	Catalysis Communications	2.986	TRF & CHE
12	"The effect of phosphorous precursor on the CO oxidation activity of P-modified TiO <sub>2</sub> supported Ag catalysts" [Nattaya Comsup, Joongjai Panpranot, <b>Piyasan Praserthdam</b> *]	11, 1238-1243, <b>2010</b>	Catalysis Communications	2.986	TRF & CHE
13	"Effects of synthesis conditions and annealing post-treatment on the photoatalytic activities of ZnO nanoparticles in the degradation of methylene blue dye" [Okorn Mekasuwandumrong, Pongspak Pawinrat, Piyasan Praserthdam, Joongjai Panpranot*]	164, 77-84, <b>2010</b>	Chemical Engineering Journal	3.461	TRF&CHE
14	"Influence of mixed activators on ethylene polymerization and ethylene/1-hexene copolymerization with silica-supported Ziegler-Natta catalyst" [Nichapat Senso, Supaporn Khaubunsongserm, Bunjerd Jongsomjit, <b>Piyasan Praserthdam</b> *]	15, 9323-9339, <b>2010</b>	Molecules	2.386	TRF&CHE

No	Title	Volume/Page/Year	Journal	IF (2011)	Acknowledgement (in paper)
15	"Observation of different catalytic activity of various 1-olefins during ethylene/1-olefin copolymerization with homogeneous metallocene catalysts" [Mingkwan Wannaborworn, Piyasan Praserthdam, Bunjerd Jongsomjit *]	16, 373-383, <b>2011</b>	Molecules	2.386	TRF&CHE
16	"Behaviors in ethylene polymerization of MgCl <sub>2</sub> -SiO <sub>2</sub> /TiCl <sub>4</sub> /THF Ziegler-Natta catalysts with differently treated SiO <sub>2</sub> " [Nichapat Senso, Bunjerd Jongsomjit, <b>Piyasan Praserthdam</b> *]	16, 1323-1335, <b>2011</b>	Molecules	2.386	TRF&CHE
17	"The influence of comonomer on ethylene/α-olefins copolymers derived from [Bis(N-(3-tert butylsalicylidene) anilinato)] titanium (IV) dichloride complex" [Patcharaporn Kaivalchatchawal, Pattiya Suttipitakwong, Sutheerawat Samingprai, <b>Piyasan Praserthdam,</b> Bunjerd Jongsomjit <sup>*</sup> ]	16, 1655-1666, <b>2011</b>	Molecules	2.386	TRF&CHE
18	"Effect of Ga modification on different pore size silicas in synthesis of LLDPE by copolymerization of ethylene and 1-hexene with [t-BuNSiMe <sub>2</sub> Flu]TiMe <sub>2</sub> /MMAO catalyst" [Ekrachan Chaichana, Supaporn Khaubunsongserm, <b>Piyasan Praserthdam</b> , Bunjerd Jongsomjit*]	66, 1301-1312, <b>2011</b>	Polymer Bulletin	1.532	TRF&CHE

No	Title	Volume/Page/Year	Journal	IF (2011)	Acknowledgement (in paper)
19	"Flow patterns of liquid multiphase flow in microreactors with different guideline structures" [Chayanoot Kositanont, Sompong Putivisutisak, <b>Piyasan Praserthdam</b> , Suttichai Assabumrungrat, Hiroshi Yamada, Tomohiko Tagawa*]	44, 649-652, 2011	Journal of Chemical Engineering of Japan	0.662	TRF&CHE
20	"Production of propylene from an unconventional metathesis of ethylene and 2-pentene over Re <sub>2</sub> O <sub>7</sub> /SiO <sub>2</sub> -Al <sub>2</sub> O <sub>3</sub> " [Weena Phongsawat, Benjamas Netivorruksa, Kongkiat Suriye, Siraprapa Dokjampa, Piyasan Praserthdam, Joongjai Panpranot <sup>*</sup> ]	21, 83-90, 2012	Journal of Natural Gas Chemistry	1.348	TRF&CHE

**Note** No. 11-20 are the output for 2<sup>nd</sup> year, including in the previous 24-month progress report.

# 3<sup>rd</sup> Year

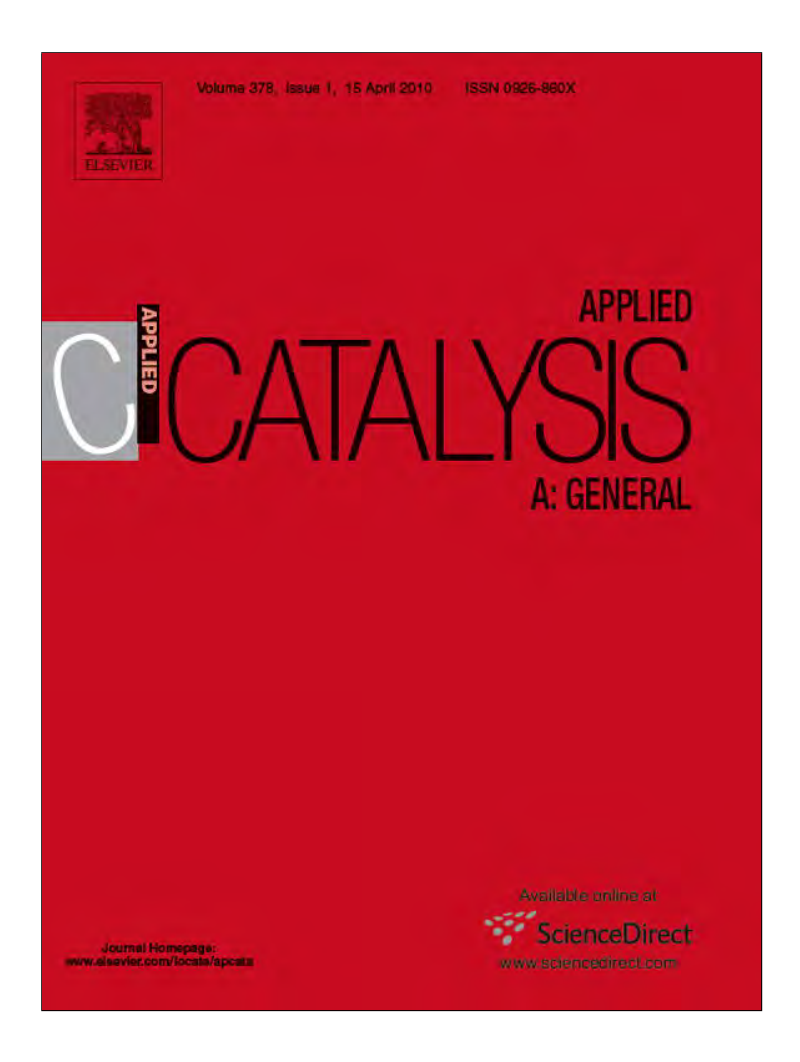
No	Title	Volume/Page/Year	Journal	IF (2011)	Acknowledgement (in paper)
21	"Effect of calcination treatment of zirconia on W/ZrO <sub>2</sub> catalysts for transesterification" [Nichapat Senso, Bunjerd Jongsomjit <sup>*</sup> , <b>Piyasan Praserthdam</b> ]	92, 1537-1542, <b>2011</b>	Fuel Processing Technology	2.945	TRF & CHE
22	"The influence of the t-butyl and cyclododecyl substitution based on ansafluorenylamidodimethyltitanium derivatives on ethylene/1-hexene copolymerization" [Patcharaporn Kaivalchatchawal, <b>Piyasan Praserthdam</b> , Yuuichi Sogo, Zhengguo Cai, Takeshi Shiono, Bunjerd Jongsomjit*]	16, 4122-4130, <b>2011</b>	Molecules	2.386	TRF & CHE
23	"Effect of Ti oxidation state on ethylene, 1-hexene comonomer polymerization by MgCl <sub>2</sub> -supported Ziegler-Natta catalysts" [Nichapat Senso, <b>Piyasan Praserthdam</b> , Bunjerd Jongsomjit, Toshiaki Taniike, Minoru Terano*]	67, 1979-1989, <b>2011</b>	Polymer Bulletin	1.532	TRF&CHE
24	"Investigation of Ti-Si composite oxide- supported cobalt catalysts over CO <sub>2</sub> hydrogenation" [Jakrapan Janlamool, <b>Piyasan</b> <b>Prserthdam</b> , Bunjerd Jongsomjit <sup>*</sup> ]	20, 558-564, <b>2011</b>	Journal of Natural Gas Chemistry	1.348	TRF&CHE

No	Title	Volume/Page/Year	Journal	IF (2011)	Acknowledgement (in paper)
25	"LLDPE synthesis via SiO <sub>2</sub> -Ga-supported zirconocene/MMAO catalyst" [Mingkwan Wannaborworn, <b>Piyasan Praserthdam</b> , Bunjerd Jongsomjit*]	18, 373-377, <b>2012</b>	Journal of Industrial and Engineering Chemistry	1.977	TRF & CHE
26	"Effect of Ga- and BCl <sub>3</sub> -modified silica- supported t-BuNSiMe <sub>2</sub> (2,7-t-Bu <sub>2</sub> Flu)] TiMe <sub>2</sub> /MAO catalyst on ethylene/1-hexene copolymerization" [Patcharaporn Kaivalchatchawal, Sutheerawat Samingprai, Takeshi Shiono, <b>Piyasan Praserthdam</b> , Bunjerd Jongsomjit <sup>*</sup> ]	48, 1304-1312 , <b>2012</b>	European Polymer Journal	2.739	TRF & CHE
27	"Role of support nature (γ-Al <sub>2</sub> O <sub>3</sub> and SiO <sub>2</sub> -Al <sub>2</sub> O <sub>3</sub> ) on the performances of rhenium oxide catalysts in the metathesis of ethylene and 2-pentene" [Weena Phongsawat, Benjamas Netiworaruksa, Kongkiat Suriye, Siraprapha Dokjampa, <b>Piyasan Praserthdam</b> , and Joongjai Panpranot <sup>*</sup> ]	21, 158-164, <b>2012</b>	Journal of Natural Gas Chemistry	1.348	TRF & CHE
28	"Effect of SiO <sub>2</sub> -Al <sub>2</sub> O <sub>3</sub> composition on the catalytic performance of the Re2O7 catalysts in the metathesis of ethylene and 2-propylene production" [[Weena Phongsawat, Benjamas Netiworaruksa, Kongkiat Suriye, <b>Piyasan Praserthdam</b> , and Joongjai Panpranot*]	142, 1141-1149, <b>2012</b>	Catalysis Letters	2.242	TRF & CHE
29	"Observation on inhibition of Ti 3+ reduction by fumed silica addition in Ziegler-Natta catalyst with in situ ESR" [Jirawat Pinyocheep, Sirachaya Kunjara Na Ayudhya, Bunjerd Jongsomjit*, <b>Piyasan Praserthdam</b> ]	In press, 2012	Journal of Industrial and Engineering Chemistry	1.977	TRF & CHE

No	Title	Volume/Page/Year	Journal	IF (2011)	Acknowledgement (in paper)
30	"Effect of nanocrystallite size of TiO <sub>2</sub> on Co/TiO <sub>2</sub> and Co/TiO <sub>2</sub> -Ru catalysts over methanation" [Kitima Pinkaew, <b>Piyasan Praserthdam</b> , Bunjerd Jongsomjit <sup>*</sup> ]	In press, <b>2012</b>	Korean Journal of Chemical Engineering	0.991	TRF & CHE
31	"Integrated methane decomposition and solid oxide fuel cell for efficient electrical power generation and carbon capture" [Narisra Triphob, Suwimol Wongsakulphasatch, Worapon Kiatkittipong, Tawatchai Charinpanitkul, Piyasan Praserthdam, Suttichai Assabumrungrat*]	In press, <b>2012</b>	Chemical Engineering Research & Design	1.968	TRF & CHE
32	"Formation of CoAl <sub>2</sub> O <sub>4</sub> nanoparticles via low temperature solid-state reaction of fine gibbsite and cobalt precursor" [Natpakan Srisawad, Wasu Chaitree, Okorn Mekasuwandumrong, <b>Piyasan Praserthdam</b> , and Joongjai Panpranot*]	Accepted	Journal of Nanomaterials	1.376	TRF & CHE

**Note** No. 21-32 are the output for 3<sup>rd</sup> year, including in this present progress report.

Provided for non-commercial research and education use. Not for reproduction, distribution or commercial use.



This article appeared in a journal published by Elsevier. The attached copy is furnished to the author for internal non-commercial research and education use, including for instruction at the authors institution and sharing with colleagues.

Other uses, including reproduction and distribution, or selling or licensing copies, or posting to personal, institutional or third party websites are prohibited.

In most cases authors are permitted to post their version of the article (e.g. in Word or Tex form) to their personal website or institutional repository. Authors requiring further information regarding Elsevier's archiving and manuscript policies are encouraged to visit:

http://www.elsevier.com/copyright

## Author's personal copy

Applied Catalysis A: General 378 (2010) 119-123



Contents lists available at ScienceDirect

## Applied Catalysis A: General

journal homepage: www.elsevier.com/locate/apcata



# Modification of acid properties and catalytic properties of AlPO<sub>4</sub> by hydrothermal pretreatment for methanol dehydration to dimethyl ether

Krit Lertjiamratn<sup>a</sup>, Piyasan Praserthdam<sup>a</sup>, Masahiko Arai<sup>b</sup>, Joongjai Panpranot<sup>a,\*</sup>

- <sup>a</sup> Center of Excellence on Catalysis and Catalytic Reaction Engineering, Department of Chemical Engineering, Faculty of Engineering, Chulalongkorn University, Bangkok 10330. Thailand
- b Division of Chemical Process Engineering, Graduate School of Engineering, Hokkaido University, Sapporo, 060-8628, Japan

#### ARTICLE INFO

Article history:
Received 26 November 2009
Received in revised form 5 February 2010
Accepted 9 February 2010
Available online 17 February 2010

Keywords: Dimethyl ether Methanol dehydration AIPO<sub>4</sub> Hydrothermal treatment Acid properties

#### ABSTRACT

An amorphous AlPO $_4$  catalyst prepared by precipitation method was subjected to pretreatment with  $10\,\text{mol}\%$  water vapor at  $100-300\,^\circ\text{C}$  for  $15\,\text{min}$  prior to activity tests in the dehydration of methanol to dimethyl ether (DME). The catalysts pretreated at  $200-300\,^\circ\text{C}$  exhibited higher methanol conversion than the non-treated catalyst while the one treated at a lower temperature of  $100\,^\circ\text{C}$  showed lower activity. As revealed by FT-IR and FT-Raman results, there was an increase of lattice hydroxyls on the hydrothermally treated catalysts in the form of P-OH group (weak Brønsted acid sites). Amine titration using Hammett indicators confirmed the increase of both strength and number of acid sites on these catalysts. However, hydrothermal pretreatment at  $100\,^\circ\text{C}$  may result in catalyst poisoning by weakly bonded water molecules instead so that lower catalyst activity was obtained. More than 99% selectivity to DME was achieved on both non-treated and hydrothermally treated AlPO $_4$  catalysts in this study.

© 2010 Elsevier B.V. All rights reserved.

#### 1. Introduction

Dimethyl ether (DME) is one of the promising alternative fuels that can be used to replace liquefied petroleum gas (LPG) and diesel fuels because of their similar properties to those of LPG and their high cetane number [1–3]. Moreover, DME was identified as the ultraclean alternative fuel for diesel engines with emission levels meeting the California ULEV standards [4]. DME could be produced from either synthesis gas or methanol. The production of DME via methanol dehydration is more favorable as regards thermodynamics and economy [2,5].

Methanol dehydration to DME is usually carried out over solidacid catalysts such as H-ZSM-5, steam de-aluminated H-Y zeolite (SDY), and  $\gamma$ -Al $_2$ O $_3$ . The most widely used material is probably  $\gamma$ -Al $_2$ O $_3$ , due to its suitable acidity for this reaction that yields good performance in terms of methanol conversion and DME selectivity. Aluminum phosphate (AlPO $_4$ ) is also one of the promising catalysts in this reaction, because of its lower amounts of coking and byproducts and water resistant property [3,4]. The catalytic activity of AlPO $_4$  in methanol dehydration was found to be dependent on

Water may be a poison in methanol dehydration reactions because it could block active sites and impede methanol from adsorption on the catalyst surface [7,8]. Nevertheless, there are a number of studies reporting opposite results. For example, Ludmány et al. [4] have shown that the presence of water in a reaction can increase the catalytic activity of amorphous titanium hydrogenphosphate (Ti(HPO<sub>4</sub>)<sub>2</sub>) in alcohol dehydration due to swollen effect resulting in an increase of the inter layer of Ti(HPO<sub>4</sub>)<sub>2</sub>. The swollen catalyst with water and alcohol inside the layers retains its high activity until it loses the alcohol and water by evaporation. Fu et al. [9] also reported a slight increase of activity of SDY zeolite catalyst in methanol dehydration after regeneration under hydrothermal conditions at 500 °C for 2 h. Another hypothesis about why water could increase the activity of alumina-based catalyst is that the Lewis acid sites could change to weak Brønsted acid sites upon contact with humidity [7].

In the present work, an amorphous AlPO<sub>4</sub> catalyst was pretreated under various hydrothermal conditions prior to activity test in the dehydration of methanol. The catalysts were characterized by X-ray diffraction (XRD), N<sub>2</sub> physisorption, Fourier transform infrared spectroscopy (FT-IR), Fourier transform Raman spectroscopy (FT-Raman), and amine titration with Hammett indicators. The catalyst activities were correlated with their surface characteristics and acid properties.

the preparation method, chemical composition (AI/P molar ratio), and activation temperature [3,6].

<sup>\*</sup> Corresponding author. Tel.: +66 2218 6869; fax: +66 2218 6877. E-mail address: joongjai.p@chula.ac.th (J. Panpranot).

#### 2. Experimental

## 2.1. Catalyst preparation

An amorphous AlPO<sub>4</sub> catalyst with Al/P molar ratio = 1 was prepared by a modified version of the aqueous solution precipitation method of Bautista et al. [10]. Firstly, Al(NO<sub>3</sub>)<sub>3</sub>·9H<sub>2</sub>O (analytical grade, Aldrich) was diluted in deionized water and mixed with H<sub>3</sub>PO<sub>4</sub> (85%, v/v Aldrich) by stirring at a controlled temperature of 0 °C. Then aqueous ammonia solution was added drop-wise until the precipitation occurred at pH of solution ca. 7. The precipitate was filtered out and washed with distilled water to remove excess substances and any contaminants, and then washed again with 2-propanol. The filtrated mass was dried at 110 °C overnight and calcined at 650 °C in air flow for 3 h.

The AlPO<sub>4</sub> so prepared was subjected to hydrothermal pretreatments at different temperatures. It was exposed to a stream of  $10 \, \text{mol}\%$  water vapor in helium at a GHSV  $5300 \, \text{h}^{-1} \, \text{cm}^3/\text{min}$  and at temperatures of  $100-300 \, ^{\circ}\text{C}$  for  $15 \, \text{min}$ .

## 2.2. Catalyst characterization

The XRD patterns of the prepared catalysts were measured from  $10^{\circ}$  to  $80^{\circ}$   $2\theta$  using a SIEMENS D5000 X-ray diffractometer and Cu  $K\alpha$  radiation with a Ni filter. Surface area, pore volume, and average pore diameter were measured by N2 physisorption using a Micromeritics ASAP 2020. FT-IR was performed using a Nicolet 6700 spectrometer in the range of  $4000-400\,\mathrm{cm}^{-1}$  at a resolution of 2.0 cm<sup>-1</sup>. FT-Raman was performed using a PerkinElmer, spectrum GX in the Raman shift range of 200-3600 cm<sup>-1</sup> at a resolution of 4.0 cm<sup>-1</sup>. The acidity of the catalyst samples was determined by amine titration method using Hammett indicators according to Ref. [11]. The NH<sub>3</sub>-TPD was performed in a Micromeritic Chemisorb 2750 automated system. Before adsorption, the sample was pretreated in high purity N<sub>2</sub> (50 cm<sup>3</sup>/min) at 200 °C for 1 h. Then, it was saturated with 15% NH<sub>3</sub>-He at 80 °C for 1 h (50 cm<sup>3</sup>/min) and subsequently flushed with flowing He at 100 °C for 1 h (50 cm<sup>3</sup>/min) to remove physisorbed NH<sub>3</sub>. The temperature-programmed desorption was carried out from 35 to 600 °C at a constant heating rate of 10°C/min.

## 2.3. Catalytic activity test

The dehydration of methanol over non-treated and hydrothermally treated AlPO $_4$  was carried out in a fixed-bed reactor (i.d. 6 mm) using 0.2 g of catalyst and a gas hourly space velocity (GHSV) of  $5300\,h^{-1}$ . Methanol was bubbled by helium through a glass saturator maintained at  $29\,^{\circ}$ C. The reaction was conducted at  $150-300\,^{\circ}$ C under atmospheric pressure. The reactant and products were analyzed using a gas chromatograph with a TCD detector and Porapak-Q and Porapak-N columns at  $110\,^{\circ}$ C and  $100\,^{\circ}$ C, respectively.

## 3. Results and discussion

## 3.1. Catalytic activity in the dehydration of methanol

The AIPO<sub>4</sub> synthesized by a modified precipitation method in this work had amorphous structure as determined by XRD (not shown) and possessed a BET surface area of  $171.2\,\mathrm{m}^2/\mathrm{g}$ , a pore volume of  $0.758\,\mathrm{cm}^3/\mathrm{g}$ , and an average pore radius of  $17.7\,\mathrm{nm}$ . The non-treated AIPO<sub>4</sub> catalyst was tested in the dehydration of methanol to DME at the temperature range  $150-300\,^{\circ}\mathrm{C}$  and the results are shown in Fig. 1. As compared to a commercial  $\gamma$ -Al<sub>2</sub>O<sub>3</sub> (Aldrich) that possessed BET surface area  $149\,\mathrm{m}^2/\mathrm{g}$ , pore volume  $0.23\,\mathrm{cm}^3/\mathrm{g}$ , and average pore radius  $3.7\,\mathrm{nm}$ , the catalytic activity

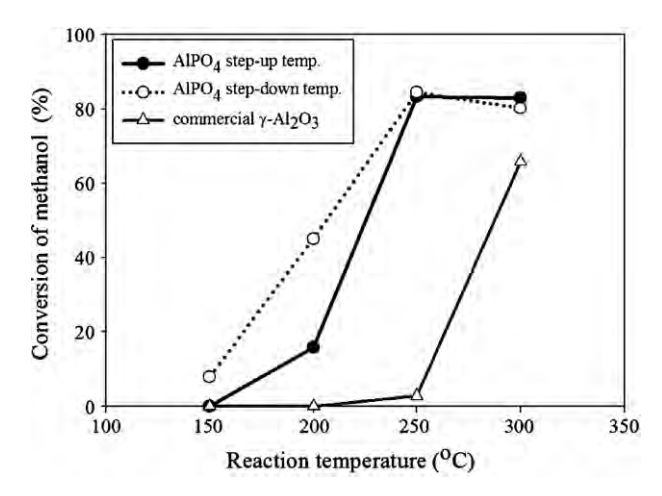


**Fig. 1.** Methanol conversion profiles of step-up and step-down reaction temperature experiments for the non-treated AlPO<sub>4</sub> catalyst as compared to a commercial  $\gamma$ -Al<sub>2</sub>O<sub>3</sub> catalyst (reaction conditions were 0.2 g catalyst, 1 atm, and GHSV = 5300 h<sup>-1</sup>).

of our synthesized AlPO $_4$  catalysts in the dehydration of methanol was much higher. Based on the NH $_3$ -TPD results (Fig. 2), the lower activity of  $\gamma$ -Al $_2$ O $_3$  was attributed to the lower number of acid sites present. Moreover, while the AlPO $_4$  catalyst exhibited a large broad peak with the highest peak intensity at ca. 125 °C, the commercial  $\gamma$ -Al $_2$ O $_3$  showed two desorption peaks at ca. 80 and 360 °C, indicating the presence of both relatively weak and strong acid sites on  $\gamma$ -Al $_2$ O $_3$ .

The catalytic activities of AlPO $_4$  catalyst were further investigated in the dehydration of methanol using step-up and step-down reaction temperature tests. For a step-up reaction temperature experiment (increasing temperature from  $150 \rightarrow 200 \rightarrow 250 \rightarrow 300\,^{\circ}\text{C}$ ), methanol conversion occurred at  $200\,^{\circ}\text{C}$  and increased with increasing reaction temperature. Equilibrium conversion ( $\sim$ 82%) was reached at  $300\,^{\circ}\text{C}$ . The AlPO $_4$  catalyst gave >99% selectivity to DME with less than 1% of by products such as carbon monoxide and methane. For a step-down reaction temperature experiment using a new catalyst sample (decreasing temperature from  $300 \rightarrow 250 \rightarrow 200 \rightarrow 150\,^{\circ}\text{C}$ ), methanol conversion at  $200\,^{\circ}\text{C}$  increased to 45.1% as compared to 15.3% for the step-up temperature one. The AlPO $_4$  catalyst also showed some conversion of methanol of ca. 8% at  $150\,^{\circ}\text{C}$ . It is hypothesized that there was an effect of water vapor and/or initial

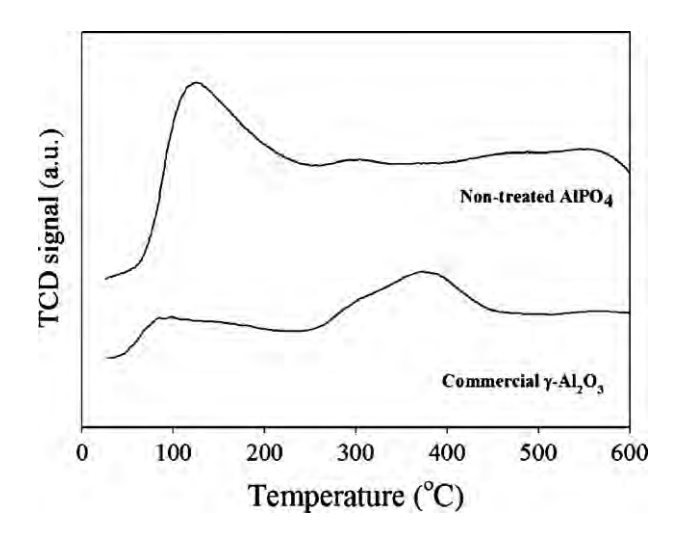


Fig. 2.  $\,$  NH $_3$  -TPD results of the synthesized-AlPO $_4$  and the commercial  $\gamma$  -Al $_2$ O $_3$  catalysts.

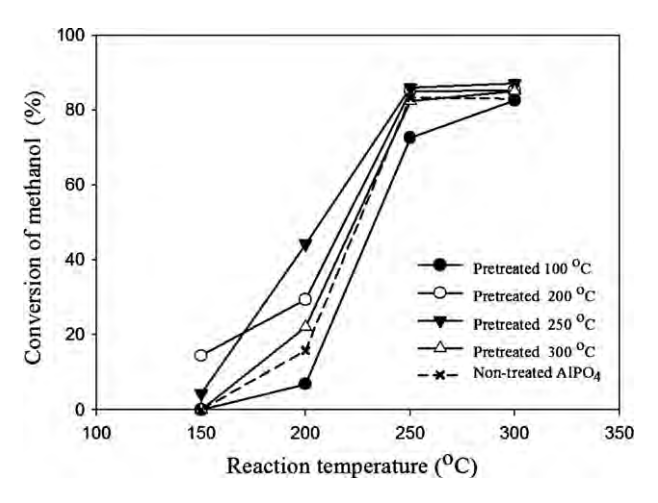
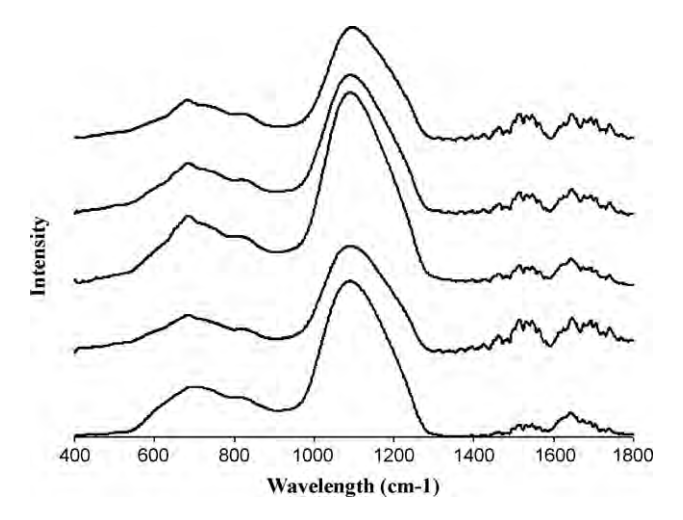


Fig. 3. Effect of water pretreatment temperature on the conversion of methanol for the hydrothermally treated and non-treated amorphous AlPO<sub>4</sub> catalysts (0.2 g catalyst and GHSV =  $5300 \, h^{-1}$ ).

high reaction temperature on the improvement of catalytic activity. The latter hypothesis, however, was rejected since treating the AlPO $_4$  catalyst at 300 °C in neutral atmosphere of helium for 1 h prior to reaction test did not result in an increase of catalytic activity (similar conversion to the step-up reaction temperature test). In order to prove the former hypothesis that the presence of water vapor could increase the activity of AlPO $_4$  in methanol dehydration, we subjected the material to pretreatment with 10 mol% water vapor at various temperatures between 100–300 °C for 15 min prior to reaction test. The activities of treated and non-treated AlPO $_4$  catalysts in methanol dehydration are shown in Fig. 3. It was found that all the treated catalysts exhibited higher activity than the non-treated one except the one that was treated at 100 °C. There was no change in product selectivity for all the catalysts in which >99% selectivity to DME was obtained.

### 3.2. Surface characteristics and acidity of the AlPO<sub>4</sub> catalysts

Surface characteristics and acidity of the catalysts were determined by FT-IR, FT-Raman, and amine titration using Hammett indicators. The AlPO $_4$  catalysts were investigated by FT-IR in two regions:  $400-1800\,\mathrm{cm}^{-1}$  and  $2500-4000\,\mathrm{cm}^{-1}$ . The results are shown in Figs. 4 and 5, respectively. According to the literature [6,12,13], there are two major types of hydroxyl groups:



**Fig. 4.** FTIR spectra at wavelength  $400-1800\,\mathrm{cm^{-1}}$  of the non-treated AlPO<sub>4</sub> and  $100-300\,^{\circ}\mathrm{C}$  water vapor pretreated AlPO<sub>4</sub> catalysts.

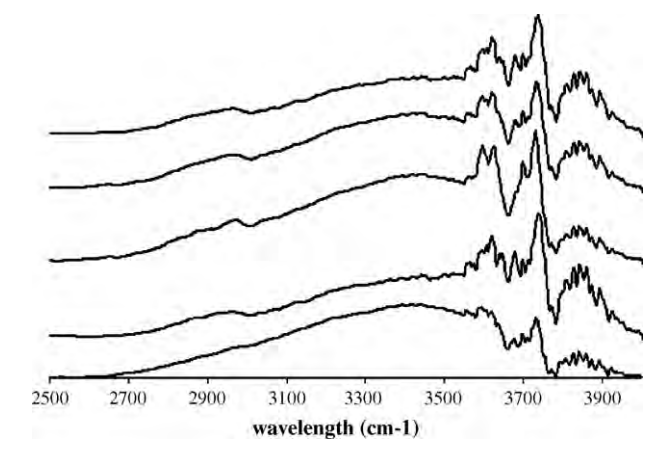


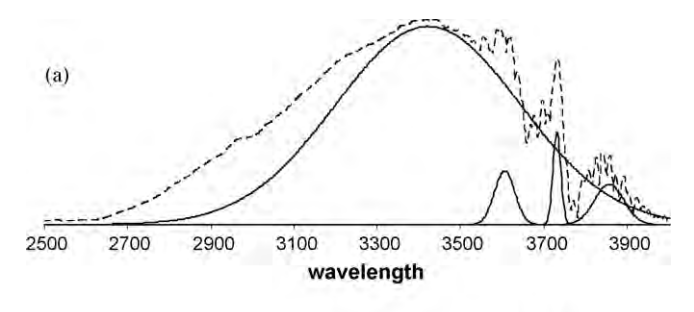
**Fig. 5.** FTIR spectra at wavelength  $2500-4000\,\mathrm{cm}^{-1}$  of the non-treated AlPO<sub>4</sub> and  $100-300\,^\circ\mathrm{C}$  water vapor pretreated AlPO<sub>4</sub> catalysts.

the hydroxyl stretching vibration bands of adsorbed molecular water absorption (surface hydroxyls) and the hydrogen-bonded hydroxyl groups (lattice hydroxyls). In Fig. 3, the peaks in the range around 400–800 cm<sup>-1</sup> were attributed to asymmetric and symmetric stretching vibrations of Al-O-P bonds, corresponding to the non-stoichiometric aluminum phosphates [6]. The peak that centered around 1100 cm<sup>-1</sup> was attributed to PO<sub>2</sub> in a chain structure with two oxygen atoms from the phosphorous coordination sphere bonded to aluminum atoms [6]. These peaks identifying Al-O-P and PO<sub>2</sub> confirmed that the catalysts were aluminum phosphate. Another peak centered around 1650 cm<sup>-1</sup> was assigned to the physisorption of water molecules (H-O-H) or surface hydroxyls on the catalysts. There was no significant difference in the water physisorption bands among the non-treated and treated catalyst samples.

The stretching vibration of hydrogen-bonded hydroxyl groups can be detected in the wavelength region of 2500-4000 cm<sup>-1</sup> with a large broad adsorption band centered near  $3400 \, \mathrm{cm}^{-1}$ . These peaks were attributed to the chemisorption of water molecules on the catalyst surface. Using the "fityk 0.7.4" curve fitting program (GNU General Public License, version 2, as published by the free software foundation), we achieved the de-convolution of FT-IR spectra of each catalyst. The results for the non-treated and 250 °C-treated AlPO<sub>4</sub> catalysts are shown as examples of the de-convoluted spectra in Fig. 6. The peaks in the region of 2500–4000 cm<sup>-1</sup> for the treated catalysts can be separated into 5 main peaks at 2950, 3400, 3600, 3750, and  $3800 \, \text{cm}^{-1}$ . There was an absence of an FT-IR peak at  $2950\,\mathrm{cm^{-1}}$  for the non-treated AlPO<sub>4</sub> catalyst. Moreover, the intensity of FT-IR bands at wavelengths of 3600 and 3750 cm<sup>-1</sup> of the pretreated AlPO<sub>4</sub> were significantly higher than those of the non-treated one. The strong sharp band around 3750 cm<sup>-1</sup> accompanied by a broad band around 3400 cm<sup>-1</sup> could be assigned to the hydroxyl stretching mode of surface phosphate or pyrophosphate species [13]. The shoulder that appeared at ca. 2950 cm<sup>-1</sup> of the pretreated catalyst suggests the presence of hydroxyl groups of various strengths attached to phosphorous in the samples [6]. These results confirmed that there was an increase of hydroxyls on phosphate groups in the AlPO<sub>4</sub> catalysts after hydrothermal pretreatment. In other words, molecules of water were adsorbed and bonded with phosphorous atoms in the catalysts in the form of P-OH.

The Raman spectra of fresh and pretreated AlPO<sub>4</sub> catalysts are shown in Fig. 7. The Raman bands at 1050 and  $1200\,\mathrm{cm^{-1}}$  indicate the presence of PO<sub>3</sub><sup>2-</sup> and PO<sub>2</sub><sup>1-</sup>, respectively [14]. A study of phosphate groups using Raman spectroscopy by de Jager and Prinsloo [15] showed that Raman shifts around 876–992 cm<sup>-1</sup> could be assigned to P-OH bands in several structures, due to matrix effects

K. Lertjiamratn et al. / Applied Catalysis A: General 378 (2010) 119-123



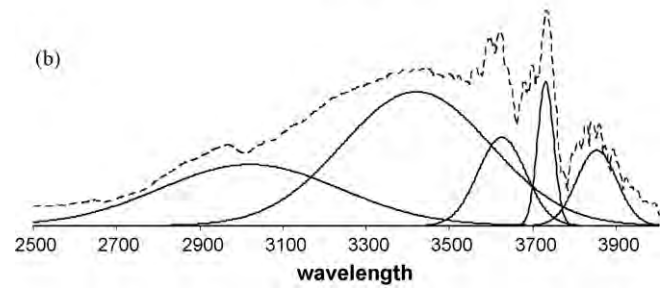


**Fig. 6.** De-convolution FT-IR spectra of hydroxyl groups of non-treated (a) and 250 °C pretreated (b) AlPO<sub>4</sub> catalysts.

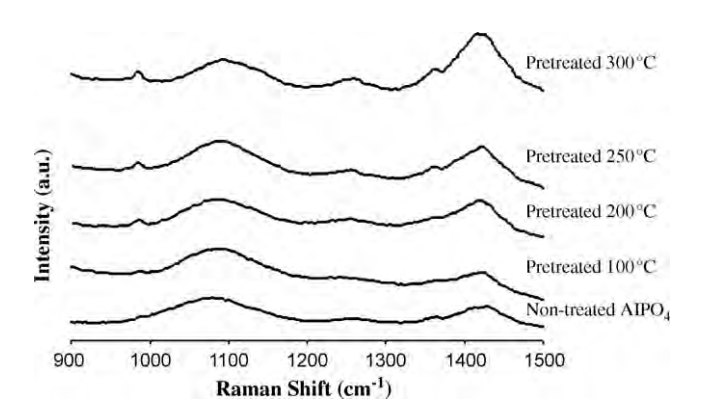


Fig. 7. FT-Raman spectra at Raman shift  $900-1500\,\mathrm{cm^{-1}}$  of the non-treated AlPO<sub>4</sub> and  $100-300\,^\circ\mathrm{C}$  water vapor pretreated AlPO<sub>4</sub> catalysts.

and different phosphate functional groups such as  $PO_2^{1-}$ ,  $PO_3^{2-}$ ,  $PO_4^{3-}$  and  $P_2O_7^{2-}$ . In the present study, the Raman shift at ca. 985 cm<sup>-1</sup> appeared after pretreatment with water vapor, indicating the formation of P-OH. Such a result was in good agreement with the FT-IR data, which suggested that pretreatment with water vapor could result in the formation of hydroxyls that are adsorbed and chemically bonded with phosphate groups in the AlPO<sub>4</sub> catalyst.

The relative amount of P-OH on the pretreated AlPO<sub>4</sub> catalysts was determined according to the semi-quantitative analysis [16]. For the FT-IR results, it is reported in term of a ratio of the area of de-convoluted hydroxyl peak at 2950 cm<sup>-1</sup> and the Al-O-P peak

at  $833\,\mathrm{cm^{-1}}$ . For the FT-Raman results, ratios of the area of P-OH at Raman shift  $985\,\mathrm{cm^{-1}}$  and  $PO_2^{-1}$  at  $1200\,\mathrm{cm^{-1}}$  were used. The relative amounts of P-OH by semi-quantitative analysis from FT-IR and FT-Raman are shown in Table 1. The highest and the lowest amounts of P-OH were obtained on the AlPO<sub>4</sub> pretreated at 250 and  $100\,^\circ\mathrm{C}$ , respectively. The amount of P-OH followed the activity trend in the dehydration of methanol to DME.

The strength and number of acid sites of the non-treated and treated AIPO<sub>4</sub> catalysts were also measured by amine titration using Hammett indicators. Values are reported in a range depending on the acid strength  $(pK_a)$  of indicators (methyl red, methyl orange, methyl yellow, and crystal violet). The numbers of acid sites in different ranges of Hammett indicators are shown in Table 1. Using methyl red as Hammett indicator, all the treated catalysts changed color to acid form of methyl red while the non-treated catalyst had color in base form. These results indicated that the non-treated AIPO<sub>4</sub> catalyst had lower acid strength than methyl red ( $pK_a = 4.8$ ). In other words, acidity of the AlPO<sub>4</sub> catalysts after pretreatement with water vapor was higher than  $pK_a = 4.8$ . However, all the treated catalysts had color in base form when Hammett indicators with higher acid strength such as methyl orange, methyl yellow, and crystal violet were used so that they could not be titrated by amine. Thus, the acid strength of treated AlPO<sub>4</sub> was in the range of  $pK_a = 4.8-3.3$ , based on the acidity of methyl red and methyl orange, respectively. It was found that the pretreatment with water vapor at 250 °C gave the highest number of acid sites, while the pretreatment at 100°C resulted in the lowest amount of acidity, in good agreement with results from FT-IR, FT-Raman, and reactions. Since there was no significant change in BET surface area and pore characteristics of the AlPO<sub>4</sub> catalysts upon hydrothermal pretreatment under the conditions used, the differences in the catalytic activities of the hydrothermal treated catalysts could also be attributed to the difference in the distribution of acid strength, in addition to the changes of numbers of acid sites and acid strengths.

#### 3.3. Reaction mechanism

The pretreatment with water vapor at 200–300 °C has been shown to result in an increase of activity of AlPO<sub>4</sub> catalyst in the dehydration of methanol. The improved catalyst performance was attributed to the increase of acid strength and acidity of the AlPO<sub>4</sub> catalyst. As shown by FT-IR and FT-Raman results, there were lattice hydroxyls that are chemically bonded with phosphate groups in the AlPO<sub>4</sub> catalyst after hydrothermal treatment. Such results also suggested a change of Lewis acid sites to Bronsted acid sites on the AlPO<sub>4</sub> catalyst. Higher acid strengths on the pretreated catalysts were confirmed by amine titration using Hammett indicators. According to the mechanism for dehydration of methanol over ZrP and TiP catalysts proposed by Clearfield et al. [17], the P-OH group is involved in water condensation at Bronsted acid sites and formation of methoxy groups on the orthophosphate surface, which are the initial steps for methanol etherification. The methoxy group is

**Table 1**The relative amount of P-OH group of hydrothermally treated AIPO<sub>4</sub> samples from FT-IR and FT-Raman calculated by semi-quantitative analysis and the amount of acid sites by amine titration using methyl red indicator.

Pretreatment temperature	Relative amount of P-OH <sup>a</sup>	Relative amount of P-OH <sup>a</sup>	
	FT-IR at 2950 cm <sup>-1</sup> Raman shift at 985 cm <sup>-1</sup>		
100 °C	0.49	0.00846	0.266
200 °C	1.23	0.02431	0.276
250 °C	1.35	0.03245	0.359
300 °C	0.91	0.02871	0.340

<sup>&</sup>lt;sup>a</sup> See the text for determination.

b Determined by amine titration using methyl red indicator

K. Lertjiamratn et al. / Applied Catalysis A: General 378 (2010) 119-123

$$P-OH+CH_3-OH \longrightarrow P-O-H_3 \longrightarrow P-O-CH_3+H_2O$$

$$CH_3-OH$$

$$P-O-CH_3+CH_3-OH \implies P-O-C-H_3 \implies P-OH+CH_3-O-CH_3$$
 [2]

P-O-CH<sub>3</sub> + H<sub>2</sub>O

Scheme 1. Possible reaction mechanism for dehydration of methanol to DME over AlPO4 catalyst.

considered to be highly polar due to the strong electronegativity of the phosphate group. The methoxy species can then react with methanol through a four-member ring electron transfer process to form DME. The proposed mechanism is illustrated in Scheme 1. We have clearly shown that P-OH is an important intermediate for the dehydration of methanol over AlPO<sub>4</sub> catalyst.

#### 4. Conclusions

The pretreatment with 10 mol% water vapor at 200–300 °C has been shown to result in an increase of catalytic activity of AlPO<sub>4</sub> catalyst in the dehydration of methanol to DME. The improved catalyst performance was attributed to the increased acid strength and acidity of the AlPO<sub>4</sub> catalyst. The peaks corresponding to P-OH were observed by both FT-IR and FT-Raman techniques. Such results suggested that Lewis acid sites could be changed to Bronsted acid sites on the pretreated AlPO<sub>4</sub> catalysts which would result in higher acid strength, as also confirmed by amine titration with Hammett indicators. However, hydrothermal pretreatment at 100 °C resulted in lower catalytic activity than the non-treated one, due probably to blocking of catalyst active sites by the weakly bonded hydroxyl groups.

#### Acknowledgements

Financial supports from the Thailand Research Fund (TRF) and, the Office of Higher Education Commission, Ministry of Education are gratefully acknowledged.

#### References

- [1] J.H. Fei, Z.Y. Hou, B. Zhu, H. Lou, X.M. Zheng, Appl. Catal. A: Gen. 304 (2006)
- [2] F. Yaripour, F. Baghaei, I. Schmidt, J. Perregaard, Catal. Commun. 6 (2005) 147-152
- [3] F. Yaripour, F. Baghaei, I. Schmidt, J. Perregaard, Catal. Commun. 6 (2005) 542-549.
- [4] A. Ludmany, S.S. Kurek, A. Stoklosa, G. Wilczynski, A. Wojtowicz, J. Zajecki, Appl. Catal. A: Gen. 267 (2004) 149-156.
- [5] S. Jiang, J.S. Hwang, T. Jin, T. Cai, W. Cho, Y.S. Baek, S.E. Park, Bull. Korean Chem. Soc. 25 (2004) 185-189.
- [6] V.S. Kumar, A.H. Padmasri, C.V.V. Satyanarayana, I.A.K. Reddy, B.D. Raju, K.S.R. Rao, Catal. Commun. 7 (2006) 745-751.
- [7] M.T. Xu, J.H. Lunsford, D.W. Goodman, A. Bhattacharyya, Appl. Catal. A: Gen. 149 (1997) 289-301.
- K.W. Jun, H.S. Lee, H.S. Roh, S.E. Park, Bull. Korean Chem. Soc. 23 (2002) 803-806.
- [9] Y.C. Fu, T. Hong, J.P. Chen, A. Auroux, J.Y. Shen, Thermochim. Acta 434 (2005) 22-26
- [10] F.M. Bautista, J.M. Campelo, A. Garcia, D. Luna, J.M. Marinas, Appl. Catal. A: Gen. 243 (2003) 93-107
- [11] M. Yurdakoc, M. Akcay, Y. Tonbul, K. Yurdakoc, Turkish J. Chem. 23 (1999) 319-327.
- [12] S. Kaewgun, C.A. Nolph, B.I. Lee, L.Q. Wang, Mater. Chem. Phys. 114 (2009) 439-445
- [13] T. Armaroli, M. Trombetta, A.G. Alejandre, J.R. Solis, G. Busca, Phys. Chem. Chem. Phys. 2 (2000) 3341-3348
- [14] M. Hernandez, J. Genesca, J. Uruchurtu, F. Galliano, D. Landolt, Prog. Organ. Coat.
- 56 (2006) 199-206.
- [15] H.J. de Jager, L.C. Prinsloo, Thermochim. Acta 376 (2001) 187-196.
- [16] L. Qi, B.I. Lee, P. Badheka, L.Q. Wang, P. Gilmour, W.D. Samuels, G.J. Exarhos, Mater. Lett. 59 (2005) 2794-2798.
- [17] S. Cheng, G.Z. Peng, A. Clearfleld, Ind. Eng. Chem. Prod. Res. Dev. 23 (1984) 219-225.





CERAMICS INTERNATIONAL

www.elsevier.com/locate/ceramint

Ceramics International 36 (2010) 1439-1446

# Impact of Si and Zr addition on the surface defect and photocatalytic activity of the nanocrystalline TiO<sub>2</sub> synthesized by the solvothermal method

Piyawat Supphasrirongjaroen <sup>a</sup>, Piyasan Praserthdam <sup>a</sup>, Okorn Mekasuwandumrong <sup>b</sup>, Joongjai Panpranot <sup>a,\*</sup>

## Abstract

In the present work, the effects of Si and Zr addition on the surface defect and photocatalytic activity of the solvothermal-derived  $TiO_2$  were investigated. The metal-doped  $TiO_2$  samples were prepared with the molar ratio Si/Ti and Zr/Ti ranging from 0.002 to 0.1 and were subjected to two different cooling temperatures (room temperature and 77 K) after calcination as a post-synthesis treatment. The presence of a small amount of metal dopant caused a slight change in the  $TiO_2$  crystallite and BET surface area (ranging from 7.8 to 10.6 nm and corresponding surface area 95 to  $159 \text{ m}^2/\text{g}$ ). The photocatalytic activity of  $TiO_2$  did not depend solely on the surface area but rather affected by the concentration of  $Ti^{3+}$  on the catalyst surface as shown by a linear ascending trend of the ethylene conversion and the amount of  $Ti^{3+}$ /surface area of the catalysts. It is noted that addition of Zr had more positive effect than Si and the effect of post-treatment on the photocatalytic activity of  $TiO_2$  catalysts was more pronounced than the addition of metal dopants.

© 2010 Elsevier Ltd and Techna Group S.r.l. All rights reserved.

Keywords: B. Defects; Semiconductor; Nanostructures; Solvothermal; Catalytic properties

## 1. Introduction

Titanium (IV) dioxide or titania (TiO<sub>2</sub>) has a wide range of applications due to its excellent physical and chemical properties. Titania is commercialized as the most powerful photocatalyst because it has high photoactivity for most photocatalytic reactions and is nonexpensive as well as nontoxic to human life [1,2]. The photocatalytic activity of TiO<sub>2</sub> is greatly influenced by its crystal structure, crystallite size, crystallinity, surface area, incident light intensity, and porosity [3]. With the decrease in particle size to nanometer scale, the catalytic activity of titania is enhanced because the optical band gap is widened due to an increase in surface area [4,5], surface defect [6,7], and a shift of the absorption/luminescence spectra towards shorter wavelengths (so-called "blue shift").

Surface defects in titania crystal are the results of surface oxygen vacancies, which leave Ti<sup>3+</sup> sites exposed [8,9]. The surface Ti<sup>3+</sup> sites play an essential role in photocatalytic process over titania photocatalyst [10–12]. Yamazaki et al. [13] reported that the competitive adsorption of water and ethylene molecules occurred on the same Ti<sup>4+</sup> sites while the oxygen molecules adsorbed separately on the Ti<sup>3+</sup> sites. Thus, an increase of Ti<sup>3+</sup> sites substantially increased oxygen adsorption and photocatalytic oxidation efficiency. In addition, Park et al. [14] showed that the photoelectrons were trapped by the surface defects (Ti<sup>3+</sup>) leading to the inhibition of the e<sup>-</sup>-h<sup>+</sup> recombination. Relationship between the amount of Ti<sup>3+</sup> defects on TiO<sub>2</sub> surface and their photocatalytic activities have been reported by many authors [15–18].

Many methods have been proposed to synthesize nanocrystalline  $TiO_2$  in anatase phase such as sol-gel [19,20], solvothermal [21] and hydrothermal methods [22]. Solvothermal synthesis, in which chemical reactions occur in aqueous or organic media under the self-produced pressure at low temperature (usually lower than 250 °C), is an advantageous

<sup>&</sup>lt;sup>a</sup> Center of Excellence on Catalysis and Catalytic Reaction Engineering, Department of Chemical Engineering, Faculty of Engineering, Chulalongkorn University, Bangkok 10330, Thailand

b Department of Chemical Engineering, Faculty of Engineering and Industrial Technology, Silpakorn University, Nakhonphatom 73000, Thailand
Received 23 July 2009; received in revised form 30 July 2009; accepted 28 January 2010
Available online 1 March 2010

<sup>\*</sup> Corresponding author. Tel.: +66 2218 6869; fax: +66 2218 6877. *E-mail address:* joongjai.p@eng.chula.ac.th (J. Panpranot).

method because it does not require high temperature treatment step that usually causes grain growth, reduction in specific surface area, and phase transformation of the TiO<sub>2</sub> particles as occurred in the sol–gel process [23]. The solvothermal method has been used to successfully synthesize various types of nanosized metal oxides with large surface area, high crystal-linity, and high thermal stability [24,25].

Incorporation of metals into anatase phase TiO<sub>2</sub> has been frequently studied as a way to improve the photocatalytic activity of TiO<sub>2</sub> nanoparticles. Addition of a second metal such as silicon [26,27], zirconium [28], tungsten [29], cerium [30] and aluminium [31] has shown to enhance the thermal stability for phase transformation of titania particles from anatase to rutile and increase the surface area of titania. For example [32], anatase-type TiO<sub>2</sub> doped with 4.7 and 12.4 mol\% ZrO<sub>2</sub> that were directly precipitated as nanometer-sized particles from acidic precursor solutions of TiOSO<sub>4</sub> and Zr(SO<sub>4</sub>)<sub>2</sub> by simultaneous hydrolysis under hydrothermal conditions at 200 °C, showed higher photocatalytic activity than pure anatase-type TiO<sub>2</sub> for the decomposition of methylene blue. The thermal stability for phase transition from anatase to rutile of TiO2 doped with ZrO2 was greatly improved. Cheng et al. [33] reported that silica-doped TiO<sub>2</sub> showed high photocatalytic activity due to the suppression of phase transformation of titania from anatase to rutile and formation of oxygen vacancies.

However, in most of the aforementioned studies, the effect of second metal addition on the photocatalytic activity of TiO<sub>2</sub> was studied at relatively high metal contents (10–50 wt.%). Thus, it is of interest for this study to investigate the effect of second metal addition (Si and Zr) at relatively low metal content (Si/Ti and Zr/Ti molar ratio between 0.002 and 0.1) on both surface defect and photocatalytic activity of the TiO<sub>2</sub>-based catalysts. The properties of TiO<sub>2</sub> samples were characterized using various analytical methods such as X-ray diffraction (XRD), N<sub>2</sub> physisorption, electron spin resonance spectroscopy (ESR), and X-ray photoelectron spectroscopy (XPS). Photocatalytic activity of the TiO<sub>2</sub> was tested in a gasphase decomposition of ethylene under UV irradiation.

#### 2. Experimental

#### 2.1. Preparation of nanocrystalline TiO<sub>2</sub>

The TiO<sub>2</sub> catalyst was prepared with a procedure reported by Payakgul et al. [34] using titanium (IV) *n*-butoxide (TNB, Aldrich) as a titanium source. The Si- and Zr-doped TiO<sub>2</sub> were prepared by adding a small amount of TEOS (tetraethylorthosilicate, Aldrich) and zirconium (IV) *n*-butoxide (Aldrich) into the solution of 25 g TNB (Aldrich) in 100 ml toluene, respectively. The molar ratios of Si/Ti and Zr/Ti calculated were in the range 0.002–0.1. Then, set up the test tube in a 300 cm<sup>3</sup> autoclave. The gap between the test tube and the autoclave wall was filled with 30 cm<sup>3</sup> of the same solvent used in the test tube. The autoclave was purged completely by nitrogen before heating up to the desired temperature, in the range of 573 K at a rate of 2.5 K/min. Autogenously pressure during the reaction gradually increased as the temperature was

raised. Once the prescribed temperature was reached, the temperature was held constant for 2 h. After the system was cooled down, the resulting powders were repeatedly washed with methanol and dried in air.

## 2.2. Quenching treatment

The detailed experiment has already been reported in our earlier works [35,36]. Prior to quenching, the synthesized catalysts were calcined in air atmosphere at 573 K with a heating rate of 10 K/min for 1 h, and then it was taken out and immediately quenched in air at room temperature and 77 K. After the samples were quenched, all the catalyst samples were dried in air at room temperature and stored in a desiccator.

#### 2.3. Sample nomenclature

The base samples were  $TiO_2$ -RT and  $TiO_2$ -77 K which referred to the  $TiO_2$  catalysts without a second metal addition that were cooled down in air at room temperature (RT) and 77 K after calcination, respectively. The nomenclature used for the metal-doped  $TiO_2$ , for example "0.002-(Si)- $TiO_2$ -RT" was referred to the Si-doped  $TiO_2$  with Si/Ti molar ratio 0.002 that was cooled down in air at room temperature.

#### 2.4. Characterization

Phase identification and crystallite size of pure and modified nanocrystalline titania were investigated by X-ray diffraction (SIEMENS D5000) using Ni filter Cu  $K_{\alpha}$  radiation from  $20^{\circ}$  to  $80^{\circ} 2\theta$ . The crystallite size of TiO<sub>2</sub> was determined from halfheight width of the 101 diffraction peak of anatase using the Scherrer equation. The BET surface area was obtained from the N<sub>2</sub> adsorption isotherms measured at 77 K in a Micromeritics ASAP 2000. Electron spin resonance spectroscopy (ESR) was conducted in vacuum at room temperature and without illumination using a JEOL, JES-RE2X electron spin resonance spectrometer. To obtain the "g" value, MnSO<sub>4</sub> was used as reference standard material. The intensity of ESR was calculated using a computer software program ES-PRIT ESR DATA SYSTEM (version 1.6). The XPS measurement was carried out using an AMICUS photoelectron spectrometer equipped with an Mg  $K_{\alpha}$  X-ray as a primary excitation and KRATOS VISION2 software. XPS elemental spectra were acquired with 0.1 eV energy step at a pass energy of 75 kV. The background pressure during the spectra accumulation was typically  $10^{-6}$  Pa. Detailed spectral scans were taken over Ti 2p, O 1s, Zr 3d, Si 2p and C 1s regions. All the binding energies were referenced to the C1s peak at 285.0 eV of the surface adventitious carbon.

## 2.5. Photocatalytic activity measurement

In photocatalytic experiments, the catalysts were packed into a 60 cm long 9 mm diameter horizontal quartz fixed bed reactor. The weights of the catalysts were kept constant at 0.40 g, and in all cases the illuminated length of catalyst was identical. High purity grade air containing 0.1 vol.% ethylene was continuously

fed at a constant flow rate with a gas hourly space velocity (GHSV) of  $120 \,\mathrm{h}^{-1}$ . An air stream with 0.1 vol.% ethylene was first passed through the reactor without irradiation until reaching gas-solid adsorption equilibrium. Then, UV light ( $\lambda = 365 \text{ nm}$ ) was irradiated on the surface of the catalyst using 125 W mercury lamp (Philips, HPLN). The distance between the lamp and the reactor was 20 cm. The light irradiance at surface of the reactor was 0.65 mW/cm<sup>2</sup>. The irradiated sample area was approximately 4 cm<sup>2</sup>. Analysis of the ethylene feed and other hydrocarbon products were conducted with an on-line SHI-MADZU GC-14B gas chromatograph equipped with a flame ionization detector (FID) and VZ-10 column. The retention time of ethylene was approximately around 30 s. Other degradation products such as CO and CO<sub>2</sub> were detected using SHIMADZU GC-8A gas chromatograph equipped with a thermal conductivity detector (TCD) equipped with Molecular sieve 5A and Poropak-Q columns, respectively. Steady state was achieved within ca. 3 h after illumination.

#### 3. Results and discussion

#### 3.1. Textural properties of the $TiO_2$ photocatalysts

X-ray diffraction patterns of the base TiO<sub>2</sub> and the metal-doped TiO<sub>2</sub> samples with metal/titanium molar ratio 0.1 are shown in Fig. 1. All the samples exhibited the XRD patterns of only pure anatase phase TiO<sub>2</sub> without any contamination of other phases. However, the peak intensities of anatase TiO<sub>2</sub> decreased with the insertion of second metal due probably to the formation of amorphous phases [37]. No diffraction lines of zirconia or silica were observed due to the very small amount and/or the small crystallite sizes of the dopant phase lower than XRD detection limit. Incorporation of Zr and Si into anatase TiO<sub>2</sub> structure has been reported by others [38,39]. The average crystallite sizes of TiO<sub>2</sub> samples were determined from the full

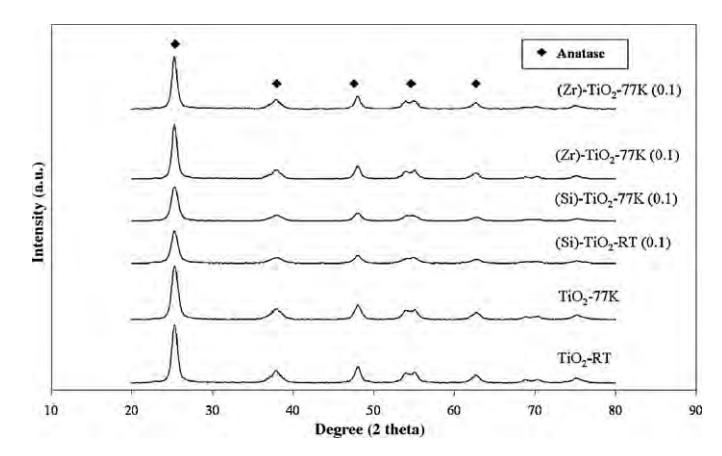


Fig. 1. X-ray diffraction patterns of pure TiO<sub>2</sub> and metal-doped TiO<sub>2</sub>.

width at half maximum of the XRD peak at  $2\theta = 25^{\circ}$  using Scherrer's equation. As shown in Table 1, addition of a small amount of Si or Zr to TiO<sub>2</sub> powder, the average crystallite size of TiO<sub>2</sub> decreased slightly from 11.0 to 9.0 nm. It is likely that second metal doping suppressed crystal growth of TiO2 thus smaller crystallite sizes were obtained. According to the BET analysis, it can be observed that the Si- and Zr-doped TiO<sub>2</sub> samples have larger BET surface area than pure TiO<sub>2</sub>. The effect was more pronounced for the Si-doped than the Zr-doped ones. The increase in BET surface area can be related with the lower degree of crystallisation of the mixed oxides with respect to the pure TiO<sub>2</sub>. According to Daturi et al. [40], a maximum increase of BET surface area for Zr-modified TiO2 was observed at the 0.5:0.5 atomic ratio. Thus, we can probably say that addition of relatively small amount of dopant (atomic ratio <0.1) in this study did not have much impact on the BET surface area of TiO<sub>2</sub> powders. The BET equivalent particle diameters were also calculated and summarized in Table 1. The BET equivalent particle diameters were found to be larger than

Table 1 Physical properties and activities of Si- and Zr-doped  $TiO_2$  samples synthesized by solvothermal method.

Sample nomenclature	BET surface area <sup>a</sup> (m <sup>2</sup> /g)	${d_{ m XRD}}^{ m b}$ (nm)	$d_{\mathrm{BET}}^{}^{}}}$ (nm)	Intensity of ESR/BET	Ethylene conversion <sup>d</sup> (%)	TON <sup>e</sup>
TiO <sub>2</sub> -RT	93	10.6	16.8	47	21.5	3.6
TiO <sub>2</sub> -77 K	97	10.6	16.1	257	34.6	5.6
(Si)-TiO <sub>2</sub> -RT (0.002)	159	9.0	9.8	77	23.5	2.3
(Si)-TiO <sub>2</sub> -77 K (0.002)	156	9.0	10.0	199	31.5	3.2
(Si)-TiO <sub>2</sub> -RT (0.005)	133	8.9	11.7	144	27.9	3.3
(Si)-TiO <sub>2</sub> -77 K (0.005)	136	8.6	11.5	213	32.4	3.7
(Si)-TiO <sub>2</sub> -RT (0.1)	133	9.0	11.7	56	22.1	2.6
(Si)-TiO <sub>2</sub> -77 K (0.1)	136	8.4	11.5	62	22.5	2.6
$(Zr)$ - $TiO_2$ - $RT (0.002)$	95	9.5	16.4	111	25.7	4.2
(Zr)-TiO <sub>2</sub> -77 K (0.002)	99	9.7	15.8	225	33.2	5.2
(Zr)-TiO <sub>2</sub> -RT $(0.005)$	101	7.7	15.5	245	34.5	5.3
(Zr)-TiO <sub>2</sub> -77 K (0.005)	106	7.8	14.7	322	39.5	5.8
(Zr)-TiO <sub>2</sub> -RT (0.1)	104	8.2	15.0	57	22.2	3.3
(Zr)-TiO <sub>2</sub> -77 K $(0.1)$	105	8.4	14.9	79	23.5	3.5

<sup>&</sup>lt;sup>a</sup> Determined using BET method.

<sup>&</sup>lt;sup>b</sup> Determined using Scherrer's equation.

Calculated from  $d_{\text{BET}} = 6/(\text{SSA} \times \rho_{\text{p}})$ , where  $\rho_{\text{p}}$  is the weighted density of TiO<sub>2</sub> (3840 kg/m<sup>3</sup>).

<sup>&</sup>lt;sup>d</sup> Photocatalytic reaction was carried out at 313-328 K, 1 bar, and 0.1% ethylene in air.

e Turnover number.

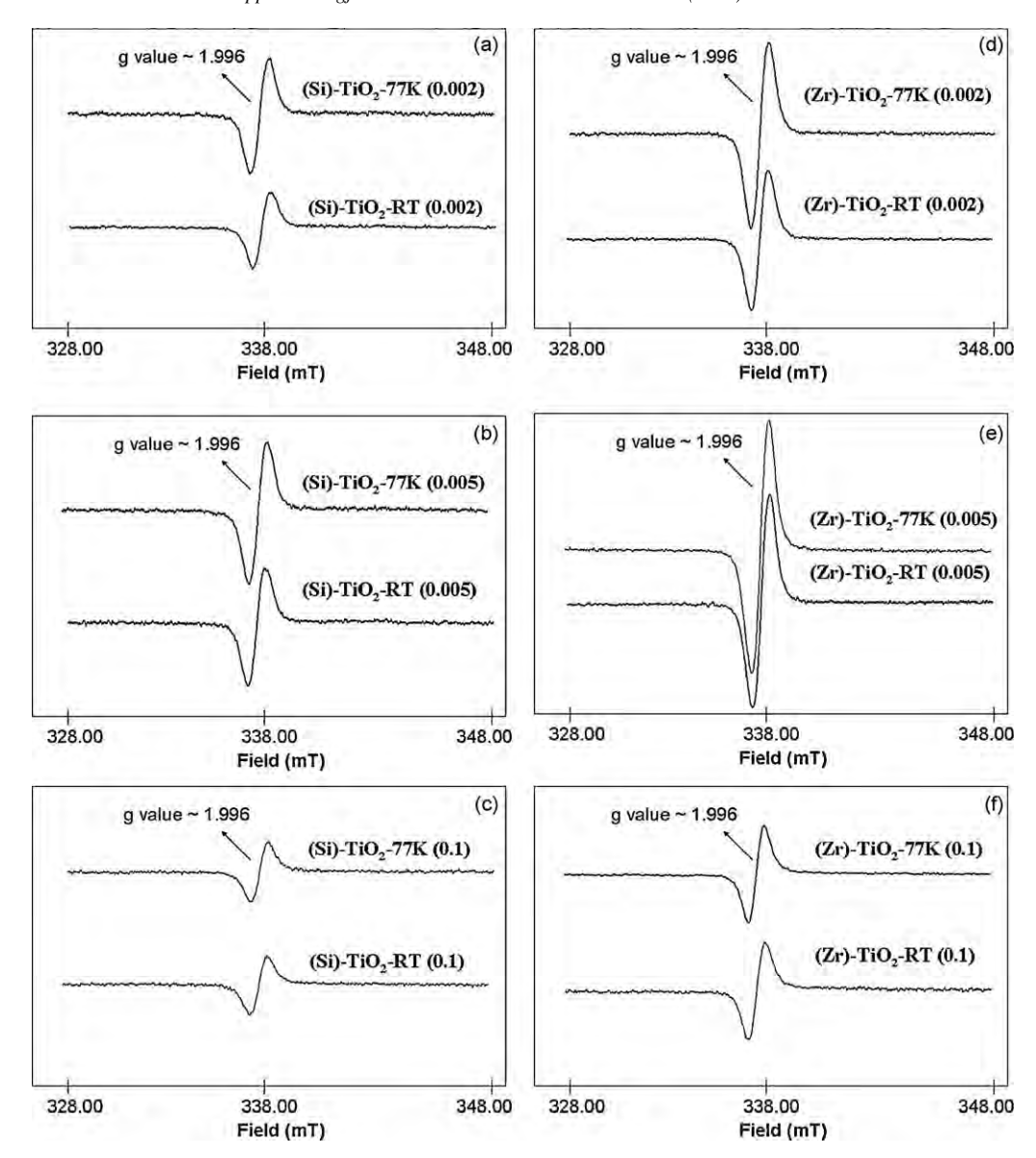


Fig. 2. ESR spectra of (a) 0.002 Si-doped TiO<sub>2</sub>, (b) 0.005 Si-doped TiO<sub>2</sub>, (c) 0.1 Si-doped TiO<sub>2</sub>, (d) 0.002 Zr-doped TiO<sub>2</sub>, (e) 0.005 Zr-doped TiO<sub>2</sub>, and (f) 0.1 Zr-doped TiO<sub>2</sub>.

the ones calculated from XRD results. This can be explained by the agglomeration of  $TiO_2$  particles, which could inhibit the adsorption of  $N_2$  molecules.

It is believed that the process of annealing or calcination has shown to result in a variety of surface defects, strains, and reconstructions of materials [41]. So, the variation of cooling temperature was applied as a post-synthesis treatment with the aim to create more defects on the  $TiO_2$  surface and as a consequence, improve their photocatalytic activities. Moreover, the post-synthesis treatment in cooling temperature did not significantly alter the specific surface area and the average crystallite size of the  $TiO_2$  (see Table 1).

## 3.2. Electron spin resonance spectroscopy (ESR) study

The number of defective sites of TiO<sub>2</sub> or Ti<sup>3+</sup> was determined using electron spin resonance spectroscopy

technique and the results are shown in Fig. 2. Nakamura et al. [42] and Serwicka [43] reported two signals occurring on the surface of TiO2 during ESR analysis without illumination indicating: (i) the surface Ti<sup>3+</sup> and (ii) the bulk defect. Nakaoka and Nosaka [44] reported six signals in ESR measurement on the surface of titania namely (i) Ti<sup>4+</sup>OH<sup>-</sup>, (ii) surface Ti<sup>3+</sup>, (iii) adsorbed oxygen (O<sup>2-</sup>), (iv) Ti<sup>4+</sup>O<sup>2-</sup>, (v) inner Ti<sup>3+</sup>, and (vi) adsorbed water. In the present study, all the TiO2 samples exhibited similar ESR spectra, in which mainly one signal at the g value of 1.996 was observed. According to Nakaoka et al. [42], this peak was attributed to the Ti<sup>3+</sup> sites on surface TiO<sub>2</sub>. It is clearly seen that the Zrdoped TiO2 exhibited higher intensity of the ESR signals than the Si-doped ones. The intensity of ESR spectra per surface area of the TiO<sub>2</sub> is given in Table 1. The results indicate that Zr-doped TiO2 possessed higher concentration of Ti<sup>3+</sup> defective sites than Si-doped TiO<sub>2</sub>.

Table 2 XPS binding energies (eV) and FWHM (eV) values of Si- and Zr-doped  $TiO_2$  catalysts.

Sample nomenclature	Ti 2p		O 1s		Zr 3d		Si 2p	
	BE	FWHM	BE	FWHM	BE	FWHM	BE	FWHM
TiO <sub>2</sub> -RT	459.3	1.7	530.8	1.5	_	_	_	_
TiO <sub>2</sub> -77 K	459.2	1.7	530.6	1.4	_	_	_	_
(Si)-TiO <sub>2</sub> -RT (0.002)	458.8	1.4	530.1	1.5	_	_	102.1	2
(Si)-TiO <sub>2</sub> -77 K (0.002)	458.9	1.4	530.2	1.5	_	_	102	1.9
(Si)-TiO <sub>2</sub> -RT (0.005)	458.3	1.4	530.1	1.5	_	_	102.1	2.1
(Si)-TiO <sub>2</sub> -77 K (0.005)	458.4	1.4	530.2	1.5	_	_	102.1	2.3
$(Si)$ - $TiO_2$ - $RT(0.1)$	458.5	1.5	530.2	1.6	_	_	102.3	2.2
(Si)-TiO <sub>2</sub> -77 K (0.1)	458.6	1.5	530.3	1.6	_	_	102.4	2.1
(Zr)-TiO <sub>2</sub> -RT $(0.002)$	458.5	1.4	530.2	1.5	182.1	1.8	_	_
(Zr)-TiO <sub>2</sub> -77 K $(0.002)$	458.3	1.4	530.1	1.6	182	2	_	_
(Zr)-TiO <sub>2</sub> -RT $(0.005)$	458.3	1.5	530.3	1.4	182.1	1.9	_	_
(Zr)-TiO <sub>2</sub> -77 K (0.005)	458.6	1.4	530.3	1.6	182.4	1.8	_	-
$(Zr)$ - $TiO_2$ - $RT$ $(0.1)$	458.2	1.4	530.1	1.5	182.3	2.2	_	_
(Zr)-TiO <sub>2</sub> -77 K $(0.1)$	458.4	1.4	530.3	1.5	182.1	2.1	-	-

#### 3.3. X-ray photoelectron spectroscopy (XPS) study

It is well known that XPS is a surface probe detecting electrons that are generated from a depth of a few nanometers on the surface of the sample. To make the XPS results comparable to those of ESR measurement, elemental composition and chemical states on the surface of metal-doped TiO2 samples that were subjected to two different cooling temperatures were studied. The binding energy values and the full width at half maximum (FWHM) values of Zr 3d, O 1s, Si 2p and Ti 2p photoelectron peaks as determined by XPS of the various TiO<sub>2</sub> samples are summarized in Table 2. The binding energies for Si 2p and Zr 3d levels are in agreement with those reported for pure SiO<sub>2</sub> [45] and ZrO<sub>2</sub> [46] at 103.0 and 183.5 eV, respectively. No significant variation has been observed for these elements over the metal-doped TiO<sub>2</sub> samples. However, the binding energy of the Ti 2p band for the metal-doped samples was found to be lower than that of the pure TiO2. For better comparison, the XPS bands of Ti 2p for Si- and Zr-doped TiO<sub>2</sub> are shown in Fig. 3. Normally, the Ti 2p XPS spectra of TiO<sub>2</sub> sample show two shoulder peaks at lower binding energy (Ti  $2p_{3/2}$ ) and higher binding energy (Ti  $2p_{1/2}$ ), respectively, in line with the earlier reports by Mukhopadhyay

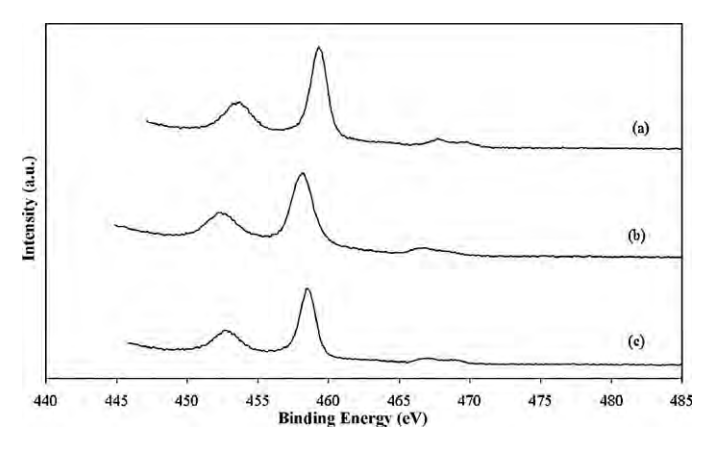


Fig. 3. Ti 2p XPS spectra of various  $TiO_2$  samples: (a)  $TiO_2$ -RT, (b) 0.1-(Zr)- $TiO_2$ -RT, and (c) 0.1-(Si)- $TiO_2$ -RT.

and Garofalini [47]. The presence of defect is visible as a shoulder in the XPS spectra which was assigned to Ti<sup>3+</sup> oxidation state. From Fig. 3, the binding energy of Ti 2p electrons was found to be lower than the value normally published for Ti<sup>4+</sup> ions in TiO<sub>2</sub> (459.2 eV) [48,49]. However, the Ti 2p spectrum was slightly broadened and a shoulder band appeared at 1.6 eV lower than the Ti<sup>4+</sup> binding energy, this could be associated with the Ti<sup>3+</sup> defect state [50].

#### 3.4. Photocatalytic activity test

The photocatalytic activity of the  ${\rm TiO_2}$  and metal-doped  ${\rm TiO_2}$  samples was tested for the photocatalytic decomposition of ethylene in gas-phase under UV illumination. Under these conditions, the only products detected by gas chromatography were  ${\rm CO_2}$  and  ${\rm H_2O}$ . The mechanism of photocatalytic decomposition of ethylene has been reported by many researchers [13,51]. The mechanism is believed to involve absorption of an UV photo by  ${\rm TiO_2}$  to produce an electron-hole pair. Both hole and electron play an important role on creating the reaction intermediate, which react further and form  ${\rm CO_2}$  as the final product.

Photocatalytic activities of the TiO<sub>2</sub> samples with different proportions of Si/Ti and Zr/Ti were evaluated in the decomposition of ethylene in gas-phase and the results are shown in Table 1. In our previous studies [35,36], the effects of cooling media and temperature on the photocatalytic activities of solvothermal-derived TiO2 have been reported. It was found in this study that the photocatalytic activity of the metal-doped TiO<sub>2</sub> cooled down in different cooling temperatures is also evidently different. The ethylene conversion results show that the metal-doped TiO<sub>2</sub> at lower amounts of metal exhibited higher photocatalytic activity than the pure titania. Ethylene conversions at steady state for the metal-doped TiO<sub>2</sub> samples after cooling at room temperature were ranging from ca. 22% to 39% while pure TiO<sub>2</sub> sample under similar reaction conditions gave ca. 21% ethylene conversion. The turnover number (TON) was calculated from the ratio of the number of photoinduced transformation for a given period of time and the number of

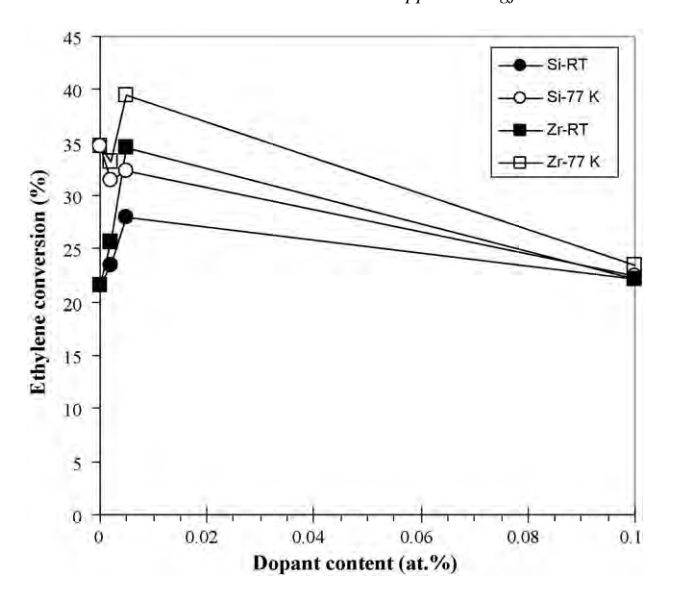


Fig. 4. Plot between ethylene conversion at steady state (ca.  $3\,\mathrm{h}$ ) and dopant content.

photocatalytic sites (surface area). From Table 1, TONs for all the catalysts were greater than unity, the (photo) catalytic character of the reaction or process was confirmed.

The photocatalytic activity of metal-doped TiO<sub>2</sub> depended on the cooling temperature applied after calcination. It was found that metal-doped TiO2 samples cooled at lower temperature exhibited higher photocatalytic activity than those cooled in high temperature ones. For example, the ethylene conversion of 0.005 Zr-doped TiO<sub>2</sub> was 34.5% and 39.5% for the sample cooled down at room temperature and at 77 K, respectively. Additionally, the metal content has an obvious effect on the activity of the metal-modified TiO<sub>2</sub> catalysts. The plots of ethylene conversion versus metal content (Fig. 4) show that there existed an optimal metal content (atomic ratio) to achieve the highest photocatalytic activity. If the concentration of metal is too low, the promotional effect is not significant while for high metal content, the active sites of TiO<sub>2</sub> may be blocked and lower catalytic activity would be obtained. An optimum metal content on photocatalytic activity of the Zr- and Si-doped TiO<sub>2</sub> has also been suggested by Fu et al. [28] for much higher metal loading range. The specific activity of TiO<sub>2</sub> synthesized by sol-gel method was enhanced by the addition of SiO<sub>2</sub> (optimum at 16 wt.%) or ZrO<sub>2</sub> (optimum at 12 wt.%). The increase in activity of the modified catalysts was attributed to both an increase in surface area (ranging between 250 and 400 m<sup>2</sup>/g) and chemical change on the catalyst surface.

The results in this study show that for a similar metal content, the Zr-doped TiO<sub>2</sub> exhibited higher photocatalytic activity than the Si-doped ones. However, one may notice that the Si-doped TiO<sub>2</sub> had larger BET surface areas than the Zr-doped ones and in general, anatase TiO<sub>2</sub> nanoparticles with higher specific surface area typically exhibit higher photocatalytic activity. The increase of surface area means the increase of the number of active sites on which the electron acceptor and donor are adsorbed and participate in the photocatalytic reaction. In our present study, the presence of

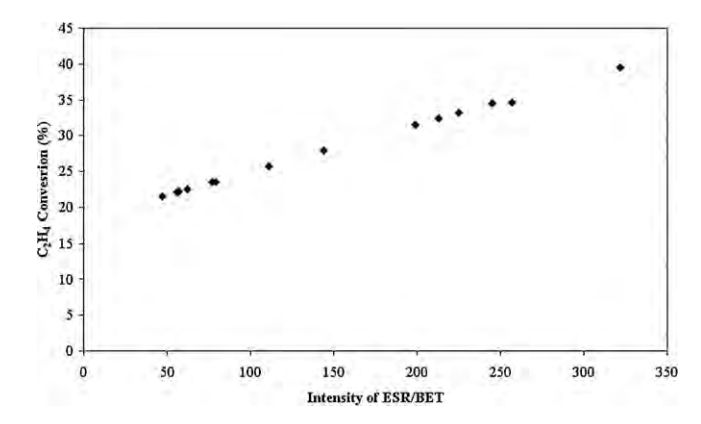


Fig. 5. Photocatalytic activity at steady state (ca. 3 h) of metal-doped TiO<sub>2</sub> for ethylene decomposition as a function of the intensity of ESR/BET.

very small amount of metal dopants caused only a slight change in the  $TiO_2$  crystallite and BET surface area (ranging from 7.8 to 10.6 nm and corresponding surface area 95 to 159 m²/g). The photocatalytic activity of  $TiO_2$  did not depend solely on the surface area but were found to be correlated well with the concentration of  $Ti^{3+}$  on the catalyst surface as illustrated by a linear ascending trend of the ethylene conversion and the amount of  $Ti^{3+}$ /surface area of the catalysts in Fig. 5. It should also be noted that the effect of post-treatment on enhancing the concentration of  $Ti^{3+}$  on the  $TiO_2$  was more pronounced than the addition of metal dopants.

#### 4. Conclusions

The Si- and Zr-doped TiO<sub>2</sub> with Si/Ti and Zr/Ti molar ratios ranging from 0.002% to 0.1% were prepared via the solvothermal method using titanium n-butoxide as the titanium precursor and toluene as the solvent. It was found that selection of a suitable second metal doping can enhance photocatalytic activity of the TiO<sub>2</sub>. Based on ESR and XPS analyses, the improved photocatalytic activity of the TiO<sub>2</sub> is suggested to be due to the presence of Ti<sup>3+</sup> defect sites on the surface of TiO<sub>2</sub>. Moreover, a post-synthesis treatment by cooling in air at 77 K effectively enhanced the amount of Ti<sup>3+</sup> and photocatalytic activity of the TiO<sub>2</sub> and the metal-doped TiO<sub>2</sub>.

## Acknowledgements

The financial supports from the Thailand Research Fund (TRF) and Commission on Higher Education are gratefully acknowledged.

#### References

- C.H. Chen, E.M. Kelder, J. Schoonman, Electrostatic sol-spray deposition (ESSD) and characterization of nanostructured TiO<sub>2</sub> thin films, Thin Solid Films 342 (1999) 35–41.
- [2] A. Fujwashima, T.N. Rao, D.A. Tryk, Titanium dioxide photocatalysis, J. Photochem. Photobiol. C: Photochem. Rev. (2000) 1–21.
- [3] B. Ohtani, Y. Ogawa, S. Nishimoto, Photocatalytic activity of amorphousanatase mixture of titanium(IV) oxide particles suspended in aqueous solutions, J. Phys. Chem. B 101 (1997) 3746–3752.

- [4] K.M. Reddy, C.V.G. Reddy, S.V. Manorama, Preparation, characterization, and spectral studies on nanocrystalline anatase TiO<sub>2</sub>, J. Solid State Chem. 158 (2001) 180–186.
- [5] T. Toyoda, H. Kawano, Q. Shen, A. Kotera, M. Ohmori, Characterization of electronic states of TiO<sub>2</sub> powders by photoacoustic spectroscopy, Jpn. J. Appl. Phys. Part 1 39 (2000) 3160–3163.
- [6] C. Shifu, C. Gengyu, The effect of different preparation conditions on the photocatalytic activity of TiO<sub>2</sub>·SiO<sub>2</sub>/beads, Surf. Coat. Technol. 200 (2006) 3637–3643.
- [7] K. Suriye, P. Praserthdam, B. Jongsomjit, Impact of Ti<sup>3+</sup> present in titania on characteristics and catalytic properties of the Co/TiO<sub>2</sub> catalyst, Ind. Eng. Chem. Res. 44 (2005) 6599–6604.
- [8] G. Lu, A. Linsebigler, J.T. Yates Jr., Ti<sup>3+</sup> defect sites on TiO<sub>2</sub>(1 1 0): production and chemical detection of active sites, J. Phys. Chem. 98 (1994) 11733–11738.
- [9] V. Henrich, R.L. Kurtz, Surface electronic structure of TiO<sub>2</sub>: atomic geometry, ligand coordination, and the effect of adsorbed hydrogen, Phys. Rev. B 23 (1981) 6280–6287.
- [10] U. Diebold, J. Lehman, T. Mahmoud, M. Kuhn, G. Leonardelli, W. Hebenstreit, M. Schmid, P. Varga, Intrinsic defects on a TiO<sub>2</sub>(1 1 0)(1 × 1) surface and their reaction with oxygen: a scanning tunneling microscopy study, Surf. Sci. 411 (1998) 137–153.
- [11] R. Schaub, P. Thostrup, N. Lopez, E. Laegsgaard, I. Stensgaard, J.K. Norskov, F. Besenbacher, Oxygen vacancies as active sites for water dissociation on rutile TiO<sub>2</sub>(1 1 0), Phys. Rev. Lett. 87 (2001) 2661041– 2661044.
- [12] R. Schaub, E. Wahlstrom, A. Ronnau, E. Laegsgaard, I. Stensgaard, F. Besenbacher, Oxygen-mediated diffusion of oxygen vacancies on the TiO<sub>2</sub>(1 1 0) surface, Science 299 (2003) 377–379.
- [13] S. Yamazaki, S. Tanaka, H. Tsukamoto, Kinetic studies of oxidation of ethylene over a TiO<sub>2</sub> photocatalyst, J. Photochem. Photobiol. A 121 (1999) 55–61.
- [14] D.-R. Park, J. Zhang, K. Ikenue, H. Yanashita, M. Anpo, Photocatalytic oxidation of ethylene to CO<sub>2</sub> and H<sub>2</sub>O on ultrafine powdered TiO<sub>2</sub> photocatalysts in the presence of O<sub>2</sub> and H<sub>2</sub>O, J. Catal. 185 (1999) 114–119.
- [15] F.B. Li, X.Z. Li, Photocatalytic properties of gold/gold ion-modified titanium dioxide for wastewater treatment, Appl. Catal. A 228 (2002) 15–27.
- [16] F.B. Li, X.Z. Li, C.H. Ao, S.C. Lee, M.F. Hou, Enhanced photocatalytic degradation of VOCs using Ln<sup>3+</sup>-TiO<sub>2</sub> catalysts for indoor air purification, Chemosphere 59 (2005) 787–800.
- [17] W. Kongsuebchart, P. Praserthdam, J. Panpranot, A. Sirisuk, P. Supphasrirongjaroen, C. Satayaprasert, Effect of crystallite size on the surface defect of nano-TiO<sub>2</sub> prepared via solvothermal synthesis, J. Cryst. Growth 297 (2006) 234–238.
- [18] K. Suriye, P. Praserthdam, B. Jongsomjit, Control of Ti<sup>3+</sup> surface defect on TiO<sub>2</sub> nanocrystal using various calcination atmospheres as the first step for surface defect creation and its application in photocatalysis, Appl. Surf. Sci. 253 (2007) 3849–3855.
- [19] K.H. Yoon, J.S. Noh, C.H. Kwon, M. Muhammed, Photocatalytic behavior of TiO<sub>2</sub> thin films prepared by sol-gel process, Mater. Chem. Phys. 95 (2006) 79–83.
- [20] C.H. Kwon, H. Shin, J.H. Kim, W.S. Choi, K.H. Yoon, Degradation of methylene blue via photocatalysis of titanium dioxide, Mater. Chem. Phys. 86 (2004) 78–82.
- [21] C.-S. Kim, B.K. Moon, J.-H. Park, S.T. Chung, S.-M. Son, Synthesis of nanocrystalline TiO<sub>2</sub> in toluene by a solvothermal route, J. Cryst. Growth 254 (2003) 405–410.
- [22] Y.V. Kolen'ko, A.A. Burukhin, B.R. Churagulov, N.N. Oleynikov, Synthesis of nanocrystalline TiO<sub>2</sub> powders from aqueous TiOSO<sub>4</sub> solutions under hydrothermal conditions, Mater. Lett. 57 (2003) 1124–1129.
- [23] O. Carp, C.L. Huisman, A. Reller, Photoinduced reactivity of titanium dioxide, Prog. Solid State Chem. 32 (2004) 33–177.
- [24] S. Kongwudthiti, P. Praserthdam, P.L. Silveston, M. Inoue, Influence of synthesis conditions on the preparation of zirconia powder by the glycothermal method, Ceram. Int. 29 (2003) 807–814.

- [25] O. Mekasuwandumrong, P.L. Silveston, P. Praserthdam, M. Inoue, V. Pavarajarn, W. Tanakulrungsank, Synthesis of thermally stable micro spherical χ-alumina by thermal decomposition of aluminum isopropoxide in mineral oil, Inorg. Chem. Commun. 6 (2003) 930–934.
- [26] K.Y. Jung, S.B. Park, Enhanced photoactivity of silica-embedded titania particles prepared by sol–gel process for the decomposition of trichloroethylene, Appl. Catal. B: Environ. 25 (2000) 249–256.
- [27] S.R. Kumar, C. Suresh, K.A. Vasudevan, N.R. Suja, P. Mukundan, K.G.K. Warrier, Phase transformation in sol–gel titania containing silica, Mater. Lett. 38 (1999) 161–166.
- [28] X. Fu, L.A. Clark, Q. Yang, M.A. Anderson, Enhanced photocatalytic performance of titania-based binary metal oxides: TiO<sub>2</sub>/SiO<sub>2</sub> and TiO<sub>2</sub>/ ZrO<sub>2</sub>, Environ. Sci. Technol. 30 (1996) 647–653.
- [29] H. Yang, D. Zhang, L. Wang, Synthesis and characterization of tungsten oxide-doped titania nanocrystallites, Mater. Lett. 57 (2002) 674–678.
- [30] T. López, F. Rojas, R.A. -Katz, F.F. Galindo, A. Balankin, A. Buljan, Porosity, structural and fractal study of sol-gel TiO<sub>2</sub>-CeO<sub>2</sub> mixed oxides, J. Solid State Chem. 177 (2004) 1873–1885.
- [31] S. Sivakumar, C.P. Sibu, P. Mukundan, P.K. Pillai, K.G.K. Warrier, Nanoporous titania-alumina mixed oxides—an alkoxide free sol-gel synthesis, Mater. Lett. 58 (2004) 2664–2669.
- [32] M. Hirano, Ch. Nakahara, K. Ota, O. Tanaike, M. Inagaki, Photoactivity and phase stability of ZrO<sub>2</sub>-doped anatase-type TiO<sub>2</sub> directly formed as nanometer-sized particles by hydrolysis under hydrothermal conditions, J. Solid State Chem. 170 (2003) 39–47.
- [33] P. Cheng, M. Zheng, Y. Jin, Q. Huang, M. Gu, Preparation and characterization of silica-doped titania photocatalyst through sol–gel method, Mater. Lett. 57 (2003) 2989–2994.
- [34] W. Payakgul, O. Mekasuwandumrong, V. Pavarajarn, P. Praserthdam, Effects of reaction medium on the synthesis of TiO<sub>2</sub> nanocrystals by thermal decomposition of titanium (IV) n-butoxide, Ceram. Int. 31 (2005) 391–397.
- [35] P. Supphasrirongjaroen, P. Praserthdam, J. Panpranot, D. Na-Ranong, O. Mekasuwandumrong, Effect of quenching medium on photocatalytic activity of nano-TiO<sub>2</sub> prepared by solvothermal method, Chem. Eng. J. 138 (2008) 622–627.
- [36] P. Supphasrirongjaroen, W. Kongsuebchart, J. Panpranot, O. Mekasuwandumrong, C. Satayaprasert, P. Praserthdam, Dependence of quenching process on the photocatalytic activity of solvothermal-derived TiO<sub>2</sub> with various crystallite sizes, Indust. Eng. Chem. Res. 47 (2008) 693–697.
- [37] M. Yoshinaka, K. Hirota, O. Yamaguchi, Formation and sintering of TiO<sub>2</sub> (anatase) solid solution in the system TiO<sub>2</sub>–SiO<sub>2</sub>, J. Am. Ceram. Soc. 80 (1997) 2749–2753.
- [38] M. Inoue, K. Sato, T. Nakamura, T. Inui, Glycothermal synthesis of zirconia–rare earth oxide solid solutions, Catal. Lett. 65 (2000) 79–83.
- [39] S. Iwamoto, W. Tanakulrungsank, M. Inoue, K. Kagawa, P. Praserthdam, Synthesis of large-surface area silica-modified titania ultrafine particles by the glycothermal method, J. Mater. Sci. Lett. 19 (2000) 1439–1443.
- [40] M. Daturi, A. Cremona, F. Milella, G. Buca, E.J. Vogna, Characterisation of zirconia–titania powders prepared by coprecipitation, Eur. Ceram. Soc. 18 (1998) 1079–1087.
- [41] M.A. Henderson, An HREELS and TPD study of water on TiO<sub>2</sub>(1 1 0): the extent of molecular versus dissociative adsorption, Surf. Sci. 355 (1996) 151–166.
- [42] I. Nakamura, N. Negishi, S. Kutsuna, T. Ihara, S. Sugihara, K. Takeuchi, Role of oxygen vacancy in the plasma-treated TiO<sub>2</sub> photocatalyst with visible light activity for NO removal, J. Mol. Catal. A 161 (2000) 205–212.
- [43] E. Serwicka, ESR study on the interaction of water vapour with polycrystalline TiO<sub>2</sub> under illumination, Colloids Surf. 13 (1985) 287–293.
- [44] Y. Nakaoka, Y. Nosaka, ESR Investigation into the effects of heat treatment and crystal structure on radicals produced over irradiated TiO<sub>2</sub> powder, J. Photochem. Photobiol. A 110 (1997) 299–305.
- [45] H.J.M. Bosman, A.P. Pijpers, A.W.M.A. Jaspers, An X-ray photoelectron spectroscopy study of the acidity of SiO<sub>2</sub>–ZrO<sub>2</sub> mixed oxides, J. Catal. 161 (1996) 551–559.
- [46] Z. Bastl, A.I. Senkevich, I. Spirovova, V. Vrtilkova, Angle-resolved corelevel spectroscopy of Zr1Nb alloy oxidation by oxygen, water and hydrogen peroxide, Surf. Interface Anal. 34 (2002) 477–480.

- [47] S. Mukhopadhyay, S. Garofalini, Surface studies of  $TiO_2 \cdot SiO_2$  glasses by X-ray photoelectron spectroscopy, J. Non-Cryst. Solids 126 (1990) 202–208.
- [48] P.M. Kumar, S. Badrinarayanan, M. Sastry, Nanocrystalline TiO<sub>2</sub> studied by optical, FTIR and X-ray photoelectron spectroscopy: correlation to presence of surface states, Thin Solid Films 358 (2000) 122–130.
- [49] Z. Wei, Q. Xin, X. Guo, E.L. Sham, P. Grange, B. Delmon, Titaniamodified hydrodesulphurization catalysts. I. Effect of preparation tech-
- niques on morphology and properties of  ${\rm TiO_2-Al_2O_3}$  carrier, Appl. Catal. 63 (1990) 305–317.
- [50] L.Q. Wang, D.R. Baer, M.H. Engelhard, A.N. Schultz, Adsorption of liquid and vapor water on TiO<sub>2</sub>(1 1 0) surfaces: the role of defects, Surf. Sci. 344 (1995) 237–250.
- [51] A. Sirisuk, C.G. Hill, M.A. Anderson, Photocatalytic degradation of ethylene over thin films of titania supported on glass rings, Catal. Today 54 (1999) 159–164.



# Effect of Milling on the Formation of Nanocrystalline $\chi$ -Al<sub>2</sub>O<sub>3</sub> from Gibbsite

Wasu Chaitree,<sup>‡</sup> Sirithan Jiemsirilers,<sup>§</sup> Okorn Mekasuwandumrong,<sup>¶</sup> Piyasan Praserthdam,<sup>‡</sup> Tawatchai Charinpanitkul,<sup>‡</sup> and Joongjai Panpranot<sup>†,‡</sup>

<sup>‡</sup>Department of Chemical Engineering, Faculty of Engineering, Chulalongkorn University, Bangkok 10330, Thailand

§Department of Materials Science, Faculty of Science, Chulalongkorn University, Bangkok 10330, Thailand

Department of Chemical Engineering, Faculty of Engineering and Industrial Technology, Silpakorn University, Nakorn Phathom 73000, Thailand

Gibbsite (FG) with mean particle diameter ( $d_{50} = 13 \mu m$ ) was milled in an attrition mill for 12 and 24 h using alumina balls as grinding media and calcined at different temperatures in the range of 350°-600°C. The properties of the alumina obtained were determined by X-ray diffraction, N<sub>2</sub> physisorption, thermogravimetric/differential thermal analyses, and transmission electron microscopy. Without milling, the alumina obtained normally contained the mixed phases between  $\gamma$ - and  $\gamma$ -phase alumina. On the other hand, high purity of nanocrystalline  $\chi$ phase alumina (100 wt%) can be produced by calcination of the 24-h milled FG at 600°C. The isothermal kinetics measurements revealed that the rate constant (k) for phase transformation increased as the particle size of gibbsite decreased and the calculated activation energy for transformation from FG to alumina decreased from 20.6 to 14.7 and 6.8 kJ/mol after milling for 12 and 24 h, respectively. The physical properties of nanocrystalline y-alumina obtained by the calcination of milled FG were comparable to those produced by the solvothermal method. The present results offer a simple way to prepare a large amount of pure  $\chi$ -phase alumina for particular industrial applications.

#### I. Introduction

A LUMINA (Al<sub>2</sub>O<sub>3</sub>) is one of the most common crystalline materials used as catalysts, catalyst supports, sorbent, coating, and ceramics. <sup>1-4</sup> Compared with the other oxides, alumina has high surface area, good catalytic activity, high mechanical resistance, good thermal stability, high strength, and toughness. <sup>5-7</sup> There are many methods to synthesize alumina such as solvothermal, <sup>5-7</sup> molten salt synthesis, <sup>8</sup> shock wave action, <sup>9</sup> sol–gel, <sup>10</sup> spray pyrolysis, <sup>11</sup> and thermal decomposition of aluminum hydroxide (boehmite and gibbsite). <sup>12,13</sup>

 $\chi$ -alumina is a crystallographic form of series of alumina, which is normally obtained by dehydration of gibbsite (<200 nm). When it is fired,  $\chi$ -alumina will transform to  $\kappa$ -alumina at a temperature in the range of 650°–750°C and consequently form  $\alpha$ -alumina at a temperature around 1000°C. The  $\chi$ -phase alumina has been used as catalysts and catalyst supports and interesting results were obtained. So reasonable of Co/Al<sub>2</sub>O<sub>3</sub> catalysts increased when the catalysts were prepared on the mixed  $\gamma$ - and  $\chi$ -phase Al<sub>2</sub>O<sub>3</sub>. Khom-in *et al.* Studied the solvothermal-derived nanocrystal-

A. Krell-contributing editor

Author to whom correspondence should be addressed. e-mail: joongjai.p@chula.ac.th

line pure  $\gamma$ -Al<sub>2</sub>O<sub>3</sub>,  $\chi$ -Al<sub>2</sub>O<sub>3</sub>, and mixed-phase  $\gamma$ - and  $\chi$ -Al<sub>2</sub>O<sub>3</sub> in the dehydration reaction of methanol to dimethyl ether. Meephoka *et al.*<sup>17</sup> used both  $\gamma$ - and  $\chi$ -Al<sub>2</sub>O<sub>3</sub> as supports for the preparation of Pt/Al<sub>2</sub>O<sub>3</sub> for CO oxidation reaction. Most of the recent studies show that highly stable nanocrystalline  $\chi$ -Al<sub>2</sub>O<sub>3</sub> can be prepared by the solvothermal method using aluminum iso-propoxide as the precursor. Such a technique, however, is quite tedious and costly because it requires a high-pressure reactor, high temperature, and long reaction time.

Gibbsite ( $\alpha$ -Al(OH)<sub>3</sub>) is a cheap starting material widely used in the transformation of alumina because it can be dehydrated to various phases ( $\chi, \gamma, \theta, \kappa, \alpha$ ). <sup>18,19</sup> Figure 1 shows the diagram of phase transformation of alumina from gibbsite. The transformation route depended on temperature, heating environment, particle size of staring gibbsite, and heating rate. <sup>20</sup> Typically, for small particles (<1  $\mu$ m), the phase transformation process occurs by route 1 and produces  $\chi$ -alumina. <sup>14</sup> In addition, the transformation of bayerite <sup>21</sup> and diaspore <sup>22</sup> to  $\alpha$ -Al<sub>2</sub>O<sub>3</sub> has been studied. It was indicated that  $\chi$ -alumina was not formed from these starting materials.

The formation of  $\chi$ -alumina from gibbsite has been observed in previous works. Jang *et al.*<sup>12</sup> studied the effect of grinding on the phase transformation of gibbsite (starting particle size 64.2  $\mu$ m). The  $\chi$ -phase alumina was observed at 450°C for the sample grind for 5 h (particle size 9.7  $\mu$ m) and completed at around 910°C. Bhattacharya *et al.*<sup>20</sup> investigated the thermal decomposition of fine gibbsite (1.5  $\mu$ m) and the formation of  $\chi$ -alumina appeared at 500°C and its crystal remained until around 800°C. Mercury *et al.*<sup>23</sup> studied the decomposition of synthetic gibbsite by neutron thermodiffractometry and found that  $\chi$ -alumina was formed at the temperature above 500°C. The grinding method is an effective method for the reduction of particle size due to its simplicity, minimal environmental problems, convenient operation, and absence of wastes. Attrition mills are widely used in order to reduce particle size; moreover, they are ideally appropriate for the industrial process due to their high efficiency and availability in large scale.<sup>24</sup>

In the present study, the effect of milling on the phase transformation behavior of gibbsite was extensively investigated. The properties of the alumina obtained were investigated using a laser diffraction-based size analyzer, X-ray diffraction (XRD), thermogravimetric/differential thermal analyses (TGA/DTA), N<sub>2</sub> physisorption, transmission electron microscopy (TEM), and isothermal kinetics measurement.

## II. Experimental Procedure

#### (1) Sample Preparation

Gibbsite with  $d_{50} = 13.0$  m (Merck, Darmstadt, Germany) was used as a starting material. In order to reduce its particle size,

Manuscript No. 27288. Received December 23, 2009; approved April 8, 2010. This work was financially supported by the Thailand Research Fund (TRF) and the Office of Higher Education Commission, Ministry of Education, Thailand.

Gibbsite 
$$\longrightarrow \chi$$
-Al<sub>2</sub>O<sub>3</sub>  $\longrightarrow \kappa$ - Al<sub>2</sub>O<sub>3</sub>  $\longrightarrow \alpha$ - Al<sub>2</sub>O<sub>4</sub> (route I)  
Boehmite  $\longrightarrow \gamma$ -Al<sub>2</sub>O<sub>3</sub>  $\longrightarrow \delta$ - Al<sub>2</sub>O<sub>3</sub>  $\longrightarrow \theta$ -Al<sub>2</sub>O<sub>3</sub>  $\longrightarrow \alpha$ -Al<sub>2</sub>O<sub>4</sub> (route 2)

Fig. 1. Phase transformation of alumina from gibbsite to α-alumina.

the starting material was milled in an attrition mill for 12 and 24 h using alumina balls as grinding media and water as milling fluid. Approximately 100 g of gibbsite and water 300 mL were first mixed in a plastic pot. Alumina balls were weighed before and after milling as well as filled to a half volume of the milling pot. Cooling water was fed continuously in the attrition mill in order to remove heat. Rotational speed of the mill was fixed at 500 rpm. The sample was collected every 2 h and dried at  $105^{\circ}\mathrm{C}$  overnight in an oven to remove water. The dried sample was subsequently milled using a mortar to deagglomerate. The samples were calcined in a tube furnace in air (95 mL/min) by heating to a desired temperature at a rate of  $10^{\circ}\mathrm{C/min}$  and was held at this temperature for 4 h. Then, the samples were cooled down to room temperature in  $N_2$  flow (75 mL/min). The products are designed as  $FG^{**}h^{***}C$  where the first two

The products are designed as FG\*\*h\*\*\*C where the first two asterisks represent the milling time and the latter three asterisks represent the temperature of calcination. The abbreviation of FG is gibbsite (starting material).

#### (2) Characterization

Particle size distribution was measured using a laser diffractionbased size analyzer (reflective index 1.57; Malvern Mastersizer, Worcester Shire, England). All the samples were measured on DI water as dispersant. Dispersion and deagglomeration of particles were ensured by ultrasonic treatment before measurement. XRD analysis was carried out using a Siemens D5000 diffractometer (Karlsruhe, Germany) with  $CuK\alpha$  radiation with Ni filter. The scans were recorded in the  $2\theta$  range of  $10^{\circ}$ – $80^{\circ}$  using a step size of 0.04°. The average crystallite size was estimated using the Scherrer equation. The surface areas of samples were measured by N<sub>2</sub> physisorption using a micromerities chemisorb 2750 (Norcross, GA). TGA/DTA of the ground and unground samples were performed (SDT Analyzer Model Q600 from TA Instruments, New Castle, DE) at a heating rate of 10°C/min in flowing air (100 mL/min). The morphology of samples was investigated by TEM (JEOL JEM 2010, Tokyo, Japan), operating at 200 kV.

The fraction of  $\chi$ -Al<sub>2</sub>O<sub>3</sub> was determined by quantitative XRD analysis, using CaF<sub>2</sub> (Merck, Germany) as an internal standard. A  $0.2000\pm0.0001$  g of sample was placed in a porcelain dish. One tenth of the sample weight of CaF<sub>2</sub> was weighed and mixed with the sample for 5 min. The analysis was calculated by the ratio of the integrated intensities of the 43° (CuK $\alpha$  2 $\theta$ ) of  $\chi$ -Al<sub>2</sub>O<sub>3</sub> and integrated intensities of the 28.1° (CuK $\alpha$  2 $\theta$ ) of CaF<sub>2</sub>. Their ratios were compared against a standard calibration curve of  $\chi$ -Al<sub>2</sub>O<sub>3</sub>/CaF<sub>2</sub>. The calibration curve was determined using a mixture of  $\chi$ -alumina and the same amount of CaF<sub>2</sub>, spanning the range of 20–90 wt%  $\chi$ -alumina.

## (3) Isothermal Kinetic Measurements

The samples were heated at three different temperatures in the range of  $450^{\circ}$ – $600^{\circ}$ C with different holding times. The activation energy for the transformation of gibbsite to  $\chi$ -Al<sub>2</sub>O<sub>3</sub> was estimated by isothermal experiments according to the Arrhenius method. First of all, the value of the rate constant (*k*) was calculated by the Johnsom–Mehl–Avrami equation (Eq. (1)). The value of the rate constant (*k*) was calculated by the Johnsom–Mehl–Avrami equation (Eq. (1)).

$$x(t) = 1 - \exp[-(kt)^n]$$
 (1)

where x is the phase fraction of  $\chi$ -Al<sub>2</sub>O<sub>3</sub> at time (t) and n is the reaction exponent. For analyzing Eq. (1), it can be rewritten in the form of the following Eq. (2).

$$\ln(-\ln(1-x)) = n\ln k + n\ln t \tag{2}$$

The value of k and n can be calculated from the slope and interception of a linear plot of  $\ln t$  and  $\ln(-\ln(1-x))$ . After the value of k is obtained, the activation energy  $(E_a)$  can be estimated by the Arrhenius equation (Eq. (3)).

$$\ln k = \ln A - \frac{E_{\rm a}}{RT} \tag{3}$$

where A is a constant, R is the gas constant (8.314  $J \cdot (K \cdot mol)^{-1}$ ), and T is the working temperature. The value of  $E_a$  can be calculated from the slope of a linear plot of  $\ln k$  and l/T.

#### III. Results and Discussion

#### (1) Particle Size Distribution

The size distributions of gibbsite agglomerates and particles before and after milling are shown in Fig. 2. The median particle size ( $d_{50}$ ) decreased from 13 to 3 µm and 0.6 µm after milling for 12 and 24 h, respectively. Moreover, the unimodal pore size distribution in the starting gibbsite changed to bimodal distribution after milling for 24 h. During milling, the evolution of the distribution of gibbsite is lower, and the mean size decreased.<sup>24</sup> Regarding the starting specific surface area of 25 m<sup>2</sup>/g and microscopic evidence (shown in Fig. 9), the 13 µm is referred to the agglomerate size of the raw powder, whereas the particle size in the as-delivered state was ca. 2-3 μm. It is noted that particle size distribution of the samples did not come from alumina balls because the weight loss of balls was determined to be <1% (initial weight 761.9 g and after milling 759.9 g). Milling run of the alumina balls for 24 h in pure water without gibbsite was carried out in order to determine the typical mean particle size of the wear debris (possible  $\alpha$  seeds and abrasives coming from the grinding media). The result is also shown in Fig. 2 and the typical mean particle size was determined to be 24 m.

## (2) XRD and TGA/DTA Results

Figures 3 and 4 show the results from the TGA and DTA plots, of the gibbsite powder after milling for various times. Two weight processes were detected corresponding to two endothermic and one exothermic process. The decrease in mass at around 150°-600°C, accompanied by the endothermic peaks in DTA

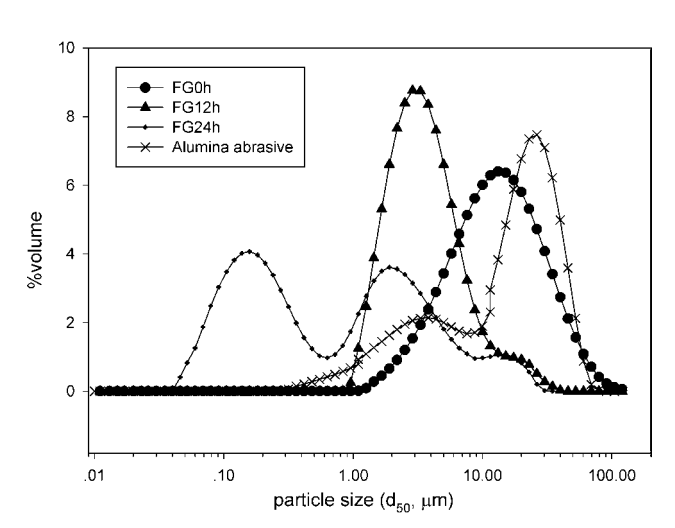


Fig. 2. The particle size distribution of unmilled and milled gibbsite at various milling times.

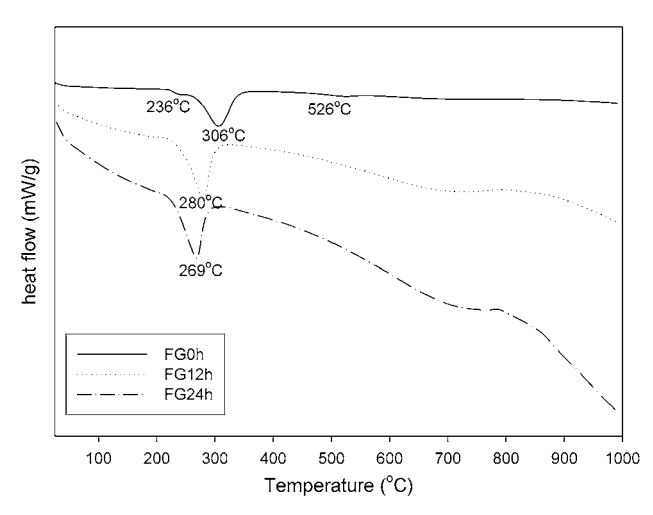


Fig. 3. The thermogravimetric curves of unmilled and milled gibbsite at various milling times.

signal, is attributed to the dehydration of gibbsite to form alumina. The endothermic peak was shifted toward the lower temperature with an increasing milling time, indicating an acceleration of the dehydration of gibbsite by the milling process. The overall weight losses of all the samples were approximately around 35%, which were in good agreement with the calculated value of 34.6% for the dehydration reaction

$$2Al(OH)_3 \rightarrow Al_2O_3 + 3H_2O \tag{4}$$

The dehydration of FG0h (Fig. 4(a)) in first endothermic step (236°C) was due to loss of water in the sample. The second endothermic peak (306°C) is corresponding to a weight loss of 22.5%, XRD measurements of FG0h treated at 400°C also show a peak at  $2\theta = 14.4^{\circ}$  (Fig. 6(d)). It points out that boehmite formed at this range of temperature. In addition, the endothermic peak at around 526°C indicated that boehmite transforms to alumina. Figure 6(b) shows that diffraction peaks of mixed phases of alumina were observed at 500°C. However, this endothermic peak disappeared when milling time increased, indicating that the milling conditions affected the transformation sequence of gibbsite. 12

XRD data were undertaken to study the transformation phases from gibbsite at various temperatures. The XRD patterns of FG0h, FG12h, and FG24h are shown in Fig. 5. The intensities of XRD peaks decreased and became wider as the milling time increased. It is due to decreasing of the crystallinity and particle size of gibbsite. Figures 6–8 shows the XRD pat-

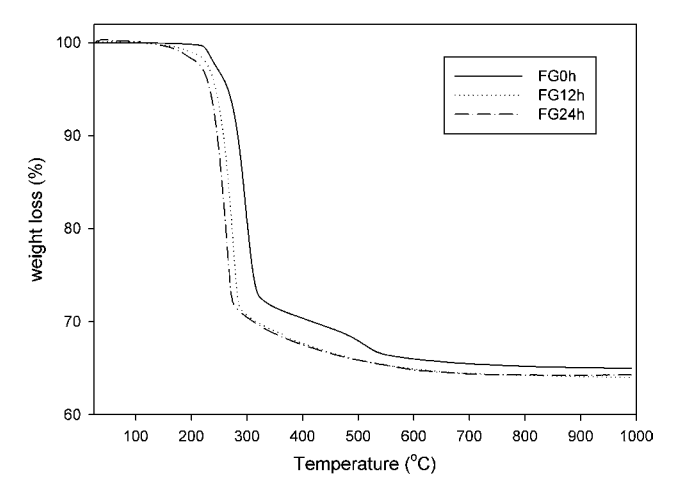


**Fig. 4.** The differential thermal analyses curves of unmilled and milled gibbsite at various milling times.

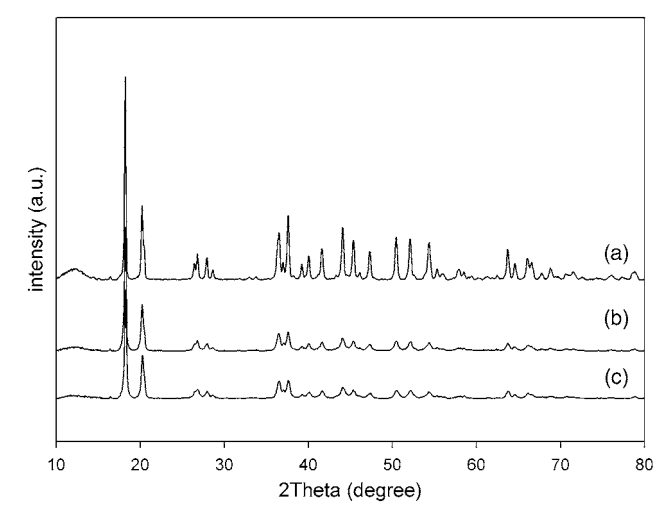


**Fig. 5.** The X-ray diffraction patterns of unmilled and milled gibbsite at various milling times; (a) FG0h, (b) FG12h, and (c) FG24h.

terns of calcined FG0h, FG12h, and FG24h at various temperatures. For the calcined FG12h, the mixture between boehmite and  $\chi$ -phases was found at 400°C and the  $\chi$ -phase was observed at a higher calcination temperature. In the case of prolonged milling (FG24h), the transformation of gibbsite to  $\chi$ -alumina was completed at 350°C. This implies that the small particle sizes are effective for reduction in the transformation temperature of gibbsite to  $\chi$ -alumina.

When particle size of gibbsite is small, the dominant peak  $(2\theta = 14.4^{\circ})$  of boehmite would be reduced (Figs. 6(d) and 7(d)). As a result, y-alumina occurred from the small particle size of gibbsite. It has been known that the dehydration sequence of gibbsite in air is affected by its particle size. In small gibbsite particles ( $<10 \,\mu\text{m}$ ), boehmite is rarely formed, but in the case of larger particles (>100 μm), boehmite is formed because the water formed by the decomposition of the gibbsite cannot rapidly escape from the larger particles.<sup>2,12,20,27</sup> Consequently, transformation of gibbsite occurred through route 1 (Fig. 1). However, the boehmite phase may be observed from the small particle size of gibbsite, if the gibbsite particle is a crystal.<sup>20</sup> Bhattacharya et  $al.^{20}$  found that crystal gibbsite (0.25 µm) can produce boehmite at 400°C. Nevertheless, Jang et  $al.^{12}$  used ground gibbsite losing the crystalline structure, and boehmite was not observed at low temperature. When FG0h was heated, boehmite was observed at 400°C and χ-alumina was formed at 450°C. However, χ-alumina was not the only phase of alumina that occurred

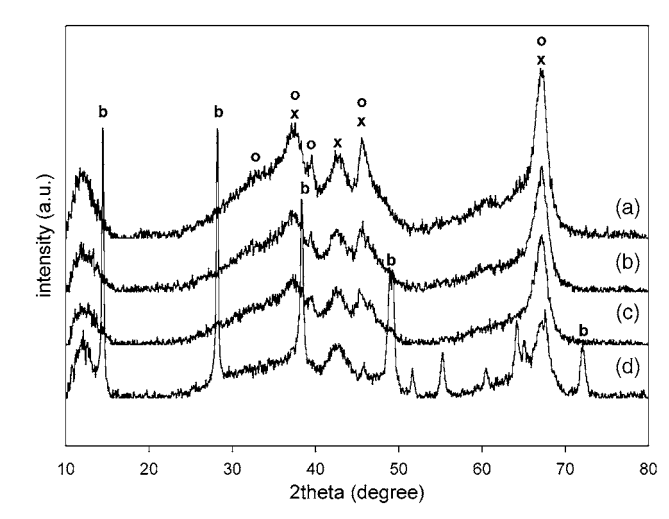


**Fig. 6.** The X-ray diffraction patterns of FG0h calcined at various temperatures, b, boehmite; x,  $\chi$ -Al<sub>2</sub>O<sub>3</sub>; o,  $\gamma$ -Al<sub>2</sub>O<sub>3</sub> (a) 600°C, (b) 500°C, (c) 450°C, and (d) 400°C.

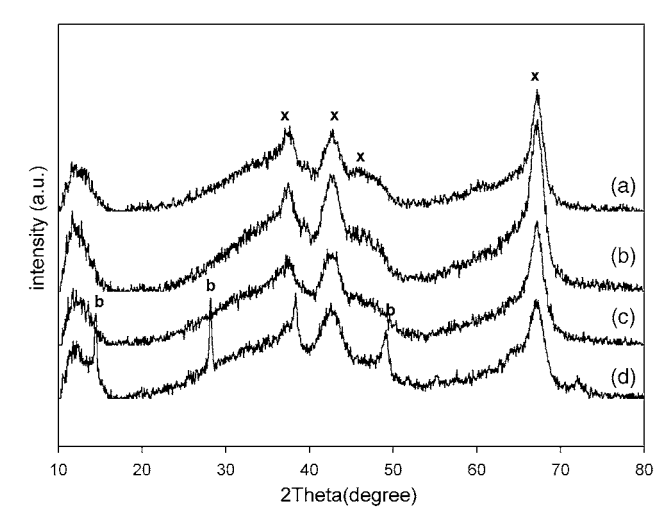


**Fig. 7.** The X-ray diffraction patterns of FG12h calcined at various temperatures, b, boehmite; x,  $\chi$ -Al<sub>2</sub>O<sub>3</sub> (a) 600°C, (b) 500°C, (c) 450°C, and (d) 400°C.

at this temperature; the peak of  $\gamma$ -alumina was also observed. For the micrometer sizes, both transition routes (Fig. 1) may possibly occur, which depends on the heat treatment conditions. The decomposition of boehmite would occur at 300°C at atmospheric pressure. The typical temperature reported for the decomposition of boehmite to  $\gamma$ -Al<sub>2</sub>O<sub>3</sub> is 450°C. The decomposition of boehmite to  $\gamma$ -Al<sub>2</sub>O<sub>3</sub> is 450°C.

In the past, α-seeding has been shown to influence phase development and transformation kinetics of alumina. 26,30 It may be possible that the γ peaks in Figs. 6-8 could have been enhanced by such a seeding effect. However, in the present study, the contamination from abrasives appeared to have very little impact on the reduction of transformation temperature of gibbsite to χ-alumina due to the very small amount presented. The amounts of wear debris obtained by milling the alumina balls in water for 24 h with and without gibbsite were only 2 and 3 wt% of the gibbsite weight, respectively. According to the literature, the effect of  $\alpha$ -seeding was dependent not only on the size of the seeds but also on the amount of the seeds presented. For examples, Kano et al.26 showed that the presence of 50 wt% αalumina seeding reduced the transformation temperature of gibbsite to α-alumina by 120°C (from 1030° to 910°C), while for 5 wt% α-alumina seeding, the transformation temperature decreased only about 30°C. Similarly, Xie et al.30 reported that Al(OH)<sub>3</sub> can be transformed to α-Al<sub>2</sub>O<sub>3</sub> at a relatively lower temperature (1100°C) with the help of seeds by wet grinding of

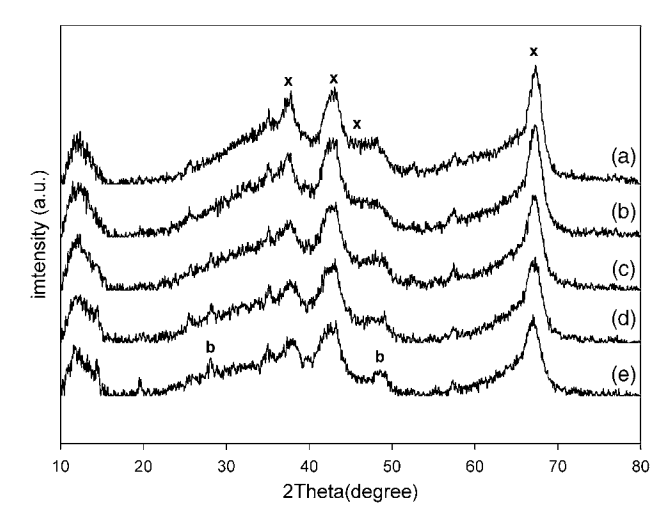


**Fig. 8.** The X-ray diffraction patterns of FG24h calcined at various temperatures, b, boehmite; x,  $\chi$ -Al<sub>2</sub>O<sub>3</sub> (a) 600°C, (b) 500°C, (c) 400°C, (d) 350°C, and (e) 300°C.

Table I. The BET Surface Area and Alumina Phase of Unmilled and Milled Samples after Calcination at 600°C

Samples	Phase	Surface area (m <sup>2</sup> /g	
FG0h	_	25.1	
FG0h600C	$\gamma$ and $\chi$	101.8	
FG12h600C	χ	110.5	
FG24h600C	χ	122.6	

high-purity  $Al_2O_3$  balls when the seed concentration was increased to >10 wt%. Moreover, the average particle size of the abrasives in this study was much larger than those reported in the literature for reduction in the transformation temperature of gibbsite powder (i.e.,  $24~\mu m$  (this work) as compared with  $0.6~\mu m$  in Xie et~al.<sup>30</sup>).

### (3) BET Surface Area

Based on BET surface analyses of calcined samples summarized in Table I, the FG0h had significantly smaller surface area. After calcinations, the structure of gibbsite was destroyed, resulting in a drastic increase in surface area of the calcined samples. With the same calcination temperature, FG24h600C had the highest surface area of 122.6  $\rm m^2/g$ . The increase in the surface area of treated samples is due to the decrease in particle size. These results are in good agreement with that of Ogata  $et\,al.,^{19}$  who used gibbsite as the starting material and found that the specific surface area increased when the calcination temperature increased.

Table II summarizes the crystallite size  $(d_{XRD})$  and the fraction of  $\chi$ -phase of the calcined samples. It can be seen that the increase in calcination temperature resulted in a larger crystallite size. Meanwhile, the fraction of χ-alumina increased with the increasing calcination temperature. These results indicated that high-purity  $\chi$ -alumina can form at the higher temperature. Du et al.<sup>21</sup> also reported that the fraction of  $\alpha$ -phase in  $\alpha$ -alumina synthesized from bayerite would increase with increasing calcination temperature. Macêdo et al.<sup>25</sup> found that the high fraction of  $\alpha$ -alumina can be produced from  $\gamma$ -alumina when the calcination temperature increased from 750° to 900°C. At low temperature (450°C), the fraction of χ-alumina rapidly increased from 0.58 to 0.89. It is implied that mechanical activation affected the formation of χ-alumina. Under isothermal condition, the fraction of  $\chi$ -alumina increased when the particle size decreased. It is confirmed that the small particle size of gibbsite can produce high purity of χ-alumina. In comparison with pure χ-alumina prepared by the solvothermal method as reported previously by our group (crystallite size 6 nm and BET surface area 168 m<sup>2</sup>/g),<sup>17</sup> the physical properties of χ-alumina obtained by the calcination of FG24h were comparable to those of the solvothermally derived ones.

#### (4) Kinetics Measurements

Table III summarizes the transformation rate constants (k) of unmilled and milled gibbsite, which was calcined at different

Table II. The Particle Size (d<sub>XRD</sub>) of the Samples after Calcination and the Fraction of χ-Phase

Samples	T (°C)	$d_{\mathrm{XRD}} \left(\mathrm{nm}\right)^{\dagger}$	Fraction of χ-phase <sup>‡</sup>
FG0h	450	3.8	0.58
	500	4.1	0.72
	600	4.4	0.88
FG12h	450	3.7	0.68
	500	3.8	0.94
	600	4.2	0.95
FG24h	450	3.3	0.90
	500	3.7	0.99
	600	3.8	1

<sup>†</sup>Calculated by the Scherrer equation. <sup>‡</sup>Calculated by quantitative XRD.

Table III. Rate Constant (k) for Milled and Unmilled Gibbsite at Different Temperature

Milling time (h)	$k  (\text{min}^{-1})$
$T = 600^{\circ}\text{C}$	
0	0.0142
12	0.0178
24	0.0359
$T = 500^{\circ} \text{C}$	
0	0.0110
12	0.0153
24	0.0248
$T = 450^{\circ} \text{C}$	
0	0.0033
12	0.0054
24	0.0188

temperatures. For any constant temperature, k increased with the increasing milling time. At a low temperature, the milling can increase k more significantly. For example, at  $450^{\circ}$ C activation of the sample, milling for 24 h increased the reaction rate constant 5.7 times (compared with the sample for 0 h), but at  $600^{\circ}$ C it increased only 2.5 times. Panchula and Ying<sup>31</sup> synthesizing  $\alpha$ -alumina from milled and unmilled  $\gamma$ -alumina reported that k increased with the increase in calcination temperature and milling time from 30 to 120 min.

Table IV. Activation Energy of Milled and Unmilled Gibbsite

Sample	$E_{\rm a}$ (kJ/mol)
FG0h	20.6
FG12h	14.7
FG24h	6.8

Table IV shows the activation energy for phase transformation of unmilled and milled gibbsite to χ-alumina. The activation energy decreased from 20.6 to 14.7 and 6.8 kJ/mol after milling for 12 and 24 h, respectively. This result indicated that the activation energy decreased with the decreasing particle size of the starting gibbsite. In general, reducing the particle size would lead to an increasing surface energy of the particle, thereby resulting in the decreasing of activation energy for phase transformation and transformation temperature as shown in the DTA profile.<sup>28</sup> The XRD patterns also confirmed that the transformation temperature of gibbsite to χ-alumina reduced from 450° to 350°C after milling for 24 h. It may be attributed to the fact that gibbsite grows to the critical size of phase transformation and then transform to  $\chi$ -alumina at a lower temperature. 28,31 Moreover, the milling of gibbsite for 12 and 24 h can be up to 28% and 67% of the activation energy compared with that of the unmilled gibbsite. Several researchers observed the kinetics of transition alumina. Macêdo *et al.*<sup>25</sup> studied the ki-

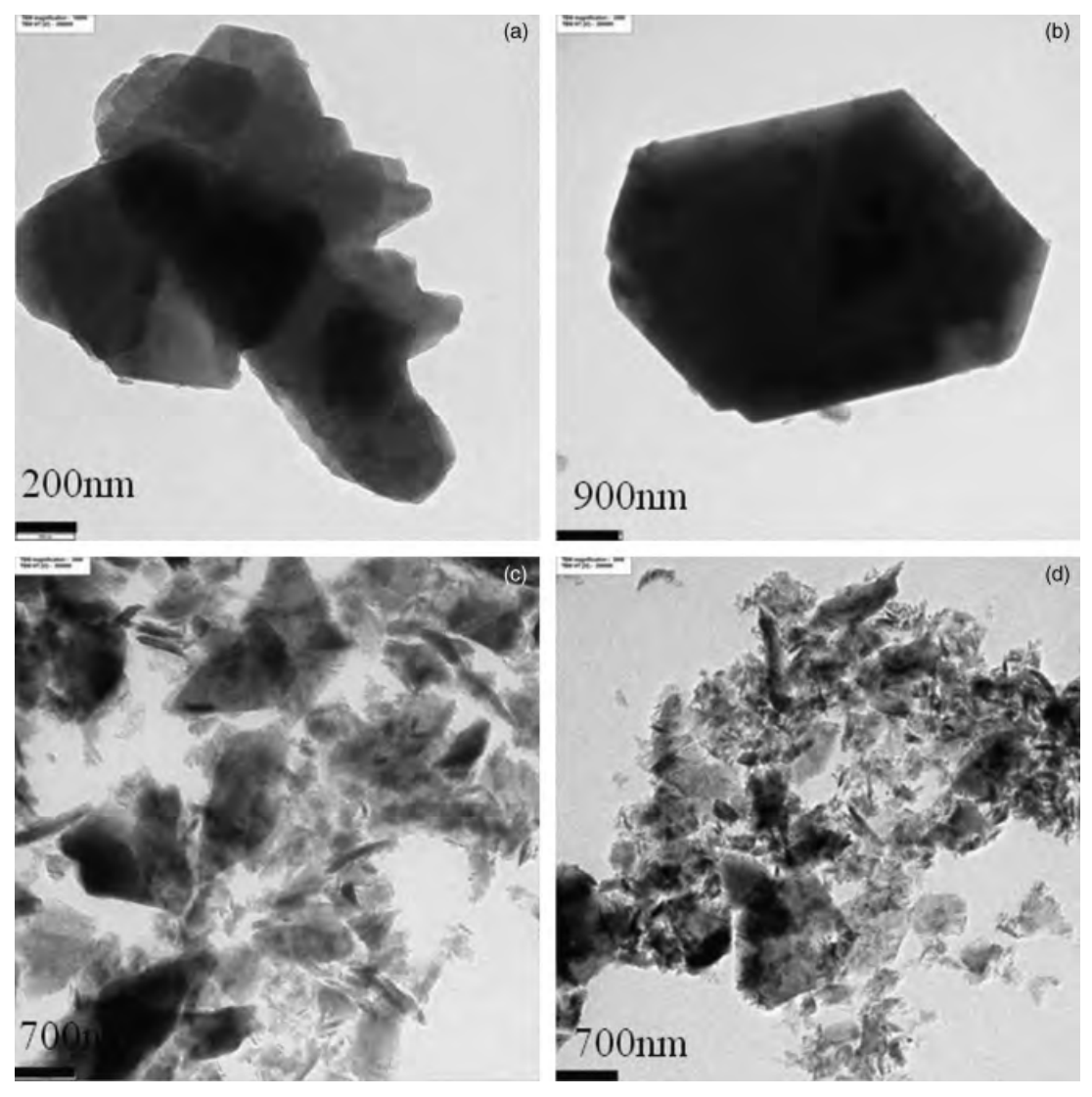


Fig. 9. The transmission electron micrographs of FG0h (a, b), FG12h (c), and FG24h (d).

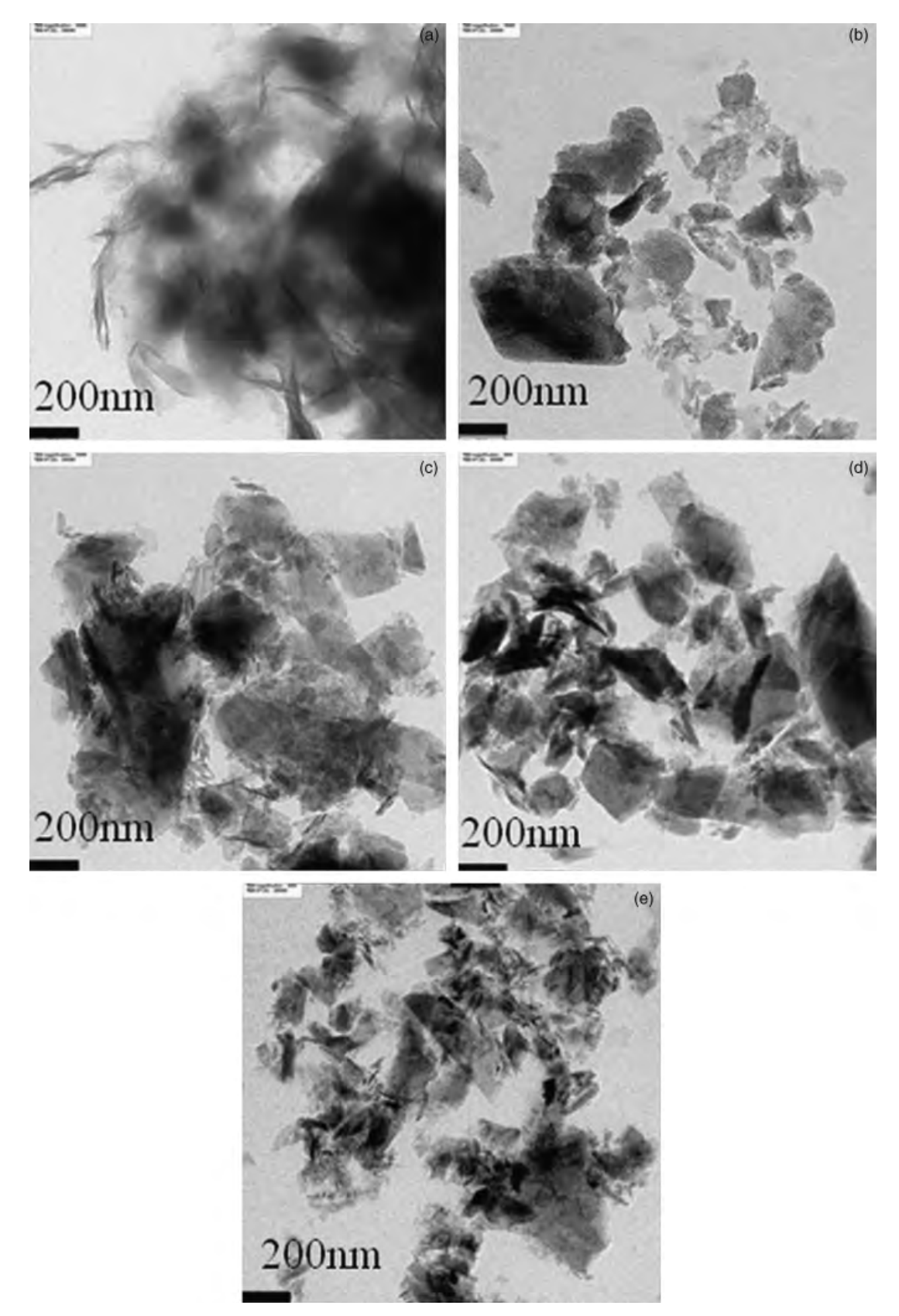


Fig. 10. The transmission electron micrographs of FG0h400C (a), FG0h600C (b), FG12h400C (c), FG12h600C (d), and FG24h600C (e).

netics of  $\gamma$ - to  $\alpha$ -alumina. They found that the activation energy of this phase transformation was  $201 \pm 4$  kJ/mol. Chang *et al.*<sup>28</sup> studied the size effect of  $\chi$ -alumina to  $\alpha$ -alumina. The activation energy reduced from 506 to 321 kJ/mol when  $d_{50}$  of  $\chi$ -alumina decreased from 155 to 40, respectively. Yang *et al.*<sup>32</sup> presented the formation during  $\theta$ -Al<sub>2</sub>O<sub>3</sub> to  $\alpha$ -Al<sub>2</sub>O<sub>3</sub> transformation. They

used three kinds of  $\theta$ -powder (as-received, homogenized, homogenized, and additionally unaxial-pressed compact) as the starting material. The activation energy was 299, 189, and 148 kJ/mol, respectively. Candela and Perlmutter<sup>33</sup> studied the kinetics of boehmite formation by the thermal decomposition of gibbsite under water vapor pressure from 100 to 3200 Pa. The

activation energy was 142±10 kJ/mol. In the present work, the value of activation energy was lower than those reported in the above-mentioned works due to the lower transformation temperature.

#### (5) TEM Observation

The effect of grinding on the morphology of gibbsite and χ-Al<sub>2</sub>O<sub>3</sub> were studied by TEM observation. Figure 9 shows the TEM micrographs of unmilled (a and b) and milled (c and d) gibbsite powder. The unmilled fine gibbsite clearly consisted of pseudohexagonal plates, while irregular and flaky particles were observed for milled samples. It revealed that the milling effectively changed the morphology of gibbsite and reduced particle size. Figures 10(a) and (b) show the TEM micrographs of FG0h400C and FG0h600C, respectively. Figure 10(a) shows that the structure is a strip. It was due to the formation of boehmite. However, this structure disappeared when gibbsite was milled for 12 h and calcined at the same temperature (Fig. 10(c)). It was probably due to the decreasing of boehmite phase in calcined samples. Figures 10(b), (d), and (e) exhibited the TEM micrographs of FG0h600C, FG12h600C, and FG24h600C, respectively. Figures 10(d) and (e) indicated that the dispersed y-alumina with narrow size distribution was obtained from milled gibbsite, whereas the larger particle of mixed phase  $(\chi, \gamma)$  was obtained from unmilled one (Fig. 10(b)). Besides, the morphology of samples is similar to that of gibbsite treated by mechanical milling.

#### IV. Conclusions

High-purity nanocrystalline χ-alumina can be produced from milled gibbsite (FG12h and FG24h). The transformation temperature of gibbsite to χ-alumina decreased from 450° to 350°C when the milling time of gibbsite was increased from 12 to 24 h, respectively. For the unmilled gibbsite (FG0h), the mixed  $\chi$  and γ-phase Al<sub>2</sub>O<sub>3</sub> were formed at 450°C. The fraction of χ-alumina increased with the increase in the milling time and calcination temperature. The activation energy for phase transformation of gibbsite to χ-Al<sub>2</sub>O<sub>3</sub> also decreased with the reducing particle size of the starting gibbsite.

#### Acknowledgments

The authors also would like to thank the Research Unit of Advanced Ceramic and Polymeric Materials, National Center of Excellence for Petroleum, Petrochemicals and Advanced Materials, Chulalongkorn University, Bangkok, Thailand for providing the attrition mill.

#### References

- <sup>1</sup>B. P. Zolotovskii, O. P. Krivoruchko, R. A. Buyanov, T. A. Kriger, and G. N. Krjukova, "Study of the Effect of the Size of Hydrargillite Crystals on the Peculiarities of its Thermal Decomposition and Formation of the Phase Composition of Al (III) Oxide," React. Kinet. Catal. Lett., 22, 153-7 (1983).
- <sup>2</sup>W. H. Gitzen, Alumina as a ceramic material, pp. 17–8. The American Ceramic Society, Westerville, OH, 1970.
- <sup>3</sup>M. Lacroix, G. M. Pajonk, and S. J. Teichner, "Silica and Alumina Catalysts, Activated by Hydrogen Spillover, for the Conversion of n-Heptane at 270°C, J. Catal., 101, 314-22 (1986).
- <sup>4</sup>J. S. Church, N. W. Cant, and D. L. Trimm, "Stabilisation of Aluminas by Rare Earth and Alkaline Earth Ions," *Appl. Catal.*, **101**, 105–16 (1993).
- O. Mekasuwandumrong, H. Kominami, P. Praserthdam, and M. Inoue, "Synthesis of Thermally Stable x-Alumina by Thermal Decomposition of Aluminum Isopropoxide in Toluene," *J. Am. Ceram. Soc*, **87**, 1543–9 (2004).
- O. Mekasuwandumrong, V. Pavarajarn, M. Inoue, and P. Praserthdam, "Preparation and Phase Transformation Behavior of χ-Alumina Via Solvothermal Synthesis," Mater. Chem. Phys, 100, 445-50 (2006).

- <sup>7</sup>O. Mekasuwandumrong, P. Tantichuwet, C. Chaisuk, and P. Praserthdam, "Impact of Concentration and Si Doping on the Properties and Phase Transformation Behavior of Nocrystalline Alumina Prepared Via Solvothermal Synthesis," Mater. Chem. Phys, 107, 208-14 (2008).
- <sup>8</sup>J. He, W. Liu, L.-H. Zhu, and Q.-W. Huang, "Phase Transformation Behaviors of Aluminum Hydroxides to Alpha Alumina in Air and Molten Salt," J. Mater. Sci., 40, 3259-60 (2005).
- <sup>9</sup>A. N. Tsvigunov, V. G. Khotin, A. S. Krasikov, A. S. Valasov, and B. S. Svetlov, "Synthesis of New Modification of Aluminium Oxide with the Spinel Structure Under Shock-Wave Action on Gibbsite," Glass Ceram., 56, 7-8
- (1999).

  10A. L. Ahmad and N. N. N. Muatafa, "Sol-Gel Synthesized of Nanocomposite

  Nambrane for Ha Permeability: Preparation and Characterization," Int. J. Hydrogen Energy, 32, 2010–21 (2007).
- <sup>1</sup>J. H. Kim, K. Y. Jung, K. Y. Park, and S. B. Cho, "Characterization of Mesoporous Alumina Particle Prepared by Spray Pyrolysis of Al(NO<sub>3</sub>)<sub>2</sub>.9H<sub>2</sub>O Precursor: Effect of CTAB and Urea," Micropor. Mesopor. Mater., 128, 85-90
- 12S.-W. Jang, H.-Y. Lee, S.-M. Lee, S. W. Lee, and K.-B. Shim, "Mechanical Activation Effect on the Transition of Gibbsite to α-Alumina," J. Mater. Sci. Lett., 19, 507–10 (2000).

  13A. Boumaza, L. Favaro, J. Lédion, G. Attonnay, J. B. Brubach, P. Berthet,
- A. M. Huntz, P. Roy, and R. Tétot, "Transition Alumina Phases Induced by Heat Treatment of Boehmite: An X-Ray Diffraction and Infrared Spectroscopy Study, J. Solid State Chem., **182**, 1171-6 (2009).

  <sup>14</sup>F. G. W. Brindley and J. O. Choe, "The Reaction Series, Gibbsite→chi
- Alumina → kappa Alumina → Corundum," J. Mineral. Soc. Am., 46, 771-85
- (1961).

  15 K. Pansanga, J. Panpranot, O. Mekasuwandumrong, C. Satayaprasert, J. G. Goodwin, and P. Praserthdam, "Effect of Mixed γ- and χ-Crystalline Phases in Nanocrystalline Al<sub>2</sub>O<sub>3</sub> on the Dispersion of Cobalt on Al<sub>2</sub>O<sub>3</sub>," Catal. Commun., 9, 207–12 (2008). <sup>16</sup>J. Khom-in, P. Praserthdam, J. Panpranot, and O. Mekasuwandumrong,
- "Dehydration of Methanol to Dimethyl Ether over Nocrystalline Al2O3 with Mixed χ- and γ- Crystallite Phases," Catal. Commun., 9, 1955–8 (2008).
- <sup>7</sup>C. Meephoka, C. Chaisuk, P. Samparnpiboon, and P. Praserthdam, "Effect of Phase Composition Between Nano γ- and χ-Al<sub>2</sub>O<sub>3</sub> on Pd/Al<sub>2</sub>O<sub>3</sub> Catalyst in CO Oxidation," Catal. Commun., 9, 546-50 (2008).
- <sup>18</sup>P. Souza Santos, H. Souza Santos, and S. P. Toledo, "Standard Transition Aluminas. Electron Microscopy Studies," *Mater. Res.*, 3, 104–14 (2000).
- <sup>19</sup>F. Ogata, N. Kawasaki, M. Kabayama, T. Nakamura, and S. Tanada, "Structure Transformation of Gibbsite by Calcinations," J. Surf. Sci. Nanotech.,
- **4**, 267–9 (2006).

  <sup>20</sup>I. N. Bhattacharya, S. C. Das, P. S. Mukherjee, S. Paul, and P. K. Mitra, "Thermal Decomposition of Precipitated Fine Aluminium Trihydroxide," Scand.
- J. Metall., 33, 211–9 (2004).

  <sup>21</sup>X. Du, X. Su, Y. Wang, and J. Li, "Thermal Decomposition of Grinding Activated Bayerite," Mater. Res. Bull., 44, 660–5 (2009).

  <sup>22</sup>L. Löffler and W. Mader, "Transformation Mechanism of the Dehydration of
- Diaspore," *J. Am. Ceram. Soc.*, **86** [4] 534–40 (2003).

  <sup>23</sup>J. M. R. Mercury, P. Pena, and A. H. de Aza, "On the Decomposition of SyntheticGibbsite Studied by Neutron Thermodiffractometry," J. Am. Ceram.
- Soc., 89 [12] 3728–33 (2006).

  <sup>24</sup>T. C. Alex, R. Kumar, S. K. Roy, and S. P. Mehrotra, "Stirred Bead Mill Grinding of Gibbsite: Surface and Morphological Change," Adv. Powder Technol., 19, 483–391 (2008).  $^{25}$ M. I. F. Macêdo, C. A. Bertran, and C. C. Osawa, "Kinetic of the  $\gamma^{\text{\tiny \$}}\alpha$ -Al-
- umina Phase Transformation by Quantitative X-Ray Diffraction," J. Mater. Sci., 42, 2830-6 (2007).

  <sup>26</sup>J. Kano, S. Saeki, F. Saito, M. Tanjo, and S. Yamazaki, "Application of Dry
- Grinding to Reduction in Transformation Temperature of Aluminum Hydroxides," Int. J. Miner. Process., **60**, 91–100 (2000).

  <sup>27</sup>C. Misra, Industrial Alumina Chemicals. American Chemical Society, Wash-
- ington, DC, 1986 75pp..

  <sup>28</sup>P.-L. Chang, Y.-C. Wu, S.-J Lai, and F. S. Yen, "Size Effects on the χ-to α-Al<sub>2</sub>O<sub>3</sub> Phase Transformation," *J. Eur. Ceram. Soc.*, **29**, 3341–8 (2009).

  <sup>29</sup>S. Serena, M. A. Raso, M. A. Rodríguez, A. Caballero, and T. J. Leo, "Ther-
- modynamic Evaluation of the Al<sub>2</sub>O<sub>3</sub>-H<sub>2</sub>O Binary System at Pressures Up to 30 MPa," *Ceram. Int.*, **35**, 3081–90 (2009).

  <sup>30</sup>Z.-P. Xie, J.-W. Lu, Y. Huang, and Y.-B. Cheng, "Influence of α-Alumina
- Seed on Morphology of Grain Growth in Alumina Ceramics from Bayer Aluminum Hydroxide," Mater. Lett., 57, 2501-8 (2003).
- <sup>31</sup>M. L. Panchula and J. Y. Ying, "Mechanical Synthesis of Nanocrytalline α-Al<sub>2</sub>O<sub>3</sub> Seeds for Enhanced Transformation Kinetics," Nanostruct. Mater., 9,
- <sup>32</sup>R.-J. Yang, F. S. Yen, S.-M. Lin, and C. C. Chen, "Microstructure-Controlled Effects on Temperature Reduction of α-Al<sub>2</sub>O<sub>3</sub> Crystallite Formation," J. Cryst. Growth, 299, 429-45 (2007).
- 33L. Candela and D. D. Perlmutter, "Kinetics of Boehmite Formation by Thermal Decomposition of Gibbsite," Ind. Eng. Chem. Res., 31, 694-700 (1992).

# Improvement of propane oxidation activity over $Pt/Al_2O_3$ by the use of MIXED $\gamma$ - and $\chi$ -Al<sub>2</sub>O<sub>3</sub> supports

Thongchai Glinrun · Okorn Mekasuwandumrong · Joongjai Panpranot · Choowong Chaisuk · Piyasan Praserthdam

Received: 13 August 2009/Accepted: 20 January 2010/Published online: 30 April 2010 © Akadémiai Kiadó, Budapest, Hungary 2010

**Abstract** The use of mixed  $\gamma$ - and  $\chi$ -phase  $Al_2O_3$  as supports for preparation of  $Pt/Al_2O_3$  catalysts resulted in higher acidity of  $Al_2O_3$  and higher Pt dispersion compared to the pure phase supports. As a consequence, higher propane oxidation activities were obtained.

**Keywords** Chi alumina · Phase composition · Pt/Al<sub>2</sub>O<sub>3</sub> · Propane oxidation

#### Introduction

The catalytic combustion of hydrocarbons has widely been used for power generation in gas turbine combustors and emission control of automotive exhausts. Pt/Al<sub>2</sub>O<sub>3</sub> is recognized as the most active catalyst for the catalytic combustion of lower alkanes such as propane, while supported palladium catalysts are more active for methane oxidation [1–5]. The reaction mechanism of alkane oxidation over precious metal supported on alumina under oxygen rich conditions has been reported [6–9]. It is suggested that oxygen adsorbs much more effectively than alkanes resulting in high coverage of chemisorbed oxygen on the metal surface. The slowest reaction step has been postulated to be the dissociative chemisorption of alkane on the bare metal surface with breakage of the weakest C–H bond [10–13] followed by its interaction with oxygen adsorbed on an adjacent site. Many researchers reported "structure-sensitiveness" of the reaction in the case of methane

Department of Chemical Engineering, Center of Excellence on Catalysis and Catalytic Reaction Engineering, Faculty of Engineering, Chulalongkorn University, Bangkok 10330, Thailand e-mail: piyasan.p@chula.ac.th

Department of Chemical Engineering, Faculty of Engineering and Industrial Technology, Silpakorn University, Nakhon Pathom 73000, Thailand



T. Glinrun  $\cdot$  J. Panpranot  $\cdot$  P. Praserthdam ( $\boxtimes$ )

O. Mekasuwandumrong · C. Chaisuk

442 T. Glinrun et al.

combustion over supported metal catalysts [1, 2, 14, 15]. Yazawa et al. [16] reported that propane combustion over Pt catalysts was structure-sensitive in which the turnover frequency increased with an increase in acid strength of support materials and a decrease in platinum dispersion.

 $\chi$ -Al<sub>2</sub>O<sub>3</sub> is one of the metastable polymorphs of transition alumina with relatively high thermal stability compared to  $\gamma$ -Al<sub>2</sub>O<sub>3</sub>. Nanocrystalline transition alumina has been synthesized by decomposition of aluminum isopropoxide under solvothermal conditions [17–20]. Pansanga et al. [21] showed that high catalytic activities for CO hydrogenation of Co/Al<sub>2</sub>O<sub>3</sub> can be obtained over the ones supported on mixed  $\gamma$ - and  $\chi$ -Al<sub>2</sub>O<sub>3</sub>. Mephoka et al. [22] synthesized alumina supports with various  $\chi/\gamma$  ratios by solvothermal synthesis and found that the ones with 30–70%  $\chi$ -phase Al<sub>2</sub>O<sub>3</sub> gave higher Pt dispersion than pure  $\gamma$ -phase and improved catalytic activity in CO oxidation. In those studies, the effect of mixed  $\gamma$ - and  $\chi$ -crystalline phase Al<sub>2</sub>O<sub>3</sub> on the catalytic activity of Al<sub>2</sub>O<sub>3</sub> supported catalysts in structure-insensitive reactions such as CO oxidation and CO hydrogenation has been clearly demonstrated.

Thus, it is the goal of this study to investigate the catalytic activity of the Pt catalysts supported on mixed  $\gamma$ - and  $\chi$ -Al<sub>2</sub>O<sub>3</sub> with various  $\chi/\gamma$  ratios in a structure-sensitive reaction such as propane oxidation reaction. The catalyst activities were evaluated in terms of propane conversion and light-off temperature. The catalysts were also characterized by N<sub>2</sub> physisorption, X-ray diffraction (XRD), transmission electron microscopy (TEM), C<sub>3</sub>H<sub>8</sub> temperature program desorption (C<sub>3</sub>H<sub>8</sub>-TPD), and NH<sub>3</sub> temperature program desorption (NH<sub>3</sub>-TPD).

#### **Experimental**

Preparation of Al<sub>2</sub>O<sub>3</sub> and Pt/Al<sub>2</sub>O<sub>3</sub>

Nanocrystalline  $Al_2O_3$  samples with various  $\chi/\gamma$  compositions were prepared by the solvothermal method using approximately 25 g of aluminum isopropoxide dissolved in a mixed solution of toluene and 1-butanol as starting materials according to the method described by Meephoka et al. [22]. The as-synthesized powders were calcined in a flow of air at 600 °C for 6 h. The 0.3% Pt/Al<sub>2</sub>O<sub>3</sub> catalysts were prepared by incipient wetness impregnation with a desired amount of an aqueous solution of hexachloroplatinic acid hexahydrate and then calcined in air at 380 °C for 2 h.

#### Catalyst characterization

XRD patterns of the samples were collected using a SIEMENS D-5000 X-ray diffractometer with Cu  $K_{\alpha}$  radiation and a Ni filter in the  $2\theta$  range of  $20^{\circ}$ – $80^{\circ}$ . The BET surface areas were measured by  $N_2$  adsorption–desorption isotherm at liquid nitrogen temperature (-196 °C) using a Micromeritics ASAP 2020. The morphologies of catalyst samples were determined by TEM using a JEOL JEM-2010 transmission electron miscroscope.  $C_3H_8$ -TPD and  $NH_3$ -TPD experiments were carried out using a Micromeritics Chemisorp 2750 system. The dispersion of active



Pt metals was measured using CO pulse-chemisorption technique in a flow of helium in a Micromeritics ASAP 2750.

#### Reaction study

Propane oxidation over various Pt/Al<sub>2</sub>O<sub>3</sub> catalysts was performed in a quartz tube (i.d. 6 mm). Approximately 0.2 g of catalyst was loaded in the reactor. It was then reduced by hydrogen for 1 h at a flow rate of 100 cm<sup>3</sup>/min at 500 °C and then cooled to room temperature before the reaction. The composition of products was analyzed on-line using a gas chromatograph with a TCD detector (SHIMADZU GC 8A) with a Porapak QS column. The reaction gas of 1% C<sub>3</sub>H<sub>8</sub> and 7% O<sub>2</sub> was fed to the catalyst bed at a space velocity of 16,000 h<sup>-1</sup>. The reaction temperature was raised by 50 °C steps from 100 to 450 °C. At each temperature, the reaction products were analyzed 20 min after the bed temperature attained predetermined value.

#### Result and discussion

The XRD patterns of Pt/Al<sub>2</sub>O<sub>3</sub> catalysts with various  $\chi$ - and  $\gamma$ -Al<sub>2</sub>O<sub>3</sub> compositions are shown in Fig. 1. All the catalyst samples exhibited the typical pattern for transition alumina without any additional peaks for Pt phases due probably to the very low amount of Pt present (0.3 wt%). Nanocrystalline Al<sub>2</sub>O<sub>3</sub> supports with pure  $\chi$ - and  $\gamma$ -phase were obtained by the reaction of aluminum isopropoxide (AIP) in toluene and 1-butanol, while the mixed-phase Al<sub>2</sub>O<sub>3</sub> were obtained by the reaction in the mixed solvents. In this paper, the Pt catalysts supported on Al<sub>2</sub>O<sub>3</sub> support with 0, 30, 50, 70 and 100%  $\chi$ -Al<sub>2</sub>O<sub>3</sub> are referred to as Pt/C0G100, Pt/C30G70, Pt/C50G50, Pt/C70G30, and Pt/C100G0, in order. The XRD characteristic peak at  $2\theta = 43^{\circ}$  was used for the calculation of  $\chi$ -phase (%) according to those reported by Meephoka et al. [22].

The TEM images of 0.3 wt% of Pt/Al<sub>2</sub>O<sub>3</sub> containing different compositions of  $\gamma$ - and of  $\chi$ -phase Al<sub>2</sub>O<sub>3</sub> are shown in Fig. 2. The wrinkled sheet morphology was attributed to the presence of  $\gamma$ -Al<sub>2</sub>O<sub>3</sub> while  $\chi$ -Al<sub>2</sub>O<sub>3</sub> were shown as spherical particles [17], [23], [24]. As the percent  $\chi$ -Al<sub>2</sub>O<sub>3</sub> increased, the wrinkled sheets morphology became less apparent and more spherical particles structure was seen. However, Pt/PtO metal clusters/particles were not distinguishable in all the TEM images.

The acidity of the  $Pt/Al_2O_3$  catalysts was determined by  $NH_3$ -TPD experiments and the results are shown in Fig. 3. Two broad peaks with a maximum temperature at 80–110 °C and 290–310 °C were observed in all cases. Compared to the pure phase  $Al_2O_3$ , the mixed-phases showed a slight peak shift toward higher temperature. The amounts of  $NH_3$  adsorbed on  $Pt/Al_2O_3$  catalysts were calculated from the peak areas and the results are given in Table 1. The results indicated that acidity of  $Pt/Al_2O_3$  was higher and stronger when they were supported on the mixed  $\gamma$ - and of  $\chi$ -phase  $Al_2O_3$  than those supported on the pure phase ones.



T. Glinrun et al.

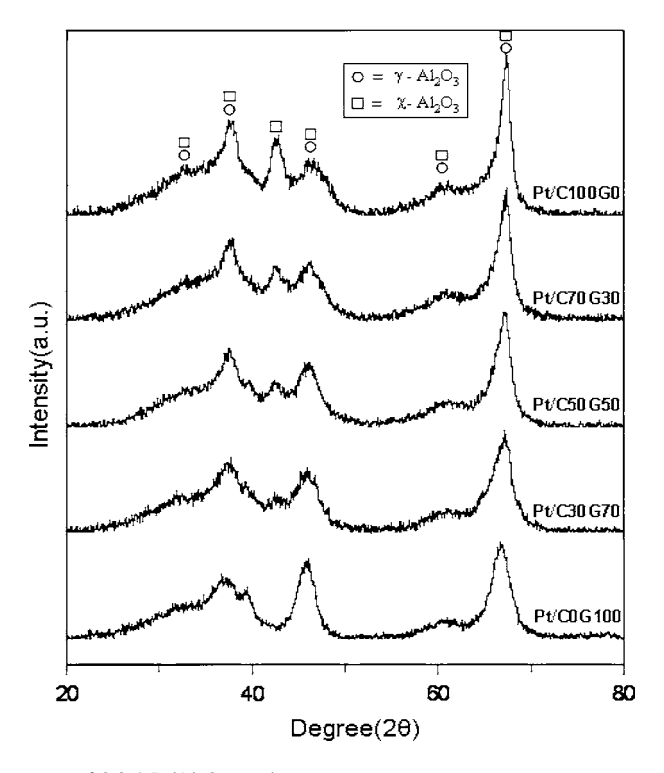


Fig. 1 XRD patterns of 0.3% Pt/Al<sub>2</sub>O<sub>3</sub> catalyst

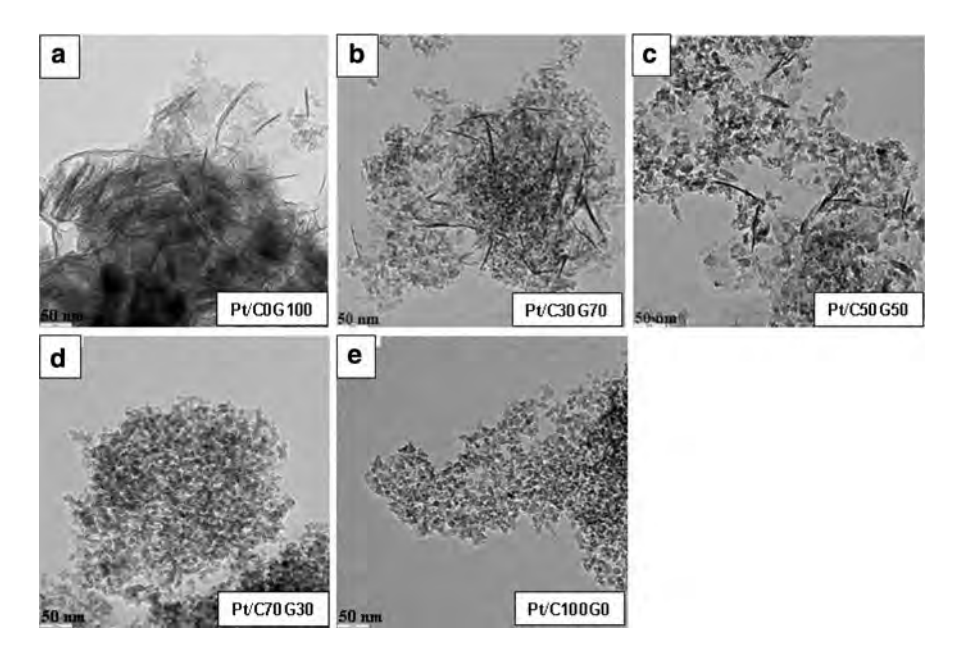


Fig. 2  $\,$  TEM images of 0.3%  $Pt/Al_2O_3$  catalyst with various phase composition



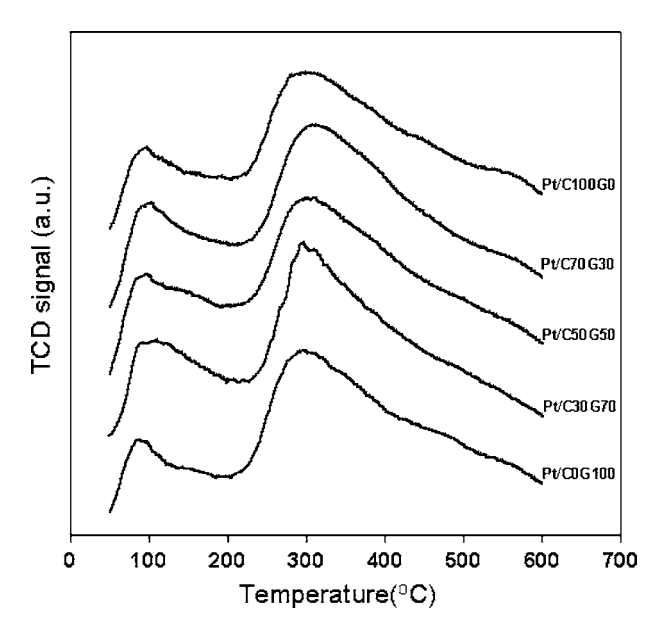


Fig. 3 NH<sub>3</sub>-TPD profiles of catalysts with various phase composition

Table 1 Physiochemical properties of 0.3% Pt/Al<sub>2</sub>O<sub>3</sub> catalyst

Sample	BET surface area (m²/g) <sup>a</sup>	Crystallite size (nm)	Acidity $(\mu mol \ g^{-1})^b$	CO chemisorption × 10 <sup>-18</sup> (molecule CO/ g catalyst) <sup>c</sup>	Pt dispersion (%) <sup>d</sup>
Pt/C0G100	203	5	733	3.25	38.9
Pt/C30G70	189	5	768	3.56	42.6
Pt/C50G50	177	6	775	3.55	42.5
Pt/C70G30	163	6	770	3.58	42.8
Pt/C100G0	151	6	724	3.18	38.1

<sup>&</sup>lt;sup>a</sup> Error = 4%, SD = 5.1

The BET surface area, crystallite size, and CO chemisorptions results of the Pt/  $Al_2O_3$  catalysts are summarized in Table 1. The BET surface area decreased from 203 to 151 m<sup>2</sup>/g as the  $\chi$ -phase content increased from 0 to 100% although the average crystallite size of  $Al_2O_3$  supports remained constant at around 5 to 6 nm. The amounts of active Pt metals on the catalyst surface were calculated from CO chemisorption experiments at room temperature. The calculation of Pt active sites was based on the assumption that one carbon monoxide molecule adsorbs on one platinum site. The metal active sites of Pt supported on pure  $\chi$ - and  $\gamma$ -Al<sub>2</sub>O<sub>3</sub> were



<sup>&</sup>lt;sup>b</sup> Error = 3%, SD = 13.4

<sup>&</sup>lt;sup>c</sup> Error = 3%, SD = 0.1

<sup>&</sup>lt;sup>d</sup> Error = 3%, SD = 0.9

446 T. Glinrun et al.

essentially similar at around 3.2  $\times$  10<sup>18</sup> molecules CO/g cat., while the active sites of Pt supported on mixed phase Al<sub>2</sub>O<sub>3</sub> (30, 50, and 70% of  $\chi$ -phase) were higher than those on the pure phase Al<sub>2</sub>O<sub>3</sub> (approximately 3.6  $\times$  10<sup>18</sup> molecules CO/g cat.). This can be explained by the difference between particle morphologies of the different alumina phase structures.

The characteristics of the surface active sites of Pt/Al<sub>2</sub>O<sub>3</sub> catalysts were studied by means of the temperature programmed desorption of  $C_3H_8$  from 50–500 °C and the results are shown in Fig. 4. The major  $C_3H_8$  desorption peak appeared at ca. 425 °C for those supported on the single phase Al<sub>2</sub>O<sub>3</sub> (either pure  $\gamma$ - or  $\chi$ -Al<sub>2</sub>O<sub>3</sub>). It is clearly seen that the same peak was significantly shifted towards lower temperature (to ca. 320 °C) for the Pt/Al<sub>2</sub>O<sub>3</sub> catalysts containing mixed  $\gamma$ - and  $\chi$ -Al<sub>2</sub>O<sub>3</sub> supports. It is suggested that the Pt may interact more strongly on the mixed Al<sub>2</sub>O<sub>3</sub> structures than on the single phase ones so that the adsorption strength of  $C_3H_8$  was altered (lower).

Fig. 5 shows the activities of Pt/Al<sub>2</sub>O<sub>3</sub> catalysts in propane oxidation as a function of reaction temperature. The catalytic activity of supported platinum catalyst depended on the platinum dispersion. Moreover, the activity of Pt-based catalysts for propane combustion also increased with increasing support acidity. A similar trend has been reported by Garetto et al. [25]. Since the C<sub>3</sub>H<sub>8</sub>-TPD experiments showed that propane desorption behaviors were different between the mixed phase Al<sub>2</sub>O<sub>3</sub> supported Pt catalysts and the single phase supported ones. Faster desorption of C<sub>3</sub>H<sub>8</sub> from Pt surface would, therefore, result in more active Pt surface available for reaction to proceed; as a consequence an increase in oxidation activity was obtained. According to the reaction mechanism in the literature, the rate of propane oxidation increases by increasing the active sites for both dissociation

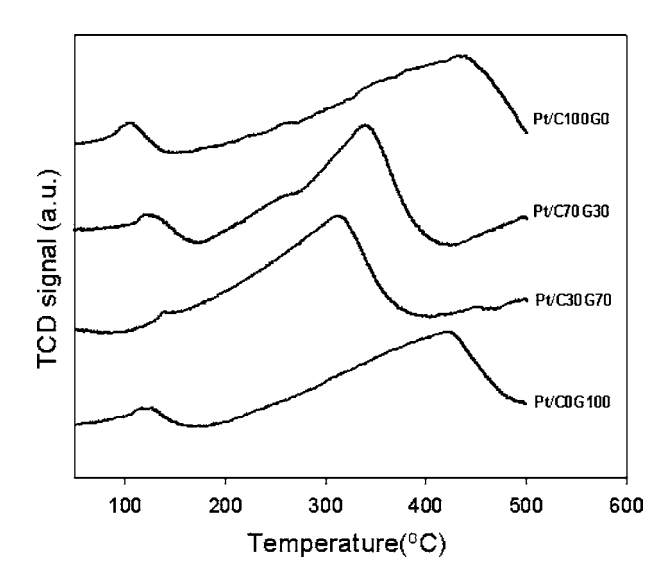


Fig. 4 C<sub>3</sub>H<sub>8</sub>-TPD profiles of catalysts with various phase composition



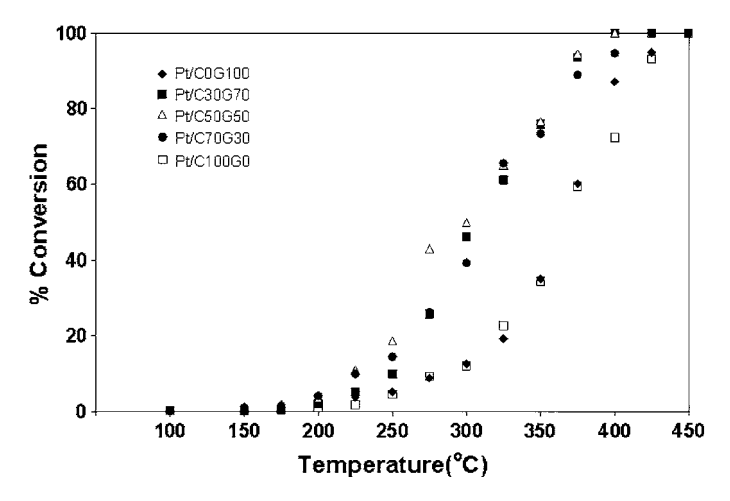


Fig. 5 C<sub>3</sub>H<sub>8</sub> conversion profiles of 0.3% Pt/Al<sub>2</sub>O<sub>3</sub> for the propane oxidation

of C–H bond and oxygen adsorption [8, 10, 26]. The advantages of mixed phase composition effect on the activity and selectivity characteristics have also been reported for other catalyst systems [22, 23, 27–29].

**Acknowledgement** Financial support from the Thailand Research Fund (TRF) and the Office of Higher Education Commission, Ministry of Education, Thailand are gratefully acknowledged.

#### References

- 1. Hicks RF, Qi H, Young ML, Lee RG (1990) J Catal 122:280
- 2. Kooh AB, Han WJ, Lee RG, Hicks RF (1991) J Catal 130:374
- 3. Mouaddib N, Feumi-Jantou C, Garbowski E, Primet M (1992) Appl Catal A 87:129
- 4. Muto KI, Katada N, Niwa M (1996) Appl Catal A 134:203
- 5. Bera P, Patil KC, Hegde MS (2000) Phys Chem Chem Phys 2:377
- Ertl GL, Koch J (1973) Proceedings of 5th International congress on catalysis. American Elsevier, New York
- 7. Campbell CT, Foyt DC, White JW (1977) J Phys Chem 81:491
- 8. Yao YFY (1980) Ind Eng Chem Prod Res Dev 19:293
- 9. Burch R, Crittle DJ, Hayes MJ (1999) Catal Today 47:229
- 10. Hiam L, Wise H, Khaikin S (1968) J Catal 272:9
- 11. Cullis CF, Keene DE, Trimm DL (1970) J Catal 18:864
- 12. Schwartz A, Holbrook LL, Wlse H (1971) J Catal 21:199
- 13. Otto K (1989) Langmuir 5:1364
- 14. Briot P, Auroux A, Jones D, Primet M (1990) Appl Catal 59:141
- 15. Baldwin TR, Burch R (1990) Appl Catal 66:337
- 16. Yazawa Y, Yoshida H, Hattori T (2002) Appl Catal A 237:147
- Praserthdam P, Inoue M, Mekasuvandumrong O, Thanakulrangsan W, Phatanasri S (2000) Inorg Chem Commu 3:671
- Mekasuwandumrong O, Silveston PL, Praserthdam P, Inoue M, Pavarajarn V, Tanakulrungsank W (2003) Inorg Chem Commu 6:930
- Mekasuwandumrong O, Kominami H, Praserthdam P, Inoue M, Blendell JE (2004) J Am Ceram Soc 87:1543



T. Glinrun et al.

 Mekasuwandumrong O, Praserthdam P, Inoue M, Pavarajarn V, Tanakulrungsank W (2004) J Mater Sci 39:2417

- 21. Pansanga K, Mekasuwandumrong O, Panpranot J, Praserthdam P (2007) Korean J Chem Eng 24:397
- 22. Meephoka C, Chaisuk C, Samparnpiboon P, Praserthdam P (2008) Catal Commun 9:546
- Pansanga K, Panpranot J, Mekasuwandumrong O, Satayaprasert C, Goodwin JG, Praserthdam P (2008) Catal Commun 9:207
- 24. Inoue M, Otsu H, Kominami H, Inui T (1996) Ind Eng Chem Res 35:295
- 25. Garetto TF, Rincon E, Apesteguia CR (2004) Appl Catal B 48:167
- 26. Garetto TF, Rincon E, Apesteguia CR (2007) Appl Catal B 73:65
- 27. Jongsomjit B, Wongsalee T, Praserthdam P (2005) Mater Chem Phys 92:572
- 28. Jongsomjit B, Wongsalee T, Praserthdam P (2005) Catal Commun 6:705
- 29. Komhom S, Mekasuwandumrong O, Praserthdam P, Panpranot J (2008) Catal Commun 10:86



ELSEVIER

Contents lists available at ScienceDirect

#### Journal of Industrial and Engineering Chemistry

journal homepage: www.elsevier.com/locate/jiec



#### Solvent effect on synthesis of zirconia support for tungstated zirconia catalysts

#### Peangpit Wongmaneenil, Bunjerd Jongsomjit\*, Piyasan Praserthdam

Center of Excellence on Catalysis and Catalytic Reaction Engineering, Department of Chemical Engineering, Faculty of Engineering, Chulalongkorn University, Bangkok 10330 Thailand

#### ARTICLE INFO

Article history: Received 14 October 2009 Accepted 11 December 2009

Keywords: ZrO<sub>2</sub> W/ZrO<sub>2</sub> Solvothermal synthesis Surface acidity Carbon residue Esterification

#### ABSTRACT

Solvothermal reaction of zirconium n-butoxide (ZNB) in different solvent media, such as 1,3-pentanediol, 1,4-butanediol, 1,5-pentanediol and 1,6-hexanediol resulted in the formation of zirconium dioxide (ZrO<sub>2</sub>) nanostructure. Then, the 15%W/ZrO<sub>2</sub> (WZ) catalysts using different zirconia supports were prepared by impregnation method. The effects of solvent on preparation of zirconia on the catalytic performance of WZ catalysts in esterification of acetic acid and methanol at 60 °C were investigated. The experimental results showed that ZrO<sub>2</sub> particles prepared in 1,4-butanediol (ZrO<sub>2</sub>-BG) have a spherical shape, while in other glycols the samples were irregularly-shaped particles. The reaction results of esterification illustrated that the W/ZrO<sub>2</sub>-BG catalysts had high surface acidity and showed high acetic acid conversion. The W/ZrO<sub>2</sub>-PeG catalysts (ZrO<sub>2</sub> particles prepared in 1,5-pentanediol, PeG) exhibited the lowest surface acidity among other samples due to strong interaction of proton species and the zirconia supports as proven by TGA. One of the possible reasons can be attributed to different amounts of carbon residue on the surface of catalysts.

© 2010 The Korean Society of Industrial and Engineering Chemistry. Published by Elsevier B.V. All rights reserved.

#### 1. Introduction

Tungstated zirconia [WO<sub>x</sub>/ZrO<sub>2</sub> (WZ)] catalysts have attracted much attention because of their ability to catalyze a wide range of reactions, such as dehydration [1], isomerization [2–4], and esterification [5,6]. The advantages of WO<sub>x</sub>/ZrO<sub>2</sub>, such as higher stability under high-temperature treatments and reductive atmospheres, lower deactivation rates during catalysis, and easier regeneration [7–9] are of considerable interest for practical applications in the petrochemical industry. Several authors revealed that the catalytic properties of WO<sub>x</sub>/ZrO<sub>2</sub> only depend on the *W* surface density (W/nm²). This surface density can be modified by varying the tungsten loading and the calcination temperature [10–12]. The tungsten oxide overlayer can be present as isolated surface monotungstates, polymeric surface polytungstates, and crystalline WO<sub>3</sub> particles on the oxide supports [13].

Since the preparation of tungstated zirconia by impregnation of hydrated zirconia was reported by Hino and Arata [14], several investigations about the influence of the preparation method on the activity of  $WO_x/ZrO_2$  materials have been investigated [15–17]. Some of the general conclusions are that the incorporation of tungsten into the zirconia favors the formation of the

tetragonal phase, inhibits sintering of the support and enhances the acid strength of these solids by the slight reduction of the  $WO_x$ species. Since then, many papers have been focused on the properties of catalysts prepared from zirconium oxyhydroxide [7,15,18-25]. Systems based on the W deposited on crystallized zirconia were studied to a smaller extent [3,4,6,26-28]. In addition, the influences of the initial state of the support on the acidic properties of the catalyst and their relation with the activity and surface structure are not fully understood. Recently, we have reported the characteristics and catalytic behaviors of tungstated zirconia catalysts, which can be altered by different calcination atmospheres [6]. It revealed that the presence of F-center (electrons stabilized in oxygen vacancies) on zirconia surface occurred during reduction treatments leading to enhancement of activity for tungstated zirconia catalyst due to the formation of monotungstate surface morphology resulted into high acidity of the catalyst.

In the present study, four different solvent media were used to prepare the nanocrystalline zirconia prepared by the solvothermal method. The application of synthesized zirconia as supports for tungsten catalysts was further investigated. The influences of the solvent used during preparation on the physicochemical properties of the zirconia were investigated by means of N<sub>2</sub> physisorption, XRD, XPS, and SEM. The corresponding solvothermal-derived zirconia supported tungsten catalysts were further characterized by Raman spectroscopy, TGA, XPS and were tested for catalytic activities in the acetic acid esterification reaction.

<sup>\*</sup> Corresponding author. Tel.: +66 2 1 2186869; fax: +66 2 2186877. E-mail address: bunjerd.j@chula.ac.th (B. Jongsomjit).

#### 2. Experimental

#### 2.1. Preparation of zirconia

Zirconium dioxide was prepared by methods previously reported [6]. Approximately 25 g of zirconium tetra-n-butoxide 80 wt% solution in 1-butanol (ZNB, Aldrich) was suspended in 100 ml of the desired solvent in a test tube, which was then placed in a 300 ml autoclave. The solvents used in this work were 1,3-propanediol (PG, purity 98%, Aldrich), 1,4-butanediol (BG, purity 99%, Sigma–Aldrich), 1,5-pentanediol (PeG, purity 98%, Merck) and 1,6-hexanediol (HG, purity 97%, Merck). The gap between autoclave wall and the test tube was filled with 30 ml of the same solvent. The autoclave was completely sealed and purged with nitrogen, the mixture was heated to 300 °C at a heating rate of 2.5 °C/min and was kept at that temperature for 2 h. After cooling to room temperature, the resulting powders were collected after repeated washing with methanol by centrifugation. The products were then air-dried and were used without further calcinations.

#### 2.2. Preparation of W/ZrO<sub>2</sub>

The zirconia samples obtained from 2.1 were used as supports. The zirconia doped with tungsten catalysts were prepared by the incipient wetness impregnation method using tungsten (VI) chloride (WCl $_6$ , Aldrich, 99.9%) sufficient for yield materials having 15 wt% of W loading. The catalysts were dried at 110 °C for 12 h and calcined in air at 500 °C for 3 h.

#### 2.3. Catalyst nomenclature

The different solvothermal-derived zirconia supports are designated as  $ZrO_2$ -PG,  $ZrO_2$ -BG,  $ZrO_2$ -PeG and  $ZrO_2$ -HG in which PG, BG, PeG and HG refer to the solvent used (PG = 1,3-propanediol, BG = 1,4-butanediol, PeG = 1,5-pentanediol and HG = 1,6-hexanediol). The tungsten catalysts supported on different zirconia supports are designated as W/ZrO<sub>2</sub>-PG, W/ZrO<sub>2</sub>-BG, W/ZrO<sub>2</sub>-PeG and W/ZrO<sub>2</sub>-HG.

#### 2.4. Catalyst characterization

#### 2.4.1. XRD measurements

X-ray powder diffractograms of various investigated samples were determined using a D5000 (Siemens) using Ni filter Cu K $\alpha$  radiation from 20° to 80°. Crystallite size was calculated from the Scherrer equation using 1 0 1 diffraction peak of tetragonal zirconia. The fraction of tetragonal ( $f_t$ ) phase in the W/ZrO<sub>2</sub> catalysts are estimated by the following formula [22]

$$f_{t} = \frac{A_{t}(101)}{A_{tot}(ZrO_{2})} \tag{1}$$

where  $A_t(1\ 0\ 1)$  stands for the area of the  $(1\ 0\ 1)$  peak of the tetragonal phase and  $A_{tot}$  the area of all the tetragonal and monoclinic peaks in the pattern.

#### 2.4.2. Surface area measurements

The specific surface areas ( $S_{\rm BET}$ ) of various samples were determined from nitrogen adsorption studies conducted at  $-196\,^{\circ}{\rm C}$  in a Micrometrics ASAP 2020 device. Prior to the adsorption measurements, the sample was degassed at 300  $^{\circ}{\rm C}$  for 3 h under reduced pressure of  $10^{-3}$  mmHg.

#### 2.4.3. Acidity measurements

The number of acid sites was also estimated by using a method involving an aqueous ion-exchange step of the catalyst H<sup>+</sup> ions with Na<sup>+</sup> ions, followed by titration of the resulting solution [29].

#### 2.4.4. Raman spectroscopy

The molecular structure of the supported tungsten oxide phases was determined using Raman spectroscopy since this technique has the ability to discriminate between the different tungsten oxide molecular structures [2,14,16,19]. The Raman spectra of the samples were recorded using a PerkinElmer Spectrum GX spectrometer, collected by projecting a continuous wave YAG laser of Nd (810 nm) through the samples at room temperature. A scanning range of  $700-1400~\rm cm^{-1}$  with a resolution of  $2~\rm cm^{-1}$  was applied.

#### 2.4.5. X-ray photoelectron spectroscopy (XPS)

The XPS measurement was carried out using an AMICUS photoelectron spectrometer equipped with an Mg K $\alpha$  X-ray as a primary excitation and KRATOS VISION2 software. XPS elemental spectra were acquired with 0.1 eV energy step at a pass energy of 75 kV. All the binding energies were referenced to the C 1s peak at 285.0 eV of the surface adventitious carbon.

#### 2.4.6. Thermogravimetric analysis (TGA)

TGA was performed using a TA Instruments SDT Q 600 analyzer. The samples of 10–20 mg and a temperature ramping from room temperature up to 800  $^{\circ}\text{C}$  at 10  $^{\circ}\text{C/min}$  were used in the operation. The carrier gas was  $N_2$  UHP.

#### 2.4.7. Electron spin resonance spectroscopy (ESR)

JEOL JESRE2X A model ESR was used to measure the surface F-center and  $Zr^{3+}$  on the surface of  $ZrO_2$  and  $W/ZrO_2$  [30]. Before measurement, the sample was dried at 120 °C overnight. A 0.1 g of sample was placed in a sample tube, which was sealed at atmospheric pressure and room temperature.

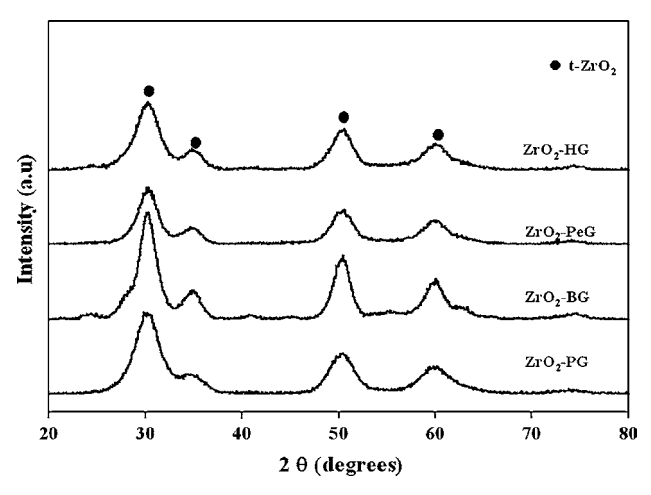
#### 2.5. Activity test

The activity test was performed on the basis of esterification reaction between acetic acid and methanol. The reaction was conducted at 60 °C with magnetic stirring in a closed 250 ml regular glass reactor using 20 g of acetic acid (99.9%) and 2 wt% of catalyst heated to the desired temperature, and the methanol (99.9%) was then added to the mixture (3 eq. molar). Sample was withdrawn periodically from the reactor, quenched to room temperature, and centrifuged in order to separate the solid catalyst from product to prevent further reaction. Concentration of reacted samples was determined using a SHIMADZU gas chromatograph (GC–14B) equipped with Chrompack SE52 column and flame ionization detector. UHP  $\rm N_2$  was used as the carrier gas. Reactions were tested in batch process for 6 h.

#### 3. Results and discussion

#### 3.1. Textural properties and crystalline structure of the catalysts

The X-ray diffraction patterns of the zirconia powders prepared by the solvothermal method in various solvents are shown in Fig. 1. The XRD patterns indicate only tetragonal crystalline zirconia (t-ZrO<sub>2</sub>) for all as-synthesized products. No other crystal structures were observed. The average crystallite sizes calculated from the XRD line broadening using the Scherrer equation and the BET surface areas of the zirconia are reported in Table 1. The average crystallite sizes of zirconia were approximately 2.7–4.0 nm. Within experimental error, there was significant difference in the crystallite sizes and BET surface areas of the zirconia prepared in different glycols, the crystallization pathway of zirconia in the various glycols is probably different [31]. The isotherms of products obtained from ZNB with different glycols are shown in Fig. 2. The isotherms of all parent materials are of IV type (IUPAC





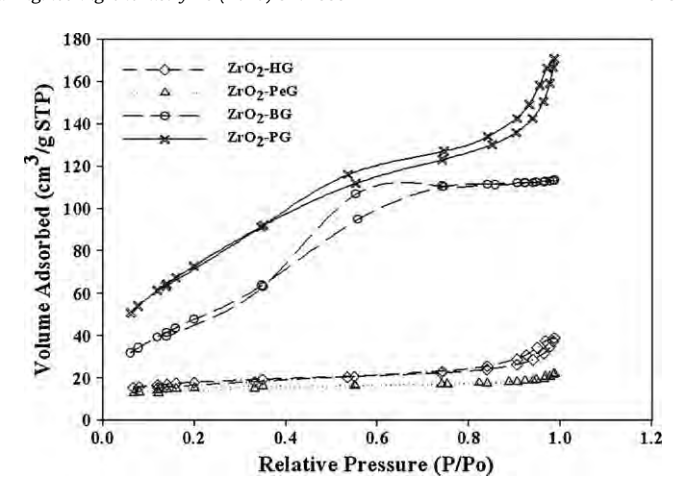


**Fig. 2.** Typical adsorption/desorption isotherms of the ZrO<sub>2</sub>.

classification) with a capillary condensation step above  $0.4\ P/P_0$ , which is typical of ordered mesoporous structures. Fig. 3a–d shows SEM images of the products synthesized in 1,3-propanediol, 1,4-butanediol, 1,5-pentanediol and 1,6-hexanediol, respectively. It was reported that when the starting material were completely dissolved into the glycol, nanocrystals were formed [32]. Each particle was, therefore, a single crystal grown from a nucleus. It was found that the samples prepared in 1,4-butanediol have a

spherical shape and a dense mass while in other glycols the samples were irregularly-shaped particles. The secondary particles which appeared as separate spherical particles when prepared in 1,4-butanediol seem to be formed by aggregation of primary particles. These results were found to be in agreement with our previous work [33]. It has been proposed by Kongwudthiti et al. [31] that the mechanisms during crystallization of zirconia in the different glycols were completely different. The ESR was used to

**Table 1**Textural characterization of zirconia supports.

Sample	Crystallite size (nm)	XRD phases	BET surface area (m <sup>2</sup> /g)	Pore volume (cm <sup>3</sup> /g)	Pore Size (nm)
ZrO <sub>2</sub> -PG	2.7	t-ZrO <sub>2</sub>	276	0.29	3.60
ZrO <sub>2</sub> -BG	4.0	t-ZrO <sub>2</sub>	184	0.19	2.69
ZrO <sub>2</sub> -PeG	3.1	t-ZrO <sub>2</sub>	54	0.02	3.84
ZrO <sub>2</sub> -HG	2.8	t-ZrO <sub>2</sub>	63	0.05	5.70

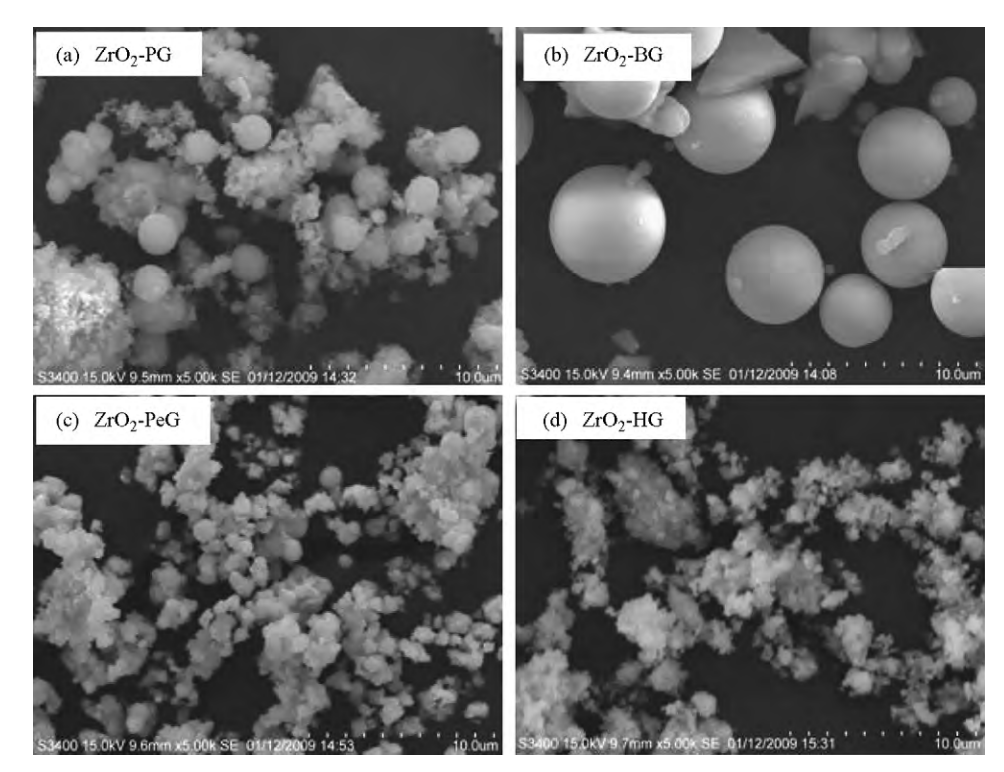


Fig. 3. SEM micrographs of (a) ZrO<sub>2</sub>-PG (b) ZrO<sub>2</sub>-BG (c) ZrO<sub>2</sub>-PeG, and (d) ZrO<sub>2</sub>-HG.

**Table 2** Physicochemical properties of W/ZrO<sub>2</sub> catalysts.

Sample	Crystallite size (nm)	XRD phases	Fraction of tetragonal phase <sup>a</sup>	BET surface area (m²/g)	W surface density (W-atom/nm <sup>2</sup> )	Surface acidity <sup>b</sup> (µmol/g)	Monotungstate/ polytungstate intensity ratio
W/ZrO <sub>2</sub> -PG	4.6	t-ZrO <sub>2</sub> , m-ZrO <sub>2</sub>	0.41	79	6.2	70	1.8
W/ZrO <sub>2</sub> -BG	4.6	t-ZrO <sub>2</sub> , $m$ -ZrO <sub>2</sub>	0.50	124	3.9	110	2.8
W/ZrO <sub>2</sub> -PeG	3.6	t-ZrO <sub>2</sub> , $m$ -ZrO <sub>2</sub>	0.36	49	10.0	55	1.1
W/ZrO <sub>2</sub> -HG	3.1	t-ZrO <sub>2</sub> , $m$ -ZrO <sub>2</sub>	0.43	62	7.9	75	2.5

<sup>&</sup>lt;sup>a</sup> Calculated from tetragonal zirconia (101) reflection from the equation  $f_t = \frac{A_t(101)}{A_{tot}(Zt02)}$ 

identify the surface nature of  $ZrO_2$ . The ESR spectra of all samples show a symmetrical singlet with g = 2.00 assigned to F-center, i.e., electrons stabilized in oxygen vacancies [34,35] as shown in Fig. 4. According to the present results, the order of F-center of zirconia prepared by different solvents was as follows:  $ZrO_2$ -PG  $> ZrO_2$ -PeG  $> ZrO_2$ -HG, which should be the origin of the formation of different morphologies for  $ZrO_2$  in the specified system.

The characteristics of various tungstated zirconia catalysts are shown in Table 2. In this study, the zirconia was impregnated with 15 wt% of tungsten and calcined in air at 500 °C for 3 h. The BET surface areas of the tungstated zirconia catalysts were slightly less than that of the original zirconia supports suggesting that tungsten was deposited in some of the pores of zirconia. This loss of surface area is significantly inhibited by the presence of WO<sub>x</sub> species [36] or the emergence of monoclinic zirconia (m-ZrO<sub>2</sub>). Among all these catalysts. W/ZrO<sub>2</sub>-BG shows higher surface area followed by W/ ZrO<sub>2</sub>-PG, W/ZrO<sub>2</sub>-HG, and W/ZrO<sub>2</sub>-PeG, respectively. Based on the values of surface area (at different solvents) and the same amount of W loading, it is possible to estimate nominal W surface densities [37]. The W surface coverage of W/ZrO<sub>2</sub>-BG sample can be achieved at the density of 3.9 W-atom/nm<sup>2</sup>, which was in good agreement with monotungstates surface coverage value (0-4 W/nm<sup>2</sup>) reported by earlier works [10]. While the W surface coverage of W/ZrO<sub>2</sub>-PG, W/ZrO<sub>2</sub>-PeG and W/ZrO<sub>2</sub>-HG are more than 4 Watom/nm<sup>2</sup> (6.2, 10.0 and 7.9 W-atom/m<sup>2</sup>, respectively). The X-ray diffraction patterns of the tungstated zirconia catalysts are shown in Fig. 5. The XRD patterns of W/ZrO<sub>2</sub> revealed the partial phase transformation from t-ZrO<sub>2</sub> to m-ZrO<sub>2</sub> in all samples due to calcination temperature with W loading. No diffraction peaks of WO<sub>3</sub> crystallites ( $2\theta = 23.2^{\circ}, 23.6^{\circ}$  and  $24.48^{\circ}$ ) were observed for all samples, indicating that tungsten oxide was well dispersed on zirconia. It should be noted that the XRD peak at ca. 24.3° for all samples was assigned to the monoclinic zirconia and not WO<sub>x</sub> crystallites [38].

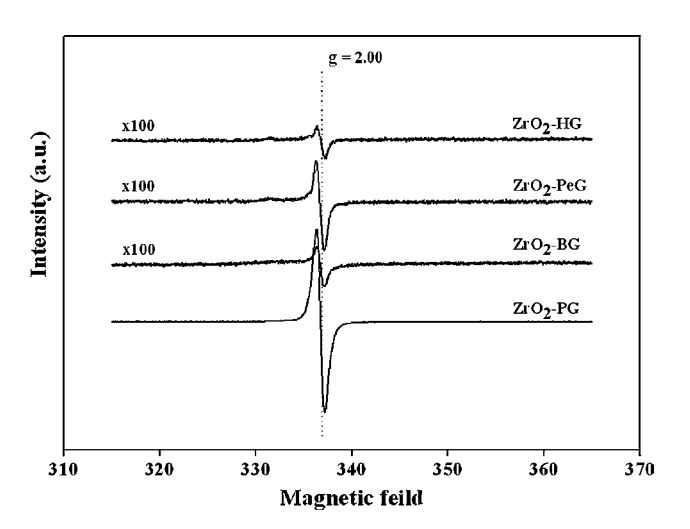


**Fig. 4.** ESR spectra of the ZrO<sub>2</sub>.

The Raman spectra of W/ZrO<sub>2</sub> catalysts are shown in Fig. 6. The Raman spectra of the tungsten oxide component are generally found at the 700–1400 cm<sup>-1</sup> region because the strong crystalline ZrO<sub>2</sub> support vibrations tend to dominate the spectra below 700 cm<sup>-1</sup> [39,40]. Crystalline WO<sub>3</sub> shows characteristic Raman bands at 807, 715, and 274 cm<sup>-1</sup> [41]. Absence of these bands indicates that microcrystalline WO<sub>3</sub> is not formed on the surface of W/ZrO<sub>2</sub> catalyst. These results are in well agreement with the XRD results, where no independent peaks due to crystalline WO<sub>3</sub> are observed. All the catalysts show broad bands of two components at 1020 and 850 cm<sup>-1</sup>, which are attributed to the symmetric stretch of the terminal W=O of monotungstate and asymmetric stretch of the W-O-W bonds of polytungstate, respectively [27,41], indicating that polytungstates coexist with monotungstate under monolayer

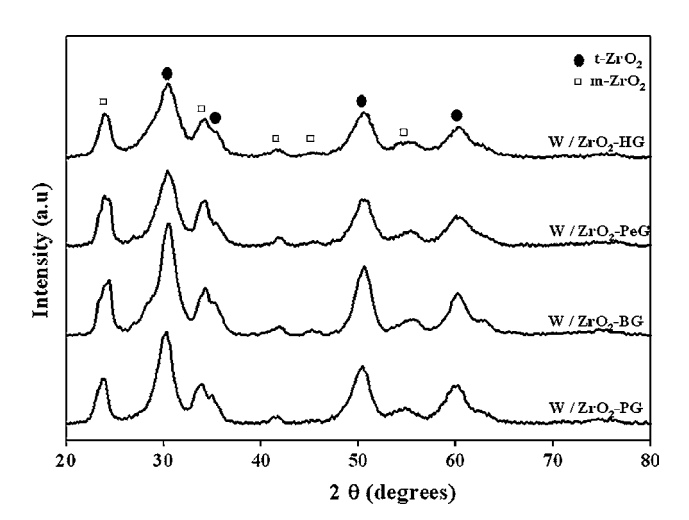


Fig. 5. XRD patterns for W/ZrO<sub>2</sub> calcined at 500 °C for 3 h.

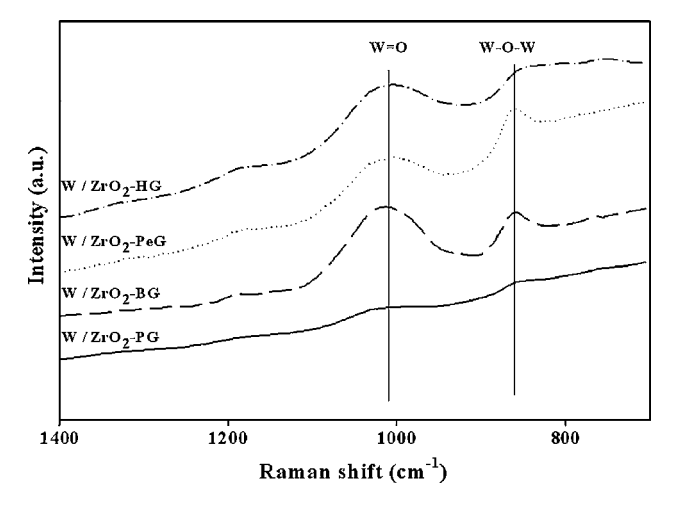


Fig. 6. Raman spectra of various W/ZrO<sub>2</sub>.

<sup>&</sup>lt;sup>b</sup> Measured by ion-exchange and titration with 0.05 N NaOH.

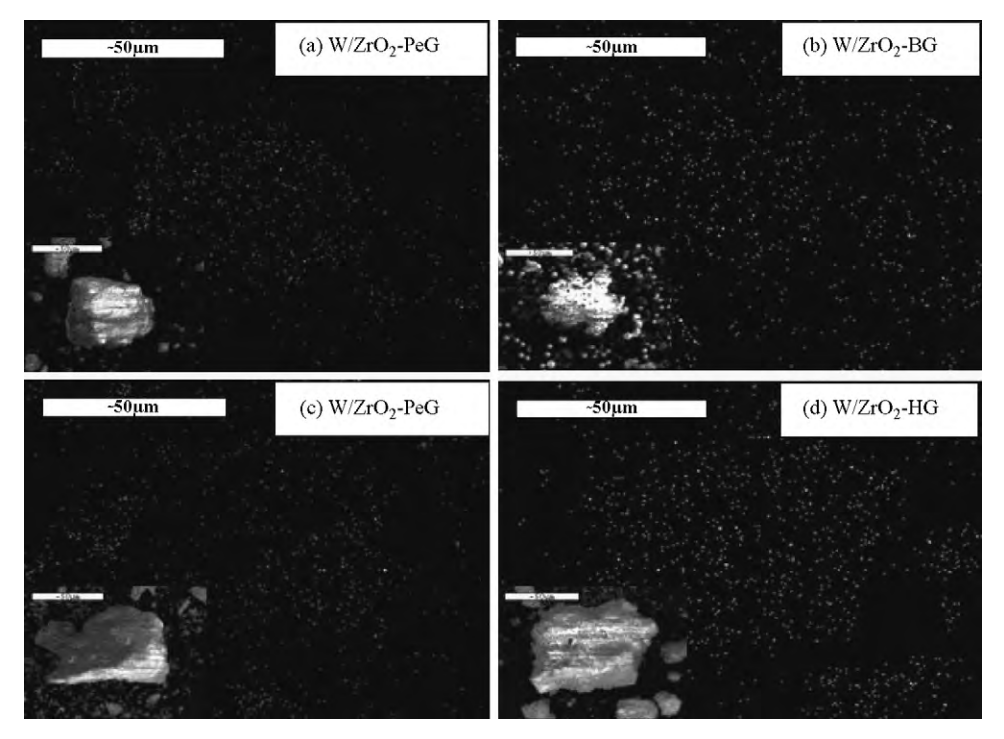


Fig. 7. SEM/EDX mapping for W distributions of (a) W/ZrO<sub>2</sub>-PG, (b) W/ZrO<sub>2</sub>-BG, (c) W/ZrO<sub>2</sub>-PG, and (d) W/ZrO<sub>2</sub>-PG.

coverage. Moreover, the complex WO<sub>v</sub> feature could be resolved by curve fitting procedures only in the range 800–1200 cm<sup>-1</sup> (not shown here), the surface monotungstate/polytungstate ratio of W/ ZrO<sub>2</sub>-BG(ca. 2.8) is larger than those prepared with other solvents as shown in Table 2. The elemental distribution was also performed using SEM/EDX mapping on the external surface. The W distribution in the various supports is shown in Fig. 7. As seen, all samples exhibited good distributions of W without any changes in the zirconia morphology. The typical measurement curve for the quantitative analysis using EDX is shown in Fig. 8. The amounts of W in various zirconia are also listed. Results revealed that the ZrO<sub>2</sub>-BG exhibited the lowest amount of W present on the surface, which can be attributed to the monotungstates surface coverage. The ESR signals for all tungstated zirconia catalysts are shown in Fig. 9. All catalysts exhibited the ESR signals of  $Zr^{3+}$  ( $g_{\perp}$  = 1.97, i.e., oxygen vacancy site) and F-center. It is known that the intensity of F- center signal on zirconia surface is disproportional to that of Zr<sup>3+</sup> signal [34,35]. The amounts of Zr<sup>3+</sup> present on the surface of zirconia are in the following order as; W/ZrO<sub>2</sub>-PeG > W/ZrO<sub>2</sub>-HG > W/ZrO<sub>2</sub>-BG > W/ZrO<sub>2</sub>-PG. It is known from previous work [6] that by calcinations in reductive and oxidative ambient, the electronic density can move to F-center and Zr<sup>3+</sup>. In addition we found that the presence of F-center on zirconia surface is able to enhance the catalytic activity of tungstated zirconia catalyst. However, in our present work, the highest amounts of F-center on the surface of ZrO<sub>2</sub>-PG did not show the highest activity of tungstated zirconia catalysts. It is therefore possible to explain these results by carbon residue on the surface of catalysts obtained from the XPS analysis (Table 3). The carbon residues on the surface of catalyst were found to be in the order:  $W/ZrO_2-PeG > W/ZrO_2-PG > W/ZrO_2-HG > W/$ ZrO<sub>2</sub>-BG. On the other words, the higher amounts of carbon residue on zirconia, the lower activity of WZ catalyst was.

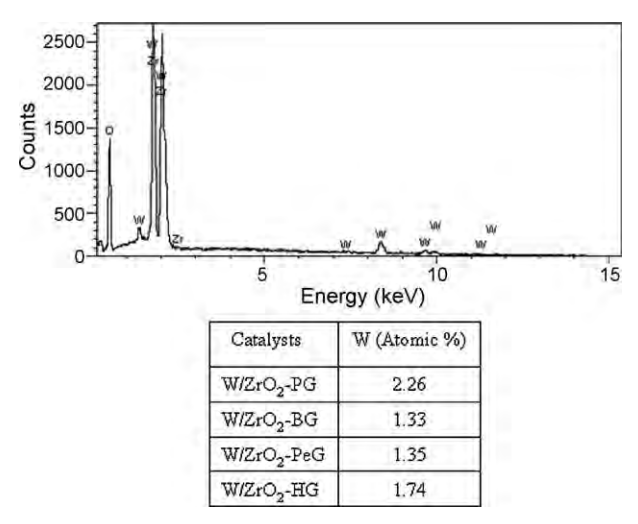


Fig. 8. A typical EDX spectrum for a W/ZrO<sub>2</sub> catalyst.

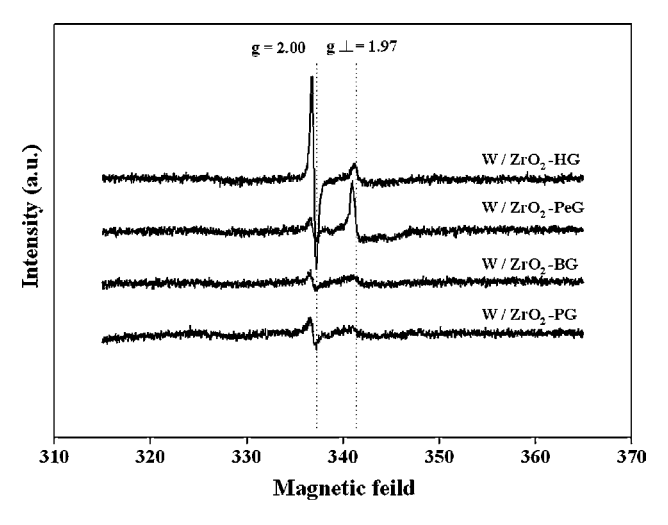


Fig. 9. ESR spectra of various  $W/ZrO_2$  catalysts.

Table 3 XPS results.

Sample	B.E. (eV	B.E. (eV)			Atomic concentration		
	Zr 3d	O 1s	W 4f	W/Zr	W/O	Zr/O	C (%)
ZrO <sub>2</sub> -PG	184.4	531.0	-	-	-	0.267	42.74
ZrO <sub>2</sub> -BG	184.1	530.2	-	-	-	0.330	11.91
ZrO <sub>2</sub> -PeG	185.1	531.3	-	-	-	0.337	39.86
ZrO <sub>2</sub> -HG	184.3	530.5	-	-	-	0.334	30.89
W/ZrO <sub>2</sub> -PG	185.7	531.3	36.2	0.311	0.079	0.265	29.74
W/ZrO <sub>2</sub> -BG	184.9	530.7	36.6	0.146	0.047	0.320	14.04
W/ZrO <sub>2</sub> -PeG	185.0	531.3	35.0	0.377	0.098	0.260	36.74
W/ZrO <sub>2</sub> -HG	185.5	530.8	37.7	0.171	0.054	0.314	23.49

#### 3.2. Surface acidity of the samples

In order to form a catalytically active form, it is usually necessary to anchor the amorphous WO<sub>x</sub> with ZrO<sub>2</sub> tetragonal crystal phase [5,14,41]. Surface acidity is the most important function of tungstated zirconia. The acidity measurements of the catalysts by means of acid-base titration with NaOH allow us to estimate the surface acidity. It was found that they are in the range of ca. 70, 110, 55 and 75 µmol/g for W/ZrO<sub>2</sub>-PG, W/ZrO<sub>2</sub>-BG, W/ ZrO<sub>2</sub>-PeG and W/ZrO<sub>2</sub>-HG samples, respectively (Table 2). It was observed that for W/ZrO<sub>2</sub>-BG catalyst showed the highest surface acidity among all catalysts. The number of acid sites decreases in parallel with the increase of W surface density content. Probably as a result of the generation of new acid sites due to interaction and dispersion of WO<sub>x</sub> on the surface of the support. When the dispersion of WO<sub>x</sub> is maximum (at the theoretical monolayer coverage) for W/ZrO<sub>2</sub>-BG sample, the acidity is maximum. Moreover, samples with higher W surface density content show loss of acidity that is probably due to the agglomeration of  $WO_x$  on the surface.

#### 3.3. Reaction study

Acetic acid conversion in the esterification reaction of acetic acid and methanol over the four tungstated zirconia catalysts as mentioned before were shown in Fig. 10, indicating increased conversion in the order of:W/ZrO<sub>2</sub>-PeG < W/ZrO<sub>2</sub>-PG < W/ZrO<sub>2</sub>-HG < W/ZrO<sub>2</sub>-BG. The increased activity of W/ZrO<sub>2</sub>-BG can be attributed to its higher acidity as observed from acid-base titration techniques (Table 2). It is well known that the *W* surface density

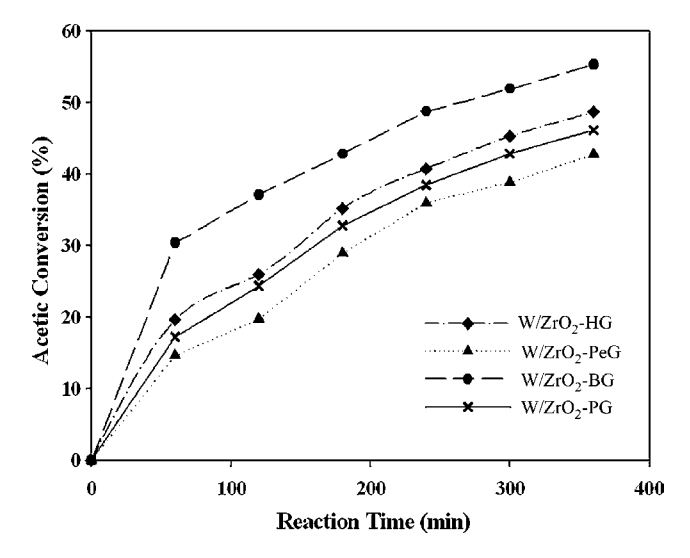


Fig. 10. Catalytic activity on the different W/ZrO<sub>2</sub> catalysts.

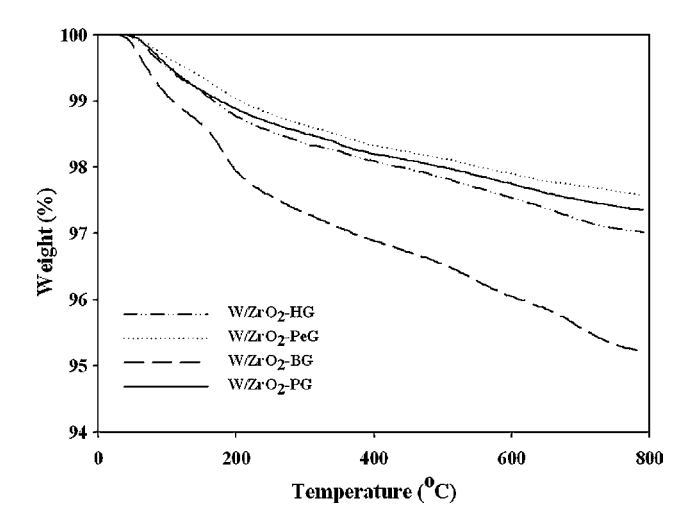


Fig. 11. TGA profiles of various W/ZrO<sub>2</sub> catalysts.

content of the catalysts and the formation of WO<sub>x</sub> surface species is an essential factor for remaining the acidity of the catalysts, which may greatly influence the catalytic activity [10–28]. The formation of WO<sub>x</sub> surface species was observed by Raman spectroscopy. Based on this study, activity of catalyst is related to the increasing surface monotungstate/polytungstate ratio with surface tungsten oxide coverage. One of the possible reasons is that the interaction and dispersion of WO<sub>x</sub> on the surface of the support. The degree of interaction between the zirconia and adsorbed species can be determined by the TGA measurement [42–45]. The TGA profiles for all catalysts are shown in Fig. 11, indicating similar profiles for various supports showing the desorption of similar species. We observed that the weight losses of samples were in the order of W/  $ZrO_2$ -BG (4.8%) > W/ $ZrO_2$ -HG (3.0%) > W/ $ZrO_2$ -PG (2.7%) > W/ ZrO<sub>2</sub>-PeG (2.4%). This indicated that adsorbed species present on ZrO<sub>2</sub>-PeG had the strongest interaction, and thus the lowest observed esterification activity. The adsorbed species are presumably involving with desorption of oxygenated and proton species relating to acidity of catalysts [46]. As seen, the carbon residue on the surface of catalysts apparently resulted in increased interaction leading to decreased acidity of catalysts. It should be mentioned that the acetic acid conversion in this present study was less than our previous work [6]. This was due to different calcination treatments for ZrO<sub>2</sub> prepared from the same solvent. As mentioned in the previous work [6], the H<sub>2</sub> treatment during calcination can result in increased F-center of ZrO2 samples leading to increased catalytic activity.

#### 4. Conclusions

This study revealed the effects of solvent on morphology and other characteristics of zirconia and their performance as tungstated zirconia catalyst. It was found that a series of  $WO_x/ZrO_2$  catalysts exhibited the tungsten density in the range of 3.9 to 10.0 W-atoms/nm². XRD and Raman spectroscopy results indicated that the W phase is present as a surface interaction species. No evidence for the formation of  $WO_3$  was found. The zirconia prepared in 1,4-butanediol as the support resulted in the highest surface acidity consequently having the highest activity. The lower activities of tungstated zirconia catalysts prepared in other solvents were due to stronger interaction of proton species and the zirconia supports as shown by weight losses of samples in the TGA profiles. The types of solvent used for preparation of the glycothermal-derived zirconia may affect the amount of carbon residue and  $WO_x$  monotungstate/polytungstate ratio on the

surface of catalysts resulting in the difference in proton speciessupport interaction behavior.

#### Acknowledgments

The authors thank the Thailand Research Fund (TRF) and Office of the Higher Education Commission (CHE) for the financial support of this project.

#### References

- [1] C.D. Baertsch, K.T. Komala, Y. Chua, E. Iglesia, J. Catal. 205 (2002) 44.
- M. Scheithauer, T.K. Cheung, R.E. Jentoft, R.K. Grasselli, B.C. Gates, H. Knözinger, J. Catal. 180 (1998) 1;
   (a) G. Talebi, M. Sohrabi, S.I. Rovaee, Ind. Eng. Chem. 14 (5) (2008) 614.
- (a) G. Ferraris, M. Valigi, D. Gazzoli, Appl. Catal. A Gen. 231 (2002) 173.
- [4] F.D. Gregorio, N. Keller, V. Keller, J. Catal. 256 (2008) 159.
- [5] S. Ramu, N. Lingaiah, B.L.A.P. Devi, R.B.N. Prasad, I. Suryanarayana, P.S.S. Prasad, Appl. Catal. A Gen. 276 (2004) 163.
- [6] P. Wongmaneenil, B. Jongsomjit, P. Praserthdam, Catal. Commun. 10 (2009) 1079.
- [7] (a) E. Iglesia, D.G. Barton, S.L. Soled, S. Miseo, J.E. Baumgartner, W.E. Gates, G.A. Fuentes, G.D. Meitzner, Stud. Surf. Sci. Catal. 101 (1996) 533;
   (b) B.S. Kang, W.G. Lee, Ind. Eng. Chem. 15 (5) (2009) 694.
- [8] G. Larsen, E. Lotero, R.D. Parra, L.M. Petkovic, H.S. Silva, S. Raghavan, Appl. Catal. A Gen. 130 (1995) 213.
- [9] F.T.T. Ng, N. Horvát, Appl. Catal. A Gen. 123 (1995) L197.
- [10] D.G. Barton, M. Shtein, R.D. Wilson, S.L. Soled, E. Iglesia, J. Phys. Chem. B 103 (1999) 630.
- [11] D.G. Barton, S.L. Soled, G.D. Meitzer, G.A. Fuentes, E. Iglesia, J. Catal. 181 (1999) 57.
- [12] D.G. Barton, S.L. Soled, E. Iglesia, Topics Catal. 6 (1998) 87.
- [13] I.E. Wachs, T. Kim, E.I. Ross, Catal. Today 116 (2006) 162.
- [14] M. Hino, K. Arata, J. Chem. Soc. Chem. Commun. 18 (1987) 1259.
- [15] J.C. Vartuli, J.G. Santiesteban, P. Traverso, N. Cardona-Martínez, C.D. Chang, S.A. Stevenson, J. Catal. 187 (1999) 131.
- [16] J.G. Santiesteban, J.C. Vartuli, S. Han, D. Bastian, C.D. Chang, J. Catal. 168 (1997) 431.

- [17] S.R. Vaudagna, S.A. Canavese, R.A. Comelli, N.S. Fígoli, Appl. Catal. 168 (1998) 93.
- [18] G. Larsen, E. Lotero, L.M. Petkovic, D.S. Shobe, J. Catal. 169 (1997) 67.
- [19] R.A. Boyse, E.I. Ko, J. Catal. 171 (1997) 191.
- [20] M. Scheithauer, R.K. Grasselli, H. Knözinger, Langmuir 14 (1998) 3019.
- [21] J.R. Sohn, M.Y. Park, Langmuir 14 (1998) 6140.
- [22] M. Valigi, D. Gazzoli, I. Pettiti, G. Mattei, S. Colonna, S. De Rossi, G. Ferraris, Appl. Catal. A Gen. 231 (2002) 159.
- [23] S. Kuba, P. Lukinskas, R.K. Grasselli, B.C. Gates, H. Knözinger, J. Catal. 216 (2003) 353.
- [24] A. Galano, G. Rodriguez-Gattorno, E. Torres-García, Phys. Chem. Chem. Phys. 10 (2008) 4181.
- [25] B.M. Reddy, M.K. Patil, B.T. Reddy, Catal. Lett. 125 (2008) 97.
- [26] D. Gazzoli, M. Valigi, R. Dragone, J. Phys. Chem. B 101 (1997) 11129.
- [27] D.S. Kim, M. Ostromecki, I.E. Wachs, J. Mol. Catal. A 106 (1996) 93.
- [28] T. Onfroy, G. Clet, M. Houalla, J. Phys. Chem. B 109 (2005) 3345.
- [29] D.E. López, J.G. Goodwin Jr., D.A. Bruce, J. Catal. 245 (2007) 381.
- [30] E.V. Frolova, M.I. Ivanovskaya, Mater. Sci. Eng. C 26 (2006) 1106.
- [31] S. Kongwudthiti, P. Praserthdam, P.L. Silveston, M. Inoue, Ceram. Int. 29 (2003) 807.
- [32] M. Inoue, Adv. Sci. Technol. 29 (2000) 855.
- [33] S. Kongwudthiti, D. Eng Thesis, Chulalongkorn University, Thailand (2002).
- [34] H. Liu, L. Feng, X. Zhang, Q. Xue, J. Phys. Chem. 99 (1995) 332.
- [35] C. Morterra, E. Giamello, L. Orio, M. Volante, J. Phys. Chem. 7 (1990) 3111.
- [36] D.E. López, K. Suwannakarn, D.A. Bruce, J.G. Goodwin Jr., J. Catal. 247 (2007) 43.
- [37] B.M. Reddy, M.K. Patil, G.K. Reddy, B.T. Reddy, K.N. Rao, Appl. Catal. A Gen. 332 (2007) 183.
- [38] V.V. Srdic, M. Winterer, Chem. Mater. 15 (2003) 2668.
- [39] J. Macht, C.D. Baertsch, M. May-Lozano, S.L. Soled, Y. Wang, E. Iglesia, J. Catal. 227 (2004) 479.
- [40] N. Vaidyanathan, M. Houalla, D. Hercules, Surf. Interf. Anal. 26 (1998) 415.
- [41] E. Torres-García, G. Rosas, J.A. Ascencio, E. Haro-Poniatowski, R. Pérez, Appl. Phys. A 79 (2004) 401.
- [42] B. Jongsomjit, T. Womgsalee, P. Praserthdam, Catal. Commun. 6 (2005) 192.
- [43] C. Ketloy, B. Jongsomjit, P. Praserthdam, Appl. Catal. A Gen. 327 (2007) 270.
- [44] S. Srijumnong, P. Suttipitakwong, B. Jongsomjit, P. Praserthdam, J. Mol. Catal. A 294 (2008) 1.
- [45] B. Jongsomjit, S. Ngamposri, P. Praserthdam, Ind. Eng. Chem. Res. 44 (2005) 9059.
- [46] F.D. Gregorio, V. Keller, J. Catal. 225 (2004) 45.

# The Role of Zirconia Surface on Catalytic Activity of Tungstated Zirconia via Two-Phase Esterification of Acetic Acid and 1-Heptanol

Kanokwan Ngaosuwan · Bunjerd Jongsomjit · Pivasan Praserthdam

Received: 26 August 2009 / Accepted: 19 October 2009 / Published online: 3 November 2009 © Springer Science+Business Media, LLC 2009

**Abstract** It is proven that surface nature of zirconia can play crucial roles on determining the catalytic activity of tungstated zirconia catalysts. The solvothermal method for preparation of crystalline zirconia support can result in the formation of Zr–OH bond on its surface. This surface species related to the Zr-heteropolyacid, acting as strong Brønsted acid sites. It consequently affected on the catalytic activity.

**Keywords** Zirconia · Tungstated zirconia · Solvothermal method · Zr–OH bond · Zr-heteropolyacid

#### 1 Introduction

Currently, the replacement of homogeneous catalysts with suitable heterogeneous ones is a major key to develop many processes, since heterogeneous catalysts are environmental friendly and potentially used for a long time and/ or multiple reaction cycles. Moreover, it readily allows for the implementation of continuous processes. Interestingly, the heterogeneous catalyst demonstrated the remarkable performance for two-phase esterification system (organic and aqueous phases). It has been also known that the replacement of adsorbed water molecule by acetic acid molecule was only carried out by a solid acid catalyst. In our previous study [1], we reported that the Amberlyst 15 exhibited higher turnover number (TON) than sulfuric acid

K. Ngaosuwan · B. Jongsomjit · P. Praserthdam (☒) Center of Excellence on Catalysis and Catalytic Reaction Engineering, Department of Chemical Engineering, Faculty of Engineering, Chulalongkorn University, Bangkok 10330, Thailand

e-mail: piyasan.p@chula.ac.th

 $\underline{\underline{\mathscr{D}}}$  Springer

(H<sub>2</sub>SO<sub>4</sub>) in the two-phase acid catalyzed esterification of dilute acetic acid and 1-heptanol. It was proposed that the Amberlyst 15 with adsorbed acetic acid on active sites can move into the organic phase (upper phase) by agitator, and then react with 1-heptanol leading to increased catalytic activity because the reaction occurs in the organic phase. In addition, increased activity can be also attributed to the decrease of solvation effect by water.

A heterogeneous catalyst as a tungsten oxide supported on zirconia (WZ) has been tremendously used for alkane isomerization [2-5], alcohol dehydration [6, 7] and recently biodiesel forming reaction [8–13]. This is because of their acid properties, stability under reducing and oxidizing conditions and regenerability [14]. The nature of active site is a key factor in order to achieve the high catalytic performance. For instance, the calcination temperature and tungsten loading affects on the structure of WO<sub>x</sub> presented in an isolated surface monotungstates, polymerics surface polytungstates and crystalline WO<sub>3</sub> particles on a zirconia support as reported in numerous studies [3, 4, 6, 7, 15, 16]. Barton et al. [4] reported that the maximum activity for tungsten loading was slightly rather than monolayer coverage, so called polytungstate species for hydrocarbon isomerization. Gregorio et al. [17] suggested that the 15% of tungsten loading is a critical value to achieve high activity, selectivity, and stability of the catalyst on stream and good activity for saturated hydrocarbon isomerization. Lopez et al. [11] reported that the calcination temperature of 800 °C contributed with tungsten oxide polymeric structure can achieve the highest catalytic activity for both esterification and transesterification. In many cases, the preparation method of zirconia is allowing to make different surface species formed [18-21]. The generation of new active sites on the surface can bring about various influences on activity and selectivity for certain types of reactions [22]. Lebarbier et al. [23] reported that no significant effect of the initial form of the support (Zr oxyhydroxide versus predominantly tetragonal zirconia) was observed for *n*-hexane isomerization. Wongmaneenil et al. [24] found that the calcination of ZrO<sub>2</sub> support in the reductive atmosphere (H<sub>2</sub>) can achieve higher conversion for esterification of acetic acid than that of oxidative atmosphere (O<sub>2</sub>). Although, the numerous studies have been investigated, the influence of the ZrO<sub>2</sub> support on the acid properties of the WZ catalysts and their relation with the activity and surface structure are still unclear.

This work has been focused on the behaviors of surface nature for the ZrO<sub>2</sub> support prepared by the solvothermal method before and after loading of 15 wt% of tungsten. Based on the similar texture properties, non-treated ZrO<sub>2</sub> support (crystalline zirconia bonding with hydroxide, Zr-OH) was compared to the thermal treated ZrO<sub>2</sub> under H<sub>2</sub> as a reduction atmosphere (crystalline zirconia, ZrO<sub>2</sub>). All catalyst characteristics have been investigated by means of XRD, N<sub>2</sub> physisorption, FT-IR spectroscopy, Raman spectroscopy, and electron spin resonance (ESR). The twophase esterification of dilute acetic acid and 1-heptanol was performed to measure the catalytic activity of WZ catalysts in a batch reactor. This is due to the outstanding properties of WZ (distribution of acid site between Brønsted and Lewis acid sites) that would gain more beneficial for the two-phase esterification, which requires the heterogeneous catalyzed reaction [6, 12, 25, 26].

#### 2 Experimental

#### 2.1 Materials

Acetic acid (99.8%) and 1-heptanol (99%) were purchased from Merck and used as received. Heptyl acetate (98%) as standard of product was purchased from Wako Pure Chemical Industries. Tungstated zirconia (WZ-X) was prepared as described in Sect. 2.2

Aldrich) in a test tube, which was then placed in a 300 mL autoclave. A 30 mL of 1,4-butanediol was filled in the gab between the test tube and the autoclave wall. The autoclave was purged with nitrogen. The mixture was heated to 300 °C at a rate of 2.5 °C/min. The temperature was held constantly at 300 °C for 2 h. After reaction, this autoclave was cooled and the resulting powder yield was repeatedly washed with methanol by centrifugation. Subsequently, they were dried in air and designated as Z-NT (non-treated zirconia). Another ZrO<sub>2</sub> support was treated at 400 °C with heating rate of 10 °C/min under flowing H<sub>2</sub> atmosphere (UHP grade of gases from TIG) for 2 h, designated as Z-H<sub>2</sub> (H<sub>2</sub> treated zirconia).

Tungstated zirconia (WZ) catalysts were prepared by the incipient wetness impregnation of zirconia with an aqueous solution of WCl<sub>6</sub> to obtain the final catalyst having 15 wt% of tungsten loading. The hydrolysis of WCl<sub>6</sub> possibly resulted in the well dispersion of WCl<sub>6</sub> species in the aqueous solution, which is corresponding to work reported by Kob et al. [28]. This probably leads to obtain well dispersion on the zirconia support. The freshly impregnated catalyst was dried at 110 °C for 12 h. Then, it was calcined at 500 °C for 3 h [24]. The retained chlorine on WZ catalyst was less than 10 ppm, which was verified by the AgNO<sub>3</sub> titration with  $K_2$ CrO<sub>4</sub> indicator. The nomenclatures given as WZ-NT and WZ-H<sub>2</sub> were used for the tungstated on non-treated zirconia and H<sub>2</sub> treated zirconia surface, respectively.

#### 2.3 Catalysts Characterization

Powder X-ray diffraction (XRD) was performed by SIE-MENS XRD D5000 using  $CuK_{\alpha}$  radiation. The average crystallite size was determined using Scherrer's equation calculated from peak broadening as applied to the tetragonal (101) peak.

Physical properties, such as BET surface area ( $S_{\rm BET}$ ), pore diameters and BJH cumulative pore volumes were evaluated with N<sub>2</sub> adsorption–desorption at –196 °C in a Micromeritics ASAP 2020 [12]. The tungsten surface density was calculated based on the BET surface area of WZ and tungsten loading (15 wt%) as follows [24, 29]:

$$Surface \ density = \frac{\text{Promoterloading}(\%) \, / \, 100 \times 6.023 \times 10^{23}}{\text{Formula weight of promoter} \times \text{BET surface area} \ (m^2/g^{-1}) \times 100^{18}}$$

#### 2.2 Catalyst Preparation

Zirconia as a support was prepared via a solvothermal method as reported by Kongwudthiti et al. [27]. Zirconium tetra-*n*-butoxide 80 wt% solution in 1-butanol (Aldrich) was suspended in 100 mL of 1,4-butanediol (99%, Sigma—

A JEOL, JESRE2X model electron spin resonance spectroscopy (ESR) was used to measure the surface F-center and  $Zr^{3+}$  on the surface of  $ZrO_2$  and WZ. Before measurement, the sample was dried at 110 °C overnight. 0.1 g of sample was placed in a sample tube, which was sealed at atmospheric pressure and room temperature.



K. Ngaosuwan et al.

FT-IR analysis of ZrO<sub>2</sub> support was carried out in a Nicol model 6700 of the IR spectrometer using the wavenumber ranging from 400 to 4,000 cm<sup>-1</sup> with a resolution of 4 cm<sup>-1</sup>. A small amount of sample (0.2 g) was thoroughly mixed with ground KBr in an agate mortar and pressed as pellets.

The Raman spectra of the samples were collected by projecting a continuous wave YAG laser of Nd (810 nm) through samples at room temperature. A scanning range of 200–1,400 cm<sup>-1</sup> with a resolution of 2 cm<sup>-1</sup> was applied.

#### 2.4 Reaction Test

The catalyst activity via the esterification reaction between dilute acetic acid (6 wt%) and 1-heptanol was conducted in a stirred batch reflux system at temperature 90 °C. A threenecked flask equipped with a condenser and stirrer was charged with certain amount of 6 wt% of dilute acetic acid (6.8 mL) and catalyst samples (0.3 g). Then, the system was heated up to the reaction temperature after which the pre-heated heptanol (3.2 mL) was added. Sufficient stirring of the mixture was used to avoid external mass or heat transport limitations. The reaction temperature was maintained by means of a thermostatic paraffin bath in which the reactor was immersed. For catalytic activity measurement, samples were diluted with 2-propanol (10 mL) to stop reaction and perform in a single phase, and then analyzed by GC (Shimudzu) equipped with a flame ionization detector and Chrompack SE52 column. The reaction was repeated at different reaction times in order to obtain the acetic conversion profiles. All catalysts were employed under similar reaction conditions. GC analysis confirmed that no by-products were formed. The acetic acid conversion (%) was calculated as follows:

% acetic acid conversion

 $= \frac{\text{initial acetic acid conc.} - \text{acetic acid conc. at time } (t)}{\text{initial acetic acid conc.}}$ 

 $\times 100$ 

#### 3 Results and Discussion

Upon different treatments of zirconia, it was observed that the color of Z-NT was white, whereas the color of the  $Z-H_2$  changed from white to dark yellow with the treatment of  $H_2$ . This suggested that the thermal treatment under reductive atmosphere generated the F-center (color center) [30] due to the strong Zr–O bond energy that is less likely reduced by  $H_2$  [24]. However, the color of catalyst (WZ and WZ- $H_2$ ) has returned to white again after calcination because re-oxidation was obtained [2]. This phenomenon supports the hypothesis in the color change with the presence of F-center which is only observed on the Z- $H_2$ 

support. Figure 1 shows the XRD patterns of ZrO<sub>2</sub> support as synthesized (Z-NT) and treated in H<sub>2</sub> atmosphere (Z-H<sub>2</sub>). Tetragonal phase (t-ZrO<sub>2</sub>) is the primary crystalline structure for Z-NT and Z-H<sub>2</sub> with the diffraction peaks at 30.2, 35.3 and 49.8° [11]. A crystallite size was calculated from Scherrer's equation of the tetragonal (101) peak [31] as shown in Table 1. After the thermal treatment under reduction atmosphere (H<sub>2</sub>) was applied on the ZrO<sub>2</sub>, it was found that the crystallite size and the fraction of tetragonal phase structure of Z-H<sub>2</sub> were still similar to those of Z-NT sample. The crystallite sizes of WZ-NT (4.5 nm) and WZ-H<sub>2</sub> (4.7 nm) were slightly larger than those zirconia supports before the tungsten loading when increasing of the calcination temperature to 500 °C. The increase calcination temperature was also allowing to present a fraction of monoclinic phase (m-ZrO<sub>2</sub>) with the diffraction peak at 24.3° (Fig. 1), which is in agreement with the work reported by Wongmaneenil [24]. For this study, the deposit of tungsten did not exhibit to stabilize t-ZrO<sub>2</sub> phase because the impregnation method appeared to permit tungsten being present on the ZrO<sub>2</sub> crystallite surface. It is known that the co-precipitation and sol-gel synthesis are the methods for incorporating tungsten atom into ZrO<sub>2</sub> lattice, which stabilizes the tetragonal structure [18, 19, 32]. WO<sub>3</sub>, on the other hand, has not been detected for both WZ-NT and WZ-H<sub>2</sub>. This may be due to either relatively low calcination temperature or tungsten loading [3, 4, 6, 7, 16, 33].

The catalyst textural properties determined by the BET method and acid site concentrations as measured by ion-exchange titration are listed in Table 1. The surface areas of Z-H<sub>2</sub> and Z-NT were comparable within the experimental error. This result suggested that the reductive calcination treatment did not affect on the surface area as corresponding to our previous study [24]. In general, the

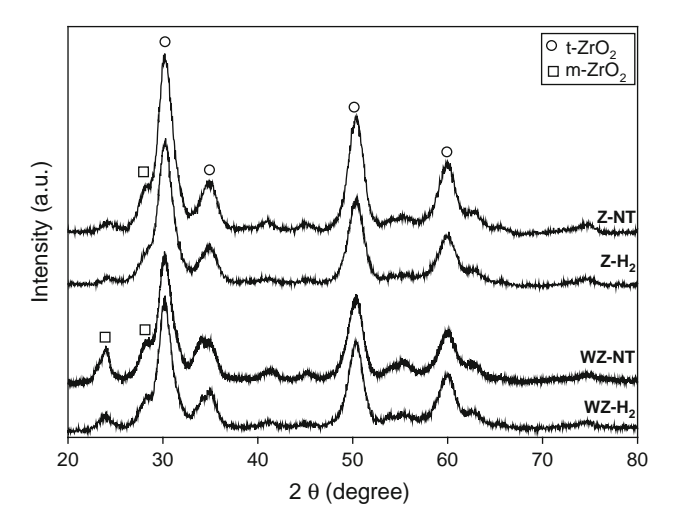


Fig. 1 XRD patterns for ZrO<sub>2</sub> supports and WZ catalysts



Table 1 Surface area, theoretical W surface density, surface acidity, crystallite size and XRD phases for ZrO<sub>2</sub> support and WZ samples

Sample	BET surface area $(m^2/g)^a$	W surface density (W-atom/nm <sup>2</sup> )	Surface acidity by exchange/titration (μmol/g) <sup>b</sup>	Crystallite size (nm)	XRD phases
Z-NT	161	_	-	4.1	t-ZrO <sub>2</sub> , m-ZrO <sub>2</sub>
$Z-H_2$	155	_	_	4.3	$t$ - $ZrO_2$
WZ-NT	125	3.93	233.0	4.5	t-ZrO <sub>2</sub> , m-ZrO <sub>2</sub>
$WZ-H_2$	125	3.93	133.0	4.7	$t$ - $ZrO_2$ , $m$ - $ZrO_2$

<sup>&</sup>lt;sup>a</sup> Experimental error ± 7%

penetration of tungsten species into the pore of  $ZrO_2$  support could reduce the surface area of WZ-NT and WZ-H<sub>2</sub> [34]. In order to estimate the theoretical nominal W surface densities, WZ surface area and amount of tungsten loading were used [29]. It was found that the W surface coverage of both WZ-NT and WZ-H<sub>2</sub> were presented as the growing surface polytungstated domain and crystalline of WO<sub>3</sub> ( $\sim$ 4 W atom/nm<sup>2</sup>) [15, 35, 36].

The other physical properties, such as crystallite size, tetragonal structure, and BET surface area for both Z-H<sub>2</sub> and Z-NT were almost similar, except for the surface defect. The electron spin resonance (ESR) spectroscopy is one of the most powerful techniques used to detect the structural defect, as shown in Fig. 2. The ESR signal of  $ZrO_2$  can be found with g values,  $g_{\perp} = 1.97$  assigned to  $Zr^{3+}$  [37] and g = 2.00 assigned to F-center [38]. As seen, no ESR signal for the Z-NT sample was observed in the magnetic field ranging between 310 and 370 indicating that no defect occurred on the surface of Z-NT sample. When the ZrO<sub>2</sub> was treated in a reductive atmosphere (H<sub>2</sub>), the F-center was present. The dominated intensity of F-center on Z-H<sub>2</sub> may be produced by the reduction of hydroxyl group on ZrO2 surface, which is corresponding to the previous reports [24, 30, 39, 40]. Due to the strong Zr-O bond energy, H2 may not reduce the ZrO2 surface allowing to insignificant intensity of Zr<sup>3+</sup> obtained [37]. The ESR spectra of WZ catalysts were also illustrated in Fig. 2. WZ catalysts were in the oxidation atmosphere during the deposition of tungsten onto ZrO2 support. Thus, the ESR signals of Zr<sup>3+</sup> were detected on the ZrO<sub>2</sub> support for both WZ-NT and WZ-H<sub>2</sub> because the oxygen coordinatively unsaturated Zr sites under oxidation atmosphere [40]. In addition, the shift of F-center  $(V_0^-)$  to  $Zr^{3+}$   $(g_{\perp} = 1.97)$  for WZ-H<sub>2</sub> was also observed within a good agreement to the previous reports [24, 30].

FT-IR spectroscopy was used to clarify the chemical bonding of  $\rm ZrO_2$  support obtained by different thermal treatments in the range of 400–4,000 cm $^{-1}$  as presented in Fig. 3. It was found that five transmittance peaks were observed over this range. A very broad band with the highest frequency at 3,421 cm $^{-1}$  contributed to the

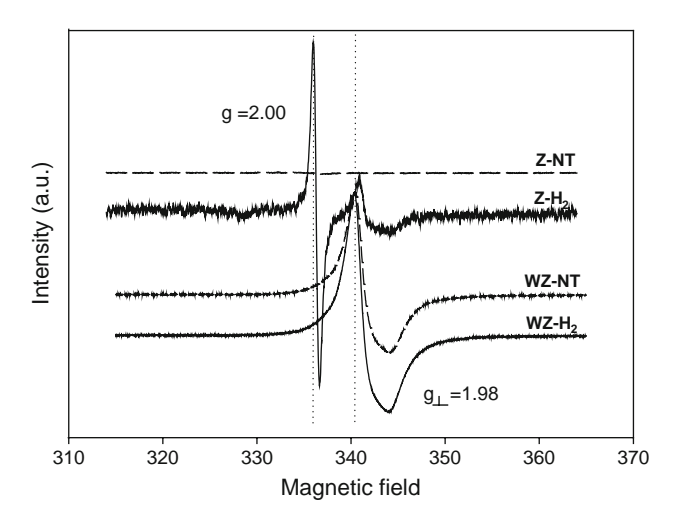


Fig. 2 ESR spectra of ZrO<sub>2</sub> supports and WZ catalysts

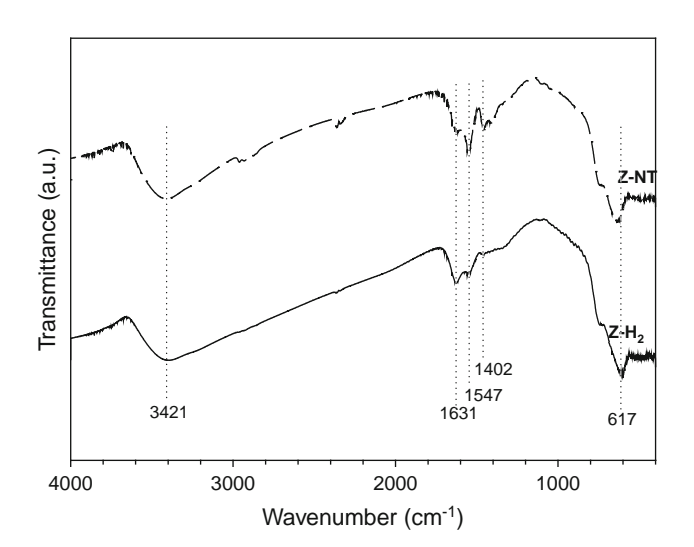


Fig. 3 FT-IR spectra of ZrO<sub>2</sub> supports

physically adsorbed water molecular as reported in those literatures [41–43]. In addition, the band at 1,631 cm<sup>-1</sup> should be attributed to the OH group of free water related to alcohol. The IR band within the range of 617–632 cm<sup>-1</sup> was corresponding to the bond of metal and oxygen (Zr–O)



b Experimental error ± 10%

K. Ngaosuwan et al.

as presented for both ZrO<sub>2</sub> supports [43]. There were other two peaks observed at 1,547 and 1,402 cm<sup>-1</sup>, which are corresponding to the metal and hydroxide (Zr–OH) bond [42, 43]. It can be concluded that ZrO<sub>2</sub> supported prepared from solvothermal method [27] exhibited the Zr–OH group. However, this metal hydroxide bond can be eliminated by the thermal treatment in the reduction atmosphere (H<sub>2</sub>) indicated by the decrement of these characteristic peaks. The FT-IR spectrum of ZrO<sub>2</sub> support is corresponding to the ESR signal with the presence of F-center on the Z-H<sub>2</sub> surface. Therefore, the F-center is probably produced by the reduction of hydroxyl group on ZrO<sub>2</sub> surface through the following reaction [39, 40]:

$$Zr^{4+} - OH^- + \frac{1}{2}H_2 \to Zr^{4+} + F^- + H_2O$$

In order to obtain a better insight for the changes upon molecular level structure of the tungsten oxide overlayer for WZ catalysts, the Raman spectroscopy was performed as seen in Fig. 4. The Raman bands at 310, 402, and 473 cm<sup>-1</sup> were assigned to the tetragonal phase of ZrO<sub>2</sub> [11, 35, 44] as presented in both catalysts. Both WZ-NT and WZ-H<sub>2</sub> showed the characteristic peak of the terminal W=O band of the dehydrated surface WO<sub>x</sub> species at 910-1,030 cm<sup>-1</sup> [11, 36]. The WZ-H<sub>2</sub> exhibited slightly higher intensity of crystalline WO<sub>3</sub> nano-particle (799 cm<sup>-1</sup>) than that of WZ-NT. The crystalline WO<sub>3</sub> nano-particle was observed upon the W surface density at  $\sim 4 \text{ W/nm}^2$  as reported by Wachs et al. [36]. The stretching and bending modes of the bridging for W-O-W were assigned at  $\sim 500-800$  and  $\sim 200-300$  cm<sup>-1</sup> [35, 45]. As illustrated in Fig. 4, WZ-NT had higher intensity of bending mode of the bridging W-O-W than that for the WZ-H<sub>2</sub>, whereas the stretching modes of bridging W-O-W were comparable. In summary, three different tungsten species (W=O, WO<sub>3</sub>, and W-O-W) were observed for both catalysts, which

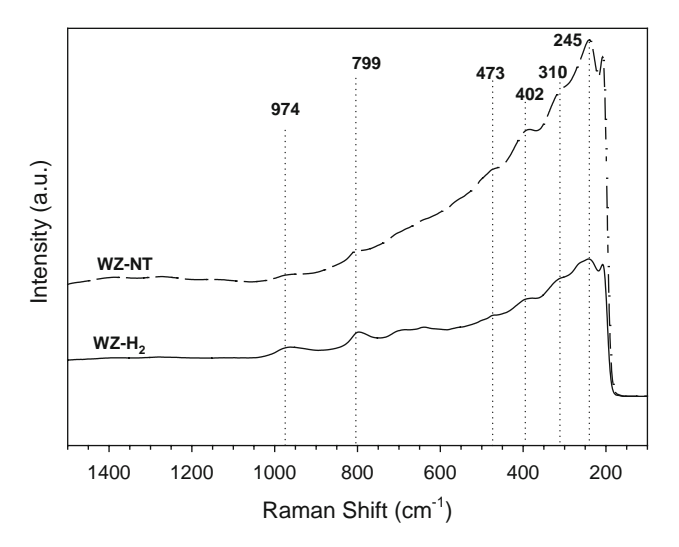


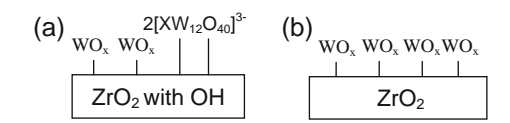
Fig. 4 Raman spectra of WZ-NT and WZ-H<sub>2</sub> catalysts



were probably due to the similar W surface density at  $\sim 4 \text{ W/nm}^2$ .

As known, acidity of WZ catalyst is a key factor to enhance the catalytic activity for several reactions by generation of active sites [2–13]. The catalytic active sites were plausible for high surface acidity form with a monolayer of polytungstated species (WO<sub>x</sub>) [3, 4, 11]. The surface acidity was obtained from a larger population of Brønsted acid sites and the presence of stronger Brønsted acid sites [19]. WZ-NT and WZ-H2 catalysts exhibited the growing surface polytungstated domain and crystalline of WO<sub>3</sub> nano-particle. It is more likely to obtain the similar Brønsted acid site density based on the similar polytangstated domain. However, the WZ-NT has higher acidity compared to WZ-H<sub>2</sub> as presented in Table 1. The higher surface acidity of WZ-NT should be derived from the different forms of polytungsted domain. The FT-IR spectra of zirconia support suggested that the Zr-OH bonding presented in Z-NT appeared to result in a super acid center (heteropolyacid of W,  $[XW_{12}O_{40}]^{3-}$ ), which was proposed by Afanasiev et al. [46] and Scheithauer et al. [18, 44, 47]. In addition, the Raman spectrum of WZ-NT was resemble the finger print of Raman spectrum of tungstophosphoric heteropolyacid  $(H_6P_2W_{18}O_{62})$  as a super acid [45]. The only substantial difference between the WZ-NT and WZ-H<sub>2</sub> catalysts in the monolayer region is the presence of the Zr-heteropolyacid spices for the WZ-NT catalysts as illustrated in Scheme 1. The catalytic activity sites seem to be fully oxidized from noncrystalline surface polytungstate networks incorporating trace levels of surface-exposed Zr capable of stabilizing delocalized protons for Brønsted acid sites as well as heteropolyacids did [18, 44, 47].

As expected, after 9 h reaction period, WZ-NT exhibited 17% higher for an acetic acid conversion than that for WZ-H<sub>2</sub>, as shown in Fig. 4. Heteropolyacid as the strong Brønsted acid sites related to acid site density and catalytic activity of esterification as corresponding to the work reported by Park et al. [48]. This could be obtained from the crystalline zirconia with Zr–OH bonding. Our result is in good agreement to the work claimed by Scheithauer group [18, 44, 47] indicating that the Zr–OH group is required to create the strong Brønsted acid sites. This reveals that the crystalline zirconia support prepared from the solvothermal method also created Zr–OH bonding as well as amorphous zirconium oxide precursor. Based on the TON of catalyst the appreciable catalytic activity



**Scheme 1** Proposed catalytic active species presented in **a** WZ-NT and **b** WZ-H<sub>2</sub> catalyst

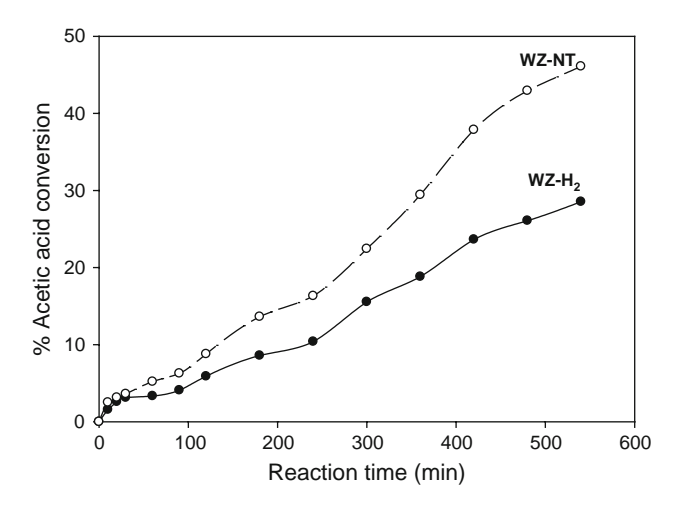


Fig. 5 Reaction profiles of acetic acid conversion using the different WZ catalysts

of both WZ-NT and WZ-H2 were 100 times greater than that of the Amberlyst 15 as presented by Preserthdam and Jongsomjit [1]. As known, the somewhat difference in response of water flow rate for the Amberlyst 15 versus WZ may have been caused by the presence of Lewis acid sites on WZ resulting in enhanced activity [6, 25, 26]. In addition, the WZ catalyst does not deactivate by leaching of active species in the liquid phase transesterification [8, 49], which is different from the SZ (sulfated zirconia) under similar condition. In order to prove that, the leaching experiment was also performed based on the procedure of Suwannakarn et al. [49]. It was found that the acetic acid conversion was less than 3%. This suggested that the leaching of active spices in WZ catalyst did not occur for the WZ catalyst Fig. 5 upon the preparation used in this work [8, 12, 49].

#### 4 Conclusions

In summary, the surface nature of zirconia was found to be crucial for determining the catalytic properties of WZ catalysts. The formation of Zr-heteropolyacid can be obtained from crystalline zirconia with Zr–OH bonding as presented in WZ-NT. This active species provided the strong Brønsted acid sites, which are essential for the esterification of dilute acetic acid and 1-heptanol. The Zr–OH bonding for WZ-H<sub>2</sub> was eliminated by the thermal treatment in the reduction atmosphere of the crystalline zirconia support allowing to the presence of only polytungstated domain.

**Acknowledgments** This research was supported by the Commission on Higher Education (CHE) and the Thailand Research Fund (TRF).

#### References

- 1. Praserthdam S, Jongsomjit B (2009) Catal Lett 130:583
- 2. Hino M, Arata K (1988) J Chem Soc. Chem Comm 18:1259
- Iglesia E, Barton DG, Soled SL, Miseo S, Baumgartner JE, Gates WE, Fuentes GA, Meitzner GD (1996) Stud Surf Sci Catal 101:533
- 4. Barton DG, Soled SL, Meitzner GA, Fuentes GA, Iglesia E (1999) J Catal 181:57
- Martinez A, Prieto G, Arribas MA, Concepcion P, Sanchez-Royo JF (2007) J Catal 248:288
- Macht J, Baertsch CD, May-Lozano M, Soled SL, Wang Y, Iglesia E (2004) J Catal 227:479
- 7. Baertsch CD, Komala KT, Chua YH, Iglesia E (2002) J Catal
- 8. Lopez DE, Goodwin JG Jr, Bruce DA, Lotero E (2005) App Catal A-General 295:97
- 9. Furuta S, Matsuhashi H, Arata K (2004) Catal Comm 5:721
- Lopez DE, Suwannakarn K, Goodwin JG Jr, Bruce DA (2008) Ind Eng Chem Res 47:2221
- Lopez DE, Suwannakarn K, Bruce DA, Goodwin JG Jr (2007)
   J Catal 247:43
- Ngaosuwan K, Lotero E, Suwannakarn K, Goodwin JG Jr, Praserthdam P (2009) Ind Eng Chem Res 48:4757
- Ngaosuwan K, Mo X, Goodwin Jr. JG, Praserthdam P (2009) Top Catal (in press)
- Kuba S, Lukinskas P, Ahmad R, Jentoft FC, Grasselli RK, Gates BC, Knozinger H J Catal 219:376
- Barton DG, Shtein M, Wilson RD, Soled SL, Iglesia E (1999)
   J Phy Chem B 103:630
- 16. Barton DG, Soled SL, Iglesia E (1998) Top Catal 6:87
- 17. Di Gregorio F, Keller V (2004) J Catal 225:45
- Santiesteban JG, Vartuli JC, Han S, Bastian RD, Chang CD (1997) J Catal 168:431
- 19. Boyse RA, Ko EI (1997) J Catal 171:191
- Occhiuzzi M, Cordischi D, Gazzoli D, Valigi M, Heydorn PC (2004) App Catal A: General 269:169
- 21. Ward DA, Ko EI (1994) J Catal 150:18
- 22. Wachs IE (2005) Catal Today 100:79
- 23. Lebarbier V, Clet G, Houalla M (2006) J Phys Chem B 110:22608
- Wongmaneenil P, Jongsomjit B, Praserthdam P (2009) Catal Comm 10:1079
- Suwannakarn K, Lotero E, Goodwin JG Jr (2007) Catal Lett 114:122
- 26. Li LS, Yoshinaga Y, Okuhara T (2002) Phys Chem Chem Phys 4:6129
- Kongwudthiti S, Praserthdam P, Silveston P, Inoue M (2003)
   Ceram Int 29:807
- 28. Kob N, Drago RS, Young V (1997) Inor Chem 36:5127
- Reddy BM, Patil MK, Reddy GK, Reddy BT, Rao KN (2007) Appl Catal A: General 332:183
- Ivanovskaya MI, Frolova EV (2007) Russian Journal of General Chemistry 77:524
- Kongwudthiti S, Praserthdam P, Tanakulrungsank W, Inoue M (2003) J Mater Process Technol 136:186
- Cortes-Jacome MA, Angeles-Chavez C, Bokhimi X, Toledo-Antonio JA (2006) J Solid State Chem 179:2663
- Benaissa M, Santiesteban JG, Daz G, Chang CD, Jose-Yacaman M (1996) J Catal 161:694
- 34. Reddy BM, Sreekanth PM, Lakshmanan P (2005) J Mol Catal A: Chemical 237:93
- Ross-Medgaarden EI, Knowles WV, Kim T, Wong MS, Zhou W, Kiely CJ, Wachs IE (2008) J Catal 256:108
- 36. Wachs IE, Kim T, Ross EI (2006) Catal Today 116:162



140 K. Ngaosuwan et al.

- 37. Morterra C, Giamello E, Orio L, Volante M (1990) J Phys Chem 94:3111
- 38. Liu H, Feng L, Zhang X, Xue Q (1995) J Phys Chem 99:332
- 39. Frolova EV, Ivanovskaya MI (2006) Mater Sci Eng C 26:1106
- 40. Zhao Q, Wang X, Cai T (2004) App Surf Sci 225:7
- 41. Zhu J, van Ommen JG, Lefferts L (2006) Catal Today 117:163
- 42. Sarkar D, Mohapatra D, Ray S, Bhattacharyya S, Adak S, Mitra N (2007) Ceram Int 33:1275
- Matos JME, Anjos FM Jr, Cavalcante LS, Santos V, Leal SH, Santos LS Jr, Santos MRMC, Longo E (2009) Mater Chem Phys 117:455
- 44. Scheithauer M, Grasselli RK, Knozinger H (1998) Langmuir 14:3019

- 45. Ross-Medgaarden EI, Wachs IE (2007) J Phys Chem C 111:15089
- Afanasiev P, Geantet C, Breysse M, Coudurier G, Vedrine JC (1994) J Chem Soc. Faraday Trans 90:193
- Scheithauer M, Cheung TK, Jentoft RE, Grasselli RK, Gates BC, Knozinger H (1998) J Catal 180:1
- 48. Park YM, Lee DW, Kim DK, Lee JS, Lee KY (2008) Catal Today 131:238
- Suwannakarn K, Lotero E, Ngaosuwan K, Goodwin JG Jr (2009)
   Ind Eng Chem Res 48:2810





## Ethylene-hexene copolymer derived from [t-butylfluorenylsilyl-amido] dimethyl titanium complex

E. Chaichana<sup>1</sup>, S. Khaubunsongserm<sup>2</sup>, P. Praserthdam<sup>1</sup>, B. Jongsomjit<sup>1\*</sup>

<sup>1</sup>Center of Excellence on Catalysis and Catalytic Reaction Engineering, Department of Chemical Engineering, Faculty of Engineering, Chulalongkorn University, Bangkok 10330, Thailand

<sup>2</sup>PTT Public Company Limited, PTT Research and Technology Institute, Wangnoi, Ayuthaya 13170, Thailand

Received 15 September 2009; accepted in revised form 16 November 2009

**Abstract.** The copolymers of ethylene and 1-hexene were prepared with half-metallocene titanium complex ([t-BuNSiMe<sub>2</sub>Flu]TiMe<sub>2</sub>) and modified methylaluminoxane (MMAO). The initial concentrations of 1-hexene were varied to investigate how the different amounts of comonomer affect on the catalytic activity of copolymerization system and microstructure of the copolymers. It has been found that this catalytic system was not active for hexene polymerization, however, it can be active when ethylene was introduced to perform ethylene-hexene copolymerization. As comonomer, 1-hexene provides positive comonomer effect on the system although very high concentration of 1-hexene was introduced. However, the microstructures of the obtained copolymers, which were examined by <sup>13</sup>C-NMR need to be improved because with highly alternating sequence distribution of comonomer causing them losing some essential specific thermal properties.

Keywords: polymer synthesis, molecular engineering, metallocene, copolymer, LLDPE

#### 1. Introduction

It is generally presumed that crystallinity of polymer plays an important role in determining the polymer properties, such as mechanical and thermal properties [1, 2]. We have known that, in synthesis of linear low-density polyethylene (LLDPE) by copolymerization of ethylene with  $\alpha$ -olefins, the crystallinity depends mainly on the amount of  $\alpha$ -olefin (comonomer) content in copolymer [3]. So, if the comonomer content can be controlled, properties of copolymer can be also altered. Appropriate crystallinity or comonomer content is varied depending on the application of polymer. The high comonomer content of copolymer has been commercially produced, named plastomers [1]. The advantages of plastomers are low density, high elongation, and low haze in film form. In order to obtain the plastomer derived from the metallocene catalysts, the open structure of metallocene catalyst is crucial. Half-metallocenes and/or constrained geometry catalysts (CGCs) are subset of general metallocene catalyst, which pose the open structure because they have just one cyclopentadienyl ring (or their family, such as, indenyl or fluorenyl rings) bonded with the group IV transition metal leaving the opposite side of that ring large enough space for comonomer incorporation with less hindrance [4]. Therefore, plastomers or LLDPE with high comonomer content can be obtained with this type of catalyst.

As mentioned, comonomer contents are sensitive to many factors, such as the structure of catalyst, type of catalyst activators and the initial concentration of comonomer in the system. When considering the initial concentration, it has been found that the initial comonomer concentration not only affects

<sup>\*</sup>Corresponding author, e-mail: bunjerd.j@chula.ac.th © BME-PT

directly on the comonomer contents, but it also affects on the catalytic activity of system [5, 6]. Therefore, in this present study the effect of the initial comonomer concentration in ethylene-1-hexene copolymerization with half-metallocene is investigated to determine both the catalytic performance and the specification of the obtained copolymers.

#### 2. Experimental

#### 2.1. Materials

All operations were manipulated under an argon atmosphere using glove box and/or standard Schlenk techniques. The [t-BuNSiMe<sub>2</sub>Flu]TiMe<sub>2</sub> (Ti-complex) was synthesized according to the procedure described by Hagihara et al. [7]. Ethylene (polymerization grade) was obtained from the National Petrochemical Co. Ltd., Thailand. 1-Hexene (≥ 97%) was purchased from Aldrich Chemical Company, Thailand and further purified by distilling over CaH<sub>2</sub> for 6 h. Modified methyl aluminoxane, MMAO  $[(Me-Al-O-)_m-(i-Bu-Al-O-)_n]$  having 1.86 M in toluene, was donated by Tosoh Akzo, Japan. Toluene (commercial grade) was donated by the Exxon Chemical, Thailand Co. Ltd. It was dried over dehydrated CaCl2 and distilled over sodium/ benzophenone.

#### 2.2. Polymerization procedure

Ethylene/1-hexene copolymerization reaction was carried out in a 100 ml semibatch stainless steel autoclave reactor equipped with a magnetic stirrer. At first, the desired amounts of MMAO and the toluene were introduced into the reactor. The titanium complex in toluene (10 µmol·ml-1) was put into the reactor to make the  $[Al]_{MMAO}/[Ti]_{cat} = 400$ . Then, the reactor was immersed in liquid nitrogen. 1-hexene was added into the frozen reactor (to stop or prevent possible polymerization of 1-hexene). The reactor was heated up to the polymerization temperature at 343 K. The polymerization was started by feeding ethylene (0.018 moles) into the reactor. The ethylene pressure and reactor temperature were kept constant during the polymerization (pressure in reactor = 349 kPa (50 psi)). Due to the fixed ethylene consumption (at 0.018 moles), the polymerization time was defined as the time that all ethylene gas was totally consumed (the equivalent pressure drop of 42 kPa (6 psi) was observed). The polymerization time was recorded to calculate the activity. The reaction was terminated by adding acidic methanol and the material was stirred for 30 min. After filtration, the copolymer obtained was washed with methanol and dried at room temperature.

#### 2.3. <sup>13</sup>C-NMR spectroscopy

<sup>13</sup>C-NMR spectroscopy was used to determine the α-olefin incorporation and copolymer microstructure. Chemical shifts were referenced internally to the CDCl<sub>3</sub> and calculated according to the method described by Randall [8]. Each sample solution was prepared by dissolving 50 mg of copolymer in 1,2,4-trichlorobenzene and CDCl<sub>3</sub>. <sup>13</sup>C-NMR spectra were taken at 333 K using a BRUKER AVANCE II 400 operating at 100 MHz with an acquisition time of 1.5 s and a delay time of 4 s.

#### 2.4. Differential scanning calorimetry

The melting temperature of ethylene/1-octene copolymer products was determined with a Perkin-Elmer diamond DSC. The analyses were performed at the heating rate of 20°C/min in the temperature range of 50–150°C. The heating cycle was run twice. In the first scan, samples were heated, and then cooled to room temperature. In the second scan, samples were reheated at the same rate, but only the results of the second scan were reported because the first scan was influenced by the mechanical and thermal history of samples.

#### 3. Results and discussion

#### 3.1. Reactivity of (co)monomer to catalyst

The catalytic activities based on polymer product are shown in Table 1. It can be seen that there is no catalytic activity for system conducted with only 1-hexene as monomer (entry 1). The opposite occurred on entry 2 for the system that used only ethylene as monomer. It suggests that this half-metallocene catalyst ([t-BuNSiMe<sub>2</sub>Flu]TiMe<sub>2</sub>) is active for ethylene polymerization, but not for 1-hexene polymerization. This result agreed with the finding of Intaragamjon *et al.* [9], who reported that this catalyst cannot proceed 1-hexene polymerization under the specified condition. It has been known that ethylene is the most reactive olefin

Table 1. Activities of system with various monomer concentrations

Entry	Ethylenea	1-Hexene	Time	Weight	Activityb
Entry	[mol/l]	[mol/l]	[s]	[g]	(kg polymer/mol Ti .h)
1	0.0	0.6	475	-	-
2	0.6	0.0	475	0.2468	187
3	0.6	0.3	500	1.0596	763
4	0.6	0.6	248	1.4030	2037
5	0.6	1.2	326	1.9241	2125

<sup>&</sup>lt;sup>a</sup>Ethylene addition into the system

[10], so it can react with itself for polymerization in the absence of any comonomer. Although 1-hexene was not reactive in its homopolymerization, it can be reacted in the system of copolymerization with ethylene (entry 3–5). Thus, this should be clarified in this finding that why 1-hexene was not active unless ethylene was introduced together in the system, even with the small amount of ethylene as seen for entry 5.

The mechanism of polymerization by metallocene catalyst system is reviewed here to explain the result. There are three main steps for completing the copolymerization (excluding chain transfer step), as shown in Figure 1 [10]. The first step is the 'activation' of metallocene catalyst typically achieving via contact with an appropriate cocatalyst species (MMAO in this case). The second is the 'initiation' of the polymerization occurring as a result of the displacement of the anion and coordination of the monomer in the primary complex. In our study, this step seems to be a problem for obtaining the 1-hexene polymerization, since the ion-pairs still stay in their coordinated tightly. Therefore, only the strong reactive monomer like ethylene is able to insert in this coordination, and consequently displace the anion and make coordination with catalyst active site. This step can generate an available coordination site on the metal center, which provides high enough space for a large molecule, such as 1-hexene to coordinate with it in the next step. As the result, the final step that is the 'propagation' step will be the open competition between ethylene monomer and 1-hexene comonemer for insertion into the growing chain of polymer.

As describe above, for this catalytic system, if ethylene was not introduced into the system first, 1-hexene would not be reactive for this half-metal-locene catalyst even open structure. However, in many cases, 1-hexene can perform polymerization by itself with some metallocenes such as  $iPr(Cp)(Flu)ZrCl_2$  and  $En(Ind)_2ZrCl_2$  [11] indicating that reactivities of  $\alpha$ -olefin also depend on the catalyst structure [12].

## **3.2.** Effect of the amount of 1-hexene on catalytic activity

In **entry 3–5**, introducing of 1-hexene into copolymerization enhanced catalytic activity higher than

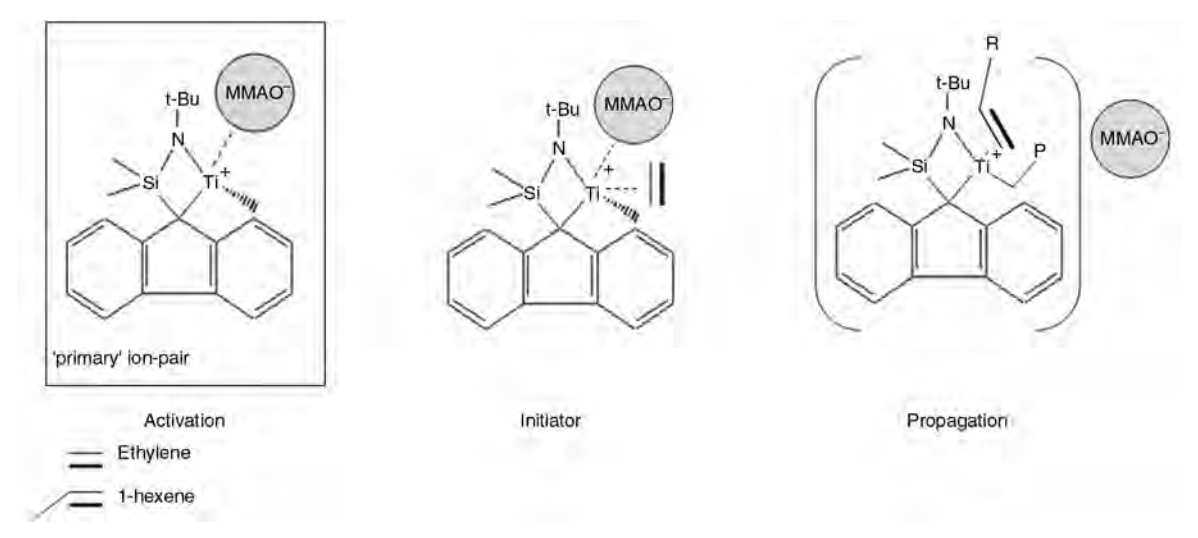
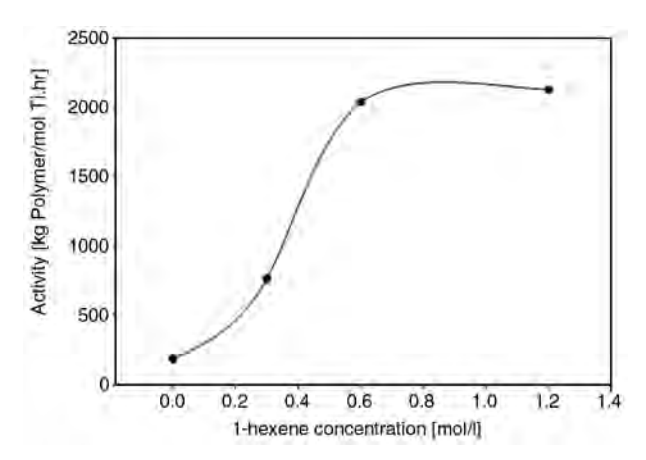


Figure 1. Schematic representation of copolymerization mechanism

<sup>&</sup>lt;sup>b</sup>Copolymerization condition: Ti = 10 μmol, Al/Ti = 400, temperature = 343 K, 349 kPa (50 psi) of ethylene pressure was applied



**Figure 2.** Activity profile with various 1-hexene concentrations

that of system without 1-hexene (entry 2). When the amounts of 1-hexene were increased, the catalytic activities were also increased. They increased pronouncedly when the amount of 1-hexene was raised from 0.3 to 0.6 mol/l. However, they gradually increased when the amount of 1-hexene was raised two times again from 0.6 to 1.2 mol/l. A comparison of activities is also shown in Figure 2. It can be explained that the first range of increasing is because of comonomer effect in copolymerization behavior [13]. The chain structure of 1-hexene can increase the gap between the cationic active species and counter anion more separately in propagation step (Figure 1). Then, the propagation rate of polymerization can be raised leading to enhancing the activity of copolymerization. However, at 1.2 mol/l of 1-hexene concentration (entry 5), the anticipated activity can not be attained. This is because high excess of 1-hexene obstructed active sites of catalyst from reacting with ethylene monomer, and consequently reduce rate of ethylene insertion into the chain of growing polymer. The explanation can be supported by polymerization time of entry 5, which was longer than that of entry 4. The longer polymerization time suggests that, in entry 5, the rate of ethylene consumption for polymerization was slower than that of **entry 4**. Although the rate of ethylene consumption in entry 4 was faster, activity or productivity of entry 5 was higher. This is because initial concentration of 1-hexene of entry 5 was higher then it can produce more product than entry 4 did resulting in high catalytic activity for the system.

### **3.3.** Effect of the amount of 1-hexene on microstructure of copolymers

As seen in Table 2, the comonomer incorporations apparently increased with increasing the amount of 1-hexene in copolymerization. In this copolymerization process, which fixed the amount of ethylene addition and kept ethylene pressure constant during copolymerization, the incorporation of 1-hexene can be increased by two primary reasons. One is that enhancing the reactivity of 1-hexene or two, diminishing the reactivity of ethylene. It can be seen from Table 2 that reactivities of ethylene decreased dramatically with increasing the concentration of 1-hexene in the system while reactivities of 1-hexene just slightly increased. So, it can be concluded that the initial concentrations of 1-hexene in the system have more effect on the reactivity of ethylene than itself. The increase of 1-hexene reactivity enables it to still incorporate continuously into the growing chain even at high concentration. The open structure of half-metallocene catalyst is one of the important factors that retains high reactivity of 1-hexene and encourages high comonomer incorporation. As compared with the works done by our group previously with normal metallocene, it has been found that with the same initial comonomer concentration in copolymerization, the obtained copolymer from those studies exhibited much lower comonomer incorporation than in this study [14, 15].

On account of the fact that the uniform comonomer incorporation is the key feature for producing lowdensity plastomer, which exhibited plastic and elas-

Table 2. Comonomer incorporation and the reactivity ratios

Entry	Ethylene 1-Hexene		Incorpo	Incorporationa		Reactivity <sup>b</sup>		
Entry	[mol/l]	[mol/l]	E [mol%]	H [mol%]	r <sub>E</sub>	$\mathbf{r}_{\mathrm{H}}$	r <sub>E</sub> r <sub>H</sub>	
3	0.6	0.3	68.4	31.6	1.121	0.658	0.737	
4	0.6	0.6	43.7	56.3	0.797	0.738	0.588	
5	0.6	1.2	23.0	77.0	0.621	0.784	0.487	

<sup>&</sup>lt;sup>a</sup>Examined by <sup>13</sup>C-NMR by Randall method [8]

<sup>&</sup>lt;sup>b</sup>Relative comonomer reactivities ( $r_E$  for ethylene and  $r_H$  for 1-hexene) calculated by  $r_E$  = 2[EE]/[EC]X,  $r_H$  = 2X[CC]/[EC], [EE] = [EEE] + 0.5[CEE], [CC] = [CCC] + 0.5[ECC], [EC] = [CEC] + 0.5[CEE] + [ECE] + 0.5[ECC]

Entry	Ethylene [mol/l]	1-Hexene [mol/l]	EEE	ЕЕН	нен	ЕНЕ	ЕНН	ннн
3	0.6	0.3	0.345	0.292	0.048	0.172	0.144	0.000
4	0.6	0.6	0.091	0.270	0.076	0.185	0.339	0.039
5	0.6	1.2	0.015	0.130	0.085	0.154	0.424	0.192

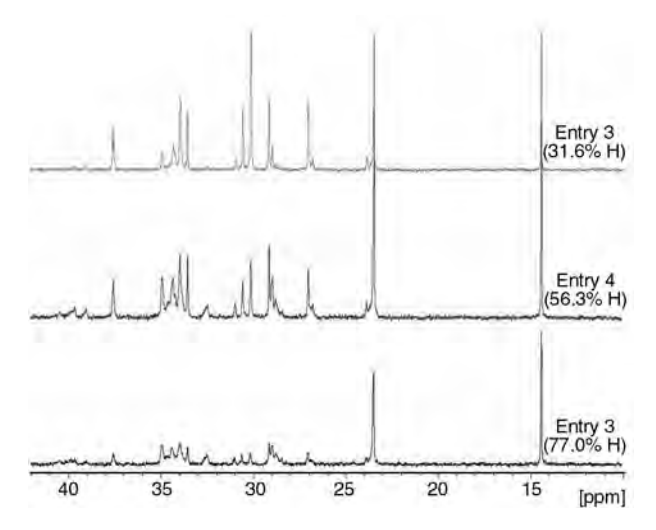


Figure 3. <sup>13</sup>C-NMR spectra of copolymers

tomeric behavior [16], the distribution of comonomer in the copolymers needs to be concerned in order to obtain plastomers with desired specification. The triad distribution for all copolymers obtained from <sup>13</sup>C-NMR is shown in Table 3. Triad block of comonomer (HHH) was detected in samples having 1-hexene incorporation above 31.6% (entry 4, 5). It was also noticed from Figure 3, which showed <sup>13</sup>C-NMR spectrum of the copolymers that the peaks between 39.5 and 42 ppm (proportional to the HHH triad) occurred obviously in the copolymer from entry 4 and 5. Nevertheless, the number of HHH triad was not converted directly from the area under these peaks. There are other peaks, which are more pronounced in the calculation. Therefore, the larger area of these peaks of entry 4 than entry 5 did not mean that entry 4 had more HHH triad than entry 5.

The presence of HHH triad can imply that the good distribution of comonomer throughout the copolymer chain was interrupted at high incorporation of comonomer. Although the copolymers with high 1-hexene incorporation contain the block of comonomer, they are still not the block copolymer. It can be observed from the product of reactivity ratio ( $r_{ETH}$ ), which is one of the parameters that can identify types of copolymer. A value  $r_{ETH} > 1$  indicates a block copolymer structure and  $r_{ETH} < 1$ 

reveals an alternating copolymer structure. Therefore, all the obtained copolymers are alternating copolymers having the  $r_{ETH}$  value being lower than 1. Once the alternating copolymers were obtained, it means the comonomers in their chain are distributed moderately well along the backbone, then shortening the average backbone sequence length for crystallization and therefore low crystallinity, including low density, would be gained. Thus, with these properties, the obtained copolymers are in closing proximately to be low-density plastomer. However, these copolymers might not meet all properties required for the use in plastic industry because they probably lost completely the thermal properties.

As a result of the fact that disadvantages of alternating copolymer, which have been found by Hung et al. [17] that the polymer with a highly alternating sequence distribution did not exhibit any melting behavior. Based on the result, when the incorporations of comonomers increased, the obtained polymer tended to exhibit more highly alternating copolymer structure ( $r_E r_H < 1$ ). Therefore, they might lose the melting behavior at high level of 1-hexene incorporation. To prove that, melting temperatures of the obtained polymers were investigated by differential scanning calorimetry (DSC). From the investigation, it was found that only the sample from entry 2, which is the polyethylene sample, has the melting temperature (130°C) and the remaining samples cannot be found the melting temperatures. Thus, the losses of thermal properties existed in all obtained copolymers even the one that had low comonomer content (entry 3, 31.6%).

Copolymers were formed the gel-like structure as seen in Figure 4 when the 1-hexene was introduced into the system, especially at the high level of incorporation. With this structure, it is obviously shown the character of amorphous material. Therefore, it accords with the results from <sup>13</sup>C-NMR and DSC that the obtained copolymers should not have the melting temperature.

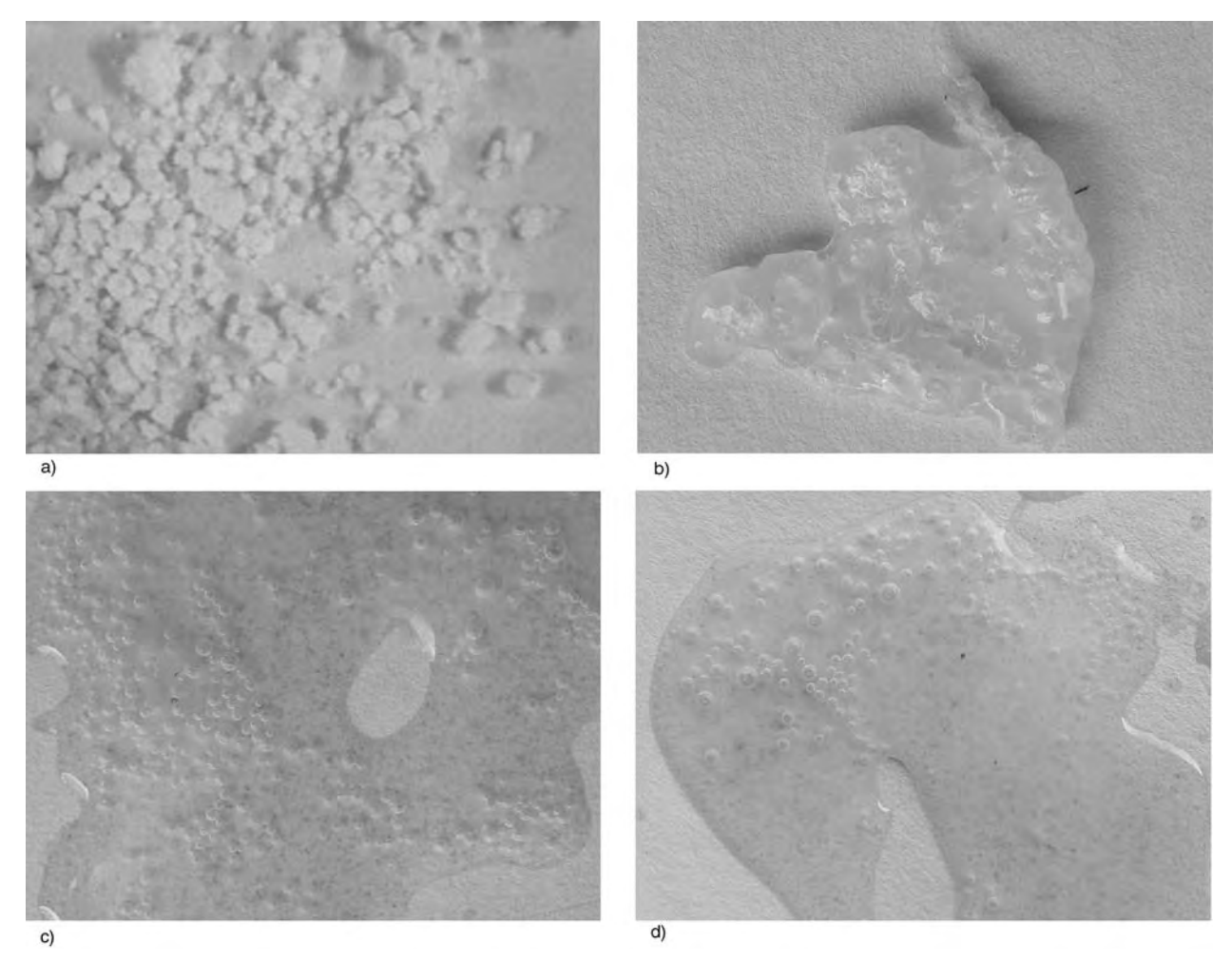


Figure 4. Digital photograph of copolymer with various 1-hexene contents a) 0%, b) 31.6%, c) 56.3% and d) 77.0%

#### 4. Conclusions

It was found that the positive comonomer effect occurred even though a very high concentration of 1-hexene that was introduced into the system. However, the microstructures of the obtained copolymer examined by <sup>13</sup>C-NMR need to be improved because the highly alternating sequence distributions of copolymer cause the loss of essential specific thermal properties.

#### Acknowledgements

We thank the Thailand Research Fund (TRF), the Commission of Higher Education (CHE) of Thailand and PTT Research and Technology Institute for the financial support of this project.

#### References

- [1] Speed C. S., Trudell B. C., Mehta A. K., Stehling F. C.: Structure/property relationships in EXPOL<sup>TM</sup> polymers. in 'Society of plastics engineers polyolefins, VII International conference, Houston, Texas' 45–66 (1991).
- [2] Jongsomjit B., Chaichana E., Praserthdam P.: LLDPE/ nano-silica composites synthesized via in situ polymerization of ethylene/1-hexene with MAO/metallocene catalyst. Journal of Material Science, 40, 2043– 2045 (2005).

DOI: <u>10.1007/s10853-005-1229-z</u>

- [3] Hong H., Zhang Z., Chung T. C. M., Lee R. W.: Synthesis of new 1-decene-based LLDPE resins and comparison with the corresponding 1-octene- and 1-hexene-based LLDPE resins. Journal of Polymer Science Part A: Polymer Chemistry, **45**, 639–649 (2007). DOI: 10.1002/pola.21825
- [4] Kaminsky W., Tran P-D., Weingarten U.: New materials by polymerisation of olefins and styrene with metallocene catalysts. Macromolecular Symposia, **193**, 1–11 (2003).

DOI: 10.1002/masy.200390053

[5] van Grieken R., Carrero A., Suarez I., Paredes B.: Effect of 1-hexene comonomer on polyethylene particle growth and kinetic profiles. Macromolecular Symposia, 259, 243–252 (2007).

DOI: <u>10.1002/masy.200751329</u>

[6] Galland G. B., Seferin M., Mauler R. S., Dos Santos J. H. Z.: Linear low-density polyethylene synthesis promoted by homogeneous and supported catalysts. Polymer International, 48, 660–664 (1999).

DOI: 10.1002/(SICI)1097-0126(199908)48:8<660:: AID-PI212>3.0.CO;2-L

[7] Hagihara H., Shiono T., Ikeda T.: Living polymerization of propene and 1-hexene with the [t-BuNSiMe<sub>2</sub>Flu]TiMe<sub>2</sub>/B(C<sub>6</sub>F<sub>5</sub>)<sub>3</sub> catalyst. Macromolecules, **31**, 3184–3188 (1998).

DOI: 10.1021/ma971697k

[8] Randall J. C.: A review of high resolution liquid 13carbon nuclear magnetic resonance characterizations of ethylene-based polymers. Polymer Reviews, **29**, 201–317 (1989).

DOI: <u>10.1080/07366578908055172</u>

[9] Intaragamjon N., Shiono T., Jongsomjit B., Praserth-dam P.: Elucidation of solvent effects on the catalytic behaviors for [t-BuNSiMe<sub>2</sub>Flu]TiMe<sub>2</sub> complex during ethylene/1-hexene copolymerization. Catalysis Communications, 7, 721–727 (2006).

DOI: 10.1016/j.catcom.2006.02.022

- [10] Severn J. R., Chadwick J. C.: Tailor-made polymers: Via immobilization of alpha-olefin polymerization catalysts. Wiley-VCH, Weinheim (2008).
- [11] Kawahara N., Saito J., Matsuo S., Kaneko H., Matsugi T., Toda Y., Kashiwa N.: Study on unsaturated structures of polyhexene, poly(4-methylpentene) and poly(3-methylpentene) prepared with metallocene catalysts. Polymer, **48**, 425–428 (2007).

DOI: 10.1016/j.polymer.2006.11.001

- [12] Krenstel B. A., Kissin Y. V., Kleiner V. J., Stotskaya L. L.: Polymer and copolymer of higher α-olefins. Hanser Publishers, Munich (1997).
- [13] Forlini F., Fan Z-Q., Tritto I., Locatelli P., Sacchi M. C.: Metallocene-catalyzed propene/1-hexene copolymerization: Influence of amount and bulkiness of cocatalyst and of solvent polarity. Macromolecular Chemistry and Physics, 198, 2397–2408 (1997). DOI: 10.1002/macp.1997.021980804
- [14] Jongsomjit B., Ngamposri S., Praserthdam P.: Application of silica/titania mixed oxide supported zirconocene catalyst for synthesis of linear low-density polyethylene. Industrial and Engineering Chemistry Research, 44, 9059–9063 (2005).

DOI: 10.1021/ie050806d

[15] Bunchongturakarn S., Jongsomjit B., Praserthdam P.: Impact of bimodal pore MCM-41-supported zir-conocene/dMMAO catalyst on copolymerization of ethylene/1-octene. Catalysis Communications, **9**, 789–795 (2008).

DOI: <u>10.1016/j.catcom.2007.09.001</u>

[16] Yu T. C.: Metallocene plastomer modification of polypropylenes. Polymer Engineering and Science, 41, 656–671 (2001).

DOI: <u>10.1002/pen.10761</u>

[17] Hung J., Cole A. P., Waymouth R. M.: Control of sequence distribution of ethylene copolymers: Influence of comonomer sequence on the melting behavior of ethylene copolymers. Macromolecules, **36**, 2454–2463 (2003).

DOI: <u>10.1021/ma021779v</u>

#### Study on Solvent/Alkoxide Molar Ratios on Synthesis Zirconia Nanoparticles for Tungstated Zirconia Catalysts Over Esterification

Peangpit Wongmaneenil · Bunjerd Jongsomjit · Piyasan Praserthdam

Received: 9 April 2010/Accepted: 21 June 2010/Published online: 2 July 2010 © Springer Science+Business Media, LLC 2010

**Abstract** A series of nanocrystal zirconia samples were synthesized, characterized and studied for the esterification reaction. The results showed that the solvothermal method under different solvent/alkoxide molar ratios led to remarkable effect on the amount of carbon residue remained on the surface of catalysts resulting in the difference in proton species-support interaction behavior. Moreover, the esterification activity of W/ZrO<sub>2</sub> varied distinctly with the solvothermal synthesis condition of nanocrystal zirconia.

**Keywords** W/ZrO<sub>2</sub> · Solvothermal synthesis · Solvent content · Carbon residue · Esterification

#### 1 Introduction

A large number of industrially important reactions are catalyzed by solid acids. To improve their performance, a detailed characterization of these catalysts is important. Specifically, a systematic study of the development of acid sites in relation to the nature of the surface structure is of particular interest. Solid acids catalysts of the type  $WO_x/ZrO_2$  have attracted much interest recently due to their structural feature which can present strong acidic sites, and thus are active for isomerization, alkylation and esterification [1–6].

P. Wongmaneenil · B. Jongsomjit (☒) · P. Praserthdam
Department of Chemical Engineering, Faculty of Engineering,
Center of Excellence on Catalysis and Catalytic Reaction
Engineering, Chulalongkorn University, Bangkok 10330,
Thailand

e-mail: bunjerd.j@chula.ac.th

The structural feature of the WO<sub>x</sub>/ZrO<sub>2</sub> catalysts have been studied [7-12] and was showed that the active species-support interaction plays an important role in controlling the active phase features and in affecting the support properties. Some authors suggest that the catalytic activity is associated with interconnecting amorphous WO<sub>x</sub> species on the surface of tetragonal zirconia. The creation of strong acidic centers appears to require the presence of WO<sub>x</sub> clusters in the presence of a significant proportion of tetragonal zirconium oxide (ZrO<sub>2</sub>) [10, 13]. Several works have shown that the catalytic properties of the WO<sub>x</sub>/ZrO<sub>2</sub> are strongly affected by every step of the preparation including the choice of the synthesis method and tungsten loading. The main influences of the preparation method are on: (i) the type of the active species formed; (ii) the dispersion of the active species; (iii) the acidity of the catalyst; (iv) the different types of phases formed and (v) the surface area. Synthesis methods, such as impregnation, coimpregnation, hydrothermal, sol-gel, and solvothermal, have been widely studied to optimize the preparation of such catalysts with properties being appropriate for different purposes [14–17]. Among these methods, the most used one for the preparation of pure tetragonal zirconia phase is the solvothermal method. In this case, the procedure consists of impregnation of crystal zirconium oxide with a solution containing tungsten precursor [18]. After the calcination, the tungsten species formed were composed of isolated surface monotungstates and/or polymeric surface polytungstates species (WO<sub>x</sub>) and WO<sub>3</sub> crystallites [19]. Previous studies have emphasized on the amounts of residual carbon remained the surface of catalysts certain characteristics of the degree of interaction between the zirconia and adsorbed species [20]. It revealed that ZrO<sub>2</sub> particles prepared in 1,4-butanediol (ZrO<sub>2</sub>-BG) have the lowest amounts of residual carbon on the surface of catalysts leading to enhanced activity for tungstated zirconia catalyst.

In the present research, we synthesized the nanocrystalline zirconia by the solvothermal method under different solvent (glycol)/alkoxide molar ratios and investigated the effects of the properties of zirconia obtained on the esterification performances of W/ZrO<sub>2</sub>. It was confirmed that carbon residue present on the surface of catalysts affects the activity for tungstated zirconia catalyst in acetic acid esterification reaction.

#### 2 Experimental Section

#### 2.1 W/ZrO<sub>2</sub> Catalyst Synthesis

W/ZrO<sub>2</sub> samples were prepared by the adsorption of a W precursor on the surface of nanocrystalline zirconia (ZrO<sub>2</sub>). First the zirconia support was prepared by the solvothermal method of zirconium tetra-n-butoxide 80 wt% solution in 1-butanol [ZNB, Zr(O(CH<sub>2</sub>)<sub>3</sub>CH<sub>3</sub>)<sub>4</sub>, Aldrich] and 1,4-butanediol [HO(CH<sub>2</sub>)<sub>4</sub>OH, Sigma-Aldrich, 99%]. A desired amount of an alkoxide was suspended in 100 mL of 1,4-butanediol in a glass vessel, and then placed in a 300-mL autoclave filled with 30 mL of the same solvent. The autoclave was completely sealed and purged with nitrogen. The mixture was heated to the desired temperature at a constant rate of 2.5 °C min<sup>-1</sup> and held at that temperature for 2 h. After the autoclave was cooled, the resulting powder was washed repeatedly with methanol by centrifugation, and then air-dried at room temperature. The products were then air-dried and used without further calcinations. The molar ratios of solvent/alkoxide used in this work were ranged from 12 to 29.

A series of samples was prepared by the incipient wetness impregnation method using tungsten(VI) chloride (WCl<sub>6</sub>, Aldrich, 99.9%) sufficient for yield materials having 15 wt% of W loading. The catalysts were dried at 110 °C for 12 h and finally calcined at 500 °C in air for 3 h

Samples are designated as ZrO<sub>2</sub>-x and W/ZrO<sub>2</sub>-x, where x refers to the molar ratios of solvent/alkoxide.

#### 2.2 X-Ray Diffraction

X-ray powder diffraction spectra were recorded using a Siemens (D5000, Germany) powder diffractometer with a copper anode (Cu K $\alpha$ ,  $\lambda = 0.15418$  nm) and a scanning rate of  $0.04^{\circ}$  s<sup>-1</sup>. The crystalline planes of phases t-ZrO<sub>2</sub> and m-ZrO<sub>2</sub> were indexed following the Joint Committee on Powder Diffraction Standards (JCPDS) cards and the crystallite size was calculated from the Scherrer equation.

#### 2.3 BET Surface Area

Nitrogen adsorption was measured at -196 °C with an automatic adsorptiometer (Micromeritics ASAP 2020, USA). The samples were pretreated at 300 °C for 3 h under vacuum. The surface areas were determined from adsorption values for relative pressures ( $P/P_0$ ) ranging from 0.1 to 1.0 using the Brunauer–Emmett–Teller (BET) method.

#### 2.4 Scanning Electron Microscope

Surface morphology of the samples was observed on Hitachi S-3400N (Japan) scanning electron microscope (SEM) with an acceleration voltage of 15 kV. Catalyst samples were gold coated prior to scanning.

#### 2.5 Transmission Electron Micrographs

The TEM measurement was obtained using a JEOL JEM-2010 (Japan) transmission electron microscope. The samples were supported on carbon-coated copper grids for the experiment.

#### 2.6 Thermogravimetric Analysis

The thermogravimetric (TG) analyses were performed on a TA Instruments SDT Q 600 analyzer (USA). The samples of 10–20 mg and a temperature range between 30 to 800 °C at 10 °C  $\rm min^{-1}$  were used in the operation with  $\rm N_2$  UHP carrier gas.

#### 2.7 X-Ray Photoelectron Spectroscopy

The XPS measurement was carried out using an AMICUS photoelectron spectrometer (UK) equipped with an Mg K $\alpha$  X-ray as a primary excitation and KRATOS VISION2 software. XPS elemental spectra were acquired with 0.1 eV energy step at a pass energy of 75 kV. The background pressure during the spectra accumulation was typically  $10^{-6}$  Pa. Detailed spectral scans were taken over Zr 3d, O 1s, W 4f, C 1s and Ag 3d regions. The binding energy scale of the spectra was calibrated to the silver Ag  $3d_{5/2}$  peak at the energy of 368.2 eV [21].

#### 2.8 Acidity Measurements

The number of acid sites was also estimated by using a method involving an aqueous ion-exchange step, in which 0.2 g of catalyst was added to 10 mL of a 3.42 M aqueous solution of NaCl under stirring. The exchange ions between H<sup>+</sup> of catalyst and Na<sup>+</sup> in the solution were carried out for 30 h at room temperature; the liquid was filtered off and titrated with a 0.05 N aqueous NaOH solution.



P. Wongmaneenil et al.

The endpoint for titration was determined using a pH meter (pH  $\sim$  7) and corroborated using pH paper [4, 22].

#### 2.9 Catalytic Activity

The esterification of acetic acid with methanol has been used as a probe reaction for studying the activity of the catalysts. The reaction was carried out in liquid phase batch reactor. The WZ catalyst taken was 2 wt% of acetic acid, and acetic acid and methanol were taken in 1:3 molar ratio. In a typical procedure, a 250-mL round bottom flask equipped with a water condenser and magnetic stirrer was kept in a constant temperature of oil bath. The reaction was carried out at atmospheric pressure at 60 °C. Sample was withdrawn periodically from the reactor, quenched to room temperature, and centrifuged in order to separate the solid catalyst from product to prevent further reaction. Concentration of reacted samples was determined using a SHIMADZU gas chromatograph (GC-14B) equipped with Chrompack SE52 column and flame ionization detector. UHP N<sub>2</sub> was used as the carrier gas.

#### 3 Results and Discussion

The XRD patterns are shown in Fig. 1. It reveals that zirconia in the samples existed mainly in the form of tetragonal phase (*t*-ZrO<sub>2</sub>) and only very few percentages of monoclinic zirconia (*m*-ZrO<sub>2</sub>) were detected in ZrO<sub>2</sub>-15 and ZrO<sub>2</sub>-12 [23]. The average crystallite sizes calculated from the XRD line broadening using the Scherrer equation and the BET surface areas of the zirconia are reported in Table 1. The average crystallite sizes of zirconia were approximately 3.4–4.0 nm. Within experimental error, there was no significant difference in BET surface areas

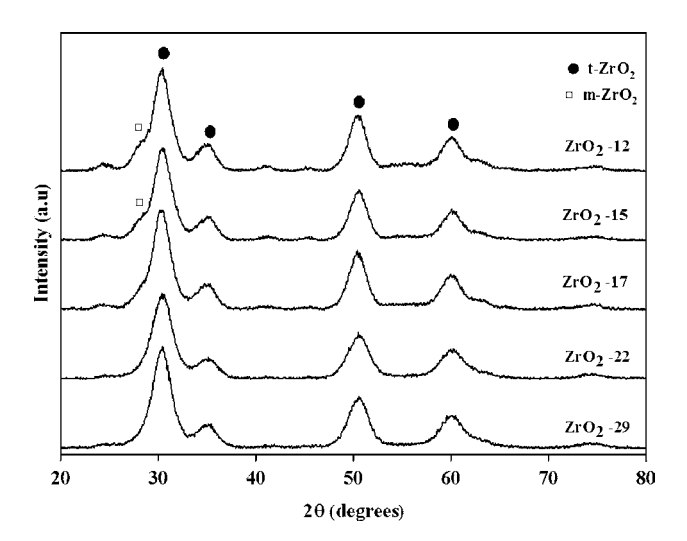


Fig. 1 XRD patterns of the  $ZrO_2$ 



**Table 1** Textural characterization of zirconia supports

Sample	Crystallite size <sup>a</sup> (nm)	BET surface area (m²/g)	Pore size (nm)	Pore volume (cm <sup>3</sup> /g)
ZrO <sub>2</sub> -29	3.8	171	2.60	0.10
$ZrO_2$ -22	3.4	170	2.52	0.09
ZrO <sub>2</sub> -17	3.9	186	2.64	0.17
ZrO <sub>2</sub> -15	3.8	187	2.68	0.18
ZrO <sub>2</sub> -12	4.0	185	2.72	0.19

<sup>&</sup>lt;sup>a</sup> Calculated from XRD measurement based on Scherrer equation

and the crystallite sizes of the zirconia prepared in different solvent/alkoxide molar ratios (different ZNB concentrations). To check accuracy of the crystal size obtained from the XRD analysis, TEM photographs of products were also taken in comparison. Figure 2 shows an agglomeration of crystals with an average diameter of 4.4 nm in ZrO<sub>2</sub>-17. Since the crystal sizes from TEM and X-ray analysis are in good agreement, it has been concluded that each primary particles of the obtained products are single crystals of zirconia. These results were found to be in agreement with our previous work [24].

Typical SEM micrographs of zirconia samples prepared in 1,4-butanediol with different molar ratios of solvent/alkoxide are shown in Fig. 3a–e. The powders have a spherical shape and a dense mass and seem to be formed by aggregations of primary particles. The SEM photograph shows these secondary particles as separate microspheres. Interestingly, the lower solvent/alkoxide ratios (higher the initial ZNB concentration), the larger the size of the

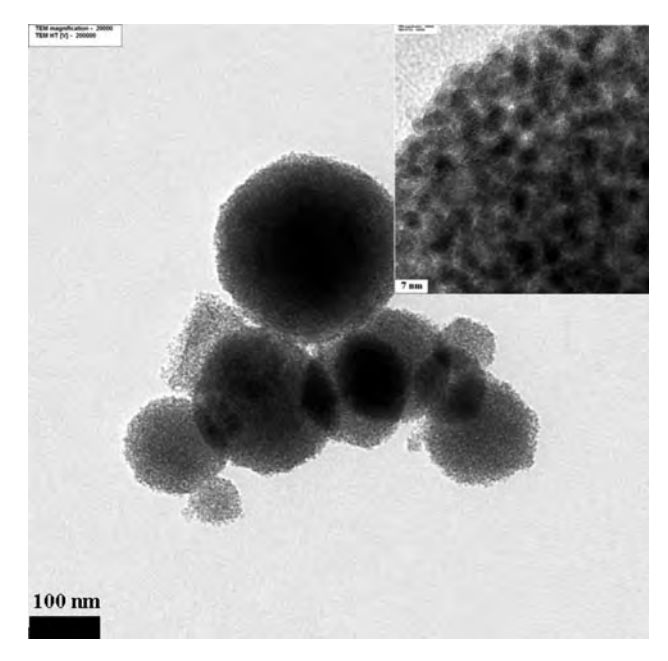


Fig. 2 TEM image of ZrO<sub>2</sub>-17

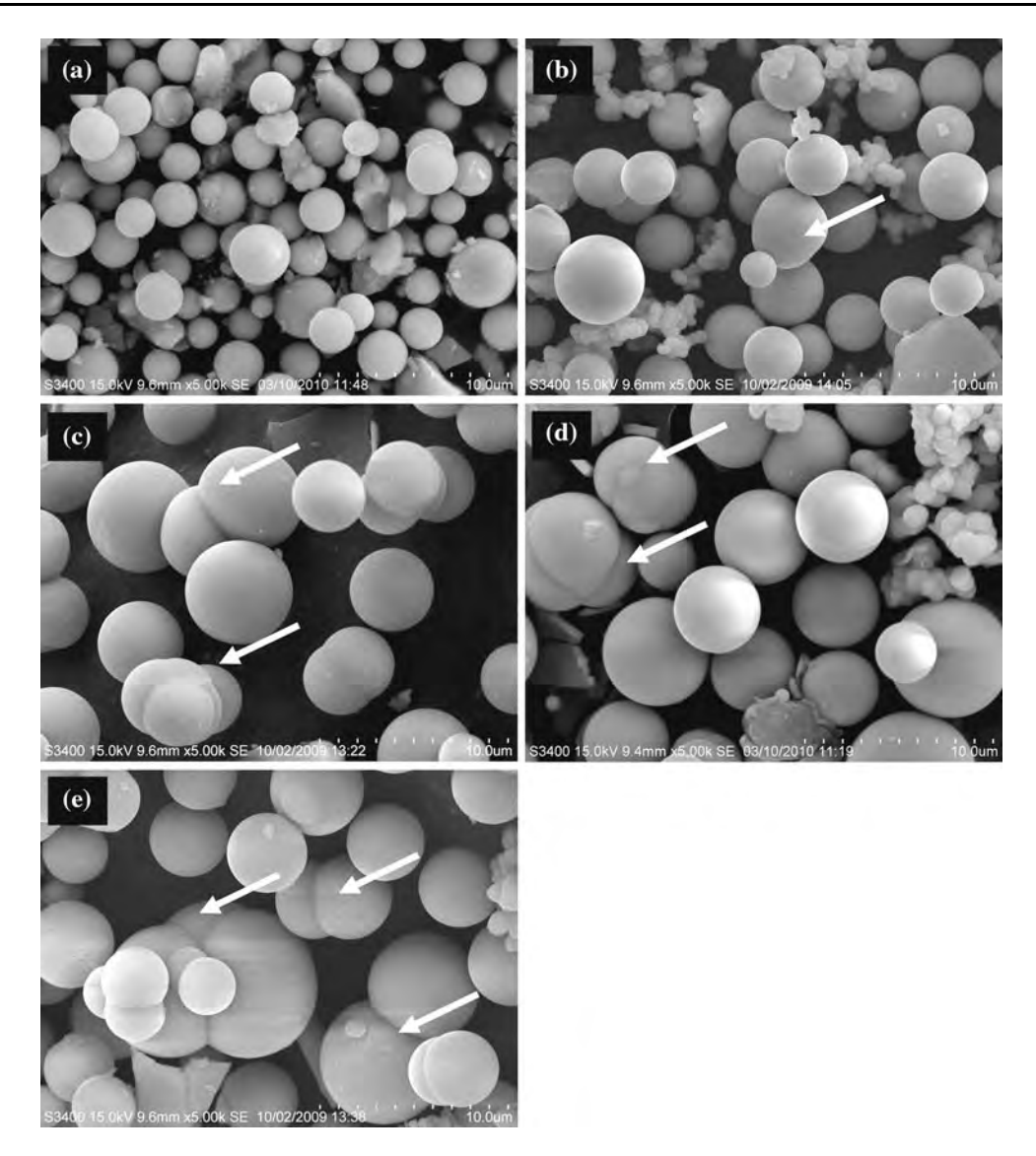


Fig. 3 SEM photographs of products synthesized in 1,4 butanediol at 250 °C of a ZrO<sub>2</sub>-29, b ZrO<sub>2</sub>-22, c ZrO<sub>2</sub>-17, d ZrO<sub>2</sub>-15 and e ZrO<sub>2</sub>-12

secondary particle. Furthermore, we can see boundaries of small microspheres that agglomerated to form larger secondary particles. These boundaries are indicated by arrows in Fig. 3. Increasing solvent/alkoxide ratios decreases mean microsphere diameter while reducing sharply the number of small microspheres.

Table 2, compares the catalytic properties of various zirconia supported tungsten catalysts. In this study, the zirconia was impregnated with 15 wt% of tungsten and calcined in air at 500 °C for 3 h. In general, the penetration of tungsten species into the pore of ZrO<sub>2</sub> support could reduce the surface area of the tungstated zirconia catalysts. This loss of surface area is significantly inhibited by the presence of WO<sub>x</sub> species [4] or the emergence of monoclinic zirconia (*m*-ZrO<sub>2</sub>). In order to estimate the theoretical nominal W surface densities, W/ZrO<sub>2</sub> surface area and

amount of tungsten loading were used [25]. It was found that the W surface coverage of all catalysts were presented as the growing surface monotungstated domain (approximately 3.6–4.0 W/nm<sup>2</sup>) [7]. It would appear that the surface area and particle size of the catalyst particles were not affected by solvent/alkoxide ratio since no physical changes were observed. The X-ray diffraction patterns of the zirconia-supported tungsten catalysts are shown in Fig. 4. The increased calcination temperature was also allowing to present a fraction of m-ZrO<sub>2</sub>. It should be noted that the XRD peak at ca. 24.3° for all samples was assigned to the monoclinic zirconia (not WO<sub>x</sub> crystallites) [26–28]. The results were found to be in agreement with the work previously reported by our group, the catalysts did not show diffraction peaks at  $2\theta = 23.2$ , 23.6 and 24.48 and did not show Raman bands at 720 and 807 cm<sup>-1</sup> that



P. Wongmaneenil et al.

Table 2 Physicochemical properties of W/ZrO<sub>2</sub> catalysts

Sample	Crystallite size <sup>a</sup> (nm)	BET surface area (m²/g)	W surface density <sup>b</sup> (W atom/nm <sup>2</sup> )	Surface acidity <sup>c</sup> (µmol/g)	C atomic concentration <sup>d</sup> (%)
W/ZrO <sub>2</sub> -29	4.5	123	4.0	88	20.03
W/ZrO <sub>2</sub> -22	4.7	128	3.8	94	16.30
W/ZrO <sub>2</sub> -17	4.4	134	3.7	112	14.63
W/ZrO <sub>2</sub> -15	4.6	135	3.6	120	13.32
W/ZrO <sub>2</sub> -12	4.4	136	3.6	128	12.08

<sup>&</sup>lt;sup>a</sup> Calculated from XRD measurement based on Scherrer equation

<sup>&</sup>lt;sup>d</sup> Measured from XPS measurement

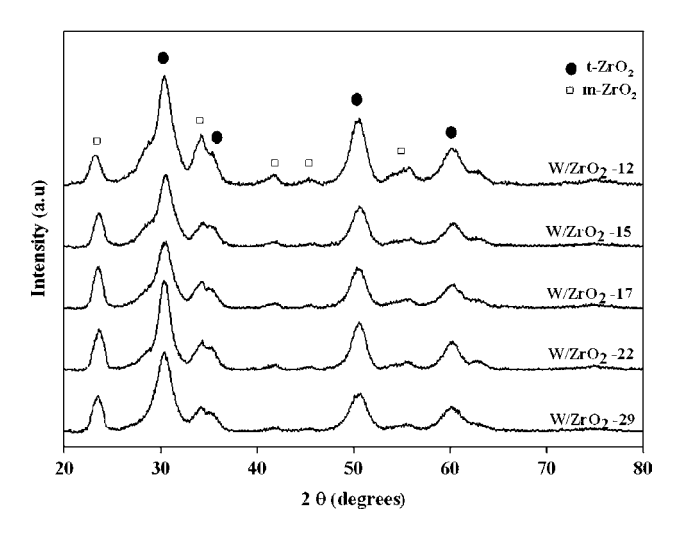


Fig. 4 XRD patterns for W/ZrO<sub>2</sub> calcined at 500 °C for 3 h

are characteristic of  $WO_3$  [18, 20, 29]. No diffraction peaks of  $WO_3$  crystallites were observed for all samples, indicating that tungsten oxide was well dispersed on zirconia.

The acid site concentrations as measured by ion-exchange titration are also listed in Table 2. It was found that they are in the range of ca. 88, 94, 112, 120 and 128 μmol/g for W/ZrO<sub>2</sub>-29, W/ZrO<sub>2</sub>-22, W/ZrO<sub>2</sub>-17, W/ZrO<sub>2</sub>-15 and W/ZrO<sub>2</sub>-12 samples, respectively. The number of acid sites increases in parallel with the decreased solvent/alkoxide molar ratio. Probably as a result of the residue carbon deposit on the surface of catalyst. The

amounts of residue carbon on the surface of catalysts were characterized by XPS, as shown in Table 3. The C 1s envelopes were analyzed and peak-fitted after subtraction of a Shirley background using a Gaussian peak shapes is shown in Fig. 5. In this deconvolution operation, the FWHM value adopted for all the C 1s lines were not higher than 2.4 eV. High residual carbon concentrations are apparently evident for the W/ZrO<sub>2</sub>-29. It can be seen that when the solvent ratio was decreased from 29 to 12, the carbon concentration decreased ca. 40%. These results indicate a more pronounced effect of solvent ratio on the carbon residual concentration and the acid site concentration of tungstated zirconia catalyst.

The esterification of acetic acid with methanol was carried out over the catalysts of W/ZrO<sub>2</sub>-29, W/ZrO<sub>2</sub>-22, W/ZrO<sub>2</sub>-17, W/ZrO<sub>2</sub>-15, and W/ZrO<sub>2</sub>-12 at 60 °C; the conversions of acetic acid after 6 h of time on stream are shown as a function of time in Fig. 6. The figure shows that the W/ZrO<sub>2</sub> catalysts are quite effective for the reaction, the W/ZrO<sub>2</sub>-12 catalyst showed especially high activities for the esterification of acetic acid. This is due to the highest acidity present as observed from acid–base titration techniques (Table 2). It is interesting to note that the ratio of solvent/glycol of the zirconia support synthesis has an influence on the catalytic activity of the tunstated zirconia catalysts. It is found that the conversion of acetic acid decreases with increasing the solvent/glycol ratio from 12 to 29 as shown in Fig. 6. This is mainly due to the fact that

Table 3 C 1s XPS results

Sample	Position BE (eV)	FWHM (eV)	Raw area (CPS)	$R^2$	Carbon concentration	
					Atomic%	Mass%
W/ZrO <sub>2</sub> -29	285.063	2.180	2643.5	0.98859	20.03	6.0
W/ZrO <sub>2</sub> -22	284.832	2.306	2340.9	0.97740	16.30	4.7
W/ZrO <sub>2</sub> -17	284.708	2.192	1927.2	0.98559	14.63	4.5
W/ZrO <sub>2</sub> -15	284.849	2.162	1870.1	0.98092	13.32	3.9
W/ZrO <sub>2</sub> -12	285.052	2.122	1549.9	0.98396	12.08	3.6



<sup>&</sup>lt;sup>b</sup> Calculated from the equation [25] Surface density =  $\frac{1}{\text{Formula weight of promoter} \times \text{BET surface area } (\text{m}^2 \, \text{g}^{-1}) \times 10^{18}}$ 

<sup>&</sup>lt;sup>c</sup> Measured by ion-exchange and titration with 0.05 N NaOH

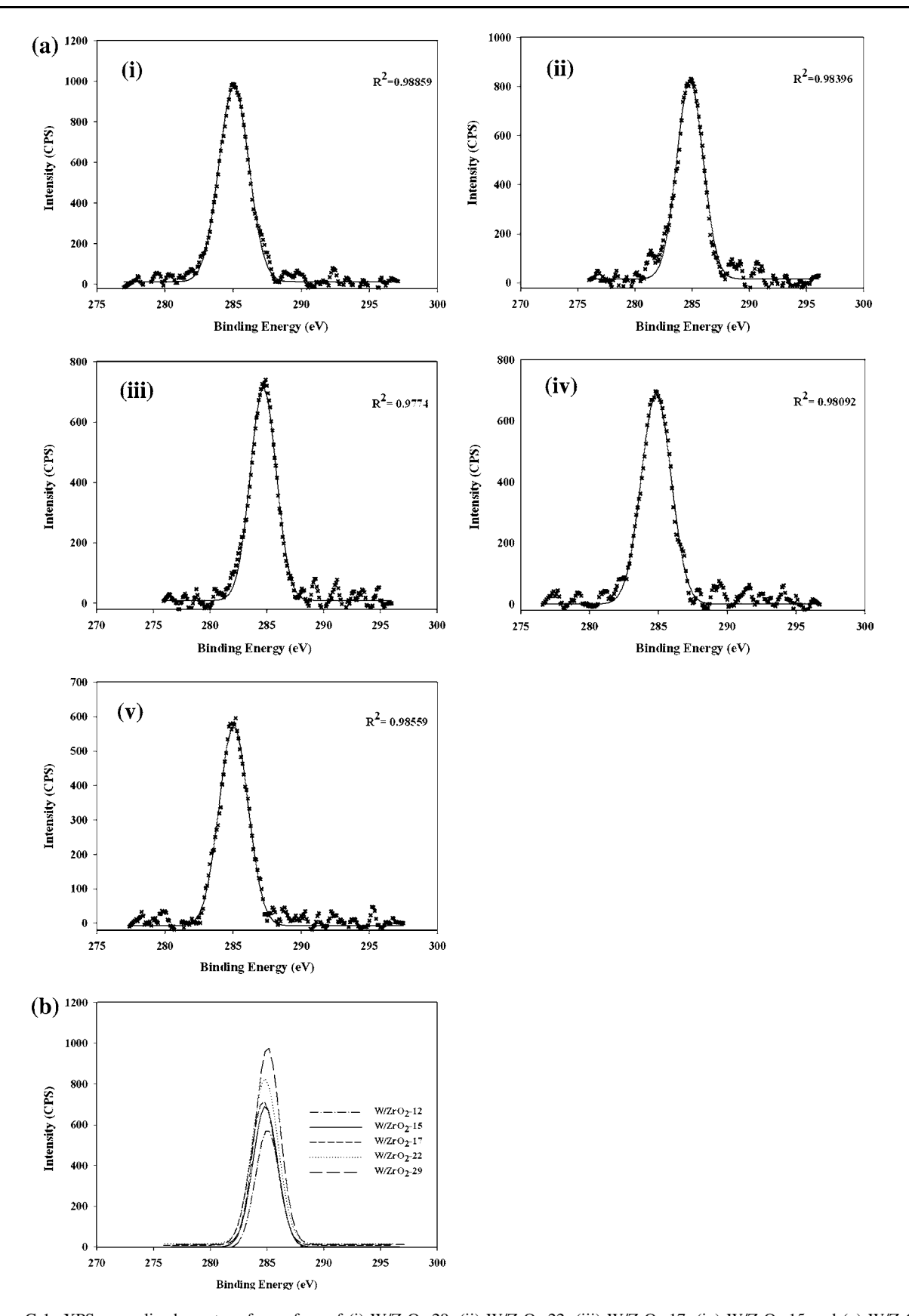


Fig. 5 a C 1s XPS normalized spectra of a surface of (i)  $W/ZrO_2-29$ , (ii)  $W/ZrO_2-27$ , (iii)  $W/ZrO_2-17$ , (iv)  $W/ZrO_2-15$  and (v)  $W/ZrO_2-12$ . b Evolution of C 1s XPS spectrum of a surface of various tungstated zirconia catalysts



P. Wongmaneenil et al.

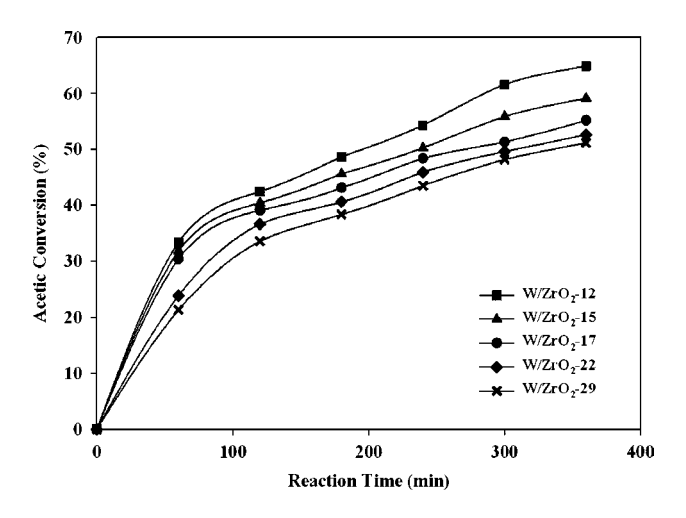


Fig. 6 Catalytic activity on the different W/ZrO2 catalysts

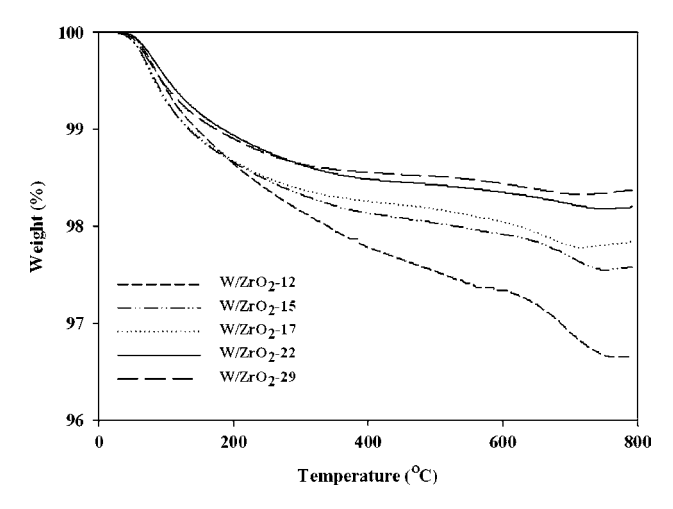
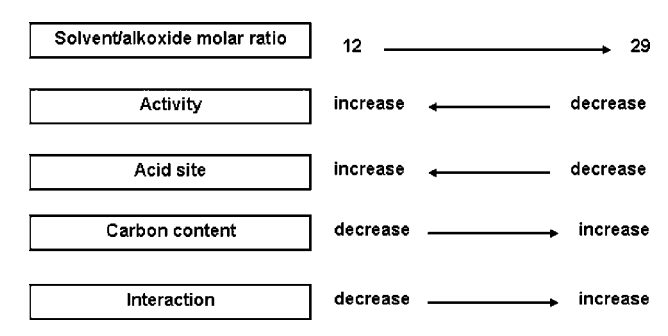


Fig. 7 TGA profiles of tungsten oxide on different supports

W/ZrO<sub>2</sub>-29 catalyst has the maximum residue carbon on the surface (Table 3 and Fig. 5). The results clearly show, in agreement with previous reports [20], an increased carbon residue on the surface of catalysts. The acidity of the solids after calcination at 500 °C was affected by the residue carbon deposition on the surface of the catalysts. One of the possible reasons is that the interaction between the support and the dispersed oxide species. In order to prove the interaction between the tungsten oxide and support, TGA measurement was performed. The TGA can provide the useful information on the degree of interaction for adsorbed species bound to support in terms of weight loss and removal temperature [20, 30–33]. The TGA profiles for all catalysts are shown in Fig. 7. We observed that the weight losses of samples were in the order of W/ZrO<sub>2</sub>-12  $(3.3\%) > W/ZrO_2-15$   $(2.4\%) > W/ZrO_2-17$  (2.2%) > $W/ZrO_2-22$  (1.8%) >  $W/ZrO_2-29$  (1.6%). This indicated that adsorbed species present on ZrO<sub>2</sub>-29 had the strongest interaction among other supports, resulted in the lowest



Scheme 1 Relationship between solvent/alkoxide molar ratios and other parameters

activity obtained. In addition, the relationship between the solvent/alkoxide ratios and other parameters is summarized as shown in Scheme 1.

#### 4 Conclusions

The liquid-phase esterification of acetic acid with methanol at 60 °C was investigated to characterize the effect of solvent/alkoxide molar ratios on synthesis nanocrystal zirconia support on the esterification performances of W/ZrO<sub>2</sub>. The catalytic activity of W/ZrO<sub>2</sub>-12, zirconia support prepared by solvothermal method with the molar ratio of solvent/alkoxide = 12 showed highest surface acidity consequently having the highest activity. It can be concluded that the molar ratios of solvent/alkoxide remarkably affect the amount of carbon residue on the surface of catalysts resulting in the difference in acidity of catalyst.

**Acknowledgments** The authors thank the Thailand Research Fund (TRF) and Office of the Higher Education Commission (CHE) for the financial support of this project.

#### References

- Bordoloi A, Mathew NT, Devassy BM, Mirajkar SP, Halligudi SB (2006) J Mol Catal A Chem 247:58
- Khurshid M, Al-Daous MA, Hattori H, Al-Khattaf SS (2009) Appl Catal A Gen 362:75
- 3. Khurshid M, Al-Khattaf SS (2009) Appl Catal A Gen 368:56
- López DE, Suwannakarn K, Bruce DA, Goodwin JG Jr (2007) J Catal 247:43
- 5. Park Y, Lee JY, Chung S, Park IS, Lee S, Kim D, Lee J, Lee K (2010) Bioresour Technol 101:S59
- Sun W, Zhao Z, Guo C, Ye X, Wu Y (2000) Ind Eng Chem Res 39:3717
- Barton DG, Shtein M, Wilson RD, Soled SL, Iglesia E (1999) J Phys Chem B 103:630
- 8. Barton DG, Soled SL, Meitzner GD, Fuentes GA, Iglesia E (1999) J Catal 181:57
- 9. Boyse RA, Ko EI (1997) J Catal 171:191
- 10. Gregorio FD, Keller V (2004) J Catal 225:45



- Pedrosa AMG, Souza MJB, Marinkovic BA, Melo DM, Araujo AS (2008) Appl Catal A Gen 342:56
- 12. Valigi M, Gazzoli D, Pettiti I, Maattei G, Colonna S, Rossi S, Ferraris G (2002) Appl Catal A Gen 231:159
- Iglesia E, Barton DG, Soled SL, Miseo S, Baumgartner J, Gates WE, Fuentes GA, Meitzner GD (1996) Stud Surf Sci Catal 101:533
- Vaudagna SR, Comelli RA, Fígoli NS (1997) Appl Catal A Gen 164:265
- Sun W, Xu L, Chu Y, Shi W (2003) J Colloid Interface Sci 266:99
- 16. Arribas MA, Márquez F, Martínez A (2000) J Catal 190:309
- 17. Hino M, Arata K (1988) J Chem Soc Chem Commun 18:1259
- 18. Wongmaneenil P, Jongsomjit B, Praserthdam P (2009) Catal Commun 10:1079
- 19. Wachs IE, Kim T, Ross EI (2006) Catal Today 116:162
- Wongmaneenil P, Jongsomjit B, Praserthdam P (2010) J Ind Eng Chem 16:327
- 21. Anthony MT, Seah MP (1984) Surf Interface Anal 6:95
- 22. López DE, Goodwin JG Jr, Bruce DA (2007) J Catal 245:381

- Li M, Feng Z, Xiong G, Ying P, Xin Q, Li C (2001) J Phys Chem B 105:8107
- Panpranot J, Taochaiyaphum N, Praserthdam P (2005) Mater Chem Phys 94:207
- Reddy BM, Patil MK, Reddy GK, Reddy BT, Rao KN (2007) Appl Catal A Gen 332:183
- 26. Wong ST, Hwang CC, Mou CY (2006) Appl Catal B Environ 63:1
- 27. Reddy BM, Patil MK, Reddy BT (2008) Catal Lett 125:97
- 28. Srdić VV, Winterer M (2003) Chem Mater 15:2666
- Ngaosuwan K, Jongsomjit B, Praserthdam P (2010) Catal Lett 136:134
- Ketloy C, Jongsomjit B, Praserthdam P (2007) Appl Catal A Gen 327:270
- 31. Bunchongturakarn S, Jongsomjit B, Praserthdam P (2008) Catal Commun 9:789
- 32. Pothirat T, Jongsomjit B, Praserthdam P (2008) Catal Lett 121:266
- Suriye K, Praserthdam P, Jongsomjit B (2007) Appl Sur Sci 253:3849



S.S. C. ELSEVIER

Contents lists available at ScienceDirect

#### Journal of Industrial and Engineering Chemistry

journal homepage: www.elsevier.com/locate/jiec



#### The influence of Si-modified TiO<sub>2</sub> on the activity of Ag/TiO<sub>2</sub> in CO oxidation

Nattaya Comsup, Joongjai Panpranot, Piyasan Praserthdam\*

Center of Excellence on Catalysis and Catalytic Reaction Engineering, Department of Chemical Engineering, Faculty of Engineering, Chulalongkorn University, Bangkok 10330, Thailand

#### ARTICLE INFO

Article history: Received 1 February 2010 Accepted 14 April 2010

Keywords: Si-modified TiO<sub>2</sub> CO oxidation Ag/TiO<sub>2</sub>

#### ABSTRACT

Nanocrystalline  $TiO_2$  and Si-modified  $TiO_2$  with Si/Ti ratios 0.01, 0.05, 0.1, and 0.3 were prepared by the solvothermal method and employed as the supports for  $Ag/TiO_2$  catalysts for CO oxidation reaction. The incorporation of Si into the  $TiO_2$  lattice in the form of Ti-O-Si as revealed by FT-IR results could inhibit the agglomeration of  $TiO_2$  crystallites, resulting in an increase of both surface area and metal dispersion. However, there existed an optimum content of Si/Ti at ca. 0.05-0.1 which resulted in an improved catalytic activity of  $Ag/TiO_2$  in CO oxidation. Based on the  $O_2$ -temperature program desorption ( $O_2$ -TPD) results, the catalysts with appropriate amounts of Si/Ti exhibited higher amount of  $O_2$  adsorption and much lower desorption temperature. It is suggested that the presence of Ti-O-Si promoted the formation of active oxygen species and increased the mobility of lattice oxygen so that the catalytic activity was enhanced. There was no improvement in CO oxidation activity of the  $Ag/TiO_2$  catalyst when the Si/Ti was further increased to 0.3 due probably to the formation of amorphous  $SiO_2$  instead of the Ti-O-Si bond.

© 2010 The Korean Society of Industrial and Engineering Chemistry. Published by Elsevier B.V. All rights reserved.

#### 1. Introduction

The main purpose of support modification is generally to obtain high dispersion of metal catalyst or high active sites for catalytic reaction. Support modification usually brings about changes in surface properties of the support such as surface area and interaction between metal particles and support, which are a crucial factor affecting catalytic activity of the metal. The modification of support with trace element has been investigated widely by many researchers. This method can result in changes in surface chemistry, crystal structure and size, and crystal defects of support. For TiO<sub>2</sub> support, various doping elements have been studied including silicon [1–6] lanthanum [7,8], yttrium [9–11], zirconium [12–14], etc. The incorporation of trace element has shown to increase both surface area and thermal stability of the support.

It is well known that titanium dioxide ( $TiO_2$ ) is reducible metal oxide that stronger interacts with group VIII noble metals than other metal oxides such as  $SiO_2$ ,  $Al_2O_3$ , and MgO [15–19]. For this reason, titanium dioxide has attracted much attention for the application as noble metal catalyst support in many reactions. CO oxidation is one of the reactions that have been frequently investigated using  $TiO_2$  as the support. Nevertheless, only a few studies have reported about the modification of  $TiO_2$  with trace

elements for application as catalyst support in CO oxidation reaction. For examples, Tai et al. [20] have shown that modification of TiO<sub>2</sub> aerogel support with silica-coating improved the catalytic activity of Au/TiO<sub>2</sub> compared to that on pure TiO<sub>2</sub> support. Yu et al. [8] reported that doping of La in TiO<sub>2</sub> support during the sol–gel synthesis also enhanced the catalytic activity of Au/TiO<sub>2</sub> in CO oxidation.

In this work, the effect of Si doping in  $TiO_2$  support synthesized by solvothermal method on the physicochemical properties of  $TiO_2$  and the catalytic activities of  $Ag/TiO_2$  catalysts in the CO oxidation reaction were investigated. The catalysts were also characterized by X-ray diffraction (XRD), Fourier transformed spectroscopy (FT-IR), temperature programmed desorption of oxygen ( $O_2$ -TPD), and pulse chemisorption.

#### 2. Experimental

#### 2.1. Preparation of $TiO_2$ and Si-modified $TiO_2$

The  $TiO_2$  nanoparticles were prepared by the solvothermal method according to that of Ref. [21]. Titanium (IV) n-butoxide (TNB) (97%, Aldrich) and 1,4-butanediol (Aldrich) were used as  $TiO_2$  precursor and organic solvent, respectively. Firstly, 25 g of TNB was dissolved in  $100~\rm cm^3$  of 1,4-butanediol. The solution was mixed in the test tube and placed in  $300~\rm cm^3$  autoclave. Additional 1,4-butanediol, with a volume of about  $30~\rm cm^3$ , was filled into the gap between the test tube and the autoclave wall. The nitrogen gas was purged into the autoclave reactor before heating up to  $320~\rm ^{\circ}C$ 

<sup>\*</sup> Corresponding author. Tel.: +66 2218 6883; fax: +66 2218 6769. E-mail address: Piyasan.p@chula.ac.th (P. Praserthdam).

at a rate of  $2.5~^{\circ}$ C/min and held constant at that temperature for 4 h. The Si-modified  $TiO_2$  was prepared by addition of a certain amount of tetraethylorthosilicate (TEOS, Aldrich) into the mixed solution of TNB and 1,4-butanediol before setting up in the autoclave. The molar ratios of Si/Ti were varied in the range of 0.01–0.3. After cooling naturally to room temperature, the products were repeatedly washed with methanol and dried in air.

#### 2.2. Preparation of Ag/TiO<sub>2</sub> catalysts

The obtained  ${\rm TiO_2}$  powder was used as support for preparation of Ag/TiO<sub>2</sub> catalyst. A certain amount of AgNO<sub>3</sub> was dissolved in deionized water and loaded on the support by the incipient wetness impregnation method. After impregnation, the samples were dried at room temperature for 6 h and then at 110 °C overnight in an oven. The obtained samples were calcined in air at 450 °C for 3 h. The metal content was maintained at 10 at.%Ag with respect to the atomic weight of the  ${\rm TiO_2}$  support. The series of catalysts are denoted by their atomic percentages of metal loading and the silicon content in the  ${\rm TiO_2}$  supports. For example, 10%Ag/TiO<sub>2</sub>-0.01Si is referred to the catalyst containing 10 at.%Ag on the Si-modified  ${\rm TiO_2}$  with the molar ratio of Si/Ti 0.01.

#### 2.3. Catalyst characterization

The XRD analysis was performed using the SIEMENS D5000 diffractometer with Cu  $K_{\alpha}$  radiation. The crystallite size and crystalline phase of Si-modified TiO2 were estimated by the Scherrer equation. The XRD patterns were collected at a rate of  $2.4^{\circ}$  min<sup>-1</sup> in the range of  $2\theta = 20-80^{\circ}$ . The particle sizes of Simodified TiO<sub>2</sub> were investigated by transmission electron microscopy (TEM) with a Philips CM100 microscope. The specific surface area of samples was determined by the Brunauer-Emmet-Teller (BET) method using N<sub>2</sub> adsorption at 77 K in a Micromeritics ASAP 2020 instrument. The FT-IR spectra were collected at room temperature using a NICOLET 6700 spectrometer in the range of  $400-4000 \text{ cm}^{-1}$  with  $4 \text{ cm}^{-1}$  resolution by the KBr technique. The sample and KBr were dried at 110 °C for 24 h before analysis. The samples were measured in a controlled humidity room. The amount of metal active sites for Ag/TiO<sub>2</sub> catalysts was determined using N<sub>2</sub>O pulse chemisorption according to the method described previously by our group [22]. Approximately 100 mg of the catalyst sample was reduced in hydrogen flow (50 cm<sup>3</sup>/min) at 200 °C. After that the temperature was cooled down to 150 °C in He stream and a certain amount of N2O was injected. The N2O was analyzed by TCD gas chromatography using a packed Porapak N column. The metal active site of the Ag/TiO<sub>2</sub> catalyst was calculated assuming a reaction stoichiometry of two Ag per oxygen atom.

The  $O_2$ -TPD experiment was performed in order to study the characteristics of oxygen adsorption and desorption on the catalyst surface. This method was adapted from Yu et al. [8]. Approximately, 0.1 g of the catalyst was reduced at 200 °C in hydrogen flow (50 cm³/min) for 1 h. The temperature was then cooled down to 30 °C in He stream (30 cm³/min) and followed by oxygen adsorption at 30 °C for 1 h with a flow of oxygen (30 cm³/min). The physically adsorbed oxygen on the catalyst surface was swept out with He stream until no signal of oxygen could be detected and then the temperature was ramped with a heating rate of 10 °C/min to 600 °C. The oxygen desorption signal was detected by the thermal conductivity detector (TCD) during programmed heating.

#### 2.4. Reaction study

A fixed-bed glass tube microreactor (i.d. 5 mm) was use to test the catalytic activity of the catalyst samples in CO oxidation. Approximately 100 mg of the catalyst powder was packed in the middle of tubular microreactor between plugs of quartz wool. A thermocouple was inserted into the reactor below the catalyst bed to measure temperature at the catalyst outlet. The tubular reactor was heated from room temperature to the desired temperature in a vertical tubular furnace. The reactant gas mixture of 1% CO, 2% O<sub>2</sub>, and the balanced He was introduced at a total flow rate of 100 cm<sup>3</sup>/ min or a gas hourly space velocity (GHSV)  $\approx 30,600 \, h^{-1}$ . The catalyst was first reduced in situ at 200 °C in flowing hydrogen (50 cm<sup>3</sup>/min) for Ag/TiO<sub>2</sub> for 1 h. After the reduction, the reactant gas mixture was switched into the reactor and maintained at a desired temperature for 20 min. The concentration of CO was monitored by an on-line GC-8ATP (Shimadzu) gas chromatograph equipped with a TCD detector and a Porapak Q column. The conversion of CO was defined as the number of moles of CO converted per the total number of CO in feed stream. The temperature at which conversion reaches 50% (defined as lightoff temperature) is used to compare the catalytic activities of the catalyst samples.

#### 3. Results and discussion

#### 3.1. Effect of Si doping on the properties of TiO<sub>2</sub>

The XRD patterns of TiO<sub>2</sub> and Si-modified TiO<sub>2</sub> prepared by the solvothermal method are shown in Fig. 1. All the samples exhibited only pure anatase phase TiO<sub>2</sub> without any other phase contamination. The XRD patterns of Si-modified TiO<sub>2</sub> showed the major peak of anatase TiO<sub>2</sub> at  $2\theta$  around 25°. Increasing of Si content can affect the broadening of XRD peaks [23]. However, the peak intensity of anatase TiO<sub>2</sub> decreased with increasing Si content, indicating that the crystallite size of TiO<sub>2</sub> became smaller. The crystallite sizes of TiO<sub>2</sub> and Si-modified TiO<sub>2</sub> are shown in Table 1. The crystallite sizes of all Si-modified TiO<sub>2</sub> were smaller than the unmodified TiO<sub>2</sub>. The peak position of anatase (101) and lattice

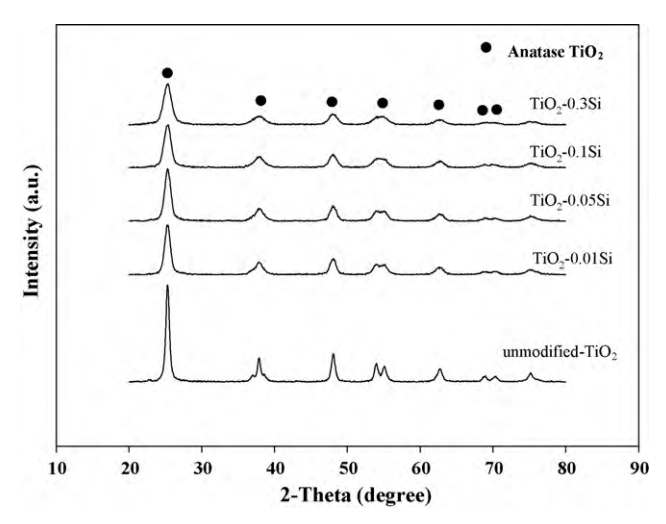


Fig. 1. XRD patterns of Si-modified TiO<sub>2</sub> with different Si/Ti molar ratios.

Table 1 Physical properties and amount of active sites of unmodified  $TiO_2$ , Si-modified  $TiO_2$  support and 10%Ag/ $TiO_2$ -xSi catalysts.

Sample	Crystallite size (nm)	BET surface area (m <sup>2</sup> /g)	Active site of 10%Ag/TiO <sub>2</sub> -xSi (×10 <sup>20</sup> atom/g-catalyst)
Unmodified TiO <sub>2</sub>	15.0	77	1.27
TiO <sub>2</sub> -0.01Si	9.8	103	2.10
TiO <sub>2</sub> -0.05Si	8.5	125	2.02
TiO <sub>2</sub> -0.1Si	7.0	136	1.98
TiO <sub>2</sub> -0.3Si	6.4	96	2.46

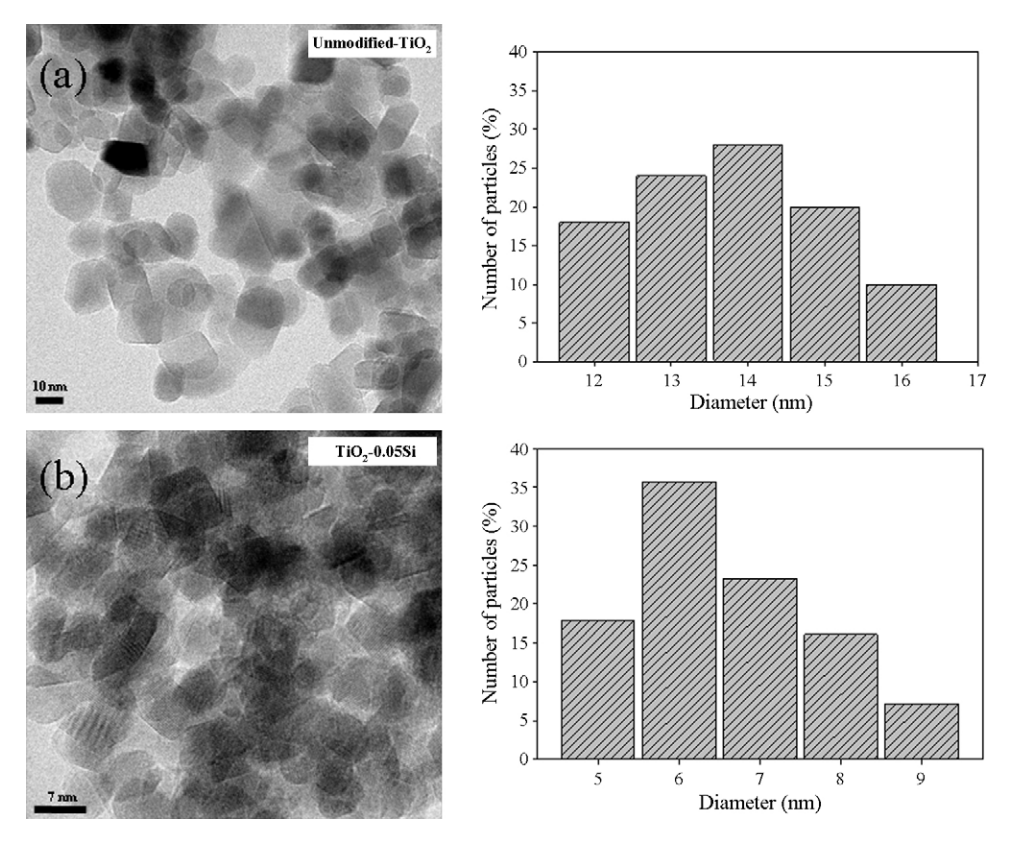


Fig. 2. TEM images and the size distribution of (a) unmodified TiO<sub>2</sub> and (b) TiO<sub>2</sub>-0.05Si.

parameters of TiO $_2$  and Si-modified TiO $_2$  support are given in Table 2. The anatase (1 0 1) diffraction peaks for all the Si-modified TiO $_2$  were shifted slightly to a higher angle compared to that of the TiO $_2$  support, indicating a decrease of the distance between crystal planes which related to the lattice parameters [24]. The decrease of the lattice parameters for the Si-modified TiO $_2$  compared to the TiO $_2$  was attributed to an insertion of the smaller ionic radius of Si (0.042 nm) into the lattice of TiO $_2$  (ionic radius 0.064 nm) [25]. Moreover, the peak intensity of anatase TiO $_2$  decreased with increasing Si content, indicating that the crystallite size of TiO $_2$  became smaller.

Fig. 2 shows the TEM images of  $TiO_2$  and  $TiO_2$ –0.05Si. The particle size distributions were in the range of 12–16 nm and 5–9 nm for the  $TiO_2$  and the  $TiO_2$ –0.05Si, respectively. Such results were in good agreement the XRD results in which the crystallite size of  $TiO_2$  supports decreased with Si doping. The existence of Si in the  $TiO_2$  framework may inhibit the  $TiO_2$  moiety to form large crystal [26]. Moreover, the replacement of Ti by Si atom in  $TiO_2$  lattice can also produce Ti–0–Si bond and the lattice shrinkage because the bond length of Si–0 bond (1.59 Å) is shorter than that of Ti–0 (1.79 Å) [27], as a consequence the crystallite size of  $TiO_2$  is decreased. As also shown in Table 1, BET surface area of the  $TiO_2$ 

 $\begin{tabular}{ll} \textbf{Table 2} \\ \textbf{The peak position of anatase and lattice parameters of unmodified $TiO_2$ and $Simodified $TiO_2$ support. \end{tabular}$ 

Sample	Peak position of anatase (101)	Lattice param- eters (Å)	
	$(2\theta)$ (degree)	a (=b)	С
Unmodified TiO <sub>2</sub>	25.28	3.7934	9.5003
TiO <sub>2</sub> -0.01Si	25.52	3.7528	9.5003
TiO <sub>2</sub> -0.05Si	25.32	3.7896	9.4523
TiO <sub>2</sub> -0.1Si	25.40	3.7766	9.4427
TiO <sub>2</sub> -0.3Si	25.40	3.7766	9.4427

supports increased with increasing Si content and reached a maximum value of 136 m<sup>2</sup>/g for the TiO<sub>2</sub>–0.1Si. Further increase of Si/Ti to 0.3 resulted in the decrease of BET surface area. Similar results were observed by Jin et al. that the BET surface area of silicadoped TiO<sub>2</sub> prepared by hydrothermal process decreased when the molar ratio of Si/Ti was higher than 0.05 [28].

Fig. 3 shows the FT-IR spectra of Si-modified TiO<sub>2</sub> with the Si/Ti molar ratio between 0.01 and 0.3 in the wave number ranging from 400 to 4000 cm<sup>-1</sup>. The spectra bands at ca. 1630 and 3400 cm<sup>-1</sup> were attributed to H-OH bonds of adsorbed water molecules and hydroxyl group of Ti-OH bonds, respectively [29–31]. The hydroxyl group at 3400 cm<sup>-1</sup> of all Si-modified TiO<sub>2</sub> seems to increase compared with the TiO<sub>2</sub> support. These results are in agreement with Chen et al. [32], who reported that the hydroxyl

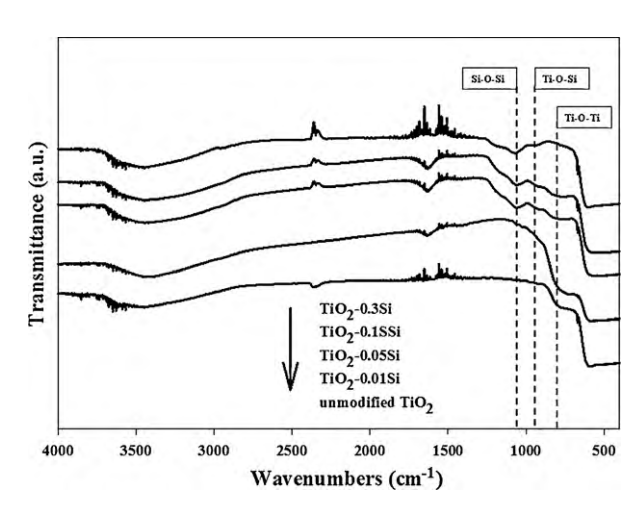


Fig. 3. FT-IR spectra of Si-modified TiO<sub>2</sub> with different Si/Ti molar ratios.

groups of TiO<sub>2</sub> increased after Si doping in non-humidity system. The IR spectra at ca. 700 and 800 cm<sup>-1</sup> were attributed to Ti-O-Ti bonds in the TiO<sub>2</sub> lattice [33]. It is noticed that the spectra band in the 400-850 cm<sup>-1</sup> region became weaker with the increase of Si content, suggesting that the formation of Ti-O-Ti structure was suppressed due to the formation of Ti-O-Si and/or Si-O-Si structure. The presence of Ti-O-Si bond was confirmed by the IR spectra band at ca.  $950 \text{ cm}^{-1}$  [34–36]. The intensity of Si–O–Si bonds at ca. 1070 cm<sup>-1</sup> also increased with increasing the Si content. The presence of the amorphous silica could prevent the agglomeration of TiO<sub>2</sub> nanoparticles, leading to a decrease of TiO<sub>2</sub> particle size [37,38]. The metal active sites of Ag/TiO<sub>2</sub> catalysts were determined by pulse chemisorption and are given in Table 1. It is clearly shown that higher metal dispersion was obtained on the Si-modified TiO<sub>2</sub>. The amount of metal active sites on the Simodified TiO<sub>2</sub> supported catalysts were nearly two times higher than those supported on the unmodified ones. However, the amount of metal active sites on the Si-modified TiO2 was quite similar especially for those with the Si/Ti ratio 0.01-0.1.

#### 3.2. Effect of Si doping on the activity of CO oxidation

The CO conversions as a function of reaction temperature for  $10\% Ag/TiO_2$  with different Si contents in the  $TiO_2$  are shown in Fig. 4. Addition of trace amount of Si in the  $TiO_2$  supports can improve the CO oxidation activity of the  $TiO_2$  supported Ag catalysts. However, there existed an appropriate amount of Si/Ti molar ratio that yielded the higher CO oxidation activity at around 0.05-0.1. At their optimum Si/Ti ratios, the Si-modified  $TiO_2$  supported Ag catalysts showed light-off temperature at 68 °C, which were much lower than the corresponding unmodified ones. When the Si contents were higher than their optimum values, the Si-modified  $TiO_2$  supported catalysts exhibited lower CO oxidation activity although these catalysts possessed higher amount of metal active sites as measured by pulse chemisorption. Thus, the modification of  $TiO_2$  with Si atoms not only improved the metal dispersion, but also affected the mechanism of CO oxidation.

The reaction mechanism for catalytic CO oxidation is known to compose of two possible mechanisms (1) the CO molecule and oxygen atom from external source are coadsorbed on metal active site to produce  $CO_2$  and (2) the CO molecule is adsorbed on metal catalyst surface to form intermediate complex and then reacted with surface lattice oxygen atom of  $TiO_2$  support to generate  $CO_2$ . The oxygen from external source in gas phase then dissociates into atomic oxygen and is adsorbed on the oxygen vacancies sites of the  $TiO_2$  support. As suggested by Mguig et al. [39], the latter

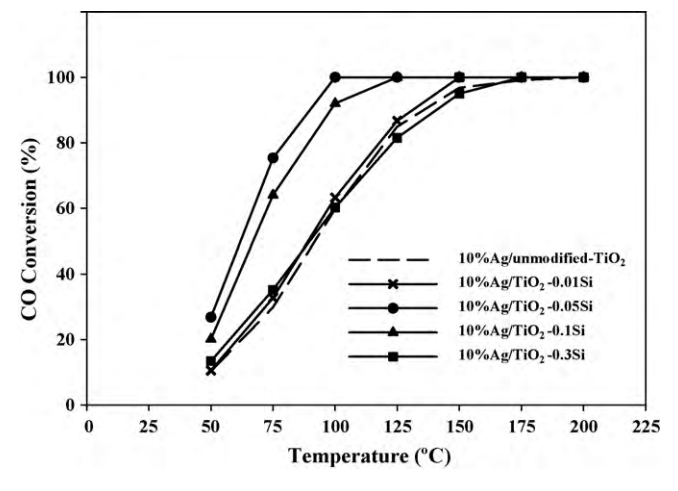


Fig. 4. CO conversion over 10 at.%Ag catalysts supported on Si-modified  $TiO_2$  with different Si/Ti molar ratios.

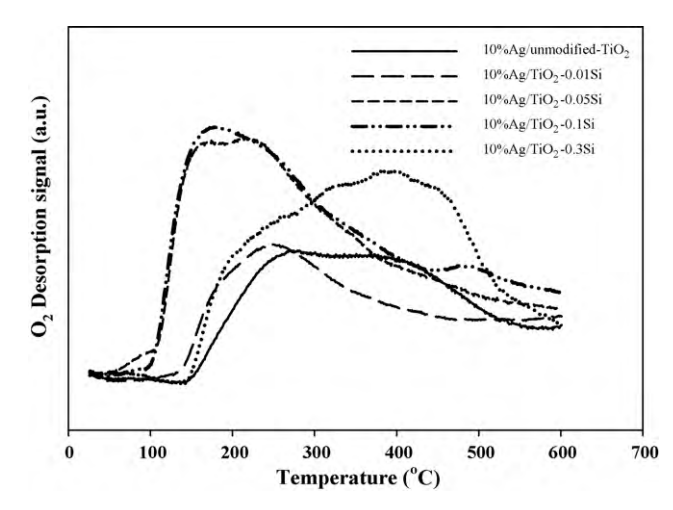


Fig. 5.  $O_2$ -TPD patterns of 10 at.%Ag catalysts supported on Si-modified  $TiO_2$  with different Si/Ti molar ratios.

mechanism occurs more easily on defective surface or basic site surface of metal oxide support. In the present study, the modification of TiO<sub>2</sub> support with trace amount of Si resulted in an increase of the amounts of hydroxyl group and the formation of basic site surface and improved CO oxidation activities. Thus, it is likely that CO oxidation on the Si-modified TiO<sub>2</sub> supported Ag catalysts occurred via such mechanism.

According to the mechanism proposed by Bollinger and Vannice [40] for CO oxidation over Au/TiO<sub>2</sub> catalysts, the adsorption of CO and O2 occurred on two different sites, CO adsorbed on Au and O2 adsorbed on TiO2. Then CO reacted with surface lattice oxygen of TiO<sub>2</sub> to form CO<sub>2</sub> leading to the formation of surface oxygen vacancies. During the CO oxidation, these oxygen vacancies were filled by chemisorbed oxygen species from gas phase. The oxygen adsorption and desorption behaviors of the Ag/TiO<sub>2</sub> catalysts were investigated by using O<sub>2</sub>-TPD experiments and the results are shown in Fig. 5. The Si-modified TiO<sub>2</sub> supported Ag catalysts with optimum Si/Ti ratios exhibited much lower desorption temperature and larger amount of desorbed O<sub>2</sub> compared to the non-modified ones and the ones with excess Si. According to Iwamoto et al. [41], there are three kinds of adsorbed oxygen species on TiO2 surface. The adsorbed oxygen consists of weakly adsorbed surface oxygen, strongly adsorbed surface oxygen and surface lattice oxygen. The weakly adsorbed oxygen desorption in the range of 100–180  $^{\circ}$ C and  $\sim$ 230  $^{\circ}$ C were assigned to  $O_2^-$  and  $O^-$  species, respectively [42]. The desorption temperature of strongly adsorbed surface oxygen and surface lattice oxygen were reported in the range of 470–490 °C, and 810-870 °C, respectively [43,44]. The results demonstrated that the Si-modified TiO<sub>2</sub> supported Ag catalysts with optimum Si/Ti ratios produced the highest amount of O<sub>2</sub><sup>-</sup> and O<sup>-</sup> species whereas the non-modified ones and the ones with excess Si produced O<sup>-</sup> species and strongly adsorbed surface oxygen. It has been reported that the adsorbed O<sup>-</sup> species were the most active species for CO oxidation [8]. In addition, Qu et al. [45] suggested that the strongly adsorbed surface oxygen species blocks the adsorption and diffusion of weakly adsorbed surface oxygen, causing a decrease in the CO oxidation activity of the catalysts.

The results in this work show that oxygen in  $Ag/TiO_2$ –0.05Si and  $Ag/TiO_2$ –0.1Si catalysts desorbed more easily so that the catalysts exhibited higher CO oxidation activity. It is suggested that the formation of Ti–O–Si bonds produced an appreciable change in the electronic properties of these catalysts. Generally,  $TiO_2$  was classified as a support which exhibits the strong metal-support interaction with precious metals. Bernal et al. [46] reported that the temperatures of oxygen desorption from metal catalyst surface

increased when a strong interaction between the metal particles and support occurred. The addition of Si into TiO<sub>2</sub> lattice to form Ti–O–Si bonds may lead to a decrease of the metal-support interaction and resulted in a decrease of oxygen desorption temperature. In other words, the adsorbed oxygen on the Si-modified TiO<sub>2</sub> with optimum Si/Ti ratios can be dissociated to atomic species which desorbed at lower temperature. Moreover, the presence of Si in TiO<sub>2</sub> could decrease the strength of surface lattice oxygen bonding, resulted in higher mobility of lattice oxygen which has been reported to be beneficial for CO oxidation [47,44].

On the other hand, an excess Si content in the  $TiO_2$  support (i.e., for Si/Ti = 0.3) exhibited the increase of amorphous  $SiO_2$  formation which revealed by Si–O–Si bonds from FT-IR results. Qu et al. [48] reported that interaction between Ag and  $SiO_2$  became strongly when the catalyst was pretreated in oxygen at high temperature like a calcination of the catalyst in an oxygen atmosphere. Thus, the formation of  $SiO_2$  in  $TiO_2$  lattice led to a shift of oxygen desorption temperature towards higher temperature and decreased the catalytic activity in CO oxidation.

#### 4. Conclusions

The presence of trace amount of Si atoms in the  $TiO_2$  supports with Si/Ti = 0.05-0.1 has resulted in an improved catalytic performance of  $Ag/TiO_2$  catalysts in the CO oxidation. The insertion of Si atoms into the  $TiO_2$  lattice in the form of Ti-O-Si not only increased the metal active sites by increasing specific surface area of the catalyst and inhibition the agglomeration of  $TiO_2$  crystallites but also altered the strength of  $O_2$  adsorption–desorption behavior on the catalyst surface. As shown by the  $O_2$ -TPD results, the Si-modified  $TiO_2$  supported catalysts exhibited higher amount of oxygen adsorption and lower desorption temperature, which could promote the formation of active oxygen species and increase the mobility of lattice oxygen so that the catalytic activity was enhanced. An excess Si content (i.e., Si/Ti = 0.3), on the other hand, resulted in higher oxygen desorption temperature and no improvement of the catalyst activity, due probably to the formation of amorphous  $SiO_2$ .

#### Acknowledgments

The financial supports from the Thailand Research Fund (TRF) and the Office of Higher Education Commission, Ministry of Education, Thailand are gratefully acknowledged.

#### References

 S. Kongwudthiti, P. Praserthdam, W. Tanakulrungsank, M. Inoue, J. Mater. Process. Technol. 136 (2003) 186.

- [2] F.D. Monte, W. Larsen, J.D. Mackenzie, J. Am. Ceram. Soc. 83 (2000) 1506.
- [3] J. Wiwattanapongpan, O. Mekasuwandumrong, C. Chaisuk, P. Praserthdam, Ceram. Int. 33 (2007) 1469.
- [4] P. Soisuwan, P. Praserthdam, J. Panpranot, D.L. Trimm, Catal. Commun. 7 (2006) 761
- [5] G. Fan, B. Zou, S. Cheng, L. Zheng, J. Ind. Eng. Chem. 16 (2010) 220.
- [6] K. Cho, H. Chang, J.H. Park, B.G. Kim, H.D. Jang, J. Ind. Eng. Chem. 14 (2008) 860.
- [7] C.K. Loong, J.W. Richardson Jr., M. Ozawa, M. Kimura, J. Alloy Compd. 207–208 (1994) 174.
- [8] J. Yu, G. Wu, D. Mao, G. Lu, Acta Phys.-Chim. Sin. 24 (2008) 1751.
- 9] K. Yasuda, S. Arai, M. Itoh, K. Wada, J. Mater. Sci. 34 (1999) 3597.
- [10] J. Ballard, J. Davenport, C. Lewis, R. Doremus, L. Schadler, W. Nelson, J. Therm. Spray Technol. 12 (2003) 34.
- [11] M.R. Alvarez, M.J. Torralvo, Colloids Surf. A 113 (1996) 165.
- [12] S.-M. Chang, C.-Y. Hou, P.-H. Lo, C.-T. Chang, Appl. Catal. B: Environ. 90 (2009) 233.
- [13] J. Luk, M. Klementov, P. Bezdicka, S. Bakardjieva, J. Subrt, L. Szatmry, Z. Bastl, J. Jirkovsk, Appl. Catal. B: Environ. 74 (2007) 83.
- [14] B.N. Narayanan, Z. Yaakob, R. Koodathil, S. Chandralayam, S. Sugunan, F.K. Saidu, V. Malayattil, Eur. J. Sci. Res. 28 (2009) 566.
- [15] S.J. Tauster, S.C. Fung, R.L. Garten, J. Am. Chem. Soc. 100 (1978) 170.
- [16] G.L. Haller, D.E. Resasco, H.P.D.D. Eley, B.W. Paul, Adv. Catal. 36 (1989) 173.
- [17] M.A. Vannice, B. Sen, J. Catal. 115 (1989) 65.
- [18] P. Claus, S. Schimpf, R. Schdel, P. Kraak, W. Mrke, D. Hnicke, Appl. Catal. A: Gen. 165 (1997) 429.
- [165] (1997) 429.[19] L.L. Murrell, D.J.C. Yates, T. Seiyama, K. Tanabe, Stud. Surf. Sci. Catal. 7 (1981) 1470.
- [20] Y. Tai, J. Murakami, K. Tajiri, F. Ohashi, M. Date', S. Tsubota, Appl. Catal. A: Gen. 268 (2004) 183.
- [21] W. Payakgul, O. Mekasuwandumrong, V. Pavarajarn, P. Praserthdam, Ceram. Int. 31 (2005) 391.
- [22] N. Comsup, J. Panpranot, P. Praserthdam, Catal. Lett. 133 (2009) 76.
- [23] I. Djerdj, A.M. Tonejc, J. Alloy Compd. 413 (2006) 159.
- [24] B. Gao, T.M. Lim, D.P. Subagio, T.-T. Lim, Appl. Catal. A: Gen. 375 (2010) 107.
- [25] H. Yang, R. Shi, K. Zhang, Y. Hu, A. Tang, X. Li, J. Alloy Compd. 398 (2005) 200.
- [26] K.Y. Jung, S.B. Park, M. Matsuoka, M. Anpo, Int. J. Photoenergy 5 (2003) 31.
- [27] K. Yang, Y. Dai, B. Huang, Chem. Phys. Lett. 456 (2008) 71.
- [28] R. Jin, Z. Wu, Y. Liu, B. Jiang, H. Wang, J. Hazard. Mater. 161 (2009) 42.
- [29] G. Xu, Z. Zheng, Y. Wu, N. Feng, Ceram. Int. 35 (2009) 1.
- [30] C. Kang, L. Jing, T. Guo, H. Cui, J. Zhou, H. Fu, J. Phys. Chem. C 113 (2009) 1006.
- [31] B. Braconnier, C.A. Paez, S. Lambert, C. Alie, C. Henrist, D. Poelman, J.-P. Pirard, R. Cloots, B. Heinrichs, Micropor. Mesopor. Mater. 122 (2009) 247.
- [32] Q. Chen, D. Jiang, W. Shi, D. Wu, Y. Xu, Appl. Surf. Sci. 255 (2009) 7918.
- [33] J. Liqiang, F. Honggang, W. Baiqi, W. Dejun, X. Baifu, L. Shudan, S. Jiazhong, Appl. Catal. B: Environ. 62 (2006) 282.
- 34] I.N. Martyanov, S. Uma, S. Rodrigues, K.J. Klabunde, Langmuir 21 (2005) 2273.
- [35] H. Nur, Mater. Sci. Eng. B 133 (2006) 49.
- [36] J. Ren, Z. Li, S. Liu, Y. Xing, K. Xie, Catal. Lett. 124 (2008) 185.
- [37] Y.K. Kim, E.Y. Kim, C.M. Whang, Y.H. Kim, W.I. Lee, J. Sol-Gel Sci. Technol. 33 (2005) 87.
- [38] I. Lee, T. Jung, J. Kim, S. Ro, C. Kim, Y. Lee, Y. Kim, J. Lee, M. Kang, J. Ind. Eng. Chem. 14 (2008) 869.
- [39] B. Mguig, M. Calatayud, C. Minot, J. Mol. Struct. Theochem. 709 (2004) 73.
- [40] M.A. Bollinger, M.A. Vannice, Appl. Catal. B: Environ. 8 (1996) 417.
- [41] M. Iwamoto, Y. Yoda, N. Yamazoe, T. Seiyama, J. Phys. Chem. 82 (1978) 2564.
- [42] H. Chon, J. Pajares, J. Catal. 14 (1969) 257.
- [43] R. Li, J. Ma, J. Xu, X. Zhou, Z. Su, React. Kinet. Catal. Lett. 70 (2000) 363.
- [44] L. Luo, G. Shao, Z. Duan, Turk. J. Chem. 29 (2005) 597.
- [45] Z. Qu, M. Cheng, C. Shi, X. Bao, J. Nat. Gas Chem. 14 (2005) 4.
- [46] S. Bernal, J.J. Calvino, M.A. Cauqui, J.M. Gatica, C. Larese, J.A. Perez Omil, J.M. Pintado, Catal. Today 50 (1999) 175.
- [47] L. Rui, R.-R. Inmaculada, B.-B. Belen, G.-R. Antonio, G. Sun, Q. Xin, Chin. J. Catal. 27 (2006) 109.
- [48] Z. Qu, M. Cheng, X. Dong, X. Bao, Catal. Today 93-95 (2004) 247.

Provided for non-commercial research and education use. Not for reproduction, distribution or commercial use.



This article appeared in a journal published by Elsevier. The attached copy is furnished to the author for internal non-commercial research and education use, including for instruction at the authors institution and sharing with colleagues.

Other uses, including reproduction and distribution, or selling or licensing copies, or posting to personal, institutional or third party websites are prohibited.

In most cases authors are permitted to post their version of the article (e.g. in Word or Tex form) to their personal website or institutional repository. Authors requiring further information regarding Elsevier's archiving and manuscript policies are encouraged to visit:

http://www.elsevier.com/copyright

# Author's personal copy

Journal of Industrial and Engineering Chemistry 16 (2010) 785-789



Contents lists available at ScienceDirect

### Journal of Industrial and Engineering Chemistry

journal homepage: www.elsevier.com/locate/jiec



# Thermodynamic analysis of calcium oxide assisted hydrogen production from biogas

S. Assabumrungrat <sup>a,\*</sup>, P. Sonthisanga <sup>a</sup>, W. Kiatkittipong <sup>b</sup>, N. Laosiripojana <sup>c</sup>, A. Arpornwichanop <sup>a</sup>, A. Soottitantawat <sup>a</sup>, W. Wiyaratn <sup>d</sup>, P. Praserthdam <sup>a</sup>

- <sup>a</sup> Department of Chemical Engineering, Faculty of Engineering, Chulalongkorn University, Bangkok 10330, Thailand
- Department of Chemical Engineering, Faculty of Engineering and Industrial Technology, Silpakorn University, Nakhon Pathom 73000, Thailand
- <sup>c</sup> The Joint Graduate School of Energy and Environment, King Mongkut's University of Technology Thonburi, Bangkok 10140, Thailand
- Department of Production Technology Education, Faculty of Industrial Education and Technology, King Mongkut's University of Technology Thonburi, Bangkok 10140, Thailand

#### ARTICLE INFO

Article history: Received 23 October 2009 Accepted 5 April 2010

Keywords: Hydrogen Biogas Multifunctional reactor Process intensification

#### ABSTRACT

This paper investigates calcium oxide assisted hydrogen production from biogas. Preliminary experiments were performed to compare the catalytic performance of combined carbon dioxide reforming and partial oxidation of biogas among four different adsorbent (CaO)/catalyst (Ni/SiO<sub>2</sub>-MgO) arrangements; i.e. (i) Ni/SiO<sub>2</sub>-MgO before CaO, (ii) CaO before Ni/SiO<sub>2</sub>-MgO, (iii) Ni/SiO<sub>2</sub>-MgO mixed with CaO, and (iv) Ni/SiO<sub>2</sub>-MgO without CaO. The mixture of CaO and Ni/SiO<sub>2</sub>-MgO was found to be the best arrangement, offering the highest hydrogen yield. Thermodynamic investigation of the integrated sorption-reaction systems for hydrogen production from biogas was performed. The system can be operated under thermal neutral condition when appropriate operating parameters are adjusted. Finally based on the thermal neutral operation, the effects of H<sub>2</sub>O/CH<sub>4</sub> and CaO/CH<sub>4</sub> ratios on the required O<sub>2</sub>/CH<sub>4</sub> ratio, hydrogen yield, hydrogen concentration and CO/H<sub>2</sub> ratio in product were determined. Obviously the use of CaO adsorbent can improve hydrogen production and there is an optimum H<sub>2</sub>O/CH<sub>4</sub> ratio which offers the highest hydrogen production at each CaO/CH<sub>4</sub> ratio. Increasing H<sub>2</sub>O/CH<sub>4</sub> ratio generally increases H<sub>2</sub>/CO ratio but decreases hydrogen concentration in the product.

© 2010 The Korean Society of Industrial and Engineering Chemistry. Published by Elsevier B.V. All rights reserved.

#### 1. Introduction

Energy production from renewable sources is one of several approaches to reduce emissions of greenhouse gases (GHG). Nowadays, GHG is one of significant problems that have a great impact on global warming. About 75% of the anthropogenic carbon dioxide (CO<sub>2</sub>) emissions to the atmosphere during the past 20 years are due to fossil fuel burning [1,2]. In addition to CO<sub>2</sub>, methane (CH<sub>4</sub>) produced in natural environments from anaerobic degradation of organic substrates is another major constituent significantly contributing to a greenhouse effect with a 23-fold higher global warming potential than CO<sub>2</sub> [3,4]. With the increasing concern on environmental problems, many countries are pursuing efforts to develop renewable energy sources and fuels with lower carbon content as an alternative future energy resource. Increasing fuel combustion efficiency and capturing/ storing CO<sub>2</sub> produced are also important aspects in developing new energy technologies.

Hydrogen is considered to be the most promising future energy carrier [2,5]. A hydrogen-based energy economy coupled with the anticipated limits on CO<sub>2</sub> emissions provides a good opportunity for the investigation of H<sub>2</sub> production processes that are more energy-efficient and environmental friendly. A sorption-enhanced H<sub>2</sub> production (SEHP) in which the hydrocarbon reforming, watergas shift, and CO<sub>2</sub> removal reactions occur simultaneously at high temperatures over a mixture of reforming catalyst and CO2 sorbent, could be a potential alternative. In the SEHP process, CO<sub>2</sub> is reacted with a solid sorbent (adsorption/carbonation step) and converted to a solid carbonate. Regenerating the sorbent (desorption/calcination step) results in releasing CO2 which is in a form suitable for storage. Several sorbent materials, i.e. calcium oxide [6], lithium oxides [6–9], hydrotalcites [6,10,11], double salts [6,12], and basic alumina [6,13], have been studied for the sorption of CO<sub>2</sub> at high temperatures. Recently, calcium oxide (CaO) has been examined thoroughly as a suitable sorbent for SEHP processes [6,14-20]. It was reported to be thermodynamically the best candidate among various metal oxides for CO2 capture in zero emission power generation systems [2,20]. In addition, CaO is cheap and readily available in nature. Thus, the CaO sorption process has been a well-known CO<sub>2</sub> capture technology nowadays.

<sup>\*</sup> Corresponding author. Fax: +66 2 218 6877. E-mail address: Suttichai.A@chula.ac.th (S. Assabumrungrat).

This study concentrates on the production of  $H_2$  from biogas via a sorption-enhanced system. The experiment of the combined carbon dioxide reforming and partial oxidation of biogas over an industrial Ni/SiO<sub>2</sub>·MgO catalyst and a CaO adsorbent was carried out to investigate the effect of an adsorbent and catalyst bed arrangement on the reaction performance. Further, a thermodynamic analysis was performed to investigate the effects of temperature, oxygen, water, and CaO sorbent under a thermal neutral operation in which no external heat is required to sustain the reactor operation.

#### 2. Theory

#### 2.1. Sorption-enhanced dry reforming and partial oxidation of biogas

#### 2.1.1. Reforming and partial oxidation

The main reactions taking place in the system are: Methane dry reforming with carbon dioxide:

$$CH_4 + CO_2 \leftrightarrow 2CO + 2H_2 \quad \Delta H_{298}^\circ = 261 \text{ kJ/mol}$$
 (1)

Methane partial oxidation with oxygen:

$$CH_4 + 1/2O_2 \leftrightarrow CO + 2H_2$$
  $\Delta H_{298}^{\circ} = -36 \text{ kJ/mol}$  (2)

When steam is introduced to the reaction system, the steam reforming of methane and the water gas shift reaction can be occurred as follows.

Methane steam reforming reaction:

$$CH_4 + H_2O \leftrightarrow CO + 3H_2$$
  $\Delta H_{298}^{\circ} = 206 \text{ kJ/mol}$  (3)

Water gas shift reaction:

$$CO + H_2O \leftrightarrow CO_2 + H_2$$
  $\Delta H_{298}^{\circ} = -41.5 \text{ kJ/mol}$  (4)

Methane reforming with carbon dioxide (Eq. (1)) and steam (Eq. (3)) are highly endothermic, the forward reaction are thermodynamically favored with high operating temperature and low pressure while methane partial oxidation (Eq. (2)) and water gas shift reaction (Eq. (4)) are mildly exothermic.

#### 2.1.2. Sorption of carbon dioxide on calcium oxide

Carbon dioxide sorption (carbonation reaction) on calcium oxide can be explained by the following reaction:

$$CO_2 + CaO \rightarrow CaCO_3$$
  $\Delta H_{298}^{\circ} = -178 \text{ kJ/mol}$  (5)

Utilization of CaO to capture carbon dioxide can improve the operation performance as the exothermic heat from carbon dioxide sorption can be utilized for the endothermic reactions.

#### 2.2. Thermodynamic analysis

For understanding the advantages of combining sorption and reaction for  $H_2$  production and studying of suitable operating condition, a thermodynamic analysis of the important reactions (Eqs. (1)–(5)) were investigated. Aspen Plus simulator was used for equilibrium calculations. The minimization of Gibbs free energy method has been used for predicting the product compositions at equilibrium. The products are in both gas phase i.e.  $CH_4$ , CO,  $CO_2$ ,  $O_2$ ,  $O_2$ ,  $O_2$ ,  $O_2$ ,  $O_2$ ,  $O_3$ ,  $O_4$ 

#### 3. Experimental

A commercial-grade reforming catalyst, Ni/SiO<sub>2</sub>·MgO, containing 55 wt.% of nickel supplied from Japan and a commercial-grade calcium oxide adsorbent supplied from Riedel-de Haën were employed in this study. The catalyst was cylindrical extrudate with a diameter of 3 mm and a length of 3 mm. Silicon carbide supplied from Fluka with an average size of 40-100 mesh was used as a dilution material for the catalyst. The reaction was carried out in a reaction system described in our previous work [21]. The reactor was a quartz tube (internal diameter = 0.011 m, length = 0.5 m) heated by a temperature-controlled electric oven. Experiments were performed using Ni/SiO<sub>2</sub>·MgO catalyst (0.1314 g) diluted with silicon carbide (0.438 g) and CaO adsorbent (0.657 g). CaO adsorbent acts as a CO<sub>2</sub> acceptor in the sorption-enhanced system. As shown in Fig. 1, four different bed arrangements in the sorptionenhanced operation were considered as follows: (i) Ni/SiO2·MgO before CaO, (ii) CaO before Ni/SiO2·MgO, (iii) Ni/SiO2·MgO mixed with CaO, and (iv) Ni/SiO<sub>2</sub>·MgO without adsorbent. High pure CH<sub>4</sub> (99.999%),  $CO_2$  (99.999%) and  $O_2$  (99.99%) were used as the reactant gases. Argon was used for purging the system. The reaction was taken place at 1023 K and atmospheric pressure. The catalyst was reduced in a hydrogen flow (30 cm<sup>3</sup>/min) for 1 h and then the gas feed containing CH<sub>4</sub> (12.5 cm<sup>3</sup>/min), CO<sub>2</sub>  $(12.5 \text{ cm}^3/\text{min})$  and  $O_2(6.25 \text{ cm}^3/\text{min})$  was switched to the reactor. It should be noted that with the difference in bed arrangements it becomes difficult to keep the same space velocity and contact time for each configuration. Therefore, the comparison of reaction performance among the different arrangements was based on the

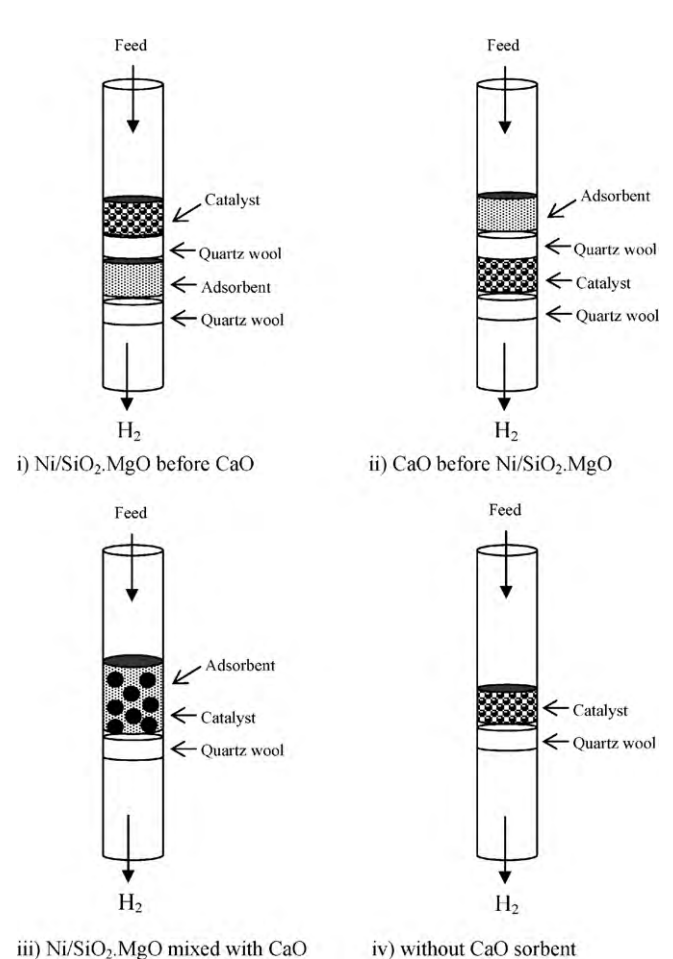


**Fig. 1.** Different adsorbent/catalyst arrangements in the sorption-enhanced operation.

same ratio of gas feed rate per catalyst weight. The composition of exit gas effluent was analyzed every 10 min by a TCD gas chromatograph (Shimadzu GC-8A, Japan) equipped with a Porapak-Q and Molecular Sieve 5A column. The  $\rm H_2$  yield were defined as

$$H_2 \, yield = \frac{H_2 \, molar \, flow \, rate/2}{CH_4 \, molar \, feed \, flow \, rate} \tag{6}$$

#### 4. Results and discussion

A preliminary set of experiments was performed to determine a suitable adsorbent/catalyst arrangement for hydrogen production from simulated biogas, a mixture of CH<sub>4</sub> (50 mol%) and CO<sub>2</sub> (50 mol%). Hydrogen yields achieved from the operation under four different bed arrangements are shown in Fig. 2. It can be seen that for the case without CaO (conventional operation), hydrogen yield initially increases and levels off at a hydrogen yield of about 57%. For the case of packing Ni/SiO<sub>2</sub>·MgO before CaO, it shows similar behavior as the first case in term of hydrogen yield, indicating that the presence of CaO after the catalyst bed does not help improving the reactions in the system. However, it was observed that hydrogen concentration in the exit gas is considerably higher than the first case since CO<sub>2</sub> in the reaction product was adsorbed by CaO. Importantly, the improvement in hydrogen yield was observed for the cases of packing CaO before Ni/SiO2·MgO and Ni/SiO2·MgO mixed with CaO with. For the case of packing CaO before the catalyst, in which some CO<sub>2</sub> in the feed was removed before reaching the subsequent catalyst bed, the increasing of hydrogen yield was observed over 20 min of reaction time. As for the case of mixing CaO with the catalyst in the bed, the improvement of hydrogen yield becomes more significant and the superior yield is observed until 80 min of reaction time. Previous report suggested that with pure CO<sub>2</sub> of 1 atm, the minimum temperature for CO<sub>2</sub> desorption from CaCO<sub>3</sub> is 1173 K [22]. Hence, CaO could be assumed effective for CO<sub>2</sub> adsorption in the range of operating temperature in our study. However, it should be noted that for all experiments, hydrogen yields always approached the same value of about 57% after prolonged period since the sorption of CO<sub>2</sub> by CaO become insignificant when most of CaO is converted to CaCO<sub>3</sub>. In addition, the study further demonstrated that when sorbent bed is appropriately integrated in the reaction system, the values of hydrogen yield higher than the equilibrium value (75%) can be achieved.

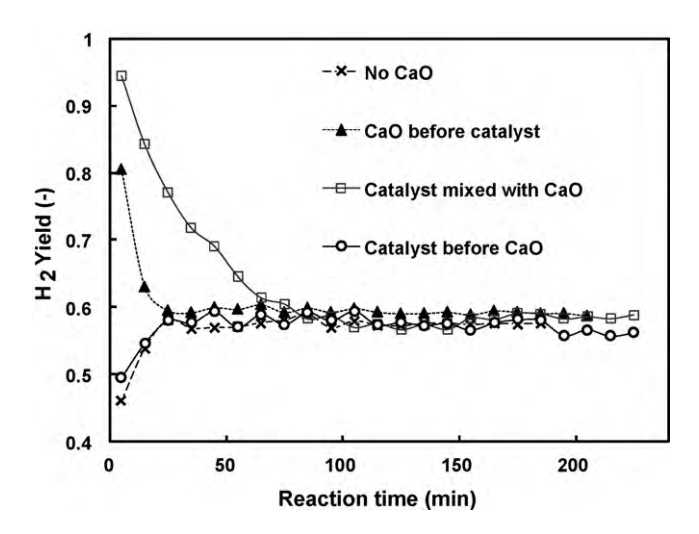


**Fig. 2.** Hydrogen yield achieved from different adsorbent/catalyst arrangements (T = 1023 K,  $\text{CH}_4$ : $\text{CO}_2$ : $\text{O}_2 = 1$ :1:0.5).

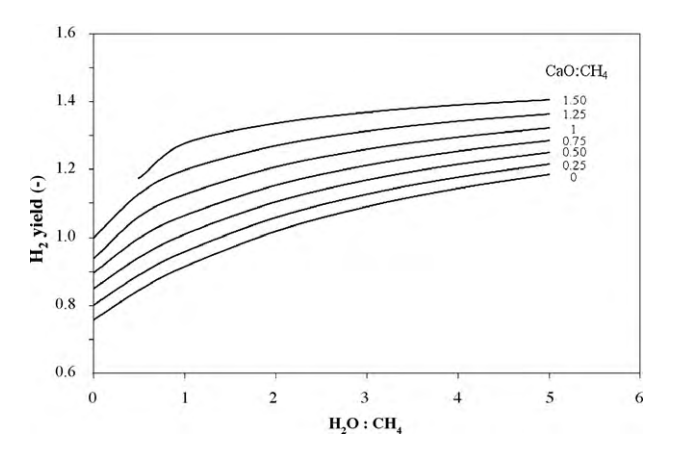


**Fig. 3.** Hydrogen yield in the CaO assisted hydrogen production system (T = 1073 K and  $O_2$ :CH<sub>4</sub> = 0.5).

According to these preliminary results, it is obvious that the use of CaO in the combined carbon dioxide reforming and partial oxidation of biogas particularly under the mode of mixture of CaO and Ni/SiO<sub>2</sub>·MgO can improve the hydrogen yield compared to the conventional system without CaO. Therefore, the reaction system under the mode of mixture of CaO and Ni/SiO2:MgO was selected for further studies. It is noted that for practical application of this adsorbent/catalyst system under steady-state condition, a fluidized bed reactor with continuous feeds of a gas mixture and CaO is generally considered as a suitable option for the sorptionenhanced hydrogen production from biogas. When this reactor is equipped with a regenerator for regenerating CaCO<sub>3</sub> to CaO, the system can be operated continuously under steady-state condition. In addition, the removed CO<sub>2</sub> can be further sequestrated, if necessary, in order to reduce the amount of CO2 released to the environment.

As the next step, the technical feasibility of the above system without a regenerator was studied based on thermodynamic analysis. The reactions taking place are assumed at equilibrium compositions and the feed biogas is assumed to consist of 50% CH<sub>4</sub> and 50% CO<sub>2</sub>. The effects of some major operating parameters; i.e.  $\rm H_2O/CH_4$ , and  $\rm CaO/CH_4$  ratios on hydrogen yield, hydrogen concentration,  $\rm CO/H_2$  ratio in product gas, and overall enthalpy change were investigated in order to understand the role and behavior of CaO assisted hydrogen production from biogas. It is noted that the inlet  $\rm O_2/CH_4$  ratio and operating temperature was fixed at 0.5 and 1073 K, respectively.

Figs. 3 and 4 show the hydrogen yield and enthalpy change of the system at various values of  $H_2O/CH_4$  and  $CaO/CH_4$  ratios. It was

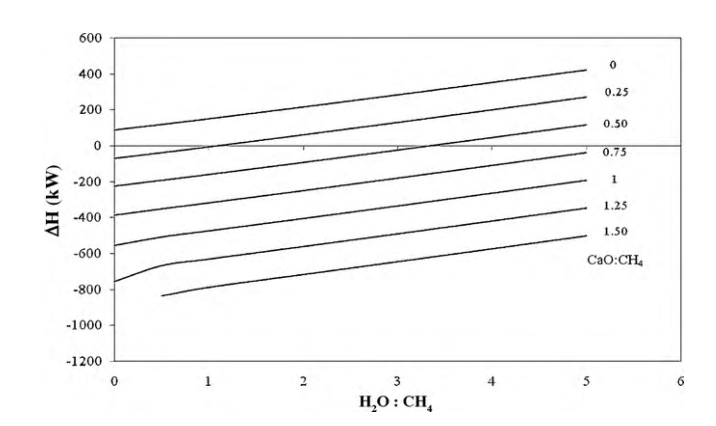


**Fig. 4.** Overall enthalpy change in the CaO assisted hydrogen production system (T = 1073 K and  $O_2$ :CH<sub>4</sub> = 0.5).

S. Assabumrungrat et al./Journal of Industrial and Engineering Chemistry 16 (2010) 785-789

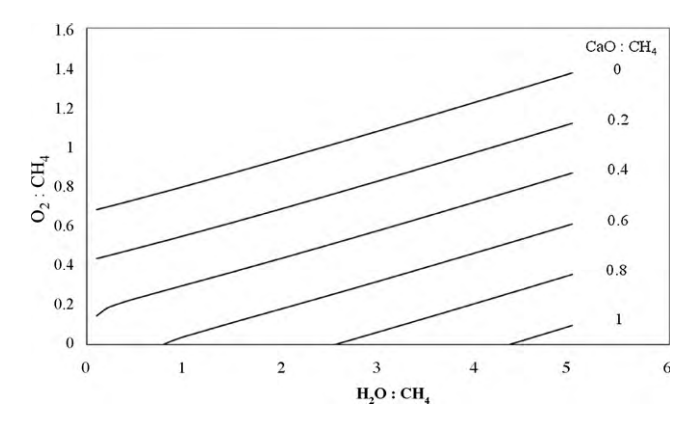


**Fig. 5.**  $O_2/CH_4$  ratio required for thermal neutral operation of the CaO assisted hydrogen production system (T = 1073 K).

**Fig. 7.**  $H_2/CO$  ratio at the thermal neutral operation of the CaO assisted hydrogen production system (T = 1073 K).

demonstrated that at low H<sub>2</sub>O/CH<sub>4</sub> ratio and without the presence of CaO, hydrogen yield as low as 37.5% is achieved because the hydrogen production is predominately governed by the carbon dioxide reforming and partial oxidation which offer low hydrogen. When water is added in the reaction system, more hydrogen is observed according to the promotion of methane stream reforming and water gas shift reaction. The highly endothermic stream reforming causes the enthalpy change to become less negative (Fig. 4). Under the presence of CaO in the system, the removal of carbon dioxide can further increase the hydrogen yield by shifting the water gas shift reaction and consequently shifting the methane steam reforming. The enthalpy change becomes more negative as the carbonation (Eq. (5)) is a highly exothermic reaction. From Fig. 4, it is evident that when the operating parameters are carefully adjusted, the system can be operated at a thermal neutral condition ( $\Delta H = 0$ ) in which the heat generated is equal to the heat consumed. For example, at  $O_2/CH_4 = 0.5$ , the suitable values of H<sub>2</sub>O/CH<sub>4</sub> ratio are 1.1 and 3.3 when the CaO/CH<sub>4</sub> ratios are 0.25 and 0.5, respectively.

In the following studies, only the results at thermal neutral condition are determined as it is a desirable condition for practical operations – no effort on heat addition to or heat removal from the system is required. The values of O<sub>2</sub>/CH<sub>4</sub> ratio required at different H<sub>2</sub>O/CH<sub>4</sub> and CaO/CH<sub>4</sub> ratios are shown in Fig. 5. It is obvious that higher O<sub>2</sub>/CH<sub>4</sub> ratios are required when the system is operated at higher H<sub>2</sub>O/CH<sub>4</sub> ratios while lower O<sub>2</sub>/CH<sub>4</sub> ratios are needed at higher CaO/CH<sub>4</sub> ratios. This is because of the endothermic and exothermic natures of the steam reforming and carbonation reactions, respectively. Figs. 6–8 show the corresponding hydrogen yield, H<sub>2</sub>/CO ratio and hydrogen concentration in product,

respectively. Unlike the results shown in Fig. 2 (isothermal condition), there is an optimum H<sub>2</sub>O/CH<sub>4</sub> ratio which provides the highest hydrogen yield for each CaO/CH<sub>4</sub> ratio in the thermal neutral operation (Fig. 6). At low H<sub>2</sub>O/CH<sub>4</sub> ratio, low hydrogen yield is obtained as most hydrogen is derived from the carbon dioxide reforming and the partial oxidation of methane which give lower hydrogen than does the steam reforming. When operating at a higher H<sub>2</sub>O/CH<sub>4</sub> ratio, higher hydrogen yield is achieved from the promotion of methane steam reforming and water gas shift reaction as evident by the observed higher H<sub>2</sub>/CO ratio in the product (Fig. 7). However, when the system is operated at too high values of H<sub>2</sub>O/CH<sub>4</sub>, operation at higher O<sub>2</sub>/CH<sub>4</sub> ratios is required as shown in Fig. 5 so that the exothermic heat generated from the partial oxidation and complete combustion of methane is sufficient for providing the increased endothermic heat demand from the presence of higher extent of steam. Therefore, less hydrogen is generated. From Fig. 8, it is observed that the addition of extra steam lowers the hydrogen concentration in most cases due to the dilution of gas product by excess water and the requirement of higher oxygen in the system.

When the reactions are incorporated with the addition of CaO, it is evident that the CaO assisted hydrogen production shows beneficial effects on all the hydrogen yield,  $H_2/CO$  ratio and hydrogen concentration. The removal of  $CO_2$  from the reaction system by CaO sorption promotes the water gas shift reaction and subsequently the steam reforming, and therefore, increases all the hydrogen yield, hydrogen concentration and  $H_2/CO$  ratio. In addition, the exothermic heat generated from the carbonation reduces the requirement of  $O_2/CH_4$  ratio and thus suppresses the hydrogen production from the partial oxidation

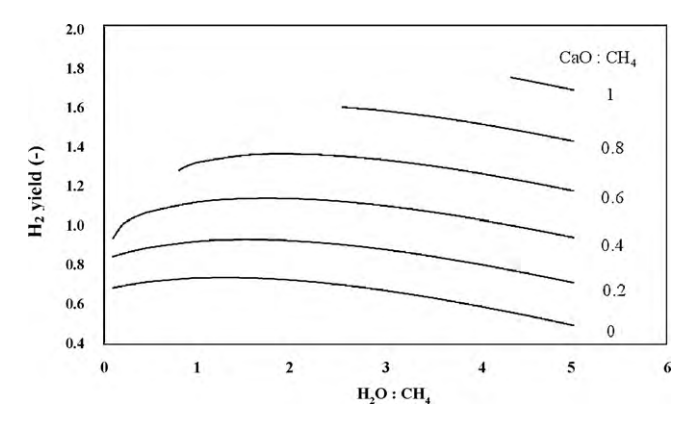


**Fig. 6.** Hydrogen yield at the thermal neutral operation of the CaO assisted hydrogen production system (T = 1073 K).

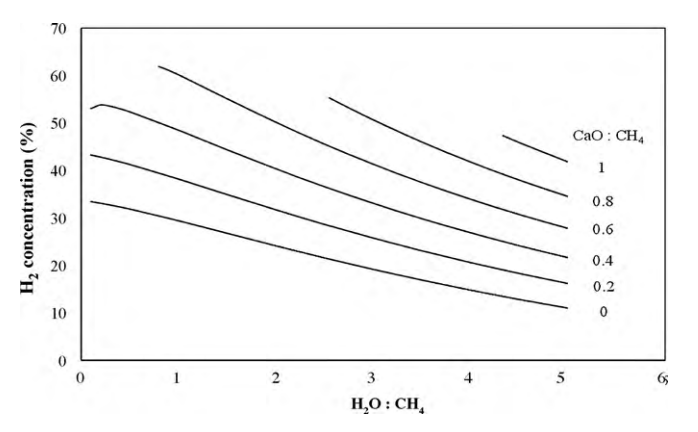


**Fig. 8.** Hydrogen concentration at the thermal neutral operation of the CaO assisted hydrogen production system (T = 1073 K).

reaction which offers lower hydrogen production and hydrogen concentration.

#### 5. Conclusion

The reaction tests for hydrogen production from biogas using four different adsorbent/catalyst arrangements; (i) Ni/SiO2:MgO before CaO, (ii) CaO before Ni/SiO<sub>2</sub>·MgO, (iii) Ni/SiO<sub>2</sub>·MgO mixed with CaO, and (iv) Ni/SiO2·MgO without CaO, indicated that the CaO assisted hydrogen production is best to be performed under an operation with mixture of CaO and Ni/SiO2·MgO. The thermodynamic investigation revealed that the H<sub>2</sub>O/CH<sub>4</sub>, CaO/CH<sub>4</sub> and O<sub>2</sub>/ CH<sub>4</sub> ratios can be appropriately adjusted to achieve thermal neutral condition in which the system requires no external heat source for the operation. Based on this condition, at a higher H<sub>2</sub>O/ CH<sub>4</sub> feed ratio, the system requires either higher O<sub>2</sub>/CH<sub>4</sub> or CaO/ CH<sub>4</sub> ratio to maintain the thermal neutral operation. It is clearly demonstrated that the use of CaO adsorbent can promote the hydrogen production and hydrogen concentration in the product. In addition, there is an optimum H<sub>2</sub>O/CH<sub>4</sub> ratio which offers the highest hydrogen production at each CaO/CH<sub>4</sub> ratio.

#### Acknowledgements

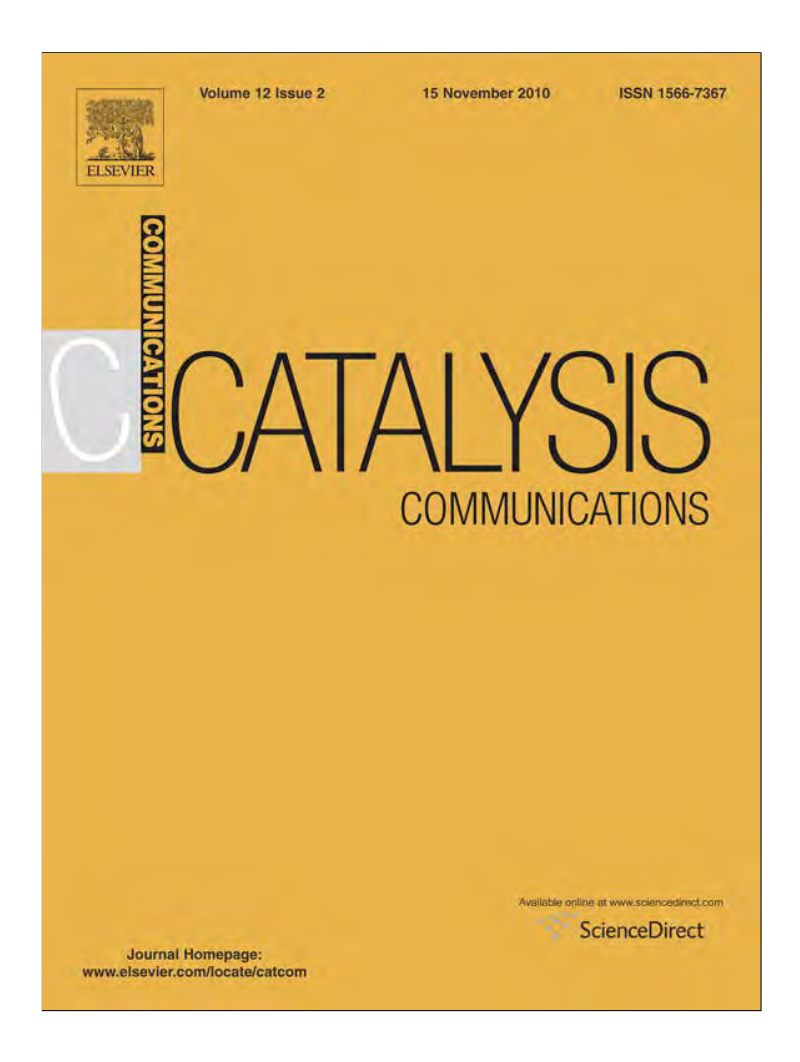
This research is financially supported by the Thailand Research Fund and Commission on Higher Education. The authors also would like to acknowledge great helps from Mr. Watcharapong Khaodee and Mr. Parinya Intaracharoen.

#### References

[1] B. Metz, O. Davidson, H. de Coninck, M. Loss, L. Meyer, IPCC Special Report on Carbon Dioxide Capture and Storage, Prepared by Working Group III of the

- Intergovernmental Panel on Climate Change, Published for the Intergovernmental Panel on Climate Change, Cambridge University Press, 2005
- [2] (a) A.A.A. Solieman, J.W. Dijkstra, W.G. Haije, P.D. Cobden, R.W. van den Brink, Int. J. Greenhouse Gas Control. 3 (2009) 393;
- (b) B.H. Um, Y.S. Kim, J. Ind. Eng. Chem. 15 (2009) 297.
- F. Eric, B. Roda, R. Denis, J. Membr. Sci. 328 (2009) 11.
- O. Davidson, B. Metz, Special Report on Carbon Dioxide Capture and Storage, International Panel on Climate Change, Geneva, Switzerland, 2005 (www.
- [5] A.H. Stromman, E.G. Hertwich, Hybrid life cycle assessment of large scale hydrogen production facilities, Reports and Working Papers from Norwegian University of Science and Technology (NTNU) Industrial Ecology Programme (IndEcol), Working Papers No. 3/2004, 2004, ISSN:1504-3681.
- H.T. Reijers, J. Valster-Schiermeier, S.E.A. Cobden, P.D. Ruud, W. van den Brink, Ind. Eng. Chem. Res. 45 (2006) 2522.
- J.-I. Ida, Y.S. Lin, Environ. Sci. Technol. 37 (2003) 1999.
- M. Kato, S. Yoshikawa, K. Nakagawa, J. Mater. Sci. Lett. 21 (2002) 485. E. Ochoa-Fernandez, H.K. Rusten, H.A. Jakobsen, M. Ronning, A. Holmen, D. Chen, in: Proceedings of the International Conference on Gas-Fuel 05, Brugge, (2005), p.
- [10] J.R. Hufton, S. Mayorga, S. Sircar, AIChE J. 45 (1999) 248.
- [11] Z. Yong, V. Mata, A.E. Rodrigues, Ind. Eng. Chem. Res. 40 (2001) 204.
- [12] S.G. Mayorga, T.R. Gaffney, J.R. Brzozowski, S.J. Weigel, European Patent 1,074, 297 (2001)
- [13] Z. Yong, V. Mata, A.E. Rodrigues, Sep. Purif. Technol. 26 (2002) 95.
- [14] D.P. Harrison, Ind. Eng. Chem. Res. 47 (2008) 6486.
- [15] E. Ochoa-Fernandez, G. Haugen, T. Zhao, M. Rønning, I. Aartun, B. Børresen, E. Rytter, M. Rønnekleiv, D. Chen, Green Chem. 9 (2007) 654.
- [16] A. Bjørnar, B. Richard, B. Egil, D. Ival, J. Jana, R. Petter, Energy Procedia. 1 (2009)
- [17] S.C. Lee, B.Y. Choi, T.J. Lee, C.K. Ryu, Y.S. Ahn, J.C. Kim, Catal. Today 111 (2006) 385.
- [18] J. Abbasian, A.H. Khayyat, Development of highly durable and reactive regenerable magnesium-based sorbents for CO<sub>2</sub> separation in coal gasification process. Final Technical Report for U.S. Department of Energy, National Energy Technology Laboratory, 2005. [19] B. Feng, W. Liu, X. Li, H. An, Energy Fuels 21 (2007) 426.
- [20] J.C. Abanades, Chem. Eng. J. 90 (2002) 303.
- B. Pholjaroen, N. Laosiripojana, P. Praserthdam, S. Assabumrungrat, J. Ind. Eng. Chem. 15 (2009) 488.
- [22] A.L. Ortiz, D.P. Harrison, Ind. Eng. Chem. Res. 40 (2001) 5102.

Provided for non-commercial research and education use. Not for reproduction, distribution or commercial use.



This article appeared in a journal published by Elsevier. The attached copy is furnished to the author for internal non-commercial research and education use, including for instruction at the authors institution and sharing with colleagues.

Other uses, including reproduction and distribution, or selling or licensing copies, or posting to personal, institutional or third party websites are prohibited.

In most cases authors are permitted to post their version of the article (e.g. in Word or Tex form) to their personal website or institutional repository. Authors requiring further information regarding Elsevier's archiving and manuscript policies are encouraged to visit:

http://www.elsevier.com/copyright

# Author's personal copy

Catalysis Communications 12 (2010) 80-85



Contents lists available at ScienceDirect

### **Catalysis Communications**

journal homepage: www.elsevier.com/locate/catcom



# Elucidation of the basicity dependence of 1-butene isomerization on MgO/Mg(OH)<sub>2</sub> catalysts

Jiraporn Puriwat <sup>a</sup>, Wasu Chaitree <sup>a</sup>, Kongkiat Suriye <sup>b</sup>, Siraprapa Dokjampa <sup>b</sup>, Piyasan Praserthdam <sup>a</sup>, Joongjai Panpranot <sup>a,\*</sup>

<sup>a</sup> Center of Excellence on Catalysis and Catalytic Reaction Engineering, Department of Chemical Engineering, Faculty of Engineering, Chulalongkorn University, Bangkok 10330, Thailand <sup>b</sup> SCG Chemicals, Co., Ltd., 1 Siam Cement Road, Bangsue, Bangkok 10800, Thailand

#### ARTICLE INFO

Article history:
Received 18 May 2010
Received in revised form 18 August 2010
Accepted 21 August 2010
Available online 25 September 2010

Keywords: MgO Mg(OH)<sub>2</sub> Basicity Isomerization 1-butene

#### ABSTRACT

The gas-phase isomerization of 1-butene to 2-butene was investigated on the  $MgO/Mg(OH)_2$  catalysts containing different basicities (i.e., weak, medium, and strong basic sites). The isomerization reaction mainly proceeded on either the strong or the medium strength basic sites while the weak basic sites had little impact on the isomerization activity. As revealed by  $CO_2$ -temperature program desorption ( $CO_2$ -TPD), Fourier-transformed-infrared spectroscopy (FT-IR), and electron spin resonance (ESR), the crystalline MgO contained both weak and strong basic sites while the  $Mg(OH)_2$  phase exhibited only the medium strength one. The strong basic sites of MgO were correlated well with the presence of oxygen atoms in the lattice of crystalline MgO. The medium strength basic sites in  $Mg(OH)_2$ , on the other hand, were arisen from the hydroxyl groups in the  $Mg(OH)_2$  structure.

© 2010 Elsevier B.V. All rights reserved.

#### 1. Introduction

In the field of heterogeneous catalysis, many reactions involve acidic-basic properties of the catalyst surface. Compared to the wide use of heterogeneous acid catalysts, commercialization of heterogeneous base catalysts and characterization of solid bases have been less reported [1,2]. According to a survey by Tanabe and Holderich [2], the number of industrial processes that use solid acids, solid bases, and acid-base bifunctional catalysts are 103, 10, and 14, respectively. Basic catalysts are active and selective for various reactions including isomerization, dehydrogenation, amination, hydrogenation, alkylation, and condensation [3]. Many of these reactions have been carried out industrially using liquid base catalysts. The replacement of liquid bases by solid base catalysts would have the advantage such as decreasing corrosion and environmental problems and easier separation and recovery of the catalysts [4]. The fundamental study on the structure, reactivity, and deactivation of solid bases are, therefore, necessary before they can be widely used as the solid acid catalysts [5].

Magnesium oxide (MgO) is one of the well-known basic catalysts. It is interesting in its essential basic surface character, which makes an effective catalyst and catalyst support [6]. Besides O<sup>2-</sup> sites, hydroxyl groups also act as basic sites and have been shown to promote basic

reactions [7]. In addition, it has the ability to stabilize metals in unusual oxidation states and to retard sintering and evaporation of the metal atoms [8,9].

Due to the rising demand of propylene, the isomerization of 1-butene to 2-butene on MgO catalysts has now become an important reaction in the metathesis of ethylene and 2-butene for propylene production [10,11]. However, little is known about the active sites of the MgO basic catalyst in 1-butene isomerization reaction and controversy still exists. For examples, Baird and Lunsford [12] suggested that electron donors, presumably the strongly basic  $\mathrm{O}^{2-}$  ions located on the corners of the cubic oxide lattice are related to the active site for the isomerization of 1-butene. Matsuda et al. [13,14] reported that the isomerization activity could be correlated with stronger basicity than  $\mathrm{H}^{\bullet}=22.3$  and was inactive on MgO catalysts existing only in the weak basic sites. In addition, Klabunde and Matsuhashi [15] concluded that surface defects are responsible for 1-butene isomerization.

The purpose of this study was to elucidate the dependence of basicity of the isomerization of 1-butene on MgO and Mg(OH)<sub>2</sub> catalysts. The catalysts were prepared by co-precipitation method using Mg(NO<sub>3</sub>)<sub>2</sub> and KOH. The basic properties of the catalysts were varied by changing the calcination temperature. The catalyst activities were evaluated in the gas-phase isomerization of 1-butene to 2-butene. Various analytic techniques have been employed in order to determine the physical and basic properties of the catalysts including X-ray diffraction (XRD), N<sub>2</sub> physisorption, CO<sub>2</sub>-TPD, Fourier-transformed-infrared spectroscopy (FT-IR), and electron spin resonance (ESR).

<sup>\*</sup> Corresponding author. Tel.: +66 2218 6869; fax: +66 2218 6877. E-mail address: joongjai.p@chula.ac.th (J. Panpranot).

#### 2. Experimental

#### 2.1. Catalyst preparation

The catalysts were synthesized by co-precipitation method using magnesium nitrate hexahydrate (Mg(NO<sub>3</sub>)<sub>2</sub>.6H<sub>2</sub>O) (Sigma Aldrich) and potassium hydroxide (KOH) (AnalaR) as the starting materials. Firstly, 0.8 M of Mg(NO<sub>3</sub>)<sub>2</sub>.6H<sub>2</sub>O and 0.9 M of KOH solutions were prepared in de-ionized water. These two solutions were added dropwise into 200 cm<sup>3</sup> of de-ionized water under vigorous stirring. The pH was controlled at 11–12. Then, the complete solution was first separated by centrifuging and the solid product washed 5 times in deionized water. The white paste was subsequently dried in ambient air overnight and in an oven at 80 °C for 24 h. Finally, the white solid was calcined at various temperatures of 200, 400, 600 and 800 °C for 2 h in air with a ramp rate of 4 °C/min. After thermal treatment, the synthesized catalysts were immediately kept in vials and then preserved in a desiccator to prevent from surface hydration. The calcined samples were denoted as MgO200, MgO400, MgO600, and MgO800 according to the calcination temperature used.

#### 2.2. Catalyst characterization

The XRD patterns were collected using a SIEMENS XRD D5000 diffractometer with Cu  $K_{\alpha}$  radiation and a Ni filter in 10-80° 20 angular regions. The crystallite size of samples was calculated using the Scherrer's equation. The BET surface area was determined by N<sub>2</sub> physisorption using a Micrometritics ASAP 2000 automated system. Each sample was degassed at 200 °C for 4 h prior to N<sub>2</sub> physisorption. The CO<sub>2</sub>-TPD was performed to determine the basicity of MgO catalysts using a Micromeritic Chemisorb 2750 automated system. Before adsorption, the sample was pretreated in He for 1 h (flow rate 50 cm<sup>3</sup>/min) at the temperature which MgO was calcined. Then, it was cooled down to 100 °C and subsequently adsorbed by CO<sub>2</sub> for 1 h. The temperature-programmed desorption was carried out at a constant rate of 10 °C/min from ambient to 750 °C. The ESR was performed in a JEOL model JES-RE2X at room temperature. The hydroxyl groups of the catalysts were identified by FT-IR using a Nicolet 6700™ spectrometer in the range of 3800–3400 cm<sup>-1</sup> at a resolution of 4.0 cm<sup>-1</sup>. The catalyst morphology was observed using a Hitachi S-3400N scanning electron microscope. For the pre-adsorbed CO<sub>2</sub> FT-IR experiments, the catalysts were first pretreated ex-situ in He flow 50 cm<sup>3</sup>/min in a quartz cell at the temperature which they were calcined. Then, the samples were cooled down to  $100\,^{\circ}\text{C}$  and subsequently followed by  $CO_2$  adsorption for 1 h and purging with He for 30 min. The infrared spectra of the pre-adsorbed  $CO_2$  samples were collected using the Nicolet 6700 spectrometer.

#### 2.3. Reaction study

The gas-phase isomerization of 1-butene was carried out in a stainless steel 316 down flow reactor at 300 °C and atmospheric pressure. For a typical run, 10% 1-butene in nitrogen was used as reactant and approximately 0.3 g of catalyst was packed in the reactor. The total flow rate was 26 cm³/min composed of 2.6 cm³/min of the reactant and 23.4 cm³/min of  $N_2$  carrier gas. The composition of products and feed stream were analyzed by a Shimadzu GC-2014 gas chromatograph equipped with FID detector (aluminum oxide porous layer open tubular capillary column).

#### 3. Results and discussion

#### 3.1. Physical properties of the prepared catalysts

The XRD patterns of the prepared catalysts are shown in Fig. 1. For the uncalcined powder and the MgO200 sample, the characteristic diffraction peaks corresponding to Mg(OH)<sub>2</sub> phase were apparent at  $2\theta$  degrees =  $18.6^{\circ}$ ,  $32.9^{\circ}$ ,  $38.1^{\circ}$ ,  $50.9^{\circ}$ ,  $58.7^{\circ}$ ,  $62.1^{\circ}$ ,  $68.3^{\circ}$  and  $72.1^{\circ}$  [16–19]. For those calcined at  $400^{\circ}$ C and higher temperature, the diffraction peaks corresponding to MgO crystalline can be observed at  $2\theta$  degrees =  $37.0^{\circ}$ ,  $43.0^{\circ}$ ,  $62.4^{\circ}$ ,  $74.8^{\circ}$  and  $78.7^{\circ}$  [16,18]. The TGA results (not shown) confirmed that the Mg(OH)<sub>2</sub> was completely transformed into MgO at the temperature  $\geq 400^{\circ}$ C.

The physical properties of the uncalcined and calcined MgO at various calcination temperatures are shown in Table 1. The average crystallite sizes of Mg(OH) $_2$  phase in the uncalcined and the MgO200 samples were determined to be 17.1–17.4 nm with the corresponding BET surface area 42–46 m $^2$ /g. For the sample calcined at 400 °C in which only the MgO crystalline phase was observed, the crystallite size was 6.8 nm. A significant decrease of primary particle size when Mg(OH) $_2$  was transformed into MgO crystalline phase can be explained by the elimination of water and fragmentation of primary particle [20]. An increase in calcination temperature of MgO from 400 to 800 °C led to an increase of crystallize size from 6.8 to 16.0 nm and as a consequence the BET surface area decreased from 160 to 59 m $^2$ /g, respectively due to sintering of the MgO particles. Moreover, the

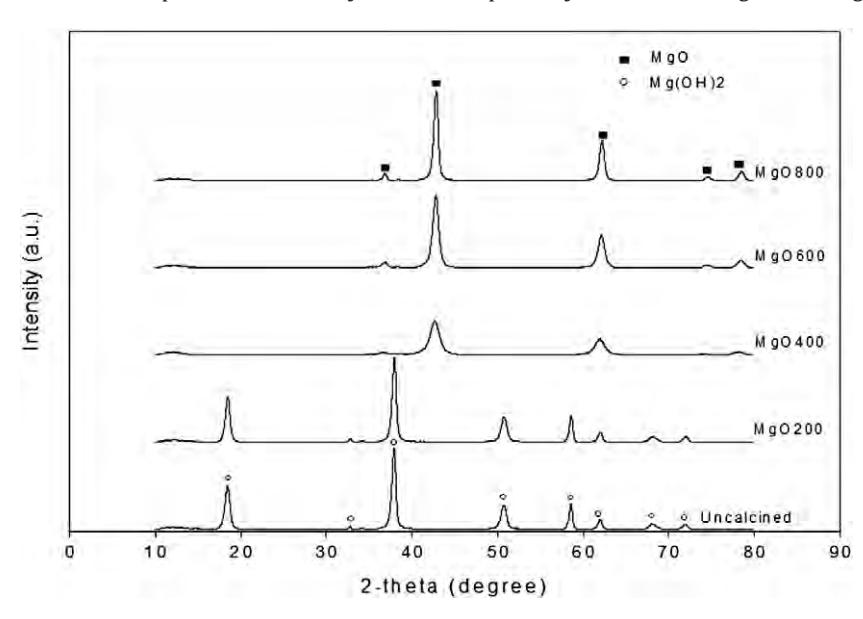


Fig. 1. The XRD patterns of MgO/Mg(OH)<sub>2</sub> catalysts calcined at various temperatures.

**Table 1**The phase transformation and physical properties of MgO/Mg(OH)<sub>2</sub> calcined at various temperatures.

Temperature (°C)	Phase <sup>a</sup>	Crystallite size (nm) <sup>a</sup>	Surface area $(m^2/g)^b$	Pore size (nm) <sup>b</sup>
Uncalcined	$Mg(OH)_2$	17.4	42	34
200	$Mg(OH)_2$	17.1	46	37
400	MgO	6.8	180	3, 43
600	MgO	11.1	91	15
800	MgO	16.0	59	24

<sup>&</sup>lt;sup>a</sup> Based on the XRD results.

bimodal pore structure was observed for the MgO400 sample while the other samples contained only unimodal pore. The SEM micrographs of the various MgO/Mg(OH)<sub>2</sub> catalysts calcined at different temperatures are provided in Fig. 2. There was no difference in particle size/shape of the catalysts in which a flower-like shape was observed.

#### 3.2. Identification of the basicity by FT-IR, CO<sub>2</sub>-TPD, and ESR

The hydroxyl groups in the prepared catalysts were determined from FT-IR analysis. Fig. 3(a) shows intense narrow peaks around  $3700 \, \mathrm{cm}^{-1}$ , indicating the presence of hydroxyl groups in the Mg (OH)<sub>2</sub> phase [19,21–23] while Fig. 3(b) shows broad band peaks in the range of 3400– $3750 \, \mathrm{cm}^{-1}$ , which were attributed to the isolated hydroxyl groups on the MgO samples [24,25].

The TPD profiles of  $CO_2$  desorbed in the temperature range of 100–750 °C are shown in Fig. 4. The  $CO_2$  desorption profiles consisted of three major peaks corresponding to different interactions of  $CO_2$  with MgO surface sites. The desorption peaks in the range of 100-300 °C, 300-550 °C, and 550-750 °C were categorized into the weak, the medium, and the strong basic sites, respectively. The amounts of  $CO_2$  desorption in each temperature range were calculated based on the area under the desorption peaks and are given Table 2. For the uncalcined sample and the MgO200, only the medium strength basic sites were presented. The uncalcined sample showed a higher amount of medium basic sites compared to the MgO200.

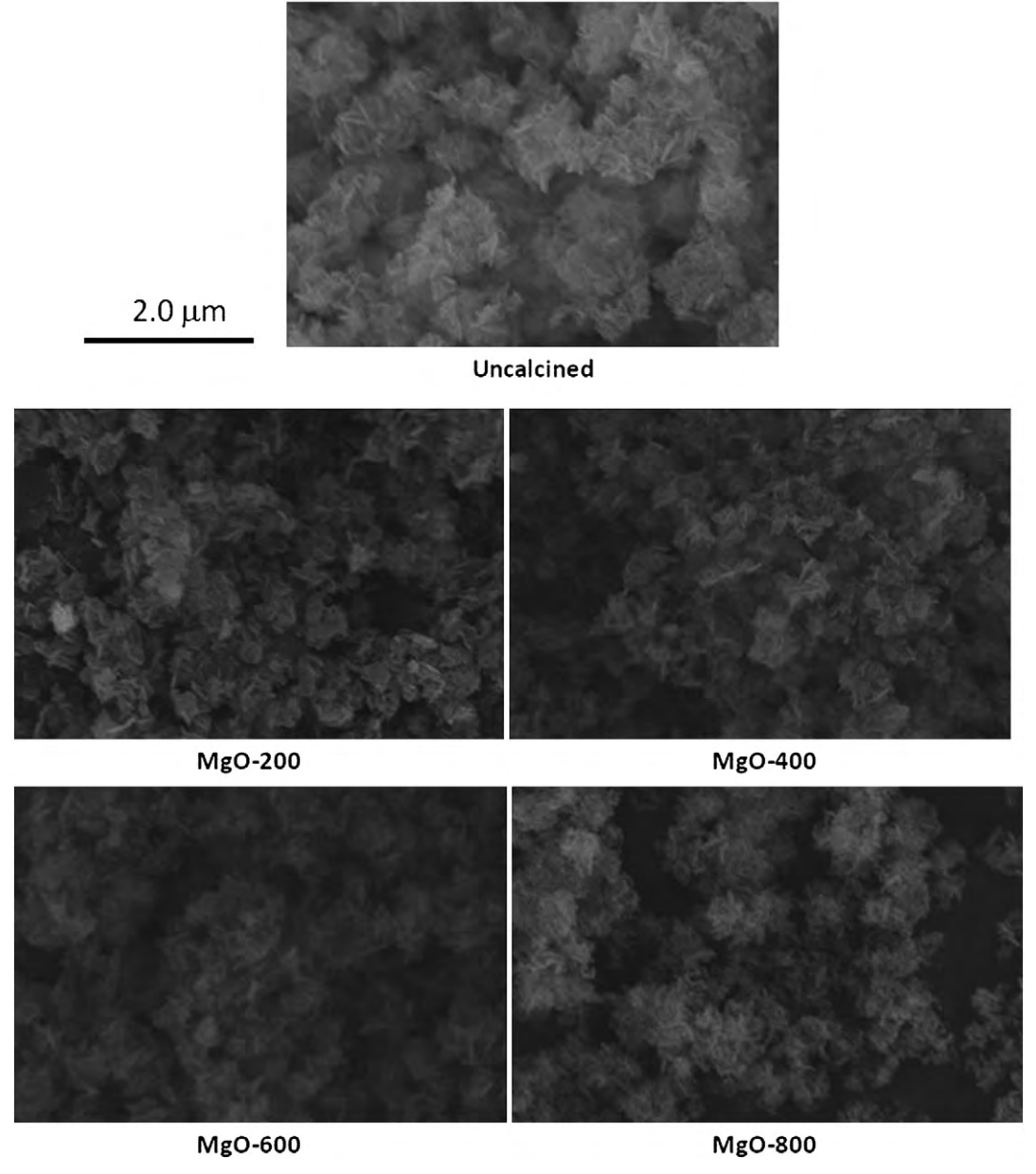
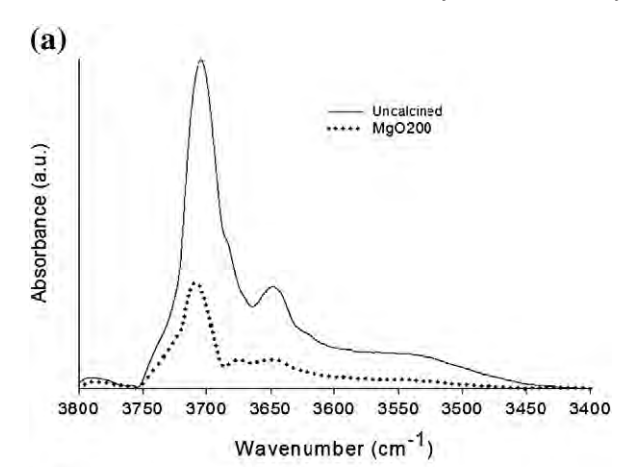


Fig. 2. The SEM micrographs of the Mg(OH)<sub>2</sub> and the MgO catalysts calcined at different temperatures.

<sup>&</sup>lt;sup>b</sup> Based on N<sub>2</sub> physisorption and the BJH method.



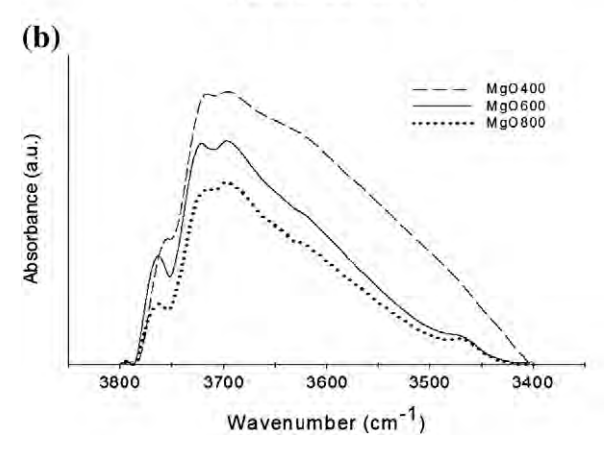


Fig. 3. The FT-IR spectra of  $MgO/Mg(OH)_2$  calcined at various temperatures (a)  $Mg(OH)_2$  phase, (b) MgO phase.

Fig. 5 shows the FT-IR results of the pre-adsorbed  $CO_2$  at 100 °C on the various catalyst samples. According to the literature, the absorption bands in the  $2000-2400~\rm cm^{-1}$  region were assigned to the physisorbed and end-on chemisorbed  $CO_2$  molecules [26,27] and the bands in the region below  $1000~\rm cm^{-1}$  were derived from an overtone of a fundamental lattice vibration of Mg–O stretching [28]. The Mg–O stretching bands were clearly observed for all the MgO samples calcined at 400 °C and higher, confirming the formation of MgO structure. In most of the *in-situ* IR studies of pre-adsorbed  $CO_2$  at room temperature on MgO, bicarbonate, bidentate, and unidentate carbonate species were observed in the  $1200-1700~\rm cm^{-1}$  region [29].

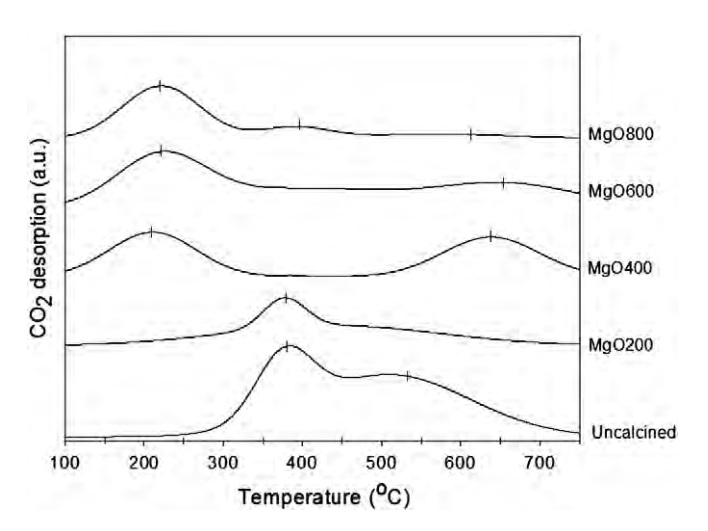


Fig. 4. The CO<sub>2</sub>-TPD profiles of MgO/Mg(OH)<sub>2</sub> calcined at various temperatures.

**Table 2** The amount of CO<sub>2</sub> desorption from CO<sub>2</sub>-TPD profiles.

T <sub>calcined</sub>	Amount of CO <sub>2</sub> desorption (unit area/g)					
(°C)	1st peak	2nd peak	3rd peak	Total		
Uncalcined	-	5.90	=	5.90		
MgO200	_	2.46	_	2.46		
MgO400	1.71	_	1.34	3.05		
MgO600	1.82	_	0.91	2.73		
MgO800	1.78	0.33	0.29	2.40		

The bicarbonate is the most labile species and disappears after evacuation at 373 K while both the unidentate and bidentate carbonates remain on the surface after evacuation at 573 K. However, only the unidentate bands are observed upon evacuation at higher temperatures [29]. In the present work, the absorption at 1500–1506 cm<sup>-1</sup> which was assigned to the unidentate species [27–29] was presented on the MgO catalysts and was found to be relatively more obvious on the MgO400. The results were correlated well with the CO<sub>2</sub>-TPD results in which the MgO400 contained the highest amount of strong basic sites.

Fig. 6 shows the ESR results of the various MgO catalyst samples. There was almost no signal for the uncalcined catalyst and the MgO200. For those containing MgO crystalline phase (MgO400, MgO600, and MgO800), two signals of the g factor were observed. The sharp peak at g=1.980 was assigned to the unpaired  $e^-$  unstable oxygen radicals associated with lattice defects [30]. The broad one at g=2.002 was assigned to one anion vacancies [31,32]. The intensity of both ESR signals increased with increasing calcination temperature.

The strength of basicity of the MgO and Mg(OH) $_2$  catalysts in this study was categorized into 3 types corresponding to the three desorption temperature ranges in the CO $_2$ -TPD profiles, viz. 100–300 °C (weak basic sites), 300–550 °C (medium basic sites), and 550–750 °C (strong basic sites). It was found that the uncalcined sample and the MgO200 contained only the medium strength basic sites

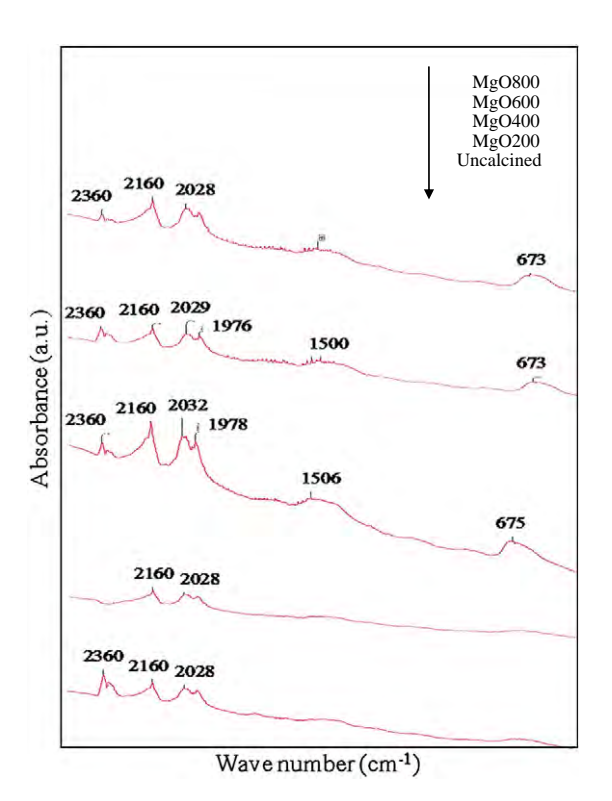


Fig. 5. The FT-IR spectra of pre-adsorbed  ${\rm CO_2}$  at 100  $^{\circ}{\rm C}$  on the various MgO/Mg(OH) $_2$  catalysts.

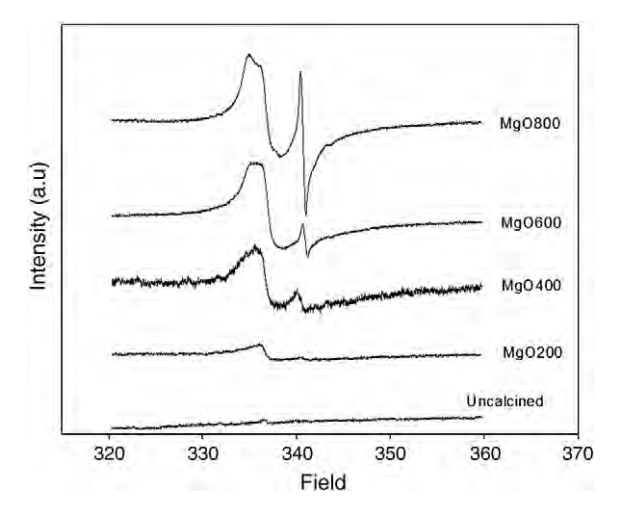


Fig. 6. The ESR spectra of MgO/Mg(OH)<sub>2</sub> calcined at various temperatures.

whereas the MgO400, MgO600, and MgO800 contained both weak and strong basic sites. The interactions of CO<sub>2</sub> with MgO surface sites have been investigated by Aramendia et al. [18] using in-situ IR measurements. Three kinds of adsorbed species were correlated to the different basic site strength: the unidentate carbonate forms on isolated surface O<sup>2-</sup> ions, the bidentate carbonate forms on Lewis-acid-Brönsted-base pairs  $(Mg^{2+}-O^{2-})$ , and the bicarbonate species formation which involves surface hydroxyl groups. The strength order for surface basic sites was determined to be O<sup>2-</sup> ions>oxygen in Mg-O pairs>OH groups. In the present study, the strong basic sites of MgO catalysts decreased significantly with increasing calcination temperature while the weak basic sites remained unaltered. The strong basic sites were correlated to the oxygen in Mg-O pairs because the more the lattice defects (as shown by increased ESR signals in Fig. 6), the lower the amount of strong basic sites. In other words, an increase of the calcination temperature gave rise to a significant reduction of lattice oxygen.

It has been reported that different types of OH groups were presented on the surface of magnesium oxide, which will not disappear completely at calcination temperatures below 900 °C [33]. Based on our FT-IR results, a sharp and intense —OH stretching vibration peak at 3700 cm<sup>-1</sup> indicated the presence of a hydroxyl group at the low-coordination sites in the Mg(OH)<sub>2</sub> structure [34] while smaller broad band peaks in the range of 3400–3750 cm<sup>-1</sup> were attributed to the isolated hydroxyl groups on the MgO samples [24,25]. It is likely that these OH groups contributed to the medium and the weak basic sites of Mg(OH)<sub>2</sub> and MgO, respectively. The different structures contributing to the basicity of MgO are illustrated in Fig. 7.

#### 3.3. Isomerization of 1-butene

The activity and selectivity of the catalysts with different basic properties were investigated in the isomerization of 1-butene to 2-butene at 300 °C and ambient pressure. Fig. 8 shows the conversion of 1-butene as a function of time-on-stream obtained on the various

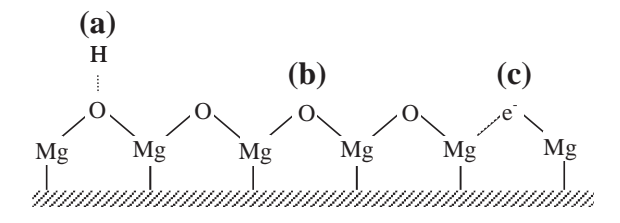


**Fig. 7.** The possible MgO structures contributing to the basicity (a) the isolated hydroxyl groups, (b) oxygen in MgO lattice, and (c) one anion vacancies.

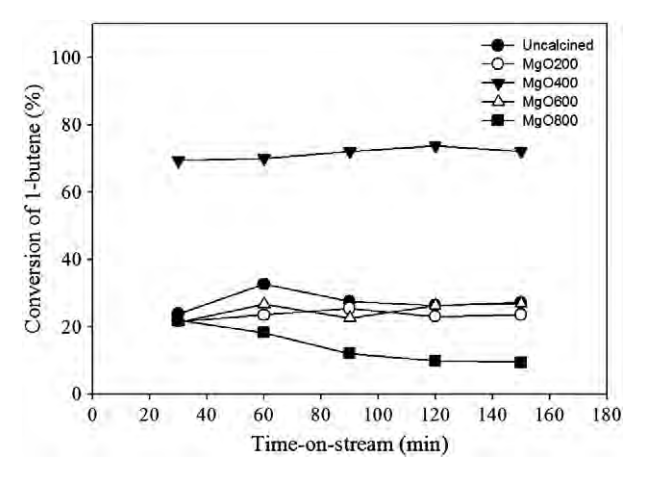


Fig. 8. Catalyst performances in the gas-phase isomerization of 1-butene to 2-butene at 300  $^{\circ}\mathrm{C}$ 

catalysts. The 1-butene conversions were found to be in the order of MgO400>MgO600 ≈ uncalcined catalyst>MgO200>MgO800. The selectivity to 2-butene was more than 99% for all the catalysts under the reaction conditions used. There was no significant catalyst deactivation during the 150 min time-on-stream. The isomerization of 1-butene has been suggested to proceed via a carbanion intermediate on the strong basic sites [14] as illustrated in Scheme 1. The basic oxide ion facilitated the abstraction of an allylic proton and transferred to the terminal methyl group [7].

In the present study, we can divide the catalysts into two groups according to their structures: (1) the  $Mg(OH)_2$  phase containing only medium strength basic sites (uncalcined catalyst and MgO200) and (2) the MgO crystalline phase (MgO400, MgO600, and MgO800) containing both weak and strong basic sites. For any surface catalytic reaction, high specific surface area available for adsorption of reactant is necessary. However, it appeared that the basicity of MgO and Mg ( $OH)_2$  catalysts played a more decisive role in 1-butene isomerization reaction than the available surface area. For example, the BET surface area of MgO400 was twice that of MgO600 but the percent conversion of 1-butene obtained over the MgO400 catalyst was almost 3 times higher than that of MgO600. The MgO800 possessed BET surface area of SP but exhibited very low conversion of 1-butene isomerization (ca. SP) compared to the SP000 with a BET surface area of SP1 m²/g that exhibited 27% conversion of 1-butene.

The catalyst activity in 1-butene isomerization activity was found to be dependent not only on the amount of basic sites but also the distribution of basic strength. The MgO400 catalyst had the highest amount of strong basic sites and exhibited the highest isomerization activity. The MgO600 with less amounts of strong basic sites showed similar isomerization activity to that of the uncalcined catalyst containing only medium strength basic sites. Based on the CO<sub>2</sub> TPD results, there was no significant difference in the amount of weak basic sites on the various MgO catalysts, suggesting that the weak basic sites in MgO catalysts had little impact on the isomerization activity of MgO catalysts. Similar to the weak basic sites, the presence of the unpaired e unstable oxygen radicals did not promote the reaction. Considering the Mg(OH)<sub>2</sub> phase catalysts, the conversion of 1-butene was found to decrease with decreasing amount of the medium basic sites. It is proposed that the medium strength basic sites were also responsible for 1-butene isomerization. Moreover, the corner O<sup>2-</sup> ions at low-coordination number have been proposed to be capable of abstracting an allylic hydrogen from 1-butene [13].

#### 4. Conclusions

The co-precipitation of Mg(NO<sub>3</sub>)<sub>2</sub>.6H<sub>2</sub>O and KOH resulted in the formation of Mg(OH)<sub>2</sub> with an average crystallite size of 17.4 nm and

J. Puriwat et al. / Catalysis Communications 12 (2010) 80-85

$$CH_2 = CH - CH_2 - CH_3 \xrightarrow{-H^+} CH_2 - CH - CH - CH_3 \xrightarrow{+H^+} CH_3 - CH = CH - CH_3$$
1-butene Carbanion intermediate 2-butene

**Scheme 1.** Mechanism for 1-butene isomerization to 2-butene.

BET surface area 42 m<sup>2</sup>/g. The MgO crystalline phase (average crystallite size 6.8 nm and surface area 180 m<sup>2</sup>/g) was obtained by calcination of the Mg(OH)<sub>2</sub> at 400 °C. Increasing calcination temperature from 400 to 800 °C resulted in the sintering of MgO and as a consequence, the BET surface area decrease to 59 m<sup>2</sup>/g. As revealed by CO<sub>2</sub>-TPD results, the Mg(OH)<sub>2</sub> phase contained only medium strength basic sites while the MgO phase exhibited both weak and strong basic strengths. The activity of the catalyst increased in the order of MgO400>MgO600≈uncalcined sample>MgO200>MgO800 with more than 99% selectivity to 2-butene. The isomerization activity mainly proceeded on the strong basic sites of MgO while the medium basic sites from hydroxyl groups were the responsible active sites for the Mg(OH)<sub>2</sub> phase. The weak basic sites in MgO catalysts did not participate much in the reaction. The strong basic sites of MgO were correlated well with the presence of oxygen atoms in the lattice of crystalline MgO.

#### Acknowledgments

The financial supports from the Thailand Research Fund (TRF) and the Office of the Commission on Higher Education are gratefully acknowledged. The authors would like to thank the SCG Chemicals Co., Ltd., Thailand for the scholarship for Jiraporn Puriwat and the provision of facilities.

#### References

- M.-L. Bailly, C. Chizallet, G. Costentin, J.-M. Krafft, H. Lauron-Pernot, M. Che, J. Catal. 235 (2005) 413–422.
- [2] K. Tanabe, W.F. Holderich, Appl. Catal. A 181 (1999) 399-434.
- [3] J. Li, R.J. Davis, J. Phys. Chem. B 109 (2005) 7141–7148.
- [4] Y. Ono, T. Baba, Catal. Today 38 (1997) 321-337.
- [5] C. Chizallet, G. Costentin, H. Lauron-Pernot, J.M. Krafft, P. Bazin, J. Saussey, F. Delbecq, P. Sautet, M. Che, Oil and Gas Sci. Tech.-Rev. IFP 61 (2006) 479–488.

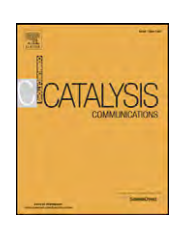
- [6] M.A. Aramendía, J.A. Benítez, V. Borau, C. Jiménez, J.M. Marinas, J.R. Ruiz, F. Urbano, Langmuir 15 (1999) 1192–1197.
- [7] G. Zhang, H. Hattori, K. Tanabe, Appl. Catal. 36 (1988) 189-197.
- 8] J. Schwank, S. Galvagno, G. Parravano, J. Catal. 63 (1980) 415-424.
- [9] J.M. Driessen, E.K. Poels, J.P. Hindermann, V. Ponec, J. Catal. 82 (1983) 26–34.
- 10] S. Huang, S. Liu, W. Xin, J. Bai, S. Xie, Q. Wang, L. Xu, J. Mol. Catal. A 226 (2005) 61–68.
- [11] J.C. Mol, J. Mol. Catal. A 213 (2004) 39-45.
- [12] M.J. Baird, J.H. Lunsford, J. Catal. 26 (1972) 440-450.
- [13] T. Matsuda, M. Sugimoto, React. Kinet. Catal. Lett. 44 (1991) 69-73.
- [14] T. Matsuda, J. Tanabe, N. Hayashi, Y. Sasaki, H. Miura, K. Sugiyama, Bull. Chem. Soc. Japan 55 (1982) 990–994.
- [15] K.J. Klabunde, H. Matsuhashi, J. Am. Chem. Soc. 109 (2002) 1111-1114.
- [16] M.A. Aramendia, J.A. Betez, V. Borau, C. Jimnez, J.M. Marinas, J.R. Ruiz, F. Urbano, J. Solid State Chem. 144 (1999) 25–29.
- [17] M.A. Aramendia, J.A. Bentez, V. Borau, C. Jimnez, J.M. Marinas, J.R. Ruiz, F.J. Urbano, Colloids Surf., A 168 (2000) 27–33.
- [18] M.A. Aramendia, V. Borau, C. Jimnez, J.M. Marinas, J.R. Ruiz, F.J. Urbano, Appl. Catal. A 244 (2003) 207–215.
- [19] X.-F. Wu, G.-S. Hu, B.-B. Wang, Y.-F. Yang, J. Crystal Growth 310 (2008) 457–461.
- [20] I.F. Mironyuk, V.M. Gun'ko, M.O. Povazhnyak, V.I. Zarko, V.M. Chelyadin, R. Leboda, J. Skubiszewska-Zieba, W. Janusz, Appl. Surf. Sci. 252 (2006) 4071–4082.
- [21] W. Jiang, X. Hua, Q. Han, X. Yang, L. Lu, X. Wang, Powder Tech. 191 (2009) 227–230.
- 22] J.-P. Hsu, A. Nacu, Colloids Surf., A 262 (2005) 220–231.
- [23] D. An, X. Ding, Z. Wang, Y. Liu, Colloids Surf., A 356 (2010) 28–31.
- [24] A. Kumar, J. Kumar, J. Phys. Chem. Solids 69 (2008) 2764-2772.
- 25] C. Chizallet, G. Costentin, H. Lauron-Pernot, J.M. Krafft, P. Bazin, J. Saussey, F. Delbecq, P. Saufet, M. Che, Oil and Gas Sci. Tech. 61 (2006) 479–488.
- [26] G. Busca, V. Lorenzelli, Mater. Chem. 7 (1982) 89.
- [27] G.A.H. Mekhemer, S.A. Halawy, M.A. Mohamed, M.I. Zaki, J. Phys. Chem. B 108 (2004) 13379.
- [28] K. Teramura, T. Tanaka, H. Ishikawa, Y. Kohno, T. Funabiki, J. Phys. Chem. B 108 (2004) 346–354.
- [29] V.K. D´ıez, C.R. Apestegu´ıa, J.I. Di Cosimo, Catal. Today 63 (2000) 53-62.
- [30] M.J. Larsen, Y. Ma, H. Qian, H. Toftlund, P.B. Lund, E.M. Skou, Solid State Ionics 181 (2009) 201–205.
- [31] E. Giamello, A. Ferrero, S. Coluccia, A. Zecchina, J. Phys. Chem. 95 (1991) 9385–9391.
- [32] H. Matsuhashi, M. Oikawa, K. Arata, Langmuir 16 (2000) 8201–8205.
- [33] J. Li, W.-L. Dai, K. Fan, J. Phys. Chem. C 112 (2008) 17657–17663.
- [34] M. Foster, M. Furse, D. Passno, Surf. Sci. 502–503 (2002) 102–108.



Contents lists available at ScienceDirect

# **Catalysis Communications**

journal homepage: www.elsevier.com/locate/catcom



# The effect of phosphorous precursor on the CO oxidation activity of P-modified TiO<sub>2</sub> supported Ag catalysts

Nattaya Comsup, Joongjai Panpranot, Piyasan Praserthdam\*

Center of Excellence on Catalysis and Catalytic Reaction Engineering, Department of Chemical Engineering, Faculty of Engineering, Chulalongkorn University, Bangkok 10330, Thailand

#### ARTICLE INFO

Article history:
Received 20 April 2010
Received in revised form 18 June 2010
Accepted 23 June 2010
Available online 1 July 2010

Keywords: P-modified TiO<sub>2</sub> CO oxidation Ag/TiO<sub>2</sub> Phosphorous precursor

#### ABSTRACT

Nanocrystalline  ${\rm TiO_2}$  and P-modified  ${\rm TiO_2}$  with P/Ti atomic ratio 0.01 were prepared by the solvothermal method and employed as the supports for  ${\rm Ag/TiO_2}$  catalysts for CO oxidation reaction. The incorporation of phosphorus into the  ${\rm TiO_2}$  lattice in the form of  ${\rm Ti-O-P}$  resulted in an increase of both surface area and metal dispersion. The P-modified  ${\rm TiO_2}$  supported Ag catalysts using phosphorus precursor in the form of oxide promoted the weak adsorbed oxygen species and resulted in catalytic activity improvement in CO oxidation. However, the use of phosphorous precursor in the form of phosphate such as  ${\rm H_3PO_4}$ ,  $({\rm NH_4})_2{\rm HPO_4}$ ,  $({\rm C_2H_5})_3{\rm PO_4}$  could result in the strongly adsorbed oxygen species and/or the bidentate of phosphate species blocking the active sites instead.

© 2010 Elsevier B.V. All rights reserved.

#### 1. Introduction

Titanium dioxide  $(TiO_2)$  is a reducible metal oxide that has been widely used as a support for noble metal catalysts in CO oxidation because it exhibits a stronger interaction with group VIII noble metals than other metal oxides [1–6]. The strong metal–support interaction has been shown to play an important role in increasing the metal dispersion, which leads to enhancing the catalytic activity for CO oxidation. Additionally, the promoting effect of the reducible support may result from the creation of second active sites at the metal–support interface [7].

The addition of trace element to TiO<sub>2</sub> support is a simple way to modify its physicochemical properties such as crystallite size, crystal defects, surface area, thermal stability, and the interaction between metal and support. Support modification has been shown to result in an improved CO oxidation activity in many catalyst systems. For examples, Yu et al. [8] reported that doping of La in TiO<sub>2</sub> during the solgel synthesis induced the creation of the second active site on the surface of Au/TiO<sub>2</sub> which promoted the fast CO oxidation. Peza-Ledesma et al. [9] reported that the use of SBA-15 modified with 10 wt. % of TiO<sub>2</sub> as support materials led to a high dispersion of supported gold catalysts which promoted the catalytic activity toward CO oxidation. Similarly, Hernandez et al. [10] found that the well dispersion of gold catalyst on the cerium-modified silica support provided the formation of small gold particle and the coverage of

Despite a number of studies reporting the support modification effect in CO oxidation activity, the modification of support with a nonmetallic modifier has received little attention as compared to the metallic ones. Most of the non-metallic modifier reported in the literature was in the form of anionic species such as nitrate ion [11,12], sulfate ion [13,14], and phosphate ion [15]. Both positive and negative effects of the non-metallic modifier on CO oxidation activities have been found. The negative effect of sulfate ion was reported by Ruth et al. [13] in which the Au/TiO2 catalyst was deactivated by the blocking of SO<sub>2</sub> at the interface between an Au particle and the TiO<sub>2</sub> support. Kim and Woo [14] reported that SO<sub>2</sub> treatment increased the adsorption strength between Au and CO which suppressed the migration of absorbed CO on the Au particles to Au–TiO<sub>2</sub> interface to form CO<sub>2</sub>, resulting in a decrease of CO oxidation activity. On the other hand, modification with phosphate ion showed a positive effect on CO oxidation activity. Incorporation of phosphate ion in TiO<sub>2</sub> support could prevent sintering of Au particles at high temperature treatment, as a consequence higher CO oxidation activity was obtained [12,15]. However, an over-loading of phosphate ions may block the active sites instead.

In the present study, the effect of phosphorus precursors on the P-modified TiO<sub>2</sub> supported Ag catalysts has been extensively investigated. The catalysts were characterized by N<sub>2</sub> physisorption, X-ray diffraction (XRD), transmission electron microscopy (TEM), X-ray photoelectron spectroscopy (XPS), Fourier transformed infrared spectroscopy (FT-IR), temperature programmed desorption of oxygen (O<sub>2</sub>-TPD), and pulse chemisorption. The catalyst activities were evaluated in the CO oxidation in a fixed-bed reactor.

cerium on the silica support promoted the effectiveness of oxygen mobility, which led to higher catalytic activity in CO oxidation.

<sup>\*</sup> Corresponding author. Tel.: +66 2218 6883; fax: +66 2218 6766. E-mail address: piyasan.p@chula.ac.th (P. Praserthdam).

#### 2. Experimental

#### 2.1. Preparation of TiO2 and P-modified TiO2

The TiO<sub>2</sub> nanoparticles were prepared by the solvothermal method according the procedure described in our previous work in Ref [16]. Typically, about 25 g of Titanium (IV) *n*-butoxide (TNB) was mixed with 100 cm<sup>3</sup> of 1,4-butanediol in a test tube. The mixed solution in the test tube was placed in a 300 cm<sup>3</sup> autoclave. An addition of 30 cm<sup>3</sup> of 1,4-butanediol was added to the gap between the test tube and the autoclave wall. After purging with nitrogen into the autoclave reactor, the system was heated to 320 °C at a rate of 2.5 °C/min and held at that temperature for 4 h. The P-modified TiO<sub>2</sub> supports were prepared by addition of a certain amount of phosphorus precursor into the mixed solution of TNB and 1,4-butanediol before setting up in the autoclave. Four phosphorus precursors used in this study were H<sub>3</sub>PO<sub>4</sub>, (NH<sub>4</sub>)<sub>2</sub>HPO<sub>4</sub>, (C<sub>2</sub>H<sub>5</sub>)<sub>3</sub>PO<sub>4</sub>, and P<sub>2</sub>O<sub>5</sub>. After the autoclave was naturally cooled to room temperature, the resulting powder was repeatedly washed with methanol and dried in air for 12 h. As determined by the inductively coupled plasma optical emission spectroscopy (Agilent Optima 2100 DV ICP-OES), the mean value of P/Ti molar ratio for all the P-modified TiO<sub>2</sub> samples was  $0.01 \pm 6\%$ .

#### 2.2. Preparation of Ag/TiO<sub>2</sub> catalysts

The  $TiO_2$  supported Ag catalysts were prepared by the incipient wetness impregnation method. An aqueous solution of 1.98~M of  $AgNO_3$  equal to the pore volume of the  $TiO_2$  support, i.e.  $0.7~cm^3g^{-1}$  STP, was added drop-wise to the support during intensive mixing to give a metal content of 10~at.% with respect to the atomic weight of the  $TiO_2$  support. After impregnation, the catalysts were dried at room temperature for 6~h and then at 110~C overnight in an oven. The dried catalysts were calcined in air at 450~C for 3~h. The series of catalysts are denoted by their atomic percentages of silver loading, the phosphorus content in the  $TiO_2$  supports, and type of phosphorus precursor. For example,  $10\%Ag/TiO_2-H_3PO_4$  is referred to the catalyst containing 10~at.% Ag on the P-modified  $TiO_2$  support prepared from  $H_3PO_4$  precursor. The actual amount of Ag loading determined by the ICP-AES was  $6.7\pm6\%$ .

#### 2.3. Catalyst characterization

The XRD measurements were performed using the SIEMENS D5000 diffractometer with Cu  $K_{\alpha}$  radiation. The average crystallite size and phase composition of P-modified TiO $_2$  were determined by the Scherrer equation. The XRD patterns were scanned at a rate of  $2.4^{\circ}\,\text{min}^{-1}$  in the range of  $2\theta = 20-80^{\circ}$ . The BET specific surface area of the samples was measured by  $N_2$  adsorption at 77 K using a Micromeritics ASAP 2020 instrument. The FT-IR spectra were recorded at room temperature on a Nicolet 6700 spectrometer using a KBr pellet for sample preparation, in the range of 400–4000 cm $^{-1}$  with 4 cm $^{-1}$  resolution. The particle sizes of Ag/TiO $_2$  catalysts were investigated by transmission electron microscopy (TEM) with a Philips CM100 microscope. The chemical states of the elements were measured by XPS technique using an Amicus photoelectron spectrometer with Mg  $K_{\alpha}$  X-ray source at current of 20 mA and 10 keV, resolution of 0.1 ev/step, and pass energy of 75 eV. The binding energy was calibrated by the C 1s peak at 285.0 eV.

The amount of metal active sites for Ag/TiO $_2$  catalysts were determined using N $_2$ O pulse chemisorption according to the method previously reported by our group [17]. About 100 mg of the catalyst sample was first reduced in hydrogen (50 cm $^3$ /min) at 200 °C for 1. Then the catalyst was cooled down to 150 °C in He stream and a certain amount of N $_2$ O was injected into the He stream in front of the catalyst bed. The N $_2$ O was analyzed by TCD gas chromatography using a packed Porapak N column. The metal active site of the Ag/TiO $_2$  catalyst was calculated assuming a simplified reaction stoichiometry of Ag:O = 2.

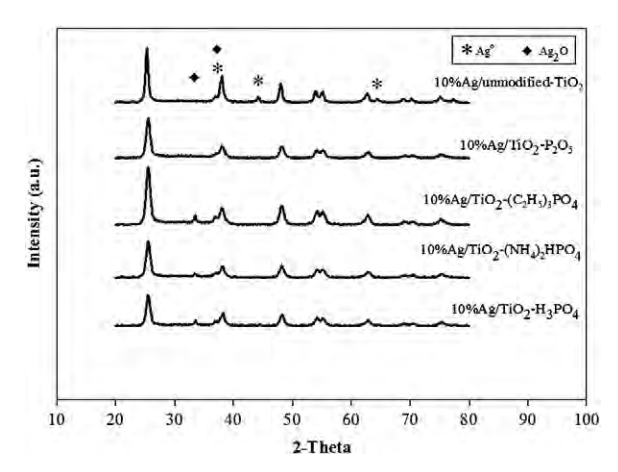


**Fig. 1.** XRD patterns of 10 at.% Ag catalysts supported on TiO<sub>2</sub> and P-modified TiO<sub>2</sub> with different phosphorus precursors.

The  $O_2$ -TPD profiles were performed in order to study the characteristics of oxygen adsorption and desorption on the catalyst surface. Approximately, 0.1 g of the catalyst was reduced in hydrogen flow ( $50 \text{ cm}^3/\text{min}$ ) at  $200 \,^{\circ}\text{C}$  for 1 h. Subsequently the sample was cooled down to room temperature in He stream ( $30 \, \text{cm}^3/\text{min}$ ) and held at that temperature in oxygen stream ( $30 \, \text{cm}^3/\text{min}$ ) for 1 h to adsorb oxygen on the catalyst surface. Then the gas flow was switched to He gas flow ( $30 \, \text{cm}^3/\text{min}$ ) for 1 h in order to remove the physically adsorbed oxygen on the catalyst surface. The temperature was ramped with a heating rate of  $10 \,^{\circ}\text{C}/\text{min}$  to  $600 \,^{\circ}\text{C}$ . The oxygen desorption signal was detected by the thermal conductivity detector (TCD) during programmed heating.

#### 2.4. Reaction study

The activity of the catalyst samples in CO oxidation was carried out in a fixed-bed glass tube microreactor (i.d. 5 mm) with 100 mg of catalyst packed at the center of the reactor between two quartz wool plugs. The catalyst bed temperature was measured by inserting a thermocouple into the reactor below the catalyst bed. The reactant feed gas consisted of 1% CO, 2% O<sub>2</sub> and He as balance, with a total flow rate of  $100 \text{ cm}^3/\text{min}$  (GHSV  $\approx 30,600 \text{ h}^{-1}$ ). Prior to the start of the reaction, the catalyst was first reduced in-situ in flowing H2 at 200 °C for 1 h with a flow rate of 50 cm<sup>3</sup>/min. Following the *in-situ* reduction of the catalyst, the reactant gas mixture was switched into the reactor. The temperature of the furnace was increased from room temperature to the desired temperature and held at that temperature for 20 min. The concentration of CO in the exit stream from the reactor was analyzed on line by gas chromatography with a Shimadzu GC-8ATP gas chromatograph provided with a thermal conductivity detector (TCD) and a Porapak Q column with He as the carrier gas. The conversion of CO was defined as the percentage of the CO in feed

**Table 1**Physical properties and amount of active sites of 10 at.% Ag catalyst supported on TiO<sub>2</sub> and P-modified TiO<sub>2</sub> with different phosphorus precursors.

Catalyst	TiO <sub>2</sub> crystallit	te size (nm)	BET	Active site (×10 <sup>20</sup> atom-Ag/g-cat.)	
	Before Ag loading	After Ag loading	surface (m <sup>2</sup> /g)		
10%Ag/unmodified-TiO <sub>2</sub>	15.2	16.2	52	1.27	
10%Ag/TiO <sub>2</sub> $-$ H <sub>3</sub> PO <sub>4</sub>	10.8	11.2	75	3.57	
$10\%$ Ag/TiO <sub>2</sub> $-(NH_4)_2$ HPO <sub>4</sub>	10.0	10.0	76	3.76	
$10\%$ Ag/TiO <sub>2</sub> $-(C_2H_5)_3$ PO <sub>4</sub>	9.8	10.1	74	3.64	
10%Ag/TiO <sub>2</sub> -P <sub>2</sub> O <sub>5</sub>	9.5	10.4	75	3.89	

stream that was converted to analyzed product. The temperature at which the conversion of CO equals 50% (defined as light-off temperature) is used for evaluation of the catalyst performance.

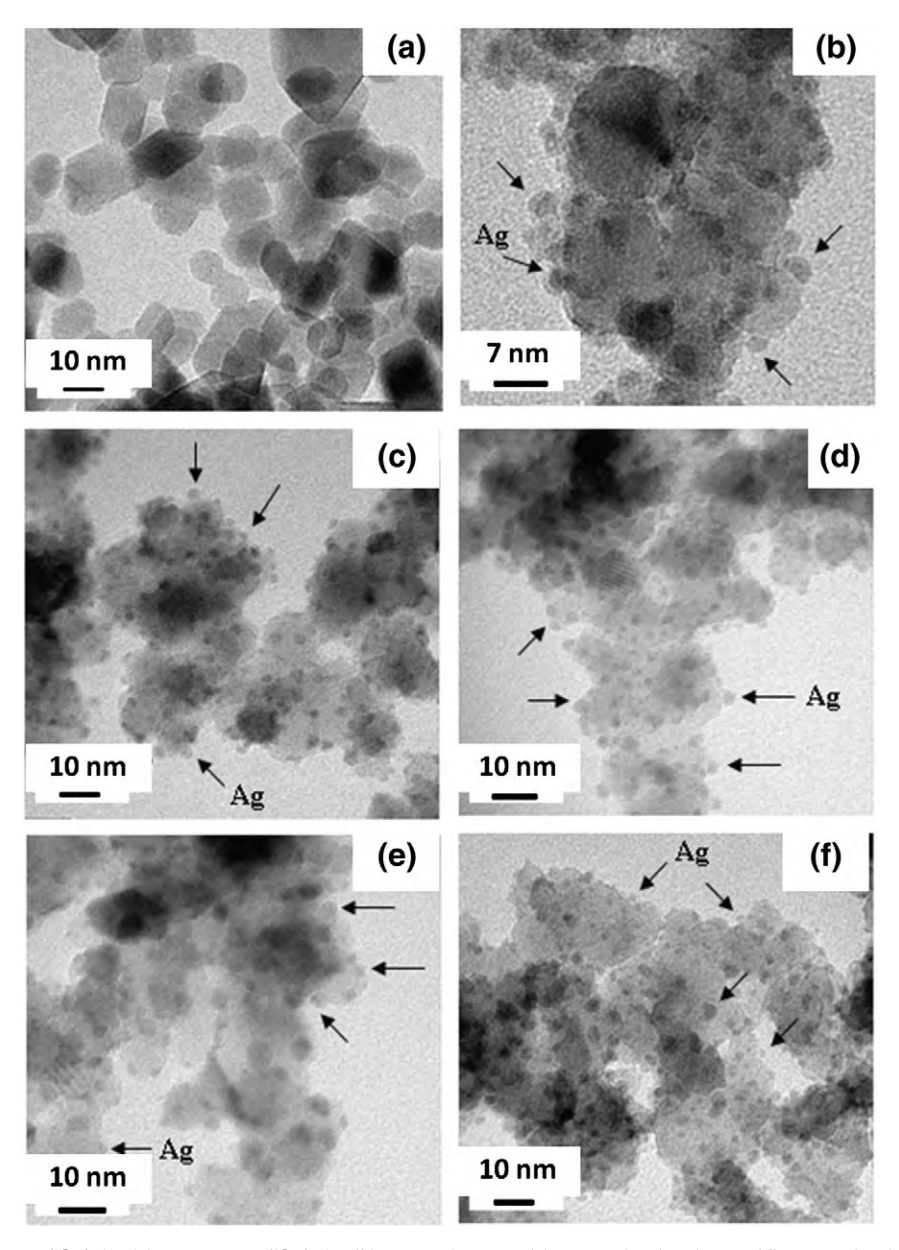
#### 3. Results and discussion

3.1. Effect of P doping on the physicochemical properties of  $Ag/TiO_2$  catalysts

The XRD patterns of the unmodified  $TiO_2$  and P-modified  $TiO_2$  supported Ag catalysts prepared with different precursors of phosphorus modifier are shown in Fig. 1. The major peak of pure anatase (101) phase  $TiO_2$  was observed at  $2\theta$  around  $25^\circ$  for all the catalyst samples. Doping of  $TiO_2$  with P led to broadening of the XRD peaks as well as a slight shift of the XRD reflections towards higher angles. According to the Bragg's law, an increase of  $2\theta$  values indicated a decrease of the distance between crystal planes, which is in close relationship with the lattice parameters. For the 10%Ag/unmodified- $TiO_2$ , diffraction peaks corresponding to metallic Ag appeared at  $2\theta = 38.1^\circ$ ,  $44.4^\circ$ , and  $64.5^\circ$ 

and the peaks at 32.8° and 38° were assigned to Ag<sub>2</sub>O [18,19]. The intensities of the XRD characteristic peaks of metallic Ag (44.4° and 64.5°) for the P-modified TiO<sub>2</sub> samples became weak, whereas the peaks of Ag<sub>2</sub>O (32.8°) became strong except those of 10%Ag/TiO<sub>2</sub>–P<sub>2</sub>O<sub>5</sub> in which the peaks corresponding to any Ag species were not clearly seen. The low intensity of Ag metallic peaks for the P-modified TiO<sub>2</sub> may be ascribed to the smaller Ag particles and/or the oxidation of some of the metallic Ag to Ag<sub>2</sub>O.

Table 1 summarizes the crystallite size of the unmodified and the P-modified TiO<sub>2</sub> supported Ag catalysts, which was calculated from the Scherrer equation. The crystallite sizes of all the P-modified TiO<sub>2</sub> were found to be smaller than the unmodified one, and as a consequence the BET surface areas increased. The existence of phosphorus in the TiO<sub>2</sub> framework may inhibit the growth of anatase TiO<sub>2</sub> crystals [20]. There was little impact of phosphorous precursor on the crystallite size and BET surface area of P-modified TiO<sub>2</sub>. All the P-modified TiO<sub>2</sub> had an average crystallite size of ~10 nm and BET surface area of 75 m<sup>2</sup>/g. The XRD results were found to be in good agreement with those observed from the TEM micrographs (Fig. 2). The average crystallite sizes of



 $\textbf{Fig. 2.} \ \ The TEM \ micrographs of unmodified TiO_2\ (a), 10\% Ag/unmodified-TiO_2\ (b), 10\% Ag/TiO_2-HPO_4\ (c), 10\% Ag/TiO_2-(NH_4)_2HPO_4\ (d), 10\% Ag/TiO_2-(C_2H_5)_3PO_4\ (e), 10\% Ag/TiO_2-P_2O_5\ (f)\ catalysts.$ 

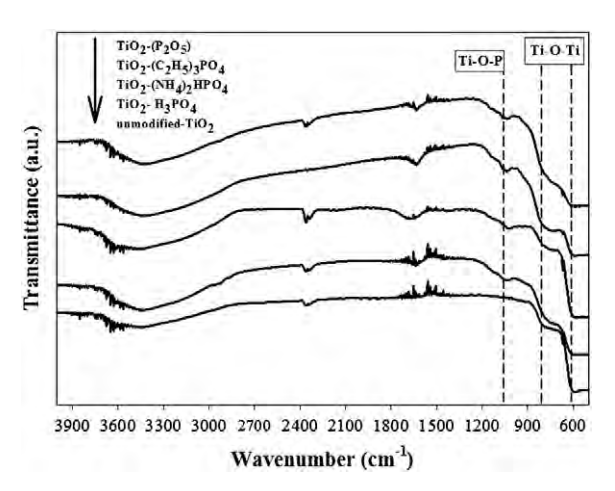
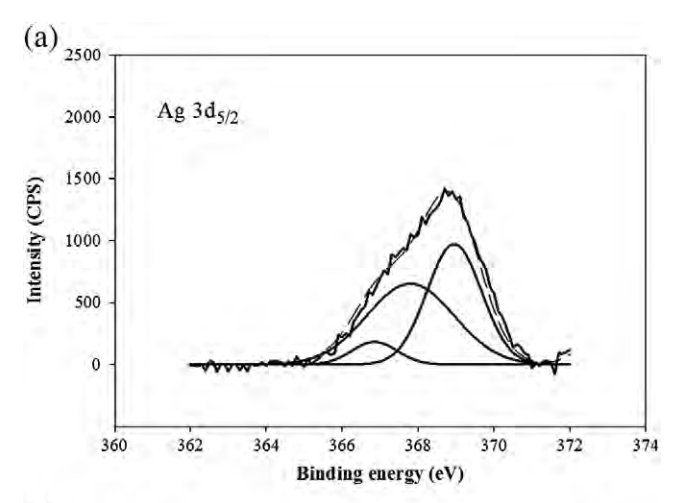


Fig. 3. FT-IR spectra of TiO<sub>2</sub> and P-modified TiO<sub>2</sub> with different phosphorus precursors.

unmodified-TiO<sub>2</sub> support decreased from ~15 to ~11 nm when the TiO<sub>2</sub> support was modified with phosphorus. The particle sizes of Ag/Ag<sub>2</sub>O on the P-modified TiO<sub>2</sub> supports were determined to be ca. 2.3 nm which were smaller than those dispersed on the unmodified-TiO<sub>2</sub> (ca. 3 nm). The higher metal dispersion on the P-modified TiO<sub>2</sub> supported Ag catalysts was confirmed by the chemisorption results (see also Table 1). The amount of metal active sites on the P-modified TiO<sub>2</sub> supported Ag catalysts was nearly three times higher than the unmodified ones. However, the amount of metal active sites on the P-modified TiO<sub>2</sub> supported Ag catalysts prepared from different phosphorous precursors were found to be essentially similar in the range of 3.57–3.89 × 10<sup>20</sup> atoms Ag/g cat.

The FT-IR spectra of unmodified and P-modified TiO<sub>2</sub> are shown in Fig. 3. The spectra bands at ca. 1600 cm<sup>-1</sup> and 3200 cm<sup>-1</sup> were attributed to the surface-absorbed water and hydroxyl group, respectively [21,22]. The IR spectra bands at ca. 400–800 cm<sup>-1</sup> were attributed to Ti–O–Ti bond. The bands in this range became weak when the TiO<sub>2</sub> support was modified with phosphorus while the bands corresponding to Ti–O–P appeared at ca. 1100 cm<sup>-1</sup> [23–25]. It is likely that the formation of Ti–O–Ti was suppressed by the formation of Ti–O–P. The incorporation of phosphorus into TiO<sub>2</sub> support could inhibit the agglomeration of TiO<sub>2</sub> crystal, leading to a decrease of TiO<sub>2</sub> crystallite size. The FT-IR results support the characterization by XRD and TEM in which smaller TiO<sub>2</sub> crystallite size was obtained after P doping.

The oxidation state of element on the catalyst surface was examined by XPS and is summarized in Table 2. The binding energies of Ti 2p, O 1s, Ag 3d, and P 2p were slightly different among the various catalysts. The Ti 2p peaks consisting of Ti  $2p_{3/2}$  and Ti  $2p_{1/2}$ , with a separation around 5.3 eV, were assigned to the  $Ti^{4+}$  in pure anatase  $TiO_2$  [26,27]. The binding energy of O 1s in all the samples was at ca. 530.0 eV, which was assigned to the Ti-O-Ti lattice oxygen of  $TiO_2$  [28]. The P 2p of all the P-modified  $TiO_2$  shows only one peak in the range of 133.8–134.4 eV, indicating that the oxidation state of phosphorus in  $TiO_2$  was  $P^{5+}$ . The absence of P 2p spectra at 129 eV suggested that  $Ti^{4+}$  in the lattice of  $TiO_2$  was replaced by  $P^{5+}$  [29]. For all the samples, the binding energies of Ag  $3d_{5/2}$  and Ag  $3d_{3/2}$  were



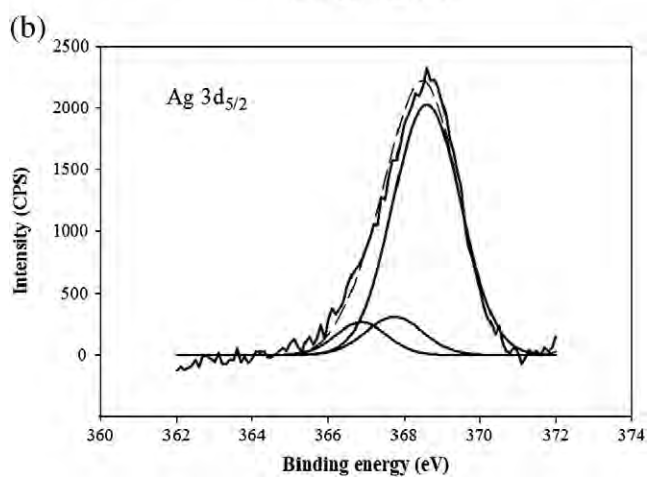


Fig. 4. The Ag 3d XPS spectra of (a) 10%Ag/unmodified-TiO $_2$  and (b) 10%Ag/TiO $_2$ –  $(C_2H_5)_3PO_4$  catalysts.

centered at ca. 368 and 374 eV, respectively. According to the literature [30], the binding energy of Ag  $3d_{5/2}$  at 368.2 eV and the splitting between Ag  $3d_{5/2}$  and Ag  $3d_{3/2}$  6.0 eV indicates a normal state of Ag $^0$ . The deconvolution of Ag  $3d_{5/2}$  of 10%Ag/unmodified-TiO $_2$  and 10%Ag/TiO $_2$ -(C $_2$ H $_5$ ) $_3$ PO $_4$  is shown in Fig. 4. Three peaks at the binding energy of ca. 366.8 eV, 367.7 eV, and 368.5 eV were attributed to AgO, Ag $_2$ O, and Ag $_3$ 0, respectively [31]. Base on the deconvolution analysis, the 10%Ag/TiO $_2$ -(C $_2$ H $_5$ ) $_3$ PO $_4$  catalyst produced larger amount of Ag metallic (80%) than the 10%Ag/unmodified-TiO $_2$  (45%). Such results indicated that the P-modified TiO $_2$  promoted the Ag metallic formation on the TiO $_2$  support.

#### 3.2. Effect of P doping on the activity of CO oxidation

Fig. 5 shows the CO conversion as a function of reaction temperature of the unmodified TiO<sub>2</sub> and P-modified TiO<sub>2</sub> supported Ag catalysts prepared with different types of phosphorus precursor.

**Table 2**Binding energies of 10 at.% Ag catalyst supported on TiO<sub>2</sub> and P-modified TiO<sub>2</sub> with different phosphorus precursors.

Sample	Ti 2p		O 1s	Ag 3d	Ag 3d		P 2p	
	Ti 2p <sub>3/2</sub>	Ti 2p <sub>1/2</sub>		Ag 3d <sub>5/2</sub>	Ag 3d <sub>3/2</sub>	P 2p <sub>3/2</sub>	P 2p <sub>1/2</sub>	
10%Ag/unmodified-TiO <sub>2</sub>	458.75	464.55	530.0	368.90	375.00	-	-	
10%Ag/TiO <sub>2</sub> -H <sub>3</sub> PO <sub>4</sub>	459.85	465.65	531.1	368.70	375.00	133.4	-	
10%Ag/TiO <sub>2</sub> -(NH <sub>4</sub> ) <sub>2</sub> HPO <sub>4</sub>	459.35	465.15	530.70	368.70	374.60	133.80	-	
10%Ag/TiO <sub>2</sub> -(C <sub>2</sub> H <sub>5</sub> ) <sub>3</sub> PO <sub>4</sub>	459.25	464.85	530.60	368.50	374.60	133.40	135.2	
10%Ag/TiO <sub>2</sub> -P <sub>2</sub> O <sub>5</sub>	458.45	465.05	530.8	368.90	374.90	134.00	-	

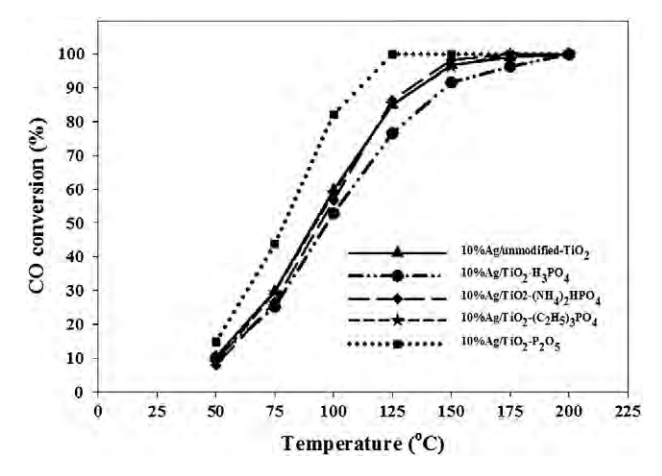


Fig. 5. CO conversion over 10 at.% Ag catalysts supported on  $TiO_2$  and P-modified  $TiO_2$  with different phosphorus precursors.

The results show that the type of phosphorus precursor affected the CO oxidation activity of the TiO<sub>2</sub> supported Ag catalysts. The P-modified TiO<sub>2</sub> supported Ag catalysts using the phosphorus precursor in the form of phosphate showed comparable (for  $10\% Ag/TiO_2-(NH_4)_2HPO_4$  and  $10\% Ag/TiO_2-(C_2H_5)_3PO_4)$  or lower activity ( $10\% Ag/TiO_2-H_3PO_4$ ) compared to the  $10\% Ag/unmodified-TiO_2$  (light-off temperature ca. 92-97 °C). On the contrary, the catalyst prepared with the phosphorus precursor in the form of oxide ( $10\% Ag/TiO_2-P_2O_5$ ) showed higher activity than the unmodified-TiO<sub>2</sub> supported catalyst (light-off temperature ~80 °C).

Since the physical properties of the P-modified TiO<sub>2</sub> supported Ag catalysts prepared from different phosphorous precursors were quite similar (i.e. in terms of BET surface area, crystallite size, and metal dispersion), the catalytic behaviors were correlated with the O2 adsorption-desorption behavior on the catalyst surface. Fig. 6 shows the O<sub>2</sub>-TPD patterns of the unmodified and P-modified TiO<sub>2</sub> supported Ag catalysts with different phosphorus precursors. The Ag catalyst modified with phosphorus exhibited lower desorption temperature compared to the unmodified ones. The desorption temperature of 10% Ag/TiO<sub>2</sub>-(C<sub>2</sub>H<sub>5</sub>)<sub>3</sub>PO<sub>4</sub> and 10%Ag/TiO<sub>2</sub>-P<sub>2</sub>O<sub>5</sub> catalyst appeared at lower temperature in comparison with the 10%Ag/unmodified-TiO<sub>2</sub>. The desorption peak appeared in the range of 250 to 265 °C was assigned to species [32]. For the 10%Ag/TiO<sub>2</sub>-(NH<sub>4</sub>)<sub>2</sub>HPO<sub>4</sub> and 10%Ag/TiO<sub>2</sub>-H<sub>3</sub>PO<sub>4</sub>, a small shoulder of O<sub>2</sub> desorption peak at around 250–265 °C and large desorption peaks at higher temperature in the range of 300-320 °C and 400-430 °C were observed.

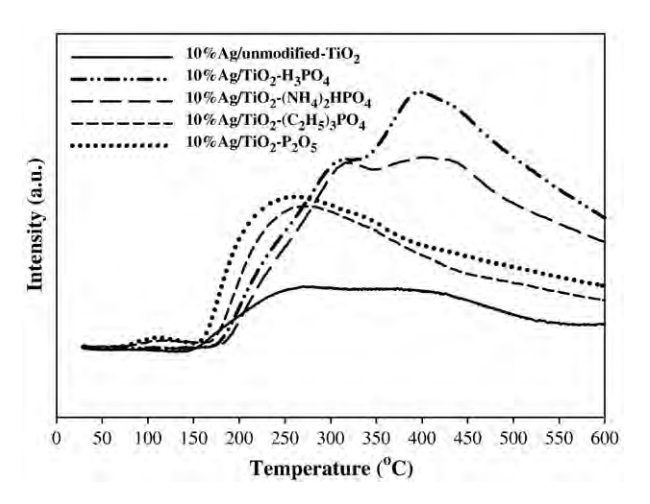


Fig. 6.  $O_2$ -TPD patterns of 10 at.% Ag catalysts supported on  $TiO_2$  and P-modified  $TiO_2$  with different phosphorus precursors.

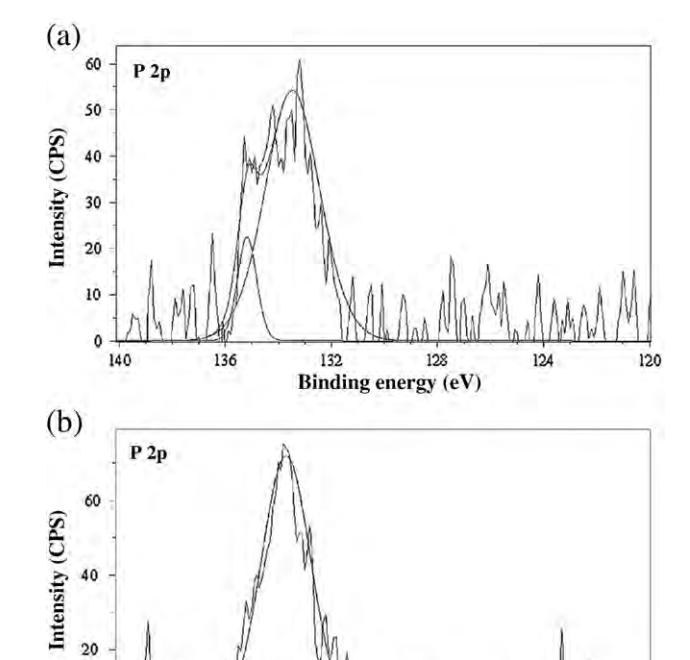


Fig. 7. The P 2p XPS spectra of (a) 10%Ag/TiO<sub>2</sub>–(C<sub>2</sub>H<sub>5</sub>)<sub>3</sub>PO<sub>4</sub> and (b) 10%Ag/TiO<sub>2</sub>–P<sub>2</sub>O<sub>5</sub> catalysts.

Binding energy (eV)

According to Masakazu et al. [33], there are three kinds of adsorbed oxygen species on  $TiO_2$  surface. The adsorbed oxygen consists of weakly adsorbed surface oxygen, strongly adsorbed surface oxygen, and surface lattice oxygen, with the oxygen desorption temperature in the range of 220–250 °C, 470–490 °C, and 810–870 °C, respectively [34,35]. The strongly adsorbed surface oxygen species blocks the adsorption and diffusion of weakly adsorbed surface oxygen, causing a decrease in the CO oxidation activity [36]. It is clearly seen from the  $O_2$ -TPD results that the 10%Ag/ $TiO_2$ - $(NH_4)_2$ HPO<sub>4</sub> and 10%Ag/ $TiO_2$ - $H_3$ PO<sub>4</sub> exhibited higher amount of strongly adsorbed oxygen than the other catalysts, thus lower CO oxidation activities were obtained. The desorption profiles of 10%Ag/ $TiO_2$ - $(C_2H_5)_3$ PO<sub>4</sub>, however, was quite similar to the 10%Ag/ $TiO_2$ - $P_2O_5$ , although the catalytic activities in CO oxidation were different.

Based on the XPS analysis (Fig. 7), the phosphate species on the P-modified  $TiO_2$  surface were identified. The P 2p spectra of 10%Ag/ $TiO_2$ – $(C_2H_5)_3$ PO<sub>4</sub> were slightly different from those of 10%Ag/ $TiO_2$ – $P_2O_5$  in which a shoulder at a binding energy of 135.2 eV appeared in addition to the major peak at 133.4 eV. The P 2p spectra at a binding energy of 133.4 eV was assigned to the monodentate surface complex, which phosphate adsorbed to the surface hydroxyl ion with one coordination number. The shoulder peak at higher binding energy (135.2 eV) was assigned to the bidentate surface complex in which phosphate was bound to two surface hydroxyl

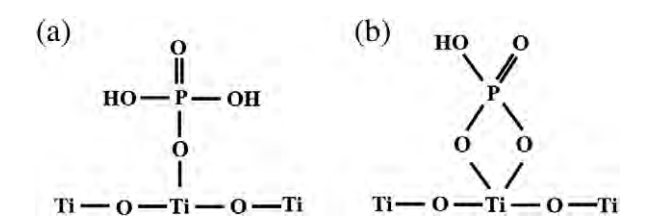


Fig. 8. Schematic illustration of (a) monodentate, (b) bidentate surface complex on the surface of  ${\rm TiO_2}$  support.

ions. The formation of monodentate and bidentate surface complexes on  ${\rm TiO_2}$  support is illustrated in Fig. 8. The bidentate adsorption is very difficult to remove by a washing step during the preparation of P-modified  ${\rm TiO_2}$  [28,37]. In other words, the  $10\%{\rm Ag/TiO_2}$ –( ${\rm C_2H_5}$ ) $_3{\rm PO_4}$  produced bidentate of phosphate species on the surface of  ${\rm TiO_2}$  that could result in the blocking of active sites and lower activity in CO oxidation.

#### 4. Conclusions

Modification of the  ${\rm TiO_2}$  supports with different phosphorus precursors altered the catalytic behaviors of  ${\rm Ag/TiO_2}$  catalysts in the CO oxidation. The insertion of phosphorus into the  ${\rm TiO_2}$  lattice in the form of Ti–O–P not only increased the metal active sites by increasing the specific surface area of the catalyst and inhibiting the agglomeration of  ${\rm TiO_2}$  crystallites but also altered the strength of  ${\rm O_2}$  adsorption—desorption behavior on the catalyst surface. The P-modified  ${\rm TiO_2}$  supported Ag catalysts using the phosphorus precursor in the form of phosphate produced the strongly adsorbed oxygen species and/or the bidentate of phosphate species on the  ${\rm TiO_2}$  supports, which resulted in no improvement in the CO oxidation activity. On the other hand, the use of phosphorus precursor in the form of oxide enhanced the CO oxidation activity of  ${\rm Ag/TiO_2}$  catalysts due to the promotion of weakly adsorbed oxygen species.

#### Acknowledgments

The financial support from the Thailand Research Fund (TRF) and the Office of Higher Education Commission (CHE), Ministry of Education, Thailand are gratefully acknowledged.

#### References

- [1] S.J. Tauster, S.C. Fung, R.L. Garten, J. Am. Chem. Soc. 100 (1978) 170–175.
- [2] G.L. Haller, D.E. Resasco, H.P.D.D. Eley, B.W. Paul, Adv. Catal. 36 (1989) 173-235.
- [3] M.A. Vannice, B. Sen, J. Catal. 115 (1989) 65–78.
- [4] P. Claus, S. Schimpf, R. Schdel, P. Kraak, W. Mrke, D. Hnicke, Appl. Catal. A Gen. 165 (1997) 429–441.

- [5] L.L. Murrell, D.J.C. Yates, T. Seiyama, K. Tanabe, Stud. Surf. Sci. Catal. 7 (1981) 1470–1471.
- [6] C.-S. Chen, J.-H. You, J.-H. Lin, Y.-Y. Chen, Catal. Commun. 9 (2008) 2381–2385.
- [7] M.A. Vannice, C. Sudhakar, J. Phys. Chem. 88 (1984) 2429–2432.
- [8] J. Yu, G. Wu, D. Mao, G. Lu, Acta Phys. Chim. Sin. 24 (2008) 1751–1755.
- [9] C.L. Peza-Ledesma, L. Escamilla-Perea, R. Nava, B. Pawelec, J.L.G. Fierro, Appl. Catal. A Gen. 375 (2010) 37–48.
- [10] J.A. Hernandez, S. Gomez, B. Pawelec, T.A. Zepeda, Appl. Catal. B Environ. 89 (2009) 128–136.
- [11] J.-N. Lin, J.-H Chen, C.-Y Hsiao, Y.-M. Kang, B.-Z. Wan, Appl. Catal. B: Environmental 36 (2002) 19–29.
- 12] J. Moma, M. Scurrell, W. Jordaan, Top. Catal. 44 (2007) 167-172.
- 13] K. Ruth, M. Hayes, R. Burch, S. Tsubota, M. Haruta, Appl. Catal. B Environ. 24 (2000) 1133–1138
- [14] M.R. Kim, S.I. Woo, Appl. Catal. A Gen. 299 (2006) 52-57.
- [15] Z. Ma, S. Brown, S.H. Overbury, S. Dai, Appl. Catal. A Gen. 327 (2007) 226–237.
- [16] W. Payakgul, O Mekasuwandumrong, V. Pavarajarn, P. Praserthdam, Ceram. Int. 31 (2005) 391–397.
- [17] N. Comsup, J. Panpranot, P. Praserthdam, Catal. Lett. 133 (2009) 76-83.
- 18] T. Nanba, S. Masukawa, J. Uchisawa, A. Obuchi, J. Catal. 259 (2008) 250–259.
- [19] L. Ren, Y.-P. Zeng, D. Jiang, Catal. Commun. 10 (2009) 645-649.
- [20] X. Fan, T. Yu, Y. Wang, J. Zheng, L. Gao, Z. Li, J. Ye, Z. Zou, Appl. Surf. Sci. 254 (2008) 5191–5198.
- [21] J. Zhu, J. Yang, Z.-F. Bian, J. Ren, Y.-M. Liu, Y. Cao, H.-X. Li, H.-Y. He, K.-N. Fan, Appl. Catal. B Environ. 76 (2007) 82–91.
- [22] K. Nagaveni, M.S. Hegde, N. Ravishankar, G.N. Subbanna, G. Madras, Langmuir 20 (2004) 2900–2907.
- 23] J.C. Yu, L. Zhang, J. Yu, Chem. Mater. 14 (2002) 4647–4653.
- 24] A. Bhaumik, S. Inagaki, J. Am. Chem. Soc. 123 (2001) 691–696.
- [25] X. Zhang, J.C. Shen, Adv. Mater. 11 (1999) 1139-1143.
- [26] G. Silversmit, G. De Doncker, R. De Gryse, Surf. Sci. Spectra 9 (2002) 21–29.
- [27] C.K. Maiti, S.K. Samanta, G.K. Dalapati, S.K. Nandi, S. Chatterjee, Microelectron. Eng. 72 (2004) 253–256.
- [28] D. Zhao, C. Chen, Y. Wang, H. Ji, W. Ma, L. Zang, J. Zhao, J. Phys. Chem. C 112 (2008) 5993–6001.
- 29] Q. Shi, D. Yang, Z. Jiang, J. Li, J. Mol. Catal. B Enzym. 43 (2006) 44-48.
- [30] H. Wang, J. Niu, X. Long, Y. He, Ultrason. Sonochem. 15 (2008) 386-392.
- [31] B. Xin, L. Jing, Z. Ren, B. Wang, H. Fu, J. Phys. Chem. B 109 (2005) 2805-2809.
- [32] H. Chon, J. Pajares, J. Catal. 14 (1969) 257-260.
- [33] M. Iwamoto, Y. Yoda, N. Yamazoe, T. Seiyama, J. Phys. Chem. 82 (1978) 2564–2570.
- [34] R. Li, J. Ma, J. Xu, X. Zhou, Z. Su, React. Kinet. Catal. Lett. 70 (2000) 363-370.
  - [5] L. Luo, G. Shao, Z. Duan, Turk. J. Chem. 29 (2005) 597-605.
- [36] Q. Zhenping, C. Mojie, S. Chuan, B. Xinhe, J. Nat. Gas Chem. 14 (2005) 4–12.
- 37] E.W. Shin, J.S. Han, M. Jang, S.-H. Min, J.K. Park, R.M. Rowell, Environ. Sci. Technol. 38 (2003) 912–917.

Provided for non-commercial research and education use. Not for reproduction, distribution or commercial use.



This article appeared in a journal published by Elsevier. The attached copy is furnished to the author for internal non-commercial research and education use, including for instruction at the authors institution and sharing with colleagues.

Other uses, including reproduction and distribution, or selling or licensing copies, or posting to personal, institutional or third party websites are prohibited.

In most cases authors are permitted to post their version of the article (e.g. in Word or Tex form) to their personal website or institutional repository. Authors requiring further information regarding Elsevier's archiving and manuscript policies are encouraged to visit:

http://www.elsevier.com/copyright

# Author's personal copy

Chemical Engineering Journal 164 (2010) 77-84

ELSEVIER

Contents lists available at ScienceDirect

# **Chemical Engineering Journal**

journal homepage: www.elsevier.com/locate/cej

Chemical Engineering Journal

# Effects of synthesis conditions and annealing post-treatment on the photocatalytic activities of ZnO nanoparticles in the degradation of methylene blue dye

Okorn Mekasuwandumrong<sup>a</sup>, Pongsapak Pawinrat<sup>b</sup>, Piyasan Praserthdam<sup>b</sup>, Joongjai Panpranot<sup>b,\*</sup>

- a Department of Chemical Engineering, Faculty of Engineering and Industrial Technology, Silpakorn University, Nakorn Phathom 73000, Thailand
- <sup>b</sup> Center of Excellence on Catalysis and Catalytic Reaction Engineering, Department of Chemical Engineering, Faculty of Engineering, Chulalongkorn University, Bangkok 10330, Thailand

#### ARTICLE INFO

#### Article history: Received 8 March 2010 Received in revised form 11 August 2010 Accepted 11 August 2010

Keywords: Flame-spray pyrolysis ZnO Particle size effect Photocatalysts Annealing

#### ABSTRACT

The effects of synthesis conditions (i.e., metal concentration, precursor flowrate, and  $O_2$  dispersion) during flame-spray pyrolysis (FSP) and annealing post-treatment on the characteristics and photocatalytic activities of ZnO nanoparticles have been investigated. The average particle size of ZnO powder prepared by one-step FSP method were in the range of 8.8–47.0 nm and were found to be increased with increasing the enthalpy density, flame height, and high-temperature residence time during FSP synthesis. The larger particle size FSP-derived ZnO nanoparticles exhibited higher photocatalytic activities in the degradation of methylene blue (MB) dye. The degradation rate over FSP-ZnO-47.0 nm was 1.7 and 7.2 times higher than those of the commercially available photocatalysts Degussa P-25 and JRC-TiO2, respectively. The better photocatalytic performance of the FSP-ZnO was correlated well with the improved crystalline quality of ZnO nanoparticles as revealed by the X-ray diffraction (XRD) and the photoluminescence (PL) results. Further increase of FSP-ZnO particle size to 52.6–103.5 nm by annealing post-treatment at high temperatures (750–900 °C), however, gradually decreased their photocatalytic activities. Our results in this study suggest a balance between high crystalline quality that enhanced photo phenomena and the surface area available for substrate adsorption in order to obtain high photocatalytic activity of ZnO nanoparticles.

© 2010 Elsevier B.V. All rights reserved.

#### 1. Introduction

Dye pollutants from textile paper and other industries are an important source of environmental contamination. Conventional treatment of such wastewater generally involves coagulation/flocculation [1,2], electrocoagulation [3], coagulation/carbon adsorption process [4] and so on. These methods, however, merely transfer dyes from the liquid-phase to the solid-phase, requiring further treatment and causing secondary pollution [5]. In the past two decades, photocatalysis by semiconductive materials such as TiO<sub>2</sub> and ZnO has attracted public concern as a promising tool among the advanced oxidation processes to substitute the traditional wastewater treatment due to their high photosensitivity, non-toxic nature, high stability, and wide band gap [6]. While TiO<sub>2</sub> is probably the most frequently used photocatalyst, ZnO is an alternative photocatalyst with low cost. It has a similar band gap energy compared to TiO<sub>2</sub> (3.2 eV) [7] and can adsorb over a larger frac-

tion of UV spectrum [8]. Higher photocatalytic efficiency of ZnO compared to  $TiO_2$  has been reported especially for degradation of organics in aqueous solutions [5,9–13]. Our recent study showed that Au–ZnO and Pt–ZnO nanocomposites prepared by one-step flame-spray pyrolysis exhibited high photocatalytic activities in degradation of methylene blue dye [14].

For semiconductor photocatalysts, particle size is an important parameter for controlling surface area and electronic structure. When the catalyst particle size is reduced down to a few nanometers, an elevate density of active sites for substrate adsorption and/or catalysis can be guaranteed, as small particles possess a significantly higher surface-to-volume ratio compared to the bulk material. When the nanocrystal size is comparable or smaller than the bulk exciton diameter, the band-gap becomes size-dependent due to quantization effects [15,16]. Moreover, an efficient photocatalytic process requires highly crystalline semiconductors to minimize electron-hole pair loss owing to the trapping of either charge carriers at defect states [17,18].

The effect of particle size on photoactivity of ZnO has been addressed by a number of researchers [19–22]. For examples, among the three different particle sizes of ZnO nanoparticles (14,

<sup>\*</sup> Corresponding author. Tel.: +66 2218 6869; fax: +66 2218 6877. E-mail address: joongjai.p@chula.ac.th (J. Panpranot).

O. Mekasuwandumrong et al. / Chemical Engineering Journal 164 (2010) 77-84

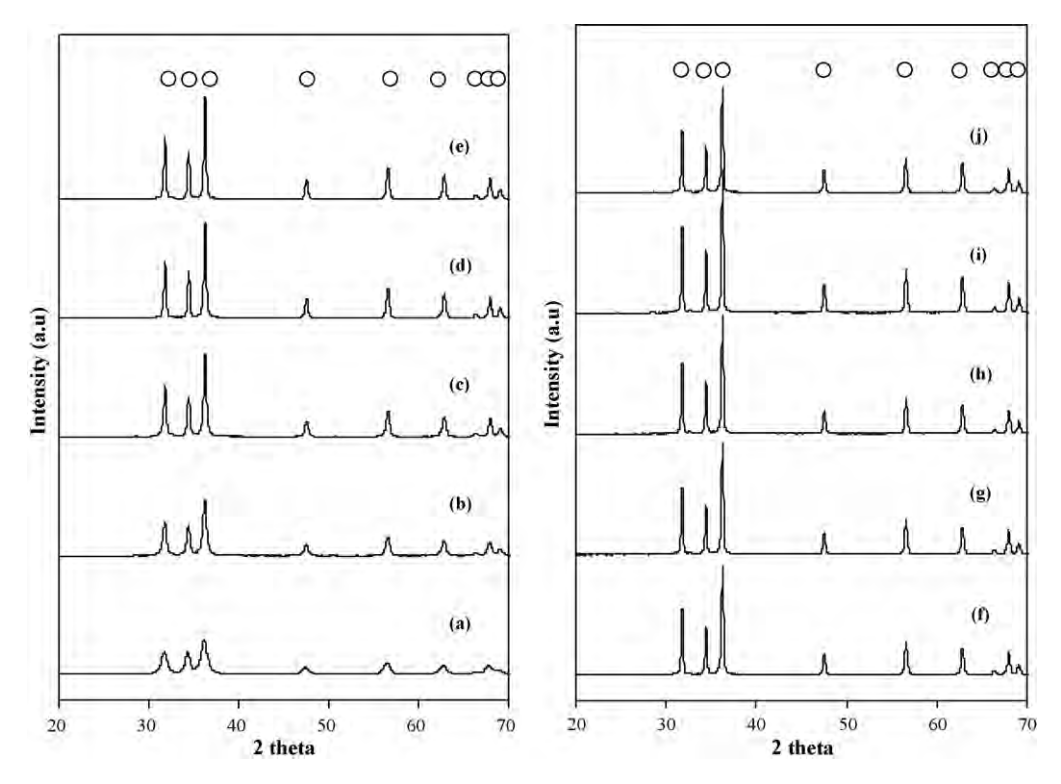


Fig. 1. XRD patterns of the as-prepared flame-made ZnO with various crystallite sizes: (a)  $8.8 \, \text{nm}$ , (b)  $19.4 \, \text{nm}$ , (c)  $30 \, \text{nm}$ , (d)  $40.7 \, \text{nm}$ , (e)  $47 \, \text{nm}$  and the annealed flame-made ZnO particles: (f)  $52.6 \, \text{nm}$ , (g)  $67.1 \, \text{nm}$ , (h)  $80.3 \, \text{nm}$ , (i)  $90.6 \, \text{nm}$ , (j)  $103.5 \, \text{nm}$ .

19, and 26 nm) prepared by precipitation process, the smaller one resulted in more surface oxygen vacancies, higher ESR intensity, stronger PL signal, and higher photocatalytic activity [20]. Dodd et al. [21] prepared ZnO nanoparticles with various particle sizes

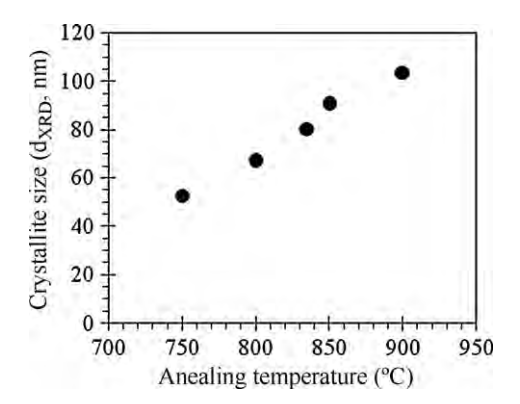


Fig. 2. Relationship between crystallite size of ZnO and annealing temperature.

in the range of 28-57 nm by mechanical milling and heat treatment. The authors found that there exists an optimum size of 33 nm for which the photocatalytic activity of ZnO is maximized. Li et al. [22] also obtained ZnO nanoparticles with average sizes 21–90 nm by varying the calcination temperature between 200 and 1000 °C and found that ZnO prismatic aggregated obtained by calcination at 800 °C demonstrated the highest photocatalytic activity. More recently, Xie et al. [19] showed that photocatalytic properties of various particle sizes of ZnO (15, 50, 200, and 1000 nm) synthesized by thermal evaporation and chemical deposition in UV-induced degradation of methyl orange depended on size, morphology, and preparation method of ZnO. Thus, in previous studies, it has clearly shown that efficiency of photocatalytic process can be maximized by optimizing the particle size of ZnO photocatalysts. However, preparation method as well as pretreatment conditions such as calcination temperature strongly affects the properties of ZnO photocatalysts.

In this report, ZnO nanoparticles with various particle sizes were obtained by flame-spray pyrolysis (FSP) method. Various particle sizes of the flame-made ZnO powder (8.8–103.5 nm) were obtained by varying the process conditions such as metal concentration in

**Table 1**Relationship between the synthesis conditions and ZnO crystallite sizes.

celutionship between the synthesis conditions and zho crystamic sizes.						
Metal concentration (molar)	Precursor flow rate (ml/min)	Dispersion oxygen flow rate (l/min)	Annealing temperature (°C)	Crystallite size d <sub>XRD</sub> (nm)	Average primary particle size $d_{\text{TEM}}$ (nm)	BET surface area (m²/g)
0.3	3	5	n/a	8.8	11.1	63.1
0.3	8	3	n/a	19.4	20.5	35.5
0.5	8	3	n/a	30.0	31.3	26.2
0.8	8	3	n/a	40.7	39.8	13.6
1	8	3	n/a	47.0	48.7	15.1
1	8	3	750	52.6	57.7	12.0
1	8	3	800	67.1	71.7	8.0
1	8	3	835	80.3	98.9	6.8
1	8	3	850	90.6	116.7	5.9
1	8	3	900	103.5	159.9	5.8

n/a = not applied.

feed, precursor flow rate, dispersion oxygen flow rate, and annealing temperature. The effects of both FSP synthesis conditions and annealing post-treatment on the characteristics and photocatalytic properties of the flame-made ZnO in photodegradation of methylene blue (MB) were discussed extensively.

#### 2. Material and methods

#### 2.1. Synthesis of ZnO nanoparticles by flame-spray pyrolysis

Synthesis of ZnO with various particle sizes by FSP technique were carried out using a spray flame reactor [24]. Zinc naphthanate (Aldrich; <50% in mineral spirits) was used as zinc precursor. The

precursor was dissolved in ethanol (J.T. Baker; 99.9%). To obtain different ZnO particle sizes during particle synthesis, precursor solution ranged from 0.3 to 1 mol/l and liquid precursor feed rates varied from 3 to 8 ml/min were fed to the flame by a syringe pump. Precursors were dispersed with 3–5 l/min oxygen forming fine spray droplets. The pressure drop at the capillary tip was maintained at 1.5 bar by adjusting the orifice gap area at the nozzle. The reactor was water-cooled to avoid evaporation or decomposition of the precursor within the feed lines. The flame was ignited by a concentric premixed methane/oxygen pilot flame (CH<sub>4</sub> 1.5 l/min, O<sub>2</sub> 3.0 l/min) that was sheathed further by flowing oxygen (25 l/min) through a sintered metal plate ring (8 mm wide,

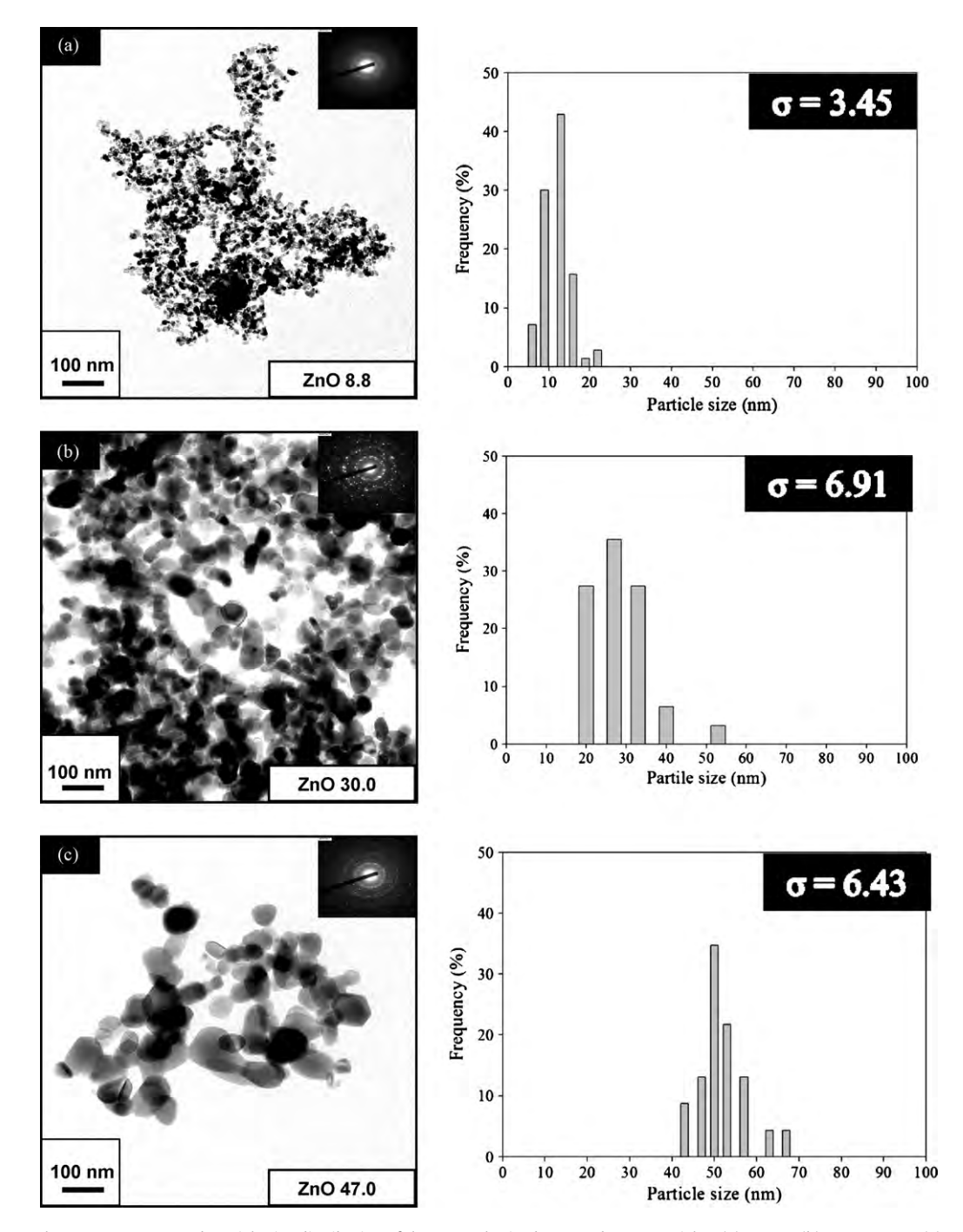


Fig. 3. TEM micrographs, SAED patterns, and particle size distribution of the as-synthesized FSP-made ZnO particles: (a) 8.8 nm, (b) ZnO 30.0 nm, (c) ZnO 47.0 nm and the annealed ZnO: (d) 67.1 nm, (e) 80.3 nm, (f) 103.5 nm.

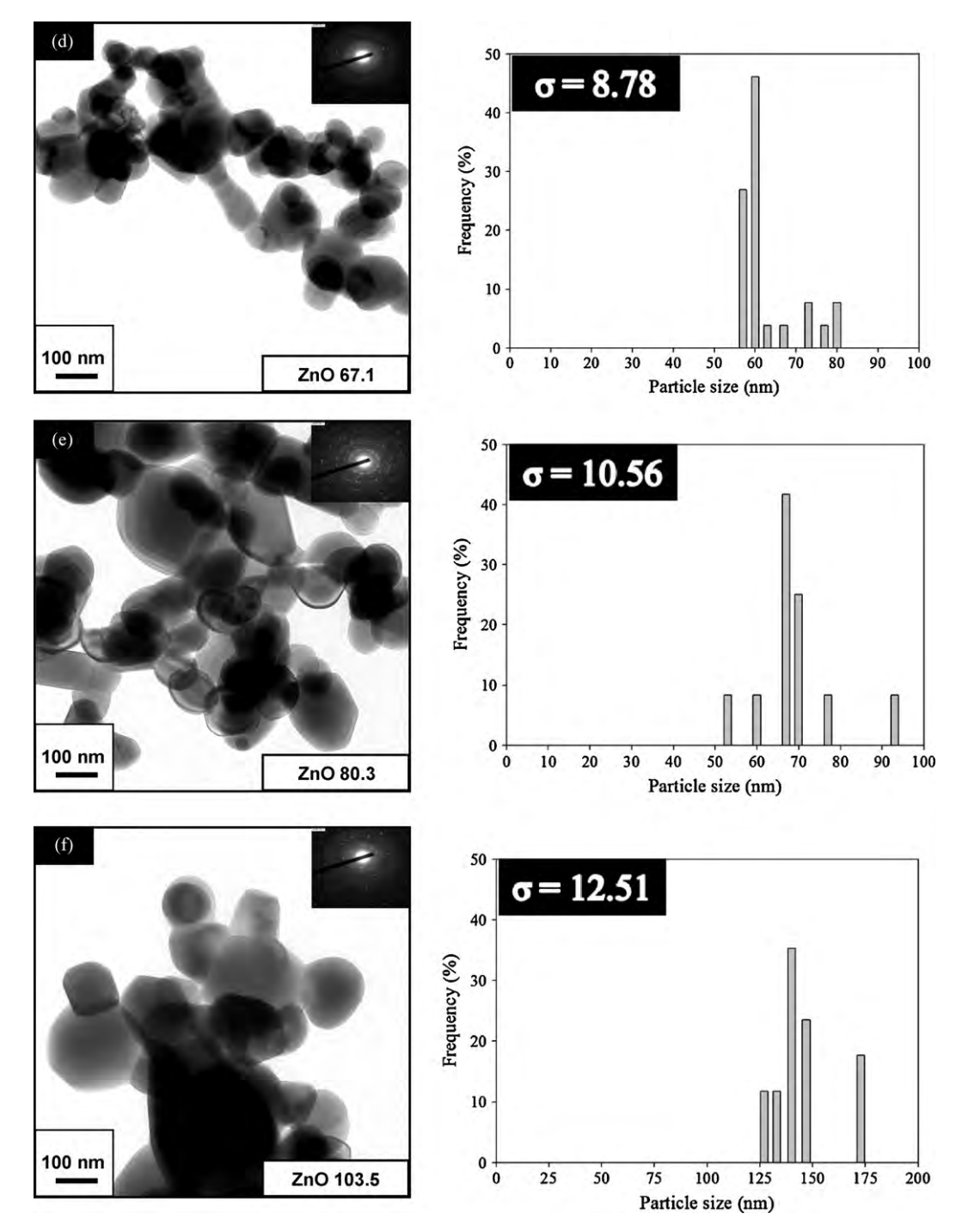


Fig. 3. (Continued)

starting at a radius of 8 mm). The powder particles were collected on a glass-fiber filter (GF/D Whatman; 257 mm diameter) with the aid of a vacuum pump.

#### 2.2. Annealing of the flame-made ZnO

Annealing of the ZnO powders was performed in a Carbolite CWF1300 temperature programmed box furnace in static air, ZnO powders with the particle size of 47 nm produced by FSP method were heated at  $10\,^{\circ}$ C/min to desired temperature (750, 800, 835, 850, or  $900\,^{\circ}$ C) and maintained at that temperature for 1 h in order to form larger particles.

#### 2.3. Characterization

Powder X-ray diffraction (XRD) was performed by a SIEMENS XRD D5000 diffractometer using Cu K $\alpha$  radiation. The crystallite size ( $d_{XRD}$ ) of FSP-ZnO powders was estimated from the full-width half-maximum breadth of the (101) diffraction peak using the Scherrer equation. The specific surface area was measured by N $_2$  physisorption using a Micromeritics ASAP 2000 automated system and the Brunauer–Emmet–Teller (BET) method. Each sample was degassed under vacuum at <1 × 10 $^{-5}$  bar in the Micromeritics system at 300 °C for 3 h prior to N $_2$  physisorption. The particle morphology was observed using JEOL Model JEM-

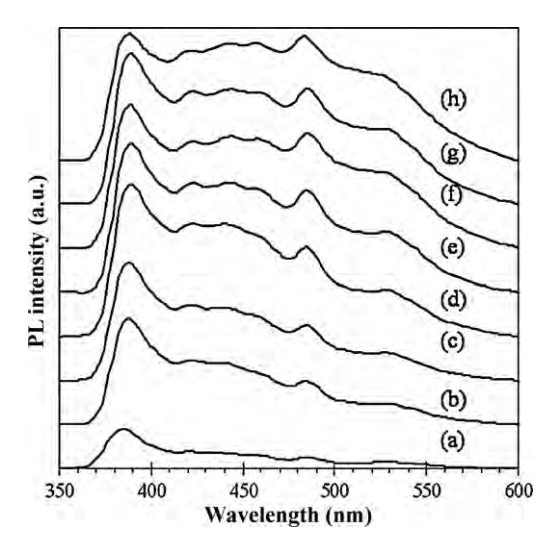


**Fig. 4.** PL spectra of various ZnO particle sizes prepared by FSP method (a) ZnO  $8.8\,\mathrm{nm}$ , (b) ZnO  $19.4\,\mathrm{nm}$ , (c) ZnO  $30.0\,\mathrm{nm}$ , (d) ZnO  $47.0\,\mathrm{nm}$ , (e) ZnO  $67.1\,\mathrm{nm}$ , (f) ZnO  $80.3\,\mathrm{nm}$ , (g) ZnO  $90.6\,\mathrm{nm}$ , and (h) ZnO  $103.5\,\mathrm{nm}$  with the excitation wavelength of  $325\,\mathrm{nm}$ .

2010 transmission electron microscope (TEM) operated at 200 keV. Photoluminescence measurement (PL) was carried out on a fluorescence spectrophotometer (Perkin-Elmer LS-50) using a Xenon lamp as the excitation source at room temperature. The sample was dispersed in ethanol using ultrasonic bath and the excitation wavelength used in PL measurement was 325 nm.

#### 2.4. Photocatalytic activity testing

A basic aniline dye, methylene blue (MB), from Unilab Asia Pacific Specialty Chemicals Limited was used as a probe molecule to evaluate the photocatalytic activities of the flame-made ZnO with various particle sizes. The photocatalytic reaction was conducted at room temperature under UV light 2 × 15 W UV tube predominantly emitting at 365 nm (Philips) with the average light intensity on the reaction beaker (pyrex) at a distance of 6 cm from the lamp was found to be  $4.7 \times 10^{-4} \, \text{W cm}^{-2}$ . The reaction was carried out with 20 mg of catalyst dispersed in 200 ml of 10 ppm methylene blue aqueous solution. The pH of solution was constant at 6.3 for all experiments. The reaction was operated with high stirring rate (1000 rpm) in order to eliminate the external mass transfer effect. Prior to irradiation, the suspensions were magnetically stirred in the dark for 15 min to establish the adsorption/desorption equilibrium of methylene blue. 2 ml samples were withdrawn every 10 min. Before analysis, the aqueous samples were centrifuged to remove any suspended solid catalyst particles. The residual concentration of methylene blue was measured at 665 nm using the UV-vis spectrophotometer (Perkin-Elmer lampda 650) in liquid cuvette configuration with de-ionized water as reference. The percentage of degradation was calculated using the equation given

Degradation (%) = 
$$\frac{C_0 - C}{C_0} \times 100$$
 (1)

in which  $C_0$  is the initial dye concentration and C is the dye concentration after the treatments.

#### 3. Results and discussion

#### 3.1. Particles characterization

Fig. 1a–e shows the XRD patterns of as-synthesized FSP-ZnO nanopowder with average crystallite sizes between 8.8 and

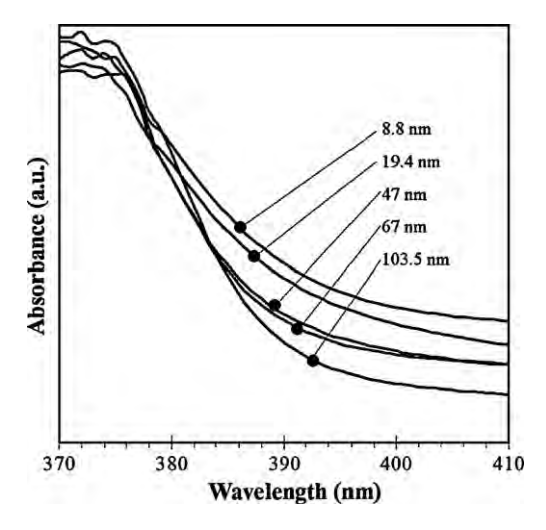
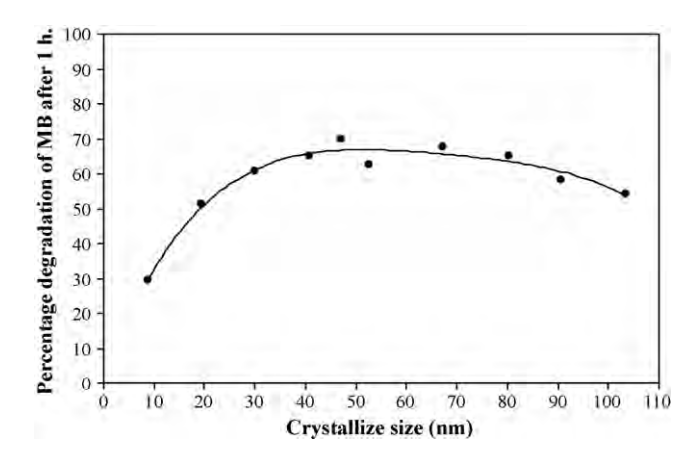


Fig. 5. UV-vis spectra of ZnO with various particle sizes.

47.0 nm. All of the indexed peaks are well matched with that of bulk ZnO (JCPDS Card No. 36-1451) possessing wurtzite hexagonal phase. No other diffraction peaks or amorphous phase was detected. The diffraction peak intensities were increased and the peaks became sharper with increasing ZnO particle sizes. The larger particle sizes of ZnO particles were obtained by increasing the precursor concentration, the ratio of the feed liquid, and decreasing the dispersion oxygen gas flow rates through the nozzle. Fig. 1f-j shows the XRD patterns of the annealed ZnO powders. The XRD characteristic peaks were similar to those of the as-synthesized ones. The calculated particle sizes of annealed ZnO were in the range of 52.6-103.5 nm indicating that annealing of the flame-made ZnO particles (47 nm) at relatively high temperature between 750 and 900 °C resulted in further crystal growth of ZnO. The relationship between synthesis conditions and corresponding ZnO particle sizes are summarized and illustrated in Table 1 and Fig. 2, respectively.

The TEM micrographs with selected area electron diffraction (SAED) patterns and particle size distribution of the as-synthesized and the annealed ZnO with various particle sizes are shown in Fig. 3. Frequency (%) was obtained by counting 50–100 ZnO particles from TEM images. All the samples consisted of polyhedral primary particles, typically seen in flame-made powders [23], with spheroidal particles and rod-like particles. The average primary particle diameters of ZnO with various particle sizes determined by TEM ( $d_{\rm TEM}$ ) are also given in Table 1. The  $d_{\rm TEM}$  data were in good agreement with the  $d_{\rm XRD}$  values. The corresponding SAED patterns are shown in the



**Fig. 6.** Relationship between for the percentage of MB degradation after 1 h and the particle size of ZnO photocatalysts prepared by FSP method.

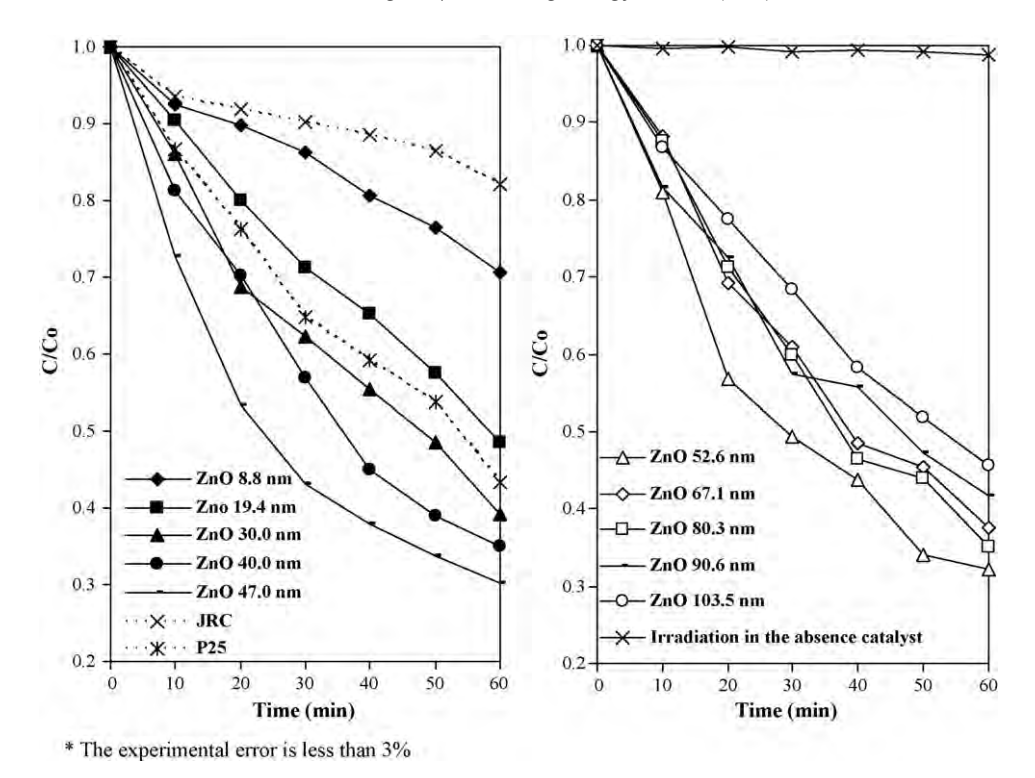


Fig. 7. The catalytic performances for photodegradation of methylene blue using FSP-made ZnO catalysts with various particle sizes (bold lines) and commercial catalysts for comparison (P25 and JRC titania) (dashed lines).

insets. The diffraction patterns of all the powders illustrate spot patterns of the hexagonal structure of ZnO, indicating that the ZnO nanoparticles are single crystalline. As also shown in Table 1, BET surface areas of the as-synthesized ZnO particles decreased from 63.1 to 15.1  $m^2/g$  as the precursor concentration increased from 0.3 to 1 M and the feed rate increased from 3 to 8 ml/min. The result was consistent with previous studies of the flame-synthesized metal oxides such as TiO<sub>2</sub> [25], SiO<sub>2</sub> [26], CeO<sub>2</sub> [27], Pt/Al<sub>2</sub>O<sub>3</sub> [28], and Ag/ZnO [29]. Typically, increasing of precursor feed flow rate and/or precursor concentration while keeping the oxygen flow rate constant results in higher enthalpy of flame, longer residence times and hotter flames [24,25]. This phenomenon is due to the fact that the combustion of the precursor is an exothermic reaction, contributing to overall increase in energy dissipation within the flame. Additionally, as the precursor feed flow rate and precursor concentration increased, Zn concentration within the flame also increased. This, coupled with the increased enthalpy content, residence time and higher flame temperature, resulted in increased coalescence and sintering of the particles. After high-temperature annealing (750–900 °C), the BET surface areas decreased further from 15.1 to  $5.8 \,\mathrm{m}^2/\mathrm{g}$  indicating that ZnO particles sintered by heat treatment.

Room temperature PL spectra of all the ZnO powders are shown in Fig. 4. The spectra mainly consisted of two emission bands. The first band is the UV near-band-edge emission (NBE) at ~385 nm [30,31]. Sharp NBE emission peak results from recombination of excitons and its position and structure is an indication of crystal quality [32,33]. The NBE emission intensities in the PL spectra increased as the particle size of as-synthesized ZnO increased. The highest value was found for the FSP-made ZnO with the crystallite size of 47 nm. Improvement of the crystal quality of ZnO can be attributed to the increase of flame enthalpy and Zn atomic concentration in gas phase that contributed typically to longer and hotter flames, which as a consequence, produced larger and more crystalline particles. However, the excitonic peak intensity for the annealed samples was remained constant and slightly decreased as the annealing temperature was raised higher than 835 °C. More-

over, the shift to the lower wavelength was also found in the FSP-made ZnO with the crystallite size of 8.8 nm. This result would be attributed to the quantum confinement effect of ZnO nanoparticles [34,35]. Madler et al. [35] prepared the ZnO quantum dots by spray combustion of Zn/Si precursors. These crystallites exhibit a quantum size effect due to the preventing of the growth and stabilized the ZnO crystals. The blue shift of the ultraviolet-vis absorption edge increased with decreasing ZnO crystal size. The other band observed in PL spectra was the visible emission that usually associates with the deep level emission (DLE) in ZnO. Most researchers believe that the DLE come from oxygen vacancies  $(V_0)$ , zinc vacancies (Zn<sub>0</sub>), interstitial zinc (Zn<sub>i</sub>), or interstitial oxygen  $(O_i)$  [36,37]. The blue emission at ~425 nm and weak blue at ~445 nm most likely occurs from the donor level of Zn interstitial  $(Zn_i)$  to acceptor energy level of Zn vacancy  $(Zn_0)$  [38]. The blue-green band around 470 nm was probably caused by radiative

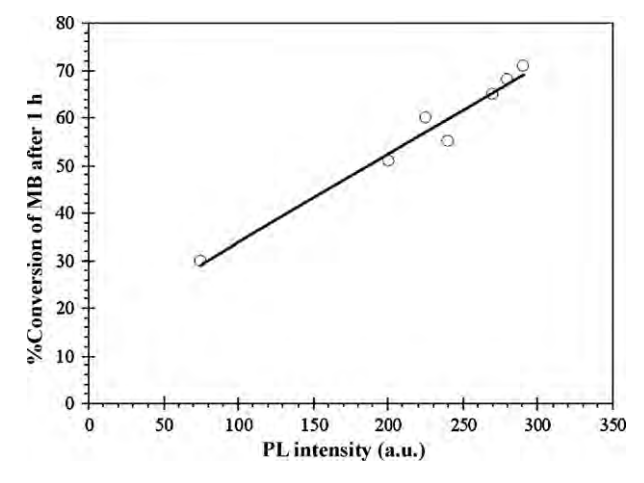


Fig. 8. Relationship between percentage of conversion of MB after 1 h of UV irradiation and PL intensity of the ZnO particles.

#### O. Mekasuwandumrong et al. / Chemical Engineering Journal 164 (2010) 77–84

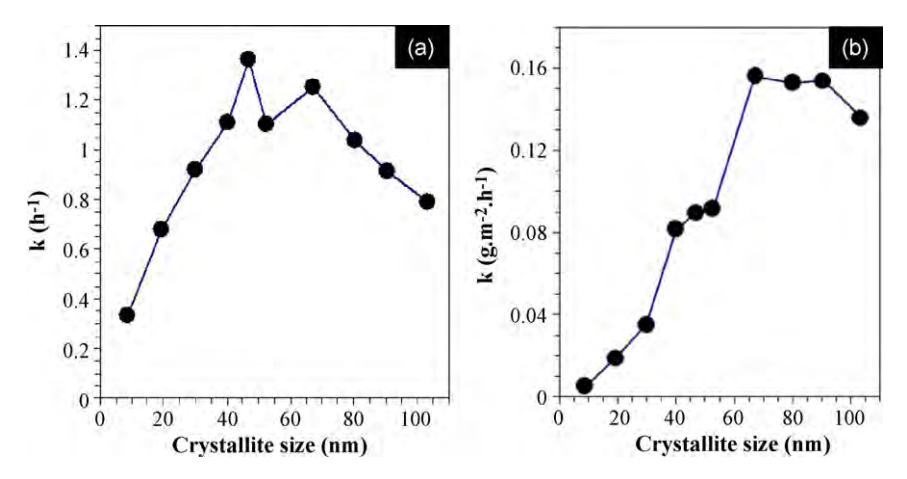


Fig. 9. Pseudo first-order rate constants for ZnO catalysts with various crystallite sizes on a mass (a) and SSA normalized (b) basis.

transition of electron from shallow donor levels, created by the oxygen vacancy to valence band [39]. The green emission at  $\sim\!\!530$  is commonly observed for ZnO, and was attributed to the singly ionized oxygen vacancy in ZnO [40]. This emission results from the recombination of a photo-generated hole with the singly ionized charge state of the specific defect [41]. The peak intensity of the blue and weak blue peak light emission increased with increasing of ZnO crystallite size from 8.8 to 47.0 nm and then was found remained unchanged. The weak blue–green band and green band emission peaks intensity slightly increased with increasing crystallite size from 8.8 to 103.5 nm.

Fig. 5 shows UV–vis absorbance spectra of the FSP-made ZnO powders. It can be seen that the slope of UV–vis spectra of the FSP-made ZnO powder was steeper from the smallest size of 8.8 nm to the size of 47 nm before reaching a plateau. A sharp UV–vis absorption curve (steep slope) indicates a high degree of crystalline quality [29]. The improved crystal structure for the larger size ZnO was in good agreement with the XRD and PL-measurements.

#### 3.2. Photocatalytic activity

The dependence of percent conversion of MB decomposition after 60 min on the particle size of ZnO powders is shown in Fig. 6. Irradiation in the absence of photocatalyst for 60 min revealed no change in the MB concentration, confirming that the MB cannot be degraded by 365 nm irradiation alone. The percentages of MB degradation increased from 30 to 70% when the particle size of as-synthesized ZnO powders increased from 8.8 to 47 nm. The photocatalytic performances for MB degradation of the as-synthesized and annealed FSP-ZnO catalysts are also shown as the plots of  $(C/C_0)$  versus time in Fig. 7 in which the results for commercial photocatalysts Degussa P25 ( $d_{XRD} = 20.1 \text{ nm}$ ) and JRC-TiO-1 titania ( $d_{XRD}$  = 15.5 nm) and irradiation in the absence of catalyst are included. The photocatalytic activity of the as-synthesized flamemade ZnO powders was superior to both P25 and JRC-TiO-1 titania when their particle sizes were larger than 30 nm with the as-syn ZnO-47 nm showed the highest activity. The rate constant assuming first-order kinetics of ZnO-47 nm was determined to be 1.7 and 7.2 times higher than those of degussa P25 and JRC-TiO-1 titania, respectively. For the larger particle sizes of ZnO powder obtained by annealing post-treatment, the percentages of MB degradation gradually decreased from 70 to 55%. The lower photocatalytic efficiency can be ascribed by the decrease in BET surface area, which lowered the adsorption of dye molecules on the catalyst surface.

In general, photocatalysis can be considered to be dominated by two linked mechanisms, namely photo phenomena or the interaction of light with the material to form electron-hole pairs, and secondly surface catalytic effects [42]. The photo aspect is sensitive to crystal defects while the surface catalytic effect is mainly dominated by the specific surface area. In this study, the photocatalytic performance of FSP-ZnO nanoparticles was found to increase with increasing crystalline quality of ZnO as illustrated by a linear relationship between the PL intensity of NBE bands and the percent conversion of MB decomposition after 60 min (Fig. 8). It is suggested that the photo phenomena (the interaction of light with the material to form electron-hole pairs) played decisive role on the photocatalytic performance of FSP-ZnO nanoparticles than the surface area for the ZnO particle size range 8.8-47.0 nm. Fig. 9a shows the corresponding rate constants (on a fixed mass basis) as a function of ZnO crystallite size. The rate constant increased from 0.33 to  $1.36 \,h^{-1}$  as the crystallite size increased from 8.8 to 47.0 nm and then slightly dropped when the crystallite size was further increased. On the other hand, when the rate constants are presented on an SSA normalized basis (Fig. 9b), an increase of photocatalytic activity of ZnO nanoparticles increased with increasing ZnO particle size from 8.8 to 67.1 nm and then remained relatively constant. The ZnO-47 nm performs best on a mass basis due to its optimum crystallinity and surface area while the ZnO-67.1 nm performs better on a surface area normalized basis, as the crystal quality within the ZnO particles was higher. For the flame-made materials, the crystalline quality would be expected to improve with increasing of the enthalpy density, flame height, and hightemperature residence time. The effect of the crystal size of ZnO on the photocatalytic activity has been reported by many researchers. They also reported the optimum size for which the photocatalytic activity of ZnO is maximized [19–23]. The optimum sizes of ZnO reported in literatures were varied depending on the preparation and pretreatment methods. The decrease of photocatalytic activity of ZnO when the particle size of ZnO was larger than optimum size was explained by the decrease of surface area.

#### 4. Conclusions

The FSP-synthesized ZnO nanoparticles have shown to be better photocatalysts for the degradation of methylene blue dye under UV irradiation, compared to the Degussa P-25 and the JRC-TiO<sub>2</sub> commercial photocatalysts. The photocatalytic activities of the FSP-ZnO nanoparticles were found to be correlated well with their crystalline quality. For those prepared by one-step FSP method with average particle size 8.8–47.0 nm, improved crystal quality as well as higher photocatalytic activities were obtained by increasing flame enthalpy density, flame height, and high-temperature residence time during the FSP synthesis. However, the larger ZnO particle sizes (52.6–103.5 nm) obtained by anneal-

ing post-treatment of the FSP-ZnO at high temperature, showed a descending trend of the photocatalytic activity due to the significant decrease of surface availability for reactant adsorption and light absorption of the annealed ZnO particles.

#### Acknowledgements

The financial supports from the Thailand Research Fund (TRF) and the Office of Higher Education Commission are gratefully acknowledged.

#### References

- C. Allegre, M. Maisseu, F. Charbit, P. Moulin, Coagulation-flocculation-decantation of dye house effluents: concentrated effluents, J. Hazard. Mater. B 116 (2004) 57–64.
- [2] V. Golob, A. Vinder, M. Simonic, Efficiency of the coagulation/flocculation method for the treatment of dyebath effluents, Dyes Pigments 67 (2005) 93–97.
- [3] A. Alinsafi, M. Khemis, M.N. Pons, J.P. Leclerc, A. Yacoubi, A. Benhammou, A. Nejmeddine, Electro-coagulation of reactive textile dyes and textile wastewater, Chem. Eng. Proc. 44 (2005) 461–470.
- [4] S. Papic, N. Koprivanac, A. LoncaricBozic, A. Metes, Removal of some reactive dyes from synthetic wastewater by combined Al(III) coagulation/carbon adsorption process, Dyes Pigments 62 (2004) 291–298.
- [5] K. Tanaka, K. Padermpole, T. Hisanaga, Photocatalytic degradation of commercial azo dyes, Water Res. 34 (2000) 327–333.
- [6] N.S. Allen, M. Edge, J. Verran, J. Stratton, J. Maltby, C. Bygott, Photocatalytic titania based surfaces: environmental benefits, Polym. Degrad. Stab. 9 (2008) 1632–1646.
- [7] S. Sakthivel, B. Neppolian, M.V. Shankar, B. Arabindoo, M. Palanichamy, V. Murugesan, Solar photocatalytic degradation of azo dye: comparison of photocatalytic efficiency of ZnO and TiO<sub>2</sub>, Sol. Energy Mater. Sol. Cells 77 (2003) 65–82
- [8] M.A. Behnajady, N. Modirshahla, R. Hamzavi, Kinetic study on photocatalytic degradation of C.I. Acid Yellow 23 by ZnO photocatalyst, J. Hazard. Mater. 133 (2006) 226–232.
- [9] A. Sharma, P. Rao, R.P. Mathur, S.C. Ameta, Photocatalytic reactions of xylidine ponceau on semiconducting zinc oxide powder, J. Photochem. Photobiol. A: Chem. 86 (1995) 197–200.
- [10] A.A. Khodja, T. Sehili, J.F. Pilichowski, P. Boule, Photocatalytic degradation of 2-phenylphenol on TiO<sub>2</sub> and ZnO in aqueous suspensions, J. Photochem. Photobiol. A: Chem. 141 (2001) 231–239.
- [11] A. Akyol, H.C. Yatmaz, M. Bayramoglu, Photocatalytic decolorization of Remazol Red RR in aqueous ZnO suspensions, Appl. Catal. B: Environ. 54 (2004) 19–24.
- [12] R. Kavitha, S. Meghani, V. Jayaram, Synthesis of titania films by combustion flame spray pyrolysis technique and its characterization for photocatalysis, Mater. Sci. Eng. B 139 (2007) 134–140.
- [13] N. Daneshvar, D. Salari, A.R. Khataee, Photocatalytic degradation of azo dye acid red 14 in water on ZnO as an alternative catalyst to TiO<sub>2</sub>, J. Photochem. Photobiol. A: Chem. 162 (2004) 317–322.
- [14] P. Pawinrat, O. Mekasuwandumrong, J. Panpranot, Synthesis of Au–ZnO and Pt–ZnO nanocomposites by one-step flame spray pyrolysis and its application for photocatalytic degradation of dyes, Catal. Commun. 10 (2009) 1380–1385.
- [15] A.P. Alivisatos, Perspectives on the physical chemistry of semiconductor nanocrystals, J. Phys. Chem. 100 (1996) 13226–13239.
- [16] A. Henglein, Small-particle research: physicochemical properties of extremely small colloidal metal and semiconductor particles, Chem. Rev. 89 (1989) 1861–1873.
- [17] M.R. Hoffmann, S.T. Martin, W. Choi, D.W. Bahnemann, Environmental applications of semiconductor photocatalysis, Chem. Rev. 95 (1995) 69–96.
- cations of semiconductor photocatalysis, Chem. Rev. 95 (1995) 69–96.
  [18] D. Beydoun, R. Amal, G. Low, S. McEvoy, Role of nanoparticles in photocatalysis,
  J. Nanopart. Res. 1 (1999) 439.

- [19] H. Wang, C. Xie, W. Zhang, S. Cai, Z. Yang, Y. Gui, Comparison of dye degradation efficiency using ZnO powders with various size scales, J. Hazard. Mater. 141 (2007) 645–652.
- [20] L. Jing, F. Yuan, H. Hou, B. Xin, W. Cai, H. Fu, Relationships of surface oxygen vacancies with photoluminescence and photocatalytic performance of ZnO nanoparticles, Sci. China Ser. B Chem. 48 (2005) 25.
- [21] A.C. Dodd, A.J. McKinley, M. Saunders, T. Tsuzuki, Effect of particle size on the photocatalytic activity of nanoparticulate zinc oxide, J. Nanopart. Res. 8 (2006) 43–51.
- [22] D. Li, V. Balek, N. Ohashi, T. Mitsuhashi, S. Hishita, H. Haneda, Self-assembly prismatic aggregates formed during the calcination of ZnO powders: in situ monitoring by ETA technique and their photocatalytic properties, J. Colloid Interface Sci. 289 (2005) 472–478.
- [23] S.E. Pratsinis, Flame aerosol synthesis of ceramic powders, Prog. Energy Combust. Sci. 24 (1998) 197–219.
- [24] T. Tani, L. Ma'dler, S.E. Pratsinis, Homogeneous ZnO nanoparticles by flame spray pyrolysis, J. Nanopart. Res. 4 (2002) 337–343.
- [25] A. Teleki, S.E. Pratsinis, K. Kalyanasundaram, P.I. Goumab, Sensing of organic vapors by flame-made TiO<sub>2</sub> nanoparticles, Sens. Actuators B 119 (2006) 683-690.
- [26] H. Briesen, A. Fuhrmann, S.E. Pratsinis, The effect of precursor in flame synthesis of  $SiO_2$ , Chem. Eng. Sci. 53 (1998) 4105–4112.
- [27] L. Mädler, W.J. Stark, S.E. Pratsinis, Flame-made ceria nanoparticles, J. Mater. Res. 17 (2002) 1356–1362.
- [28] S. Hannemann, J. Grunwaldt, P. Lienemann, D. Günther, F. Krumeich, S.E. Pratsinis, A. Baiker, Combination of flame synthesis and high-throughput experimentation: The preparation of alumina-supported noble metal particles and their application in the partial oxidation of methane, Appl. Catal. A: Gen. 316 (2007) 226–239.
- [29] M.J. Height, S.E. Pratsinis, O. Mekasuwandumrong, P. Praserthdam, Ag–ZnO catalysts for UV-photodegradation of methylene blue, Appl. Catal. B: Environ. 63 (2006) 305–312.
- [30] B. Marıĭ, F.J. Manjoĭn, M. Mollar, J. Cembrero, R. Gómez, Photoluminescence of thermal-annealed nanocolumnar ZnO thin films grown by electrodeposition, Appl. Surf. Sci. 252 (2006) 2826–2831.
- [31] J. Lim, K. Shin, H.W. Kim, C. Lee, Effect of annealing on the photoluminescence characteristics of ZnO thin films grown on the sapphire substrate by atomic layer epitaxy, Mater. Sci. Eng. B107 (2004) 301–304.
- [32] N. Serpone, D. Lawless, R. Khairlutdinov, E. Pelizzetti, Subnanosecond relaxation dynamics in TiO2 colloidal sols (particle sizes Rp=1.0-13.4 nm). Relevance to heterogeneous photocatalysis, J. Phys. Chem. 99 (1995) 16655-16661.
- [33] A. Umar, S. Lee, Y.H. Im, Y.B. Hahn, Flower-shaped ZnO nanostructures obtained by cyclic feeding chemical vapour deposition: structural and optical properties, Nanotechnology 16 (2005) 2462–2468.
- [34] T.S. Vaishnavi, P. Haridoss, C. Vijayan, Optical properties of zinc oxide nanocrystals embedded in mesoporous silica, Mater. Lett. 62 (2008) 1649–1651.
- [35] L. M\u00e4dler, W.J. Stark, S.E. Pratsinis, Rapid synthesis of stable ZnO quantum dots, J. Appl. Phys. 92 (2002) 6537–6540.
- [36] F. Leiter, H. Alves, D. Pfisterer, N.G. Romanov, D.M. Hofmann, B.K. Meyer, Oxygen vacancies in ZnO, Physica B 340–342 (2003) 201–204.
- [37] X. Li, B. Zhang, H. Zhu, X. Dong, X. Xia, Y. Cui, K. Huang, G. Du, Properties of ZnO thin films grown on Si substrates by photo-assisted MOCVD, Appl. Surf. Sci. 254 (2008) 2081–2084.
- [38] X.Q. Wei, B.Y. Man, M. Liu, C.S. Xue, H.Z. Zhuang, C. Yang, Blue luminescent centers and microstructural evaluation by XPS and Raman in ZnO thin films annealed in vacuum, N-2 and O-2, Physica B 388 (2007) 145–152.
- [39] D. Chu, Y. Zeng, D. Jiang, Hydrothermal synthesis and optical properties of Pb<sup>2+</sup> doped ZnO nanorods, Mater. Lett. 60 (2006) 2783–2785.
- [40] K. Vanheusden, W.L. Warren, C.H. Seager, D.R. Tallant, J.A. Voigt, B.E. Gnade, Mechanisms behind green photoluminescence in ZnO phosphor powders, J. Appl. Phys. 79 (1996) 7983–7990.
- [41] J. Wang, L. Gao, Hydrothermal synthesis and photoluminescence properties of ZnO nanowires, Solid State Commun. 132 (2004) 269.
- [42] Y.V. Kolenko, B.R. Churagulov, M. Kunst, L. Mazerolles, C. Colbeau-Justin, Photocatalytic properties of titania powders prepared by hydrothermal method, Appl. Catal. B: Environ. 54 (2004) 51–58.

# Flow Pattern of Liquid Multiphase Flow in Microreactors with Different Guideline Structures

Chayanoot Kositanont<sup>1</sup>, Sompong Putivisutisak<sup>2</sup>, Piyasan Praserthdam<sup>1</sup>, Suttichai Assabumrungrat<sup>1</sup>, Hiroshi Yamada<sup>3</sup> and Tomohiko Tagawa<sup>3</sup>

<sup>1</sup>Department of Chemical Engineering, Faculty of Engineering, Chulalongkorn University, Bangkok 10330, Thailand

<sup>2</sup>Department of Mechanical Engineering, Faculty of Engineering, Chulalongkorn University, Bangkok 10330, Thailand

<sup>3</sup>Department of Chemical Engineering, Nagoya University, Chikusa-ku, Nagoya-shi, Aichi 464-8603, Japan

Keywords: Microstructure, Multiphase Flow, Guideline Structure, CFD, Flow Pattern

The present study investigates CFD simulation of aqueous-organic two phase flow in microreactors with a guideline structure. The guideline structure was developed in order to stabilize and to maintain parallel flow of liquids within the microreactors. The CFD simulation can well predict the flow patterns observed in experiments. Upon determining the flow pattern and stability, it is reported that, with the presence of guideline structure, the interface became more curved and stable. Finally, the role of the guideline structure on the flow development was also investigated.

#### Introduction

A microreactor such as a miniaturized reaction system with typical channel or chamber widths in a range of  $10{\text -}500\,\mu\text{m}$  (Lowe and Ehrfeld, 1999) offers some outstanding advantages over conventional reactor systems such as intensified mass and heat transport.

A number of reactions involving immiscible systems have been studied in microreactors over the past decade (Doku et al., 2005; Kiwi-Minsker and Renken, 2005; Alibour et al., 2010). For multiphase liquid-liquid systems such as organic-aqueous reaction systems, low solubility results in very low rates of reaction and extended reaction times. Microreactors possessing a large surface-to-volume ratio can reduce the mass transfer limitations involved. A stable multiphase parallel flow in microchannels can provide a phase separation of the product mixture at the exit and then reduce the requirements of post-treatment unit operation. A microchannel with guideline structure has been proposed in order to stabilize the parallel flow for multiliquid phase systems (Surmeian et al., 2002; Tokeshi et al., 2002; Maruyama et al., 2003; Tagawa et al., 2007).

Computational fluid dynamics (CFD) is a powerful technique applying numerical methods to analyze the flow and performance of process equipment. There are

Received on April 20, 2011; accepted on June 21, 2011 Correspondence concerning this article should be addressed to T. Tagawa (E-mail address: tagawa@nuce.nagoya-u.ac.jp). many advantages in CFD over experimental approaches; for example, it can predict microscopic phenomena which occur in a very short interval. Although there are a number of works focusing on the fluid dynamics in microchannels, simulation works on the system with guideline structures are rather limited (Maruyama *et al.*, 2004). In our study, we used FLUENT (ANSYS Inc.), a well-established commercial CFD solver, to investigate the fluid dynamic behaviors of multiphase flow in microchannels with guideline structures. Different guideline structures were considered in order to achieve stable multiphase flow in the microchannels.

#### 1. Simulation

In order to simulate multiphase flow through microchannels, a 2D geometrical model was generated using the pre-processor GAMBIT. The CFD simulation was carried out with FLUENT 6.3 (Fluent Inc., 2006).

The reliability of our approach was checked by performing a set of simulations with two-phase Taylor flow in the T-shaped microchannel model shown in **Figure 1** to compare with the results reported by Guo and Chen (2009). The fluid and surface properties were set according to those in the literature. The simulated slug lengths with the effect of both phase velocities were in good agreement with the experimental and numerical results of Guo and Chen, as shown in **Figure 2**.

In our study, a 2D geometrical model having 20,040 cells was generated for the microchannel, shown in

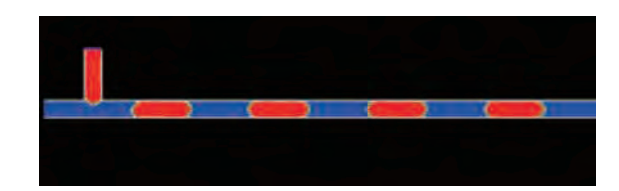
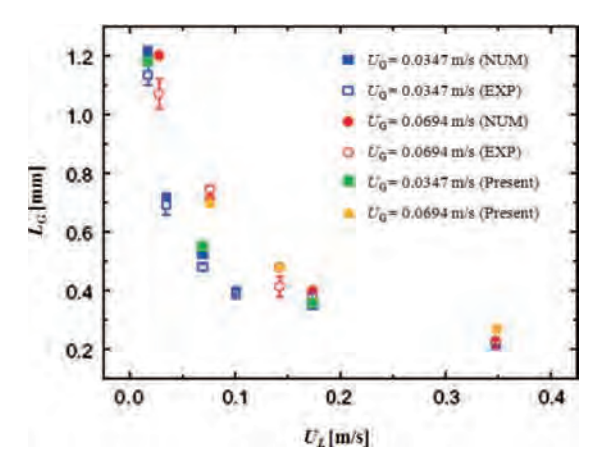


Fig. 1 The simulated Taylor flow in microchannel ( $U_{\rm G} = 0.0694 \, \text{m/s}$ ,  $U_{\rm L} = 0.0764 \, \text{m/s}$ )



**Fig. 2** Comparison of the slug length between the simulated results and results reported by Guo and Chen (2009)

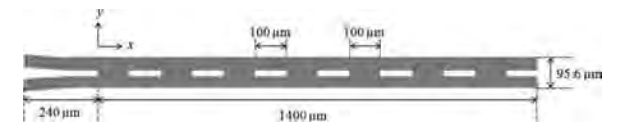


Fig. 3 The microchannel reactor with guideline structure (Model A)

Figure 3. The length and width were 1640 µm and 95.6  $\mu$ m, respectively. The grid sizes in the x direction for the reactor and the inlets were 5.56 and 7.00 µm, respectively. In the y direction, the maximum grid size was 2.51 µm and the minimum was 0.57 µm near the guideline walls. Pure water and toluene were used as aqueous and organic phases, respectively. The contact angle of water on glass in toluene and surface tension were measured at  $37^{\circ}$  and  $0.0371 \text{ kg/s}^2$  (Aota et al., 2009; Dessimoz et al., 2008). The feed flow rates of both phases were set equal at 0.02 mL/min (0.2035 m/s). The volume of fluid (VOF) method was applied to track the interface. The channel was initialized with water. For the inflows, constant velocities were specified as the boundary conditions. Fully-developed conditions were applied at outflows, and no-slip boundary conditions were used on the walls of the microchannel and guideline structures. A simulation with refined grid was carried out to confirm that the solution was independent of grid resolution. The effect of the guideline was investigated by varying the guideline structure, as summarized in **Table 1**.

Table 1 Guideline structure

Model	Length [μm]	Interval [µm]		
A	100	100		
В	100	180		
C (No guideline)	_	_		

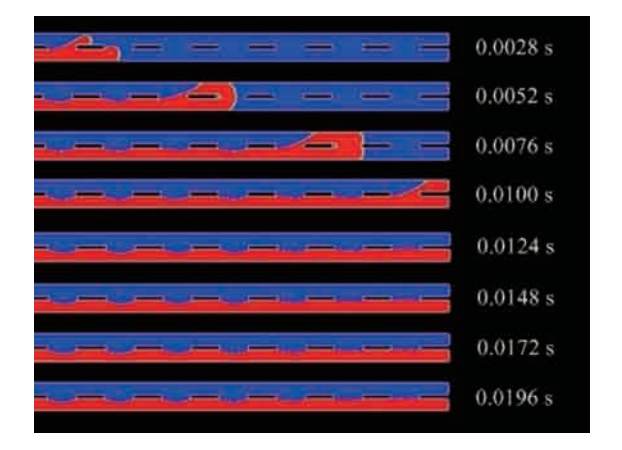


Fig. 4 The snapshots of flow development in Model A

Experiments were conducted with the microchannel sample represented by the model A under operational conditions reported in a previous paper (Tagawa *et al.*, 2007). The channel was washed and filled with distilled water before use.

#### 2. Results and Discussion

#### 2.1 Flow pattern and stability

The simulated flow development in the Model A microchannel is shown in **Figure 4**.

Before feeding the organic phase, the channel was filled with aqueous phase (blue). The top part of organic phase (toluene; red part) was spread over the entire channel and was divided from the aqueous phase to form two phase flow after passing a guideline. The parallel flow gradually stabilized with time. The flow pattern at 0.0148 s which offered the stabilized interface is compared with the experimental result under the same operation conditions in **Figure 5**. The stable interface was curved between the guideline structures (Figure 5(a)), which was in good agreement with that observed from the experiment (Figure 5(b)).

From the simulation results, the flow patterns for Models B and C are shown in **Figures 6** and **7**, respectively. For the cases with the existence of the guideline structure, Models A and B, the interface shape became more curved than the case without the guideline, Model C, at some positions along the channel length.

In Model A, which posses a smaller interval than

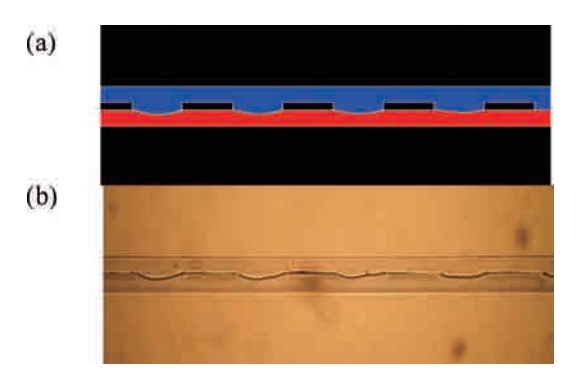


**Fig. 5** (a) The simulated stable two phase flow pattern with Model A at 0.0148 s and (b) experimental observation

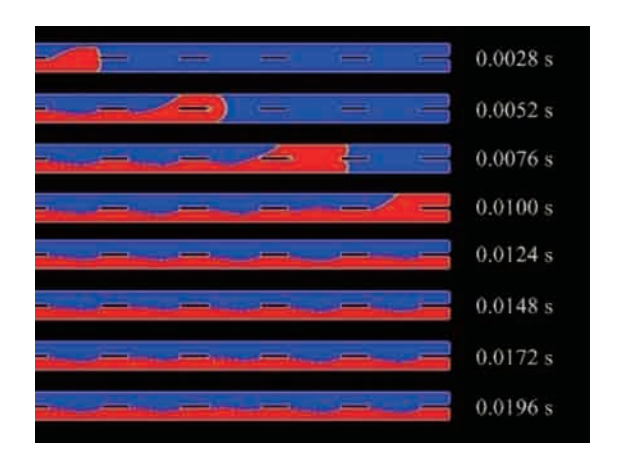


Fig. 6 The flow pattern at different times for Model B

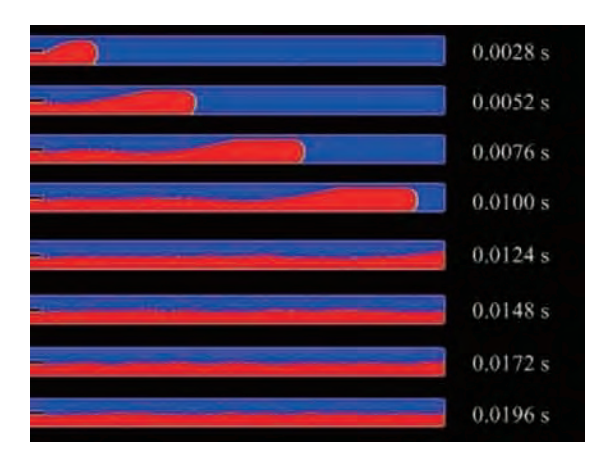


Fig. 7 The flow pattern at different times for Model C

Model B, the interface near the exits is much more flat and stable. Therefore Model A may provide better phase separation than Model B.

While the interface of Model A is stable after 0.0124 s, Model B seems to need more time to stabilize. On the other hand, the interface of Model C is more unstable with time as seen in Figure 7. Although the interface of Model C is near the center along the length of the microreactor, the instability with flow time makes



Fig. 8 The snapshots of flow developing with guideline structure in Model A

the separation uncontrollable.

#### 2.2 The role of guideline structure

The role of guideline on the flow development in the Model A microchannel is shown in **Figure 8**. It is observed that the fluids were kept in their own lanes after passing each guideline wall. The toluene stream was divided into two parts when reaching each structure. After passing the wall, the interface was pushed toward the corner of the wall and broken. Then, the fluids were guided in their own lanes.

#### **Conclusions**

The guideline structures turn the flat interface into a curve shape, which becomes more stable with flow time. The fluids are kept in their own lines after passing each guideline wall. In the smaller interval case, the interface position near the exits is close to the centerline, which is believed to provide better separation function; however, the interface area is decreased with more guideline walls and, therefore, the reaction conversion may be reduced in the case of operation with reaction. Thus, the guideline structure geometry should be further studied in more detail in order to achieve an optimized design. It is important to note that the obtained design needs to be confirmed through experiment.

#### Acknowledgements

The support of Dusadeepipat, the Thailand Research Fund and Commission on Higher Education and Nagoya University Program for Academic Exchange (NUPACE) are gratefully acknowledged.

#### Literature Cited

Aota, A., K. Mawatari, S. Takahashi, T. Matsumoto, K. Kanda, R. Anraku, A. Hibara, M. Tokeshi and T. Kitamori; "Phase Separation of Gas-Liquid and Liquid-Liquid Microflows in Microchips," *Microchim. Acta*, 164, 249–255 (2009)

Aljbour, S., H. Yamada and T. Tagawa; "Mass Transfer Performance of a Capillary Microreactor during Ultrasound Assisted Phase Transfer Catalysis," J. Chem. Eng. Japan, 43, 429–434 (2010)

Dessimoz, A. L., L. Cavin, A. Renken and L. Kiwi-Minsker; "Liquid-Liquid Two-Phase Flow Patterns and Mass Transfer

VOL. 44 NO. 9 2011 651

- Characteristics in Rectangular Glass Microreactors," *Chem. Eng. Sci.*, **63**, 4035–4044 (2008)
- Doku, G. N., W. Verboom, D. N. Reinhoudt and A. V. D. Berg; "On-Microchip Multiphase Chemistry—A Review of Microreactor Design Principles and Reagent Contacting Modes," *Tetrahedron*, 61, 2733–2742 (2005)
- Fluent Inc.; FLUENT 6.3 Documentation, Fluent Incorporated, Lebanon, U.S.A. (2006)
- Guo, F. and B. Chen; "Numerical Study on Taylor Bubble Formation in a Micro-Channel T-Junction Using VOF Method," *Microgravity Sci. Technol.*, 21, S51–S58 (2009)
- Kiwi-Minsker, L. and A. Renken; "Microstructured Reactors for Catalytic Reactions," Catal. Today, 110, 2–14 (2005)
- Lowe, H. and W. Ehrfeld; "State-of-the-Art in Microreaction Technology: Concepts, Manufacturing and Applications," *Electrochim. Acta*, 44, 3679–3689 (1999)
- Maruyama, T., J. Uchida, T. Ohkawa, T. Futami, K. Katayama, K. Nishizawa, K. Sotowa, F. Kubota, N. Kamiya and M. Goto;

- "Enzymatic Degradation of *p*-Chlorophenol in a Two-Phase Flow Microchannel System," *Lab Chip*, **3**, 308–312 (2003)
- Maruyama, T., T. Kaji, T. Ohkawa, K. Sotowa, H. Matsushita, F. Kubota, N. Kamiya, K. Kusakabea and M. Goto; "Intermittent Partition Walls Promote Solvent Extraction of Metal Ions in a Microfluidic Device," *Analyst*, 129, 1008–1013 (2004)
- Surmeian, M., M. N. Slyadnev, H. Hisamoto, A. Hibara, K. Uchiyama and T. Kitamori; "Three-Layer Flow Membrane System on a Microchip for Investigation of Molecular Transport," *Anal. Chem.*, 74, 2014–2020 (2002)
- Tagawa, T., S. Aljbour, M. Matouq and H. Yamada; "Micro-Channel Reactor with Guideline Structure for Organic-Aqueous Binary System," Chem. Eng. Sci., 62, 5123–5126 (2007)
- Tokeshi, M., T. Minagawa, K. Uchiyama, A. Hibara, K. Sato, H. Hisamoto and T. Kitamori; "Continuous-Flow Chemical Processing on a Microchip by Combining Microunit Operations and a Multiphase Flow Network," Anal. Chem., 74, 1565–1571 (2002)



Article

# The Influence of Mixed Activators on Ethylene Polymerization and Ethylene/1-Hexene Copolymerization with Silica-Supported Ziegler-Natta Catalyst

Nichapat Senso  $^1$ , Supaporn Khaubunsongserm  $^2$ , Bunjerd Jongsomjit  $^1$  and Pivasan Praserthdam  $^{1,*}$ 

- <sup>1</sup> Center of Excellence on Catalysis and Catalytic Reaction Engineering, Department of Chemical Engineering, Faculty of Engineering, Chulalongkorn University, Bangkok 10330, Thailand
- <sup>2</sup> PTT Research and Technology Institute, PTT Public Company Limited, Wangnoi, Ayuthaya 13170, Thailand
- \* Author to whom correspondence should be addressed; E-Mail: piyasan.p@chula.ac.th; Tel.: +662-218-6869; Fax: +662-218-6868.

Received: 15 November 2010; in revised form: 10 December 2010 / Accepted: 14 December 2010 / Published: 16 December 2010

**Abstract:** This article reveals the effects of mixed activators on ethylene polymerization and ethylene/1-hexene copolymerization over MgCl<sub>2</sub>/SiO<sub>2</sub>-supported Ziegler-Natta (ZN) catalysts. First, the conventional ZN catalyst was prepared with SiO<sub>2</sub> addition. Then, the catalyst was tested for ethylene polymerization and ethylene/1-hexene (E/H) co-polymerization using different activators. Triethylaluminum (TEA), tri-n-hexyl aluminum (TnHA) and diethyl aluminum chloride (DEAC), TEA+DEAC, TEA+TnHA, TnHA+ DEAC, TEA+DEAC+TnHA mixtures, were used as activators in this study. It was found that in the case of ethylene polymerization with a sole activator, TnHA exhibited the highest activity among other activators due to increased size of the alkyl group. Further investigation was focused on the use of mixed activators. The activity can be enhanced by a factor of three when the mixed activators were employed and the activity of ethylene polymerization apparently increased in the order of TEA+ DEAC+TnHA > TEA+DEAC > TEA+TnHA. Both the copolymerization activity and crystallinity of the synthesized copolymers were strongly changed when the activators were changed from TEA to TEA+DEAC+TnHA mixtures or pure TnHA and pure DEAC. As for ethylene/1-hexene copolymerization the activity apparently increased in the order of TEA+DEAC+TnHA > TEA+TnHA > TEA+DEAC > TnHA+DEAC > TEA > TnHA > DEAC. Considering the

*Molecules* **2010**, *15* 

properties of the copolymer obtained with the mixed TEA+DEAC+TnHA, its crystallinity decreased due to the presence of TnHA in the mixed activator. The activators thus exerted a strong influence on copolymer structure. An increased molecular weight distribution (MWD) was observed, without significant change in polymer morphology.

**Keywords:** Ziegler-Natta catalyst; silica support; polyethylene; mixed activator; ethylene polymerization

#### 1. Introduction

Progress in catalyst technology has lead to the synthesis of a rich set of new polymers with different structures and performances to meet the progressive demands of modern industry and life [1-12]. Recently, branched polyethylenes such as linear low-density polyethylene (LLDPE) have grown in importance in industry because of the specific properties that can be obtained by varying comonomer content and polymerization conditions. The recent development of homogeneous single-site catalyst makes it possible to synthesize the copolymers with completely different structures and performances from traditional polyethylenes [13]. The ethylene/α-olefin copolymers obtained by metallocene catalysts show homogeneous comonomer distribution and narrow molecular weight distributions in comparison with those obtained with traditional Ziegler–Natta (ZN) catalysts [14]. The correlation between the structures of the ethylene/α-olefin copolymers obtained with ZN catalysts and their properties has been extensively studied [15,16]. However, easy methods to control polymer properties and catalytic activity in polymerization system are still of concern to the industry.

One of the most important factors in ethylene and ethylene/ $\alpha$ -olefin polymerization is the choice of alkyl aluminum used to control the activity and polymer characteristics. The alkyl aluminums are often added to the reactor during slurry polymerization with ZN catalyst and conventional supported metallocene/MAO catalyst to scavenge impurities. In polymerization systems, alkyl aluminums also act as activators responsible for the generation of active sites. There are many reports on the use of alkyl aluminum as activators in the polymerization of ethylene and ethylene/α-olefins using ZN catalysts [17-23]. Trialkyl aluminum compounds are usually preferred over the halogen-containing analogues because higher polymerization rates can be obtained with the former. Alkyl aluminums such as trimethyl aluminum (TMA), triethyl aluminum (TEA), tri-n-hexyl aluminum (TnHA) and triisobutyl aluminum (TiBA), as well as diethyl aluminum chloride (DEAC) have been used in olefin polymerizations [24-31]. In general, it has been found that an increase in size of the alkyl groups  $(C_nH_{2n+1})$  up to approximately n = 11 has enhanced catalytic activity. The study by Wanke et al. [18] revealed that increasing the size of alkyl group with n < 11 produces an increase in the activity and when a very large alkyl groups (n = 18) was used, the catalytic activity was very low upon when using the ZN catalyst for ethylene polymerization. An exception to these general trends was observed by Nooijen [17]. His results showed a strong effect of activators (TEA, TiBA, TnOA and IPRA) diffusion on the rate of activation of MgCl<sub>2</sub>-supported Ziegler-Natta catalyst in slurry polymerization. At a constant ratio of activator to catalyst, the maximum activity depends on the diffusion of the activator.

*Molecules* **2010**, *15* 

The properties of polymer, such as the morphology of polymer product particles [22], were also controlled by type of activator, the product molar mass distribution, the average catalyst activity, and the shape of the activity-time profiles [22,23]. Increasing the size of the ligands attached to aluminium atoms increased the average molar masses and resulted in narrower molar weight distributions of polyethylene [18]. Terano *et al.* [23] reported that the molecular weight distribution (MWD) of the polyethylene obtained from the functionalized SiO<sub>2</sub>-supported catalyst changed markedly from broad and multimodal to narrow and unimodal depending on the type of activator used. In the case of TEA, a broad trimodal MWD was observed, while for DEAC, the MWD of polyethylene was very narrow and unimodal [23]. In the case of poly[propylene-co-(7-methyl-1,6-otadiene)], the different activators produced polypropylene with a wide range of MWD [32].

Not only single activators are used in α-olefin polymerization, but also mixtures of alkyl aluminums are interesting subjects for improvement of the catalytic activity and polymer properties. Fan *et al.* [20] synthesized PE-PP copolymers using TEA, TIBA or TEA+TIBA mixtures as activators with MgCl<sub>2</sub>/SiO<sub>2</sub>/TiCl<sub>4</sub>/diester-ZN catalyst in a slurry polymerization process. Their results showed that the behaviors of the TEA/TIBA mixture in catalytic systems were not a simple superposition of those activated by the TEA or TIBA alone. When a 50:50 TEA+TIBA mixture was used, the copolymerization activity became the highest, and the yields of both systems were highly random copolymers. In their articles, rapid exchange between the alkyl groups in mixtures of TEA with the *iso*-butyl group in TIBA may be an important reason for the increase in catalytic activity and yields of both the random copolymer and the segmented copolymer parts, which were close to the highest level in PE-PP copolymer.

In spite of these interesting results, the effect of mixed alkyl aluminum on catalytic activity of ethylene polymerization and ethylene/1-hexene copolymerization, and polymer properties has received little attention, even though it could be of crucial importance to successfully design and operate industrial polymerization processes. In the current study, the effect of various activator mixtures on activity, product morphology and molecular weight distribution of polyethylene and ethylene/1-hexene copolymere synthesized by the MgCl<sub>2</sub>/SiO<sub>2</sub>/TiCl<sub>4</sub>/THF-ZN catalyst was investigated. The obtained polymers were characterized by means of X-ray diffraction (XRD), gel permeation chromatography (GPC). differential scanning calorimetry (DSC), nuclear magnetic and resonance (<sup>13</sup>C-NMR) techniques.

#### 2. Results and Discussion

#### 2.1. Catalyst characterization

In general, the MgCl<sub>2</sub>/SiO<sub>2</sub>/TiCl<sub>4</sub>/THF-ZN catalyst has been developed for an excellent morphology control of polymer particles under the fluidized bed reactor conditions [33,34]. Kim *et al.* [34,35] reported that catalyst characteristics such as the ratio of SiO<sub>2</sub>/MgCl<sub>2</sub> had an influence on the shape and size of the MgCl<sub>2</sub>/SiO<sub>2</sub>/TiCl<sub>4</sub>/THF-ZN catalyst used for ethylene polymerization and ethylene/1-butene copolymerization. In this study, the MgCl<sub>2</sub>/SiO<sub>2</sub>/TiCl<sub>4</sub>/THF-ZN catalyst was prepared as described in the experimental part using a SiO<sub>2</sub>/MgCl<sub>2</sub> molar ratio of 1:1. Based on this preparation, the presence of Ti content in catalyst is 2.33 wt% (ICP). The shape and size of the catalyst were observed by SEM as

*Molecules* **2010**, *15* **9326** 

shown in Figure 1. The prepared catalyst exhibits a spherical shape and unimodal size distribution. Thus, the aggregated and melted form of catalyst particles seen in Figure 1 (top) are only present in a small amounts. These fractions possibly resulted from contact of catalyst particles with moisture and oxygen, when analyzed by SEM. The average diameter of obtained catalyst is approximately 30, µm as seen in Figure 1 (bottom).

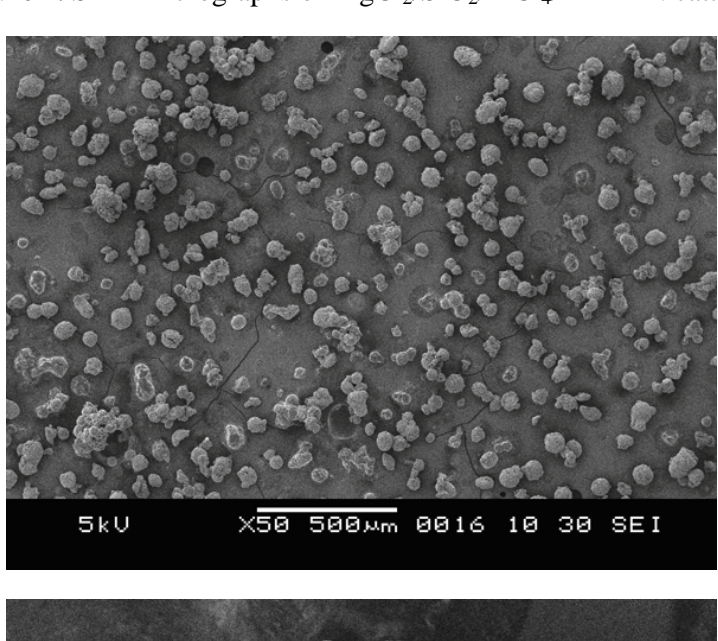
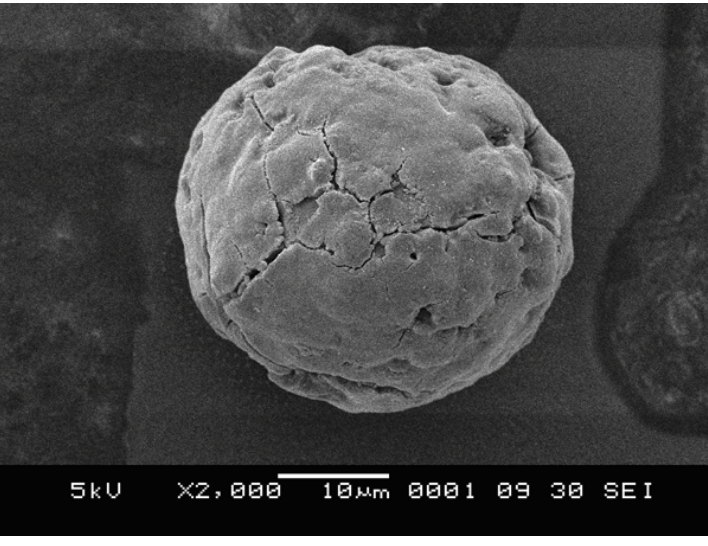


**Figure 1.** SEM micrographs of MgCl<sub>2</sub>/SiO<sub>2</sub>/TiCl<sub>4</sub>/THF-ZN catalyst.

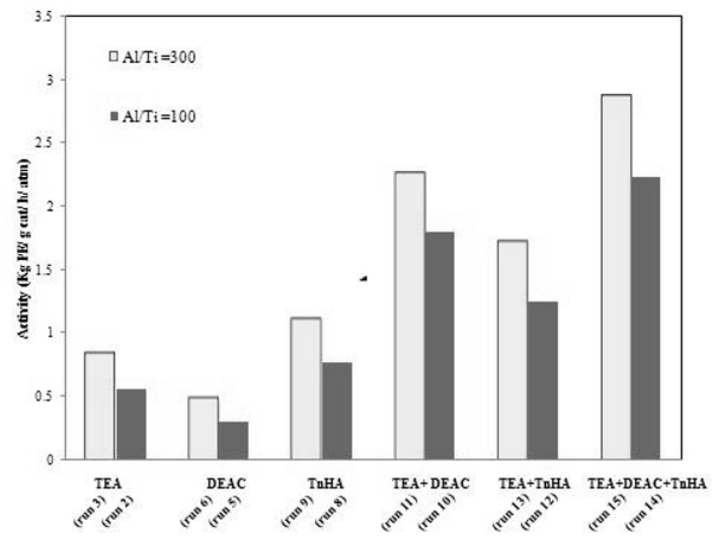


### 2.2. Ethylene homo-polymerization

For commercial production of polyethylene, the MgCl<sub>2</sub>/SiO<sub>2</sub>-supported ZN catalyst exhibits high catalytic activity when TEA is used as activator. This activator provides the highest activity among other activators, including diethyl aluminum chloride (DEAC) and tri-*n*-hexyl aluminum (TnHA) [24]. The MgCl<sub>2</sub>/SiO<sub>2</sub>/TiCl<sub>4</sub>/THF-ZN catalyst shows high catalytic activity for ethylene polymerization. In this work, the effects of different types of alkyl aluminums including TEA, DEAC, TnHA and mixed

alkyl aluminums on activity were investigated. The Al/Ti molar ratio was fixed at 100 and 300. The polymerization activities with various activators are shown in Figure 2 and Table 1.

**Figure 2.** Effect of various activators on ethylene polymerization activity using MgCl<sub>2</sub>/SiO<sub>2</sub>/TiCl<sub>4</sub>/THF-ZN catalyst.



**Note:** Total mass of supported catalyst = 0.006 mmol of Ti, titamiun content = 2.33 mmol Ti/ g cat; Polymerization temperature = 80 °C,  $P_{tot} = 8$  bar,  $P_{H2} = 3.5$  bar; Polymerization time = 2 h, ratio of Al/Ti = 100 and 300.

**Table 1.** Description of ethylene polymerization with various activators.

D		Activatora		A -4::4b	
Run – number	TEA (mol%)	DEAC (mol%)	TnHA (mol%)	Al/Ti	Activity <sup>b</sup> (kg PE/ g cat/ h/ atm)
1	100	-	-	100	0.53
2	100	-	-	100	0.55
3	100	-	-	300	0.83
4	_	100	-	100	0.32
5	-	100	-	100	0.30
6	-	100	-	300	0.48
7	-	-	100	100	0.78
8	-	-	100	100	0.76
9	-	-	100	300	1.10
10	50	50	-	100	1.79
11	50	50	-	300	2.25
12	50	-	50	100	1.25
13	50	-	50	300	1.71
14	33	33	33	100	2.23
15	33	33	33	300	2.86

<sup>&</sup>lt;sup>a</sup> Concentrations of TEA, DEAC and TnHA are 0.300 mmol/mL; <sup>b</sup> Ti concentration is 0.006 mmol/mL.

Considering the single activators, the catalytic activity was the highest when TnHA was employed, whereas DEAC exhibited the lowest activity. A similar trend was observed with regards to change in Al/Ti ratio. These results were also consistent with those reported by Lynch *et al.* [18] and Hammawa *et al.* [22]. For trialkyl aluminum with n < 11, the activity increases with the size of alkyl group [22]. It was observed that DEAC was a less effective activator than TnHA, as reported by Haward *et al.* [24].

They explained that there was an optimal ligand size for producing maximum catalyst activity. Based on this work, by mixing activators having different sizes of alkyl groups, the catalytic activity of each system was in the order of; TEA+DEAC+TnHA > TEA+DEAC > TEA+TnHA, as listed in Table 1. In addition, the mixed DEAC+TnHA (50:50) was also tested for ethylene polymerization (data not shown), but it gave low activity than seen for DEAC or TnHA alone. Hence, the catalytic activity can be enhanced by a factor of three when the suitable mixed activators are employed.

These results can be described by: (i) each type of alkyl aluminum has different reducing ability towards the catalyst, and hence produces different types of active sites [22], (ii) the optimal ligand size for producing maximum catalyst activity can be obtained by mixing the various types of activator [24], and (iii) it is related to the real mechanistic roles of alkyl aluminum activator in the formation of the active site in heterogeneous Ziegler-Natta catalysis, using either a monometallic or bimetallic active site model. Besides, changes in forms of mixed alkyl aluminums during polymerization were also a possible reason. To determine the rapid exchange of alkyl groups in the mixed alkyl aluminums, <sup>1</sup>H-NMR measurements were performed by Hatada *et al.* [36]. They found that the <sup>1</sup>H-NMR spectrum of the mixture of TEA and DEAC at room temperature displayed a rapid intermolecular exchange of ethyl groups. However, a new <sup>1</sup>H-NMR signal occurred upon the measurement at low temperature. In Scheme 1, we propose that the formation of new alkyl groups after mixing various alkyl groups may occur through various possible mechanisms. It should be noted that besides the formation of Al-ABC (as shown), other forms of mixed activator such as Al-ACC, Al-BBC, Al-BCC, and so on can occur.

**Scheme 1.** The possible formation of new alkyl groups after mixing (A, B and C refer to ethyl, *n*-hexyl and Cl).

The new alkyl groups may be suitable for adding more steric hindrance to the surface of catalyst enhancing the performance of ethylene to occupy the active species, as illustrated in Scheme 2. Moreover, the formation of catalyst might have a reducing ability to produce active sites for ethylene polymerization.

**Scheme 2.** Suggested mechanism of active site formation activated by new alkyl aluminum type (X: -Cl; A, B or C: ethyl, n-hexyl or Cl; □: coordination vacancy).

#### 2.3. Ethylene/1-hexene copolymerization

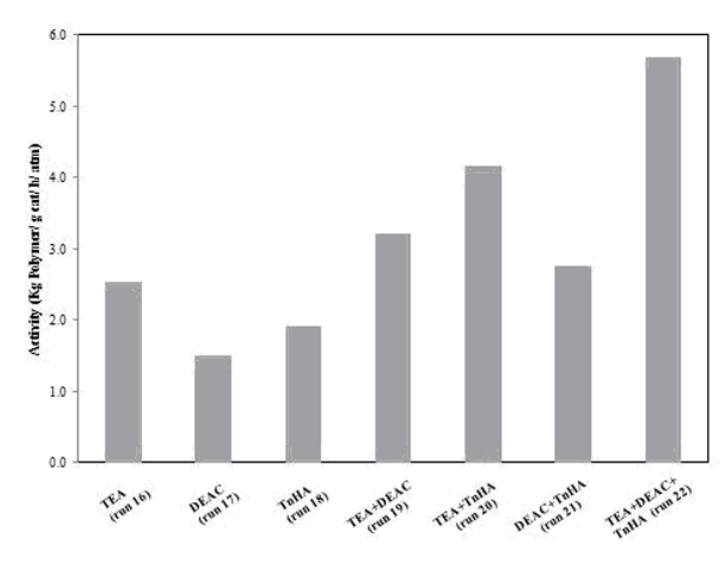
that ethylene/1-hexene (EH) polymerization catalyzed It known is also MgCl<sub>2</sub>/SiO<sub>2</sub>/TiCl<sub>4</sub>/THF-ZN catalyst in the slurry polymerization system using TEA as activator. However, the EH copolymerization with the catalyst activated by DEAC or TnHA has been found to exhibit different catalytic activity when compared to the system activated by TEA. To further explore the possibility of modifying catalytic activity and EH copolymer properties via changes in activator, TEA, DEAC, TnHA and their mixtures were employed in the equal molar ratio for each activator in the mixture. The Al/Ti molar ratio was kept constant at 300. The results are summarized in Table 2 and Figure 3.

**Table 2.** Activity of ethylene/1-hexene copolymerization with various ratios of activators and % 1-hexene insertion.

		Activator <sup>a</sup> used		Activity (kg	1-hexene	
Run number	TEA (mol%)	DEAC (mol%)	TnHA (mol%)	polymer/g cat/ h/ atm)	insertion (mol%) <sup>b</sup>	
16	100	-	-	2.53	1.27	
17	-	100	-	1.50	0.49	
18	-	-	100	1.91	1.90	
19	50	50	-	3.22	0.70	
20	50	-	50	4.15	1.26	
21	-	50	50	2.75	0.60	
22	33	33	33	5.69	1.10	

<sup>&</sup>lt;sup>a</sup> Ratio of Al/Ti =300; <sup>b</sup> 1-hexene insertion was determined by <sup>13</sup>C-NMR.

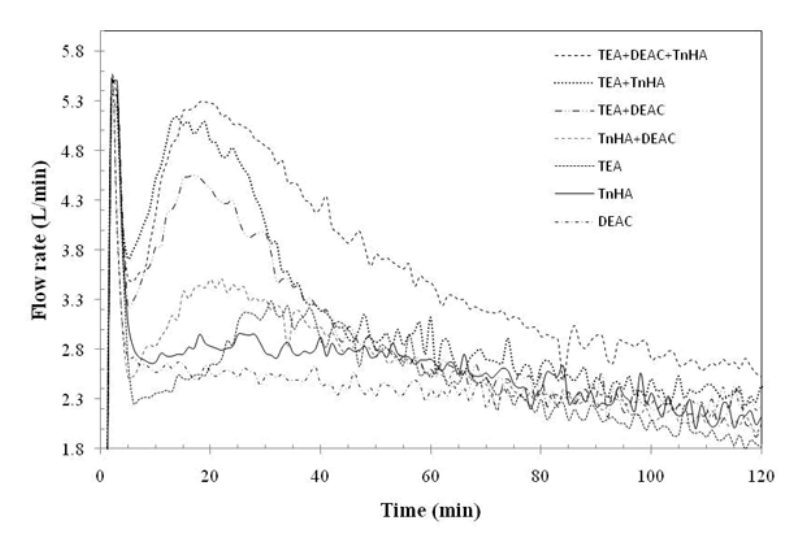
**Figure 3.** Effect of mixed activators on catalytic activity of MgCl<sub>2</sub>/SiO<sub>2</sub>/TiCl<sub>4</sub>/THF-ZN catalyst for ethylene/1-hexene copolymerization.



**Note:** Total mass of supported catalyst = 0.006 mmol Ti, titanium content = 2.33 mmol Ti/ g-cat, 1-hexene = 50 mL, polymerization temperature = 80 °C,  $P_{tot}$  = 8 bar,  $P_{H2}$  = 3.5 bar, polymerization time = 2 h, ratio of Al/Ti = 300.

Interestingly, the kinetic profile behaviors of ethylene/1-hexene copolymerization with various activators were not a simple superposition of those activated by TEA, DEAC or TnHA alone, as shown in Figure 4. From this viewpoint, this result supports the notion of a change of alkyl groups in the alkyl aluminum mixture as mentioned before. From Table 2 and Figure 3, it was evident that the activator exerted strong influence on both catalytic activity and copolymer properties. The activity increased upon mixing TEA, DEAC and TnHA (TEA+DEAC, TEA+TnHA and TEA+DEAC+TnHA). The insertion of 1-hexene in copolymer increased in the order of TnHA > TEA > DEAC > mixed activators. No relationship between the catalytic activity and 1-hexene insertion was found with the different activators.

**Figure 4.** Kinetic profile based on ethylene consumption with various activators for ethylene/1-hexene copolymerization.



**Note:** Total mass of supported catalyst = 0.006 mmol Ti, titanium content = 2.33 mmol Ti/ g-cat, 1-hexene = 50 mL, polymerization temperature = 80 °C,  $P_{tot}$  = 8 bar,  $P_{H2}$  = 3.5 bar, polymerization time = 2 h, ratio of Al/Ti = 300.

Many explanations have been put forth for the reported co-monomer effects on the enhancement of catalytic activity and can be classified as follows: (i) chemical and physical effects of co-monomer on the catalyst generation of active sites [37], (ii) increasing propagation rate constant (*kp*) [37], (iii) enhancement of the diffusion due to lower crystallinity [38], (iv) fracturing the catalyst, and (v) changing the oxidation state of Ti [38]. It seems that some of these explanations cannot possibly explain the mixed activator behavior, which should be concerned with the change in the active sites for the ZN catalyst with using different types of alkyl aluminum. Based on 1-hexene insertion, it seems that DEAC can effectively activate those active sites that produce partly crystalline copolymer, whereas the other activators such as TEA and TnHA were more efficient activators of active sites that produce amorphous copolymer. In the case of TEA+DEAC+TnHA mixture, it was able to activate both types of active sites, leading to a copolymerization system with high activity and slightly lower content of 1-hexene insertion. On the other hand, TnHA itself can produce a copolymer having relatively higher degree of 1-hexene insertion.

#### 2.4. Polymer characterization

# 2.4.1. Gel permeation chromatography (GPC) analysis

The M<sub>w</sub>, M<sub>n</sub> and MWD of the corresponding polymers are shown in Table 3. The MWD of the obtained polyethylene (Al/Ti ratio 300) gradually changed depending on the types of activator used. Apparently, TnHA produced polymers with a broader MWD as compared to polyethylene obtained from TEA and DEAC. Thus, the use of different types of activators in ethylene polymerization resulted in changes of the M<sub>w</sub> and MWD values of polyethylene. The mixed alkyl aluminum system tended to exhibit a broad polyethylene MWD, as shown in Table 3. This result was also consistent with the dependence of MWD on the type of alkyl aluminum activator as shown in a previous report [24]. This interesting phenomenon was considered to stem from the existence of multiplicity in the nature of active sites with different propagation, termination and chain transfer rates on the surface of functionalized MgCl<sub>2</sub>/SiO<sub>2</sub>-supported ZN catalyst. According to the GPC profiles (not shown), it might be speculated that mainly two kinds of active titanium precursors exist on the surface of functionalized MgCl<sub>2</sub>/SiO<sub>2</sub>-supported ZN catalyst. The various alkyl aluminum activators may provide different types of active sites and different oxidation state of Ti. The Mw, Mn and MWD results of the copolymers are also given in Table 3. The TEA, DEAC and TnHA gave M<sub>w</sub> of 295, 364 and 336 kg/mol, and MWD of 3.7, 3.6 and 4.2, respectively. The average molecular weights of copolymers obtained from mixed activators tended to decrease compared to those obtained with a single activator. On the contrary, the MWD of copolymers increased as the follows: TEA+DEAC+TnHA (5.6) > TEA+TnHA (4.5) > TnHA + (4.3) > TnHA + DEAC + (3.8) = TnHA + DEAC + (3.8) > TEA + (3.7) > DEAC + (3.6). These results showed no relationship among the  $M_w$ , MWD, reducing power and activity in copolymerization system.

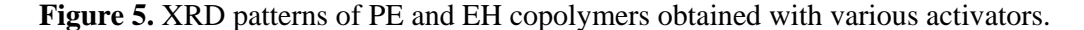
<b>Table 3.</b> $M_W$ , $M_n$ and polydispersity $(M_w/M_n)$	OU	porvetn	viene and	etny	viene/i-	nexene coporv	mer.
--	----	---------	-----------	------	----------	---------------	------

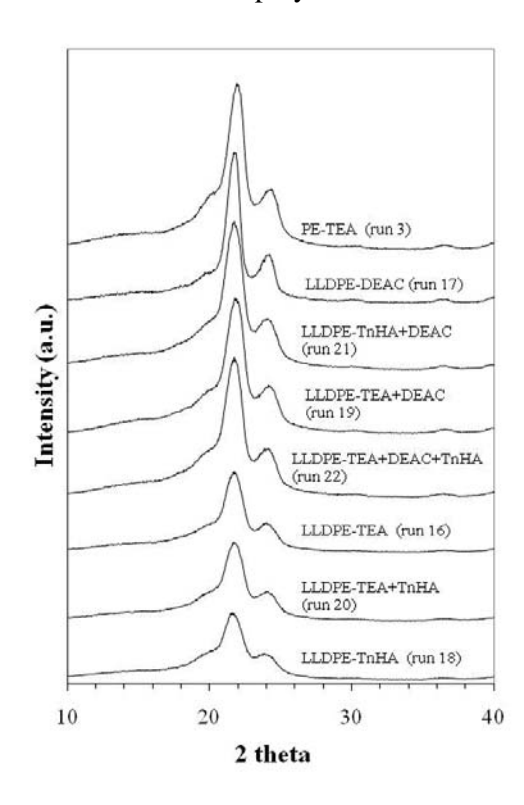
D	Manaman	Activator	M <sub>n</sub> M <sub>w</sub> M <sub>v</sub>		M <sub>w</sub> /M <sub>n</sub> <sup>a</sup>	$T_m^{\ b}$ (°C)	ď°	Crystallinity (%)	
Run	Monomer	Activator	(kg/ mol)	(kg/ mol)	NI <sub>w</sub> /NI <sub>n</sub>	1 <sub>m</sub> (°C)	(g/mL)	DSC <sup>d</sup>	X-ray <sup>e</sup>
3	Ethylene	TEA	74	299	4.0	136.5	0.955	66.0	71.3
6		DEAC	51	180	3.5	136.3	0.957	67.7	-
9		TnHA	103	474	4.6	135.9	0.956	66.3	-
11		TEA+ DEAC	31	175	5.6	136.3	0.957	67.7	-
13		TEA+ TnHA	86	344	4.0	135.9	0.957	67.7	-
15		TEA+ DEAC+	55	283	5.2	136.3	0.957	67.6	-
		TnHA							
16	Ethylene/	TEA	165	295	3.8	120.7	0.926	41.0	46.2
	1-hexene								
17		DEAC	56	364	6.5	124.4	0.943	55.5	60.1
18		TnHA	79	336	4.2	97.5	0.914	30.7	35.4
19		TEA+ DEAC	77	294	3.8	122.5	0.941	54.0	59.1
20		TEA+ TnHA	56	255	4.5	111.6	0.918	34.1	38.2
21		TnHA+ DEAC	54	209	3.8	123.7	0.943	55.3	60.3
22		TEA+ DEAC+	48	272	5.6	119.5	0.923	38.4	42.2
		TnHA							

<sup>&</sup>lt;sup>a</sup> Polydispersity index, evaluated as  $M_w/M_n$ , and determine by GPC analysis; <sup>b</sup> Melting temperature determined by DSC analysis; <sup>c</sup> Copolymer density determined according to the semi-empirical equation:  $d = (2195 + \Delta H_m)/2500$ ; <sup>d</sup> Crystallinity degree determined according to the equation:  $(\Delta H_m/\Delta H_m^{\circ}) \times 100$ , assuming  $\Delta H_m^{\circ} = 293$  J/g; <sup>e</sup> Crystallinity degree determined by XRD according to the equation:  $W_{c,x} = (I_{110} + 1.42I_{200}) / (I_{110} + 1.42I_{200} + 0.68I_a)$ .

#### 2.4.2. X-ray diffraction (XRD) and thermal properties

It is well known that the melting enthalpy  $(\Delta H_m)$  of an EH copolymer decreases with increasing comonomer content [30]. The insertion of the  $\alpha$ -olefin reduces both the degree of crystallinity and the melting temperature of the copolymer. Randall [39] found that for EH copolymer, the density of the sample decreases with increasing the comonomer content. Table 3 shows the melting temperatures of the EH copolymers obtained with different activators. It was very interesting that both melting temperature and enthalpy of melting decreased with TnHA. Figure 5 shows the XRD patterns of EH copolymers and homopolymer (PE) obtained with different activators. It was observed that the copolymers exhibit two crystalline peaks at 20 degree of 21.1 and 23.58 assigned to 110 and 200 spacing and one amorphous peak at 20 degree of 19.48. It was evident that the degree of crystallinity decreased with increasing comonomer content. The degrees of crystallinity calculated from both enthalpy and XRD are shown in Table 3. The results are very close to those reported by Mo et al. [14] and Quijada [1]. The values from XRD measurement are higher than those obtained from the DSC measurement. This can be attributed to different treatment of polymer samples prior to measurement for each technique. It can be accepted that different activators had no effect on the crystallinity of the polyethylene. However, in the case of EH copolymer, changes in activator can alter the crystallinity of copolymer due to different insertion of 1-hexene, as determined by the <sup>13</sup>C-NMR.

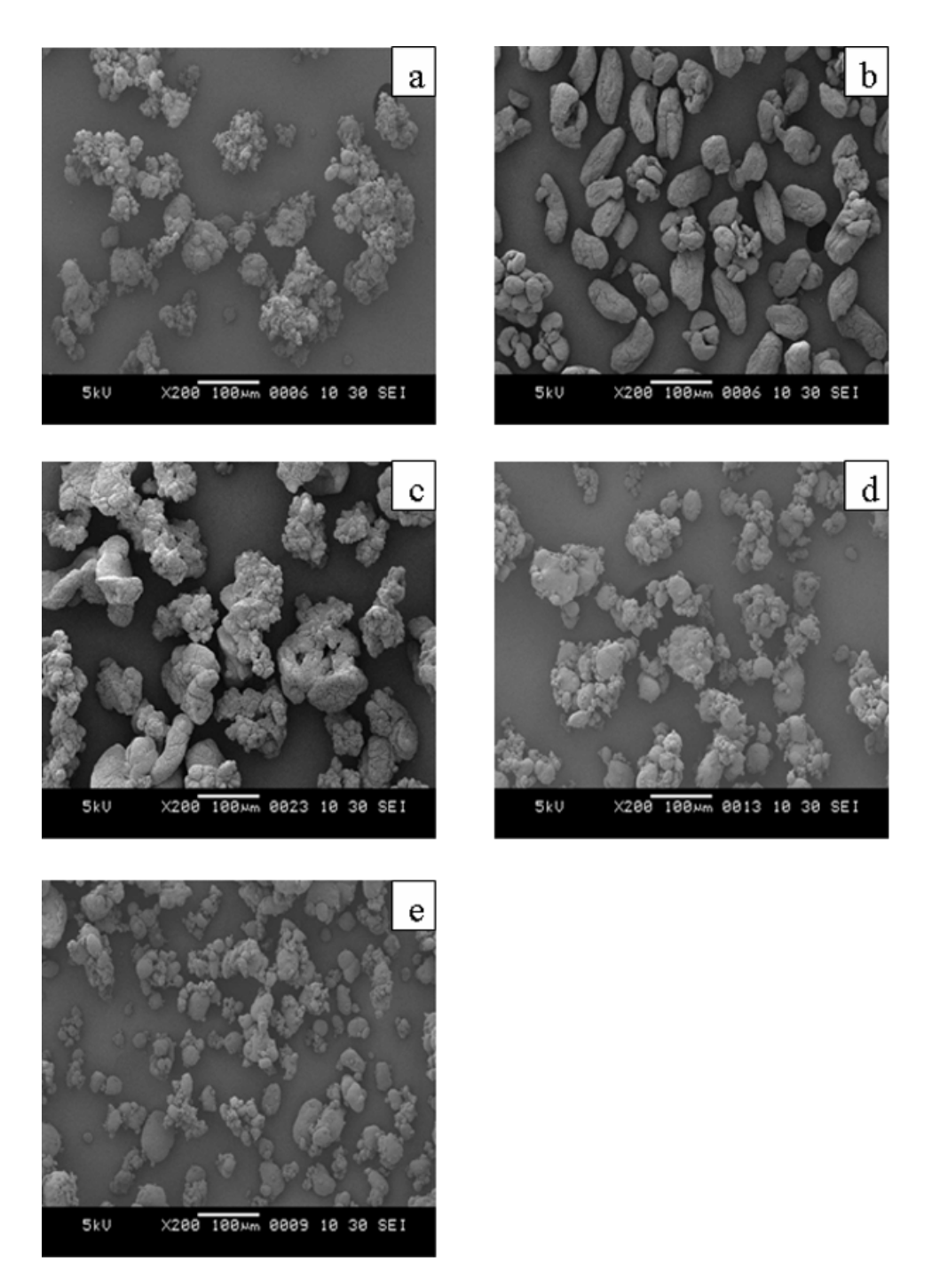




Different polymerization systems produced different polyethylene particle shapes, as seen by SEM in Figure 6. These results may result from the different reducing powers of the activators. In addition,

alkyl aluminums also participate in the termination of polymer chain growth, *i.e.* act as chain transfer agents, and/or reactivation of dormant sites [40].

**Figure 6.** SEM micrographs of secondary product particles obtained with different activators; (a) TEA, (b) DEAC, (c) TnHA, (d) TEA+DEAC, (e) TEA+DEAC+TnHA.



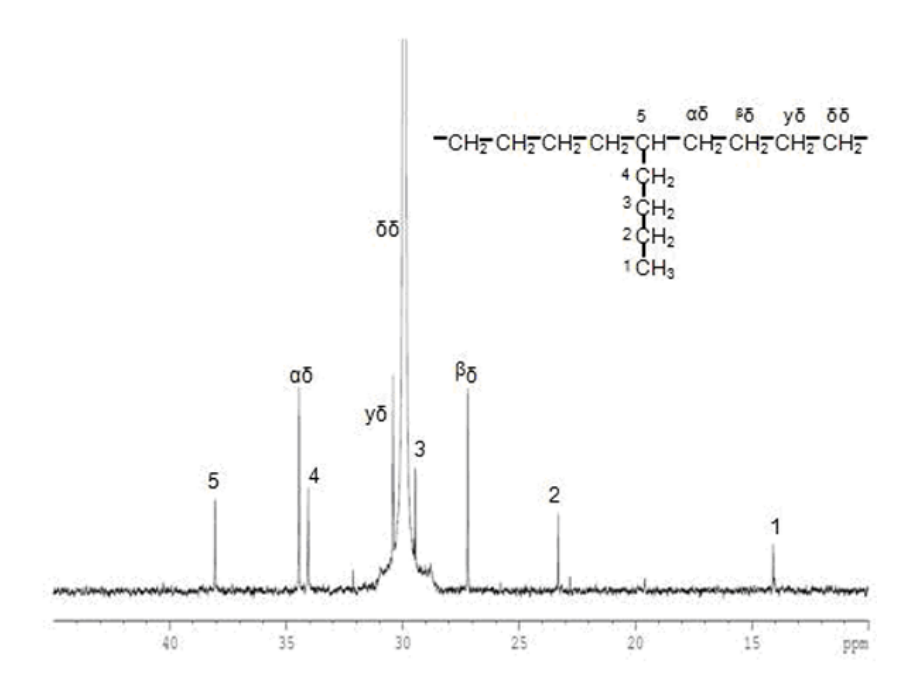
# 2.4.3. <sup>13</sup>C-NMR analysis

The incorporation of 1-hexene in copolymers was determined by <sup>13</sup>C-NMR spectroscopy. The chemical dislocations in the copolymers were calculated according to the work of Randall [39]. Table 4 shows 1-hexene incorporation in EH copolymers with different activators in the polymerization system. It was found that copolymers had 1-hexene insertion in the range of 0.49-1.90 mol%, depending on the type of activator used. Apparently, DEAC produced copolymer having the lowest 1-hexene insertion (0.49 mol%). On the contrary, TnHA gave the highest 1-hexene insertion in the copolymer (1.90 mol%). It is worth noting that the alkyl aluminum mixtures such as TEA+DEAC and TnHA+DEAC produced copolymer having 1-hexene insertion values around 0.70 and 0.60 mol%, respectively. Similarly, TEA and TEA+TnHA had a 1-hexene insertion that was very close to that of TEA alone. It should be noted that 1-hexene unit was isolated by ethylene units, and no sequence of double co-monomer units or alternating ethylene/1-hexene units were found, as shown in Figure 7. The same results were also obtained with other activators.

**Table 4.** Triad distribution based on <sup>13</sup>C-NMR for EH copolymer obtained from different activators.

Run	Activator	[HHH]	[EHH]	[EHE]	[EEE]	[HEH]	[HEE]	%Е	%Н
16	TEA	0.0	0.7	0.6	97.0	0.2	1.2	98.73	1.27
17	DEAC	0.0	0.2	0.3	98.8	0.1	0.6	99.51	0.49
18	TnHA	0.0	1.2	0.7	96.3	0.4	1.4	98.10	1.90
19	TEA+DEAC	0.0	0.2	0.5	98.2	0.1	1.0	99.30	0.70
20	TEA+TnHA	0.0	0.7	0.6	97.2	0.2	1.2	98.74	1.26
21	TnHA+DEAC	0.0	0.2	0.4	98.4	0.2	0.8	99.40	0.60
22	TEA+DEAC+TnHA	0.0	0.4	0.7	97.4	0.1	1.4	98.89	1.11

**Figure 7.** A typical <sup>13</sup>C-NMR spectrum of EH copolymer obtained with TEA.



#### 3. Experimental

#### 3.1. Chemicals

All reactions were performed under purified argon atmospheres using a standard glove box and Schlenk techniques. Polymerization grade ethylene, donated by the PTT Company, was used as received. Triethylaluminum (TEA), tri-*n*-hexylaluminum (TnHA), diethyl aluminum chloride (DEAC), donated by Tosoh Akzo Corp., were stored in a glove box and used without further purification. TiCl<sub>4</sub> (Aldrich), MgCl<sub>2</sub> (anhydrous) was donated by Tosoh Akzo Corp. Silica (specific surface area of 150 m<sup>2</sup>/g), supplied by Grace Davision, was heated under vacuum at 400 °C for 6 h. Hexane purchased from Aldrich Chemical Company Inc., was purified by passing it through a 13X molecular sieves column. Tetrahydrofuran and 1-hexene were dried over dehydrated CaCl<sub>2</sub> and distilled over sodium/benzophenone under an argon atmosphere prior to use. Ultra high purify (UHP) argon (99.999%) was purchased from Thai Industrial Gas Co., Ltd. and was further purified by passing through 3Å molecular sieves, BASF catalyst R3-11G, NaOH and phosphorus pentaoxide (P<sub>2</sub>O<sub>5</sub>) to remove traces of oxygen and moisture.

# 3.2. Catalyst preparation

The catalyst was prepared in a 500 mL vessel equipped with temperature control, and a turbine agitator. Anhydrous tetrahydrofuran (150 mL) was added to the vessel. The tetrahydrofuran was heated to 50 °C, and then magnesium metal (0.12 g) was added, followed by titanium tetrachloride (2 mL). The mixture was continuously agitated. The temperature was held at about 70 °C for 3 h. At the end of this time, magnesium dichloride (4.5 g) was added and heating was continued at 70 °C for another 3 h. Then, Grace Davision silica (4.5 g) was added over several minutes and the mixture was stirred for 1 h. This mixture was washed with hexane, and then dried under vacuum. The titanium content in the catalyst is 2.33 wt% (ICP).

#### 3.3. Polymerization reaction

The slurry polymerization was performed in hexane solution (1,000 mL) with various activator mixtures as shown in Table 1 (Al/Ti molar ratio = 100 and 300). First hexane (1,000 mL) was added into the reactor under argon atmosphere. After that, activators and catalyst were introduced into a 2 L stainless steel reactor equipped with a magnetic stirrer, and the reactor was then evacuated to remove the argon. Hydrogen ( $P_{H2} = 3.5$  bar) was fed into the reactor prior to the introduction of ethylene. The polymerization reaction was initiated by introducing the ethylene ( $P_{C2H4} = 4.5$  bar). The total pressure in the reactor was 8 bar. The polymerization reaction was held constant at 80 °C and terminated after 2 h by quenching with dilute hydrochloric acid solution in methanol. The resulting polymer was isolated and dried under vacuum.

The EH copolymerization was performed as follows; the 2 L autoclave was evacuated and purged with argon several times similar to the ethylene polymerization. After hexane (950 mL) was added at 80 °C, the solution of activator such as TEA, DEAC, TnHA and TEA+DEAC+TnHA mixtures, 1-hexene (50 mL) and the catalyst (Al/Ti = 300) were added into reactor sequentially. Then, the 3.5 bar

of hydrogen was fed into the reactor. The ethylene gas was fed into reactor and the total pressure in reactor was raised to 8 bar and held constant by continuous feed. After 2 h, the copolymerization was terminated using the same procedure as mentioned for ethylene polymerization.

#### 3.4. Polymer characterization

A high temperature GPC (PL-GPC220) equipped with a viscometric detector, differential optical refractometer and four Styragel HT type columns (HT3, HT4, HT5, and HT6) with a  $1\times10^7$  exclusion limit for polystyrene was used to determine the molecular weight (M<sub>W</sub>) and molecular weight distributions (MWD) of the polymers produced. The analyses were performed at 160 °C using 1,2,4-trichlorobenzene as the solvent. The columns were calibrated with standard narrow MWD polystyrene.

The comonomer contents of the resultant copolymers were determined by <sup>13</sup>C-NMR spectroscopy. The measurements were performed at 110 °C on Bruker 400 MHz instrument using 1,2,4trichlorobenzene as solvent. The thermal behavior of polyethylene and EH copolymers was examined with a Perkin-Elmer Pyris Diamond DSC at standard heating/cooling rate of 10 °C/min, under N<sub>2</sub> flow. The samples were first melted to 180 °C (1st scan) and kept at this temperature for 3 min, then cooled to 50 °C, and again heated up to the melting with the same heating rate (2nd scan). The reported melting temperature values are referred to the second heating scan. The melting temperature (Tm) and the melting enthalpy ( $\triangle H_m$ ) were taken from the second heating curve. Temperatures and heats of phase transitions were determined, respectively, from the maxima and areas of the crystallization and melting peaks. In this context, it was possible to relate  $\triangle H_m$  (J/g) to the density (d, g/mL) of the copolymer through the following semiempirical equation:  $d = (2195 + \Delta H_m)/2500$  [41]. Finally, using standards of known composition, a linear correlation between sample density and its content in terms of 1-hexene co-units was found, at least in the 0.92-0.94 g/mL density range [41]. The degree of crystallinity, Xc of PE and its copolymers was calculated from the ratio between the values of melting enthalpy,  $\Delta H_m$  (as calculated from the second heating scan) and the heat of fusion of 100% crystalline PE taken as  $\triangle H_m = 293 \text{ J/g } [42]$ .

X-ray diffraction patterns (XRD) analysis was carried out on a Siemens D-5000 apparatus working at 40 kV and 30 mA and using the Cu  $K_{\alpha}$  radiation ( $\lambda=0.154439~\text{Å}$ ) in the  $10^{\circ}$ - $40^{\circ}$  20 range with a scanning step of  $0.01^{\circ}$  in the reflection geometry. The crystalline degrees of the copolymers were calculated via Eq. (1) developed by Mo and Zhang [14]:

$$W_{c,X} = \frac{I_{110} + 1.42I_{200}}{I_{110} + 1.42I_{200} + 0.68I_a}$$
(1)

The morphological observations of polymers were carried out with a JEOL JSM-6400 scanning electron microscope (SEM). Micrographs were taken at a 5-kV acceleration voltage. Before SEM observations, the fracture surfaces of blends were coated with a thin layer of gold to avoid electrical charging and increase contrast during observation.

#### 4. Conclusions

The use of suitable mixed activators such as TEA+DEAC+TnHA, can result in the significant increase in catalytic activity for the bi-supported Ziegler-Natta catalyst for ethylene polymerization and ethylene/1-hexene copolymerization. This can be attributed to the change in reducing power of the mixed activators leading to generation of different active forms of the catalyst or stabilization of the active center in ethylene polymerization. The activator type had an effect on the molecular weight and molecular weight distribution of polyethylene without any significant change in polymer morphology. In the case of copolymerization, there were no relationship among the M<sub>w</sub>, MWD and catalytic activity when the mixed activators were employed.

#### Acknowledgements

The authors thank the Thailand Research Fund (TRF), Office of the Higher Education Commission (CHE), Chulalongkorn University for Royal Golden Jubilee Fund under contract No. CU-CLUSTER-Advanced-4-54-53, and PTT Company for the financial support of this project.

#### **References and Notes**

- 1. Quijada, R.; Guevara, J.L.; Galland, G.B.; Rabagliati, F.M.; Lopez-Majada, J.M. Synthesis and properties coming from the copolymerization of propene with α-olefins using different metallocene catalysts. *Polymer* **2005**, *46*, 1567–1574.
- 2. Kawahara, N.; Kojoh, S.; Toda, Y.; Mizuno, A.; Kashiwa, N. The detailed analysis of the vinylidene structure of metallocene-catalyzed polypropylene. *Polymer* **2004**, *45*, 355–357.
- 3. Cruz, V.; Ramos, J.; Mun\*oz-Escalona, A.; Lafuente, P.; Pen\*a, B.; Martinez, S. 3D-QSAR analysis of metallocene-based catalysts used in ethylene polymerization. *Polymer* **2004**, *45*, 2061–2072.
- 4. Lee, H.W.; Chung, J.S.; Choi, K.Y. Physical transitions and nascent morphology of syndiotactic polystyrene in slurry polymerization with embedded Cp\*Ti(OMe)3/methyl aluminoxane catalyst. *Polymer* **2005**, *46*, 5032–5039.
- 5. Nitta, K.H.; Shin, Y.W.; Hashiguchi, H.; Tanimoto, S.; Terano, T. Morphology and mechanical properties in the binary blends of isotactic polypropylene and novel propylene-co-olefin random copolymers with isotactic propylene sequence 1. Ethylene-propylene copolymers. *Polymer* **2005**, *46*, 965–975.
- **6.** Wooster, T.J.; Abrol, S.; Macfarlane, D.R. Cyanate ester polymerization catalysis by layered-silicates. *Polymer* **2004**, *45*, 7845–7852.
- 7. Chen, S.; Hua, Z.J.; Fang, Z.; Qi, G.R. Copolymerization of carbon dioxide and propylene oxide with highly effective zinc hexacyanocobaltate(III)-based coordination catalyst. *Polymer* **2004**, *45*, 6519–6524.
- 8. Bazzini, C.; Giarrusso, A.; Porri, L.; Pirozzi, B.; Napolitano, R. Synthesis and characterization of syndiotactic 3,4-polyisoprene prepared with diethylbis(2,2'-bipyridine)iron-MAO. *Polymer* **2004**, *45*, 2871–2875.
- 9. Liu, J.Y.; Zheng, Y.; Li, Y.S. Polymerization of methyl methacrylate by iron(II) pyridinebisimine complexes. *Polymer* **2004**, *45*, 2297–2301.
- 10. Gao, M.Z.; Liu, H.T.; Wang, J.; Li, C.X.; Ma, J.; Wei, G.S. Novel MgCl<sub>2</sub>-supported catalyst containing diol dibenzoate donor for propylene polymerization. *Polymer* **2004**, *45*, 2175–2180.

11. Kawahara, N.; Kojoh, S.I.; Toda, Y.; Mizuno, A.; Kashiwa, N. The detailed analysis of the vinylidene structure of metallocene-catalyzed polypropylene. *Polymer* **2004**, *45*, 355–357.

- 12. Lee, T.S.; Kim, J.W.; Bae, J.Y. Palladium-catalyzed selective dehalogenative homocoupling polymerization of AB2-type dihaloaryl sulfonate monomers. *Polymer* **2004**, *45*, 5065–5076.
- 13. Galland, G.B.; Quijada, R.; Rojas, R.; Bazan, G.; Zachary Komon, J.A. NMR Study of Branched Polyethylenes Obtained with Combined Fe and Zr Catalysts. *Macromolecules* **2002**, *35*, 339–345.
- 14. Mo, Z.S.; Zhang, H.F. The degree of crystallinity in polymers by wide-angle x-ray diffraction (WAXD). Macromol. *Chem. Phys.* **1995**, *C35*, 555–580.
- 15. Madri, S.; Xuejing, Z.; RoBert, B.J.; JOHN, C.C.; COR, E.K. Effect of 1-Hexene Comonomer on Polyethylene Particle Growth and Copolymer Chemical Composition Distribution. *J. Polym. Sci.: Part A: Polym. Chem.* **2006**, *44*, 2883–2890.
- 16. Yong, P.C.; Zhi, F. Ethylene/1-hexene copolymerization with TiCl4/MgCl2/AlCl3 catalyst in the presence of hydrogen. *Eur. Polym. J.* **2006**, *42*, 2441–2449.
- 17. Nooijen, G.A.H. On the importance of diffusion of cocatalyst molecules through heterogeneous ziegler/natta catalysts. *Eur. Polym. J.* **1994**, *30*, 11-15.
- 18. Lynch, T.D.; Jejelowo, M.O.; Wanke, S.E. The influence of aluminum alkyls on the polymerization of ethylene with silica/magnesium chloride-supported titanium tetrachloride catalysts. *Can. J. Chem. Eng.* **1991**, *69*, 657-664.
- 19. Siokou, A.; Ntais, S. Towards the preparation of realistic model Ziegler-Natta catalysts: XPS study of the MgCl<sub>2</sub>/TiCl<sub>4</sub> interaction with flat SiO<sub>2</sub>/Si(1 0 0). *Surf. Sci.* **2003**, *540*, 379-388.
- 20. Dong, Q.; Fu, Z.; Xu, J.; Fan, Z. Strong influences of cocatalyst on ethylene/propylene copolymerization with a MgCl<sub>2</sub>/SiO<sub>2</sub>/TiCl<sub>4</sub>/diester type Ziegler-Natta catalyst. *Eur. Polym. J.* **2007**, *43*, 3442-3451.
- 21. Lynch, D.T.; Wanke, S.E. Reactor Design and Operation for Gas-Phase Ethylene Polymerization Using Ziegler-Natta Catalysts. *Can. J. Chem. Eng.* **1991**, *69*, 332-339.
- **22.** Hammawa, H.; Mannan, T.M.; Lynch, D.T.; Wanke, S.E. Effects of aluminum alkyls on ethylene/1-hexene polymerization with supported metallocene/MAO catalysts in the gas phase. *J. Appl. Polym. Sci.* **2004**, *92*, 3549-3560.
- 23. Fukuda, K.; Liu, B.; Nakatani, H.; Nishiyama, I.; Yamahiro, M.; Terano, M. Significant variation of molecular weight distribution (MWD) of polyethylene induced by different alkyl-Al cocatalysts using a novel surface functionalized SiO2-supported Ziegler-Natta catalyst. *Catal. Commun.* **2003**, *4*, 657-662.
- 24. Haward, R.N.; Roper, A.N.; Fletcher, K.L. Highly active catalysts for ethylene polymerization by the reduction of TiCl<sub>4</sub> with organomagnesium compounds. *Polymer* **1973**, *14*, 365-372.
- 25. Gardner, K.; Parsons, I.W.; Haward, R.N. Polymerization of propene with organomagnesium-reduced titanium (IV) chloride-based catalyst. *J. Polym. Sci.: Polym. Chem.* **1978**, *16*, 1683-1696.
- 26. Kashiwa, N. Super active catalyst for olefin polymerization. *Polymer* **1980**, *12*, 603-608.
- 27. Licchelli, J.A.; Haward, R.N.; Parsons, I.W.; Caunt, A.D. Polymerization catalysts for propene from the reduction of titanium tetrachloride with halogen-free magnesium alkyls. *Polymer* **1981**, 22, 667-672.
- 28. Machon, J.P.; Hermant, R.; Houzeaux, J.P. Study of the catalytic activity of violet titanium trichloride in the high-temperature polymerization of ethylene. *J. Polym. Sci. Symp. Ser.* **1975**, *52*, 107-117.

29. Munoz, E.A.; Hernandez, J.G.; Gallardo, J.A.; Keii. T.; Soga, K. Design of supported Ziegler-Natta catalysts using silica as carrier. *Stud. Surf. Sci. Catal.* **1986**, *25*, 123-125.

- 30. Munoz, E.A.; Garcia, H.; Albornoz, A. Homo- and copolymerization of ethylene with highly active catalysts based on titanium tetrachloride and Grignard compounds. *J. Appl. Polym. Sci.* **1987**, *34*, 977-988.
- 31. Zakharov, V.A.; Bukatov, G.D.; Ermakov, Y. The Mechanism of the Catalytic Polymerisation of Olefins Based on the Number of Active Centres and the Rate Constants for Individual Stages. *Russ. Chem. Rev.* **1980**, *49*, 1097-1111.
- 32. Mori, H.; Ohnishi, K.; Terano, M. Ethene polymerization with modified-polypropene-supported highly stable Ziegler catalyst. *Macromol. Rapid Commun.* **1996**, *17*, 25-29.
- 33. Zacca, J.J.; Debling, J.A.; Ray, W.H. Reactor residence time distribution effects on the multistage polymerization of olefins I. Basic principles and illustrative examples, polypropylene. *Chem. Eng. Sci.* **1996**, *51*, 4859-4886.
- 34. Kim, I.; Chung, M.C.; Choi, H.K.; Kim, J.H.; Woo, S.I. (1990) Homo- and Co-polymerization of Ethylene with the Highly Active TiCl<sub>4</sub>/THF/MgCl<sub>2</sub> Catalyst. *Catal. Olefin Polym.* **1990**, 323.
- 35. Kim, I.; Kim, J.H.; Woo, S.I. Kinetic Study of Ethylene Polymerization by Highly Active Silica Supported TiCl<sub>4</sub> MgCl<sub>2</sub> Catalyst. *J. Appl. Polym. Sci.* **1990**, *39*, 837-854.
- 36. Hatada, K.; Yuki, H. Alkyl interchange in the mixture of triethyl aluminum and diethylaluminum chloride. *Tetrahedron Lett.* 1967, *51*, 5227-5231.
- 37. Calabro, D.C.; Lo, F.Y. A comparison of the reaction kinetics for the homo- and copolymerization of ethylene and hexene with a heterogeneous Ziegler catalyst. In *Transition Metal Cata lyzed Polymerizations: Ziegler–Natta and Methathesis Polymerization;* Quirk, R.P., Ed.; Cambridge University Press: New York, NY, USA, 1988; pp. 729-739.
- 38. Chien, J.C.W.; Nozaki, T. Ethylene-hexene copolymerization by heterogeneous and homogeneous Ziegler-Natta catalysts and the "comonomer" effect. *J. Polym. Sci.* **1993**, *31*, 227-237.
- 39. Randall, J.C. A review of high-resolution liquid carbon-13 nuclear magnetic resonance characterizations of ethylene-based polymers. *AJMS-REV. Macromol. Chem. Phys.* **1989**, *C29*, 201-317.
- 40. Zakharov, V.A.; Bukatov, G.D.; Yermakov, Y.I. On the mechanism of olefin polymerization by Ziegler-Natta catalysts. *Adv. Polym. Sci.* **1983**, *51*, 61-100.
- 41. Carlini, C.; Alessio, A.D.; Giaiacopi, S.; Po, R.; Pracella, M.; Galletti, A.M.R.; Sbrana, G. Linear low-density polyethylenes by co-polymerization of ethylene with 1-hexene in the presence of titanium precursors and organoaluminium co-catalysts. *Polymer.* **2007**, *48*, 1185-1192.
- 42. Wunderlich, B.; Czornyj, G. A study of equilibrium melting of polyethylene. *Macromolecules* **1977**, *10*, 906-913.

Sample Availability: Samples of the compounds (PEs and LLDPEs) are available from the authors.

© 2010 by the authors; licensee MDPI, Basel, Switzerland. This article is an open access article distributed under the terms and conditions of the Creative Commons Attribution license (http://creativecommons.org/licenses/by/3.0/).



Article

# Observation of Different Catalytic Activity of Various 1-Olefins during Ethylene/1-Olefin Copolymerization with Homogeneous Metallocene Catalysts

Mingkwan Wannaborworn, Piyasan Praserthdam and Bunjerd Jongsomjit \*

Center of Excellence on Catalysis and Catalytic Reaction Engineering, Department of Chemical Engineering, Faculty of Engineering, Chulalongkorn University, Bangkok 10330, Thailand

\* Author to whom correspondence should be addressed; E-Mail: bunjerd.j@chula.ac.th; Tel.: +66 2 2186869; Fax: +66 2 2186877.

Received: 18 November 2010; in revised form: 28 December 2010 / Accepted: 5 January 2011 /

Published: 7 January 2011

**Abstract:** This research aimed to investigate the copolymerization of ethylene and various 1-olefins. The comonomer lengths were varied from 1-hexene (1- $C_6$ ) up to 1-octadecene (1-C<sub>18</sub>) in order to study the effect of comonomer chain length on the activity and properties of the polymer in the metallocene/MAO catalyst system. The results indicated that two distinct cases can be described for the effect of 1-olefin chain length on the activity. Considering the short chain length comonomers, such as 1-hexene, 1-octene and 1-decene, it is obvious that the polymerization activity decreased when the length of comonomer was higher, which is probably due to increased steric hindrance at the catalytic center hindering the insertion of ethylene monomer to the active sites, hence, the polymerization rate decreased. On the contrary, for the longer chain 1-olefins, namely 1-dodecene, 1tetradecene and 1-octadecene, an increase in the comonomer chain length resulted in better activity due to the opening of the gap aperture between C<sub>p</sub>(centroid)-M-C<sub>p</sub>-(centroid), which forced the coordination site to open more. This effect facilitated the polymerization of the ethylene monomer at the catalytic sites, and thus, the activity increased. The copolymers obtained were further characterized using thermal analysis, X-ray diffraction spectroscopy and <sup>13</sup>C-NMR techniques. It could be seen that the melting temperature and comonomer distribution were not affected by the 1-olefin chain length. The polymer crystallinity decreased slightly with increasing comonomer chain length. Moreover, all the synthesized polymers were typical LLDPE having random comonomer distribution.

**Keywords:** metallocene catalyst; homogeneous catalyst; long chain olefins; copolymerization

#### 1. Introduction

Nowadays, polymers play a significant role in many applications, especially linear low-density polyethylene (LLDPE). The LLDPE has many advantages such as low density, good mechanical properties, and easy fabrication and recycling. Therefore, it has been used to produce many products such as shopping bags, food packaging film, plastic pipe and house appliances, *etc.* [1-3]. Thus, the demand for LLDPE is quite high compared with other polymers. For the production of LLDPE, the polymer can be synthesized by the polymerization of ethylene and short chain 1-olefins, namely 1-hexene, 1-octene and 1-decene, in the catalyst system for better activity. A low pressure slurry process, the gas phase process and the solution-phase process [4] can be employed for LLDPE. Some 15 million tons of LLDPE are produced worldwide using the metallocene catalyst system, since this catalyst can incorporate many types of comonomer. Moreover, it can give a narrow molecular weight distribution. Thus, there has been an increase in research and development on the synthesis of the LLDPE using metallocene catalysts [5,6].

However, the properties of LLDPE, such as the average molecular weight of the macromolecules and its distribution, the degree of crystallization, the melting temperature and the amount and distribution of the monomeric units, depend on a factor called "comonomer effect" [7-9]. Previous studies show that an increase in the quantities of 1-olefin provides higher activity which relates to a physical phenomenon improving the monomer diffusion in the lower crystalline copolymer structure. Besides the comonomer quantity, the length of the comonomer also affects the properties of LLDPE. Although short chain comonomers are normally used in the process, long chain comonomers can provide different LLDPE properties. Therefore, the use of long chain comonomers is also attractive for future production.

In this work, the effects of short and long comonomer chain length on the polymerization activity and the properties of the resulting copolymers were investigated. The synthesis of the LLDPE was performed by copolymerization of ethylene and various 1-olefins, namely 1-hexene (1- $C_6$ ), 1-octene (1- $C_8$ ), 1-decene (1- $C_{10}$ ), 1-dodecene (1- $C_{12}$ ), 1-tetradecene (1- $C_{14}$ ) and 1 -octadecene (1- $C_{18}$ ), with a metallocene catalyst.

# 2. Results and Discussion

# 2.1. Homo- and co-polymerization activities

This study is aimed to investigate the polymerization of ethylene with short and long chain 1-olefins, namely 1-hexene, 1-octene, 1-decene, 1-dodecene, 1-tetradecene and 1-octadecene. The catalytic activities obtained with different 1-olefins are shown in Table 1.

**Table 1.** Copolymerization of ethylene with long chain 1-olefins using *rac*-Et[Ind]<sub>2</sub>ZrCl<sub>2</sub>/MAO, as the catalytic system.

Run number	Olefin type	Polymerization time (s)	Polymer yield <sup>a</sup> (g)	Catalytic activity <sup>b</sup> (×10 <sup>-4</sup> kgPol/molZr h)
1	-	115	0.8703	1.8
2	1-C <sub>6</sub>	124	1.4781	2.9
3	1-C <sub>8</sub>	97	1.5529	3.8
4	$1-C_{10}$	115	1.6783	3.5
5	$1-C_{12}$	109	1.6134	3.6
6	$1-C_{14}$	89	1.3704	3.7
7	$1-C_{18}$	123	2.3157	4.5

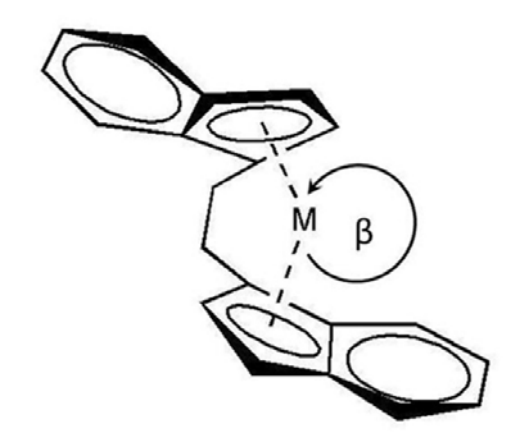
<sup>&</sup>lt;sup>a</sup> The polymer yield was limited by the amount of ethylene fed (0.018 mol). The molar ratio of ethylene:comonomer was 2:1; <sup>b</sup> Activities were measured at polymerization temperature of 343 K, [ethylene]= 0.018 mol, [Al]<sub>MMAO</sub> / [Zr]<sub>cat</sub> = 1135, in toluene with total volume = 30 mL and [Zr]<sub>cat</sub> =  $5 \times 10^{-5}$  M.

From Table 1, when comparing the activities between homo-polymerization and co-polymerization, it can be seen that the addition of the comonomer in the system yields better activity. The enhancement of polymerization rate by 1-olefin comonomers, well documented for both titanocene [7,10,11] and zirconocene catalysts [7,12,13], is called the "comonomer effect". This phenomenon in copolymerization involving the zirconocene catalysts may be related to the perturbations of the ion pairs at the active sites. Karol et al. [13] have proposed that 1-olefins can function as ligands. By coordination to the active center, the 1-olefin can alter the charge density on the cationic zirconocenium ion. Metal centers with higher mobility, lower steric interference, and higher electrophilicity are believed to form stronger ion pairs. Monomers that cause a greater separation between the cationic metal centers and the MAO aggregates can enhance the activity of the catalyst, consequently increase the rate polymerization. On the other hand, two distinct cases can be described for the effect of the comonomer length. Considering the short chain length comonomers (runs 2-4), the results indicated that the increase of the comonomer length (from C<sub>8</sub> to C<sub>10</sub>) resulted in lower activity due to increased steric hindrance. The longer chain comonomer can hinder the insertion of ethylene, and slow the propagation reaction process. This leads to lower catalytic activity for polymerization [12-15]. On the contrary, for the long chain length 1-olefins (runs 5-7), we observed an increase of polymerization activity when the length of 1-olefin was increased. This may be attributed to the opening of the gap aperture between C<sub>p</sub>(centroid)-M-C<sub>p</sub>-(centroid) in metallocene complex, which forced the coordination site to open more (Figure 1). This effect caused ethylene monomer to polymerize easier at the catalytic sites, and thus the activity increased [16,17]. A similar behavior was observed by Kaminsky et al. [17] for ethylene/ long chain 1-olefins copolymerization with a [Ph<sub>2</sub>C(2,7-di-tert-BuFlu)(Cp)]ZrCl<sub>2</sub>/MAO catalyst system, under different experimental conditions (T = 60 °C and the presence of hydrogen), but no reason was given for the trend.

The obtained result is also consistent with the study of Braunschweig and Breitling [18], which revealed that opening of the  $\beta C_p$ (centroid)-M- $C_p$ -(centroid) angle can be found in the polymerization

of ethylene and long chain olefins. Moreover, they also reported that a longer 1-olefin chain can open the  $C_p$ (centroid)-M- $C_p$ -(centroid) angle wider in metallocene complexes.

**Figure 1.** Structure of the opening gap aperture between  $C_p$ (centroid)-M- $C_p$ -(centroid) in metallocene complex, redrawn from the conceptual idea by Braunschweig and Breitling [18].



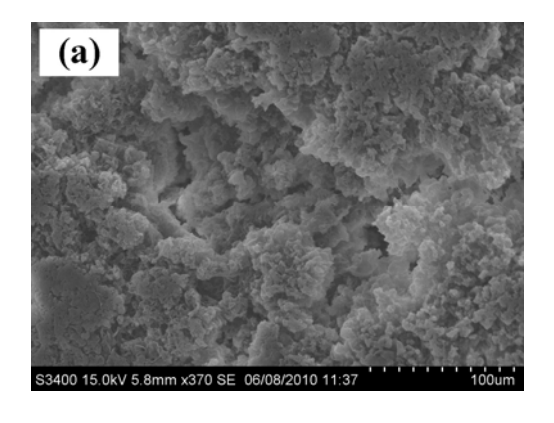
# 2.2. Polymer properties

Homo- and copolymers with different 1-olefins (copolymers containing 6 to 18 carbon atoms), synthesized by a metallocene catalyst, have been analyzed using four characterization techniques.

#### 2.2.1. SEM measurements

Figure 2 presents the scanning electron micrograph (SEM) of the polymers obtained by homo- and co-polymerization. Considering the effect of the length of comonomer on morphology, the results indicated that the crystalline structure of the obtained polymer seems to be lower with increased comonomer chain length. This is probably due to more steric hindrance caused upon introducing a longer chain length comonomer. Therefore, the amount and chain length of comonomer apparently affected on the morphology of the resulting polymer.

**Figure 2.** SEM micrograph of LLDPE produced with metallocene catalyst. (a) homopolymer (b) ethylene/1-hexene copolymer (c) ethylene/1-octadecene copolymer.



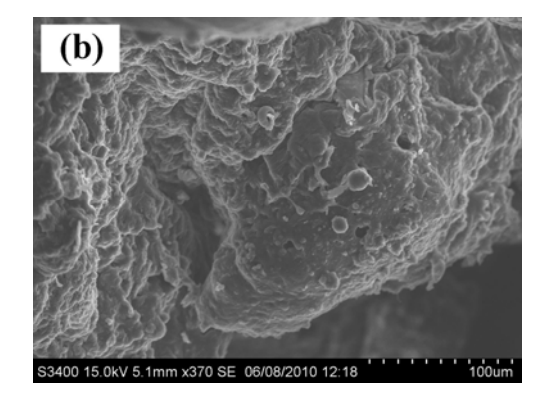
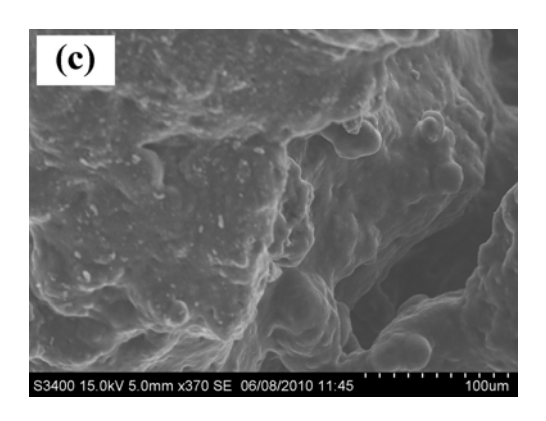


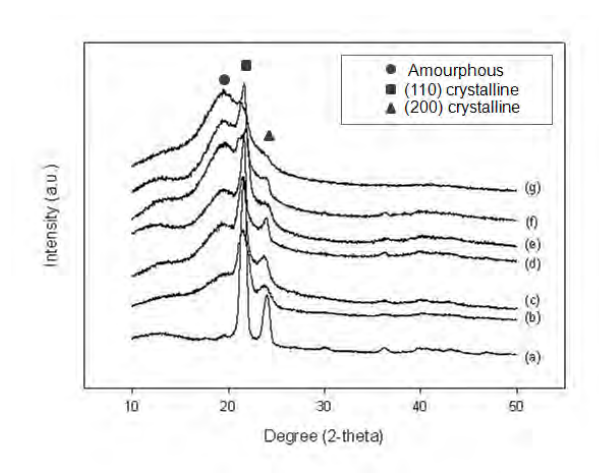
Figure 2. Cont.



# 2.2.2. X-ray Diffraction (XRD) analysis

For XRD results, the diffractograms of the different samples, which were acquired at room temperature, are shown in **Figure 3**. As expected, it can be seen that all samples display XRD peaks at three positions. A broad amorphous peak was evident centered around 19.5-20 degrees. A previous work suggested this peak as indicative of the side branches of 1- olefin participating in the crystalline structure. While the other two peaks appeared at  $2\theta = 21.8$  and 24.3 degrees are the (110) and (200) reflections, assigned to the characteristic orthorhombic cell of polyethylene [19-21]. Moreover, the longer chain length of the additional comonomers seemed to disturb the polymer recrystallization, which can probably be attributed to the increased steric hindrance, leading to a reduction in crystalline peak intensity, but clearly increasing the intensity of the amorphous peak [19,22].

**Figure 3.** X-ray diffractograms of different samples. From bottom to top. (a) homopolymer (b) ethylene/1- $C_6$  (c) ethylene/1- $C_8$  (d) ethylene/1- $C_{10}$  (e) ethylene/1- $C_{12}$  (f) ethylene/1- $C_{14}$  and (g) ethylene/1- $C_{18}$  copolymers.



# 2.2.3. NMR analysis

In order to determine the influence of chain length on the comonomer distribution, the obtained copolymers were also characterized by  $^{13}$ C-NMR measurements. The chemical-shift assignments of ethylene/ 1-C<sub>12</sub> to ethylene/ 1-C<sub>18</sub> copolymer and some resonances of the main and side chains are

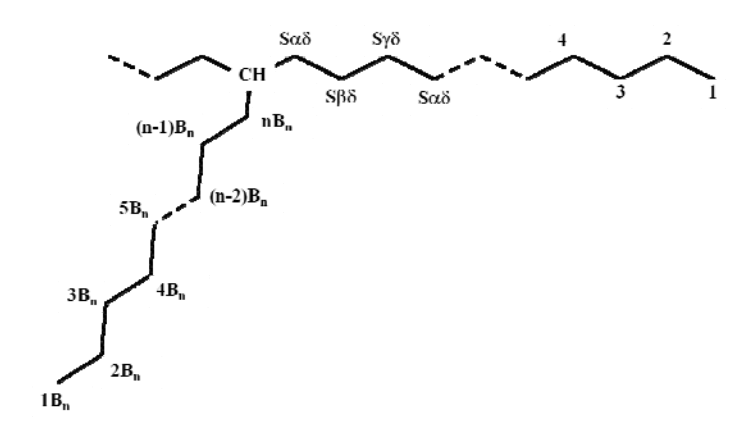
shown in Table 2 and Figure 4. The quantitative analysis of triad distribution for all copolymers is reported in Table 3.

**Table 2.** Chemical-shift assignment in <sup>13</sup>C-NMR spectra of ethylene/1-dodecene, ethylene/1-tetradecene and ethylene/1-octadecene copolymers [23].

Combon		Chemical shift <sup>b</sup> (ppm)	
Carbon trme <sup>a</sup>	ethylene/1-dodecene	ethylene/1-tetradecene	ethylene/1-octadecene
type <sup>a</sup>	$(1-C_{12})$	$(1-C_{14})$	$(1-C_{18})$
$1B_n$	14.10	14.10	14.10
$2 B_n$	22.80	22.80	22.80
$3 B_n$	32.13	32.13	32.13
$4 B_n$	29.50	29.50	29.50
$5 B_n$	29.85	29.85	29.85
$6 B_n$	$29.90^{c}$	29.90°	29.90 °
$7 B_n$	29.90 °	29.90°	29.90 °
$8 B_n$	30.36	29.90°	29.90 °
9 B <sub>n</sub>	27.18	29.90°	29.90 °
10 B <sub>n</sub>	34.45	30.37	29.90 °
11 B <sub>n</sub>	-	27.18	29.90 °
12 B <sub>n</sub>	-	34.46	29.90 °
13 B <sub>n</sub>	-	-	29.90 °
14 B <sub>n</sub>	-	-	30.37
15 B <sub>n</sub>	-	-	27.18
16 B <sub>n</sub>	-	-	34.46
CH	38.11	38.11	38.11
Sαδ	34.49	34.49	34.49
Sβδ	27.20	27.20	27.20
$S\gamma\delta$	30.38	30.38	30.38
Sδδ	29.90	29.90	29.90

<sup>&</sup>lt;sup>a</sup> See Scheme 1; <sup>b</sup> According to Randall [26]; <sup>c</sup> Overlapped to S δδ peak at 29.90 ppm.

**Figure 4.** Resonance of the main chain methylenes and the side chain of the ethylene/1-olefin copolymer.



	Olefin		,	Triad dis	tribution	$C_n$	$T_{m}$	$\chi_c$	d <sup>e</sup>		
Entry	Entry type	[EEE]	[XEE]	[EXE]	[XEX]	[EXX]	[XXX]	$(mol\%)^b$	(°C) <sup>c</sup>	(%) <sup>d</sup>	$(g\!/mL)$
2	1-C <sub>6</sub>	0.775	0.142	0.052	0.017	0.014	0.000	7	121.64	7.36	0.88
3	$1-C_8$	0.412	0.379	0.164	0.045	0.000	0.000	16	113.62	2.44	0.88
4	$1-C_{10}$	0.471	0.310	0.176	0.043	0.000	0.000	18	116.25	2.33	0.88
5	$1-C_{12}$	0.499	0.331	0.135	0.035	0.000	0.000	13	117.61	6.21	0.89
6	$1-C_{14}$	0.604	0.154	0.091	0.087	0.064	0.000	20	112.98	1.33	0.87
7	$1-C_{18}$	0.591	0.214	0.152	0.043	0.000	0.000	15	117.58	4.34	0.88

**Table 3.** Triad distribution and properties of the resulting ethylene/1-olefin copolymers.

<sup>a</sup> Obtained from <sup>13</sup>C-NMR, where E refers to ethylene monomer and X refers to 1-olefin comonomer; <sup>b</sup> Content of 1-olefin in the copolymer from <sup>13</sup>C-NMR; <sup>c</sup> Melting temperature from DSC; <sup>d</sup> Crystallinity degree:  $\chi_c = 100 \times (\Delta H/\Delta H^\circ)$ , where  $\Delta H^\circ = 290$  J/g for linear polyethylene; <sup>e</sup> Copolymer density calculated from the semi-empirical equation:  $d = (2,195 + \Delta H)/2,500$ .

From the table, it is found that ethylene incorporation in all systems gave copolymers with similar triad distribution, and only random copolymers can be produced in all systems. However, the olefin length has no effect on the comonomer distribution [12,23-25]. It should be noted that the comonomer content depends on different variables; for example, a long 1-olefin chain length forces the angle of the metallocene complex to open more. However, at the same time it causes steric hindrance to the incoming ethylene monomer. Therefore, the two effects (chain length and opened angle) can be superimposed on each other.

# 2.2.4. Differential scanning calorimetric analysis

When dealing with the thermal properties of the polymer, DSC measurements are usually considered the second melting of the sample. All the experimental results, including melting temperature (T<sub>m</sub>), % crystallinity (χ<sub>c</sub>), and density are also reported in Table 3. The PE sample (run 1) is a high density polymer with a linear microstructure, a high melting temperature (Tm~135 °C), a degree of crystallinity of 65% and a high density (0.95 g/mL) (data not shown in the Table). Based on Table 3, it can be observed that the polymer with higher incorporation of comonomers exhibited less crystallinity and lower melting temperature. This is in correspondence with the percent insertion from <sup>13</sup>C-NMR results. In addition, when the crystallinity results obtained from DSC measurements are considered, they indicate that the length of the comonomer did not affect the crystallization behavior, which was different from the XRD results. This was due to the fact that XRD was analyzed the assynpolymers at ambient conditions, whereas the DSC measurement was performed upon heating the samples. For DSC, the determination relies on the measurement of the enthalpy of melting and on the assumption of a unique enthalpy of melting for the crystal. Thus, the enthalpy of melting of long 1olefin side chains had to be taken into account for the determination of crystallinity. Therefore, the crystallinity value may be different between the various determinations. [12,13,27-29]. However, it can be concluded that the increase in the length of the comonomer chain can result in a decrease of the melting temperature. The density of all samples is in the range of 0.87-0.95 g/cm<sup>3</sup> indicating a typical LLDPE structure.

### 3. Experimental

#### 3.1. Materials

Chemicals and polymerizations were handled and operated under an argon atmosphere, using a glove box and/or Schlenk techniques. Toluene was dried over dehydrated CaCl<sub>2</sub>, and then distilled over sodium/benzophenone before use. The zirconocne, (*rac*-Et[Ind]<sub>2</sub>ZrCl<sub>2</sub>) was supplied by the Aldrich Chemical Company, Inc. Modified methylaluminoxane (MMAO) in hexane was donated by Tosoh (Akso, Japan). 1-Olefins were purchased from Aldrich Chemical Company, Inc. Ethylene gas (99.96% pure) was donated by the National Petrochemical Co., Ltd., Thailand. Ultrahigh purity argon was further purified by passing it through columns packed with BASF R3-11G catalyst (molecular-sieved to 3 Å), sodium hydroxide (NaOH), and phosphorus pentaoxide (P<sub>2</sub>O<sub>5</sub>) to remove traces of oxygen and moisture.

# 3.2. Homo- and co-polymerization

Ethylene/1-olefin copolymerizations was carried out in a 100 mL semi-batch stainless steel autoclave reactor equipped with a magnetic stirrer. In the glove box, the desired amounts of *rac*-Et[Ind]<sub>2</sub>ZrCl<sub>2</sub> and MMAO were introduced into the autoclave and then, toluene was added (to make a total volume of 30 mL). After that, the reactor was frozen in liquid nitrogen to stop any reactions and the proper amount of the comonomer was injected into the reactor (the molar ratio of ethylene:comonomer was fixed at 2:1). The reactor was evacuated to remove argon. Then, it was heated up to polymerization temperature (343 K) and the polymerization was started by feeding ethylene gas until the consumption of 0.018 mol of ethylene (6 psi was observed from the pressure gauge) was reached. The polymerization was terminated by addition of acidic methanol [30]. The time of reaction was recorded for purpose of calculating the activity. The precipitated polymer was washed with acidic methanol and dried at room temperature. Based on the system as mentioned above, the polymer yield was fixed by the amount of ethylene fed (0.018 mol). Experimentally, the polymerization was performed at least three times for each run and only the average yield and activity are reported. The error was found to be within less than 5% based on this polymerization system.

#### 3.3. Polymer characterization

Scanning electron microscopy (SEM) was used to determine the morphology of the polymeric samples. The samples were sputter-coated with a fine layer of platinum in an Edward Sputter Coater and analyzed with a JEOL (mode JSM-6400) electron microscope.

X-ray diffraction (XRD) was performed to determine the bulk crystalline phases of samples. Diffraction patterns were recorded in the reflection mode at room temperature using a Siemens D-5000 instrument. Ni-filtered Cu  $K_{\alpha}$  ( $\lambda = 1.54439$  Å) was used. The diffraction scans were collected over a period of  $2.4^{\circ}$  min 1 of  $2\theta$  from 10 to  $80^{\circ}$ .

<sup>13</sup>C-NMR spectroscopy was used to determine the triad distribution and 1-olefin insertion indicating the copolymer microstructure. Chemical shifts were referenced internally to the CDCl<sub>3</sub> peak and calculated according to the method described by Randall [26]. Sample solutions were prepared by

dissolving copolymer (50 mg) in 1,2,4-trichlorobenzene and CDCl<sub>3</sub> (0.5 mL). <sup>13</sup>C-NMR spectra were taken at 383 K using a Bruker Avance II 400 operating at 100 MHz with an acquisition time of 1.5 s and a delay time of 4 s.

The thermal properties were measured by a PerkineElmer Pyris Diamond Differential Scanning Calorimeter at a standard heating/cooling rate of 20K/min, under nitrogen flow. Both first and second melting temperatures have been analyzed. The reported melting temperature values are referred to the second heating scan. The peak temperature was assumed as melting temperature ( $T_m$ ) and the area was corresponding to the global melting enthalpy ( $\Delta H$ ). The crystallinity,  $\chi_c$ , was calculated from DSC data by using the formula  $\chi_c = 100 \cdot \times (\Delta H/\Delta H^{\circ})$  where  $\Delta H^{\circ} = 290$  J/g is the enthalpy of fusion for linear polyethylene as reported in ref. [31]. Approximately, 5-10 mg of sample was used for each DSC measurement. Moreover, it was possible to relate  $\Delta H$  (J/g) to the density (d, g/mL) of the copolymer through the following semiempirical equation:  $d = (2,195 + \Delta H)/2,500$ .

#### 4. Conclusions

In this article, we have reported the synthesis of LLDPE from the copolymerization of ethylene/1-olefin via metallocene/MAO catalysts by varying the comonomer (1-olefin) chain length. The results show that the increase in the short chain length 1-olefns (from 1-C<sub>8</sub> to 1-C<sub>10</sub>) can cause more steric hindrance of the catalytic center leading to decreased activity. However, when a long chain comonomer was used, a block of long chain 1-olefin can force the opening of the supplementary angle, therefore the coordination site was more open, resulting in increased activity. However, the increase of the chain length has no significant effects on the melting temperature and comonomer distribution. The crystallinity tended to decrease with increased chain length of comonomer, based on the XRD measurements.

# Acknowledgements

We thank the Thailand Research Fund (TRF), the Office of Higher Education Commission (CHE) of Thailand for the financial support of this project.

# References

- 1. Chum, P.S.; Swogger, K.W. Olefin polymer technologies-History and recent progress at The Dow Chemical Company. *Prog. Polym. Sci.* **2008**, *33*, 797-819.
- 2. Cano, J.; Kunz, K. How to synthesize a constrained geometry catalyst (CGC) A survey. *J. Organomet. Chem.* **2007**, *692*, 4519-4527.
- 3. Bensason, S.; Minick, J.; Moet, A.; Chum, S.; Hiltner, A.; Baer, E. Classification of homogeneous ethylene-octene copolymers based on comonomer content. *J. Polym. Sci., Part A: Polym. Phys.* **1996**, *34*, 1301-1315.
- 4. Ali, E.M.; Abasaeed, A.E.; Al-Zahrani, S.M. Optimization and control of industrial gas-phase ethylene polymerization reactors. *Ind. Eng. Chem. Res.* **1998**, *37*, 3414-3423.
- 5. Halterman, R.L. Synthesis and applications of chiral cyclopentadienylmetal complexes. *Chem. Rev.* **1992**, *92*, 965.

6. Brintzinger, H.; Beck, S.; Leclerc, M.; Stehling, U.; Röll, W. Reaction Mechanisms in Metallocene-Catalyzed Olefin Polymerization. *Stud. Surf. Sci. Catal.* **1994**, *89*, 193-200.

- 7. Chien, J.C.W.; Nozaki, T. Ethylene-hexene copolymerization by heterogeneous and homogeneous Ziegler-Natta catalysts and the "comonomer effect". *J. Polym. Sci., Part A: Polym. Chem.* **1993**, *31*, 227-237.
- 8. Simanke, A.G.; Galland, G.B.; Freitas, L.; Da Jornada, J.A.H.; Quijada, R.; Mauler, R.S. Influence of the comonomer content on the thermal and dynamic mechanical properties of metallocene ethylene/1-octene copolymers. *Polymer* **1999**, *40*, 5489-5495.
- 9. Shan, C.L.P.; Soares, J.B.P.; Penlidis, A. Ethylene/1-octene copolymerization studies with in situ supported metallocene catalysts: Effect of polymerization parameters on the catalyst activity and polymer microstructure. *J. Polym. Sci., Part A: Polym. Chem.* **2002**, *40*, 4426-4454.
- 10. Jaber, I.A.; Ray, W.H. Polymerization of olefins through heterogeneous catalysis. XIII. The influence of comonomer in the solution copolymerization of ethylene. *J. Appl. Polym. Sci.* **1993**, 49, 1709-1724.
- 11. Kim, I.; Woo, S.I. Homo- and co-polymerization of ethylene with highly active Ti/Mg bimetallic complexes Effect of crystallization conditions on structure and productivity. *Polym. Bull.* **1989**, 22, 239-246.
- 12. Koivumäki, J.; Fink, G.; Seppälä, J.V. Copolymerization of ethene/1-dodecene and ethene/1-octadecene with the stereorigid zirconium catalyst systems iPr[FluCp]ZrCl<sub>2</sub>/ MAO and Me<sub>2</sub>Si[Ind]<sub>2</sub>ZrCl<sub>2</sub>/MAO: Influence of the comonomer chain length. *Macromolecules* **1994**, 27, 6254-6258.
- 13. Karol, F.J.; Kao, S.-C.; Cann, K.J. Comonomer effects with high-activity titanium- and vanadium-based catalysts for ethylene polymerization. *J. Polym. Sci., Part A: Polym. Chem.* **1993**, *31*, 2541-2553.
- 14. Bialek, M.; Czaja, K. The effect of the comonomer on the copolymerization of ethylene with long chain α-olefins using Ziegler-Natta catalysts supported on MgCl<sub>2</sub>(THF)<sub>2</sub>. *Polymer* **2000**, *41*, 7899-7904.
- 15. Awudza, J.A.M.; Tait, P.J.T. The "comonomer effect" in ethylene/α-olefin copolymerization using homogeneous and silica-supported Cp<sub>2</sub>ZrCl<sub>2</sub>/MAO catalyst systems: Some insights from the kinetics of polymerization, active center studies, and polymerization temperature. *J. Polym. Sci.*, *Part A: Polym. Chem.* **2008**, *46*, 267-277.
- 16. McKnight, A.L.; Waymouth, R.M. Group 4 ansa-cyclopentadienyl-amido catalysts for olefin polymerization. *Chem. Rev.* **1998**, *98*, 2587-2598.
- 17. Kaminsky, W.; Piel, C.; Scharlach, K. Polymerization of ethene and longer chained olefins by metallocene catalysis. *Macromol. Symp.* **2005**, 226, 25-34.
- 18. Braunschweig, H.; Breitling, F.M. Constrained geometry complexes-synthesis and applications. *Coord. Chem. Rev.* **2006**, 250, 2691-2720.
- 19. Pérez, E.; Benavente, R.; Quijada, R.; Narváez, A.; Barrera Galland, G. Structure characterization of copolymers of ethylene and 1-octadecene. *J. Polym. Sci., Part B: Polym. Phys.* **2000**, *38*, 1440-1448.
- 20. Li, K.-T.; Dai, C.-L.; Kuo, C.-W. Ethylene polymerization over a nano-sized silica supported Cp<sub>2</sub>ZrCl<sub>2</sub>/MAO catalyst. *Catal. Commun.* **2007**, *8*, 1209-1213.

21. Krimm S.; Tobolsky A.V. Quantitative x-ray studies of order in amorphous and crystalline polymers. Quantitative x-ray determination of crystallinity in polyethylene. *J. polym. Sci.* **1951**, *7*, 57-76.

- 22. Hong, H.; Zhang, Z.; Chung, T.C.M.; Lee, R.W. Synthesis of new 1-decene-based LLDPE resins and comparison with the corresponding 1-octene- and 1-hexene-based LLDPE resins. *J. Polym. Sci., Part A: Polym. Chem.* **2007**, *45*, 639-649.
- 23. Camurati, I.; Cavicchi, B.; Dall'Occo, T.; Piemontesi, F. Synthesis and characterization of ethylene/1-olefin copolymers obtained by "single centre" catalysis. *Macromol. Chem. Phys.* **2001**, 202, 701-709.
- 24. Koivumäki, J. Properties of ethylene/1-octene, 1-tetradecene and 1-octadecene copolymers obtained with Cp2ZrCl2/MAO catalyst: Effect of composition and comonomer chain length. *Polym. Bull.* **1996**, *36*, 7-12.
- 25. Starck, P.; Löfgren, B. Thermal properties of ethylene/long chain α-olefin copolymers produced by metallocenes. *Eur. Polym. J.* **2002**, *38*, 97-107.
- 26. Randall, J.C. Carbon-13 NMR of ethylene-1-olefin copolymers: extension to the short-chain branch distribution in a low-density polyethylene. *J. Polym. Sci., Part A-2: Polym. Phys.* **1973**, *11*, 275-287.
- 27. Kim, C.; Kim, H. Copolymerization of propylene with various higher α-olefins using silica-supported *rac*-Me<sub>2</sub>Si(Ind)<sub>2</sub>ZrCl<sub>2</sub>. *J. Polym. Sci.*, *Part A: Polym. Chem.* **2001**, *39*, 3294-3303.
- 28. Quijada, R.; Galland, G.B.; Mauler, R.S. The influence of the comonomer in the copolymerization of ethylene with α-olefins using C<sub>2</sub>H<sub>4</sub>[Ind]<sub>2</sub>ZrCl<sub>2</sub>/ methylaluminoxane as catalyst system. *Macromol. Chem. Phys.* **1996**, *197*, 3091-3098.
- 29. Clas, S.D.; Mcfaddin, D.C.; Russell, K.E.; Scammell-Bullock, M.V.; Peat, I.R. Melting points of homogeneous random copolymers of ethylene and 1-alkenes. *J. Polym. Sci., Part A: Polym. Chem.* **2000**, *41*, 7899-7904.
- 30. Jongsomjit, B.; Kaewkrajang, P.; Shiono, T.; Praserthdam, P. Supporting effects of silica-supported methylaluminoxane (MAO) with zirconocene catalyst on ethylene/1-olefin copolymerization behaviors for linear low-density polyethylene (LLDPE) production. *Ind. Eng. Chem. Res.* **2004**, *43*, 7959-7963.
- 31. Carlini, C.; D'Alessio, A.; Giaiacopi, S.; Po, R.; Pracella, M.; Raspolli Galletti, A.; Sbrana, G. Linear low-density polyethylenes by co-polymerization of ethylene with 1-hexene in the presence of titanium precursors and organoaluminium co-catalysts. *Polymer* **2007**, *48*, 1185-1192.

Sample Availability: Samples of the compounds (LLDPEs) are available from the authors.

© 2011 by the authors; licensee MDPI, Basel, Switzerland. This article is an open access article distributed under the terms and conditions of the Creative Commons Attribution license (http://creativecommons.org/licenses/by/3.0/).





Journal of Natural Gas Chemistry 21(2012)83-90

# Production of propylene from an unconventional metathesis of ethylene and 2-pentene over Re<sub>2</sub>O<sub>7</sub>/SiO<sub>2</sub>-Al<sub>2</sub>O<sub>3</sub> catalysts

Weena Phongsawat<sup>1</sup>, Benjamas Netivorruksa<sup>1</sup>, Kongkiat Suriye<sup>2</sup>, Siraprapha Dokjampa<sup>2</sup>, Piyasan Praserthdam<sup>1</sup>, Joongjai Panpranot<sup>1\*</sup>

1. Center of Excellence on Catalysis and Catalytic Reaction Engineering, Department of Chemical Engineering, Faculty of Engineering, Chulalongkorn University, Bangkok 10330, Thailand; 2. SCG Chemicals CO., LTD. 1 Siam Cement Rd., Bangsue, Bangkok 10800, Thailand

[Manuscript received May 12, 2011; revised August 4, 2011]

#### Abstract

An unconventional metathesis of ethylene and 2-pentene over  $Re_2O_7/SiO_2-Al_2O_3$  catalysts has been studied as an alternative route for the production of propylene. Complete conversion of 2-pentene and propylene yield as high as 88 wt% were obtained under mild reaction conditions at 35 °C and atmospheric pressure. Unlike the conventional metathesis of ethylene and 2-butenes in which isomerization is a competing side reaction, the isomerization of 1-butene product from the unconventional metathesis of ethylene and 2-pentene to 2-butenes can further react with excess ethylene in the feed, resulting in additional increase in propylene yield. The secondary metathesis reaction was found to be favored under ethylene/2-pentene (E/2P) molar ratio  $\geqslant$ 3 and gas hourly space velocity (GHSV)  $\leqslant$ 1000 h<sup>-1</sup> at the reaction temperature of 35 °C. No catalyst deactivation was observed during the 455 min time-on-stream under the selected reaction conditions.

#### **Key words**

metathesis; propylene production; 2-pentene; rhenium; silica-alumina

#### 1. Introduction

Propylene is one of the most important feedstocks for petrochemical industries. The average annual growth of propylene global demand from 2009 to 2014 is expected to be around 5.1% per year [1-4]. Propylene supply-demand conditions and pricing are strongly dependent on refinery production, operating rates and feedstocks slates in the ethylene industry [5,6]. The main source of propylene is a byproduct from the thermal cracking of liquid feedstocks such as naphtha and LPGs. Propylene can also be produced using on-purpose technologies such as propane dehydrogenation and metathesis. The technology of propylene production from metathesis has received much attention in recent years. The commercial processes for conversion of ethylene and 2-butenes to propylene via cross-metathesis over heterogeneous catalysts have been developed [5,7-10]. This route, however, has some drawbacks because it needs access to large C4 streams that are free of isobutylene and butadiene [4]. Moreover, both cost and demand of butenes industrial feedstock increase continuously [7,11]. Metathesis between ethylene and 2-pentene is,

therefore, considered as an alternative route to produce propylene from cheaper raw materials. As shown in Equation 1, the main products from ethylene and 2-pentene are propylene and 1-butene. 1-Butene is also an important feedstock for the production of linear low density polyethylene.

$$CH_2 = CH_2 + CH_3 - CH = CH - CH_2 - CH_3 \rightarrow$$
 $CH_2 = CH - CH_3 + CH_2 = CH - CH_2 - CH_3$ 
(1)

Generally, the catalysts for olefin metathesis are based on transition metals Mo, W, Re, and Ru [7,12–16]. The catalytic systems can be carried out in both homogeneous and heterogeneous systems. The homogeneous catalysts are usually Mo, W, Re and Ru in the form of organometallic complexes while the most successful heterogeneous catalysts include Mo, W and Re in oxide form supported on high surface area inorganic oxides such as silica and alumina [7,17,18]. Due to their better handling properties and low separation problems, supported metal oxide catalysts are commercially more attractive. Industrial applications of olefin metathesis have been reviewed by Mol et al. [10].

<sup>\*</sup> Corresponding author. Tel: +66-2218-6869; Fax: +66-2218-6877; E-mail: joongjai.p@chula.ac.th
This work was supported by the financial supports from the Thailand Research Fund (TRF), the Office of Higher Education Commission, and the NRU-CU (AM1088A).

Supported Re oxide catalysts are known to be highly active for olefins metathesis under very mild reaction conditions even at room temperature [19] whereas supported W and Mo oxide catalysts requires much higher reaction temperature (150-500 °C) [7,20]. The major negative effects under high operating temperature over an acidic support were that isomerization readily occurs and as a consequence, selectivity to the primary metathesis product is much lowered [21]. High reaction temperature also leads to heavy coke formation on the metathesis active sites [22]. Another advantage of supported Re oxide catalysts is the higher tolerance to several poisons such as alkoxycarbonyl and alkoxy groups [7]. Since 1980s, the improvement of olefin metathesis over Re-based catalysts has been extensively reported. A number of studies have concluded that acidity of the support is an important factor for the active sites formation [23–29]. Recently, it has been reported that the use of mesoporous alumina supports for Re oxides has shown significant improvement in several metathesis reactions including metathesis of terminal olefins, internal olefins,  $\alpha$ -,  $\omega$ -dienes as well as ring opening metathesis polymerization (ROMP) of cycloalkenes and cross-metathesis of cycloalkenes with linear olefins [12,30–33]. Besides feed impurities, catalyst poisons, and the nature of catalysts, the activity and product selectivity in conventional olefins metathesis for propylene production depend largely on the reaction conditions such as the molar ratio of ethylene to 2-butene, GHSV, and reaction temperature.

In the present study, the gas-phase olefin metathesis between ethylene and 2-pentene as an alternative route for propylene production was investigated for the first time over the Re<sub>2</sub>O<sub>7</sub>/SiO<sub>2</sub>-Al<sub>2</sub>O<sub>3</sub> catalysts. The Re<sub>2</sub>O<sub>7</sub>/SiO<sub>2</sub>-Al<sub>2</sub>O<sub>3</sub> catalysts were selected because they have shown to produce high catalytic activity and good propylene yields under mild reaction conditions in the conventional cross metathesis between ethylene and 2-butene [19,34,35]. Moreover, reaction at relatively low temperature would be of industrial interest and more practical for the use of the alternative feed in an existing system. The catalytic performances of Re<sub>2</sub>O<sub>7</sub>/SiO<sub>2</sub>-Al<sub>2</sub>O<sub>3</sub> catalysts in the metathesis of ethylene and 2-pentene were investigated under wide operating conditions (i.e., the reaction temperature ranging from 35 to 150 °C, molar ratio of ethylene to 2-pentene (E/2P) from 2 to 6, and gas hourly space velocity (GHSV) from 500 to  $3000 \,h^{-1}$ ). The propylene yield, 2-pentene conversion and product distribution during 455 min time-on-stream were reported.

#### 2. Experimental

#### 2.1. Catalyst preparation

 $SiO_2$ -Al $_2O_3$  (99.9% Grade 135) from Aldrich was used as the support for the preparation of  $Re_2O_7/SiO_2$ -Al $_2O_3$  catalysts. The catalysts were prepared by the incipient wetness impregnation method using an aqueous solution of ammonium perrhenate (NH $_4$ ReO $_4$ , 99.999%, Aldrich). When the solution amount of the desired metal species was greater than that of the pore volume of the support, the impregnation procedure was repeated several times with drying (6 h, 110 °C) between each cycle to eliminate excess solvent. The catalysts were dried overnight at 110 °C in air and calcined at 550 °C for 8 h under oxygen flow with a heating rate of 10 °C/min. The actual amount of Re loading was determined by the inductive coupled plasma optical emission spectrometer (ICP-OES, PerkinElmer).

#### 2.2. Reaction test

Gas-phase metathesis reactions between ethylene and 2-pentene were carried out in a fixed-bed down flow stainless steel reactor with an i.d of 0.7 cm at atmospheric pressure. The reactant feed was composed of 6.75 vol% of 2pentene (≥99% mixture of isomers, Aldrich) pre-mixed with 2.25 vol% ethylene (99.999%, SCG Chemicals Co., Ltd.) in N<sub>2</sub> balance. All the reactants used in this work were in high purity grade without impurity such as oxygen, CO, water, S, and oxygenates hydrocarbons. In each experiment, approximately 1 g of the catalyst sample was placed in the middle of the reactor. A temperature sensor (type K thermocouple) was mounted into the reactor at the middle. The catalyst was first pretreated at 550 °C under nitrogen down flow for 1 h and then cooled down under the same gas to the desired operating temperature. Then, the reactant feed was introduced and both feed and reaction products were followed and analyzed every half an hour using an on-line gas chromatograph (Agilent GC 7820A) equipped with a capillary GS-Gaspro113-4362 column (60 m×0.32 mm). The GC signals were collected using an EZChrom Elite integrated peak program integrator. The conversion of limited 2-pentene reactant and the yield of products were calculated using the following equations:

2-Pentene conversion (%) = 
$$100 \times \frac{\text{Amount of 2-pentene in feed - amount of 2-pentene remained in product}}{\text{Amount of 2-pentene in feed}}$$

Yield of component  $i$  (%) = 2-Pentene conversion  $\times \frac{\text{Amount of component } i \text{ in products}}{\text{Amount of total products}}$  (2)

#### 3. Results and discussion

#### 3.1. Effect of E/2P mole ratio

The physical properties of  $SiO_2$ - $Al_2O_3$  and  $Re_2O_7/SiO_2$ - $Al_2O_3$  catalysts are summarized in Table 1.

As shown in Equation (3), the theoretical stoichiometric value of reactants in the olefin metathesis reaction is equimolar [11]. However, in the conventional metathesis process of ethylene and 2-butene, the optimal molar ratio of ethylene to 2-butene to produce high propylene yield was determined to be in excess but not more than 2.5 [36].

$$RCH=CHR+R'CH=CHR' \longrightarrow R'CH=CHR'$$

$$R'CH=CHR'$$

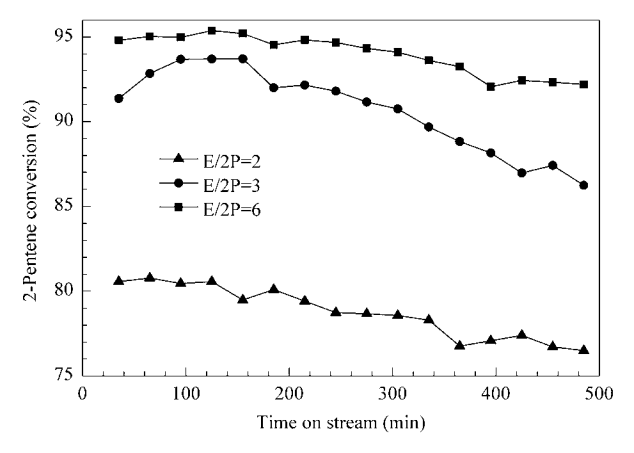
$$2RCH=CHR'$$
(3)

Table 1. The properties of the support and supported rhenium oxide catalyst

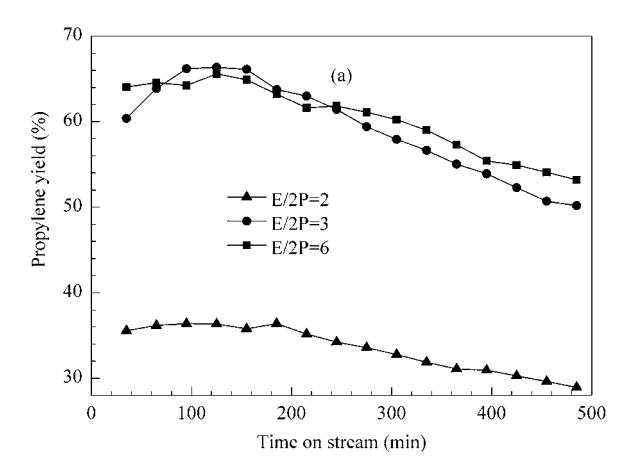
Properties	Sample			
Troperties	SiO <sub>2</sub> -Al <sub>2</sub> O <sub>3</sub>	Re <sub>2</sub> O <sub>7</sub> /SiO <sub>2</sub> -Al <sub>2</sub> O <sub>3</sub>		
BET surface area (m <sup>2</sup> ·g <sup>-1</sup> )	547.8	395.6		
Pore volume ( $cm^3 \cdot g^{-1}$ )	0.8	0.6		
Average pore size (nm)	5.6	5.9		
Al <sub>2</sub> O <sub>3</sub> support composition (wt%)	13	13		
Actual Re-metal loading (wt% Re) <sup>a</sup>	_	5.83		

<sup>&</sup>lt;sup>a</sup> The actual amount of Re-metal loading after calcination was determined by ICP-OES

In order to investigate the effect of E/2P molar ratio in the metathesis of ethylene and 2-pentene on Re<sub>2</sub>O<sub>7</sub>/SiO<sub>2</sub>-Al<sub>2</sub>O<sub>3</sub> catalysts, the reaction temperature and GHSV were set at 35 °C and 3000 h<sup>-1</sup>, respectively. All the reaction data were taken at 455 min time-on-stream. Changes of the catalyst activities in terms of 2-pentene conversion during 455 min timeon-stream were determined to be less than 5% under the selected reaction conditions. The 2-pentene concentration was kept constant while changing excess ethylene concentration to obtain the required molar ratios. The E/2P molar ratios were varied in the range of 2-6. The 2-pentene conversions under different E/2P molar ratios are shown in Figure 1. It is clear from Figure 1 that 2-pentene conversion increases from 77% to 87% with the increasing of E/2P molar ratio from 2 to 3. However, only a slight increase of 2-pentene conversion (to ca. 92%) could be observed with further increase of the E/2P molar ratio from 3 to 6. The main product yields in term of weight percent from the metathesis of ethylene and 2-pentene over Re<sub>2</sub>O<sub>7</sub>/SiO<sub>2</sub>-Al<sub>2</sub>O<sub>3</sub> catalysts as a function of time-onstream for different E/2P mole ratios are shown in Figure 2. The propylene yield increased from 39% to 59% with increasing E/2P from 2 to 3. There was no increase in propylene yield when E/2P was further increased from 3 to 6.



**Figure 1.** Effect of ethylene/2-pentene mole ratio on the 2-pentene conversion on  $Re_2O_7/SiO_2-Al_2O_3$  catalysts. Reaction conditions: Pressure = 0.1 MPa, GHSV =  $3000\,h^{-1}$ , Temperature =  $35\,^{\circ}\mathrm{C}$ 



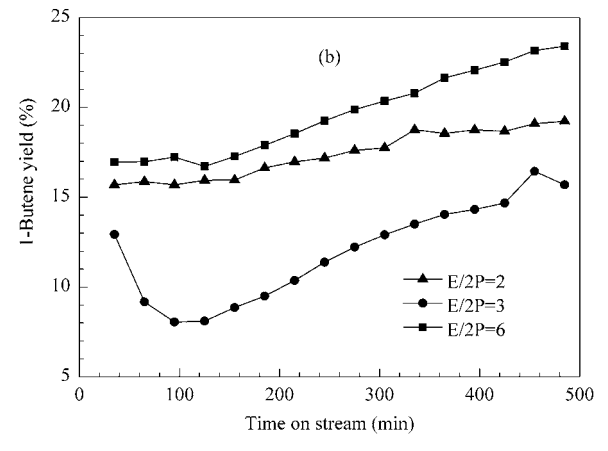


**Figure 2.** Yield of the primary metathesis products in the metathesis of ethylene and 2-pentene over  $Re_2O_7/SiO_2-Al_2O_3$  catalysts. Reaction conditions: Pressure = 0.1 MPa, GHSV =  $3000 \, h^{-1}$ , Temperature =  $35 \, ^{\circ}$ C

Besides propylene and 1-butene primary metathesis products, the other by-products were also produced including cisand tran-2-butene, 1-pentene, and  $C_{5+}$  hydrocarbons. The product distribution (yield percentage) from the metathesis reaction of ethylene and 2-pentene at 455 min time-on-stream obtained under different E/2P ratios and 35 °C are shown in Figure 3. It is known that 2-butene is more stable than 1butene so the double-bond isomerization of 1-butene to 2butene is inevitable over acidic catalyst systems even at low reaction temperature. In the conventional feed, double-bond isomerization also occurred at 21-25 °C [12,37,38]. The major  $C_{5+}$  hydrocarbon in this set of reactions was 3-hexene which were produced by self-metathesis of 2-pentene. Higher amount of C<sub>5+</sub> hydrocarbons were produced at lower E/2P mole ratio (E/2P = 2). It is suggested that excess ethylene could prevent the self-metathesis reaction of 2-pentene on the Re<sub>2</sub>O<sub>7</sub>/SiO<sub>2</sub>-Al<sub>2</sub>O<sub>3</sub> catalysts. Moreover, the amount of 2butenes was decreased with increasing E/2P mole ratio. The 2-butenes products could easily undergo a subsequent secondary metathesis reaction with excess ethylene, resulting in an additional propylene formation. The propylene yields for all the cases far exceeded the stoichiometric values (propylene selectivity of 50% (mole) or  $\sim 43\%$  (weight)). It is suggested that the isomerization of 1-butene to 2-butene was a useful side reaction assisting propylene formation in this alternative feed in the present work. A possible reaction scheme for propylene formation in the metathesis of ethylene and 2-pentene is shown in Equations (4) to (6):

Main reaction (primary metathesis)

$$CH_2 = CH_2 + CH_3 - CH = CH - CH_2 - CH_3 \rightarrow CH_2 = CH - CH_3 + CH_2 = CH - CH_2 - CH_3$$
(4)

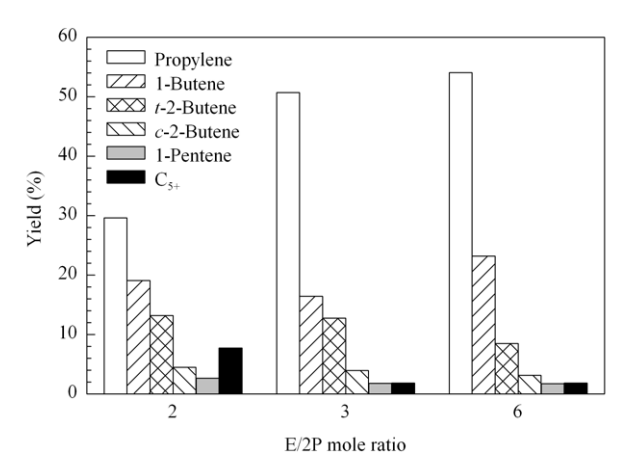
Double-bond isomerization of the primary metathesis product (1-butene)

$$CH2 = CH - CH2 - CH3 \rightarrow CH3 - CH = CH - CH3$$
 (5)

Secondary metathesis reaction

$$CH = CH + CH_3 - CH = CH - CH_3 \rightarrow$$

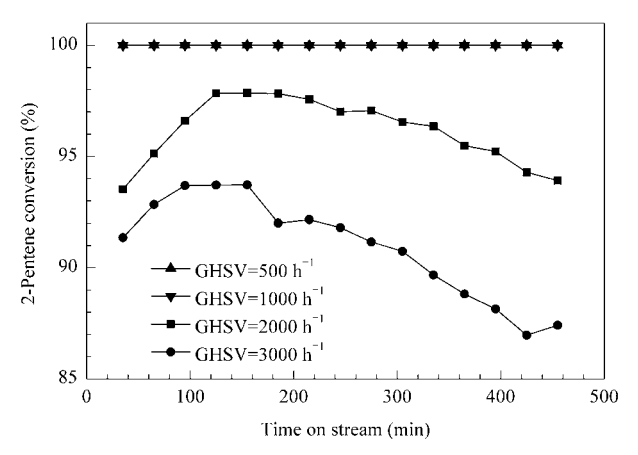
$$2CH_2 = CH - CH_3$$
(6)



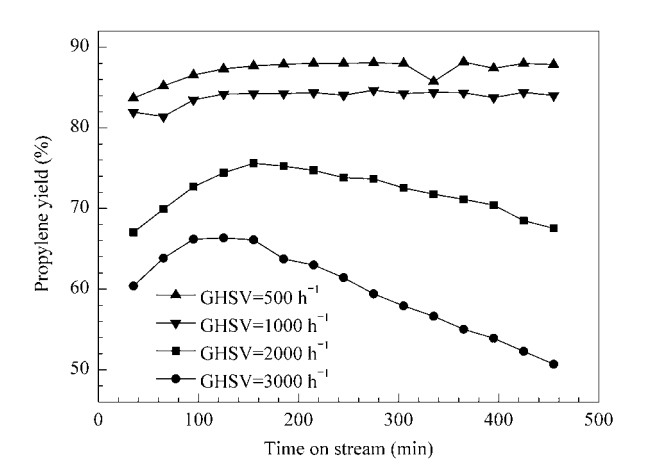
**Figure 3.** Product distribution in the metathesis reaction of ethylene and 2-pentene at different ethylene/2-pentene mole ratio at 455 min on stream. Reaction conditions: Pressure = 0.1 MPa, GHSV =  $3000 \, h^{-1}$ , Temperature =  $35 \, ^{\circ}\text{C}$ 

#### 3.2. Effect of GHSV

The effect of GHSV in the range of  $500-3000 \,h^{-1}$  on the catalytic performances of Re<sub>2</sub>O<sub>7</sub>/SiO<sub>2</sub>-Al<sub>2</sub>O<sub>3</sub> in the metathesis of ethylene and 2-pentene was investigated under the E/2P molar ratio of 3 and at 35 °C. As shown in Figure 4, the conversion of 2-pentene increased drastically from 87% to 100% when the GHSV was decreased from 3000 to  $500 \, h^{-1}$ at 455 min time-on-stream. The main product yields of the metathesis reaction between ethylene and 2-pentene as a function of time-on-stream under various GHSV are shown in Figure 5. Both propylene and 1-butene yields did not follow their stoichiometric amounts (43 wt% of propylene and 57 wt% of 1-butene) and higher amount of propylene and lower amount of 1-butene were obtained. As mentioned earlier, the isomerization of 1-butene to 2-butenes and the subsequent secondary metathesis reaction between ethylene and 2-butenes occurred readily under the selected reaction conditions, resulting in an increase in propylene yield. Table 2 summarizes the activities and the product yields obtained over Re<sub>2</sub>O<sub>7</sub>/SiO<sub>2</sub>-Al<sub>2</sub>O<sub>3</sub> catalysts at 35 °C under different GHSVs. It was found that at higher GHSV the secondary metathesis became less



**Figure 4.** Effect of gas hourly space velocity on the 2-pentene conversion over  $Re_2O_7/SiO_2-Al_2O_3$  catalysts. Reaction conditions: Pressure = 0.1 MPa, E/2P mole ratio = 3, Temperature = 35 °C



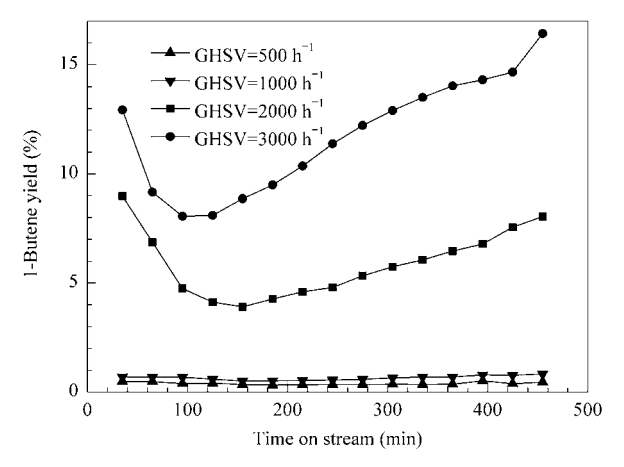


**Figure 5.** Yield of the primary metathesis products in the metathesis of ethylene and 2-pentene over  $Re_2O_7/SiO_2-Al_2O_3$  catalysts. Reaction conditions: Pressure = 0.1 MPa, E/2P mole ratio = 3, Temperature = 35 °C

pronounced while the other side reactions such as self-metathesis of 2-pentene was favored. Probably, due to the slow desorption rate of 2-pentene as compared with smaller hydrocarbon molecules such as ethylene [39–43], some of the 2-pentenes that adsorbed on the catalyst surface could interact themselves (self-metathesis reaction), forming 2-butene

and 3-hexene when the contact time was relatively short. It is noted that under the low reaction temperature conditions, oligomerization rate may be low so that the weight percentage of  $C_{5+}$  formed was mainly the 3-hexene products from 2-pentene self-metathesis reaction. Complete conversion of 2-pentene and propylene yield as high as 88% were achieved under the lowest GHSV (500 h $^{-1}$ ) and were found to be stable during the 455 min time-on-stream.

Table 2. Catalytic performance of Re<sub>2</sub>O<sub>7</sub>/SiO<sub>2</sub>-Al<sub>2</sub>O<sub>3</sub> catalyst with different GHSVs

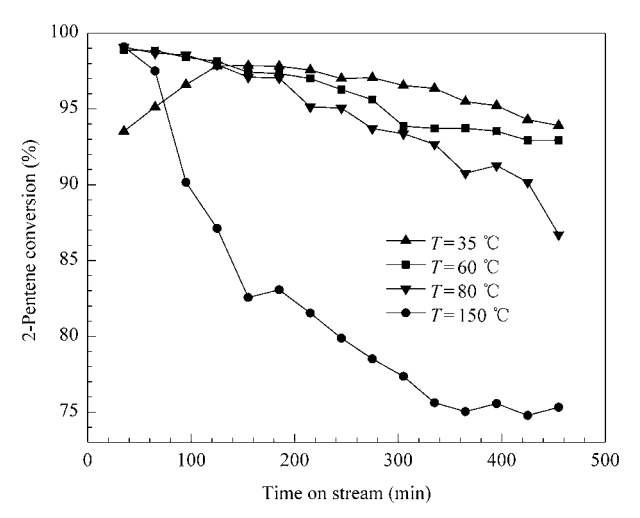
GHSV	2-C <sub>5</sub> =	Selectivity (%)					
$(h^{-1})$	conversion (%)	C <sub>3</sub> =	$1-C_4^=$	$2-C_4^=$	$1-C_5^=$	C <sub>5+</sub>	
500	100	88.0	0.5	11.7	_	_	
1000	100	83.9	0.8	15.2	_	_	
2000	93.9	70.9	8.6	19.5	_	_	
3000	87.4	58.2	8.8	19.1	2.0	2.1	

Reaction conditions: P=0.1 MPa, ethylene/2-pentene = 3 (mole ratio), T=35 °C, Time on stream = 455 min

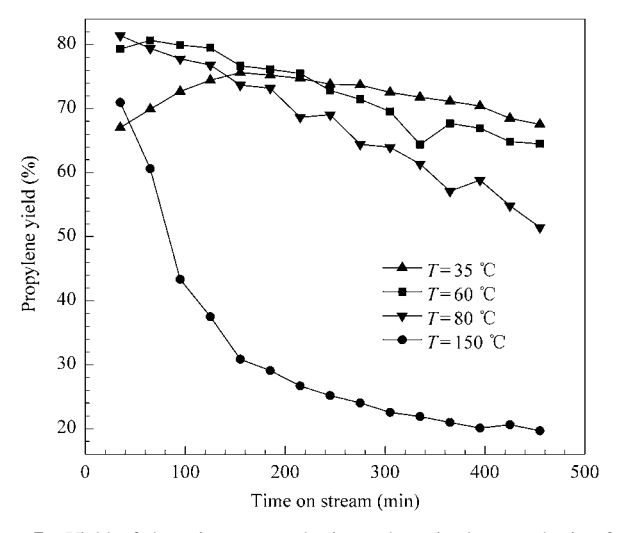
#### 3.3. Effect of reaction temperature

The metathesis of simple linear olefins is not accompanied by significant structural changes. Therefore, the reaction is almost a thermally neutral process and the variation of temperature has a negligible influence in view of the thermodynamics aspect [44]. However, for the operation aspect, it needs to know the effect of reaction temperature in the range of 35 to 150 °C on the catalytic performance of the metathesis of ethylene and 2-pentene over Re<sub>2</sub>O<sub>7</sub>/SiO<sub>2</sub>-Al<sub>2</sub>O<sub>3</sub> catalyst. And the results are shown in Figure 6. It is clear from Figure 6 that the reaction at 150 °C caused catalyst much faster deactivation than at the other temperatures. A fast drop of 2-pentene conversion from 99% to 83% was observed within the first 120 min time-on-stream. Then, it was gradually decreased to ca. 75% after 455 min time-on-stream. The main product yields of the metathesis reaction between ethylene

and 2-pentene at different reaction temperatures as a function of time-on-stream are shown in Figure 7. A trend similar to the conversion of 2-pentene was observed. If the reaction was proceeded at 150 °C, the propylene yield dramatically decreased from 70% to 37% within 120 min time-on-stream. On the other hand, 1-butene products were gradually increased along with the time-on-stream especially when the reaction was carried out at high reaction temperature. Deactivation of Re-based catalysts under high reaction temperature has been reported in Refs. [40,45–47]. The deactivation of the Rebased catalysts can mainly attribute to many aspects such as the structure change of active center, coke deposition, impurity in reactants, excessively reduction, adsorption of products and byproducts, etc. However, the reactants used in this study were high purity grade without impurity such as H<sub>2</sub>O, S, and oxygen-containing hydrocarbon so that the effect of impurity in the reactants on the catalyst activity would be minimized.



**Figure 6.** Effect of reaction temperature on the 2-pentene conversion over  $Re_2O_7/SiO_2-Al_2O_3$  catalysts. Reaction conditions: Pressure = 0.1 MPa, E/2P mole ratio = 3, GHSV =  $2000 \ h^{-1}$ 



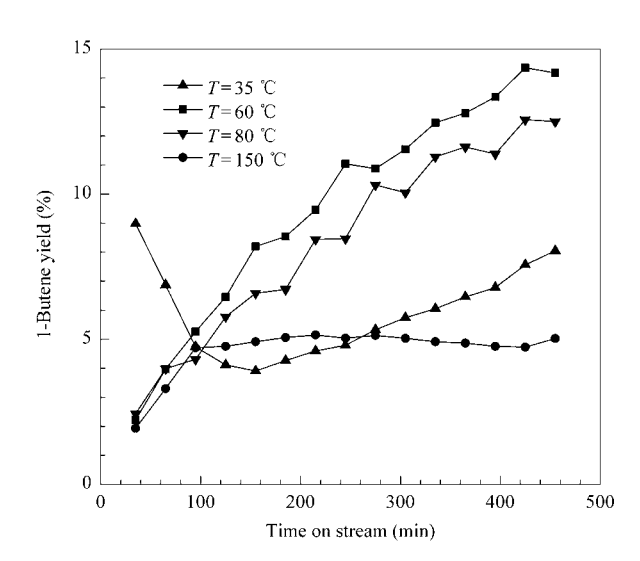


Figure 7. Yield of the primary metathesis products in the metathesis of ethylene and 2-pentene over  $Re_2O_7/SiO_2-Al_2O_3$  catalysts. Reaction conditions: Pressure = 0.1 MPa, E/2P mole ratio = 3,  $GHSV = 2000 \text{ h}^{-1}$ 

The product distributions in term of yield percentage produced after running the reaction for 35, 245, and 455 min on stream at various reaction temperatures are shown in Figure 8. It was found that much more side reactions, such as isomerization of butenes products and isomerization of 2-pentene reactant, could be observed over Re<sub>2</sub>O<sub>7</sub>/SiO<sub>2</sub>-Al<sub>2</sub>O<sub>3</sub> catalysts at the temperature higher than 60 °C. Moreover, the propylene yield decreased gradually with time-on-stream if the reaction temperature was higher than 60 °C. When the reaction temperature set at 150 °C, the propylene yield decreased by almost 40%, whereas the propylene yield remained constant

at ca. 70% – 72% when the reaction temperature set at 35 °C after running the reaction for 455 min. It has been reported that the deactivation of Re-based catalysts occurred as soon as they were in contact with alkenes and was accelerated under higher reaction temperatures [40,47]. On the one hand, larger amount of 2-butenes products were obtained at 150 °C, since most of 2-butenes did not further react with ethylene to form propylene in the subsequent secondary metathesis, resulting in poor propylene yield. On the other hand, isomerization and oligomerization were also dominated at higher reaction temperature. Although, 1-pentene product was not detected

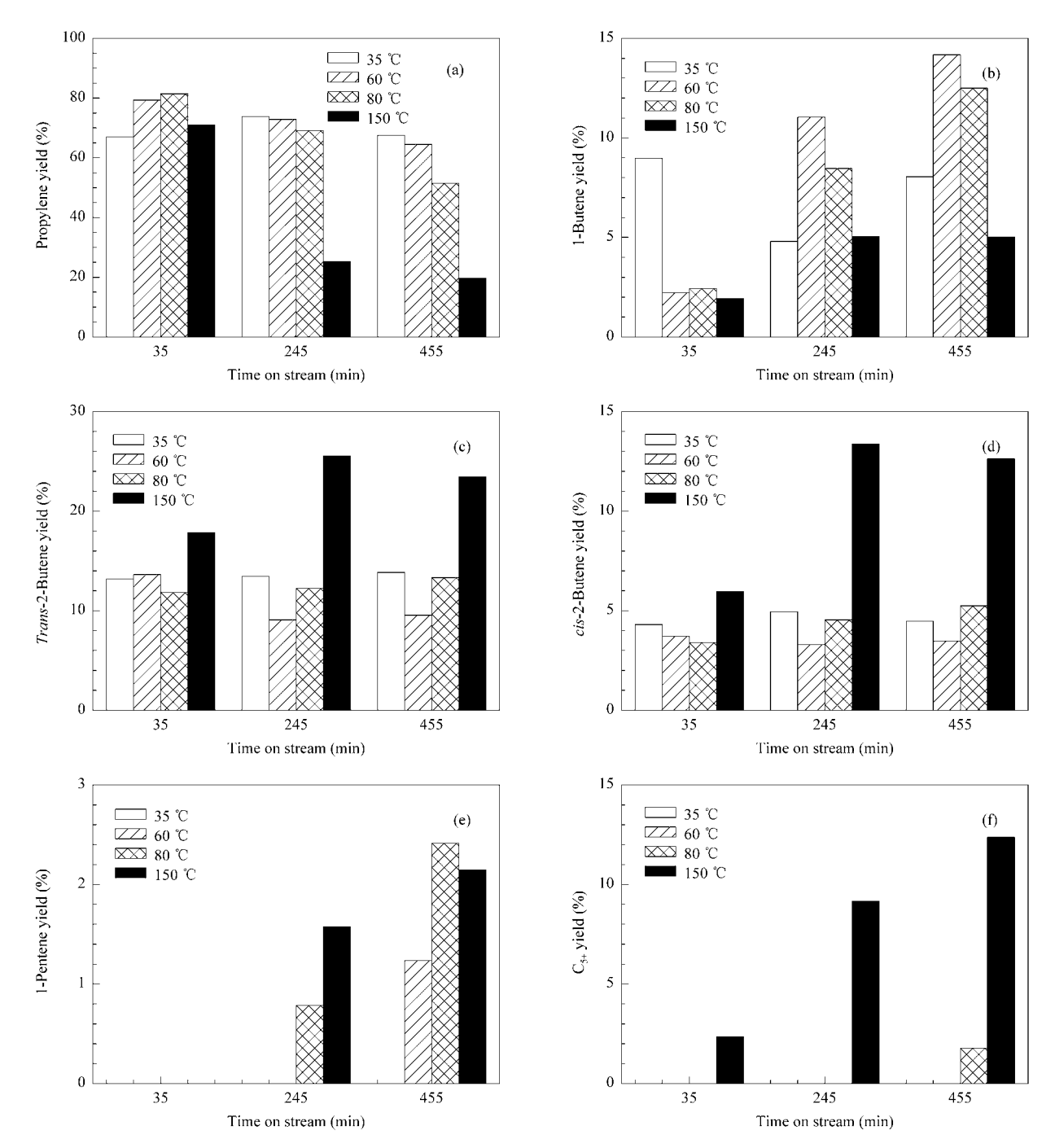
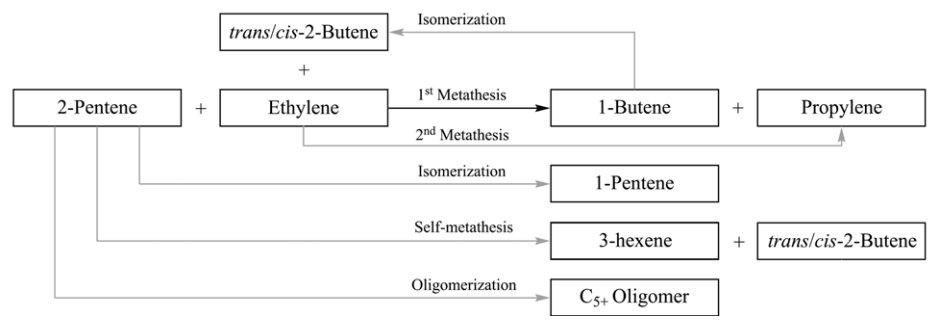


Figure 8. Product distributions along time on stream in the metathesis reaction of ethylene and 2-pentene at different reaction temperatures. Reaction conditions: Pressure = 0.1 MPa, E/2P (mole ratio) = 3, GHSV =  $2000 \text{ h}^{-1}$ 

during the first 35 min on stream at all the reaction temperatures, it became apparent (less than 2%) during 245 min on stream for the reaction temperatures at 80 and 150 °C. If the reaction temperature set at 60 °C, 1-pentene (ca. 1.2%) also produced after running the reaction for 455 min. There were very small amounts of branched isomers of butenes and hexene in the products because skeletal isomerization were also detected at the early stage of the reaction (during the first 90 min) when the reaction temperature was higher than 60 °C (results not shown), but they disappeared when the reaction time was prolonged. The results suggest that the modification of rhenium species on the catalyst surface may happen upon contacting with the reactants. It has been reported that skeletal isomerization was induced by unreduced rhenium oxide species [48]. After the rhenium-carbene species were formed, metathesis reaction was dominated and the skeletal isomerization became less pronounced. In the metathesis of 1-butene, iso-butene was found over the catalysts with relatively low activity and decreased with increasing metathesis activity [49].

As far as the formation of higher hydrocarbons is concerned, the  $C_{5+}$  products can be formed during the first 35 min on stream only at the reaction temperature as high as  $150\,^{\circ}\text{C}$ . Both 1-pentene and  $C_{5+}$  were increased with time-on-stream at high reaction temperature. Since much faster catalyst deactivation rate could be observed at  $150\,^{\circ}\text{C}$ , it is suggested that besides the self-metathesis of 2-pentene leading to the formation of 3-hexene, the formation of larger hydrocarbons via oligomerization reaction would occur under high reaction temperatures, leading to the formation of carbonaceous deposits and blocking the Re-active sites. Various reaction pathways in the metathesis of ethylene and 2-pentene over  $Re_2O_7/SiO_2-Al_2O_3$  catalysts are illustrated in Scheme 1.



Scheme 1. Various reaction pathways in the metathesis of ethylene and 2-pentene over  $Re_2O_7/SiO_2$ - $Al_2O_3$  catalysts. Dotted line represents the conventional metathesis of ethylene and 2-butenes

#### 4. Conclusions

The metathesis of ethylene and 2-pentene to propylene and 1-butene over Re<sub>2</sub>O<sub>7</sub>/SiO<sub>2</sub>-Al<sub>2</sub>O<sub>3</sub> catalysts with Re loading of 5.83 wt% has shown to be an effective alternative route for propylene production. The catalyst activity increases with increase of the reaction temperature, however, much faster catalyst deactivation is observed at 150 °C due to side reactions such as oligomerization and self-metathesis of 2pentene. The propylene yield at reaction temperature of 35 °C can be further improved when the mole ratio of E/2P higher than 3 and GHSV lesser than  $1000 \,\mathrm{h^{-1}}$  are used. The propylene yield of 88% at a 2-pentene conversion of 100% can be obtained under the optimized reaction conditions (i.e., with E/2P mole ratio of 3, GHSV of  $500 \, h^{-1}$ , and at the reaction temperature of 35 °C) without catalyst deactivation during 455 min on stream. Although double bond isomerization of 1-butene to 2-butenes occurred at the reaction temperature of 35 °C, they could further interact with excess ethylene, resulting in an increase in propylene selectivity.

#### Acknowledgements

The financial supports from the Thailand Research Fund (TRF), the Office of Higher Education Commission, and the NRU-CU (AM1088A) are gratefully acknowledged. The authors would like to thank the Royal Golden Jubilee Ph. D. scholarship from TRF and

SCG Chemicals for W. P.

#### References

- [1] Gartner E. World Petrochemicals Coverage of Propylene. World Petrochemicals. United States: IHS, Inc., 2010. 1
- [2] Eramo M. Oil Gas J, 2005, 103(45): 52
- [3] Jiao Y. Petrochem Ind Trends, 2004, (9): 9
- [4] Park Y K, Lee C W, Kang N Y, Choi W C, Choi S, Oh S H, Park D S. *Catal Surv Asia*, 2010, 14(2): 75
- [5] Parkinson G. Chem Eng, 2001, 108(8): 27
- [6] Mol J C. J Mol Catal, 1991, 65(1-2): 145
- [7] Ivin K J, Mol J C. Olefin Metathesis and Metathesis Polymerization. San Diego: Academic Press, 1997. 93
- [8] Taoufik M, Le Roux E, Thivolle-Cazat J, Basset J M. Angew Chem Int Ed, 2007, 46(38): 7202
- [9] Connon S J, Blechert S. Angew Chem Int Ed, 2003, 42(17): 1900
- [10] Mol J C. J Mol Catal A: Chem, 2004, 213(1): 39
- [11] Cornil B, Herrmann A W, Schogl R. Wong C. A Concise Encyclopedia Catalysis from A to Z. New York: Wiley-VCH, 2000
- [12] Balcar H, Hamtil R, Zilkova N, Cejka J. Catal Lett, 2004, 97(1-2): 25
- [13] Topka P, Balcar H, Rathousky J, Zilkova N, Verpoort F, Cejka J. *Microporous Mesoporous Mater*, 2006, 96(1-3): 44
- [14] Buchmeiser M R. New J Chem, 2004, 28(5): 549

- [15] Rhers B, Salameh A, Baudouin A, Quadrelli E A, Taoufik M, Coperet C, Lefebvre F, Basset J M, Solans-Monfort X, Eisenstein O, Lukens W W, Lopez L P H, Sinha A, Schrock R R. Organomet, 2006, 25(15): 3554
- [16] Rendon N, Berthoud R, Blanc F, Gajan D, Maishal T, Basset J M, Coperet C, Lesage A, Emsley L, Marinescu S C, Singh R, Schrock R R. Chem Eur J, 2009, 15(20): 5083
- [17] Li X, Zhang W, Li X, Liu S. Prog Chem, 2009, 20: 1021
- [18] Lokhat D, Starzak M, Stelmachowski M. Appl Catal A, 2008, 351(2): 137
- [19] Mol J C. Catal Today, 1999, 51(2): 289
- [20] Amigues P, Chauvin Y, Commereuc D, Hong C T, Lai C C, Liu Y H. *J Mol Catal*, 1991, 65(1-2): 39
- [21] Van Roosmalen A J, Mol J C. J Catal, 1982, 78(1): 17
- [22] Bartholomew C H. Appl Catal A, 2001, 212(1-2): 17
- [23] Duquette L G, Cieslinski R C, Jung C W, Garrou P E. *J Catal*, 1984, 90(2): 362
- [24] Piquemal J Y, Briot E, Vennat M, Bregeault J M, Chottard G, Manoli J M. Chem Commun, 1999, (13): 1195
- [25] Xiaoding X, Mol J C, Boelhouwer C. J Chem Soc, Faraday Trans 1 F, 1986, 82(9): 2707
- [26] Hsu C C. [PhD Dissertation]. Oklahoma: Oklahoma University, 1980
- [27] Buffon R, Auroux A, Lefebvre F, Leconte M, Choplin A, Basset J M, Herrmann W A. J Mol Catal, 1992, 76(1-3): 287
- [28] Amigues P, Chauvin Y, Commereuc D, Hong C T, Lai C C, Liu Y H. *J Mol Catal*, 1991, 65(1-2): 39
- [29] Schekler-Nahama F, Clause O, Commereuc D, Saussey J. Appl Catal A, 1998, 167(2): 237
- [30] Onaka M, Oikawa T. Chem Lett, 2002, (8): 850
- [31] Oikawa T, Ookoshi T, Tanaka T, Yamamoto T, Onaka M. Microporous Mesoporous Mater, 2004, 74(1-3): 93

- [32] Balcar H, Cejka J. Macromol Symp, 2010, 293(1): 43
- [33] Martin-Aranda R M, Cejka J. Top Catal, 2010, 53(3-4): 141
- [34] Mitra B, Gao X T, Wachs I E, Hirt A M, Deo G. Phys Chem Chem Phys, 2001, 3(6): 1144
- [35] Mol J C, Imamoglu i Y, Zumreoglu-Karan B, Amass A J. Olefin Metathesis and Polymerization Catalysis. Netherlands: Kluwer Academic, 1989. 173
- [36] Garside R J, Greene M I. US Patent 0124839 A1. 2005
- [37] Andreini A, Xu X D, Mol J C. Appl Catal, 1986, 27(1): 31
- [38] Mol J C, Andreini A. J Mol Catal, 1988, 46(1-3): 151
- [39] Moodley D J, van Schalkwyk C, Spamer A, Botha J M, Datye A K. Appl Catal A, 2007, 318: 155
- [40] Spronk R, Andreini A, Mol J C. J Mol Catal, 1991, 65(1-2): 219
- [41] Aguado J, Escola J M, Castro M C, Paredes B. Appl Catal A, 2005, 284(1-2): 47
- [42] Spronk R, Mol J C. Appl Catal, 1991, 70(2): 295
- [43] Hamtil R, Zilkova N, Balcar H, Cejka J. Appl Catal A, 2006, 302(2): 193
- [44] Huang S J, Liu S L, Xin W J, Xie S J, Wang Q X, Xu L Y. J Nat Gas Chem, 2006, 15(2): 93
- [45] Salameh A, Baudouin A, Soulivong D, Boehm V, Roeper M, Basset J M, Coperet C. J Catal, 2008, 253(1): 180
- [46] Stoyanova M, Rodemerck U, Bentrup U, Dingerdissen U, Linke D, Mayer R W, Lansink Rotgerink H G J L, Tacke T. Appl Catal A, 2008, 340(2): 242
- [47] Behr A, Schuller U, Bauer K, Maschmeyer D, Wiese KD, Nierlich F. Appl Catal A, 2009, 357(1): 34
- [48] Logie V, Maire G, Michel D, Vignes J L. *J Catal*, 1999, 188(1):
- [49] Harmse L, Van Schalkwyk C, Van Steen E. Catal Lett, 2010, 137(3-4): 123



Article

# Behaviors in Ethylene Polymerization of MgCl<sub>2</sub>-SiO<sub>2</sub>/TiCl<sub>4</sub>/THF Ziegler-Natta Catalysts with Differently Treated SiO<sub>2</sub>

Nichapat Senso, Bunjerd Jongsomjit and Piyasan Praserthdam \*

Center of Excellence on Catalysis and Catalytic Reaction Engineering, Department of Chemical Engineering, Faculty of Engineering, Chulalongkorn University, Bangkok 10330, Thailand

\* Author to whom correspondence should be addressed; E-Mail: piyasan.p@chula.ac.th; Tel.: +662-218-6869; Fax: +662-218-6868.

Received: 17 January 2011; in revised form: 24 January 2011 / Accepted: 27 January 2011 /

Published: 28 January 2011

Abstract: The present research focuses on investigation of the catalytic behaviors of MgCl<sub>2</sub>-SiO<sub>2</sub>/TiCl<sub>4</sub>/THF Ziegler-Natta (ZN) catalysts with fumed SiO<sub>2</sub> variously treated with silane compounds. The non-treated silica (NTS) and other silicas treated with dimethylsilicone fluid (TSDMSF), dimethyldichlorosilane (TSDMDCS), and hexamethyldisilazane (TSHMDS) were employed. It was found that the Cat-TSDMDCS and Cat-TSHMDS exhibited remarkably high activity, even with a similar bulk Ti content as the others. Thus, the more powerful technique of XPS analysis was used to determine the Ti content at the catalyst surface. It was evident that the surface concentrations of Ti could play important role on the catalyst activity. As the result, the increased activity is proportional to the surface concentration of Ti. It was mentioned that the change in surface concentration of Ti with different treated silica can be attributed to the effect of silane spacer group and steric hindrance. The distribution of Ti on the external surface can be also proven by means of EDX mapping, which matched the results obtained by XPS analysis. The treated silica also resulted in narrower molecular weight distribution (MWD) due to the more uniform active sites produced. There was no significant change in polymer morphology upon treatment of the silica.

Keywords: Ziegler-Natta catalyst; polyethylene; silica; alkyl silane; XPS

# 1. Introduction

In the polyolefin industry, the significant role of the Ziegler-Natta (ZN) catalysts is remarkable as are both industrial and academic interest in their reaction engineering [1-4]. In the production of polyolefins, the polymer particle morphology strongly affects the plant operation. The loss of polymer morphological control leads to many industrial operating problems, such as fouling and broadening reactor residence-time distribution. It is widely accepted that the polymer particle morphology is mainly determined by the morphology of a parent catalyst through the replication phenomenon [5,6]. The modification of supported-ZN catalyst is a preferred way to increase the morphology control of the polymers, increase the catalytic activity as well as increase catalytic stability.

Anhydrous magnesium dichloride (MgCl<sub>2</sub>) has been known as a preferred support for highly efficient ZN catalysts for the polymerization of olefins. MgCl<sub>2</sub> is often convenient to use in producing ZN catalysts with good morphology and the high rates of polymerization activity [7-8]. However, the frailty of MgCl<sub>2</sub> during preparation is still a problem for controlling the morphology of ZN when used in olefin polymerization. To overcome these problems, MgCl<sub>2</sub>-SiO<sub>2</sub>-bisupported titanium catalyst is preferred, especially when it is used in a gas-phase polymerization system [9-11]. For example, UCC has developed a series of MgCl<sub>2</sub>-SiO<sub>2</sub>/THF/TiCl<sub>4</sub> four-component catalyst systems for gas-phase ethylene polymerization and ethylene/1-hexene copolymerization [12-13]. This catalyst exhibits good comonomer incorporation properties, and the polyethylene products show good morphology control. Somehow, the catalytic activity of MgCl<sub>2</sub>-SiO<sub>2</sub>/THF/TiCl<sub>4</sub> system is lower than that without SiO<sub>2</sub> added. To increase the catalytic activity, the properties of SiO<sub>2</sub> such as type, shape, surface area [14] and OH content on the surface, should be considered in order to prepare a catalyst that is completely satisfactory for all purposes [15].

As is well known SiO<sub>2</sub> has OH groups on the surface, which are a very important poison for ZN catalysts. Preheated SiO<sub>2</sub> with different calcination temperatures (110–820 °C) is necessary to control the OH content on the surface of SiO<sub>2</sub>. The relationship between calcination temperature and TiCl<sub>4</sub> reaction temperature was observed by Hornytzkyj et al. [16]. It was found that the lower reaction temperature of 175 and 125 °C led to amorphous titanium species, whereas the temperature of 350 °C or higher resulted in amorphous and agglomerated titanium species. The amount of amorphous titanium species present in the high temperature samples is a function of the reaction temperature of TiCl<sub>4</sub> and of the preheat temperature of the SiO<sub>2</sub> determined by etching with sulfuric acid. Consequently, suitable calcination methods can also decrease the OH groups on the surface, but it consumes much energy and increases the production cost, so chemical treatment is one of the promising ways to decrease the OH groups on the surface of SiO<sub>2</sub> and it is practical. Hexamethyldisilazane (HMDS) and other organosilicon compounds (OSC), such as butyl dimethylsilyl (BDMS), dimethylsilicone fluid (DMSF), dimethyldichlorosilane (DMDCS), octadecyl dimethylsilyl (ODDMS) and trimethylsilyl (TMS) are commonly employed for the treatment of SiO<sub>2</sub>. This treated SiO<sub>2</sub> has a wide variety of applications, including as a support for ZN catalysts. Although the properties of surface-modified solids can be predicted, observed changes often differ from expectations. Predictions of structural changes, for instance, are almost always related to primary particles [17-19], but structural changes of highly dispersed or porous solids are often hierarchal. In the case of fumed oxides, structures are dictated by aggregates of primary particles and agglomeration of aggregates.

This hierarchal structure is difficult to predict, as it is dependent upon a balance of forces, which are altered as a result of surface modification [20,21]. This often results in unexpected changes to the modified surface of SiO<sub>2</sub>. Hertl and Hair [22] studied the treatment of silica with HMDS and used it as a support in ZN catalyst. They proposed that the reaction of HMDS occurs almost exclusively with isolated OH groups, leaving the H-bonded OH groups unoccupied. This property of HMDS has been applied successfully to study the bi-functional reactivity of TiCl4 toward H-bonded OH groups on silica in both vapor phase [22] and organic solution [23]. There were no changes of HMDS coverages on the HMDS-modified silica after the reaction with TiCl<sub>4</sub> at 175 °C [24]. Instead, the number of titanium atoms were half of that reacted without silylation, and the reaction led exclusively to doubly bonded titanium species. Consequently, the attainable trimethylsilyl surface coverage was not only determined by the steric hindrance, but also by the lower reactivity of HMDS toward H-bonded in OH groups. However, from the previous research, there is still little information about the effects of SiO<sub>2</sub> treated with different functional ethyl groups, such as dimethylsilicone fluid (DMSF), dimethyldichlorosilane (DMDCS) and hexamethyldisilazane (HMDS) on ZN catalyst properties and polymer properties although this information is of interest in both academia and industryl, especially in the surface study area. The XPS, SEM and EDX techniques were used in this investigation. Four types of CAB-O-SIL fumed silica were chosen for study based on the fact that they have well defined surface structures. They can be prepared by reproducible procedures and they are commonly used as catalyst supports. In this study, the influence of different silane compounds employed for the treatment of fumed silica in MgCl<sub>2</sub>-SiO<sub>2</sub>/TiCl<sub>4</sub>/THF catalysts on ethylene polymerization was examined The properties obtained were also determined and are discussed in detail.

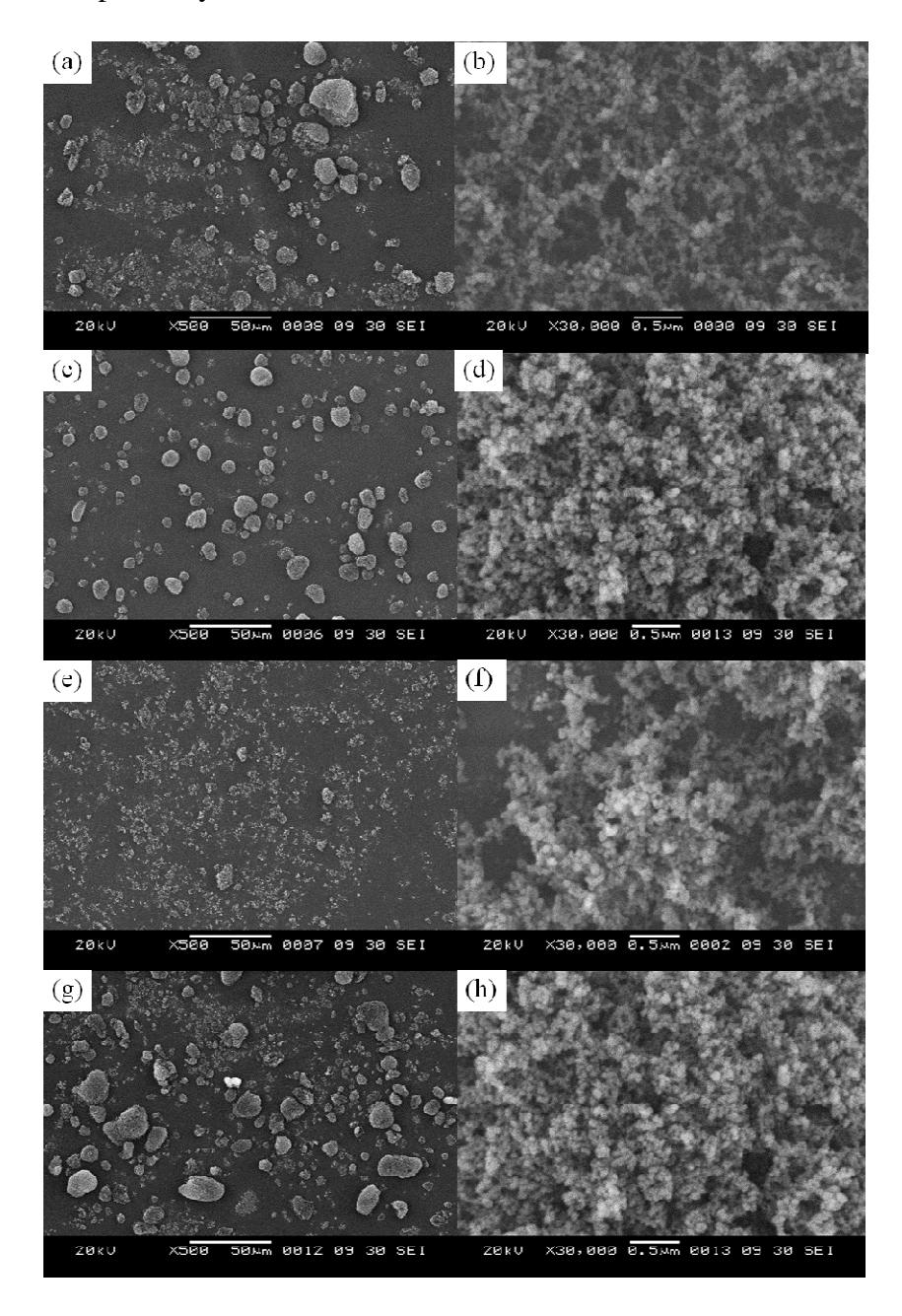
# 2. Results and Discussion

The structures of various treated fumed silicas used as supports in ZN catalysts are shown in Figure 1. There were four modified surface fumed silicas: (i) untreated SiO<sub>2</sub> (NTS); (ii) SiO<sub>2</sub> treated with dimethylsilicone fluid (TSDMSF); (iii) SiO<sub>2</sub> treated with dimethyldichlorosilane (TSDMDCS); and (iv) SiO<sub>2</sub> treated with hexamethyldisilazane (TSHMDS).

Figure 1. Different organo-silicon groups on the surface of variously treated fumed silicas.

The SEM images of all the samples are shown in Figure 2. It can be seen that the primary particles of fumed SiO<sub>2</sub> [Figures 2(b), (d), (f), and (h)] display no change in shape and size after treatment. A little agglomeration of particles occurred in TSDMSF and TSHMDS. The agglomeration of TSDMSF and TSHMDS particles results from the balance of force and type of chemical treatment. This result is supported by other research [20,21].

Figure 2. SEM images of different treated silicas; (a) NTS; (c) TSDMSF; (e) TSDMDCS; (g) TSHMDS; and (b), (d), (f), and (h) represent the primary particles of corresponding treated silicas, respectively.



After making the ZN catalysts with different treated SiO<sub>2</sub> supports, the bulk Ti content for all catalysts (Cat-NTS, Cat-TSDMSF, Cat-TSDMDCS, and Cat-TSHMDS) was analyzed by ICP. The results are shown in Table 1.

Sample	Treatment	Ti in bulk of catalysts (wt %) <sup>a</sup>	Activity b (kg PE/ mol-Ti/ h)	
Cat-NTS	Untreated silica	2.27	1,570	
Cat-TSDMSF	Dimethylsilicone Fluid	2.32	1,370	
Cat-TSDMDCS	Dimethyldichlorosilane	2.34	6,370	
Cat-TSHMDS	Hexamethyldisilazane	2.11	5,620	

**Table 1.** Ti content in bulk and activity of different catalysts.

It was found that the Ti contents in all catalyst samples were similar and within the 2.11–2.34 wt % range. Then, all catalyst samples were tested for ethylene polymerization under the specified conditions. The activity results are also shown in Table 1. It can be observed that the silica treated with silane compounds tends to show increased catalytic activity due to the effect of the spacer groups introduced by silane treatment [25]. It was also surprising that although all catalysts had similar amount of Ti contents in bulk, they exhibited different catalytic activity. As seen, Cat-TSDMDCS, and Cat-TSHMDS exhibited the remarkably high activity (about four times higher than Cat-NTS). For elucidation, another parameter such as the Ti content at surface needed to be verified. One of the most powerful techniques used to determine the surface properties is X-ray photoelectron spectroscopy (XPS). The oxidation state related to the binding energy of Ti and other elements was evaluated. Ti exhibited its binding energy at ca. 459 eV, indicating the Ti 2p state in all catalyst samples.

The surface concentrations obtained from the XPS measurements for Ti and other elements are also shown in Table 2. It was found that the surface concentrations for Ti 2p in the Cat-TSDMDCS and Cat-TSHMDS samples were remarkably high. On the other hand, for both samples Ti was located on the outer surface of the catalysts. This is probably due to less steric hindrance of the Cat-TSDMDCS and Cat-TSHMDS samples compared to the Cat-TSDMSF sample, as seen in Figure 1. The large amounts of Ti located on the surface are the main reason for the very high activities obtained from the Cat-TSDMDCS and Cat-TSHMDS samples as seen in Table 1. Therefore, the high activity of the ZN catalysts can be attributed to the large amounts of Ti content on surface, not in the bulk of catalysts.

**Table 2.** Surface concentrations of Ti, Si and Mg in all catalysts obtained by XPS analysis.

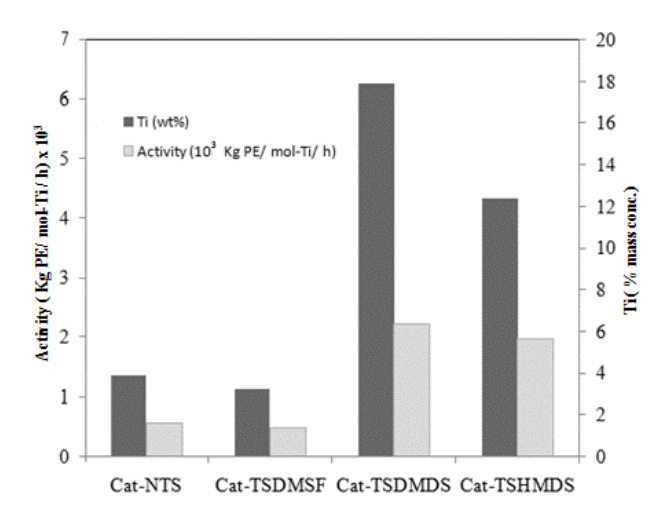
Peak	Cat-NTS	Cat-TSDMSF	Cat-TSDMDCS	Cat-TSHMDS
Ti2p	3.10	3.22	17.90	12.40
Si2p	64.05	88.55	37.81	56.13
Mg2s	32.85	8.23	44.30	31.47

In order to illustrate the relationship between the surface concentrations of Ti and the activities of catalysts, Figure 3 is constructed. It can be seen that the activities of catalysts are proportional to the surface concentrations of Ti present on the catalyst, as mentioned before.

Besides XPS measurements, the other powerful techniques used to determine the morphology and elemental distribution are SEM and EDX, respectively.

<sup>&</sup>lt;sup>a</sup> Obtained by ICP analysis; <sup>b</sup> Ethylene polymerization at 50 psi, 80 °C, Al/Ti = 100.

Figure 3. Relationship between the surface concentrations of Ti and the activities of catalysts.



The SEM and EDX mapping for all catalyst samples are shown in Figures 4 to 7 displaying the external surface of the catalysts and distribution of Mg, Si, and Ti on them. It should be mentioned that EDX only measures the concentrations in a layer less than 1 micrometer from the surface [26,27]. As a matter of fact, for whole catalyst particles, EDX measures the concentration on external surface of the particles. Figures 4–7 were all obtained with identical magnification. Considering the Ti distribution on the external surface of each catalyst represented by yellow patches (e), it can be clearly seen that the intensities of yellow patches (Ti at surface) in Figures 4 (Cat-NTS) and 5 (Cat-TSMDSF) are very low compared with those in Figures 6 (Cat-TSDMDCS) and 7 (Cat-TSDMDCS) corresponding to the XPS measurements as mentioned before. Therefore, both XPS and EDX mapping results can be used to confirm the rich Ti surface contents on the Cat-TSDMDCS and Cat-TSDMDCS samples leading to high catalytic activity. It is known that generally, TiCl<sub>4</sub> can bind to OH groups in the untreated silica. However, after treatment, it is mostly located on the MgCl<sub>2</sub> support as seen in the EDX mapping.

**Figure 4.** SEM micrograph and elemental distribution on Cat-NTS; (a) SEM image; (b) external surface; (c) Mg distribution; (d) Si distribution and (e) Ti distribution.

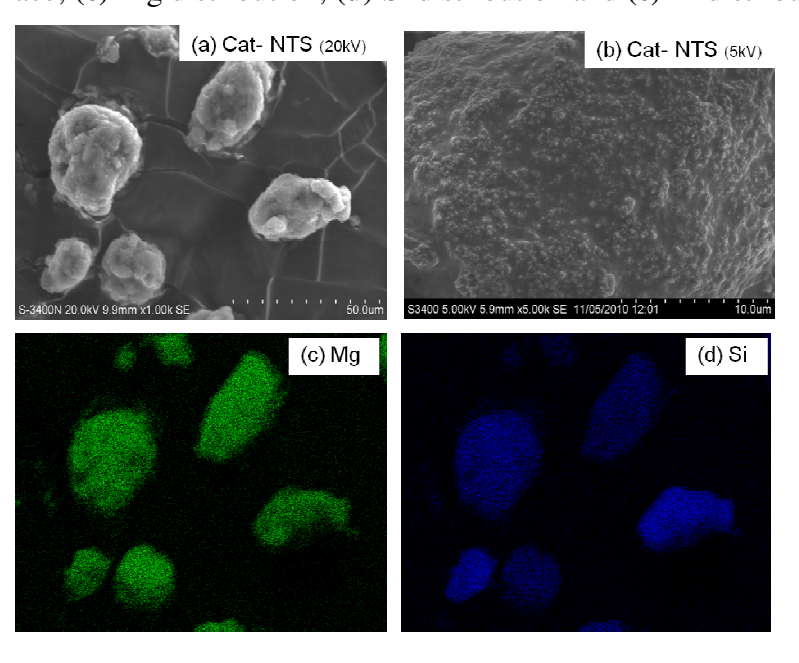
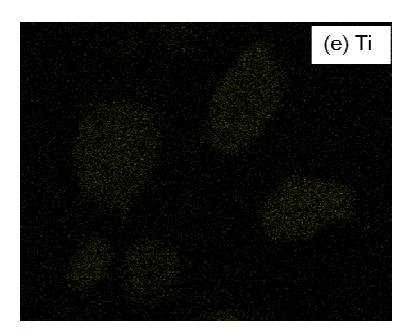
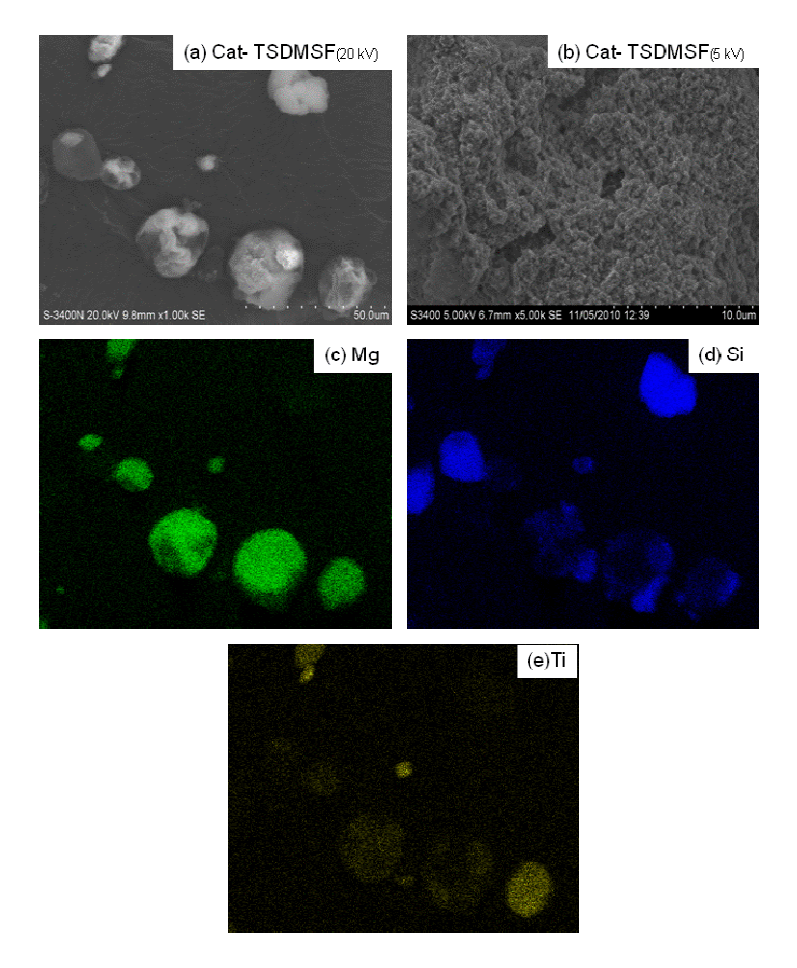


Figure 4. Cont.



**Figure 5.** SEM micrograph and elemental distribution on Cat-TSDMSF; (a) SEM image; (b) external surface; (c) Mg distribution; (d) Si distribution and (e) Ti distribution.



**Figure 6.** SEM micrograph and elemental distribution on Cat-TSDMDCS; (a) SEM image; (b) external surface; (c) Mg distribution; (d) Si distribution and (e) Ti distribution

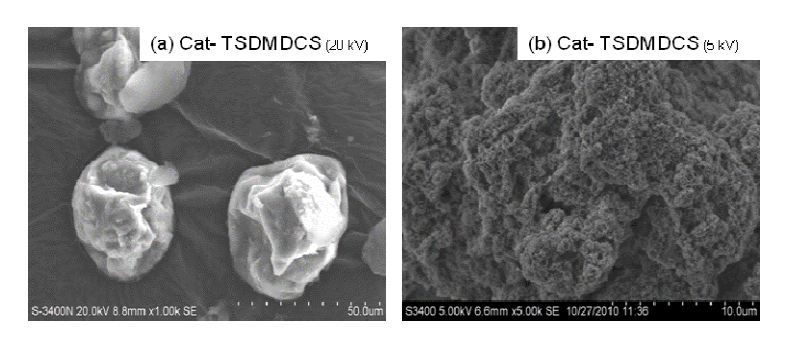
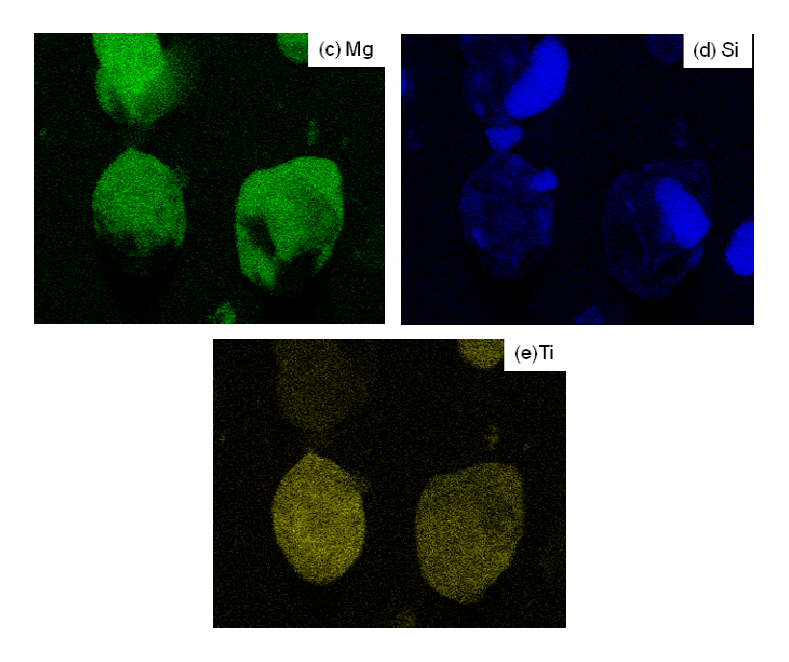
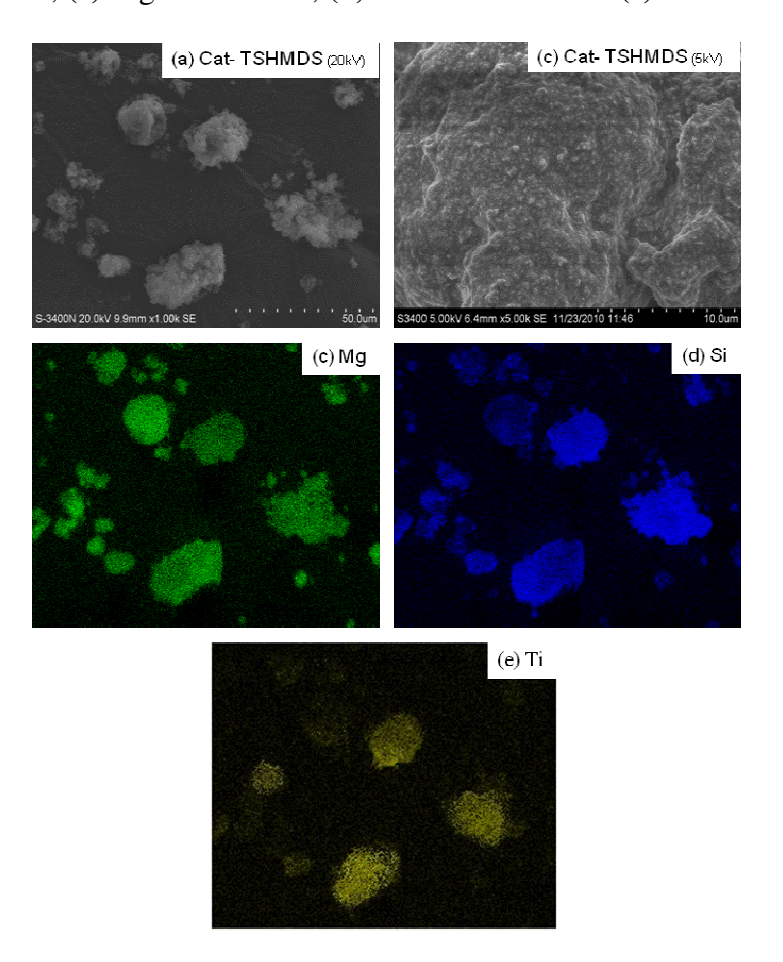


Figure 6. Cont.



**Figure 7.** SEM micrograph and elemental distribution on Cat-TSHMDS; (a) SEM image; (b) external surface; (c) Mg distribution; (d) Si distribution and (e) Ti distribution.



The molecular weight  $(M_w)$  and molecular weight distribution (MWD) of polymers obtained from different catalysts as analyzed by GPC are listed in Table 3. It can be seen that Cat-NTS produced polymer having the highest  $M_w$ ,  $M_z$ , and MWD compared to polymers obtained from other catalysts.

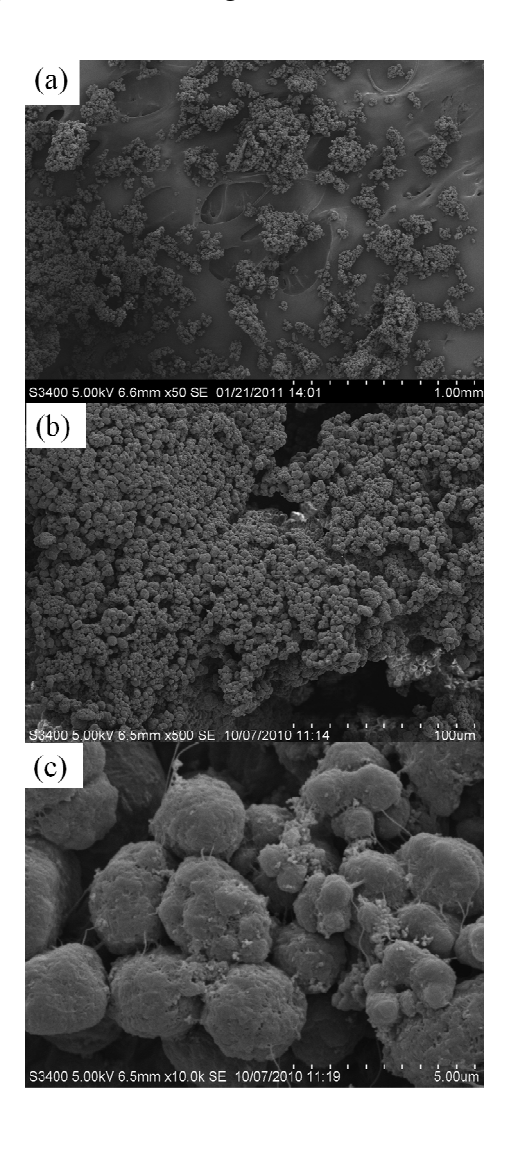
The broad MWD for Cat-NTS can be also attributed to the high molecular weight tail  $(M_z)$ . It can be observed that all treated silica for ZN catalysts apparently resulted in narrower MWD, as also reported in our previous work [25]. It was suggested that the treatment of silica with silane can result in more uniform active centers leading to narrower MWD.

<b>Table 3.</b> Molecular weights and	their distribution of po	olymers obtained from	different catalysts.

Comple	M <sub>n</sub>	$M_{\rm w}$	$M_z$	$M_{\rm v}$	MWD
Sample	(kg/mol)	(kg/mol)	(kg/mol)	(kg/mol)	$(M_w/M_n)$
Cat-NTS	40	1,028	4,574	739	25.7
Cat-TSDMSF	23	359	4,073	339	15.6
Cat-TSDMDCS	55	787	3,086	595	14.3
Cat-TSHMDS	24	437	4,064	405	18.2

A typical SEM micrograph of polymer obtained from all catalysts, which was similar, is shown in Figure 8. Hence, it indicates that the treated silica has no effect on the polymer morphologies.

**Figure 7.** A typical SEM micrograph of polyethylene samples of the treated silica ZN catalyst; (a) polyethylene at  $\times$  50 magnification; (b) polyethylene at  $\times$  500 magnification; and (b) surface of polyethylene at  $\times$  10k magnification.



# 3. Experimental

## 3.1. Chemicals

Polymerization grade ethylene and triethylaluminum (TEA) donated by PTT Chemical Plc., were used without further purification. TiCl<sub>4</sub> (Aldrich) and MgCl<sub>2</sub> (anhydrous) were donated by Toho Catalyst Co., Ltd. Fumed silica [non-treated (NTS), surface area 149.35 m<sup>2</sup>/g] and silica treated with different organic compounds [dimethylsilicone fluid (TSDMSF, surface area 121.60 m<sup>2</sup>/g), with dimethyldichlorosilane (TSDMDCS, surface area 112.00 m<sup>2</sup>/g), and with hexamethyldisilazane (TSHMDS, surface area 130.95 m<sup>2</sup>/g)] were supplied by Cabot Corporation and average particle size of all silicas were 0.2–0.3 μm as reported by the supplier. All types of silica were heated under vacuum at 120 °C for 2 h. Hexane and tetrahydrofuran were dried over dehydrated CaCl<sub>2</sub> and distilled over sodium benzophenone under an argon atmosphere prior to use. Ultra high purify (UHP) argon (99.999%) was purchased from Thai Industrial Gas Co., Ltd. and was further purified by passing through 3 Å molecular sieves., BASF catalyst R3-11G, NaOH and phosphorus pentaoxide (P<sub>2</sub>O<sub>5</sub>) to remove traces of oxygen and moisture. All chemicals were manipulated under an inert atmosphere using a vacuum glove box and Schlenk techniques.

# 3.2. Catalyst Preparation

The catalyst was prepared in a 500 mL vessel equipped with temperature control, and a turbine agitator. First, anhydrous tetrahydrofuran (150 mL) was added into the vessel and heated up to a 50 °C. Then, magnesium metal (0.12 g) was added, followed by titanium tetrachloride (2 mL). The mixture was continuously agitated and the temperature was held at about 70 °C. After that, magnesium dichloride (4.5 g) was added, and the heating process was continued at 70 °C for another 3 h. Then different treated silicas (NTS, TSDMSF, TSDMDCS and TSHMDS, 4.5 g) were slowly added to the mixture, which was stirred for 1 h to thoroughly disperse the silica in the solution. The temperature of mixture was held at 70 °C throughout this period and an argon atmosphere was maintained for all time. This mixture was washed, and then dried under vacuum.

#### 3.3. Polymerization Reaction

Ethylene polymerization was carried out in a 100 mL stainless steel autoclave reactor equipped with magnetic stirrer. The prescribed amount of hexane (30 mL), TEA and the  $SiO_2$ -MgCl<sub>2</sub>-supported ZN catalysts, such as Cat-NTS, Cat-TSDMSF, Cat-TSDMDCS and Cat-HMDS (Al/Ti molar ratio = 100) were added into the reactor. The ethylene pressure and reactor temperature were kept constant during polymerization [pressure in reactor = 50 psi and polymerization temperature was held at 80 °C]. Due to the fixed ethylene consumption (at 0.018 moles), the polymerization time was defined as the time that all ethylene gas was totally consumed [the equivalent pressure drop of 42 kPa (6 psi) was observed]. The polymerization time was recorded to calculate the activity. The reaction was terminated by adding acidic methanol and polymer was stirred for 30 min. After filtration, the polymer obtained was washed with methanol and dried at room temperature.

# 3.4. Polymer and Catalyst Characterization

# 3.4.1. Scanning electron microscopy and energy dispersive X-ray spectroscopy (SEM/EDX)

The morphological observations of polymers were carried out with a JEOL JSM-6400 scanning electron microscope. Micrographs were taken at 5-kV and 20-kV acceleration voltage. Before scanning electron microscopy (SEM) observations, the fracture surfaces of blends were coated with a thin layer of gold to avoid electrical charging and increase contrast during observation. The EDX was performed using Link Isis series 300 program, to determine the elemental distribution in catalysts.

# 3.4.2. Inductively coupled plasma (ICP)

Titanium content was measured using inductively coupled plasma atomic emission spectroscopy equipment (ICP-OES optima 2100 DV from PerkinElmer). In order to digest the sample, the catalyst was dissolved in hydrofluoric acid. The mixtures were stirred over a night. After the catalyst was completely dissolved, the solution was diluted with ID water to a volume of 100 mL.

# 3.4.3. X-ray photoelectron spectroscopy (XPS)

The chemical states and surface concentration of the elements were measured by the XPS technique using an Amicus photoelectron spectrometer with Mg  $K_{\alpha}$  X-ray source at current of 20 mA and 10 keV, resolution of 0.1 ev/step, and pass energy of 75 eV. The binding energy was calibrated by the C 1s peak at 285.0 eV. In this study, the sample was always treated under argon to prevent the sample from damage by moisture and oxygen in the atmosphere.

## 3.4.4. Gel permeation chromatography (GPC)

A high temperature GPC (Waters 150-C) equipped with a viscometric detector, differential optical refractometer and four Styragel HT type columns (HT3, HT4, HT5, and HT6) with  $1 \times 107$  exclusion limit for polystyrene was used to determine the molecular weight (M<sub>W</sub>) and molecular weight distributions (MWD) of the polymers produced. The analyses were performed at 140 °C using 1, 2, 4-trichlorobenzene as the solvent. The columns were calibrated with standard narrow MWD polystyrene.

#### 4. Conclusions

In summary, the catalytic behaviors of MgCl<sub>2</sub>-SiO<sub>2</sub>/TiCl<sub>4</sub>/THF catalysts with different treated silicas, such as Cat-NTS, Cat-TSDMSF, Cat-TSDMDCS, and Cat-TSHMDS were investigated. Although all catalysts exhibited the similar bulk Ti content, their activities were different. Therefore, the measurement of surface concentrations of Ti by means of XPS techniques was crucial. It was found that Cat-TSDMDCS and Cat-TSHMDS rendered high activities due to the large amounts of Ti at the surface of the catalyst. This could be also confirmed by the EDX mapping of Ti on the external surface. It can be concluded that for each catalyst the increased activity is proportional to the surface concentration of Ti. It is worth noting that the increased activity for the treated silica for Cat-TSDMDCS and Cat-TSHMDS catalysts can be attributed to both the effects of the silane spacer group and less steric hindrance. The treated silica in MgCl<sub>2</sub>-SiO<sub>2</sub>/TiCl<sub>4</sub>/THF catalysts apparently resulted in

narrower MWD due to the increased uniformity of the active sites. However, there was no significant change in polymer morphology with the treated silicas as seen by SEM.

# Acknowledgements

The authors thank the Thailand Research Fund (TRF), Office of the Higher Education Commission (CHE), Chulalongkorn University for Royal Golden Jubilee Fund under contract No. CU-CLUSTER-Advanced-4-54-53, Chula Unisearch (AM1088A), PTT Company and SCG chemical for the financial support of this project.

# **References and Notes**

- 1. Moore, E.P., Jr. *Polypropylene Handbook*, 1st ed.; Hanser Publishers: New York, NY, USA, 1996; pp. 86-87.
- 2. Ray, W.H. *Transition Metal Catalyzed Polymerizations*, 1st ed.; Quirk, R.P., Ed.; Cambridge University Press: New York, NY, USA, 1988; pp. 563-567.
- 3. Simonazzi, T.; Cecchin, G.; Mazzaulo, S. An outlook on progress in polypropylene-based polymer technology. *Prog. Polym. Sci.* **1991**, *16*, 303-329.
- 4. Senso, N.; Khaubunsongserm, S.; Jongsomjit, B.; Praserthdam, P. The influence of mixed activators on ethylene polymerization and ethylene/1-hexene copolymerization with silicasupported ziegler-natta catalyst. *Molecules* **2010**, *15*, 9323-9339.
- 5. Hock, C.W. How titanium chloride catalysts control the texture of as-polymerized polypropylene. *J. Polym. Sci. A-Polym. Chem.* **1966**, *4*, 3055-3064.
- 6. Kakugo, M.; Sadatoshi, H.; Sakai, J.; Yokoyama, M. Growth of polypropylene particles in heterogeneous Ziegler-Natta polymerization. *Macromolecules* **1989**, *22*, 3172-3177.
- 7. Kashiwa; N. The discovery and progress of MgCl<sub>2</sub>-supported TiCl<sub>4</sub> catalysts. *J. Polym. Sci. A-Polym. Chem.* **2004**, *42*, 1-8.
- 8. Nejad, M.H.; Ferrari, P.; Pennini, G.; Cecchin, G. Ethylene homo- and copolymerization over MgCl<sub>2</sub>-TiCl<sub>4</sub> catalysts: Polymerization kinetics and polymer particle morphology. *J. Appl. Polym. Sci.* **2008**, *108*, 3388-3402.
- 9. Lu, H.; Xiae, S. Highly isospecific silica/magnesium chloride bisupported catalyst for propene polymerization. *Makromol. Chem.* **1993**, *194*, 2095-2102.
- 10. Kim, I.I.; Woo, S.I. Morphological study of HDPE prepared with the highly active silica-supported titanium tetrachloride/magnesium chloride catalyst. *Polym. J.* **1989**, *21*, 697-707.
- 11. Pasquet, V.; Spitz, R. Preparation of bisupported catalysts for ethylene polymerization. *Makromol. Chem.* **1990**, *191*, 3084-3096.
- 12. Robert, J.J.; Belle Mead, N.J.; Elton, D.F.; Victoria, T. George, L.G.; Belle Mead, N.J. Process for producing ethylene polymers having reduced hexane extractable content. *US Patent No.* 5,290,745, 1994.
- 13. Isaac, J.L.; Frederick, J.K.; Belle Mead, N.J. Processes for preparing polyethylene catalysts by heating catalyst precursors. *US Patent No. 4,719,193*, 1988.
- 14. Lakomaa, E-L.; Haukka, S.; Suntola, T. Atomic layer growth of titania on silica. *Appl. Surf. Sci.* **1992**, 742, 60-61.

15. Haukka, S.; Lakomaa, E.-L.; Suntola, T. Analytical and chemical techniques in the study of surface species in atomic layer epitaxy. *Thin Solid Films* **1993**, 280, 225.

- 16. Haukka, S.; Lakomaa, E-L.; Jylha, O.; Vilhunen, J.; Hornytzkyj, S. Dispersion and distribution of titanium species bound to silica from TiCl<sub>4</sub>. *Langmuir* **1993**, *9*, 3497-3506.
- 17. Legrand, A.P. *The Surface Properties of Silicas*, 1st ed.; Wiley: New York, NY, USA, 1998; pp. 415-464.
- 18. Adamson, A.W.; Gast, A.P. *Physical Chemistry of Surface*, 6th ed.; Wiley: New York, NY, USA, 1997, pp. 365-369.
- 19. Gregg, S.J.; Sing, K. S.W. *Adsorption Surface Area and Porosity*, 2nd ed.; Academic Press: London, UK, 1982.
- 20. Barthel, H.; Rosch, L.; Weis, J. *Organosilicon Chemistry II. From Molecules to Materials*; Auner, N., Weis, J., Eds.; VCH: Weinheim, Germany, 1996; pp. 761-778.
- 21. Degussa, A.G. Basic Characteristics of Aerosil, Tech. Bull. Pigment. 1997, 997, 11-12.
- 22. Hertl, W.; Hair, M.L. Reaction of hexamethyldisilazane with silica, *J. Phys. Chem.* **1971**, *75*, 2181-2185.
- 23. Haukka, S.; Lakomaa, E.L. An IR and NMR study of the chemisorption of titanium tetrachloride on silica. *J. Phys. Chem.* **1993**, *97*, 5085-5094.
- 24. Blitz, J.P. Reactions of titanium tetrachloride with modified silica gel surfaces studied by diffuse reflectance FTIR spectroscopy. *Colloids Surf.* **1990**, *63*, 11-19.
- 25. Jongsomjit, B.; Kaewkrajang, P.; Wanke, S.E.; Praserthdam, P. A comparative study of ethylene/α-olefin copolymerization with silane-modified silica-supported MAO using zirconocene catalysts. *Catal. Lett.* **2004**, *94*, 205-208.
- 26. Tangjituabun, K.; Jongsomjit, B.; Praserthdam, P. Catalytic behaviors of SiO<sub>2</sub>-supported various aluminoxanes as coactivator in MgCl<sub>2</sub>/DEP/TiCl<sub>4</sub>-TEA catalysts for propylene polymerization. *Catal. Commun.* **2009**, *10*, 1319-1323.
- 27. Jongsomjit, B.; Ngamposri, S.; Praserthdam, P. Catalytic activity during copolymerization of ethylene and 1-hexene via mixed TiO<sub>2</sub>/SiO<sub>2</sub>-supported MAO with *rac*-Et[Ind]<sub>2</sub>ZrCl<sub>2</sub> metallocene catalyst, *Molecules* **2005**, *10*, 672-678.

Sample Availability: Samples of the polyethylene compounds are available from the authors.

© 2011 by the authors; licensee MDPI, Basel, Switzerland. This article is an open access article distributed under the terms and conditions of the Creative Commons Attribution license (http://creativecommons.org/licenses/by/3.0/).



Article

# The Influence of Comonomer on Ethylene/ $\alpha$ -Olefin Copolymers Prepared Using [Bis(N-(3-tert butylsalicylidene)anilinato)] Titanium (IV) Dichloride Complex

Patcharaporn Kaivalchatchawal <sup>1</sup>, Pattiya Suttipitakwong <sup>2</sup>, Sutheerawat Samingprai <sup>2</sup>, Piyasan Praserthdam <sup>1</sup> and Bunjerd Jongsomjit <sup>1</sup>,\*

- Center of Excellence on Catalysis and Catalytic Reaction Engineering, Department of Chemical Engineering, Faculty of Engineering, Chulalongkorn University, Bangkok 10330, Thailand
- Innovation & Technology, PTT Chemical Public Company Limited, Tambon Map Ta Phut, Amphoe Mueang Rayong, Rayong 21150, Thailand
- \* Author to whom correspondence should be addressed; E-Mail: bunjerd.j@chula.ac.th; Tel.: +66 2 2186869; Fax: +66 2 2186877.

Received: 25 November 2010; in revised form: 11 February 2011 / Accepted: 14 February 2011 / Published: 15 February 2011

**Abstract:** We describe the synthesis of [bis(*N*-(3-*tert*-butylsalicylidene)anilinato)] titanium (IV) dichloride (Ti-FI complex) and examine the effects of comonomer (feed concentration and type) on its catalytic performance and properties of the resulting polymers. Ethylene/1hexene and ethylene/1-octene copolymers were prepared through copolymerization using Ti-FI catalyst, activated by MAO cocatalyst at 323 K and 50 psi ethylene pressure at various initial comonomer concentrations. The obtained copolymers were characterized by DSC, GPC and <sup>13</sup>C-NMR. The results indicate that Ti-FI complex performs as a high potential catalyst, as evidenced by high activity and high molecular weight and uniform molecular weight distribution of its products. Nevertheless, the bulky structure of FI catalyst seems to hinder the insertion of  $\alpha$ -olefin comonomer, contributing to the pretty low comonomer incorporation into the polymer chain. The catalytic activity was enhanced with the comonomer feed concentration, but the molecular weight and melting temperature decreased. By comparison both sets of catalytic systems, namely ethylene/1-hexene and ethylene/1-octene copolymerization, the first one afforded better activity by reason of easier insertion of short chain comonomer. Although 1-hexene copolymers also exhibited higher molecular weight than 1-octene, no significant difference in both melting temperature and crystallinity can be noticed between these comonomers.

**Keywords:** post metallocene catalyst; homogeneous catalyst; FI catalyst; copolymerization

## 1. Introduction

Nowadays, polymers and plastics, especially linear low-density polyethylene (LLDPE), are playing the important role on the material industry due to their low density, high strength and cost-effectiveness. It is generally known that a common means of generating LLDPE is the copolymerization of ethylene and α-olefins such as 1-butene, 1-hexene, 1-octene and 1-decene [1]. The catalytic systems used have an effect on the structure and properties of the synthesized copolymers, therefore, much effort has been directed towards the development of highly active olefin polymerization catalysts. Normally, Ziegler-Natta catalysts produce copolymers with a wide molecular weight distribution (MWD) and chemical composition distribution (CCD) as a result of their multiple active sites [2,3]. Conversely, homogeneous metallocenes and post metallocenes are single sites, leading to very uniform polymers with narrow MWD and CCD. Particularly, the FI complexes (Fujita group invented catalysts) bearing phenoxyimine ligands that have been fully developed by Fujita and coworkers may be regarded in the forefront of these developments and have gained much attention in both academia and industry as potential olefin polymerization catalysts. This is probably because of high activities comparable to or exceeding those of the group 4 metallocene catalysts and the uniform properties of the polymers produced [4].

Concerning linear low-density polyethylene, it is normally accepted that comonomers (both type and concentration) play an important role in the properties of the resulting copolymers in terms of melting behavior, density, crystallinity and mechanical properties [5,6]. For instance, the introduction of short-chain branching derived from the comonomer decreases the crystallinity and melting temperature of the copolymer. In other words, the comonomer contents, which in turn are sensitive to a large number of factors, namely the catalyst and cocatalyst structure and the initial comonomer concentration in the polymerization system, govern the copolymer melting behavior [7]. Furthermore, a number of recent studies have been revealed that the film performance, such as impact and tensile strength, increases with the comonomer length [6]. The size and concentration of comonomer units also affects the catalytic activities in homogeneous metallocene systems. Hence, in this present study, in order to investigate the influence of the initial comonomer concentration and the type of comonomer (1-hexene or 1-octene) on the catalytic performance of the catalyst and the copolymer properties, the synthesis of ethylene/ $\alpha$ -olefins with Ti-FI catalysts have been performed using ethylene/comonomer in different proportions.

## 2. Results and Discussion

# 2.1. Synthesis and characterization of titanium complex (Ti-FI catalyst)

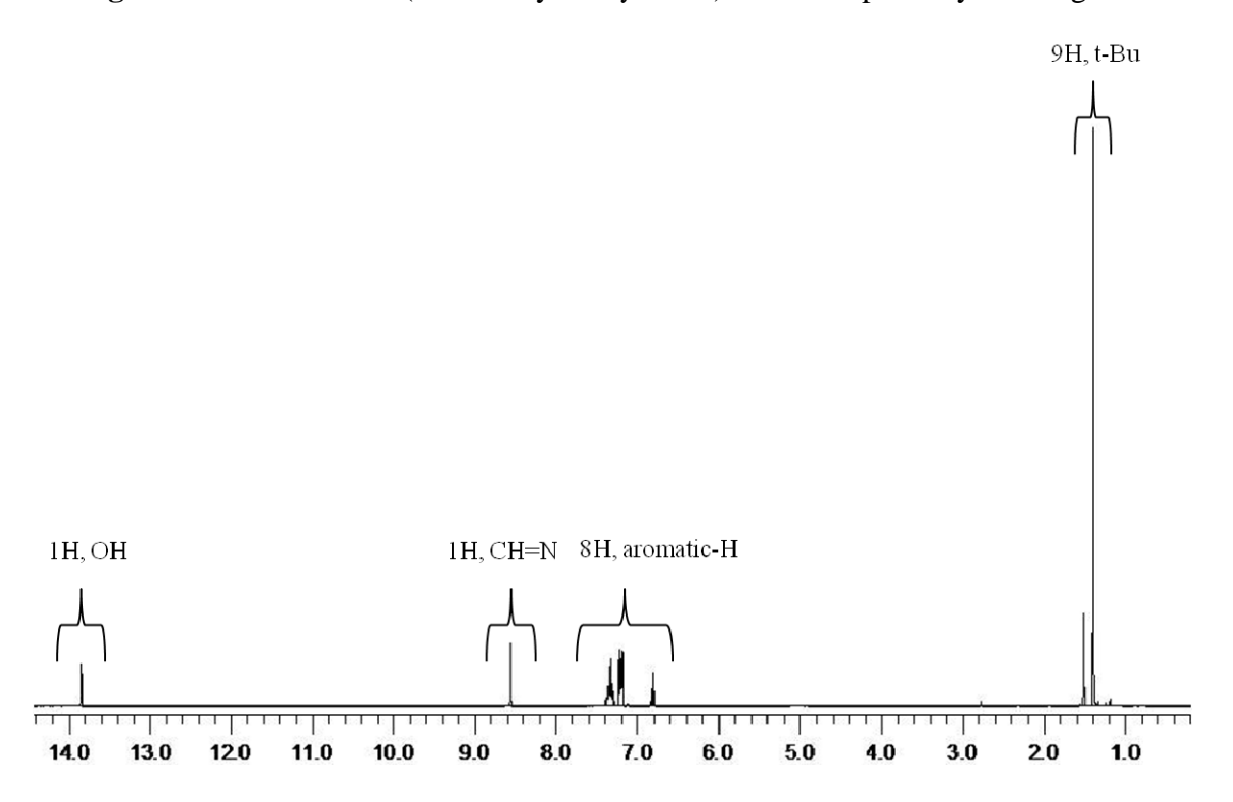
The synthetic route for titanium complex is depicted in **Scheme 1**. 3-*t*-Butylsalicylaldehyde reacted with a primary amine via Schiff base condensation in ethanol to yield a *N*-(3-*tert*butylsalycilidene)

aniline or phenoxyimine ligand. The titanium complex was obtained as reddish brown crystals by reaction of two equivalents of the lithium salt of the phenoxyimine ligand with TiCl<sub>4</sub>.

**Scheme 1.** Synthetic route to the titanium complex.

The <sup>1</sup>H-NMR spectra of the phenoxyimine chelate ligand *N*-(3-*tert*butylsalicylidene) aniline and Ti-FI complexes having phenoxyimine ligands are shown in **Figures 1** and **2**, respectively.

**Figure 1.** <sup>1</sup>H-NMR of *N*-(3-*tert*-butylsalicylidene) aniline or phenoxyimine ligand.



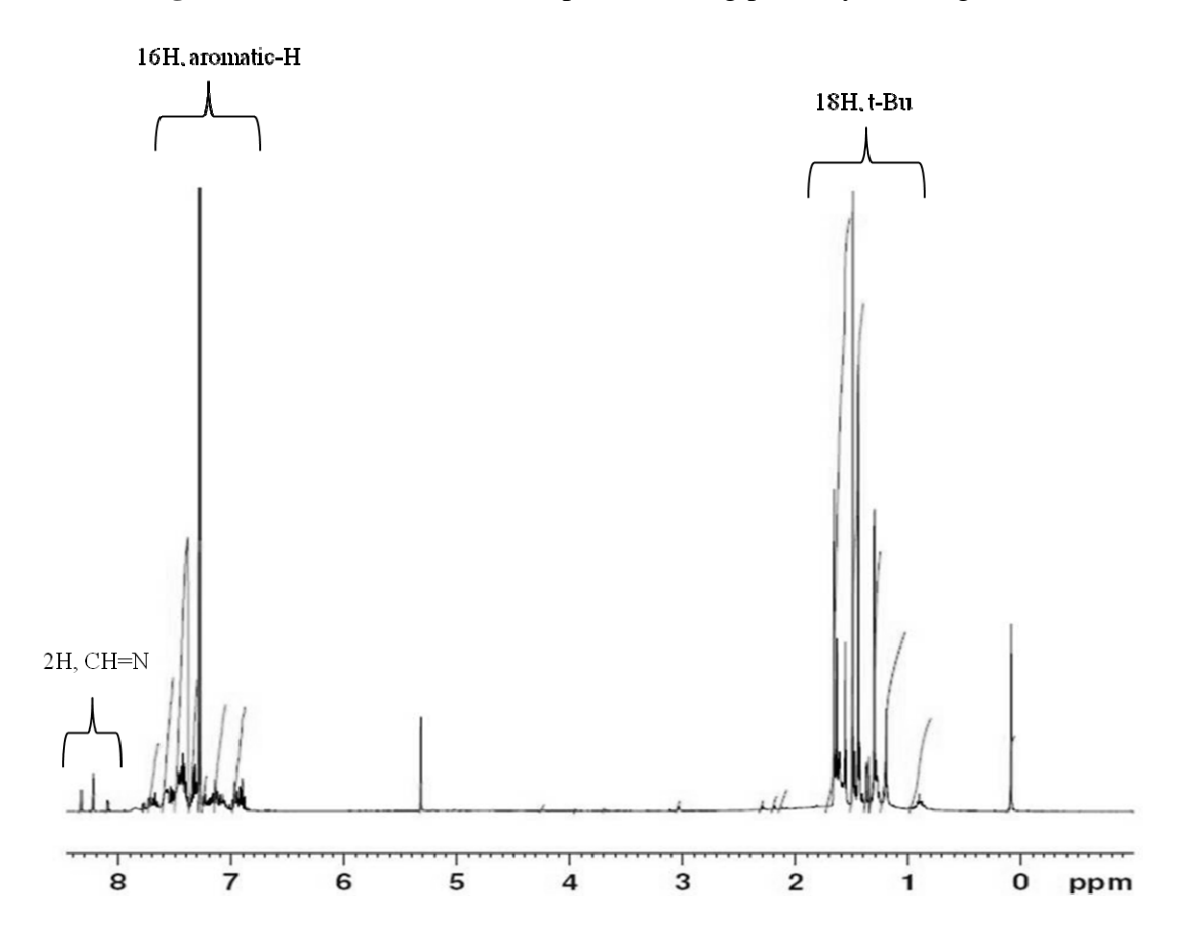
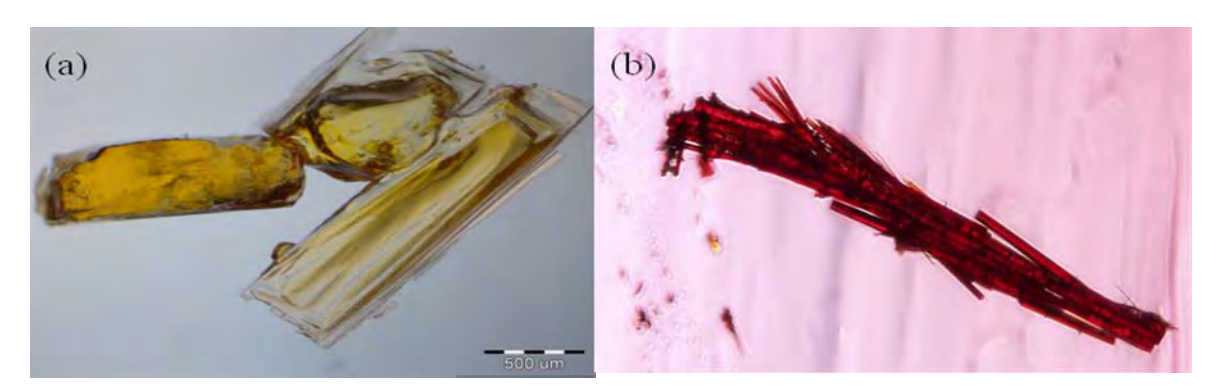


Figure 2. <sup>1</sup>H-NMR of Ti-FI complexes having phenoxyimine ligands.

In addition, using to the synthesis method mentioned, the Ti-FI ligand and complex can be crystallized into crystals and further characterized by optical microscopy to examine their morphologies, as shown in **Figure 3**. It can be seen from this figure that both of them exhibited the needle-like crystals of yellow and reddish brown color, respectively.



**Figure 3.** Optical microscope photographs of (a) Ti-FI ligand (b) Ti-FI complex.

# 2.2. Catalytic properties of ethylene and ethylene/α-olefins copolymerization

The laboratory scale Ti-FI catalyst/MAO catalyzed ethylene/ $\alpha$ -olefin copolymerization reaction was carried out at 323 K with constant ethylene pressure (50 psi). After filtration and drying, polymer was weighed and analyzed by  $^{13}$ C-NMR, GPC and DSC. The results are summarized in **Table 1**.

Entw.a	<b>Ethylene</b> <sup>b</sup>	Comonomer	Time	Weight	Activity <sup>c</sup>
Entry <sup>a</sup>	[mol/L]	[mol/L]	[s]	[g]	[kg polymer/mol Ti·h]
E-1	0.6	0	146.4	0.2881	2833
E-2	0.6	0	133.2	0.3230	3491
H-1	0.6	0.3	91.2	0.3496	5520
H-2	0.6	0.45	91.8	0.3647	5720
H-3	0.6	0.6	83.4	0.3766	6502
H-4	0	0.6	n.a. <sup>d</sup>	n.a. <sup>d</sup>	n.a. <sup>d</sup>
O-1	0.6	0.3	180	0.4405	3524
O-2	0.6	0.45	135.6	0.3748	3980
O-3	0.6	0.6	142.2	0.4470	4526
O-4	0	0.6	n.a. <sup>d</sup>	n.a. <sup>d</sup>	n.a. <sup>d</sup>

**Table 1.** Summary of ethylene/ $\alpha$ -olefins copolymerization catalytic activities.

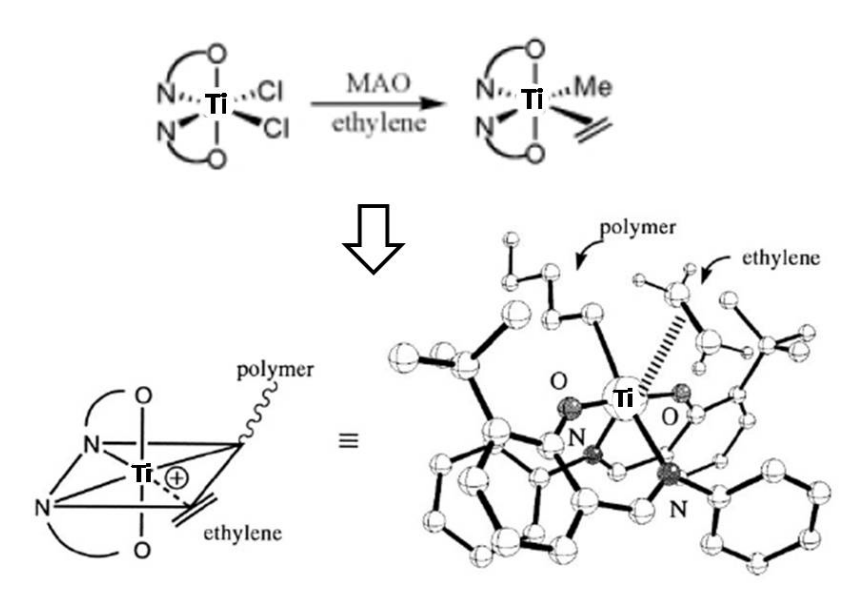
<sup>a</sup> run E1 used commercial *rac*-Et[Ind]<sub>2</sub>ZrCl<sub>2</sub> as catalyst; runs E2, H1-H4 and O1-O4 used Ti-FI as catalyst; comonomer of runs H1-H4 is 1-hexene; comonomer of runs O1-O4 is 1-octene; <sup>b</sup> Ethylene addition into the system; <sup>c</sup> Polymerization condition: [Ti] = 2.5 μmol, MAO as cocatalyst, [Al]/[Ti] = 250, liquid volume (toluene) = 30 mL, temperature = 323 K, ethylene pressure = 349 kPa (50 psi); <sup>d</sup> n.a. means not applicable (no observed polymer)

Concerning **Table 1**, the combination of Ti-FI catalyst with MAO in toluene solvent exhibited high activity (3,491 kg PE/mol Ti·h). To compare the catalytic activity of this catalyst with a metallocene catalyst, the commercial *rac*-Et[Ind]<sub>2</sub>ZrCl<sub>2</sub> catalyst was used to produce polyethylene under the same polymerization conditions. It was found that the activity value exceeded the activity obtained with the commercial cyclopentadienyl ligand metallocene catalyst, indicating that phenoxyimine chelate ligands have good potential as olefin polymerization catalysts. This may be attributed to the fact that these ligands posses moderate electron-donating properties species as well as a pair of available *cis*-located sites for polymerization [2,8]. In order to obtain more detailed insights into the catalytic activity during the polymerization, the possible active species of the titanium complex as determined by Fujita *et al.* from DFT calculations and X-ray crystallographic analysis [4,8] and the ethylene polymerization mechanism can be represented in the **Figure 4**. The mechanism begins with the activation of the catalyst with an appropriate cocatalyst – MAO in this case – to form an alkyl cationic complex, having the two available *cis*-located sites needed for polymerization. As a result, two chlorine bound sites were turned into polymerization sites, in other words, a growing polymer chain site and an ethylene coordination site, leading to the propagation of growing polymer chain.

Moreover, it can be observed from **Table 1** that no polymer was obtained from the system that was composed of only 1-hexene or 1-octene as monomer (entry H4 or O4). This result corresponded to the finding of Chaichana *et al.* [5] who examined the catalytic behavior of constrained geometry catalyst (CGC). They reported that the system presented no catalytic activity for in 1-hexene polymerization. Conversely, entry E2, which performs the ethylene homopolymerization is capable of attaining high polymer yields, suggesting that TiC<sub>34</sub>H<sub>36</sub>Cl<sub>2</sub>N<sub>2</sub>O<sub>2</sub> (Ti-FI) acts as a high potential catalyst for ethylene polymerization, despite its poor performance for 1-hexene or 1-octene homopolymerization. This may be ascribed to the fact that ethylene is the most active monomer; thus, it can insert into the active site and then form polymer chains by itself, whereas the other monomers, namely 1-hexene and 1-octene,

are too large and less active; accordingly, the initiation polymerization step cannot occur because of a lack of space for insertion of a bulkier monomer. On the other hand, when the system contains both ethylene and a bulky comonomer like 1-hexene or 1-octene, it turns out that the initiation step can be accomplished by the displacement of ethylene. This step provides higher space for longer 1-alkene and after that the propagation can proceed into the growing chain of copolymer.

Figure 4. Structure and possible active species of titanium complex [8].



The comparison of catalytic activities of two sets of catalytic system, containing using 1-hexene (H1-H4) and 1-octene (O1-O4) as comonomers by using Ti-FI as catalyst can be obtained from **Table 1**. The activities of both copolymerization systems were higher than in ethylene homopolymerization, a feature generally known as the "comonomer effect", which is a quite general effect of many comonomer pairs. Moreover, the catalytic activity increases with the increase of comonomer feed concentration. Several possible causes have been proposed to explain this behavior; however, the simplest and most supported is the improvement of monomer diffusion to the catalyst center on account of the crystallinity reduction in polymer structures when introducing a small amount of comonomer [7]. Another explanation for this phenomenon is that the inserted comonomer may resulted in the ion separation between the cationic active species and anionic cocatalyst providing more space for polymerization, thus enhancing the activity.

With regard to **Table 1**, the catalytic activity shows a general trend of 1-hexene > 1-octene under the same conditions with a fixed [ethylene]/[ $\alpha$ -olefin] monomer feed ratio. Thereby, it is fair to say that the bigger size of 1-octene comonomer has a negative effect on ethylene/ $\alpha$ -olefin copolymerization, which is probably due to more steric hindrance at the catalytic center.

## 2.3. Properties of polymers

The properties of the obtained homo and copolymers are gathered in **Table 2**. Comparing the PE obtained with both catalysts, it can be observed that the molecular weight of the homopolymer obtained with Ti-FI catalyst was considerably higher than that resulting from use of the metallocene catalyst. Besides, the commercial catalyst furnished quite high polydispersity when compared with the

corresponding value with the FI catalyst. The uniform molecular weight distribution results were also seen in all the copolymers having 1-hexene and 1-octene units synthesized with Ti-FI catalyst, implying the single site polymerization mechanism of this catalyst. Another interesting point dealing with the molecular weight result is that the average molecular weight of the copolymer decreased with the increase of comonomer feed concentration. This might suggest that 1-hexene and 1-octene incorporation promotes chain termination reactions, consequently contributing to formation of lower molecular weight copolymers [9]. Furthermore, it can be seen from **Table 2** that the copolymers derived from using 1-octene as comonomer had a lower molecular weight than those obtained from 1-hexene.

Regarding the thermal properties, 1-hexene and 1-octene incorporation resulted in a noticeable reduction of the melting temperature and crystallinity of the copolymers, when compared to the homopolymer (entry E-2), but the type of comonomer does not seem to influence both properties. This was in accord with the Flory's theory [1] that described the relationship between the melting behavior and comonomer of copolymerization system. However, this decrease was less pronounced in the case of higher comonomer feed concentration, suggesting that the bulky structure of the Ti-FI catalyst possibly reduces and limits the accessibility of the comonomer incorporation onto the active sites, especially for high comonomer concentrations, thus having a small effect on the properties.

Entry <sup>a</sup>	Feed ratio [E]/[α-olefin] [mol/mol]	Melting point <sup>c</sup> (T <sub>m</sub> )[°C]	Crystallinity <sup>d</sup> (X <sub>c</sub> )[%]	Molecular weight <sup>e</sup> (M <sub>w</sub> )[kg/mol]	PDI <sup>e</sup> (M <sub>w</sub> /M <sub>n</sub> )
E-1	1/0	134.5	38.78	432	2.5
E-2	1/0	134.3	64.01	920	1.60
H-1	1/0.5	128.7	41.94	729	1.66
H-2	1/0.75	126.3	44.93	768	1.69
H-3	1/1	127.0	43.21	675	1.67
H-4	0/1	n.a. <sup>b</sup>	n.a. <sup>b</sup>	n.a. <sup>b</sup>	n.a. <sup>b</sup>
O-1	1/0.5	128.0	42.21	668	1.64
O-2	1/0.75	127.2	48.13	641	1.63
O-3	1/1	128.3	50.37	633	1.65
O-4	0/1	n.a. <sup>b</sup>	n.a. <sup>b</sup>	n.a. <sup>b</sup>	n.a. <sup>b</sup>

**Table 2.** Properties of resulting polymers.

<sup>a</sup> run E1 used commercial *rac*-Et[Ind]<sub>2</sub>ZrCl<sub>2</sub> as catalyst; runs E2, H1-H4 and O1-O4 used Ti-FI as catalyst; comonomer of runs H1-H4 is 1-hexene; comonomer of runs O1-O4 is 1-octene; <sup>b</sup> n.a. means no observed polymer; <sup>c</sup> determined by DSC; <sup>d</sup> estimated by dividing the heat of fusion of polymer (measured by DSC) by 294 J/g of the theoretical value for 100% crystalline PE homopolymer; <sup>e</sup> determined by GPC

# 2.4. Microstructure of the polymers

The microstructure of copolymers, including the incorporation of comonomer and the comonomer triad distribution, can be determined from  $^{13}$ C-NMR spectroscopy. Nonetheless, in this work there was no peak which indicated the comonomer branch in the backbone for all copolymers, presumably due to the presence of only a small amount of  $\alpha$ -olefin insertion, contrary to the  $\alpha$ -olefin incorporation ability

of commercial rac-Et[Ind]<sub>2</sub>ZrCl<sub>2</sub>. Jongsomjit et~al. found that this commercial complex possessed a high insertion ability for 1-hexene and 1-octene, at around 40 and 29%, respectively [10-14]. In addition, this problem might occur because of the ultra high molecular weight of the resulting copolymers and the too low sample preparation temperature. Thereby, other techniques, such as CRYSTAF, infrared spectroscopy and pyrolysis gas chromatography mass spectrometry, should be further applied to investigate the copolymer microstructure in this case.

# 2.5. Morphology of polymers

The SEM micrographs of polymers are shown in **Figure 5**, indicating the typical morphologies of copolymers obtained from this catalytic system. There was no significant change in copolymer morphologies with the different comonomer lengths and initial comonomer concentrations employed. On the contrary, the morphology of polymers generated from Ti-FI catalyst seems to more rod-like comparing to those obtained from metallocene catalyst, suggesting that the catalyst microstructure might have an effect on the polymer morphology.

(e) (f)

**Figure 5.** SEM photographs of polymers (a) E-1 (b) E-2 (c) H-1 (d) H-2 (e) H-3 (f) O-1.

# 3. Experimental

#### 3.1. Materials

All operations were handled under an argon atmosphere using glove box and/or standard Schlenk techniques. Ethylene (polymerization grade) was obtained from the National Petrochemical Co. Ltd., Thailand. 3-*tert*-Butylsalicylaldehyde, aniline and TiCl<sub>4</sub> (99+%) were purchased from Aldrich Chemical Company, Inc., and used without further purification. Hexane, diethyl ether and dichloromethane (anhydrous grade) were purchased from Aldrich Chemical Company.

Methylaluminoxane, (MAO, 10% in toluene) was donated BY PTT Research and Technology Institute (Thailand). Toluene was obtained by the Exxon Chemical, Thailand Co., Ltd. It was dried over dehydrated CaCl₂ and distilled over sodium/benzophenone. Ultra-high purify (UHP) argon (99.999%) was purchased from Thai Industrial Gas Co., Ltd.. 1-Hexene and 1-octene (≥97%) was purchased from Aldrich Chemical Company, Thailand and further purified by distilling over CaH₂ for 6 h. Commercial metallocene catalyst, rac-Et[Ind]₂ZrCl₂, was purchased from Aldrich Chemical Company (Thailand). ¹H-NMR was used to investigate the structure of the ligand and catalyst complex. The spectra were recorded at ambient probe temperature (298K) using a Bruker AVANCE II 400 instrument operating at 400 MHz with an acquisition time of 1.5 s and a delay time of 4 s. Ligands and titanium complex solution were prepared using tetramethylsilane as solvent and deuterated chloroform for an internal lock. An Olympus BX51 instrument was employed to investigate the morphology of the ligand and the catalyst crystals by optical microscopy.

# 3.2. Titanium-FI complex synthesis

Bis[*N*-(3-*tert*-butylsalicylidene) anilinato]titanium (IV) dichloride (Ti-FI complex) was synthesized according to the procedure described by Saito *et al.* [15]. The synthesis of Ti-FI complex can be divided into two main steps, as follows:

# 3.2.1. Synthesis of N-(3-tert-butylsalicylidene) aniline

Firstly, a stirred mixture of 3-*tert*-butylsalicylaldehyde (2.34 g, 13.4 mmol) and 3Å molecular sieves (2 g) in ethanol (20 mL), a solution of aniline (1.41 g, 15.1 mmol) in ethanol (10 mL) was added dropwise over a 1-min period at room temperature. Then, the mixture was stirred for 16 h and filtered. The 3Å molecular sieves were washed with ethyl acetate (20 mL). The combined organic filtrates were concentrated *in vacuo* to afford the crude imine compound. Finally, purification by column chromatography on silica gel using hexane/ethyl acetate (10:1) as eluent gave *N*-(3-*tert*-butylsalicylidene) aniline as orange crystals.  $^{1}$ H-NMR (CDCl<sub>3</sub>)  $\delta$  = 1.45 (s, 9H, t-Bu), 6.81–7.35 (m, 8H, aromatic-H), 8.56 (s, 1H, CH=N), 13.84 (s, 1H, OH).

# 3.2.2. Synthesis of Bis[N-(3-tert-butylsalicylidene)anilinato] titanium (IV) dichloride

To a stirring solution of N-(3-tert-butylsalicylidene) aniline (1.552 g, 6.13 mmol) in dried diethyl ether (50 mL) at 195 K, a 1.61 M hexane solution of *n*-butyllithium (3.80 mL, 6.08 mmol) was added dropwise over a 5-min period. The solution was allowed to warm to room temperature and stirred for 4 h. The resulting solution was added dropwise over a 30 min period to a stirred solution of TiCl<sub>4</sub> (0.58 g, 3.06 mmol) in dried diethyl ether (90 mL) at 195 K. The mixture was allowed to warm to room temperature and stirred over night. After removal of the solvent, the product was extracted with CH<sub>2</sub>Cl<sub>2</sub>. Filtration following removal of the volatile gave a reddish brown solid. The solid was recrystallized from a dried dichloromethane/dried pentane (1:1) solution at room temperature to give bis[N-(3-tert-butylsalicylidene) anilinato] titanium (IV) dichloride.  $^1$ H-NMR (CDCl<sub>3</sub>):  $\delta$  = 1.26–1.66 (m, 18H, t-Bu), 6.90–7.67 (m, 16H, aromatic-H), 8.22–8.33 (m, 2H, CH=N).

# 3.3. Polymerization procedure

The ethylene/ $\alpha$ -olefin [(1-hexene, H) and (1-octene, O)] copolymerization reactions were carried out in a 100 mL semi-batch stainless steel autoclave reactor equipped with a magnetic stirrer. At first, the desired amounts of MAO ([Al]<sub>MAO</sub>/[Ti]<sub>cat</sub> = 250) and the toluene were introduced into the reactor. The Ti-FI complex in toluene was put into the reactor to make the amount of catalyst 2.5  $\mu$ mol. After that, the reactor was immersed in liquid nitrogen, followed by addition of the  $\alpha$ -olefins into the frozen reactor. The reactor was heated up to the polymerization temperature at 323 K. By feeding a fixed amount of ethylene (0.018 mole ~ 6 psi) into the reaction mixture, the ethylene consumption can be observed corresponding to the ethylene pressure drop. Lastly, the reaction was terminated by adding acidic methanol. After filtration, the resulting polymers were washed with methanol and dried at room temperature.

# 3.4. Characterization of polymers

Differential scanning calorimetry: DSC thermal analysis was used to examine the thermal properties ( $T_m$  and heat of fusion) via a DSC 204 F1 Phoenix®. The DSC measurements were recorded during the second heating/cooling cycle with the heating rate of 10 °C/min during the range of temperature 30–200 °C.

Gel Permeation Chromatography: A high temperature GPC (Waters 2200) equipped with a viscometric detector, differential optical refractometer and four Styragel HT type columns (HT3, HT4, HT5 and HT6) was used to determine the molecular weight (MW) and molecular weight distribution (MWD) of polymer. The measurement was taken at 135 °C using 1,2,4-trichlorobenzene as a solvent and a mobile phase of 1 mL/min flow rate

Scanning electron microscopy: SEM was used to determine the sample morphologies using a JEOL mode JSM-5800LV instrument.

Nuclear magnetic resonance spectroscopy: <sup>13</sup>C-NMR spectroscopy was used to determine the α-olefin incorporation and copolymer microstructure. Comparison of the positions of peak in the <sup>13</sup>C-NMR spectra of polymer sample with characteristic leads to identification of the sequence of the comonomer incorporation, referring to Randall [16]. The spectra were recorded at room temperature using a Bruker AVANCE II 400 instrument operating at 100 MHz with an acquisition time of 1.5 s and a delay time of 4 s. The samples were prepared from using 1,2,4-trichlorobenzene as a solvent and deuterated chloroform for an internal lock.

# 4. Conclusions

This article has reported the preparation of LLDPE copolymer from ethylene/ $\alpha$ -olefin copolymerization using TiC<sub>34</sub>H<sub>36</sub>Cl<sub>2</sub>N<sub>2</sub>O<sub>2</sub> (Ti-FI catalyst) by varying the initial comonomer concentration and the comonomer type. The results reveal that all copolymers achieved very high activity, high molecular weight and narrow molecular weight distribution; on the other hand, the bulkiness of the catalyst structure is likely the main feature limiting the incorporation of comonomer into the polymer backbone. The increase of initial comonomer concentration caused an increase in catalytic activity; conversely, it led to a decrease in molecular weight and melting temperature. In

addition, concerning the impact of the comonomer type on the catalytic behavior, 1-hexene exhibited apparently higher activity and molecular weight with corresponding 1-octene based copolymer. However, both melting temperature and crystallinity appeared to be independent of comonomer type.

# Acknowledgements

We gratefully thank the Dusadeepipat scholarship (Chulalongkorn University Fund), the graduate school of Chulalongkorn University, Innovation & Technology of PTT Chemical Public Company Limited, the Thailand Research Fund (TRF), the Office of Commission on Higher Education (CHE) and NRU of CU (AM1088A) for the financial support of this work.

## References

- 1. Hung, J.; Cole, A.P.; Waymouth, R.M. Control of sequence distribution of ethylene copolymers: Influence of comonomer sequence on the melting behavior of ethylene copolymers. *Macromolecules* **2003**, *36*, 2454-2463.
- 2. Makio, H.; Kashiwa, N.; Fujita, T. FI Catalysts: A New family of high performance catalysts for olefin polymerization. *Adv. Syn. Catal.* **2002**, *344*, 477-493.
- 3. Grieken, R.V.; Carrero, A.; Suarez, I.; Paredes, B. Effect of 1-hexene comonomer on polyethylene particle growth and kinetic profiles. *Macromol. Sym.* **2007**, 259, 243-252.
- 4. Ishii, S.; Saito, J.; Mitani, M.; Mohr, J.; Matsukawa, N.; Tohi, Y.; Matsui, S.; Kashiwa, N.; Fujita, T. Highly active ethylene polymerization catalysts based on titanium complexes having two phenoxy-imine chelate ligands. *J. Mol. Catal. A Chem.* **2002**, *179*, 11-16.
- 5. Chaichana, E.; Khaubunsongserm, S.; Prasethdam, P.; Jongsomjit, B. Ethylene-hexene copolymer derived from [t-butylfluorenylsilyl-amido] dimethyl titanium complex. *Express Polym. Lett.* **2010**, *4*, 94-100.
- 6. Hong, H.; Zhang, Z.; Chung, T.C.M.; Lee, R.W. Synthesis of new 1-decene-based LLDPE resins and comparison with the corresponding 1-octene- and 1-hexene-based LLDPE resins. *J. Polym. Sci. Part A Polym. Chem.* **2007**, *45*, 639-649.
- 7. Forlini, F.; Fan, Z.Q.; Tritto, I.; Locatelli, P.; Sacchi, M.C. Metallocene-catalyzed propene/1-hexene copolymerization: Influence of amount and bulkiness of cocatalyst and of solvent polarity. *Macromol. Chem. Phys.* **1997**, *198*, 2397-2408.
- 8. Matsui, S.; Fujita, T. FI Catalysts: Super active new ethylene polymerization catalysts. *Catal. Today* **2001**, *66*, 63-73.
- 9. Galland, G.B.; Seferin, M.; Mauler, R.S.; Santos, J.H.Z. Linear low-density polyethylene synthesis promoted by homogeneous and supported catalysts. *Polym. Inter.* **1999**, *48*, 660-664.
- 10. Desharun, C.; Jongsomjit, B.; Praserthdam, P. Study of LLDPE/alumina nanocomposites synthesized by in situ polymerization with zirconocene/d-MMAO catalyst. *Catal. Commun.* **2008**, *9*, 522-528.
- 11. Wongwaiwattanakul, P.; Jongsomjit, B. Copolymerization of ethylene/1-octene via different pore sized silica-based-supported zirconocene/dMMAO catalysts. *Catal. Commun.* **2008**, *10*, 118-122.

12. Bunchongturakarn, S.; Jongsomjit, B.; Praserthdam, P. Impact of bimodal pore MCM-41-supported zirconocene/dMMAO catalyst on copolymerization of ethylene/1-octene. *Catal. Commun.* **2008**, *9*, 789-795.

- 13. Jongsomjit, B.; Kaewkrajang, P.; Shiono, T.; Praserthdam, P. Supporting effects of silica-supported methylaliminoxane (MAO) with zirconocene catalyst on ethylene/1-olefin copolymerization behaviors for linear low-density polyethylene (LLDPE). *Ind. Eng. Chem. Res.* **2004**, *43*, 7959-7963.
- 14. Jongsomjit, B.; Ngamposri, S.; Praserthdam, P. Catalytic activity during copolymerization of ethylene and 1-hexene via mixed TiO<sub>2</sub>/SiO<sub>2</sub>-supported MAO with rac-Et[Ind]<sub>2</sub>ZrCl<sub>2</sub> metallocene catalysts. *Molecules* **2005**, *10*, 672-678.
- 15. Saito, J.; Mitani, M.; Matsui, S.; Tohi, Y.; Makio, H.; Nakano, T.; Tanaka, H.; Kashiwa, N; Fujita, T. A new titanium complex having two phenoxy-imine chelate ligands for ethylene polymerization. *Macromol. Chem. Phys.* **2002**, *203*, 59-65.
- 16. Randall, J.C. A review of high resolution liquid <sup>13</sup>carbon nuclear magnetic resonance characterizations of ethylene-based polymers. *J. Macromol. Sci. Rev. Macromol. Chem. Phys.* **1989**, 29, 201-317.

Sample Availability: Samples of the compounds are available from the authors.

© 2011 by the authors; licensee MDPI, Basel, Switzerland. This article is an open access article distributed under the terms and conditions of the Creative Commons Attribution license (http://creativecommons.org/licenses/by/3.0/).

FI SEVIER

Contents lists available at ScienceDirect

# **Fuel Processing Technology**

journal homepage: www.elsevier.com/locate/fuproc



# Effect of calcination treatment of zirconia on W/ZrO<sub>2</sub> catalysts for transesterification

Nichapat Senso, Bunjerd Jongsomjit\*, Piyasan Praserthdam

Center of Excellence on Catalysis and Catalytic Reaction Engineering, Department of Chemical Engineering, Faculty of Engineering, Chulalongkorn University, Bangkok 10330, Thailand

#### ARTICLE INFO

Article history: Received 15 November 2010 Received in revised form 22 February 2011 Accepted 27 March 2011 Available online 17 April 2011

Keywords: Zirconia Tungsten Biodiesel Transesterification Calcination

#### ABSTRACT

In this present study, the nanocrystalline  $ZrO_2$  particles synthesized by the solvothermal method were calcined in reductive  $(H_2)$ , inert  $(N_2)$  and oxidative  $(O_2$  and air) atmospheres prior to impregnation with tungsten (W) in order to produce the  $W/ZrO_2$  (WZ) catalysts. Based on the ESR measurement, it revealed that only the  $ZrO_2$  samples calcined in  $H_2$  and  $N_2$  exhibited the F-center (single charged oxygen vacancy) at g=2.003. None of  $Zr^{3+}$  defect was detected for all calcined  $ZrO_2$  samples. After impregnation with tungsten, the WZ catalysts were also characterized. It was present as the polycrystal, which can be seen by the selected area electron distribution (SAED). However, the presence of  $Zr^{3+}$  defect was evident in all WZ catalysts, while the F-center was absent. The highest  $Zr^{3+}$  intensity detected in the WZ catalyst using  $ZrO_2$  under  $H_2$  calcination atmosphere can be attributed to the transformation of F-center to  $Zr^{3+}$  defect. It revealed that the WZ-H<sub>2</sub> catalyst exhibited the highest conversion under transesterification of triacetin and methanol among other WZ catalysts. This can be attributed to the high surface acidity, which was probably induced by large amounts of  $Zr^{3+}$  defect.

© 2011 Elsevier B.V. All rights reserved.

#### 1. Introduction

Recently, the prices of energy from natural sources, such as petroleum gas and oil are increasing everyday because of the demand of energy for serving industries in many countries. Biodiesel is one of those renewable energy sources, which are attracted by many researchers because it can be made of bioresources, such as vegetable oils or fats from animal. Moreover, they can be readily converted to biodiesel comparing to petroleum oil and natural gas. Biodiesel itself will provide many advantages since it is effective fuel and it can reduce production cost. However, these feed stocks often contain a lot of free fatty acids (FFAs) and water, which are not suitable for homogeneous alkaline-catalyzed process and needed to pretreatment for disposal free fatty acids at the preliminary process of biodiesel production. The main reactions which play important roles on produce biodiesel are "esterification" and "transesterification", which require strong liquid acid catalysts such as sulfuric acid [1–6]. However, the use of strong liquid acid catalysts essentially causes side effects, such as high corrosive, hard to separate and having expensive cost because those catalysts are not reusable. Besides, the solid acid catalysts can be used in biodiesel production by transesterification of feedstock containing a high content of FFAs, such as waste cooking oils [7]. Hence, there are new investigation for solid acid and base catalysts, such as sulfated zirconia (SZ) and tungstated zirconia (WZ) catalysts [8] because these catalysts provide esterification and

transesterification reaction at the same time. The strong acidity of SZ catalyst has attracted much attention because of its ability to catalyze a wide range of reactions, such as cracking, alkylation, and isomerization, all needing solid acids as catalysts [9–12]. Since the SZ catalyst promoted with noble metals are subject among others to sulfate reduction and subsequent poisoning of the metallic function under reductive atmospheres [13], the W-based metal oxides originally proposed by Hino and Arata [14], seem to be good candidates for the skeletal isomerization of alkanes higher than C<sub>4</sub> requiring strong acid sites.

It is known that anionic dopants create additional electrondeficient regions that increase the Bronsted acid strength of a metal oxide surface by improving the ability of neighboring hydroxyl groups to act as proton donors [15]. As an alternative to sulfated zirconia (SZ), tungstated zirconia (WZ) was also reported to be active for the isomerization of C<sub>4</sub>–C<sub>8</sub> alkanes [14,16–19]. Although the WZ catalyst was less active than SZ, the former shows several advantages over the latter. For instance, the WZ catalyst is much more stable than the SZ one at high temperatures [12] and it undergoes significantly less deactivation during catalytic reaction [20]. Lopez et al. [8] reported that the use of WZ catalyst has active sites equal to sulfuric acid for catalyzing biodiesel-forming transesterification reaction. Another advantage of WZ catalyst is that its deactivation appears to be not rapid for transesterification reaction of triglycerides with methanol [8,21]. Ramu et al. [22] also reported that the various W loadings on zirconia and various calcination temperatures affected the phase change of zirconia and consequently the catalyst activity on esterification reaction for biodiesel production process. In addition, some papers reveal that surface structure and phase of zirconia have

<sup>\*</sup> Corresponding author. Tel.: +66 2 218 6869; fax: +66 2 218 6766. E-mail address: bunjerd.j@chula.ac.th (B. Jongsomjit).

effects on the catalyst activity as well [23–25]. Since nature of surface and defects of zirconia can affect on its properties. Therefore, it is of great benefits to investigate the deep impact of nature of surface and defect of zirconia on its catalytic properties. Among studies, Lui et al. [26] created defection on zirconia surface by calcination at different temperatures. Another research [24] showed that the surface defect of zirconia can be created by altering the calcination atmospheres.

In this present work, the nanocrystalline zirconia particles were first synthesized via the solvothermal method, and then calcined upon different atmospheres using H<sub>2</sub>, N<sub>2</sub>, O<sub>2</sub> and air. The obtained zirconia samples as supports were further impregnated with tungsten (VI) chloride to produce WZ catalyst and being used for transesterification of triacetin with methanol. In fact, the triacetin was used in this study since it is a model compound for larger triglycerides that has been found in many vegetable oils and fats [8]. Besides, it is also used to minimize the side effect of FFAs from crude oil. The effects of different calcination atmospheres of zirconia samples on the characteristics and catalytic properties of WZ catalysts were elucidated by means of various techniques, such as N<sub>2</sub> physisorption, X-ray diffraction (XRD), transmission electron microscopy (TEM) with the selected area electron distribution (SAED) and electron spin resonance (ESR).

#### 2. Experimental

#### 2.1. Preparation of nanocrystalline ZrO<sub>2</sub>

The nanocrystalline ZrO<sub>2</sub> particles were prepared using the solvothermal method in the same manner as that of Kongwudthiti et al. [27]. Zirconium n-butoxide (97%, Aldrich) was used as the starting material. Approximately, 25 g of zirconium *n*-butoxide was suspended in 100 ml of 1,4-butanediol (Aldrich) in a test tube, which was then placed in a 300 ml autoclave. The 25 ml of the same solvent was filled in the gap between the test tube and the autoclave wall. The autoclave was purged completely by nitrogen after that it was heated up to the desired temperature at 300 °C with the rate of 2.5 °C min $^{-1}$ . The temperature was held constant at 300 °C for 2 h, and then cooled down to room temperature. After the autoclave was cooled to room temperature, the resulting product was repeatedly washed with methanol by vigorous mixing and centrifuging. In fact, methanol was used to remove the impurity from the precursor during synthesis of zirconia and it is easy to evaporate during the drying process. The obtained powders were then dried in oven at 100 °C for 1 day. Finally, the obtained sample was calcined in a tube furnace in different atmospheres (H2, N2, O2, and Air, solely with the flow rate of  $30 \,\mathrm{cm^3 min^{-1}}$ ) by heating to  $500 \,^{\circ}\mathrm{C}$  with a rate of  $10 \,^{\circ}\mathrm{C} \,\mathrm{min^{-1}}$  and holding at that temperature for 2 h.

#### 2.2. Preparation of tungstated zirconia (WZ) catalyst

The WZ catalysts were prepared by the incipient wetness impregnation of the calcined zirconia samples obtained from section 2.1 with a desired amount of an aqueous solution of tungsten (VI) chloride (99 wt.%, Aldrich) to produce the WZ catalyst having 15 wt.% of W loading. The catalysts were dried at 110 °C for 24 h and calcined in air at 500 °C for 3 h.

#### 2.3. Catalyst nomenclature

The following nomenclature was used for samples in this study. The  $ZrO_2$ –X sample refers to the  $ZrO_2$  support calcined under X ( $H_2$ ,  $N_2$ ,  $O_2$ , and Air) atmosphere. The WZ–X sample refers to the WZ catalyst using  $ZrO_2$  support calcined under X atmosphere.

#### 2.4. Catalyst characterization

X-ray diffraction (XRD) patterns were recorded with a Siemens D5000 using nickel filtered  $\text{CuK}_{\alpha}$  radiation. The crystallite size was determined using the Scherrer equation by using  $\alpha$ -alumina as the external standard. The surface area of solid was determined by physisorption of nitrogen (N<sub>2</sub>) using Micromeritics ASAP 2020.

The amounts of acidity were measured by using the titration technique involved an ion-exchange step [8]. First, 0.2 g of catalyst was dissolved in 10 ml of 3.43 M NaCl solution. Stirring was taken place for 30 h at 28 °C, which caused the interchange ion between H<sup>+</sup> of catalyst and Na<sup>+</sup> of solution. Then, the solid phase was filtered out. Solution was next titrated with 0.05 M of NaOH solution. The endpoint for this titration was measured by pH meter (pH~7). The defected surface zirconia (Zr<sup>3+</sup> and F-center) was investigated by the electron spin resonance spectrometer (ESR). It was conducted on ESR spectrometer of JEOL model (JES-RE2X) on ES-IPRIT program with the X band microwave unit and frequency of 8.8–9.6 GHz. The cavity is cylindrical and it is operating in TE <sub>011</sub> mode. Transmission electron microscope (TEM) and selected area electron distribution (SAED) used to characterize the morphology, crystallite size, and diffraction patterns of the primary particles of the WZ samples were obtained using the IEOL IEM-2010 transmission electron microscope operated at 200 kV with an optical point to point resolution of 0.23 nm. The sample was dispersed in ethanol prior to measurement.

#### 2.5. Reaction study

The liquid phase transesterification reaction was carried out on well-mixed batch reactor. Hot plate and stirrer were used for heat generation and mixing. First, the solution of triacetin and methanol at molar ratio of 1:6 were mixed in the reactor [8]. The reactor was heated to 60 °C and the solid catalyst having the amounts of 2 wt.% of triacetin employed was added. Sample aliquot (1 ml) was withdrawn periodically from the reactor, quenched to room temperature, and centrifuged in order to separate out the solid catalyst and prevent further reaction. Reaction sample concentrations were determined using an SHIMADZU gas chromatograph GC-14B. The reaction was continuous on going through the stable conversion (7 h).

#### 3. Results and discussion

#### 3.1. Characteristics of zirconia calcined under different atmospheres

In this present study, the nanocrystalline  $ZrO_2$  particles were synthesized via the solvothermal method. After drying, the samples were calcined under reductive ( $H_2$ ), inert ( $N_2$ ), and oxidative ( $O_2$  and air) atmospheres. The characteristics of samples after calcinations are shown in Table 1. It was found that after calcination, all  $ZrO_2$  samples exhibited the lower surface area due to sintering at high temperature ( $500\,^{\circ}$ C). It should be noted that the  $ZrO_2-O_2$  sample had the lowest surface area ( $76.4\,^{\circ}m^2/g$ ) among other samples indicating that the  $O_2$  atmosphere apparently resulted in more sintering. In order to identify the crystallite phases of  $ZrO_2$ , the XRD was performed. The XRD

**Table 1** Characteristics of ZrO<sub>2</sub> calcined at different atmospheres.

Sample	SA	Crystal p	hase <sup>a</sup>	Crystallite size <sup>a</sup>	ESR signal (a.u.)	
	$(m^2/g)$	%t-ZrO <sub>2</sub>	%m-ZrO <sub>2</sub>	(nm)	F-center	Zr <sup>3+</sup>
ZrO <sub>2</sub> -H <sub>2</sub>	90.5	87.6	12.4	3.8	22,000	-
$ZrO_2-N_2$	90.1	87.4	12.6	3.6	15,510	-
$ZrO_2-O_2$	76.4	70.6	29.4	6.9	-	-
ZrO <sub>2</sub> -Air	94.9	78.8	21.2	4.1	-	-
ZrO <sub>2</sub> –As-syn	120.2	90.2	9.8	3.5	-	-

<sup>&</sup>lt;sup>a</sup> Based on the XRD measurement.

patterns for all calcined samples are shown in Fig. 1. Prior to calcination, the  $ZrO_2$  sample exhibited the XRD peaks at  $30.2^{\circ}$ ,  $35.3^{\circ}$  and  $49.8^{\circ}$  (strong) assigned to the tetragonal phase and at  $28.2^{\circ}$  and  $33.1^{\circ}$  (weak) assigned to the monoclinic phase. The percents of tetragonal and monoclinic phases in  $ZrO_2$  (as also shown in Tables 1 and 2) were calculated by a comparison of the area for the characteristic peaks of the tetragonal and monoclinic phases. The percent of each phase was determined by means of the Gaussian areas  $h \times w$ , where h and w are the height and half-height width of the corresponding XRD characteristic peaks as follows [28]:

% tetragonal phase;

$$= \frac{\sum (h \times w) tetragonal\ phase}{\sum (h \times w) tetragonal\ phase\ and\ monoclinic\ phase}$$

% monoclinic phase;

$$= \frac{\sum (h \times w) monoclinic\ phase}{\sum (h \times w) tetragonal\ phase\ and\ monoclinic\ phase}$$

It was found that only small fraction of monoclinic phase was present prior to calcination. However, after calcination under different atmospheres, all samples exhibited the higher fractions of monoclinic phase. It revealed that calcination under oxidative atmosphere apparently resulted in significant higher fraction of monoclinic phase present as seen for Zr-O2 and Zr-Air samples. Only small change was found in the samples calcined under reductive (Zr-H<sub>2</sub>) and inert (Zr-N<sub>2</sub>) atmospheres. In our previous works [29,30], the similar synthesized zirconia samples were calcined at only 400 °C for 2 h in the reductive and oxidative atmospheres. However, no phase transformation from tetragonal to monoclinic was observed. Thus, in this study, the increased calcination temperature at 500 °C was performed to further investigate the effect of phase transformation of zirconia along with the calcination in inert atmosphere. Upon increased calcination temperature (500 °C), the phase transformation from tetragonal to monoclinic was more pronounced under the oxidative atmosphere. The crystallite size of sample was also obtained by the XRD line broadening using Scherrer equation. As seen in Table 1, only the ZrO<sub>2</sub>-O<sub>2</sub> samples exhibited the remarkable change (largest) in the crystallite size corresponding to the lowest surface area observed. Hence, the sintering effect was more pronounced under oxidative atmosphere.

The ESR was used to identify the surface nature of ZrO<sub>2</sub> calcined under different atmospheres. The ESR spectra for all ZrO<sub>2</sub> samples are

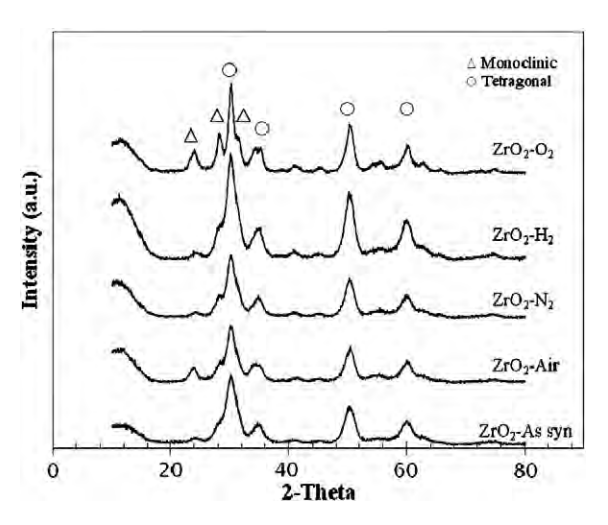


Fig. 1. XRD patterns of different ZrO<sub>2</sub> samples.

**Table 2**Characteristics of WZ catalysts obtained from different ZrO<sub>2</sub> samples.

Sample		Acidity <sup>a</sup>	Crystal p	hase <sup>b</sup>	Crystallite size <sup>b</sup>	ESR signal (a.u.)	
	(m <sup>2</sup> /g)	(µmol/g)	%t-ZrO <sub>2</sub>	%m-ZrO <sub>2</sub>	(nm)	F-center	Zr <sup>3+</sup>
WZ-H <sub>2</sub>	90.2	200	76.0	24.0	3.8	-	2362
$WZ-N_2$	90.5	150	81.4	18.6	3.6	-	2105
$WZ-O_2$	69.8	100	68.7	31.3	6.7	-	1260
WZ-Air	85.5	125	85.2	14.8	3.9	-	1315

<sup>&</sup>lt;sup>a</sup> Obtained from the ion-exchange titration.

shown in Fig. 2. It revealed that no strong ESR signals can be detected for the dried-ZrO<sub>2</sub> (As-syn), ZrO<sub>2</sub>–O<sub>2</sub>, and ZrO<sub>2</sub>–Air samples. However, the strong ESR signals for ZrO<sub>2</sub>–H<sub>2</sub> and ZrO<sub>2</sub>–N<sub>2</sub> samples were observed at g=2.003 assigned to F-center (single charged oxygen vacancy) [24]. This is confirmed that the calcination of zirconia under reductive atmosphere would lead to the formation of F-center as following reaction;

$$Zr^{4+} + OH^{-} + \frac{1}{2}H_{2} \rightarrow Zr^{4+} + F^{-} + H_{2}O$$

It is also worth noting that the intensity of F-center of  $ZrO_2-H_2$  sample was higher than that of  $ZrO_2-N_2$  sample as also shown in Table 1. Therefore,  $ZrO_2$  was hardly reduced by  $H_2$  due to strong Zr—O bond energy. Thus, the F-center was probably produced by the reduction of hydroxyl group on  $ZrO_2$  surface [24]. It should be noted that no  $Zr^{3+}$  (g = 1.975) ESR signal as seen from  $ZrO_2$  calcined at 400 °C [29,30] under oxidative atmosphere was observed. This is probably due to the presence of monoclinic phase after calcination at 500 °C inhibits the formation of  $Zr^{3+}$ . However, the existence of F-center was not affected by the presence of monoclinic phase under reductive and inert atmosphere.

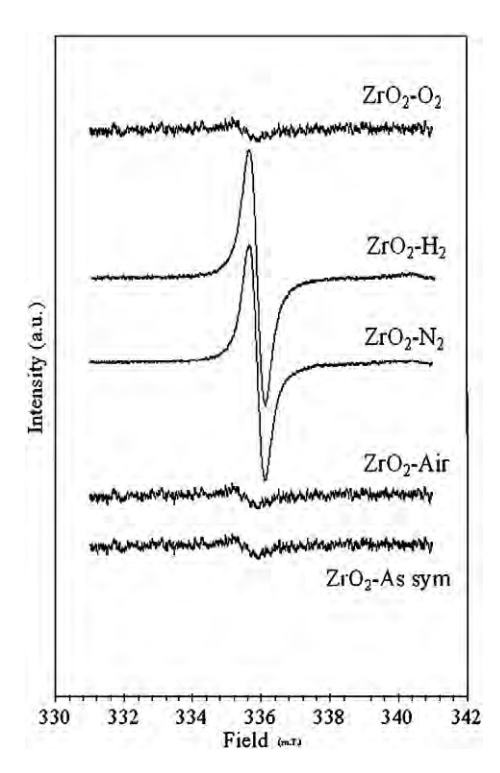


Fig. 2. ESR spectra of different ZrO<sub>2</sub> samples.

<sup>&</sup>lt;sup>b</sup> Obtained from the XRD measurement.

#### 3.2. Characteristics of tungstated zirconia (WZ) catalysts

Then, the different  $ZrO_2$  samples were impregnated with W to produce the WZ catalysts. The characteristics of different WZ catalysts are shown in Table 2. The XRD patterns of WZ catalysts are shown in Fig. 3. They are similar to the XRD patterns of the  $ZrO_2$  samples as seen in Fig. 1 indicating that tungsten is well dispersed onto the  $ZrO_2$  support and cannot be detected by XRD. Considering the characteristics of WZ catalysts, it showed that the surface area, phase composition, and crystallite size of samples were not affected by W loading. The acidity of WZ catalysts was determined using chemical titration techniques [20]. The results, as also shown in Table 2, indicated that the acidity of WZ catalysts increased within the order of WZ-H<sub>2</sub>>WZ-N<sub>2</sub>>WZ-Air>WZ-O<sub>2</sub>.

In order to elucidate the effect of W loading on surface nature of ZrO<sub>2</sub>, the ESR measurement of WZ catalysts was also performed. The ESR spectra for all WZ catalysts are shown in Fig. 4. All samples exhibited the characteristic ESR signals for  $Zr^{3+}$  at g=1.975 and g = 1.957 [24,26], while the ESR signals for F-center for  $ZrO_2-H_2$  and  $ZrO_2-N_2$  samples were absent. Zhao et al. [24] reported that the  $Zr^{3+}$ detected by ESR can be described as the oxygen coordinatively unsaturated zirconium sites on the ZrO<sub>2</sub> surface. The intensity of Zr<sup>3+</sup> obtained from ESR signal was determined and reported in Table 2. It increased upon the following order; WZ-H<sub>2</sub>>WZ-N<sub>2</sub>>WZ-Air>WZ-O<sub>2</sub>, which was related to increased acidity of WZ catalysts. It is known that the intensity of F-center signal (as seen only in ZrO<sub>2</sub>–H<sub>2</sub> and ZrO<sub>2</sub>–  $N_2$  samples) on zirconia surface is disproportional to that of  $Zr^{3+}$ signal. The appearance of these two signals is related in adverse effect. It may be because the electronic density redistribution can be relocated between  $Zr^{3+}$  and the closest oxygen vacancy. By calcination in reductive and oxidative (calcination of WZ catalysts) atmospheres, the electronic density can move to F-center and Zr<sup>3+</sup>, respectively. Hence, this reaction can be altered by calcination condition. The results of the disappearance of the F-center  $(V_0^-)$  in oxidative atmosphere can be drawn based on the work reported by Frolova and Ivanovskaya [31] as follows:

$$Zr^{3+}$$
  $-[V_0] \stackrel{\text{H}_2}{\underset{\hat{0}_2}{\longrightarrow}} Zr^{4+}$   $-[V_0^-]$ 

TEM images along with SAED for all WZ catalysts are shown in Fig. 5. They are almost similar. Primarily, the spheroid shape with

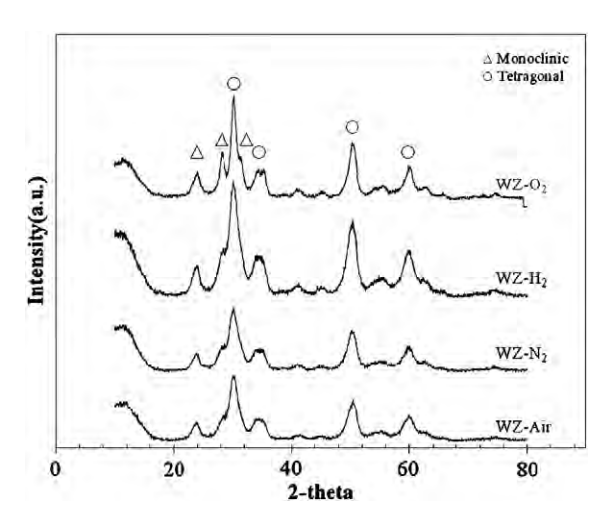


Fig. 3. XRD patterns of different WZ catalysts.

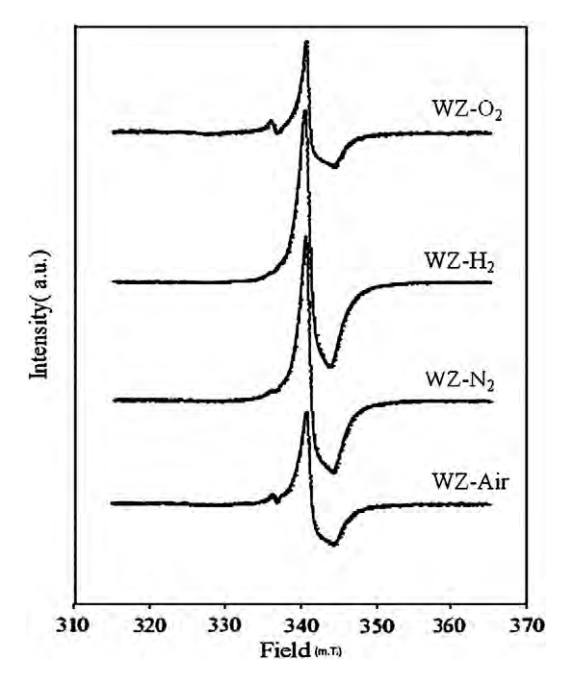


Fig. 4. ESR spectra of different WZ catalysts.

average size around 3 to 15 nm and irregular large shape overlayer are observed. From SAED analysis, the spheroid shape particles could be assigned to  $\rm ZrO_2$  particles and the irregular shape overlayer was assigned to tungsten oxide. The crystallite sizes calculated by TEM image were also in good agreement with the crystallite sizes obtained from XRD. The WZ catalysts only consisted of irregular bulk solids trapped inside the small crystal. From EDX analysis, all bulk solids comprised of tungsten and zirconium atoms, where W atoms were mixed with the Zr atoms within the crystal. This result agrees with several works, which propose that tungsten species are entrapped inside the  $\rm ZrO_2$  bulk forming a solid solution [22,25]. The results suggested that there were more dispersion of  $\rm WO_x$  species on  $\rm ZrO_2$ – $\rm H_2$  and  $\rm ZrO_2$ – $\rm N_2$  supports. All TEM images of WZ catalysts clearly display crystalline  $\rm ZrO_2$  lattice fringes.

#### 3.3. Reaction study

The liquid phase transesterification of triacetin and methanol at 60 °C was used as the model reaction for comparing the catalytic activity of all WZ catalysts. The catalytic activities of WZ catalysts are displayed in Fig. 6. The conversions were in the range of WZ-H<sub>2</sub>  $(53\%)>WZ-N_2$   $(40\%)>WZ-O_2$   $(17\%)\approx WZ-Air$  (16%). The results were in good agreement with the acidity contents of catalyst, which were related to the intensity of Zr<sup>3+</sup> in WZ catalysts after calcination. The increased acidity for WZ catalysts can be explained by the formation of WO<sub>3</sub> nanoparticles, which can be observed by Raman spectroscopy and being more acidic than the surface WO<sub>x</sub> species [32]. In earlier works, when the impregnated tungsten contents on ZrO<sub>2</sub> support increased, the tungsten species were changed from monotungstate to polytungstate surface WO<sub>x</sub> and finally to form WO<sub>3</sub> nanocrystal. However, based on this work, the W loading was fixed at 15 wt.%. Thus, the changes in the formation of WO<sub>x</sub> species should be due to the different surface structure of ZrO2 after calcination. Based on different characteristics of ZrO<sub>2</sub>, especially for the F-center that was only present in ZrO<sub>2</sub>–H<sub>2</sub> and ZrO<sub>2</sub>–N<sub>2</sub> supports, it revealed that the presence of F-center in ZrO2 can facilitate the formation of Zr<sup>3+</sup>, and then more acidity tungsten species can be formed.

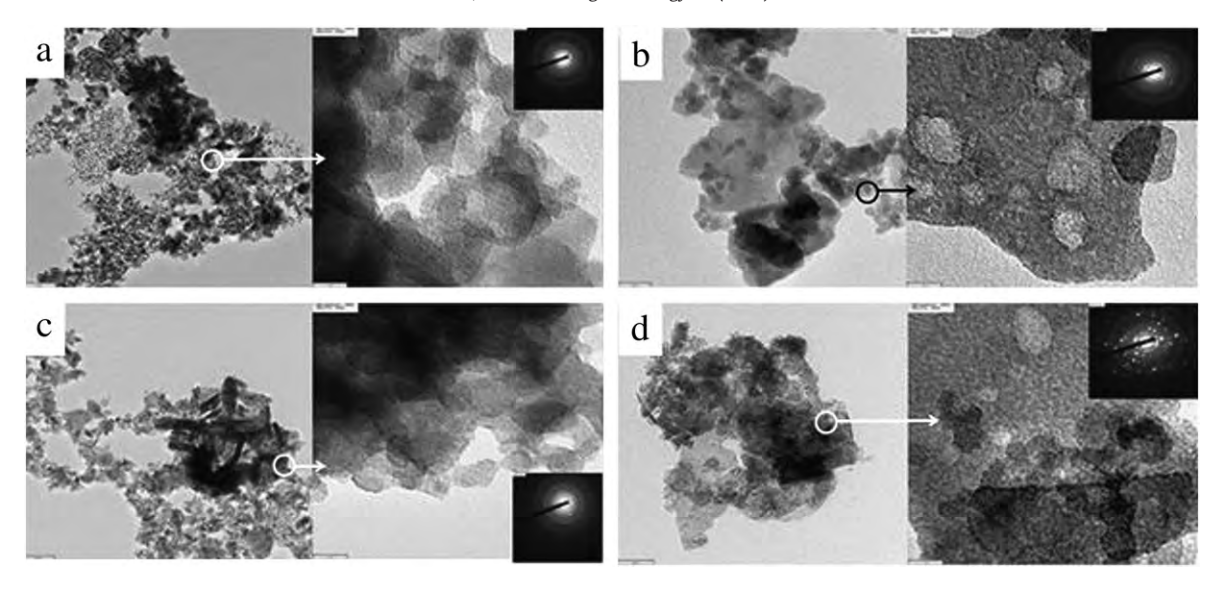


Fig. 5. TEM micrographs of (a) WZ-Air, (b) WZ-O<sub>2</sub>, (c) WZ-N<sub>2</sub>, and (d) WZ-H<sub>2</sub>.

#### 4. Conclusions

This present study revealed the effect of different calcination atmospheres on the nanocrystalline  $ZrO_2$  particles. It indicated that only  $ZrO_2$  calcined in  $H_2$  and  $N_2$  exhibited the F-center based on ESR measurement. No  $Zr^{3+}$  signal based on ESR was observed for  $ZrO_2$  calcined in  $O_2$  and air probably due to the presence of monoclinic phase. The F-center present under reductive and inert atmospheres can transform to  $Zr^{3+}$  after W loading and calcination. The large amount of  $Zr^{3+}$  apparently facilitates the formation of high acidic tungsten species that can increase the catalytic activity of WZ catalyst via transesterification.

#### Acknowledgments

The authors thank the Thailand Research Fund (TRF), Office of the Higher Education Commission (CHE) and NRU-CU (AM1088A) for the financial support of this project.

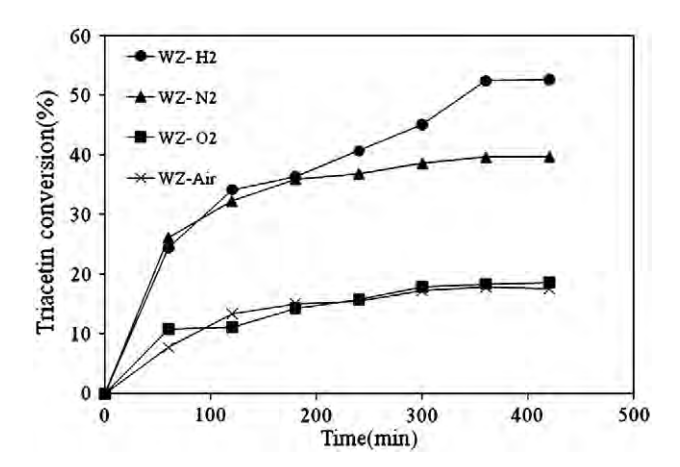


**Fig. 6.** Triacetin conversion upon different WZ catalysts; conditions: methanol:triacetin molar ratio = 6:1, reaction temperature =  $60 \, ^{\circ}$ C, solid acids =  $2 \, \text{wt.}\%$  of triacetin employed, and running time =  $7 \, \text{h.}$ 

#### References

- M.L. Pisarello, C.B. Dalla, G. Mendow, C.A. Querini, Esterification with ethanol to produce biodiesel from high acidity raw materials: kinetic studies and analysis of secondary reactions, Fuel Process. Technol. 91 (2010) 1005–1014.
- [2] B. Sarkar, S. Sridhar, K. Saravanan, V. Kale, Preparation of fatty acid methyl ester through temperature gradient driven pervaporation process, Chem. Eng. J. 162 (2010) 609–615.
- [3] M. Canakci, G.J. Van, Biodiesel production via acid catalysis, TASAE 42 (1999) 1203–1210.
- [4] M. Canakci, G.J. Van, Biodiesel production from oils and fats with high free fatty acids, TASAE 44 (2001) 1429–1439.
- [5] M.J. Goff, N.S. Bauer, S. Lopes, W.R. Sutterlin, G.J. Suppes, Acid-catalyzed alcoholysis of soybean oil, JAOCS 81 (2004) 415–420.
- [6] E. Lotero, Y. Liu, D.E. Lopez, K. Suwannakarn, D.A. Bruce, J.G. Goodwin Jr., Synthesis of biodiesel via acid catalysis, Ind. Eng. Chem. Res. 44 (2005) 5353–5363.
- [7] C. Komintarachat, S. Chuepeng, Solid acid catalyst for biodiesel production from waste used cooking oils, Ind. Eng. Chem. Res. 48 (2009) 9350–9353.
- [8] D.E. Lopez, J.G. Goodwin Jr., D.A. Bruce, E. Lotero, Transesterification of triacetin with methanol on solid acid and base catalysts, Appl. Catal. A: Gen. 295 (2005) 97–105.
- [9] E. Iglesia, S.L. Soled, G.M. Kramer, Isomerization of alkanes on sulfated zirconia: promotion by Pt and by adamantyl hydride transfer species, J. Catal. 144 (1993) 238–253.
- [10] K.F. Yee, J. Kansedo, K.T. Lee, Biodiesel production from palm oil via heterogeneous transesterification: optimization study, Chem. Eng. Commun. 197 (2010) 1597–1611.
- [11] K. Suwannakarn, E. Lotero, J.G. Goodwin Jr., C. Lu, Stability of sulfated zirconia and the nature of the catalytically active species in the transesterification of triglycerides, J. Catal. 255 (2008) 279–286.
- [12] M. Busto, K. Shimizu, C.R. Vera, J.M. Grau, C.L. Pieck, M.A. D'Amato, M.T. Causa, M. Tovar, Influence of hydrothermal aging on the catalytic activity of sulfated zirconia, Appl. Catal. A: Gen. 348 (2008) 173–182.
- [13] X. Li, K. Nagaoka, L.J. Simon, R. Olindo, J.A. Lercher, Influence of calcination procedure on the catalytic property of sulfated zirconia, Catal. Lett. 113 (2007) 34–40.
- [14] M. Hino, K. Arata, Synthesis of solid superacid of tungsten oxide supported on zirconia and its catalytic action for reactions of butane and pentane, J. Chem. Soc. Chem. Commun. 18 (1988) 1259–1260.
- [15] E. Iglesia, D.G. Barton, S.L. Soled, S. Miseo, J.E. Baumgartner, W.E. Gates, G.A. Fuentes, G.D. Meitzner, Selective isomerization of alkanes on supported tungsten oxide acids, Stud. Surf. Sci. Catal. 101 (1996) 533–542.
- [16] J.G. Santiesteban, J.C. Vartuli, S. Han, R.D. Bastian, C.D. Chang, Influence of the preparative method on the activity of highly acidic WO<sub>x</sub>/ZrO<sub>2</sub> and the relative acid activity compared with zeolites, J. Catal. 168 (1997) 431–441.
- [17] M. Busto, M.E. Lovato, C.R. Vera, K. Shimizu, J.M. Grau, Silica supported tungstazirconia catalysts for hydroisomerization-cracking of long alkanes, Appl. Catal. A: Gen. 355 (2009) 123–131.
- [18] X. Chen, C. Chen, N. Xu, C.Y. Mou, Catalytic activity of Al<sub>2</sub>O<sub>3</sub>/WO<sub>3</sub>/ZrO<sub>2</sub> strong solid acid catalyst for n-butane isomerization, Chin. J. Catal. 24 (2003) 924–928.
- [19] X.R. Chen, C.L. Chen, N.P. Xu, C.Y. Mou, Al- and Ga-promoted WO<sub>3</sub>/ZrO<sub>2</sub> strong solid acid catalysts and their catalytic activities in n-butane isomerization, Catal. Today. 93 (2004) 129–134.
- [20] D.E. López, J.G. Goodwin Jr., D.A. Bruce, S. Furuta, Esterification and transesterification using modified-zirconia catalysts, Appl. Catal. A: Gen. 339 (2008) 76–83

- [21] S. Furuta, H. Matsuhashi, K. Arata, Biodiesel fuel production with solid superacid catalysis in fixed bed reactor under atmospheric pressure, Catal. Commun. 5 (2004) 721–723.
- [22] S. Ramu, N. Lingaiah, B.L.A.P. Devi, R.B.N. Prasad, I. Suryanarayana, P.S.S. Prasad, Esterification of palmitic acid with methanol over tungsten oxide supported on zirconia solid acid catalysts: effect of method of preparation of the catalyst on its structural stability and reactivity, Appl. Catal. A: Gen. 276 (2004) 163–168.
   [23] D.E. López, K. Suwannakarn, D.A. Bruce, J.G. Goodwin Jr., Esterification and
- [23] D.E. López, K. Suwannakarn, D.A. Bruce, J.G. Goodwin Jr., Esterification and transesterification on tungstated zirconia: effect of calcination temperature, J. Catal. 247 (2007) 43–50.
- [24] Q. Zhao, X. Wang, T. Cai, The study of surface properties of ZrO<sub>2</sub>, Appl. Surf. Sci. 225 (2004) 7–13.
- [25] V. Lebarbier, G. Clet, M.A. Houalla, Comparative study of the surface structure, acidity, and catalytic performance of tungstated zirconia prepared from crystalline zirconia or amorphous zirconium oxyhydroxide, J. Phys. Chem. B 110 (2006) 13.905–13.911.
- [26] H. Liu, L. Feng, X. Zhang, Q. Xue, ESR characterization of ZrO<sub>2</sub> nanopowder, J. Phys. Chem. 99 (1995) 332–334.

- [27] S. Kongwudthiti, P. Praserthdam, P. Silveston, M. Inoue, Influence of synthesis conditions on the preparation of zirconia powder by the glycothermal method, Ceram. Int. 29 (2003) 807–814.
- [28] C. Su, J. Li, D. He, Z. Cheng, Q. Zhu, Synthesis of isobutene from synthesis gas over nanosize zirconia catalyst, Appl. Catal. A: Gen. 202 (2000) 81–89.
   [29] P. Wongmaneenil, B. Jongsomjit, P. Praserthdam, Influence of calcinations
- [29] P. Wongmaneenil, B. Jongsomjit, P. Praserthdam, Influence of calcinations treatment on the activity of tungstated zirconia catalysts towards esterification, Catal. Commun. 10 (2009) 1079–1084.
- [30] K. Ngaosuwan, B. Jongsomjit, P. Praserthdam, The role of zirconia surface on catalytic activity of tungstated zirconia via two-phase esterification of acetic acid and 1-heptanol, Catal. Lett. 136 (2010) 134–140.
- [31] E.V. Frolova, M.I. Ivanovskaya, The origin of defects formation in nanosized zirconia, Mater. Sci. Eng. C 26 (2006) 1106–1110.
- [32] A. Martínez, G. Prieto, M.A. Arribas, P. Concepción, J.F. Sánchez-Royo, Influence of the preparative route on the properties of WO<sub>x</sub>–ZrO<sub>2</sub> catalysts: a detailed structural, spectroscopic, and catalytic study, J. Catal. 248 (2007) 288–302.

#### ORIGINAL PAPER

# Effect of Ga modification on different pore size silicas in synthesis of LLDPE by copolymerization of ethylene and 1-hexene with [t-BuNSiMe<sub>2</sub>Flu]TiMe<sub>2</sub>/MMAO catalyst

Ekrachan Chaichana ·
Supaporn Khaubunsongserm ·
Piyasan Praserthdam · Bunjerd Jongsomjit

Received: 2 June 2010/Revised: 27 December 2010/Accepted: 30 December 2010/

Published online: 19 January 2011

© Springer-Verlag 2011

**Abstract** Copolymerization of ethylene and 1-hexene for obtaining the linear low-density polyethylene was conducted along with silicas as supports for [t-BuN-SiMe<sub>2</sub>Flu]TiMe<sub>2</sub>/MMAO catalyst. Two silicas with different pore sizes were used to investigate the effect of pore sizes on copolymerization. In addition, gallium was also introduced into both silicas to improve their properties and enhance the catalytic activities of the system. It was found that before modification, the larger pore silica exhibited higher catalytic activity than the smaller one due to low internal diffusion resistance. After modification, both silicas exhibited higher catalytic activity comparing to their pristine condition. However, 1-hexene incorporation in the obtained copolymers was lower. The reduced surface area of silica after modification was the main reason for the decrease in 1-hexene incorporation. The properties of the copolymers by means of differential scanning calorimetry, gel permeation chromatography, and <sup>13</sup>C NMR spectroscopy were further discussed in more detail.

**Keywords** Polymer synthesis · Silica · Metallocene · LLDPE

#### Introduction

First commercialize in the late 1970s by Union Carbide and Dow Chemical [1], linear low-density polyethylene (LLDPE) has continued a fast growth rate in usage

PTT Public Company Limited, PTT Research and Technology Institute, Wangnoi, Ayuthaya 13170, Thailand



E. Chaichana · P. Praserthdam · B. Jongsomjit (⋈)

Center of Excellence on Catalysis and Catalytic Reaction Engineering, Department of Chemical Engineering, Faculty of Engineering, Chulalongkorn University, Bangkok 10330, Thailand e-mail: bunjerd.j@chula.ac.th

S. Khaubunsongserm

from that time to this day. For using LLDPE in an efficient way, the specific properties of LLDPE, such as molecular weight (M<sub>w</sub>) distribution, stereoregularity, and comonomer content need to be considered carefully. Metallocene is one of the most widely used catalysts for control those properties, and thus, many studies have been conducted with this type of catalyst [2–4]. However, the industrial application of metallocene is usually processed in a gas or slurry phase, so the development of supported metallocene is very important. Inorganic materials, such as SiO<sub>2</sub>, Al<sub>2</sub>O<sub>3</sub>, and ZrO2 were applied for supported metallocene. It was, nevertheless, SiO2 that has been reported as the most attractive support. Therefore, the studies of silica on the role of support for metallocene catalyst have been conducted by many researchers in many aspects. Silveira et al. [5] have reported that textural properties of silica support were shown to influence several parameters and properties of supported metallocene catalysts, for example, the particle size influencing on catalytic activity. Besides the particle size, pore size is another factor that has been investigated. Kumkaew et al. [6, 7] have discovered that pore sizes influence the nature of the catalytic sites for supported metallocene catalyst, and then, also influence the comonomer incorporation rate of copolymerization. Ko et al. [8] reported that the certain pore size of support had different levels of impact on different sizes of (co)monomer. The effect of pore size not only exists in a system during copolymerization, but also does previously during preparation or modification of support. Therefore, properties of support before and after modification need to be considered to further clarify all phenomena occurring in the supported system.

In our previous study, the copolymerization of ethylene/1-hexene using the [t-BuNSiMe<sub>2</sub>Flu]TiMe<sub>3</sub>/MMAO catalyst under homogeneous system was investigated [9]. However, in this study, the similar copolymerization under the heterogeneous or supported system using silica support was further investigated. In addition, the effects of pore size of silica were studied by using different pore size silicasupported MMAO. Moreover, the effect of gallium (Ga) modification on silica was also examined to give a better understanding on how the catalytic activity apparently changes with Ga modification on different pore size silicas. In fact, the Ga modification on silica was chosen because it can enhance activity in zirconocene/ MMAO catalytic system as reported by Wannaborworn et al. [10].

#### **Experimental**

#### Materials

All operations were manipulated under an argon atmosphere using glove box and/or standard Schlenk techniques. [t-BuNSiMe<sub>2</sub>Flu]TiMe<sub>2</sub> was synthesized according to the procedure described by Hagihara et al. [11]. Ethylene was obtained from the National Petrochemical Co. Ltd., Thailand. 1-Hexene was purchased from Aldrich Chemical Company. Modified methyl aluminoxane (MMAO) (1.86 M in toluene) was donated by Tosoh Akzo, Japan. Toluene was donated by the Exxon Chemical, Thailand Co. Ltd. It was dried over dehydrated CaCl<sub>2</sub> and distilled over sodium/ benzophenone. Silica gel from Fuji Silysia Chemical Ltd., Japan (Cariact Q-50 and



P-10) was calcined at 400 °C for 6 h under vacuum. Gallium nitrate was purchased from Aldrich Chemical Company, Inc., and use as received.

#### Preparation of Ga-modified silica support

The Ga modification of the silica support was prepared by the conventional incipient-wetness impregnation method according to the procedure described previously [12]. The Ga source in this case was  $Ga(NO_3)$ . Ga was impregnated onto silica gel (Cariact Q-50 and P-10) by 1.0 wt% of Ga. The support was dried in oven at 110 °C for 12 h, and then calcined in air at 400 °C for 2 h.

#### Preparation of supported MMAO

The silica supports were prepared by in situ impregnation method which was described by Wannaborworn et al. [10]. Silica (0.1 g) was allowed in contact with 4 mmol of MMAO for at least 2 h in a reactor with magnetic stirring, and then the slurry of MMAO/support was obtained and ready to be used in polymerization. To verify that all MMAO was immobilized onto the support, a batch test was conducted together with the preparation method for the entire samples. For the batch test, after stirring the mixture of support and MMAO for 2 h and leaving for precipitate for 1 h, 1 mL of clarified liquid was taken and injected into the polymerization reactor, where a desired amount of catalyst was already present. If no formation of any amount of polymer is observed, it will be evident that this clarified liquid does not contain the free MMAO. Thus, all MMAO was immobilized on the supports completely.

#### Polymerization procedure

The prepared MMAO/support (0.1 g support and 4 mmol MMAO) and toluene were introduced into the reactor. The titanium complex in toluene (10  $\mu$ mol mL<sup>-1</sup>) was put into the reactor to make the [Al]<sub>MMAO</sub>/[Ti]<sub>cat</sub> = 400. Then, the reactor was immersed in liquid nitrogen. 0.018 mol of 1-hexene was added into the frozen reactor (to stop or prevent possible polymerization of 1-hexene). The reactor was heated up to the polymerization temperature at 70 °C. The polymerization was started by feeding ethylene into the reactor, and then stopped when ethylene consumption reached to 0.018 mol (6 psi on the pressure gauge). The reactor temperature was kept constant during the polymerization. The reaction was terminated by adding acidic methanol and the material was stirred for 30 min. After filtration, the copolymer obtained was washed with methanol and dried at room temperature.

#### Characterization

#### Characterization of supports

 $N_2$  physisorption: Measurement of BET surface area, average pore diameter, and pore size distribution were determined by  $N_2$  physisorption using a Micromeritics



ASAP 2000 automated system. *X-ray diffraction*: XRD was performed to determine the bulk crystalline phases of samples. It was conducted using a SIEMENS D-5000 X-ray diffractometer with Cu  $K_{\alpha}$  (l=1.54439~Å). The spectra were scanned at a rate of 2.4 min<sup>-1</sup> in the range of  $2\theta=10^{\circ}-80^{\circ}$ .

#### Characterization of polymers

<sup>13</sup>C NMR spectroscopy: The copolymers were characterized using <sup>13</sup>C NMR spectroscopy (BRUKER AVANCE II 400) to determine the 1-hexene incorporation. Each sample solution was prepared by dissolving 50 mg of copolymer in 1,2,4-trichlorobenzene and CDCl<sub>3</sub>. Spectra were taken at 60 °C operated at 100 MHz with an acquisition time of 1.5 s and a delay time of 4 s.

Differential scanning calorimetry (DSC): Thermal analysis measurements were performed using a Perkin-Elmer DSC P7 calorimeter. The DSC measurements reported here were recorded during the second heating/cooling cycle with the rate of 20 °C/min. This procedure ensured that the previous thermal history was erased and provided comparable conditions for all samples. Approximately, 10 mg of sample was used for each DSC measurement.

Gel permeation chromatography (GPC): The  $M_{\rm w}$  of polymer was determined using GPC (GPC, PL-GPC-220). Samples were prepared having approximately concentration of 1–2 mg/mL in trichlorobenzene (mobile phase) by using the sample preparation unit (PL-SP 260) with filtration system at a temperature of 140 °C. The dissolved and filtered samples were transferred into the GPC instrument at 140 °C. The calibration was conducted using the universal calibration curve based on narrow polystyrene standards.

#### Results and discussion

#### Characterization of supports

In this study, two kinds of silica with different pore diameters were used as a supporting material for catalyst. By investigating their porous properties with N<sub>2</sub> physisorption, they were classified according to the size of pores. Large pore (LP) denotes the Q-50 silica having an average pore diameter of 380 Å, and small pore (SP) denotes the P-10 silica having an average pore diameter of 170 Å. Besides using both silicas in pristine condition, they were modified by gallium (SP-Ga and LP-Ga) for improving some specific properties before use. Thus, there were four kinds of supports used in this polymerization system. The specific properties of them are shown in Table 1. It can be seen from this table that after modification by Ga, both supports (SP and LP) exhibited decreased surface area and also pore volume compared to the supports before modification (SP-Ga and LP-Ga). This was due to the partial blockage of pore by Ga nitrate used for the modification procedure. In addition, according to the XPS investigation on Ga-modified supports conducted by Campos et al. [13], it was suggested that Ga modifiers were mostly deposited at the surface of the supports, but some of them can penetrate into the



Supports	Pore diameter (Å)	Pore volume (cm <sup>3</sup> /g)	Surface area (m <sup>2</sup> /g)
SP	171	6.5	216.8
LP	369	1.36	70.9
SP-Ga	190	1.4	169.7
LP-Ga	320	0.2	68.8

Table 1 Specific properties of various supports obtained from N2 physisorption

surface and being present in the bulk of the support. The average pore diameters of the supports before and after modification slightly changed. The XRD patterns (not shown) for all supports were similar exhibited only a board peak between 20° and 30°, as seen typically for the conventional amorphous silica. No XRD peaks of Ga were observed after impregnation due to its highly dispersed form.

#### Effect of pore size of silica supports

As seen in Table 2, the LP silica exhibited higher catalytic activity than that of the SP silica. Although most MMAO is presumed located mostly at the external surface [10], some is located at the internal surface too. This can be observed from the effect of pore size of the silica support which still existed in this comparison. To grasp the effect of pore size, the internal diffusion resistance needs to be considered. In general, the supports with SP size result in poor intra-pellet diffusion efficiency and slow transportation of reactants and products due to strong diffusion resistance [14], contrasting with the supports with LP size, which are able to diminish the diffusion resistance by their large pores. Then, copolymerization conducted with LP size support exhibited higher catalytic activity than that with SP size support. Another parameter which provides compelling evidence is the copolymerization time of the systems. It can be obviously seen that copolymerization time of the LP silica system (LP and LP-Ga) was shorter than that of the SP silica system (SP and SP-Ga) indicating that propagation rate of system with the LP silica was higher, due to monomer and comonomer being able to reach to the catalytic active sites more easily even located inside the pores. In addition, silica with smaller diameters could

	-	- ·	
Supports	Time <sup>a</sup> (s)	Yields (g)	Catalytic activity <sup>b</sup> (kg polymer/mol Ti h)
SP	233	0.8681	1341
LP	170	0.7941	1682
SP-Ga	186	0.9919	1920
LP-Ga	140	0.7632	1893

Table 2 Catalytic activities in ethylene/1-hexene copolymerization with different supports

 $<sup>^</sup>b$  Copolymerization condition: Ti = 10  $\mu$ mol, Al/Ti = 400, temperature = 70  $^{\circ}$ C, 50 psi of ethylene pressure was applied



<sup>&</sup>lt;sup>a</sup> Time when all ethylene (0.018 mol) was consumed

display the lower catalytic activities probably due to the higher probability of formation for the bimolecular species as described by Silveira et al. [15].

#### Effect of Ga modification on silica surface

To investigate an effect of Ga as modifying agent for silica support, comparisons were drawn between modified and unmodified supports on both types of silica. As seen from Table 2 (SP vs. SP-Ga, LP vs. LP-Ga), Ga modification can increase catalytic activity in both types of silica. It has been known that adding Ga into silica surface normally increases acidic sites to the silica support [13, 16]. These sites are required to activate metallocene catalyst to be an active species in supported system. Many inorganic supports which possess the strong Lewis acidic property, such as Al<sub>2</sub>O<sub>3</sub> and MgCl<sub>2</sub> have been used as support for this purpose [17]. For silica, directly using as a support for metallocene catalysts preparation resulted in inactive catalysts formation [18]. However, in this method, MMAO took charge of main activating agent as usual in metallocene catalyst system and Ga can assist in the activation by increase Lewis acidity in support as mentioned. Furthermore, Ga can be anchored on the surface of silica, thus lower interaction between active sites and support. The result of higher catalytic activity by Ga modification accorded with the finding of Campos et al. [19], which found that introducing Ga into supports can improve the ability of the supports to immobilize metallocene, and then enhancing the catalytic activity of the systems. Improving ability to immobilize (grafting the substances) by Ga was also reported by Morrow and McFarlane [20]. They found that the introduction of species such as PH<sub>3</sub> and AsH<sub>3</sub> into the silica surface was more strongly adsorbed when silica was first reacted with the Ga.

When comparing the activities of system with Ga modification on both silica types, it revealed that the SP silica showed slightly higher catalytic activity. This was opposite to the result of activities before modifying the support. This is because the SP silica has higher surface area than that of the LP silica. Then, Ga modification, which mainly affected on the surface properties of support, can more efficiently influence catalytic behavior in higher surface area support than the lower surface area support. Therefore, after modification the SP silica would give the higher activity than that of the LP silica due to higher surface area.

#### Characterization of copolymers

The triad distribution for all copolymers investigated by  $^{13}$ C NMR is also shown in Table 3. The triad block of comonomer (HHH) was not detected for all samples. This suggests that the good distribution of comonomer throughout the copolymer chain existed in the systems. In addition, the products of reactivity ( $r_{\rm E}r_{\rm H}$ ) of some sample (SP-Ga) also showed the characteristic of random copolymers ( $r_{\rm E}r_{\rm H} > 1$ ), and the rest of them showed the typical alternating copolymer character ( $r_{\rm E}r_{\rm H} < 1$ ). Both silicas provided higher  $M_{\rm w}s$  for the copolymers after Ga modification. This was probably due to Ga modifier enhanced propagation rate, but reduced termination rate (chain transfer) in polymerization. It was also observed that Ga



had more effect on the  $M_{\rm w}$  of polymer obtained by the smaller pore silica than the larger one due to higher surface area of the smaller pore silica as mentioned earlier.

#### Effect of pore size of silica supports

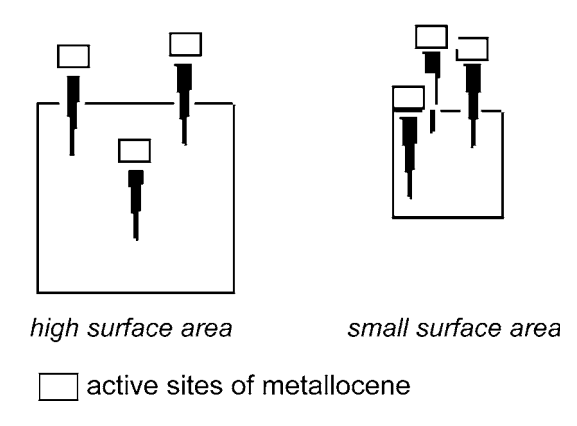
It can be observed from Table 3 that both pore size silicas produced copolymers with nearly the same incorporations of 1-hexene (SP and LP). In general, the LP silica should supply more comonomer for propagating the copolymer chain than the SP silica due to lower diffusion resistance within the pores. However, another factor which can influence on the incorporation of comonomers is the surface area of the supports. Regarding to surface area, the support with large surface area is expected to produce copolymers with high incorporation of comonomer as a result of more space between active sites dispersed on its surface area compared to the support with smaller surface area, as seen in Fig. 1. Then, the SP size silica with higher surface area would probably result in high comonomer incorporation with this effect. Therefore, from the result that showed a roughly equal amount of 1-hexene comonomer incorporation for two different textures of silicas indicated that both effects (pore size and surface area) have a profound impact at the same level upon the incorporation of 1-hexene in the obtained copolymers.

Table 3 Properties of the obtained copolymers examined by <sup>13</sup>C-NMR and GPC

Supports	EEE	EEH	HEH	EHE	EHH	ННН	$r_{\rm E} r_{\rm H}^{\rm a}$	% H <sup>b</sup>	$M_{\rm w}^{\rm c}$
SP	0.367	0.269	0.041	0.156	0.166	0.000	0.969	32.2	26
LP	0.359	0.272	0.046	0.163	0.159	0.000	0.873	32.3	24
SP-Ga	0.410	0.246	0.038	0.149	0.157	0.000	1.108	30.6	37
LP-Ga	0.422	0.280	0.039	0.159	0.099	0.000	0.737	25.8	27

<sup>&</sup>lt;sup>a</sup> Relative comonomer reactivities ( $r_{\rm E}$  for ethylene and  $r_{\rm H}$  for 1-hexene) calculated by  $r_{\rm E}=2$ [EE]/[EH]X,  $r_{\rm H}=2$ X[HH]/[EH], [EE] = [EEE] + 0.5[HEE], [HH] = [HHH] + 0.5[EHH], [EH] = [HEH] + 0.5[HEE] + [EHE] + 0.5[EHH]

**Fig. 1** Comparison of active site dispersion on the different surface areas





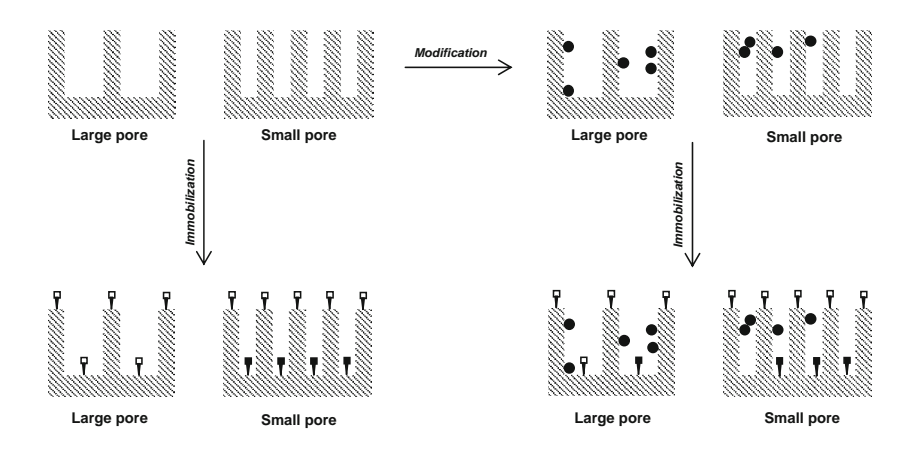
<sup>&</sup>lt;sup>b</sup> 1-Hexene incorporation

<sup>&</sup>lt;sup>c</sup> Molecular weight (kg/mol) obtained from GPC

#### Effect of Ga modification on silica surface

Comparing between SP and SP-Ga alongside LP and LP-Ga, we found that when modifying surface of silica support with Ga, the 1-hexene incorporations were decreased in both types of silica. This can be explained by the effect of surface area. Since both silicas had lower surface area through modifying procedure by Ga as follows; in LP 70.9 to 68.8 m<sup>2</sup>/g and in SP 216.8 to 169.7 m<sup>2</sup>/g. Although incipientwetness impregnation used in the modification is the easiest method of introducing a metal precursor, it results in the precipitation of small particles of the salt onto the support surface [21]. Therefore, the decrease in the surface area may be due to the partial blockage of pore by excess Ga nitrate. As seen from Fig. 2, the excess substances more seriously affect on the decrease in surface area of the SP silica than the LP silica because the SPs can be blocked by the deposit easier compared to the LP. Therefore, after modification with Ga, the significant decrease in surface area occurs in the SP silica, contrasting to that with the LP silica, which has only slight decrease. The average pore diameter shown in Table 1 also reveals that the blockage seriously affects on the smaller pore sizes by decreasing the population of the smaller pore sizes (the SPs become shallower until disappear), and then the average pore sizes are shifted to higher value (from 171 to 190 Å).

The decrease in 1-hexene incorporation in the copolymer obtained from both silicas after modification by Ga was opposite to the decrease in surface area. The significant decrease was observed for the LP silica instead. The reason for this can be explained as seen in Fig. 2. The active sites with high enough space for high 1-hexene incorporation were indicated in the figure by an open square while a filled square indicated the active sites with insufficient space for high 1-hexene incorporation. It can be seen that high space sites (open square) in the LP silica



- : Low space active site
- ¬: High space active site
- : Gallium nitrate salt

Fig. 2 Conceptual model for impact of pore blockage on supports with different pore sizes



were decreased noticeably after modification, whereas the number of the high space sites in the SP silica remained the same. The high space sites in the SP silica are always located outside the pores, and therefore they can not be affected by the deposit of excess Ga inside the pores. On the other hand, in the LP silica, these sites are sometimes located inside the pores, then the deposit on the wall of pores can hinder them from being reached by a large size molecules, especially for 1-hexene comonomer. Hence, the incorporation of 1-hexene in the LP silica system decreased significantly after the support was modified by Ga.

In addition, this proposed model (Fig. 2) can explain the previous results reported by our research group that sites with no or low 1-hexene incorporation rates (insufficient space site, filled square) were more prevalent at short polymerization times [7]. It can be seen from the model that the said sites usually located inside the pore, so therefore at initial time of polymerization it still had an impact in polymerization. After the long period of polymerization, the supports were covered by the growing chain of polymer and then, hindered the (co)monomer to reach inside of pores, thus decreasing the impact of the sites located inside the pores in polymerization. So if the polymerization time was longer, it would be found the fraction of polymer producing from sites with no or low 1-hexene incorporation rates. However, this model should be used together with the multigrain model [22] and the fragmentation of the particles should be neglected.

The model in Fig. 2 also indicated that different types of catalytic sites are present in these catalysts, according to the findings of Kumkaew et al. [7] which suggested that pore sizes can influence the type of catalytic sites present in the supports. The various sites derived from different environments which mainly point to steric hindrance as seen in the model. The hindrance is not just to the monomer to attack the site, but also to MMAO in forming cocatalysts-counterion fit and salvation, which plays a significant role in the structures and energetic of the ion pairing proposed by Lanza et al. [23]. Therefore, the alteration of selectivity by different pore sizes may be one of the reasons for the change in 1-hexene incorporations.

To support that the copolymers were obtained from different catalytic sites, one simple technique that can be used for this purpose is the DSC. As known, the DSC endotherms were influenced by many factors such as the crystallinity and  $M_{\rm w}$  of polymer, then being difficult to identify each peak occurring clearly. However, they could brief necessary information about characteristic of catalyst as recommended by Kumkaew et al. [7] that DSC of nascent polymer may provide information on heterogeneity of supported polymerization catalysts.

From Fig. 3, it can be seen that the copolymers obtained from the unmodified supports exhibited several DSC endotherm peaks, whereas the ones obtained from the Ga-modified supports exhibited broader peaks. Nevertheless, all of them indicate multiple types of catalytic sites. The slight difference in characteristic of peaks between the Ga-modified support and the unmodified one may be derived from the change in surface nature of the support after modification, particularly the heterogeneous nature. Another parameter that provides information about heterogeneity of the support is the molecular weight distribution (MWD) of the obtained polymers. The MWD as measured by GPC of the samples are; SP = 2.8, SP-Ga = 2.9, LP = 1.8, and LP-Ga = 2.3. It can be seen that after modification both silicas



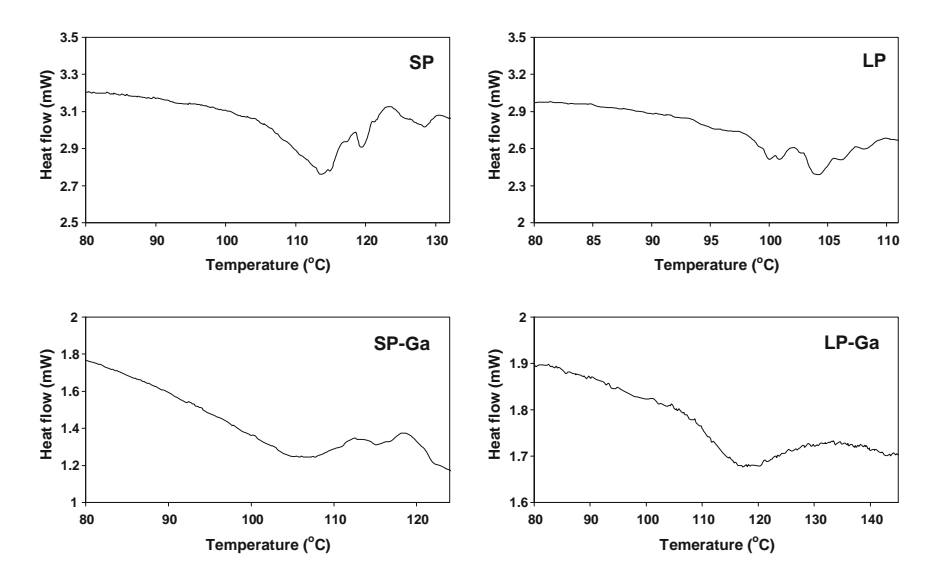


Fig. 3 DSC endotherms of LLDPE synthesized with various SiO<sub>2</sub> supports

exhibited broader MWD values, suggesting more heterogeneous nature. This may imply that silicas after modification by Ga have a greater degree of heterogeneity in catalytic sites. Therefore, it can be concluded that Ga addition into silica also changed the nature of catalyst and provide more heterogeneity in catalytic sites to supported system.

### Conclusion

The higher catalytic activity of the LP silica was observed as a result of low internal diffusion resistance. However, after Ga modification, the SP silica exhibited higher catalytic activity. This is because Ga modification, which mainly improves properties of surface, more efficiently influences properties on silica with higher surface area. Then, the SP silica with higher surface can receive more improvement from Ga and raising more catalytic activities than the LP silica with lower surface area. Moreover, effect of surface area also caused change in 1-hexene incorporation, where a decrease in 1-hexene incorporation was evident with decreased surface area. In addition, different types of catalytic sites were observed, and then used to construct a model which helped explain the results.

**Acknowledgments** The authors thank the Thailand Research Fund (TRF), Office of the Higher Education Commission (CHE) and PTT Public Company Limited for the financial support of this project.

### References

 Simpson DM, Vaughan GA (2003) Ethylene polymers, LLDPE. In: Mark HF (ed) Encyclopedia of polymer science and technology. Wiley, New York, pp 441–482. doi:10.1002/0471440264.pst122



- Severn JR, Chadwick JC, Duchateau R, Friederichs N (2005) "Bound but not gagged"—Immobilizing single-site a-olefin polymerization catalysts. Chem Rev 105:4073–4147. doi:10.1177/0010414 001034005002
- Kaminsky W, Albers I, Vathauer M (2002) New copolymers of olefins and styrene by metallocene catalysis. Des Monomers Polym 5:155–162. doi:10.1163/156855502760157881
- Shiono T, Yoshida S, Hagihara H, Ikeda T (2000) Additive effects of trialkylaluminum on propene polymerization with (t-BuNSiMe2Flu)TiMe<sub>2</sub>-based catalysts. Appl Catal A Gen 200:145–152. doi: 10.1016/S0926-860X(00)00633-5
- Silveira F, Pires GP, Petry CF, Pozebon D, Stedile FC, Santos JHZd, Rigacci A (2007) Effect of the silica texture on grafting metallocene catalysts. J Mol Catal A Chem 265:167–176. doi:10.1016/j. molcata.2006.10.008
- Kumkaew P, Wanke SE, Praserthdam P, Danumah C, Kaliaguine S (2002) Gas-phase ethylene polymerization using zirconocene supported on mesoporous molecular sieves. J Appl Polym Sci 87:1161–1177. doi:10.1002/app.11515
- Kumkaew P, Wu L, Praserthdam P, Wanke SE (2003) Rates and product properties of polyethylene produced by copolymerization of 1-hexene and ethylene in the gas phase with (n-BuCp)<sub>2</sub>ZrCl<sub>2</sub> on supports with different pore sizes. Polymer 44:4791–4803. doi:10.1016/S0032-3861(03)00473-7
- Ko YS, Woo SI (2003) Shape and diffusion of the monomer-controlled copolymerization of ethylene and a-olefins over Cp<sub>2</sub>ZrCl<sub>2</sub> confined in the nanospace of the supercage of NaY. J Polym Sci Pol Chem 41:2171–2179. doi:10.1002/pola.10762
- 9. Chaichana E, Khaubunsongserm S, Praserthdam P, Jongsomjit B (2010) Ethylene–hexene copolymer derived from [*t*-butylfluorenylsilyl-amido] dimethyl titanium complex. Express Polym Lett 4:94–100. doi:10.3144/expresspolymlett.2010.14
- Wannaborworn M, Jongsomjit B (2009) Ethylene/1-octene copolymerization over Ga-modified SiO<sub>2</sub>-supported zirconocene/MMAO catalyst using in situ and ex situ impregnation methods. Iran Polym J 18:969–979
- Hagihara H, Shiono T, Ikeda T (1998) Living polymerization of propene and 1-hexene with the [t-BuNSiMe<sub>2</sub>Flu]TiMe<sub>2</sub>/B(C6F5) 3 catalyst. Macromolecules 31:3184–3188. doi:10.1021/ma971697k
- Pothirat T, Jongsomjit B, Praserthdam P (2008) Effect of Zr-modified SiO<sub>2</sub>-supported metallocene/ MAO catalyst on copolymerization of ethylene/1-octene. Catal Lett 121:266–273. doi:10.1007/s 10562-007-9327-y
- Campos JM, Lourenco JP, Fernandes A, Rego AM, Ribeiro MR (2009) Mesoporous Ga-MCM-41 as support for metallocene catalysts: acidity-activity relationship. J Mol Catal A Chem 310:1–8. doi: 10.1016/j.molcata.2009.05.012
- 14. Iglesia E, Reyes SC, Madon RJ (1991) Transport-enhanced a-olefin readsorption pathways in Ru-catalyzed hydrocarbon synthesis. J Catal 129:238–256. doi:10.1016/0021-9517(91)90027-2
- Silveira F, MdCM Alves, Stedile FC, Pergher SB, Rigacci A, JHZd Santos (2009) Effect of the silica texture on the structure of supported metallocene catalysts. J Mol Catal A Chem 298:40–50. doi: 10.1016/j.molcata.2008.10.011
- Takahara I, Saito M, Inaba M, Murata K (2004) Effects of pre-treatment of a silica-supported gallium oxide catalyst with H<sub>2</sub> on its catalytic performance for dehydrogenation of propane. Catal Lett 96:29–32. doi:10.1023/B:CATL.0000029525.33197.89
- Finch WC, Gillespiy RD, Hedden D (1990) Organometallic molecule-inorganic surface coordination and catalytic chemistry, in Situ CPMAS NMR delineation of organoactinide adsorbate structure, dynamics, and reactivity. J Am Chem Soc 112:6221–6232. doi:10.1021/ja00173a009
- Jongsomjit B, Kaewkrajang P, Shiono T, Praserthdam P (2004) Supporting effects of silica-supported methylaluminoxane (MAO) with zirconocene catalyst on ethylene/1-olefin copolymerization behaviors for linear low-density polyethylene (LLDPE) production. Ind Eng Chem Res 43:7959–7963. doi: 10.1021/ie049548v
- Campos JM, Lourenco JP, Fernandes A, Ribeiro MR (2008) Mesoporous Ga-MCM-41: a very efficient support for the heterogenisation of metallocene catalysts. Catal Commun 10:71–73. doi: 10.1016/j.catcom.2008.07.038
- Morrow BA, McFarlane RA (1986) Trimethylgallium adsorbed on silica and its reaction with phosphine, arsine, and hydrogen chloride: an infrared and Raman study. J Phys Chem 90:3192–3197. doi:10.1021/j100405a029
- 21. Hegedus LL (1987) Catalyst design, progress and perspectives. Wiley, New York



- Laurence RL, Chiovetta MG (1983) Heat and mass transfer during olefin polymerization from the gas phase. In: Reichert KH, Geiseler W (eds) Polymer reaction engineering. Hanser, New York, pp 73–111
- 23. Lanza G, Fragala' IL, Marks TJ (2002) Energetic, structural, and dynamic aspects of ethylene polymerization mediated by homogeneous single-site "constrained geometry catalysts" in the presence of cocatalyst and solvation: an investigation at the ab initio quantum chemical level. Organometallics 21:5594–5612. doi:10.1021/om0207764





Article

## The Influence of *t*-Butyl and Cyclododecyl Substitution on Ethylene/1-Hexene Copolymerization Using Ansa-Fluorenylamidodimethyltitanium Derivatives

Patcharaporn Kaivalchatchawal <sup>1</sup>, Piyasan Praserthdam <sup>1</sup>, Yuuichi Sogo <sup>2</sup>, Zhengguo Cai <sup>2</sup>, Takeshi Shiono <sup>2</sup> and Bunjerd Jongsomjit <sup>1</sup>,\*

- <sup>1</sup> Center of Excellence on Catalysis and Catalytic Reaction Engineering, Department of Chemical Engineering, Faculty of Engineering, Chulalongkorn University, Bangkok 10330, Thailand
- <sup>2</sup> Department of Applied Chemistry, Graduate School of Engineering, Hiroshima University, Higashi-Hiroshima 739-8527, Japan
- \* Author to whom correspondence should be addressed; E-Mail: bunjerd.j@chula.ac.th; Tel.: +66 2 2186869; Fax: +66 2 2186877.

Received: 9 March 2011; in revised form: 9 May 2011 / Accepted: 12 May 2011 /

Published: 19 May 2011

Abstract: In the present study, copolymerization of ethylene and 1-hexene was conducted with a series of ansa-fluorenylamidodimethyltitanium complexes, including [t-BuNSiMe<sub>2</sub>Flu]TiMe<sub>2</sub> (complex 1), [cyclododecylNSiMe<sub>2</sub>Flu]TiMe<sub>2</sub> (complex 2) and [t-BuNSiMe<sub>2</sub>(2,7-t-Bu<sub>2</sub>Flu)]TiMe<sub>2</sub> (complex 3), activated by MMAO. The effect of these catalysts on catalytic behavior, namely activity, molecular weight and monomer reactivity ratios, has been investigated. The results showed that all of them acted by a single site polymerization mechanism and the molecular weight distribution is independent of catalyst structure. Based on the study, it revealed that the introduction of a t-butyl at the 2,7 position on the fluorenyl ligand is able to enhance both catalytic activity and copolymer molecular weight more than introducing a cyclododecyl on the amine, which is probably associated with the electronic effect exerted by the t-butyl substituent. The comonomer incorporation content was controllable over a wide range by adjusting the comonomer feed ratio. Moreover, referring to monomer reactivity ratio exploration, it seems that the substitution on the ansa-fluorenylamidodimethyltitanium complex tends to hinder the insertion of 1-hexene into the polymer chain, leading to the highest 1-hexene content for traditional complex **1**.

**Keywords:** polymer synthesis; catalytic synthesis; polyolefins; metallocene catalyst; CGC catalyst

### 1. Introduction

At present, linear low density polyethylene (LLDPE) is regarded as an important type of polyethylene and is also well recognized as economically attractive, accounting for more than half of the annual worldwide polymer production due to its distinctive processing and mechanical properties [1]. Copolymerization of ethylene and  $\alpha$ -olefins, such as 1-butene, 1-hexene and 1-octene, is a general way to generate LLDPE with short chain branching. This copolymerization usually involves a constrained geometry catalyst (CGC) which has opened active sites for easy insertion of high  $\alpha$ -olefins [2-5]. Superior to conventional Zeigler-Natta and metallocene catalysts, CGCs are capable of improving products in terms of much higher comonomer incorporation, narrower comonomer and molecular weight distribution which leads to better mechanical and physical properties. However, the incorporation of  $\alpha$ -olefins that would result in the polymer properties depends on the structure of catalyst employed during copolymerization [1,6,7]. In fact, small variations of the ligand structure or ligand substituents may cause profound changes in the catalytic activity, copolymerization behavior and properties of the resulting polymer [3-5,8]. Therefore, by knowing the nature of catalysts, properties can be controlled and altered in order to achieve the desired LLDPE.

In this research, complexes 1, 2 and 3 (Scheme 1) were synthesized and further used as the catalysts for ethylene/1-hexene copolymerization to investigate the effect of the CGC-titanium complex on the copolymerization behavior.

**Scheme 1.** Ethylene/1-hexene copolymerization system.

### 2. Results and Discussion

The ethylene/1-hexene copolymerization with catalyst complexes 1, 2 and 3 was carried out at 273 and 298 K under atmospheric pressure whereas the polymerization time of each batch was adjusted so as to keep the comonomer conversion relatively constant for the purpose of acceptable reactivity ratio evaluation. The catalytic results are tabulated in Table 1.

**Table 1.** Summary of ethylene/1-hexene copolymerization catalytic activities and properties of copolymers.

Entry a)	1- hexenem ol'L <sup>-1</sup>	Time s	Yield g	Activity b) kg·mol <sup>-1</sup> Ti·h <sup>-1</sup>	cont	$Mw^{d)}$ $kg$ mol $^{-1}$	MWD <sup>e)</sup>
T	0.75	60	0.6832	2050	-	-	-
1-1	0.075	210	0.0265	23	37.2	27	1.44
1-2	0.15	240	0.0835	63	37.8	25	1.53
1-3	0.45	360	0.2477	122	62.1	44	1.73
1-4	0.75	200	0.3688	221	74.3	49	1.53
1-5	1.5	180	0.3691	369	72.1	60	1.51
2-1	0.075	180	0.0813	81	30.1	26	1.61
2-2	0.15	120	0.1514	227	40.7	35	1.47
2-3	0.45	120	0.2250	338	57.9	36	1.54
2-4	0.75	150	0.3399	408	66.9	38	1.58
2-5	1.5	180	0.6160	616	78.0	71	1.48
3-1	0.075	45	0.0856	342	33.8	37	1.7
3-2	0.15	45	0.1167	467	47.2	64	1.48
3-3	0.45	40	0.2089	940	64.1	166	1.83
3-4	0.75	35	0.5272	2711	63.0	329	1.70
3-5	1.5	30	0.6006	3604	68.3	415	1.50

<sup>&</sup>lt;sup>a)</sup> Entry T, 1-1, 1-2, 1-3, 1-4 and 1-5 used complex 1 as catalyst; Entry 2-1, 2-2, 2-3, 2-4 and 2-5 used complex 2 as catalyst; Entry 3-1, 3-2, 3-3, 3-4 and 3-5 used complex 3 as catalyst; b) polymerization condition: [Ti] = 20 μmol, MMAO as cocatalyst, [Al]/[Ti] = 400, liquid volume (toluene) = 30 mL, ethylene pressure = 1 atm, temperature = 273 K (except Entry T (293 K)); c) 1-hexene content in copolymer determined by <sup>13</sup>C NMR; d) molecular weight determined by GPC using PS standard.

Regarding the result of Entry T in Table 1, it can be seen that the activity of the complex **1** when the reaction was performed at 293 K was very high (2,050 kg·mol<sup>-1</sup> Ti·h<sup>-1</sup>), leading to difficulty in controlling the comonomer conversion. As a consequence, the other polymerization temperature conditions were reduced to 273 K. For comparison of the three sets of catalytic systems, including using catalyst complexes **1**, **2** and **3**, the activity towards ethylene/1-hexene was in the order complex **3** > complex **2** > complex **1**. In detail, the attachment of *t*-butyl groups at the 2,7 positions of the fluorenyl ring significantly impacted the catalytic behavior of the CGC complex, causing about 7–10 times higher activity than that obtained from the original nonsubstituted complex **1**. This was in good agreement with the previous research on propylene polymerization under the specified polymerization conditions [9]. It also showed that this increased catalytic activity is presumably due to an enhancement of the propagation rate by the electronic effect of the alkyl groups. The introduction of cyclododecyl on the amine group also resulted in an increase of activity, but less pronounced.

Likewise, a similar trend in copolymerization activity for these complexes can be observed. As the 1-hexene feed concentration rose, the catalytic activity increased. Relating to Table 1, it is fair to say that the activity displayed by complex 3 was more sensitive to the comonomer concentration. This phenomenon has been generally known as "comonomer effect" and has been described in a large number of reports [2,10]. The rate-time profiles of copolymerization demonstrated that all profiles were similar, starting with the minimum initial value and then gradually increasing with time, proposing that no deactivation of catalyst occurred during the copolymerization.

The relevant GPC results of obtained copolymers are collected in Table 1. All of resultant polymers possessed middle to high molecular weight and unimodal molecular weight distribution (Mw/Mn < 2), conforming the single site polymerization behavior of the three complexes. Nevertheless, it is noticeable that the molecular weight of copolymer obtained with complex 3 was 3–5 times higher than that of the corresponding copolymers obtained with the remaining complexes. Therefore, we may concluded that the 2,7 t-butyl substituent has a profound effect on a molecular weight increase. This is probably ascribable to the fact that the electronic effect exerted by the substituent reduces the rate of chain termination. Considering the relationship between the molecular weight and comonomer feed concentration, the molecular weight of all copolymers produced by the three titanium complexes increased with the rise of concentration, contrary to the literature [2]. This trend was rather unexpected since comonomer incorporation usually favors chain termination on account of terminal double bonds formed by hydride  $\beta$ -elimination which are mainly between comonomer units, consequently causing lower molecular weight copolymers.

A quantitative analysis of triad distribution was carrried out using <sup>13</sup>C-NMR spectra assignment [11] of ethylene/1-hexene copolymer and is shown in Table 2. As expected, for each catalyst complex employed, the incorporation of comonomer increased with an increase in 1-hexene concentration in the reaction medium. Even though the content was slightly dependent on the complex used, all CGC complexes yielded the copolymers with high 1-hexene content (>30% mol).

The best way to investigate a copolymerization is to measure the reactivity ratios of the ethylene monomer ( $\mathbf{r}_E$ ) and 1-hexene comonomer ( $\mathbf{r}_H$ ) which are defined as the ratio of homopropagation to the crosspropagation rate constants. Thus, in this work, the reactivity ratios were calculated from the Fineman-Ross method and also from the Kelen-TÜdÖs method [12,13].

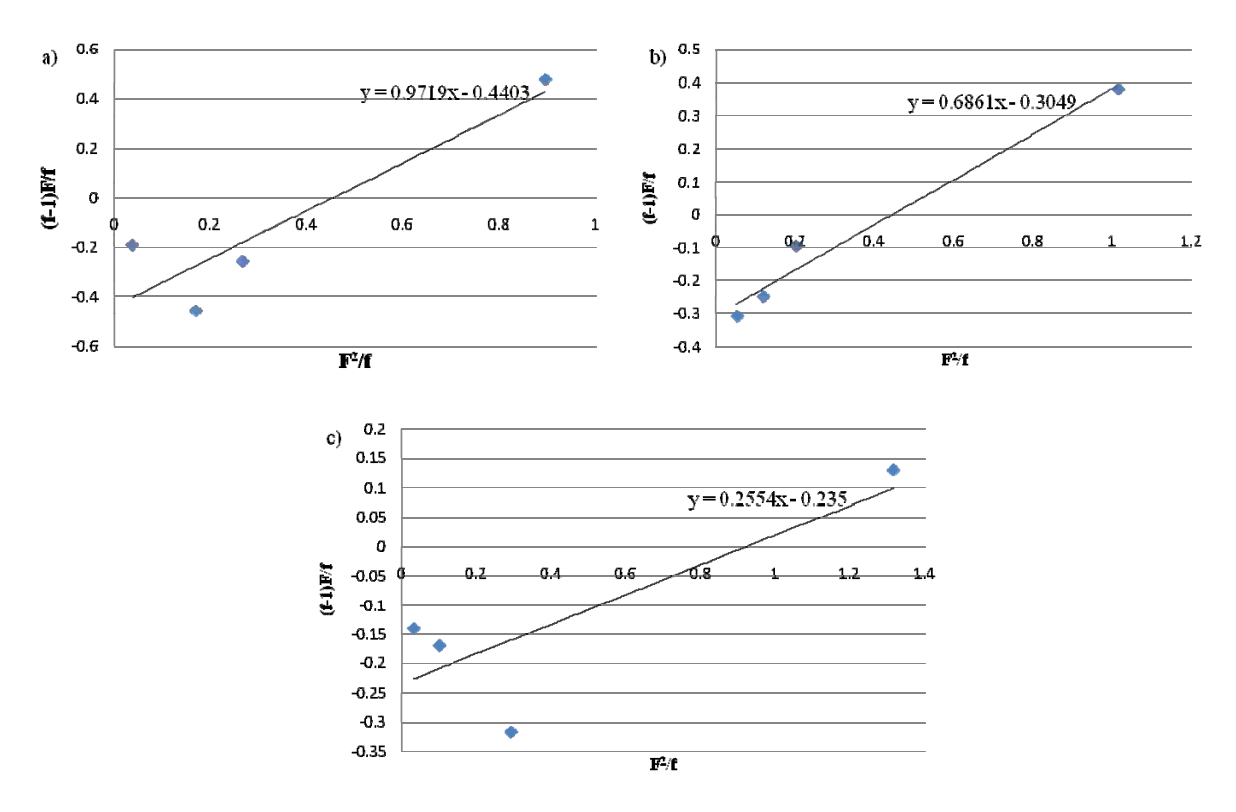
**Table 2.** Triad distributions of obtained copolymers determined by <sup>13</sup>C NMR.

Entry	1-hexene	[HHH]	[EHH]	[EHE]	[EEE]	[HEH]	[HEE]	[H]
	$mol \cdot L^{-1}$	<b>%</b>	%	%	%	%	%	<b>%</b>
1-1	0.075	0.0	23.8	13.4	15.8	10.5	36.5	37.2
1-2	0.15	0.0	21.9	15.9	19.4	10.8	32.0	37.8
1-3	0.45	19.9	32.5	9.7	4.7	18.8	14.4	62.1
1-4	0.75	36.8	33.3	4.2	0.0	15.9	9.8	74.3
1-5	1.5	28.7	37.4	3.5	0.0	14.0	16.4	72.1
2-1	0.075	0.0	11.7	18.4	28.4	7.0	34.5	30.1
2-2	0.15	7.8	14.8	18.1	21.8	13.5	24.0	40.7
2-3	0.45	16.5	28.4	13.0	6.3	18.6	17.2	57.9
2-4	0.75	48.3	11.6	7.0	13.4	19.7	0.0	66.9
2-5	1.5	43.8	34.1	0.0	0.0	12.1	9.9	78.0
3-1	0.075	4.6	10.4	18.8	28.2	10.0	27.9	33.8
3-2	0.15	8.8	20.6	17.8	11.7	15.1	26.0	47.2
3-3	0.45	29.8	24.5	9.8	5.6	13.7	16.7	64.1
3-4	0.75	27.1	25.8	10.0	6.6	15.4	15.0	63.0
3-5	1.5	31.4	32.3	4.6	2.1	11.8	17.8	68.3

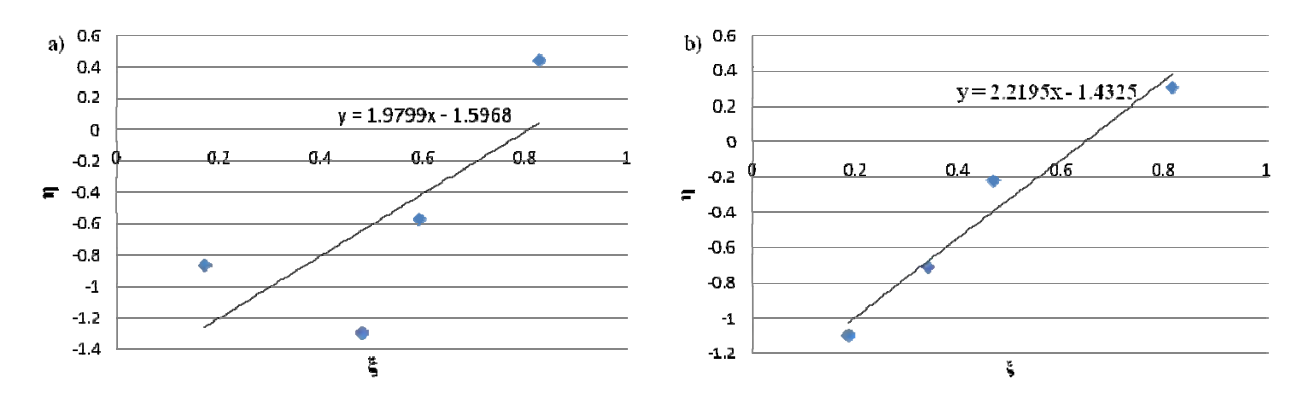
For the calculations, all copolymerizations of each series were used, except the one with the lowest concentration due to the fact it was the most affected by the experimental error. Figures 1 and 2 show the Fineman-Ross and the Kelen-TÜdÖs plots for the complexes  $\bf 1$ ,  $\bf 2$  and  $\bf 3$ , respectively, and the least squares best fit line. In general, a good fit of the experimental results in the straight line was observed in most cases. Table 3 gathers the reactivity ratios that were calculated from the mentioned methods. As seen on the Fineman-Ross and Kelen-TÜdÖs plots in Figures 1 and 2, the values of  $\bf r_E$  and  $\bf r_H$  determined by the former fitted the experimental data obtained. Thus, a straighter line can be observed. In other words, the Fineman-Ross model was likely to give a better fit to the real data than the Kelen-TÜdÖs model. In fact, the 1-hexene reactivity ratio ( $\bf r_H$ ) is able to describe the preference of 1-hexene incorporation into a polymer chain compared with the ethylene in the same chain end. Hence, with regard to Table 3, it can be observed that, all employed titanium complexes resulted in a tendency of ethylene incorporation into the polymer chain in comparison with 1-hexene. Furthermore, the difference in  $\bf r_H$  owing to the structure of the CGC catalyst was found. The increasing ratio of 1-hexene reactivity ( $\bf r_H$ ) along with the enhancing capability of catalyst complexes to provide higher 1-hexene

content in copolymer can be concluded as follows: complex 1 > complex 2 > complex 3. According to this result, it can be proposed that the attachment of each substituent group on ansa-fluorenyl amidodimethyltitanium complex seems to be an obstacle for higher  $\alpha$ -olefin insertion. Overall, the values of  $r_E r_H$  of the polymers obtained from all titanium complexes suggested a tendency of the formation of alternating copolymer structure ( $r_E r_H < 1$ ).

**Figure 1.** Fineman-Ross plots for the copolymers obtained with **a**) complex 1 **b**) complex 2 and **c**) complex 3 where F = the mole ratio of ethylene and 1-hexene in the feed and f = the mole ratio of ethylene and 1-hexene in the copolymer.



**Figure 2.** Kelen-TÜdÖs method plots for the copolymers obtained with **a**) complex 1 **b**) complex 2 and **c**) complex 3 where  $\eta = G/(\alpha+F')$ ,  $\xi = F'/(\alpha+F')$ , G = (f-1)F/f,  $F' = F^2/f$ ,  $\alpha = (F'_{max}F'_{min})^{0.5}$ , F = the mole ratio of ethylene and 1-hexene in the feed and f = the mole ratio of ethylene and 1-hexene in the copolymer.



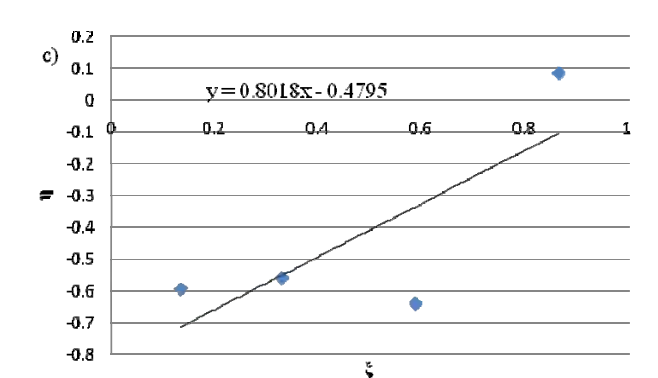


Figure 2. Cont.

**Table 3.** Reactivity ratios for each copolymerization system.

Complex	r <sub>E</sub> <sup>a)</sup>	r <sub>H</sub> b)	r <sub>E</sub> c)	r <sub>H</sub> d)
1	0.97	0.44	0.76	0.30
2	0.69	0.30	0.79	0.33
3	0.26	0.24	0.32	0.10

<sup>&</sup>lt;sup>a)</sup> Ethylene reactivity ratio calculated by Fineman-Ross method; <sup>b)</sup> 1-hexene reactivity ratio calculated by Fineman-Ross method; <sup>c)</sup> Ethylene reactivity ratio calculated by Kelen-TÜdÖs method; <sup>d)</sup> 1-hexene reactivity ratio calculated by Kelen-TÜdÖs method.

### 3. Experimental

### 3.1. Materials

All operations were performed under nitrogen gas using Schlenk techniques and all solvents were dried by usual procedures and freshly distilled before use. MMAO was donated by Tosoh-Finechem Co. Ltd. Research grade ethylene (Takachiho Chemicals Co.) was purified by passing it through columns of NaOH,  $P_2O_5$ , and 3Å molecular sieves, followed by bubbling through a NaAlH<sub>2</sub>Et<sub>2</sub>/1,2,3,4,-tetrahydronaphthalene solution. CGC complexes were synthesized according to procedures reported previously [14,15].

### 3.2. Polymerization Procedure

Ethylene/1-hexene copolymerization was performed in a 100 mL glass reactor equipped with a magnetic stirrer. After a desired amount of 1-hexene was dissolved in a toluene solution of MMAO, copolymerization was started by adding 1 mL solution of catalyst (20 μmol). The polymerization was conducted for a certain time, and then was terminated by adding HCl/methanol solution. The obtained polymers were dried under vacuum at 333 K for 6 h.

### 3.3. Analytical Procedure

The molecular weight and molecular weight distribution were determined by GPC Waters 150 CV at 408 K using o-dichlorobenzene as a solvent and calibrated with polystyrene standards. The <sup>13</sup>C-NMR spectra of copolymers were recorded at 403 K on a JEOL GX 500 spectrometer operated at 125.65 MHz in the pulse Fourier-transform mode. The samples were prepared from using 1,1,2,2-tetrachloroethane-d<sub>2</sub> and the central peak of the solvent (74.47 ppm) was used as an internal reference.

### 4. Conclusions

Three CGC complexs, comprising complex **1** (unsubstituted complex), complex **2** (cyclododecyl substituent on the amine group) and complex 3 (2,7 *t*-butyl substituents on the fluorene ring), activated by MMAO were employed for ethylene/1-hexene copolymerization at 273 K to produce LLDPE. The introduction of both substituents is able to improve the activity and copolymer molecular weight. Nonetheless, it can be noticed that the 2,7 *t*-butyl group considerably impacted those features, achieving the highest activity of 3604 kg·mol<sup>-1</sup> Ti·h<sup>-1</sup> and the highest molecular weight of 415 kg·mol<sup>-1</sup>. The polydispersity values of all obtained copolymers are less than 2, suggesting the single site behavior of all three titanium catalyst complexes. Moreover, the 1-hexene content of copolymers can be controlled by changing the comonomer feed concentration and is dependent on the catalyst structure as well. The comonomer reactivity ratio (r<sub>H</sub>) result revealed that nonsubstituted titanium CGC complex yielded the highest tendency to incorporate 1-hexene into the copolymer chain.

### Acknowledgements

The authors gratefully thank the *Dusadeepipat* scholarship (Chulalongkorn University Fund), Graduate school of Chulalongkorn University and Hiroshima University for the financial support of this work. The authors also extend the thankful for the Thailand Research Fund (TRF), Office of the Higher Education Commission (CHE), and CU-NRU (AM1088A).

### References

- 1. Mulhaupt, R. Catalytic polymerization and post polymerization catalysis fifty years after the discovery of Ziegler's catalysts. *Macromol. Chem. Phys.* **2003**, *204*, 289-327.
- 2. Hong, H.; Zhang, Z.; Chung, T.; Lee, W. Synthesis of new 1-decene-based LLDPE resins and comparison with the corresponding 1-octene- and 1-hexene-based LLDPE resins. *J. Polym. Sci. A Polym. Chem.* **2007**, *45*, 639-649.
- 3. Cano, J.; Sudupe, M.; Royo, P. How to synthesize a constrained geometry catalyst (CGC) A survey. *J. Organomet. Chem.* **2007**, *692*, 4441-4423.
- 4. Braunschweig, H.; Breitling, F.M. Constrained geometry complexes Synthesis and applications. *Coord. Chem. Rev.* **2006**, *250*, 2691-2720.
- 5. Chum, P.S.; Swogger, K.W. Olefin polymer technologies-History and recent progress at The Dow Chemical Company. *Prog. Polym. Sci.* **2008**, *33*, 797-819.

6. Schellenberg, J. Influence of the catalyst on monomer insertion in the syndiospecific copolymerization of styrene and para-methylstyrene. *J. Polym. Sci. A Polym. Chem.* **2005**, *43*, 2061-2067.

- 7 Wang, W.; Kolodka, E.; Zhu, S.; Hamielec, A.E. Continuous solution copolymerization of ethylene and octene-1 with constrained geometry metallocene catalyst. *J. Polym. Sci. A Polym. Chem.* **1999**, *37*, 2949-2957.
- 8. Liu, S.R.; Li, B.X.; Liu, J.Y.; Li, Y.S. Synthesis, structure and ethylene (co)polymerization behavior of new nonbridged half-metallocene-type titanium complexes based on bidentate beta-enaminoketonato ligands. *Polymer* **2010**, *51*, 1921-1925.
- 9. Cai, Z.; Ikeda, T.; Akita, M.; Shiono, T. Substituent effects of tert-butyl groups on fluorenyl ligand in syndiospecific living polymerization of propylene with ansa-fluorenylamidodimethyltitanium complex. *Macromolecules* **2005**, *38*, 8135-8139.
- 10. Grieken, R.V.; Carrero, A.; Suarez, I.; Paredes, B. Effect of 1-hexene comonomer on polyethylene particle growth and kinetic profiles. *Macromol. Symp.* **2007**, *259*, 243-252.
- 11. Eric, T.; Randall, C. Monomer Sequence Distributions in Ethylene-1-Hexene Copolymers. *Macromolecuels* **1986**, *15*, 1402-1411.
- 12. Tüdös, F.; Kelen, T.; Földes-Berezhnykh, T. Evaluation of high conversion copolymerization data by a linear graphical method. *React. Kinet. Cata. Lett.* **1975**, 2, 439-447.
- 13. Fineman, M.; Ross, S.D. Linear Method for Determining Monomer Reactivity Ratios in Copolymerization. *J. Polym. Sci.* **1950**, *5*, 259-265.
- 14. Nishii, K.; Hagihara, H.; Ikeda, T.; Akita, M.; Shiono, T. Stereospecific polymerization of propylene with group 4 ansa-fluorenylamidodimethyl complexes. *J. Organomet. Chem.* **2006**, *691*, 193-201.
- 15. Cai, Z.; Nakayama, Y.; Shiono, T. Catalytic synthesis of a monodisperse olefin block copolymer using a living polymerization system. *Macromol. Rapid Commun.* **2008**, *29*, 525-529.

Sample Availability: Samples of the compounds are available from the authors.

© 2011 by the authors; licensee MDPI, Basel, Switzerland. This article is an open access article distributed under the terms and conditions of the Creative Commons Attribution license (http://creativecommons.org/licenses/by/3.0/).

### ORIGINAL PAPER

### Effects of Ti oxidation state on ethylene, 1-hexene comonomer polymerization by MgCl<sub>2</sub>-supported Ziegler-Natta catalysts

Nichapat Senso · Piyasan Praserthdam · Bunjerd Jongsomjit · Toshiaki Taniike · Minoru Terano

Received: 12 November 2010/Revised: 13 June 2011/Accepted: 13 June 2011/

Published online: 31 August 2011

© Springer-Verlag 2011

**Abstract** In this study, the influences of the Ti oxidation state on the catalytic properties of MgCl<sub>2</sub>-supported Ziegler–Natta catalysts in ethylene homo- and co-polymerization with 1-hexene were investigated. Three catalysts having different Ti oxidation states were synthesized by milling TiCl<sub>4</sub>, TiCl<sub>3</sub>, or TiCl<sub>2</sub> together with MgCl<sub>2</sub>. With these catalysts having different Ti oxidation states, the polymerization conditions such as the Al concentration, temperature, and 1-hexene concentration were varied to figure out their catalytic abilities in ethylene homo- and co-polymerization. The Ti oxidation state affected the catalyst activity largely, having unique dependences on the polymerization conditions. A higher oxidation state led to a higher activity, slightly larger comonomer incorporation, and lower molecular weight as well as its narrower distribution. However, rough characteristics of copolymers were similar among the different Ti oxidation states.

**Keywords** Ziegler–Natta catalyst · Titanium oxidation state · Polyethylene · Ethylene/1-hexene copolymerization · Ethylene polymerization

### Introduction

Current industrial production of polyethylene and polypropylene still largely depends on MgCl<sub>2</sub>-supported heterogeneous Ziegler–Natta (ZN) catalysts [1–3]. The mechanical and rheological properties of polyethylene and polypropylene are

School of Materials Science, Japan Advanced Institute of Science and Technology,

1-1, Asahidai, Nomi, Ishikawa 923-1292, Japan

e-mail: terano@jaist.ac.jp



N. Senso  $\cdot$  P. Praserthdam  $\cdot$  B. Jongsomjit

Department of Chemical Engineering, Center of Excellence on Catalysis and Catalytic Reaction Engineering, Faculty of Engineering, Chulalongkorn University, Bangkok 10330, Thailand

T. Taniike ⋅ M. Terano (⋈)

strongly affected by molecular weight (MW) and molecular weight distributions (MWD) [4–6, 8, 9] as well as by chemical composition distribution (CCD) in the case of copolymer. Therefore, it is industrially crucial to control these parameters by catalyst and polymerization technologies.

Homogeneous catalysts represented by metallocene catalysts are generally single-site catalysts so as to give monodisperse MW and chemical composition, and are advantageous in the incorporation of bulky or polar co-monomers. On the other hand, ZN catalysts are multi-sites catalysts and generally lead to broad MWD and CCD, which have been regarded to be advantageous for some polymer properties.

To control the MWD and CCD of polymers with Ziegler-Natta catalysts, the nature of active sites is critically important in a sense that different active sites produce polymers with different MWs and CCs. Several factors are responsible for the nature of active sites such as Ti nucreality [4, 7], dispersion [10], oxidation state [11, 13–19], interaction with MgCl<sub>2</sub> support [7, 12], and so on. The oxidation state of Ti species has been regarded as one of the key factors to cause CCD and MWD; Ti species undergo stepwise reduction during polymerization and as a result the Ti oxidation state becomes a mixture of tetravalent (Ti<sup>4+</sup>), trivalent (Ti<sup>3+</sup>), and divalent (Ti<sup>2+</sup>) states [17]. Many researchers have investigated the relationship between Ti oxidation state and polymerization performance. Baulin et al. [13] studied the effects of the Ti oxidation state on the activity of a TiCl<sub>4</sub>/MgO catalyst by increasing alkylaluminum concentration. A contact of a TiCl<sub>4</sub>/MgO catalyst with A1Et<sub>3</sub> under conditions similar to those of polymerization (A1/Ti of 150-200 for 1 h at 70 °C), more than 90% of  $Ti^{4+}$  was reduced (96% to  $Ti^{3+}$  and 4% to  $Ti^{2+}$ ). They were not able to find any quantitative correlation between the degree of Ti reduction and catalytic activity. It was found later that the catalytic activity decreased by precontact between catalyst and alkylaluminum [14, 17]. An even stronger reduction (80% Ti<sup>2+</sup> and 20% Ti<sup>3+</sup>) has been reported by Kashiwa et al. [17] for a TiC1<sub>4</sub>/EB/MgC1<sub>2</sub> catalyst after a 2-h reaction with A1Et<sub>3</sub> (A1/Ti = 50) at 60 °C. They also observed that the catalyst thus obtained was only slightly active for the polymerization of ethylene and completely inactive for propylene polymerization; however, the activity was recovered by re-oxidizing Ti with a chlorinating agent such as t-BuCl. It was concluded that a direct relationship exists between the activity and Ti oxidation state. Kissin et al. [20] studied a relationship of the molecular weight and chemical composition with the Ti oxidation state by varying the polymerization time from 5 to 40 min. Based on deconvolution of molecular weight and crystallinity distributions in gel permeation chromatography (GPC) and temperature rising elution fractionation (TREF), they obtained the following conclusions: (i) Ti<sup>4+</sup> is active for ethylene and propylene homopolymerization and for ethylene/α-olefin copolymerization, and produces polymers with low molecular weights and high comonomer contents (ii) Ti<sup>3+</sup> is also active for the above mentioned polymerization, producing polymers with moderately high molecular weight (iii) Ti<sup>2+</sup> is active only for ethylene homopolymerization, giving very high molecular weight polymers. Zakharov et al. [6] have prepared  $Ti^{2+}$  ( $\eta^6$ -benzene-Ti<sub>2</sub>Al<sub>2</sub>Cl<sub>8</sub>), Ti<sup>3+</sup> (TiCl<sub>3</sub>·n-dibutylether), and Ti<sup>4+</sup> (TiCl<sub>4</sub>) supported on MgCl<sub>2</sub>, and investigated behaviors of different Ti oxidation states in ethylene polymerization and ethylene/1-hexene copolymerization. Their results demonstrated that Ti<sup>2+</sup>,



Ti<sup>3+</sup>, and Ti<sup>4+</sup> were highly active in both of ethylene polymerization and ethylene/ 1-hexene copolymerization, on the contrary to the results obtained by Kissin et al. [20]. The advantage of their work for the effects of the Ti oxidation state is to have prepared the catalysts from precursors with the corresponding oxidation states. However, not only the oxidation state but also the presence of the extra ligands such as *n*-dibutylether, and  $\eta^6$ -benzene and Al<sub>2</sub>Cl<sub>6</sub> might affect the catalytic behavior and polymer properties. In other words, it is not sure if the nature of  $\eta^6$ -benzene-Ti<sub>2</sub>Al<sub>2</sub>Cl<sub>8</sub> is similar to that of TiCl<sub>2</sub> formed by reaction of TiCl<sub>4</sub> with alkylaluminum. Another research [21] showed that a higher temperature or a larger alkylaluminum/TiCl<sub>4</sub> ratio increases the activity until some optimum value for the average oxidation state is achieved, while the activity starts to drop beyond the optimum value. The optimum average oxidation state was Ti<sup>2.2+</sup> for ethylene polymerization. A similar relation between the catalytic activity and optimum oxidation state was also found for different types of ZN catalysts such as TiCl<sub>2</sub>, SiO<sub>2</sub>/MgCl<sub>2</sub>/THF/TiCl<sub>4</sub>, and AlCl<sub>3</sub>/TiCl<sub>4</sub> [22-24]. In finding a relationship of the oxidation state with MW and MWD of polyethylene, Zakharov et al. [5] conducted a comprehensive study with systematically varying the Ti oxidation and dispersion states using the above-mentioned three precursors [5, 6]. They found that isolated Ti<sup>2+</sup> and Ti<sup>3+</sup> ions supported on MgCl<sub>2</sub> were more active than a supported TiCl<sub>4</sub> catalyst, which turned into a mixture of isolated and clustered Ti<sup>3+</sup> after the interaction with alkylaluminum. Moreover, it was shown that produced polyethylene had similar MW and MWD in spite of the sharp distinctions in the Ti oxidation and dispersion states for their catalysts. Thus, the source of MWD was not straightforwardly understood.

From the previous reports mentioned above, the effects of the Ti oxidation state are still controversy on the catalytic activity, polymer molecular weight, and comonomer response in olefin polymerization using Ziegler–Natta catalysts. The co-presence of different Ti oxidation states during polymerization is still an importance problem. In this study,  $TiCl_2$ ,  $TiCl_3$ , and  $TiCl_4$  were directly supported on  $MgCl_2$  to get better understanding on the role of the Ti oxidation state in ethylene homopolymerization and ethylene/1-hexene copolymerization. The activity behavior was found to be sensitive to the oxidation state of the  $TiCl_x$  precursors, while polymer structures such as MW and CC were basically insensitive, supporting the previously obtained results [5, 6].

### **Experimental**

### Materials

Anhydrous  $MgCl_2$  and  $\alpha$ -Ti $Cl_3$  (donated by Toho Titanium Co., Ltd.),  $TiCl_4$  (Wako Pure Chemical Industries, Ltd.), anhydrous  $TiCl_2$  (Aldrich) and  $AlEt_3$  (donated by Tosoh Finechem Co.) were used without further purification. Heptane (Wako Pure Chemical Industries, Ltd.) was used after dehydration by passing through a column with molecular sieve 13X, and 1-hexene (Wako Pure Chemical Industries, Ltd.) was distilled with sodium/benzophenone.



### Catalyst preparation

Three kinds of MgCl<sub>2</sub>-supported catalysts with different Ti oxidation states were prepared as follows [10].

- (i) TiCl<sub>2</sub>/MgCl<sub>2</sub>: 36 g of MgCl<sub>2</sub> and 2.34 g of TiCl<sub>2</sub> were put into a 1 L stainless steel pot containing 55 stainless steel balls (25 mm diameter) and then vibration ball-milled under nitrogen for 30 h at RT.
- (ii) TiCl<sub>3</sub>/MgCl<sub>2</sub>: 36 g of MgCl<sub>2</sub> and 3.1 g of TiCl<sub>2</sub> were similarly milled for 30 h at RT.
- (iii) TiCl<sub>4</sub>/MgCl<sub>2</sub>: 108 mL of TiCl<sub>4</sub>, 108 mL of heptane and 36 g of MgCl<sub>2</sub> were similarly milled for 30 h at RT, and then the ground product was treated with TiCl<sub>4</sub> (200 mL) at 90 °C for 2 h with stirring under nitrogen, followed by washing with heptane repeatedly.

These catalysts, TiCl<sub>2</sub>/MgCl<sub>2</sub>, TiCl<sub>3</sub>/MgCl<sub>2</sub>, and TiCl<sub>4</sub>/MgCl<sub>2</sub>, are designated as Ti2M, Ti3M, and Ti4M. Their titanium contents were 2.36, 2.31, and 1.38 wt%, respectively.

### Polymerization

Slurry polymerization in n-heptane was performed under constant ethylene pressure of 0.5 MPa at the polymerization temperature from 50 to 70 °C for 1 h. Triethylaluminum (TEA) was used as cocatalyst, whose concentration was 2.0–30.0 mmol/L. The polymerization was initiated by the injection of the catalyst slurry. The catalyst concentration in the polymerization slurry was fixed at 3.5 mg/L. Ethylene/1-hexene copolymerization was carried out under the same polymerization condition and procedure. The 1-hexene concentration was 2.5–10 vol%.

### Polymer characterization

<sup>13</sup>C NMR spectra of copolymers were recorded on a Varian Gemini-300 spectrometer at 120 °C using 1,2,4-trichlorobenzene as a diluent and 1,1,2,2-tetrachloroethane-*d2* as a solvent. MW and MWD of polymers were determined by gel permeation chromatography (GPC, Alliance GPC 2000, Waters), using 1,2,4 trichlorobenzene as a mobile phase.

### Results and discussion

### Influence of Al concentration

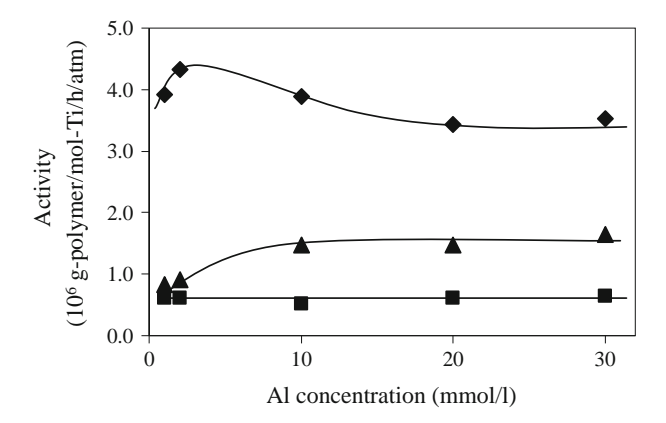
The alkylaluminum concentration largely affects on the polymerization kinetics through activation and deactivation of Ti species. The deactivation rate was known to be correlated with the rate of reduction of Ti species [17]. Figure 1 shows the effect of the Al concentration on the Ti2M, Ti3M, and Ti4M catalytic activities in ethylene polymerization. The ethylene polymerizations rates for the three catalysts



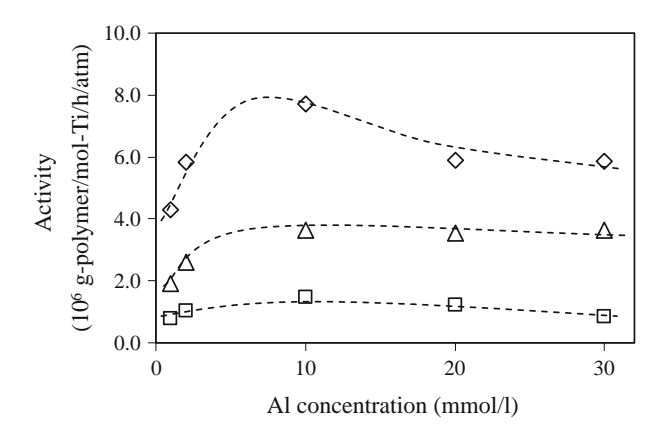
showed different trends with increasing the Al concentration. In the case of Ti2M, it was rather constant, consistent with the previously reported results [23, 25]. This could be explained by the fact that Ti species can not be reduced over Ti<sup>2+</sup> by alkylaluminum, and the formed active sites are regarded as quite stable with negligible deactivation with alkylaluminum. This conclusion was supported by previous experimental reports [5, 12, 26]. On the other hand, the ethylene polymerization rates for Ti3M and Ti4M increased, and then became nearly constant up to 10 mmol/L of the Al concentration. This trend appeared to be in agreement with the results obtained by Bresadola et al. [25]. They found that the catalytic activity for ethylene polymerization was nearly constant in the range of 50-200 Al/Ti. They observed a slow decrease of Ti<sup>4+</sup> and Ti<sup>3+</sup> amount accompanied with a small increase of Ti<sup>2+</sup>. The total amount of the Ti<sup>3+</sup> and Ti<sup>2+</sup> species, both of which are active for ethylene polymerization, was reported to be substantially constant, giving a constant activity. The catalytic activity for Ti4M once reached the maximum, and then gradually dropped over 2.0 mmol/L of the Al concentration, which differed from the constant trends for Ti2M and Ti3M. This could be explained by the fact that TiCl<sub>4</sub> easily migrates on MgCl<sub>2</sub> in the presence of alkylaluminum to aggregate with each other in the curse of the reduction, leading to the gradual decrease of the active site concentration [10]. TiCl<sub>2</sub> and TiCl<sub>3</sub>, that are originally solids, are bound much more tightly than TiCl<sub>4</sub> on MgCl<sub>2</sub>, to depress the aggregation-induced deactivation. Figure 2 shows the ethylene/1-hexene copolymerization activities with varying the alkylaluminum concentration. The activity of Ti2M was enhanced with the addition of a small amount of 1-hexene, although the activities were the lowest among the three catalysts. Interestingly, copolymers produced with Ti2M had similar composition and sequence distribution to those produced with the other two catalysts, even though the 1-hexene incorporation became lower for higher Al concentrations. These results are in disagreement with the previous explanation [20] that Ti<sup>2+</sup> is comonomer insensitive and produces homopolyethylene only. In the case of Ti3M and Ti4M, the polymerization rates were drastically increased with the addition of 1-hexene, while the activity variation in terms of the Al concentration obeyed a similar trend for the homopolymerization in Fig. 1. The observed rate enhancement by the addition of 1-hexene is known as a rate enhancement effect by comonomer [27–29]. In the case of ethylene copolymerization with α-olefin, physical explanations seem more plausible, such as the acceleration of monomer diffusion through less crystallizable copolymers [30], and the acceleration of the catalyst fragmentation in copolymerization [29]. The difference in the observed rate enhancements by 1-hexene for the three catalysts might arise from the difference of their incorporation efficiency of 1-hexene.

Table 1 shows sequence distribution of ethylene/1-hexene (E/H) copolymers obtained at different Al concentrations. The copolymers contained 0.37–0.61 mol% of 1-hexene, in which butyl branches existed in an isolated manner without any HHH, HEH, and EHH triad sequences. All of Ti2M, Ti3M, and Ti4M show a similar trend, even though a higher oxidation state tends to lead to larger incorporation: the 1-hexene incorporation is the highest at the lowest Al concentration, and then drops for higher concentrations.





**Fig. 1** Influence of the Al concentration on the ethylene homopolymerization activities. The homopolymerization was conducted at 60 °C for 1 h under 0.5 MPa of ethylene. TEA was used as cocatalyst (*filled diamond* Ti4M, *filled circle* Ti3M, and *filled square* Ti2M)



**Fig. 2** Influence of the Al concentration on the ethylene copolymerization activities. The copolymerization was conducted at 60 °C for 1 h under 0.5 MPa of ethylene. 10 vol% of 1-hexene was added as the comonomer (*open diamond* Ti4M, *open circle* Ti3M, and *open square* Ti2M)

### Influence of the polymerization temperature

The influence of the polymerization temperature on the activities of homo- and co-polymerization is shown in Fig. 3. The temperature was varied in the range of 50–70 °C. Higher catalyst activities for the ethylene homopolymerization were obtained by increasing the polymerization temperature. Although Ti4M was the most sensitive to the temperature change, the behavior was similar among the different Ti oxidation states. In comparison, the copolymerization activities increased more sharply than the homo-polymerization at 60 °C, but rather dropped at 70 °C, probably because the 1-hexene solubility was decreased upon increasing the reactor temperature.



Catalyst	Al conc. (mmol/L)	EHE	ЕНН	ННН	НЕН	ЕЕН	EEE	1-hexene incorporated (mol%)
Ti2M	2.0	0.5	0.0	0.0	0.0	1.1	98.4	0.54
	10.0	0.4	0.0	0.0	0.0	0.7	98.9	0.37
	30.0	0.4	0.0	0.0	0.0	0.8	98.7	0.42
Ti3M	2.0	0.6	0.0	0.0	0.0	1.1	98.3	0.56
	10.0	0.5	0.0	0.0	0.0	1.0	98.5	0.52
	30.0	0.5	0.0	0.0	0.0	1.1	98.4	0.53
Ti4M	2.0	0.6	0.0	0.0	0.0	1.2	98.2	0.61
	10.0	0.6	0.0	0.0	0.0	1.1	98.4	0.55
	30.0	0.6	0.0	0.0	0.0	1.1	98.3	0.57

**Table 1** Sequence distribution of ethylene/1-hexene copolymers synthesized using  $TiCl_x/MgCl_2$  catalysts (x = 2-4) at different Al concentrations

Polymerization conditions: catalyst amount = 3.5 mg/L, temperature = 60 °C, polymerization time = 1 h, ethylene pressure = 0.5 MPa, 1-hexene concentration = 10 vol%, TEA concentration = 2–30 mmol/L

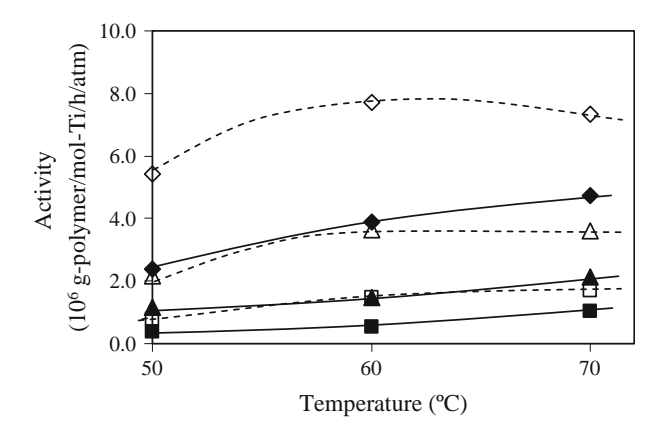


**Fig. 3** Influence of the polymerization temperature on the activities of the ethylene homo- and copolymerization. The polymerization was conducted under 0.5 MPa of ethylene for 1 h. 10 mmol/L of TEA was used as cocatalyst. 10 vol% of 1-hexene was added in copolymerization

### Influence of the 1-hexene concentration

The effects of the 1-hexene concentration on the polymerization rates and resulting polymer properties were investigated for the different Ti oxidation states. As shown in Fig. 4, all the catalysts activities were linearly increased for the 1-hexene concentration. The sequence distributions of copolymers prepared with the three catalysts are shown in Table 2. The produced copolymers again had similar composition and sequence distribution without sequential 1-hexene insertion. Incorporation of 1-hexene in copolymers was basically increased in correlation with the 1-hexene concentration, but not simply proportional to it. There might be a critical incorporation amount, below which the incorporation efficiency is lower for



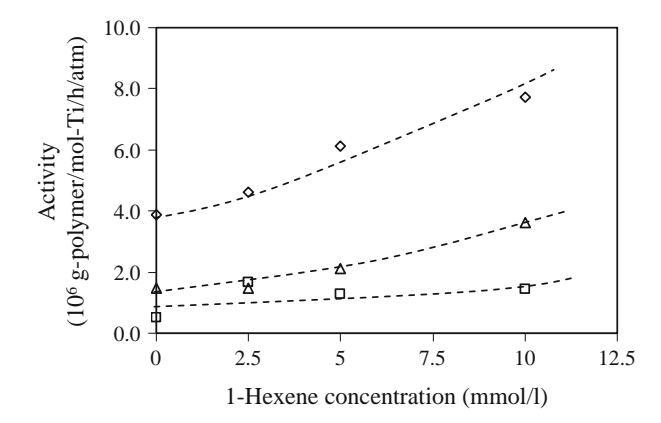


**Fig. 4** Relationship between the 1-hexene concentration and catalytic activity. The copolymerization was conducted at 60 °C for 1 h under 0.5 MPa of ethylene. 10 mmol/L of TEA was used as the cocatalyst (open diamond Ti4M, open circle Ti3M, and open square Ti2M)

**Table 2** Sequence distribution of ethylene/1-hexene copolymers synthesized using  $TiCl_x/MgCl_2$  catalysts (x = 2-4) at different 1-hexene concentrations

Catalyst	1-Hexene injected (vol%)	EHE	ЕНН	ННН	HEH	EEH	EEE	1-Hexene incorporated (mol%)
Ti2M	2.5	0.2	0.0	0.0	0.0	0.4	99.4	0.20
	5.0	0.2	0.0	0.0	0.0	0.5	99.3	0.24
	10	0.4	0.0	0.0	0.0	0.8	98.8	0.42
Ti3M	2.5	0.3	0.0	0.0	0.0	0.6	99.1	0.32
	5.0	0.4	0.0	0.0	0.0	0.7	98.9	0.37
	10	0.5	0.0	0.0	0.0	1.0	98.5	0.52
Ti4M	2.5	0.3	0.0	0.0	0.0	0.6	99.1	0.30
	5.0	0.6	0.0	0.0	0.0	1.2	98.2	0.58
	10	0.6	0.0	0.0	0.0	1.1	98.4	0.55

Polymerization conditions: catalyst amount = 3.5 mg/L, temperature = 60 °C, polymerization time = 1 h, ethylene pressure = 0.5 MPa, 1-hexene concentration = 2.5-10 vol%, TEA concentration = 10 mmol/L

the 1-hexene concentration, and above which the incorporation efficiency discontinuously increases and then becomes stable. This might be related to some discontinuous change in the monomer diffusivity, in lowering the crystallinity by incorporation of 1-hexene. It is notable that a higher oxidation sate led to higher incorporation efficiency, even with the similar response to the 1-hexene concentration. The molecular weights and their distributions of copolymers synthesized with the three catalysts are summarized in Table 3. Ti2M produced a copolymer with the broadest MWD as compared with those obtained by Ti3M and Ti4M. The broadness of MWD for Ti2M arose mainly from the formation of a high-molecular weight tail, as indicated in the highest  $M_w$ . The lowest incorporation of 1-hexene and the highest molecular weight partly agrees with the previous proposal by Kissin



Catalyst	$M_n \times 10^{-5}$	$M_w \times 10^{-5}$	$M_w/M_n$				
Ti2M	3.6	14	4.0				
Ti3M	3.2	12	3.7				
Ti4M	3.7	12	3.2				

**Table 3** Molecular weight and their distribution of copolymers synthesized using  $TiCl_x/MgCl_2$  catalysts (x = 2-4)

Polymerization conditions: catalyst amount = 3.5 mg/L, temperature = 60 °C, polymerization time = 1 h, ethylene pressure = 0.5 MPa, 1-hexene concentration = 10 vol%, TEA concentration = 10 mmol/L

et al. [20]. However, it should be stressed that the obtained copolymers had roughly similar characteristics in CC and MW, in agreement with the results by Zakharov et al. [5, 6].

### Conclusion

We have investigated the influences of the oxidation state on ethylene homo- and co-polymerization using MgCl<sub>2</sub>-based Ziegler–Natta catalysts made directly from TiCl<sub>4</sub>, TiCl<sub>3</sub>, and TiCl<sub>2</sub> precursors. The Ti oxidation state had large effects on the catalytic activity in both of ethylene homo- and co-polymerization with 1-hexene. Especially, TiCl<sub>2</sub>/MgCl<sub>2</sub> had a unique response that was very different from TiCl<sub>4</sub>/MgCl<sub>2</sub> and TiCl<sub>3</sub>/MgCl<sub>2</sub> upon varying the Al concentration and 1-hexene concentration. All the copolymers produced by the catalysts had similar sequence distribution, even though the increase of the oxidation state caused a slight enhancement of 1-hexene incorporation. Similarly, molecular weights and their distributions of the copolymers were not largely dependent on the Ti oxidation state. It is worth noting that these results are in accordance with those from Zakharov et al. [5, 6] even through the catalyst precursors to obtain the different oxidation states of Ti were different. Thus, it was concluded that the oxidation state was not important for the copolymer characteristics, while it played a major role in the catalytic activity.

**Acknowledgments** The authors thank the Thailand Research Fund (TRF), Office of the Higher Education Commission (CHE), and PTT Company for the financial support of this project.

### References

- Lynch DT, Jejelowo MO, Wanke SE (1991) The influence of aluminum alkyls on the polymerization of ethylene with silica/magnesium chloride-supported titanium tetrachloride catalysts. Can J Chem Eng 69:657–664
- Piotr S (1989) The role of magnesium chloride as supporter for the new generation of olefin polymerization catalysts. Polym Plast Tech Eng 28:493–510
- Chadwick JC, Miedema A, Ruisch BJ, Sudmeijer O (1992) Effects of procatalyst composition on the stereospecificity of a Ziegler–Natta catalyst system. Makromol Chem 193:1463–1468
- Echevskaya LG, Matsko MA, Mikenas TB, Nikitin VE, Zakharov VA (2006) Supported titanium-magnesium catalysts with different titanium content: kinetic peculiarities at ethylene homopoly-merization and copolymerization and molecular weight characteristics of polyethylene. J of Appl Polym Sci 102:5436–5442



- Tregubov AA, Zakharov VA, Mikenas TB (2009) Supported titanium-magnesium catalysts for ethylene polymerization: a comparative study of catalysts containing isolated and clustered titanium ions in different oxidation states. J Polym Sci Part A Polym Chem 47:6362–6372
- Mikenas TB, Tregubov AA, Zakharov VA, Echevskaya LG, Matsko MA (2008) Titanium-magnesium catalysts for olefin polymerization—effect of titanium oxidation state on catalyst performance. Polimery 53:353–357
- Potapov AG, Kriventsov VV, Kochubey DI, Bukatov GD, Zakharov VA (1997) EXAFS study of supported TiCl4/MgCl2 catalyst. Macromol Chem Phy 198:3477–3484
- Czaja K, Bialek M (2000) Effect of hydrogen on the ethylene polymerization process over Ziegler– Natta catalysts supported on MgCl2(THF)2 I studies of the chain-transfer reaction. J of Appl Polym Sci 79:356–360
- Giuliano C, Giampiero M, Anteo P (2001) Polypropene product innovation by reactor granule technology. Macromol Symp 173:195–209
- Wada T, Taniike T, Kouzai I, Takahashi S, Terano M (2009) Propylene polymerization performance of isolated and aggregated Ti species studied using a well-designed TiCl3/MgCl2 Ziegler–Natta model catalyst. Macromol Rapid Commun 30:887–891
- Mori H, Hasebe K, Terano M (1998) Variation in oxidation state of titanium species on MgCl2supported Ziegler catalyst and its correlation with kinetic behavior for propylene polymerization. Polymer 40:1389–1394
- Taniike T, Terano M (2008) Reductive formation of isospecific Ti dinuclear species on a MgCl<sub>2</sub> (110) surface in heterogeneous Ziegler–Natta catalysts. Macromol Rapid Commun 29:1472–1476
- Baulin AA, Novikova EI, Mal'kova GYa, Maksimov VL, Vyshinskaya LI, Ivanchev SS (1980) Correlation between the reduction of titanium in supported Ziegler catalysts and their activity in the polymerization of ethylene. Vysokomol Soed A 22:181–188
- Soga K, Chen SI, Ohnishi R (1982) Correlation between the oxidation states of titanium and the polymerization activities for higher α-olefins and diene compounds. Polym Bull 8:473–478
- Soga K, Shiono T, Doi Y (1983) Titanium (IV) chloride/magnesium chloride catalytic systems. Polym Bull 10:168–174
- Soga K, Uozumi T, Park JR (1990) Effect of catalyst isospecificity on olefin copolymerization. Makromol Chem 191:2853–2864
- Kashiwa N, Yoshitake J (1984) The influence of the valence state of titanium in magnesium chloridesupported titanium catalysts on olefin polymerization. Makromol Chem 185:1133–1138
- Kashiwa N, Yoshitake J, Tsutsui T (1987) Polymerization of styrene with a highly active magnesium dichloride supported titanium tetrachloride catalyst system. Polym Commun 28:292–296
- Kojoh SI, Kioka M, Kashiwa N (1999) The influences of cocatalyst on propylene polymerization at high temperature with MgCl<sub>2</sub>-supported TiCl<sub>4</sub> catalyst system. Eur Polym J 35:751–755
- Kissin YV, Mirabella FM, Meverden CC (2005) Multi-center nature of heterogeneous Ziegler–Natta catalysts: TREF confirmation. J Polym Sci Part A Polym Chem 43:4351–4362
- Ludlum DB, Anderson AW, Ashby CE (1958) Polymerization of ethylene by lower-valent compounds of titanium. J Amer Chem Soci 80:1380–1384
- Mobarakeh HS, Monfared MF, Vakili M (2006) Gas phase copolymerization of ethylene and 1-butene with prepolymerized MgCl2 supported Ziegler–Natta catalyst: effect of Al/Ti ratio. Iranian Polym J 15:569–575
- Benning CJ, Wszolek WR, Werber FX (1968) Crystalline titanium dichloride. Active catalyst in ethylene polymerization. II. Polymer structure, polymerization variables, and scope. J Polym Sci Part A-1 Polym Chem 6:755–762
- Skalli MK, Markovits A, Minot C, Belmajdoub A (2001) A theoretical investigation of the role of AlR<sub>3</sub> as cocatalyst. Catal Lett 76:1–2
- Fregonese D, Mortara S, Bresadola S (2001) Ziegler–Natta MgCl<sub>2</sub>-supported catalysts: relationship between titanium oxidation states distribution and activity in olefin polymerization. J Molecular Catal A Chem 172:89–95
- Ono Y, Keii T (1966) Electron spin resonance studies on Ziegler–Natta type catalyst systems.
   J Polym Sci Part A-1Polym Chem 4:2441–2446
- Ko YS, Han TK, Sadatoshi H, Woo SI (1998) Analysis of microstructure of ethylene–1-hexene copolymer prepared over thermally pretreated MgCl<sub>2</sub>/THF/TiCl<sub>4</sub> bimetallic catalyst. J Polym Sci Part A Polym Chem 36:291–300



- Kim I, Kim JH, Choi HK, Chung MC, Woo SI (1993) Comonomer enhancement effect of 1-hexene in ethylene copolymerization catalyzed over MgCl<sub>2</sub>/THF/TiCl<sub>4</sub> catalysts. J Appl Polym Sci Part A Polym Chem 48:721–730
- 29. Chien JCW, Nozaki T (1993) Ethylene/hexene copolymerization by heterogeneous and homogeneous Ziegler–Natta catalysts, and the comonomer effect. J Polym Sci 31:227–237
- Floyd S, Choi KY, Taylor TW, Ray WH (1986) Polymerization of olefins through heterogeneous catalysis. III. Polymer particle modelling with an analysis of intraparticle heat and mass transfer effects. J Appl Polym Sci 32:2935–2960





# JOURNAL OF NATURAL GAS CHEMISTRY 天然气化学

Editors-in-Chief:

Xinhe BAO Alexis T. BELL

Vol.20 No.5 Sep. 2011



### **CONTENTS**

### Communication

457 Effective modification of MgO with surface transition metal oxides for NF<sub>3</sub> decomposition

Yanan Wang, Xiufeng Xu, Pei Sheng, Hongguang Li, Tingting Wang, Youfen Huang, Fangshu Liu

### Articles

460 Preparation of activated carbons and their adsorption properties for greenhouse gases:  $CH_4$  and  $CO_2$ 

Hao Yang, Maochu Gong, Yaoqiang Chen

465 Carbon dioxide reforming of methane over Ni/Mo/SBA-15-La<sub>2</sub>O<sub>3</sub> catalyst: Its characterization and catalytic performance

Jian Huang, Renxiong Ma, Tao Huang, Anrong Zhang, Wei Huang

471 Comparison of three methods for natural gas dehydration

Michal Netusil, Pavel Ditl

477 Effect of iridium loading on HZSM-5 for isomerization of *n*-heptane

Herma Dina Setiabudi, Sugeng Triwahyono, Aishah Abdul Jalil, Nur Hidayatul Nazirah Kamarudin, Muhammad Arif Ab Aziz

483 Tuning surface active oxygen of lanthanum oxide via partial dissolution and regrowth of crystallites

Zhiming Gao, Huili Li

487 Ni/MgO catalyst prepared using atmospheric highfrequency discharge plasma for CO<sub>2</sub> reforming of methane

Pan Qin, Huiyuan Xu, Huali Long, Yi Ran, Shuyong Shang, Yongxiang Yin, Xiaoyan Dai

493 Efficient oxidative degradation of 2-chlorophenol and 4-chlorophenol over supported CuO-based catalysts

Jingjing Li, Yang Hu, Wenhui Lü, Lei Shi, Qi Sun, Yonggang Zhou, Jianfeng Xu, Jian Wang, Bizhong Shen

498 Influence of MgO contents on silica supported nanosize gold catalyst for carbon monoxide total oxidation Huiyuan Xu, Weiyi Li, Shuyong Shang, Chunrong Yan

503 Effect of heat transfer on the oscillatory behavior in partial oxidation of methane over nickel catalyst

Xiubin Ren, Xiangyun Guo

507 Quantitative interpretation to the chain mechanism of free radical reactions in cyclohexane pyrolysis

Yingxian Zhao, Bo Shen, Feng Wei

515 Gas sensing performance of polyaniline/ZnO organicinorganic hybrids for detecting VOCs at low temperature

Jing Huang, Taili Yang, Yanfei Kang, Yao Wang, Shurong Wang

520 Catalytic performance of Fe modified K/Mo<sub>2</sub>C catalyst for CO hydrogenation

Minglin Xiang, Dudu Wu, Juan Zou, Debao Li, Yuhan Sun, Xichun She

525 Correlation between hydrocarbon distribution and water-hydrocarbon ratio in Fischer-Tropsch synthesis

Xiaofeng Zhou, Qingling Chen, Yuewu Tao, Huixin Weng

531 *P-T* stability conditions of methane hydrate in sediment from South China Sea

Shicai Sun, Yuguang Ye, Changling Liu, Fengkui Xiang, Yan Ma

537 Preparation, characterization and catalytic behavior of Pt-Cu nanoparticles in methane combustion

Florica Papa, Catalin Negrila, Gianina Dobrescu, Akane Miyazaki, Ioan Balint

543 CF<sub>4</sub> decomposition without water over a solid ternary mixture consisting of NaF, silicon and one metal oxide

Xiufeng Xu, Xianjun Niu, Jie Fan, Yanan Wang, Ming Feng

547 Methane dehydro-aromatization over Mo/HZSM-5 catalysts in the absence of oxygen: Effect of steam-treatment on catalyst stability

Tingting Zhao, Hongxia Wang

553 Effects of preparation methods on the performance of Cu-Mo-Fe-O<sub>x</sub> in the hydrogen production from water Si Chen, Wei Chu, Xu Liu, Dongge Tong

558 Ti-Si composite oxide-supported cobalt catalysts for CO<sub>2</sub> hydrogenation

Jakrapan Janlamool, Piyasan Praserthdam, Bunjerd Jongsomjit

www.jngc.org www.elsevier.com/locate/jngc

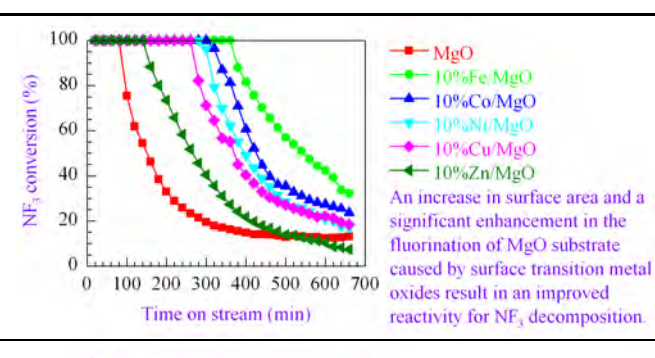
### **CONTENTS**

### Communication

457

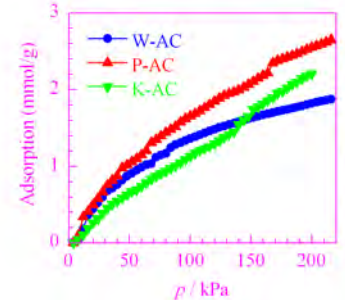
Effective modification of MgO with surface transition metal oxides for  $NF_3$  decomposition

Yanan Wang, Xiufeng Xu, Pei Sheng, Hongguang Li, Tingting Wang, Youfen Huang, Fangshu Liu



460

Preparation of activated carbons and their adsorption properties for greenhouse gases: CH<sub>4</sub> and CO<sub>2</sub>



The adsorption capacities of all activated carbons increased rapidly with the change of pressure at 25 ℃ and could be affected by activated condition sharply. The samples have enormous CO₂ adsorption capacities.

Hao Yang, Maochu Gong, Yaoqiang Chen

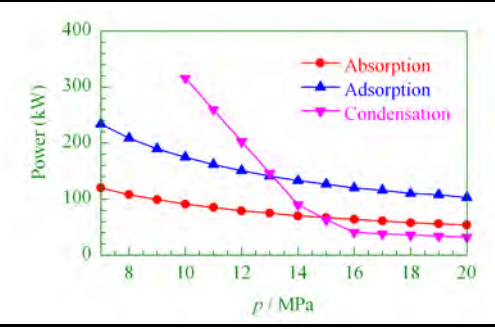
465

Carbon dioxide reforming of methane over Ni/Mo/SBA-15-La<sub>2</sub>O<sub>3</sub> catalyst: Its characterization and catalytic performance

Jian Huang, Renxiong Ma, Tao Huang, Anrong Zhang, Wei Huang

471

Comparison of three methods for natural gas dehydration

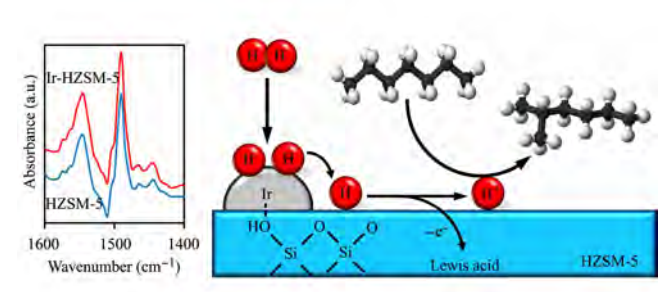


Michal Netusil, Pavel Ditl

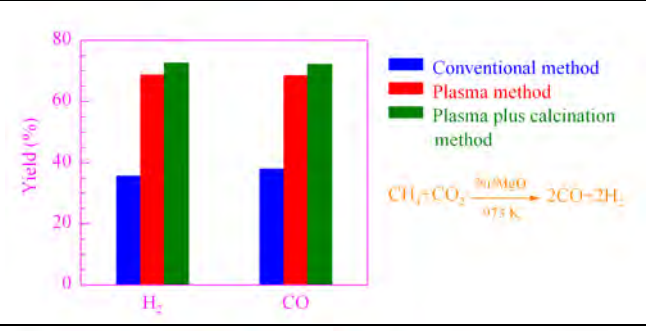
477

Effect of iridium loading on HZSM-5 for isomerization of *n*-heptane

Herma Dina Setiabudi, Sugeng Triwahyono, Aishah Abdul Jalil, Nur Hidayatul Nazirah Kamarudin, Muhammad Arif Ab Aziz



# 483 Tuning surface active oxygen of lanthanum oxide via partial dissolution and regrowth of crystallites Zhiming Gao, Huili Li 487 Ni/MgO catalyst prepared using atmospheric high-frequency discharge plasma for CO<sub>2</sub> reforming of methane Pan Qin, Huiyuan Xu, Huali Long, Yi Ran, Shuyong Shang, Yongxiang Yin, Xiaoyan Dai 493



Temperature (°C)

TPR profiles show that

the procedure of partial dissolution and regrowth of crystallites can make La<sub>2</sub>O<sub>3</sub> have an increased

amount of surface active oxygen species.

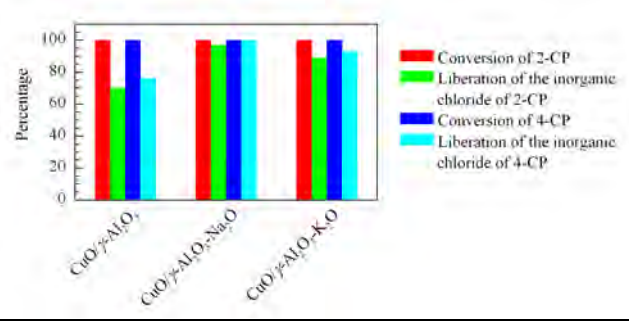
(4)

(2)

200

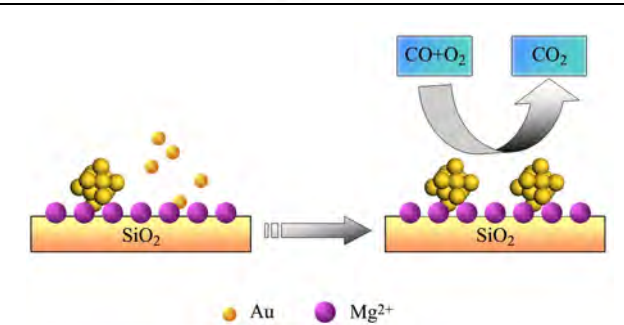
TCD signal (a.u.)

Efficient oxidative degradation of 2-chlorophenol and 4-chlorophenol over supported CuO-based catalysts



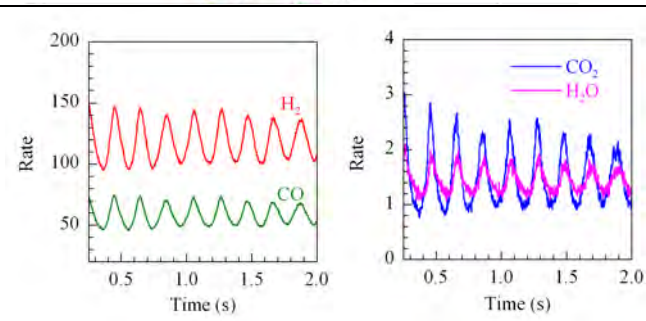
Jingjing Li, Yang Hu, Wenhui Lü, Lei Shi, Qi Sun, Yonggang Zhou, Jianfeng Xu, Jian Wang, Bizhong Shen

498
Influence of MgO contents on silica supported nanosize gold catalyst for carbon monoxide total oxidation



Huiyuan Xu, Weiyi Li, Shuyong Shang, Chunrong Yan

Effect of heat transfer on the oscillatory behavior in partial oxidation of methane over nickel catalyst



Xiubin Ren, Xiangyun Guo

### 507 Dehydrogenation Quantitative interpretation to the chain mechanism Ring opening -→ β-cracking of free radical reactions in cyclohexane pyrolysis H-abstraction lectron shifting B-cracking Initiation Propagation Yingxian Zhao, Bo Shen, Feng Wei Reaction chain of cyclohexane pyrolysis 515 18 1.2 0.05 vol% ethanol Methanol Gas sensing performance of polyaniline/ZnO organic-15 1.0 - Ethanol inorganic hybrids for detecting VOCs at low temper-Gas out - Acetone Voltage (V) 0.8 12 ature 0.6 0.4 0.2 Jing Huang, Taili Yang, Yanfei Kang, Yao Wang, 20 30 40 0 200 400 600 Shurong Wang PANI mass percentage (wt%) Time (s) 520 Catalytic performance of Fe modified K/Mo<sub>2</sub>C cata-K/Fe-Mo,C lyst for CO hydrogenation CO conversion Alcohol selectivity Methanol selectivity Methane selectivity K/Mo2C Minglin Xiang, Dudu Wu, Juan Zou, Debao Li, 40 100 Conversion or selectivity (%) Yuhan Sun, Xichun She 525 Tailed gas -Correlation between hydrocarbon distribution and water-hydrocarbon ratio in Fischer-Tropsch synthe-C5+ liquid Cold trap hydrocarbons Fischer-Tropsch Hot trap synthesis Xiaofeng Zhou, Qingling Chen, Yuewu Tao, Water Huixin Weng 531 25 Sediment from South China Sea P-T stability conditions of methane hydrate in sedi-Seawater from South China Sea The stability conditions ment from South China Sea of methane hydrate in Pressure (MPa) seafloor water and H+V+Lv 15 sediment from South

H+Lw

283

285

287

Temperature (K)

281

China Sea are depressed relative to the pure water

system.

V+Lw

291

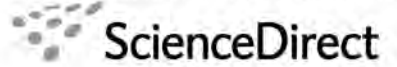
289

Shicai Sun, Yuguang Ye, Changling Liu, Fengkui Xiang, Yan Ma

537 100 Preparation, characterization and catalytic behavior CH, conversion (%) 80 Pt of Pt-Cu nanoparticles in methane combustion CuO<sub>x</sub> Al<sub>2</sub>O<sub>3</sub> 60 40 Pt 20 Al<sub>2</sub>O<sub>3</sub> Florica Papa, Catalin Negrila, Gianina Dobrescu, 350 400 450 500 550 600 Akane Miyazaki, Ioan Balint Temperature (°C) 543 100 NaF:Si:MgO= CF<sub>4</sub> decomposition without water over a solid ternary 10:30:60 21:26:53 mixture consisting of NaF, silicon and one metal oxide CF, conversion (%) -25:50:25 60 -33:34:33 40 A solid mixture of NaF-Si-MgO can effectively destruct CF4 20 without water, and the reagent with NaF/Si/MgO molar ratio of 33/34/33 exhibited a high 20 40 60 80 100 120 Xiufeng Xu, Xianjun Niu, Jie Fan, Yanan Wang, reactivity at 850 °C Time on stream (min) Ming Feng 547 Mo/HZSM-5 The smaller the Methane dehydro-aromatization over Mo/HZSM-5  $k_{\rm d}$  gets, the more catalysts in the absence of oxygen: Effect of steam $k_0 \times 10^5 (s^{-1})$ stable catalyst is. treatment on catalyst stability [Mo/HZSM-5]-813K-1h 0.0 0.5 1.0 1,5 2.0 Tingting Zhao, Hongxia Wang The number of B1 acid sites/unit cell 553 Effects of preparation methods on the performance of Cu-Mo-Fe-O<sub>x</sub> in the hydrogen production from water Fe<sub>2</sub>O<sub>3</sub> Si Chen, Wei Chu, Xu Liu, Dongge Tong 558 Role of Ti: (i) Facilitate the reduction of Co<sub>v</sub>O<sub>v</sub> (TPR) Ti-Si composite oxide-supported cobalt catalysts for (ii) Prevent the formation of silicate compounds (XPS) CO<sub>2</sub> hydrogenation (iii) Inhibit the RWGS reaction (CO2 hydrogenation) [CoTiMCM] [Co<sub>x</sub>O<sub>y</sub>/TiMCM] Jakrapan Janlamool, Piyasan Praserthdam, Bun-MCM-41 Co,O,

jerd Jongsomjit







Journal of Natural Gas Chemistry 20(2011)558-564

### Ti-Si composite oxide-supported cobalt catalysts for CO<sub>2</sub> hydrogenation

### Jakrapan Janlamool, Piyasan Praserthdam, Bunjerd Jongsomjit\*

Center of Excellence on Catalysis and Catalytic Reaction Engineering, Department of Chemical Engineering, Faculty of Engineering, Chulalongkorn University, Bangkok 10330, Thailand

[ Manuscript received January 26, 2011; revised May 27, 2011 ]

### **Abstract**

In the present work, different silica-based supported cobalt (Co) catalysts were synthesized and used for  $CO_2$  hydrogenation for methanation. Different supports, such as SSP, MCM-41, TiSSP and TiMCM were used to prepare Co catalysts with 20 wt% Co loading. The supports and catalysts were characterized by means of  $N_2$  physisorption, XRD, SEM/EDX, XPS, TPR and CO chemisorption. It is found that after calcination of catalysts, Ti is present in the form of anatase. The introduction of Ti plays important roles in the properties of Co catalysts by: (i) facilitating the reduction of Co oxides species which are strongly interacted with support, (ii) preventing the formation of silicate compounds, and (iii) inhibiting the RWGS reaction. Based on  $CO_2$  hydrogenation, the CoTiMCM catalyst exhibites the highest activity and stability.

### Key words

CO<sub>2</sub> hydrogenation; titania-silica; cobalt catalysts; methanation

### 1. Introduction

Recently, global warming, which is caused by CO<sub>2</sub> emission into the atmosphere, has become a serious problem all over the world. Among various types of methods for recovering, chemical fixation of emitted CO<sub>2</sub> is also expected to help the conservation of fossil fuels. Hydrogenation of CO<sub>2</sub> to methane is important for the purification of ammonia feedstocks, methanation of coal-derived gases and the production of process heat from reusable waste streams containing carbon dioxide [1]. Development of catalysts for CO and CO2 hydrogenation is the key technology of gas to liquid (GTL) process. The catalytic hydrogenation of carbon monoxide and carbon dioxide produces a large variety of products ranging from methane and methanol to higher molecular weight alkanes, alkenes and alcohols [2-5]. The methanation of CO<sub>2</sub> is reported to proceed with a lower activated energy than the methanation of CO [6]. The lower exothermicity of the overall reaction of CO<sub>2</sub> as compared with CO makes temperature control in a catalytic reactor easier as shown in Equations (1) and (2) [7].

$$3H_2 + CO \rightarrow H_2O + CH_4$$
  $\Delta H = -206.0 \text{ kJ/mol}$  (1)

$$4H_2 + CO_2 \rightarrow 2H_2O + CH_4$$
  $\Delta H = -164.9 \text{ kJ/mol}$  (2)

Transition metal oxides are generally regarded as good Furthermore, Weatherbee and hydrogenation catalysts. Bartholomew [8] studied the specific activities of various Group VIII metals catalysts supported on SiO2 on the methanation of CO<sub>2</sub> at 177-377 °C and 140-1030 kPa and they found that the activities decreased in order of Co>Ru>Ni>Fe. The Co and Ni-based catalysts were preferred because they required considerably milder operating pressures (about 1 atm) than the high pressure for Fe catalyst [9]. Supported cobalt catalysts were the preferred catalysts for CO<sub>2</sub> hydrogenation because of lower cost compared with Ru [10]. Moreover, the catalytic activity of metal towards carbon deposition was found to decrease in order of Ni>Co>Fe [11,12]. Previous researches revealed that supports, such as Al<sub>2</sub>O<sub>3</sub>, SiO<sub>2</sub>, ZrO<sub>2</sub>, TiO<sub>2</sub> and CeO<sub>2</sub> can efficiently affect activities and selectivities of cobalt catalysts for CO and CO<sub>2</sub> hydrogenation [13–16]. Recently, Ti-Si composite represents a novel class of materials that was attractively used as catalysts and supports for a wide variety of catalytic reactions. It was reported that the photocatalytic activity of Ti-Si is 3-fold

<sup>\*</sup> Corresponding author. Tel: +66-662-2186869; Fax: +66-662-2186877; E-mail: bunjerd.j@chula.ac.th

This work was supported by the Thailand Research Fund (TRF) and Office of the Higher Education Commission (CHE), the National Research Council of Thailand (NRCT), and NRU-CU (AM1088A).

higher than that of the corresponding TiO<sub>2</sub> [17–19]. Furthermore, heterogeneous catalysts such as SiO<sub>2</sub>-supported TiO<sub>2</sub> and Ti-Si composite are known to be effective for selective oxidation reaction [20]. The Ti-Si composite supports exhibit novel properties that are not found in single oxide supports. In addition, mesoporous SiO<sub>2</sub>, such as MCM-41 and hexagonal mesoporous silica (HMS), exhibits sufficiently large surface area, high thermal stability, excellent mechanical strength and uniform pore sizes [21]. Ti-Si composite is generally synthesized through flame hydrolysis [22], impregnation [23], coprecipitation [24] and sol-gel [25] methods by adding titanium precursor into silica framework. The titanium distribution in Ti-Si composite depends on the method of preparation [26]. The sol-gel hydrolysis is widely used because of its capability in controlling the textural and surface properties of the mixed oxides [21].

The present research focused on the application of Ti-Si composite used as support for cobalt catalysts. First, the mesoporous silicas, such as spherical silica particle (SSP) and MCM-41 were prepared. Then, titanium isopropoxide was introduced into the silica framework by hydrolysis to obtain Ti-Si composite. The cobalt catalysts were prepared by direct impregnation of cobalt precursor into different supports. The characteristics and catalytic behaviors via CO<sub>2</sub> hydrogenation were investigated and further discussed in more detail.

### 2. Experimental

### 2.1. Materials

Chemicals as follows were used: titanium isopropoxide (TiPOT, 97%, Aldrich), tetraethyl othosilicate (TEOS, 98%, Aldrich), ammonia (30%, Panreac), ethanol (99.99%, J. T. Baker), cetyltrimethylammonium bromide (CTAB, Aldrich), isopropanol (QReC), cobalt (II) nitrate hexahydrate (Co(NO<sub>3</sub>)<sub>2</sub>·6H<sub>2</sub>O, 98%, Aldrich).

### 2.2. Support and cobalt catalyst preparation

The mesoporous silica supports were synthesized by sol-gel method. The composition of the synthesized gel was as follows: molar ratio of 1 TEOS: 0.3 CTAB: 11 NH<sub>3</sub>: x ethanol: 144 H<sub>2</sub>O. Molar ratio of ethanol addition was adopted 0 for MCM-41 and 58 for SSP, respectively [27]. The mixture was further stirred for 2 h at room temperature. White precipitate was then collected by filtration and washed with deionized water. The dried sample was calcined at 550 °C for 6 h with a heating rate of 10 °C/min in air.

The desired amount of titanium isopropoxide (ca. 25 wt% of Ti) was dissolved in isopropanol (1:3 w/w). SSP or MCM-41 was then added into the mixed solution and stirred for 1 h. Hydrolysis was performed by addition of ammonia ( $H_2O$ : TiPOT = 4:1). The sol was further stirred for 20 h at room temperature. Then, the sample was dried at 110 °C for 24 h. Finally, the sample was calcined at 850 °C for 2 h in a muffle furnace.

The cobalt catalysts loading 20 wt% Co were prepared by incipient wetness impregnation using aqueous solution of cobalt (II) nitrate hexahydrate [Co(NO<sub>3</sub>)<sub>2</sub>·6H<sub>2</sub>O]. The catalysts were dried at 110  $^{\circ}$ C for 12 h, and then calcined in air at 500  $^{\circ}$ C for 4 h.

Nomenclature of samples were given as follows: SSP and MCM referred to spherical silica and MCM-41, respectively. Furthermore, TiSSP and TiMCM referred to titania spherical-silica composite and titania-MCM-41 composite, respectively. For catalysts samples, CoX referred to cobalt catalyst supported on the X support as mentioned above.

### 2.3. Catalysts characterization

Various supports and cobalt catalysts were characterized by several techniques as follows:

 $N_2$  physisorption:  $N_2$  physisorption ( $N_2$  adsorption at  $-196\,^{\circ}\text{C}$  in a Micromeritics ASPS 2020) was performed to determine surface areas of various supports and cobalt catalysts.

X-ray diffraction (XRD): XRD was used to determine the phase composition of different supports and catalysts using SIEMENS D 5000 X-ray diffractometer with Cu  $K_{\alpha}$  radiation with Ni filter in the  $2\theta$  range of  $20^{\rm o}-80^{\rm o}$  with resolution of  $0.04^{\rm o}$ .

Temperature-programmed reduction (TPR): TPR was used to determine the reducibility and reduction temperature of cobalt catalysts. Approximately, 0.05 g catalyst sample was used in the operation and temperature ramped from 35 °C to 800 °C at 10 °C/min. The carrier gas was 10%  $H_2$  in Ar. A thermal conductivity detector (TCD) was used to measure the amount of hydrogen consumption. The calibration of hydrogen consumption was performed with bulk cobalt oxide (Co<sub>3</sub>O<sub>4</sub>) under the same condition.

CO chemisorption: Static CO chemisorption at room temperature on the reduced catalysts was used to determine the number of reducible surface cobalt metal atoms. CO chemisorption was carried out following the procedure using a Micrometritics Pulse Chemisorb 2750 instrument. Prior to chemisorption, the catalysts were reduced at 350 °C for 3 h after ramping up at a rate of 10 °C/min. After that, 30  $\mu$ L CO was injected into catalyst bed and repeated until the desorption peaks were constant at room temperature. Amounts of CO adsorption on catalysts are proportional to the number of active sites.

Scanning electron microscopy (SEM) and dispersive X-ray spectroscopy (EDX): SEM (JEOL mode JSM-5800LV) and EDX (Link Isis Series 300) were used to determine the morphology and elemental distribution of the catalyst particles. The particle sizes and cobalt distributions of catalyst samples were observed using JEOL-JEM 200CX transmission electron microscope operated at 100 kV.

X-ray photoelectron spectroscopy (XPS): XPS analysis was performed originally using an AMICUS spectrometer equipped with a Mg  $K_{\alpha}$  X-ray radiation. For a typical analysis, the source was operated at a voltage of 15 kV and a current

of 12 mA. The pressure in the analysis chamber was less than  $10^{-5}$  Pa.

### 2.4. Reaction test

 $CO_2$  hydrogenation was performed to determine the overall activity and selectivity of the catalysts. Typically, 0.1 g catalyst was packed in a fixed-bed microreactor. The catalyst sample was reduced in situ in flowing  $H_2$  (50 mL/min) at 350 °C for 3 h. After reduction, a flow rate of Ar = 8 mL/min and  $H_2$  (including 8.8%  $CO_2$ ) = 22 mL/min was fed into the reactor. The  $CO_2$  hydrogenation was carried out at 220 °C at 1 atm. The product gas samples were taken in 1 h interval and analyzed by gas chromatography. The steady state was reached within 6 h.

### 3. Results and discussion

### 3.1. Characteristics

The surface areas of the different supports and catalysts are shown in Table 1. The surface areas of the mesoporous silicas (SSP and MCM-41) were remarkably large as expected. However, with the addition of Ti into the silica framework, it was found that the surface areas of Ti-Si composites (TiSSP and TiMCM) were much lower than that of the corresponding mesoporous silica. As seen, the surface areas of TiSSP and TiMCM which were calcined at 850 °C, were dramatically low ca. 385 and 137 m<sup>2</sup>/g, respectively. This can be attributed to the distribution of Ti in the silica framework. The surface areas of cobalt catalysts deposited on SSP and MCM-41 were much smaller than those of their supports, whereas CoTiSSP and CoTiMCM only had slight effect. This can be attributed to the larger pore sizes of CoSSP and CoMCM. The phase identification was carried out on the basis of data obtained from XRD. The XRD patterns for all support samples are shown in Figure 1. As seen, SSP and MCM-41 exhibited broad peak at 20°-30° indicating amorphous silica. The Ti-Si composites of TiSSP and TiMCM showed that titania was present in the anatase form  $(2\theta \text{ of } 25^{\circ}, 38^{\circ}, 48^{\circ}, 54^{\circ}, 55^{\circ} \text{ and } 75^{\circ})$ . The XRD patterns of the calcined Co catalysts are shown in Figure 2. All catalyst samples exhibited almost identical XRD patterns of  $Co_3O_4$  at  $31^{\circ}$ ,  $37^{\circ}$ ,  $45^{\circ}$ ,  $59^{\circ}$  and  $65^{\circ}$  [28]. It can be

Table 1. BET surface areas, pore volumes and pore diameters of supports and cobalt catalysts

Samples	$A_{\rm BET}~({\rm m^2/g})$	$V_{\rm p}~({\rm cm}^3/{\rm g})$	$D_{ m BJH}/ m nm$
SSP	927	0.8135	2.04
MCM	1187	1.0287	2.13
TiSSP	385	0.1587	3.23
TiMCM	137	0.1371	4.57
CoSSP	637	0.4898	2.26
CoMCM	583	0.2134	2.58
CoTiSSP	380	0.2117	2.82
CoTiMCM	126	0.1004	4.24

observed that the XRD peaks of anatase  $TiO_2$  at  $2\theta$  of  $25.3^{\circ}$  were less apparent due to the strong intensity of  $Co_3O_4$  peaks, which disturbed the observation of anatase peaks.

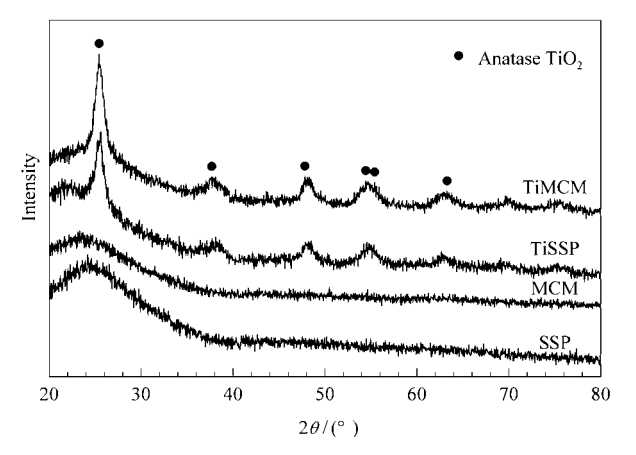


Figure 1. XRD patterns of different supports

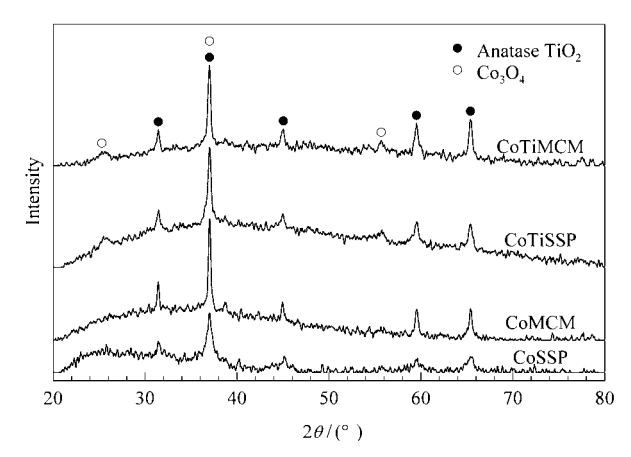


Figure 2. XRD patterns of different cobalt catalysts

TPR was performed in order to determine the reduction behaviors. The TPR profiles of all catalysts are shown in Figure 3. The reduction temperatures for all calcined catalysts were located between ca. 200 to 600  $^{\circ}$ C. One broad reduction peak with shoulder was observed for all catalysts. This can be generally assigned to the overlap of two reduction steps of  $Co_3O_4$  to CoO and then to  $Co^0$ . The two reaction steps (Equations (3) and (4)) may be whether or not observed depended upon the TPR conditions, such as ramping rate of temperature, feed gas flow rate and amount of samples.

$$H_2 + Co_3O_4 \rightarrow H_2O + 3CoO \tag{3}$$

$$3H_2 + 3CoO \rightarrow 3H_2O + 3Co$$
 (4)

The reduction temperature and reducibility results are summarized in Table 2. The reduction temperatures of CoSSP and CoMCM were located at ca. 210–330 °C and 210–360 °C, respectively. For CoTiSSP and CoTiMCM, the reduction temperatures were shifted to broad ranges (220–610 °C for CoTiSSP and 220–600 °C for CoTiMCM),

indicating the existence of larger number of reduced cobalt atoms. The higher reduction temperature represented the cobalt oxide species strongly interacted with the supports, which are reducible. Therefore, the addition of Ti into the silica framework apparently facilitated the reduction of cobalt strongly interacted with the support. Without introduction of Ti, the higher reduction peak was absent as seen for CoSSP and CoMCM samples. The strong interaction between cobalt and supports was reported following the order of Al<sub>2</sub>O<sub>3</sub>>TiO<sub>2</sub>>SiO<sub>2</sub> [29]. In addition, the reducibility of Co-TiSSP and CoTiMCM catalysts was higher than that of CoSSP and CoMCM catalysts due to the reduction of strongly interacted cobalt oxide species as mentioned earlier. It was also reported that using TiPOT for the preparation of Ti-Si composite also resulted in increased reducibility of nickel catalysts [26].

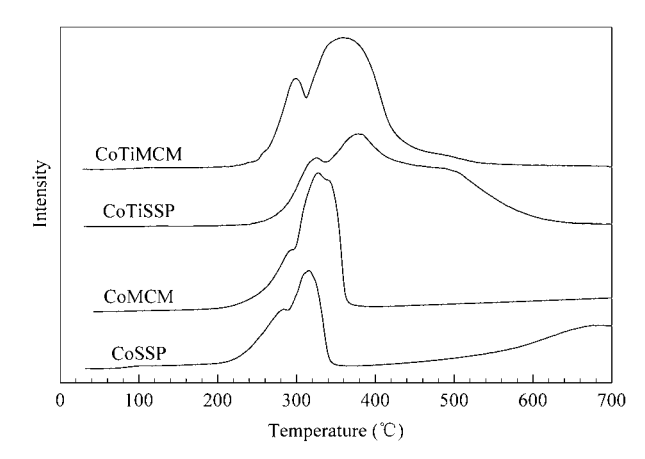


Figure 3. TPR profiles of different cobalt catalysts

Table 2. Maximum temperatures, reducibility from TPR profiles and Co dispersion of cobalt catalysts

Catalysts	Reduction temperature (°C)	Reducibility (%) <sup>a</sup>	Total CO chemisorption ( $\mu mol_{CO}/g_{cat}$ )	Dispersion of cobalt (%) <sup>b</sup>
CoSSP	210-330	30.3	28	0.84
CoMCM	210-360	21.2	37	1.10
CoTiSSP	220-610	45.4	21	0.61
CoTiMCM	220-600	45.5	19	0.56

<sup>&</sup>lt;sup>a</sup> Determined by TPR analysis; <sup>b</sup> Determined by CO chemisorption

CO chemisorption was conducted on samples reduced in hydrogen flow at 350 °C for 3 h. The amounts of carbon monoxide adsorbed on the catalysts were determined in order to obtain the number of reducible cobalt metal atoms. The adsorbed amounts of CO were directly proportional to the amounts of active sites. The amounts of CO adsorbed on the catalytic phase were ranged from 19 to 37  $\mu$ mol<sub>CO</sub>/g<sub>cat</sub> as shown in Table 2. It can be observed that in this case, the TPR and CO chemisorption results did not relate with each other due to different conditions applied. The CO chemisorption results showed that the number of reducible cobalt metal atoms slightly decreased with the addition of titania into the support. This was in accordance with the decreased number of cobalt atoms with increasing the amounts of titania in the mixed oxide supports [30]. Furthermore, the acidic property of titania-silica was quite different from that of either pure titania or pure silica, since pure titania only possesses Lewis acidity while silica has neither Brönsted nor Lewis acidity. However, new Brönsted acid sites are created when titania and silica form Ti-O-Si chemical bonds [31-33]. One possible reason for the lower CO chemisorption amounts of CoTiSSP and CoTiMCM can be explained that the electron donor additives like alkali metals enhance chemisorption, while electron acceptors inhibit chemisorption [34–36]. It should be noted that the results of CO chemisorption were different from those of TPR due to differences in measurement conditions for both techniques.

SEM and EDX were also conducted in order to study the morphologies and elemental distributions of the catalysts, respectively. The typical external surface granules and EDX mappings of the calcined cobalt catalysts are shown in Fig-

ure 4. It can be observed that the cobalt oxide species exhibited good distribution. The white spots on the external surfaces represent high concentrations of Co. The EDX analysis is not a bulk technique, but rather a surface analytical tool based on the fact that it gives information down to a depth of approximately 1  $\mu$ m from the surface that makes the information obtained from EDX comparable to atomic absorption [37]. Table 3 summarizes the element quantities of cobalt catalysts based on EDX and XPS analyses. It should be mentioned that EDX only measures the concentrations in a layer less than 1  $\mu$ m from the surface. The EDX results revealed that Ti loadings were 17.4 wt% and 23.1 wt% for CoTiSSP and CoTiMCM, respectively. In addition, Co loadings for all catalysts were ranged from 22.1 wt% and 30.8 wt%. The element compositions of surface and subsurface layers (depth of XPS analysis is about ten angstroms) indicated that the amounts of Ti were 42.6 wt% and 30.6 wt% for CoTiSSP and CoTiMCM, respectively. The amounts of Ti from XPS analysis were larger than those obtained from EDX analysis. This was due to the titania accumulation on the external surface of silica supports. Moreover, the amounts of Co for CoMCM, CoTiSSP and CoTiMCM from XPS analysis were distinctly larger than those from EDX analysis, indicating that most cobalt oxides distributed on the external surface. In contrast, the amount of Co for CoSSP from XPS measurement was remarkably smaller than that obtained from the EDX analysis, confirming that most cobalt oxides dispersed in the bulk of silica particles.

Besides the determination of surface concentration, XPS is one of the most powerful techniques used to identify the binding energy (BE) of elements. According to the BE results

obtained from XPS as shown in Table 3, it can be observed that the Co 2p core level spectra of  $\text{Co}_3\text{O}_4$  were present at the BE of  $780-782\,\text{eV}$  and  $795-796\,\text{eV}$  for  $2p_{3/2}$  and  $2p_{1/2}$ , respectively for all the catalyst samples. These values were in agreement with the reported work [38]. On the other hand, there was no change in BE for Co 2p core level with the addition of Ti. However, CoSSP and CoMCM exhibited the BE at 95.1 eV and 94.6 eV for former,  $104.2\,\text{eV}$  and  $103.5\,\text{eV}$  for latter. In fact, the BE at 95.1 eV and 94.6 eV were assigned to the formation of silicate compounds as reported by Wagner et al. [39] and Arnby et al. [40]. Previous reports

suggested that the formation of surface cobalt silicates during preliminary steps of catalyst preparation or even during reduction, was considered as a reason for partial reduction of the total cobalt presenting at the temperatures normally above 500 °C [41]. However, the presence of Ti in CoTiSSP and CoTiMCM apparently resulted in the absence of BE for silicate compound. These results were in accordance with those obtained from TPR.

TEM micrographs for all the catalysts are shown in Figure 5. The dark spots represented cobalt oxide patches dispersing on the supports after calcinating the catalysts.

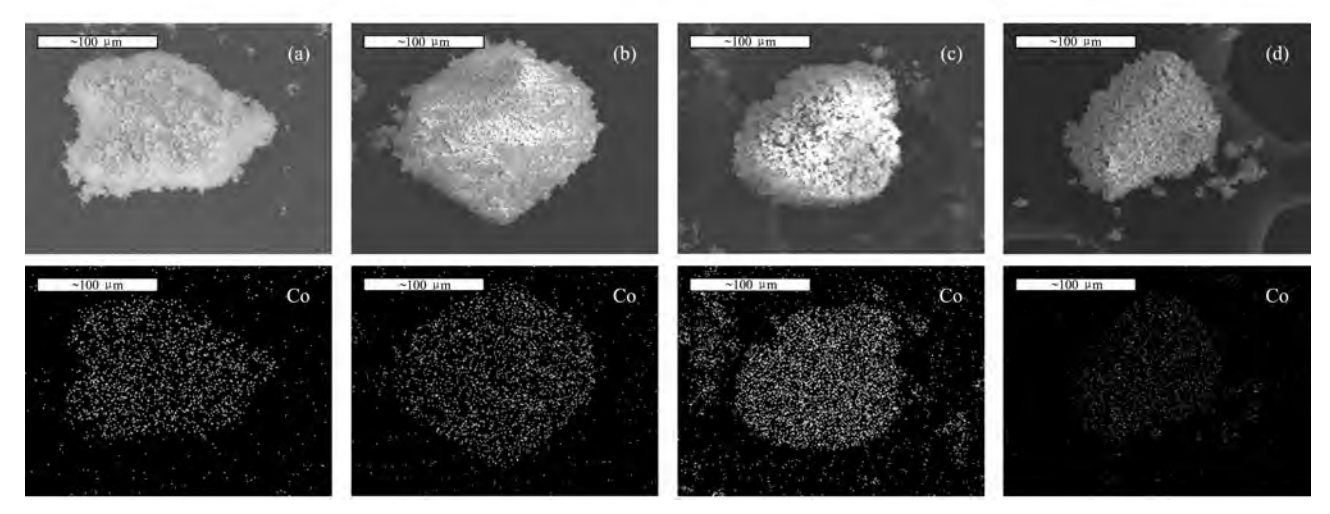


Figure 4. SEM micrographs and EDX mappings of cobalt catalysts. (a) CoSSP, (b) CoMCM, (c) CoTiSSP, (d) CoTiMCM

Amount of elements in bulk (wt%)b Binding energy (eV) Amount of elements on surface (wt%)<sup>a</sup> Catalysts Si 2pTi 2pCo 2pSi Si 90.7 75.5 CoSSP 95.1 781.0 9.3 24.3 104.2 795.8 CoMCM 94.6 780.2 59.8 40.2 69.6 30.4 103.5 795.3 CoTiSSP 17.4 103.7 460.1 781.0 19.8 42.6 37.6 60.5 22.1 465.7 796.6 CoTiMCM 103.4 459.7 780.4 34.0 30.6 35.4 46.1 23.1 30.8 465.6 795.4

Table 3. XPS data and EDX analysis of cobalt catalysts

Figure 5 (a) and (c) shows that the cobalt oxide species exhibited good distribution in CoSSP and CoTiSSP catalysts, respectively. Figure 5 (b) reveals that cobalt oxide species were agglomerated in CoMCM catalyst. In contrast, Figure 5 (d) displays the cobalt oxide species having good distribution in CoTiMCM catalyst. TEM micrographs demonstrated that the titania particles on the MCM-41 can improve the dispersion of cobalt oxide. This phenomenon was also observed with the presence of Ti in Ni catalyst [26].

### 3.2. Reaction study

 $CO_2$  hydrogenation over different cobalt catalysts at  $220\,^{\circ}C$  under methanation condition was investigated. The

reaction results are summarized in Table 4. Methane was a major product for all catalyst samples. It was found that the CoTiMCM sample exhibited the highest activity among all the samples. The selectivity to CO also decreased with the addition of Ti into MCM-41 due to the increased acidity by increasing the amount of Ti in the supports [26]. This is in agreement with the increased amount of absorbed CO<sub>2</sub> by increasing the basicity of the alkali metal oxides, which might be related to the influence on the local electron density of neighboring metal species [7]. In addition, the stability of catalyst was found to increase with the addition of Ti when compared the conversion of initial and steady states. The obtained products for methane and CO indicate that CO<sub>2</sub> hydrogenation over these catalysts occurred via a consecutive mechanism as

<sup>&</sup>lt;sup>a</sup> Determined by XPS analysis; <sup>b</sup> Determined by EDX analysis

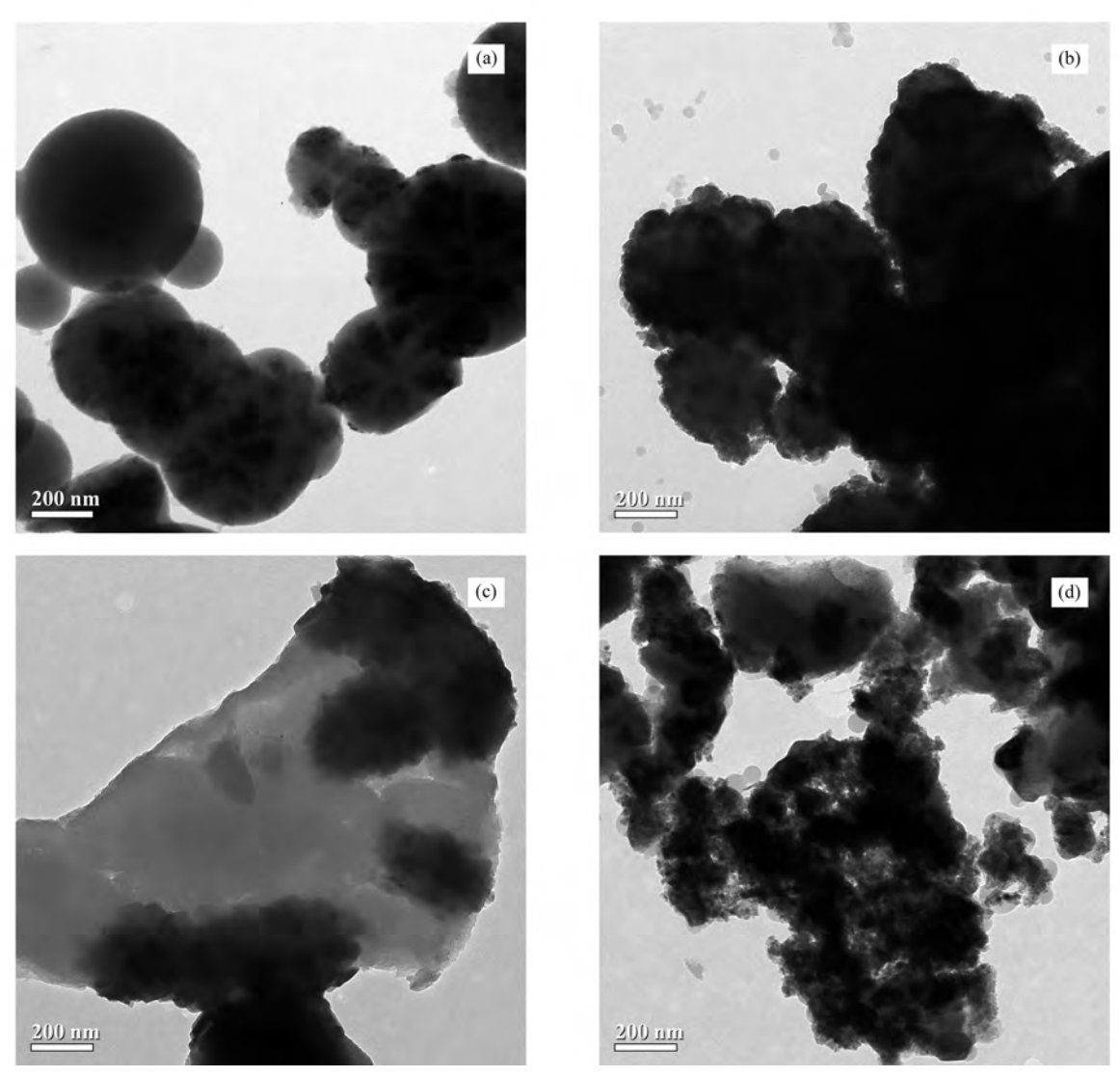


Figure 5. TEM micrographs of cobalt catalysts. (a) CoSSP, (b) CoMCM, (c) CoTiSSP, (d) CoTiMCM

shown in Equations (5) and (6). CO<sub>2</sub> is first converted to CO by reverse water gas-shift (RWGS) reaction, and then CO was hydrogenated to methane.

$$H_2 + CO_2 \rightarrow H_2O + CO \tag{5}$$

$$3H_2 + CO \rightarrow H_2O + CH_4 \tag{6}$$

For CO<sub>2</sub> hydrogenation, the operating temperature must

be rather high because of the equilibrium constraint for the reverse CO shift reaction, which limits the application of temperature in the low range for Fischer-Tropsch conversion [7]. In this study, the activities of cobalt catalysts were not related to the cobalt dispersion based on CO chemisorption. This was in accordance with the methanation turnover rate in Fischer-Tropsch synthesis which was also independent of cobalt dispersion on supported catalysts and surface orientation on Co single crystals [42].

Table 4. Activity and product selectivity of cobalt catalysts

Reaction	Catalyata	Conversion <sup>a</sup>		Rate <sup>c</sup>	Product sele	ctivity (%) <sup>c</sup>
temperature (°C)	Catalysts	initial <sup>b</sup>	steady state <sup>c</sup>	$(\times 10^2 \text{ g}_{\text{CH}_2} \cdot \text{g}_{\text{cat}}^{-1} \cdot \text{h}^{-1})$	CH <sub>4</sub>	CO
	CoSSP	38	27	16.5	89.5	10.5
220	CoMCM	35	28	18.1	91.4	8.6
	CoTiSSP	17	16	10.0	92.1	7.9
	CoTiMCM	35	34	22.3	94.9	5.1

<sup>&</sup>lt;sup>a</sup> CO<sub>2</sub> hydrogenation was carried out at 1 atm, and molar ratio of H<sub>2</sub>/CO<sub>2</sub>/Ar = 20/2/8, F/W = 18 L·g<sub>cat</sub><sup>-1</sup>·h<sup>-1</sup>; <sup>b</sup> After running the reaction for 5 min; <sup>c</sup> After running the reaction for 6 h

<sup>&</sup>lt;sup>c</sup> After running the reaction for 6 h

### 4. Conclusions

In summary, the addition of Ti into SSP and MCM-41 can alter the characteristics and catalytic properties of CoTiSSP and CoTiMCM catalysts. It is found that the presence of Ti can facilitate the reduction of cobalt oxide species which are strongly interacted with the support, resulting in the appearance of high temperature reduction peak. Based on XPS analysis, it is observed that the formed silicate is disappeared with the presence of Ti. It is worth noting that CoTiMCM catalyst exhibits the highest activity for CO<sub>2</sub> hydrogenation due to increased reducibility. The addition of Ti also inhibits the RWGS, leading to a decrease in the selectivity to CO.

### Acknowledgements

The authors thank the Thailand Research Fund (TRF) and Office of the Higher Education Commission (CHE), the National Research Council of Thailand (NRCT), and NRU-CU (AM1088A) for the financial support of this project.

### References

- [1] Weatherbee G D, Bartholomew C H. *J Catal*, 1982, 77(2): 460
- [2] Somorjai G A. Introduction to Surface Chemistry and Catalysis. New York: Wiley, 1994
- [3] Dry M E. Appl Catal A, 1996, 138(2): 319
- [4] Adesina A A. Appl Catal A, 1996, 138(2): 345
- [5] Iglesia E. Appl Catal A, 1997, 161(2): 59
- [6] Peebles D E, Goodman D W, White J M. J Phys Chem, 1983, 87(22): 4378
- [7] Riedel T, Claeys M, Schulz H, Schaub G, Nam S S, Jun K W, Choi M J, Kishan G, Lee K W. Appl Catal A, 1999, 186(1-2): 201
- [8] Weatherbee G D. Bartholomew C H. J Catal, 1984, 87(2): 352
- [9] Anderson R B. The Fischer-Tropsch Synthesis. New York: Academic Press, 1984
- [10] Jongsomjit B, Panpranot J, Goodwin J G. J Catal, 2001, 204(1): 98
- [11] Khavrus' V A, Lemesh N V, Gordeichuk S V, Tripol'skii A I, Ivashchenko T S, Strizhak P E. Theor Exp Chem, 2006, 42(4): 234
- [12] Khavrus V O, Lemesh N V, Gordijchuk S V, Tripolsky A I, Ivashchenko T S, Biliy M M, Strizhak P E. React Kinet Catal Lett, 2008, 93(2): 295
- [13] Guerrero-Ruiz A; Rodríguez-Ramos I. *React Kinet Catal Lett*, 1985, 29(1): 93
- [14] Suo Z H, Kou Y, Niu J Z, Zhang W Z, Wang H L. *Appl Catal A*, 1997, 148(2): 301

- [15] Storsaeter S, Totdal B, Walmsley J C, Tanem B S, Holmen A. J Catal, 2005, 236(1): 139
- [16] Zhao Z K, Yung M M, Ozkan U S. Catal Commun, 2008, 9(6): 1465
- [17] Anderson C, Bard A J. J Phys Chem, 1995, 99(24): 9882
- [18] Ruetten S A, Thomas J K. Photochem Photobiol Sci, 2003, 2(10): 1018
- [19] Hu C, Wang Y Z, Tang H X. Appl Catal B, 2001, 30(3-4): 277
- [20] Liu Z F, Crumbaugh G M, Davis R J. J Catal, 1996, 159(1): 83
- [21] Gao X T, Wachs I E. Catal Today, 1999, 51(2): 233
- [22] Schultz P C. J Am Ceram Soc, 1976, 59(5-6): 214
- [23] Yoshida S, Takenaka S, Tanaka T, Hirano H, Hayashi H. Stud Sur Sci Catal, 1996, 101: 871
- [24] Itoh M, Hattori H, Tanabe K. J Catal, 1974, 35(2): 225.
- [25] Ohno T, Tagawa S, Itoh H, Suzuki H, Matsuda T. Mater Chem Phys, 2009, 113(1): 119
- [26] Grzechowiak J R, Szyszka I, Masalska A. Catal Today, 2008, 137(2-4): 433
- [27] Liu S Q, Cool P, Collart O, Van Der Voort P, Vansant E F, Lebedev O I, Van Tendeloo G, Jiang M H. *J Phys Chem B*, 2003, 107(38): 10405
- [28] Rojanapipatkul S, Jongsomjit B. Catal Commun, 2008, 10(2): 232
- [29] Jacobs G, Das T K, Zhang Y Q, Li J L, Racoillet G, Davis B H. Appl Catal A, 2002, 233(1-2): 263
- [30] Jongsomjit B, Wongsalee T, Praserthdam P. Mater Chem Phys, 2006, 97(2-3): 343
- [31] Liu Z F, Tabora J, Davis R J. J Catal, 1994, 149(1): 117
- [32] Molnar A, Bartok M, Schneider M, Baiker A. Catal Lett, 1997, 43(1-2): 123
- [33] Doolin P K, Alerasool S, Zalewski D J, Hoffman J F. Catal Lett, 1994, 25(3-4): 209
- [34] Rhodin T N, Brucker C F. Solid State Commun, 1977, 23(5):
- [35] Queau R, Labroue D, Poilblanc R. J Catal, 1981, 69(2): 249
- [36] Benziger J, Madix R J. Surf Sci, 1980, 94(1): 119
- [37] Durán J D G, Guindo M C, Delgado A V, González-Caballero F. *J Colloid Interface Sci*, 1997, 193(2): 223
- [38] Morales F, de Groot F M F, Gijzeman O L J, Mens A, Stephan O, Weckhuysen B M. J Catal, 2005, 230(2): 301
- [39] Wagner C D, Naumkin A V, Kraut-Vass A, Allison J W, Powell C J, Rumble J R. NIST X-ray Photoelectron Spectroscopy Database, Version 3.4, 2004
- [40] Arnby K, Rahmani M, Sanati M, Cruise N, Carlsson A A, Skoglundh M. Appl Catal B, 2004, 54(1): 1
- [41] van Steen E, Sewell G S, Makhothe R A, Micklethwaite C, Manstein H, de Lange M, O'Connor C T. J Catal, 1996, 162(2): 220
- [42] Johnson B G, Bartholomew C H, Goodman D W. J Catal, 1991, 128(1): 231

Provided for non-commercial research and education use. Not for reproduction, distribution or commercial use.



This article appeared in a journal published by Elsevier. The attached copy is furnished to the author for internal non-commercial research and education use, including for instruction at the authors institution and sharing with colleagues.

Other uses, including reproduction and distribution, or selling or licensing copies, or posting to personal, institutional or third party websites are prohibited.

In most cases authors are permitted to post their version of the article (e.g. in Word or Tex form) to their personal website or institutional repository. Authors requiring further information regarding Elsevier's archiving and manuscript policies are encouraged to visit:

http://www.elsevier.com/copyright

## **Author's personal copy**

Journal of Industrial and Engineering Chemistry 18 (2012) 373-377



Contents lists available at SciVerse ScienceDirect

## Journal of Industrial and Engineering Chemistry

journal homepage: www.elsevier.com/locate/jiec



## LLDPE synthesis via SiO<sub>2</sub>-Ga-supported zirconocene/MMAO catalyst

Mingkwan Wannaborworn, Piyasan Praserthdam, Bunjerd Jongsomjit\*

Center of Excellence on Catalysis and Catalytic Reaction Engineering, Department of Chemical Engineering, Faculty of Engineering, Chulalongkorn University, Bangkok 10330, Thailand

#### ARTICLE INFO

Article history:
Received 28 October 2010
Accepted 13 April 2011
Available online 10 November 2011

Keywords: Polymer synthesis Molecular engineering Metallocene Copolymer LLDPE

#### ABSTRACT

In this present study, the linear low-density polyethylene (LLDPE) was synthesized via ethylene/1-octene copolymerization with the zirconocene/MMAO catalyst by *in situ* impregnation of different silica (SiO<sub>2</sub>) supports. The SiO<sub>2</sub> supports used were small-pored (SP) and large-pored (LP) sizes with and without Ga modification. It was found that the SP-SiO<sub>2</sub> support exhibited higher polymerization activity ( $\sim$ 1.5 times) than that obtained from the LP-SiO<sub>2</sub> one. This can be attributed to the lower amount of MMAO being present inside the SP-SiO<sub>2</sub> support resulting in higher content of MMAO at the external surface. The higher activity in ethylene/1-octene copolymerization was also found with the supported catalyst having Ga modification onto both SP-and LP-SiO<sub>2</sub> supports. The results demonstrated that the introduction of Ga may improve ability of supports to immobilize metallocene catalyst. Based on  $^{13}$ C NMR measurement, it indicated that all synthesized polymers were typical LLDPE having random distribution of comonomer.

© 2011 The Korean Society of Industrial and Engineering Chemistry. Published by Elsevier B.V. All rights reserved.

#### 1. Introduction

The linear low-density polyethylene (LLDPE) is very attractive polymer because of its excellent mechanical property, high thermal stability and good resistance for chemicals. Therefore, it has been widely used for various applications, especially in film and packaging industries. LLDPE is the copolymer synthesized from copolymerization of ethylene and 1-olefin [1-4]. For commercial production, it is usually produced with a catalytic system, such as Ziegler-Natta, metallocene, and metal-oxide catalysts [5]. However, the use of metallocene catalyst together with methylaluminoxane (MAO) as cocatalyst have been found to be very effective to produce polymer with high catalytic activity and give narrow molecular weight distribution. Moreover, synthesis of copolymer by using solid support as carrier has been proven to solve some disadvantages of homogeneous catalyst [6,7], including reactor fouling, low bulk density of polymer, and unable to polymerize in slurry and gas polymerization process. The most widely used supports in metallocene system are inorganic materials including silica [8,9], alumina [10], titania [11], MCM-41 [12] and zirconia [13].

In this work, we used silica with different pore sizes as a support due to the fact that pore sizes may have effects on copolymerization activity and incorporation of olefin comonomer. We also extended this study into the influence of support acidity according to Rahiala et al. [12]. They demonstrated that the use of acidic Al seems advantageous to formation of active centers resulting in high activity compared with unmodified support. Hence, the improvement of acidic material is considered as an interesting path for better heterogeneous system. Experimentally, the copolymerization of ethylene/1-octene with rac-Et[Ind]<sub>2</sub>ZrCl<sub>2</sub>/MMAO system via *in situ* impregnation over different pore sizes of silica support was performed to produce LLDPE. The Ga modification onto the support was conducted in order to increase acidity. At the end, effects of SiO<sub>2</sub> pore size and Ga modification on properties of the LLDPE produced are elucidated by means of density and <sup>13</sup>C NMR measurements.

#### 2. Experimental

#### 2.1. Materials

All chemicals and polymerization were manipulated under an argon atmosphere, using a glove box and/or Schlenk techniques. Toluene was dried over dehydrated CaCl<sub>2</sub> and distilled over sodium/benzophenone before use. The *rac*-ethylenebis (indenyl) zirconium dichloride (*rac*-Et[Ind]<sub>2</sub>ZrCl<sub>2</sub>) was supplied from Aldrich Chemical Company, Inc. Modified methylaluminoxane (MMAO) in hexane was donated by Tosoh (Akso, Japan). Trialkylaluminum (TMA, 2 M in toluene) was supplied by Nippon Aluminum Alkyls, Ltd., Japan. Ultrahigh purity argon was further purified by passing it through columns that were packed with BASF catalyst R3-11G (molecular-sieved to 3 Å), sodium hydroxide (NaOH), and phosphorus pentaoxide (P<sub>2</sub>O<sub>5</sub>) to remove traces of oxygen and

<sup>\*</sup> Corresponding author. Tel.: +66 2 2186869; fax: +66 2 2186877. E-mail address: bunjerd.j@chula.ac.th (B. Jongsomjit).

374

moisture. Ethylene gas (99.96% pure) was donated by the National Petrochemical Co., Ltd., Thailand. 1-Octene (d = 0.715) was purchased from Aldrich Chemical Company, Inc.

#### 2.1.1. Preparation of Ga-modified silica support

The Ga modification on the silica supports was prepared by the incipient-wetness impregnation method according to the procedure described previously [11]. The Ga source in this case was Ga(NO<sub>3</sub>). Ga was impregnated onto different pore-sized silica gels having 1.0 wt.% of Ga. The support was dried in oven at 383 K for 12 h, and then heated in vacuum at 673 K for 2 h.

#### 2.2. Polymerization procedure

0.2 g of the support obtained above was allowed to contact with 1.14 ml of MMAO ([Al]<sub>MMAO</sub>/[Zr]<sub>cat</sub> = 1135) for 30 min, in reactor with magnetic stirring. After this period of time, the suspension was undergone the clarified liquid test to confirm that all MMAO was immobilized on the support. About 1 ml of the clarified liquid was injected into the polymerization reactor, where the desired amount of zirconocene was already present. If any noticeable amount of polymer was formed, it means that this clarified liquid still contains MMAO. Therefore, the fixation of cocatalyst onto support was not complete. To ensure that MMAO was completely impregnated onto support, the MMAO/support ratio was then decreased until no polymer was formed [14]. After this test, the suspension was mixed with desired amount of rac- $Et[Ind]_2ZrCl_2$  and TMA ([Al]<sub>TMA</sub>/[Zr]<sub>cat</sub> = 2500). In fact, the high ratio of [Al]<sub>TMA</sub>/[Zr]<sub>cat</sub> was employed as a scavenger due to the ethylene fed was obtained from the plant containing some impurities. From an industrial point of view, it is preferable to use TEA or TIBA in place of TMA. Then, toluene (to make a total volume of 30 ml) was introduced into the reactor. The reactor was frozen in liquid nitrogen to stop reaction, and then 0.018 mol of 1-octene was injected into the reactor. The reactor was evacuated to remove argon. Then, it was heated up to polymerization temperature (343 K) and the polymerization was started by feeding ethylene gas (total pressure 50 psi in the reactor) until the consumption of ethylene at 0.018 mol was reached (6 psi was observed from the pressure gauge). The reaction of polymerization was completely terminated by addition of acidic methanol. The reaction time was recorded for purpose of calculating the activity. The precipitated polymer was washed with methanol and dried at room temperature prior to characterization.

#### 2.3. Supports characterization

#### 2.3.1. X-ray diffraction (XRD)

XRD was performed to determine the bulk crystalline phases of sample. It was conducted using a SIEMENS D-5000 X-ray diffractometer with  $\text{CuK}_{\alpha}$  ( $\lambda$  = 1.54439  $\times$  10 $^{-10}$  m). The spectra were scanned at a rate 2.4 degree/min in the range of  $2\theta$  = 20–80 degrees.

#### 2.3.2. N<sub>2</sub> physisorption

Measurement of BET surface area, average pore diameter and pore size distribution of silica support were determined by  $N_2$  physisorption using a Micromeritics ASAP 2000 automated system.

#### 2.3.3. Scanning electron microscopy (SEM)

Scanning electron microscopy was used to determine the morphologies and elemental distribution throughout the sample granules, respectively. The SEM of JEOL mode JSM-6400 was applied.

#### 2.3.4. NH<sub>3</sub>-temperature programmed desorption (TPD)

Temperature programmed desorption (TPD) of  $NH_3$  was performed in a Micromeritic ChemiSorb 2750 automated system attached with ChemiSoft TPx software. The amount of  $NH_3$  adsorbed on the surface was determined by temperature programmed desorption.

#### 2.4. Polymer characterization

#### 2.4.1. <sup>13</sup>C NMR spectroscopy

<sup>13</sup>C NMR spectroscopy was used to determine the 1-octene incorporation and copolymer microstructure. Chemical shifts were referenced internally to the CDCl<sub>3</sub> and calculated according to the method described by Randall [15]. Each sample solution was prepared by dissolving 50 mg of copolymer in 1,2,4-trichlorobenzene and CDCl<sub>3</sub>. <sup>13</sup>C NMR spectra were taken at 373 K using a BRUKER AVANCE II 400 operating at 100 MHz with an acquisition time of 1.5 s and a delay time of 4 s.

#### 2.4.2. Scanning electron microscopy (SEM)

SEM was performed to study morphologies of polymer produced. The same equipment as mentioned above was employed.

#### 2.4.3. Densimeter

Polymer density was measured with an electronic densimeter (Mirage SD-120L) in the temperature range 298–313 K.

#### 3. Results and discussion

In our research, we synthesized LLDPEs over inorganic materials with different pore-sized silica, where the large pored-silica denoted as  $SiO_2$  (LP) and the small pored-silica denoted as  $SiO_2$  (SP). In addition, we modified silica with 1.0 wt% of Ga to increase acidity of support. The XRD patterns (not shown) exhibit only a broad peak between  $ca~20^\circ$  and  $30^\circ$  for both  $SiO_2$  (LP)

 Table 1

 BET surface area and pore diameter of Ga-modified silica supports.

Support	BET surface area (m <sup>2</sup> /g)	Pore diameter (Å)
SiO <sub>2</sub> (LP)	71	146
SiO <sub>2</sub> (LP)-Ga-1.0%	69	148
SiO <sub>2</sub> (SP)	217	138
SiO <sub>2</sub> (SP)-Ga-1.0%	170	138

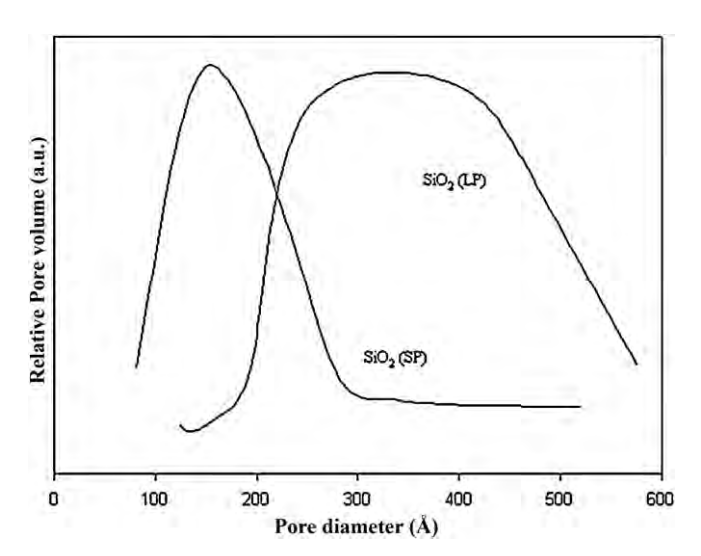
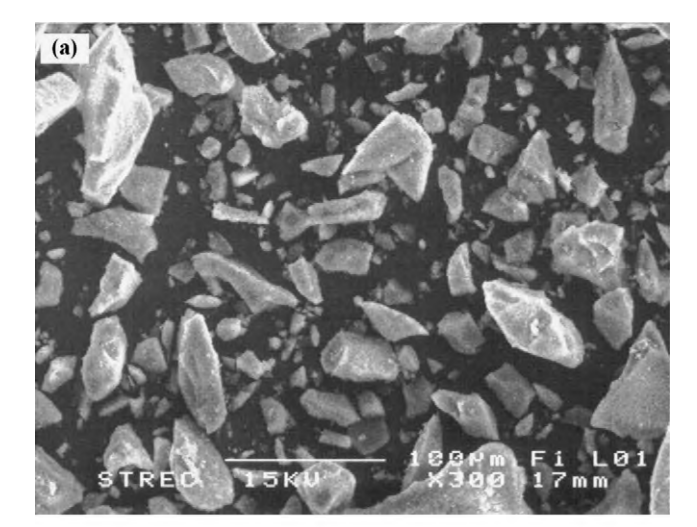


Fig. 1. Pore size distribution of different SiO<sub>2</sub>-based supports.

M. Wannaborworn et al./Journal of Industrial and Engineering Chemistry 18 (2012) 373-377



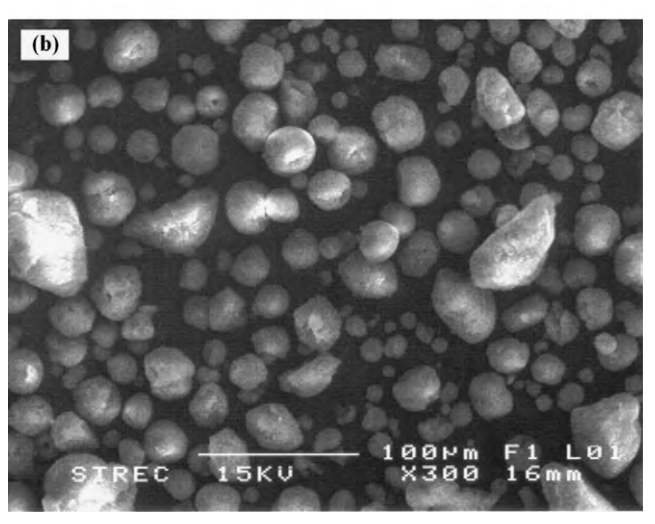


Fig. 2. SEM micrograph of Ga-modified silica (LP) and silica (SP) supports; (top) SiO<sub>2</sub> (LP), (bottom) SiO<sub>2</sub> (SP).

and  $SiO_2$  (SP) supports. As very well-known, the broad peak is due to scattering from non-crystalline area of silica. However, it does not show the Ga peak because only small amount of Ga was introduced onto the support. Moreover, Ga present on  $SiO_2$  was in the highly dispersed form.

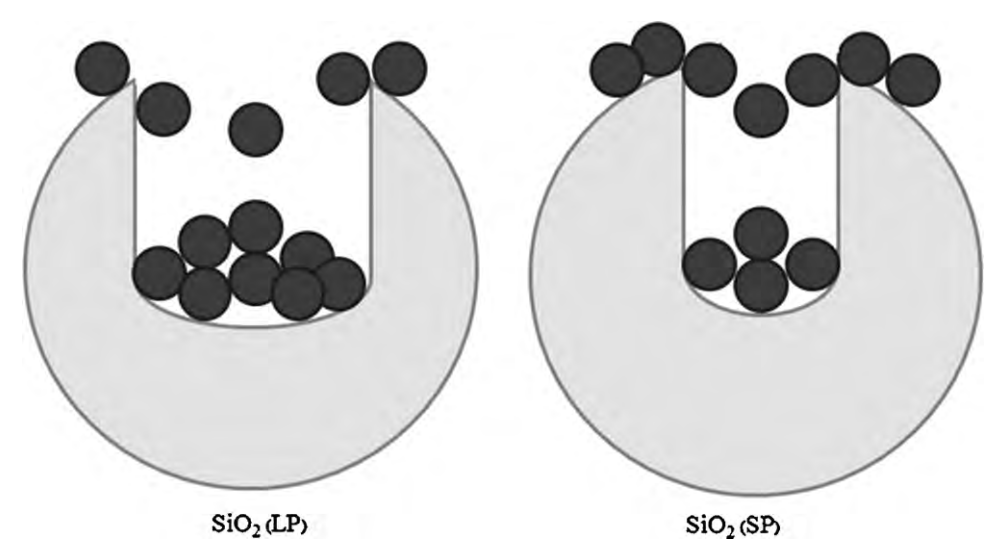


Samples	Polymerization yield <sup>a</sup> (g)	Polymerization times (s)	Catalytic activity <sup>b</sup> (kg of pol/mol Zr h)
Homogeneous	1.534	123	29,803
SiO <sub>2</sub> (LP)	1.495	88	40,405
SiO <sub>2</sub> (LP)-Ga-1.0%	1.756	76	55,329
SiO <sub>2</sub> (SP)	1.798	80	53,411
SiO <sub>2</sub> (SP)-Ga-1.0%	2.036	74	66,214

<sup>&</sup>lt;sup>a</sup> The polymer yield was fixed [limited by ethylene fed and 1-octene used (0.018 mole equally)].

The BET surface areas determined by  $N_2$  physisorption of supports are shown in Table 1. It indicates that  $SiO_2$  (SP) exhibits higher surface area than  $SiO_2$  (LP). It is also found that the addition of Ga leads to a slight decrease in the surface area for  $SiO_2$  (LP), but a remarkable decrease for the  $SiO_2$  (SP) due to the pore blockage with Ga. As seen in Fig. 1, it can be observed that the  $SiO_2$  (LP) support exhibits the large pore size distribution while the  $SiO_2$  (SP) support shows the small pore having narrow size distribution. SEM was used to determine particle morphology. The SEM micrographs of  $SiO_2$  (LP) and  $SiO_2$  (SP) supports are shown in Fig. 2. It can be observed that  $SiO_2$  (LP) has jagged shape, whereas the  $SiO_2$  (SP) has the shape of spheroid.

Table 2 displays the ethylene/1-octene copolymerization activity and activity of homogeneous system for comparison. It was found that the heterogeneous system exhibited higher catalytic activity than the homogeneous one. Based on the work done by Jungling et al. [16], a good bulk density can improve the distribution of active site. In addition, it can reduce reactor fouling, which is resulted from the adhesion of polymer to the reactor. Here, the heterogeneous system exhibited higher bulk density than the homogeneous system under this specified reaction condition. Meanwhile, it can be proposed that the SiO<sub>2</sub> support might inhibit the formation of ZrCH<sub>2</sub>CH<sub>2</sub>Zr species [17,18], which can be formed via a bimolecular process as it minimizes the steric hindrance effect of the system. It indicated that catalytic activity of  $SiO_2$  (SP) support was  $\sim 1.5$  times higher than that obtained from SiO<sub>2</sub> (LP) one. It results from the fact that, for SiO<sub>2</sub> (LP), MMAO cocatalyst can reach into its pore leading to lower MMAO present in the bulk, and hence less active species in the system. On the



**Scheme 1.** Location of active site over different supports.

<sup>&</sup>lt;sup>b</sup> Activities were measured at polymerization temperature of 343 K, [ethylene] = 0.018 mole, [1-octene] = 0.018 mole, [Al]<sub>MMAO</sub>/[Zr] = 1135, [Al]<sub>TMA</sub>/[Zr] = 2500, in toluene with total volume = 30 ml, and [Zr] =  $5 \times 10^{-5}$  M.

M. Wannaborworn et al./Journal of Industrial and Engineering Chemistry 18 (2012) 373-377

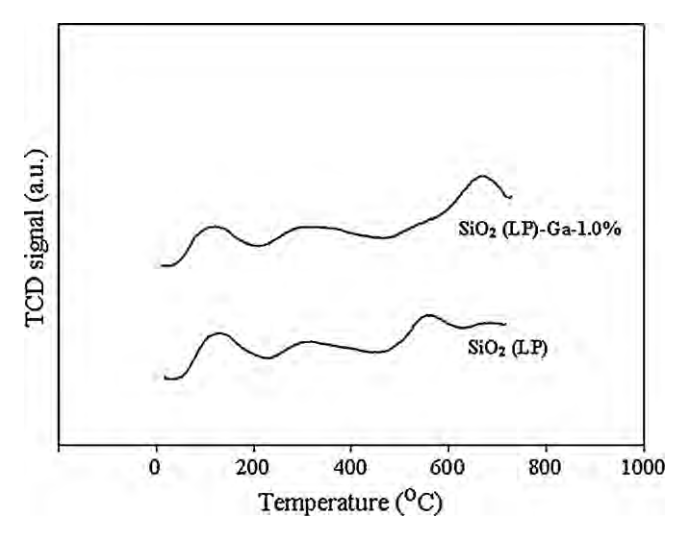
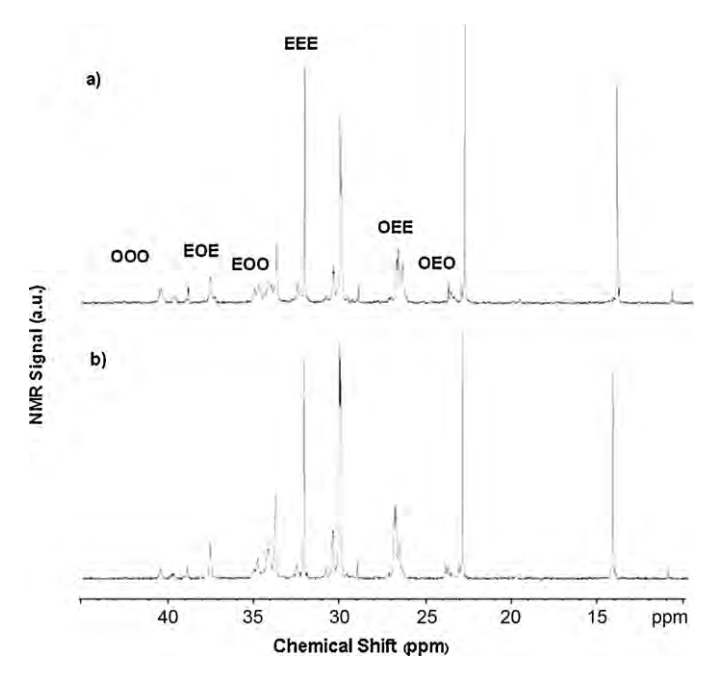


Fig. 3. NH<sub>3</sub>-TPD profiles of Ga-modified SiO<sub>2</sub> support.

**Table 3** Acidity of Ga-modified SiO<sub>2</sub> support obtained from NH<sub>3</sub>-TPD.

Support	Acid site (μmol H <sup>+</sup> /g)
SiO <sub>2</sub> (LP)	593
SiO <sub>2</sub> (LP)-Ga-1.0%	624

contrary, the higher activity was observed for SiO<sub>2</sub> (SP) support due to lower amount of MMAO in its pore. This makes MMAO remain highly in the bulk, and hence enhance the activity of polymerization (Scheme 1). Considering the effect of support modification with Ga, it was found that the polymerization activity increased with Ga loading. An increase in catalytic activity is probably due to improved ability of supports to immobilize metallocene catalyst. According to the work done by Campos et al. [14], they found that the characteristic peaks of Lewis acid center at 1457, 1492 and 1621 cm<sup>-1</sup> in the case of Ga-MCM-41, while MCM-41 does not exhibit these peaks. FTIR analysis result suggested that the interaction between zirconocene and the Lewis acid centers derived from the introduction of Ga in the support seems to play an important role in the formation of the active species and the optimization of Ga of the MCM-41 support. In addition, it can be seen from NH<sub>3</sub>-TPD method that modifying support with Ga resulted in more active site being present in the system, as shown in Fig. 3 and Table 3. All the samples exhibited two main desorption peaks around 140-170 °C and 330-340 °C, which were corresponding to weak and medium acid sites, respectively [19]. Additional peak at around 500-700 °C indicates the presence of strong acid sites of the supports [20]. The more Ga added, the more amount of acid site measured. Moreover, another reason for the higher activity of acid support is probably due to the higher efficiency of zirconocene cation generation and/or the improvement



**Fig. 4.** Typical  $^{13}$ C NMR spectra of copolymers obtained with (a) SiO $_2$  (LP) and (b) SiO $_2$  (SP) support.

of the propagation rate for polymerization. This result is consistent with Yamamoto [21], whose work revealed that  $\mathrm{SiO}_2/\mathrm{MgO}$  had strongly acid sites which helped enhance the propylene polymerization activity. Moreover, the obtained copolymers were further characterized using  $^{13}\mathrm{C}$  NMR to determine the comonomer distribution. The triad distribution and % incorporation of 1-octene comonomer are shown in Table 4 which is evaluated according to Randall [15]. From Table 4 it is apparent that only the random copolymers were produced in this system.

In addition, the  $^{13}$ C NMR spectra are shown in Fig. 4. They revealed that Ga-modification had no effect on microstructure of copolymer. However, when considered the insertion of comonomer, it can be observed that  $SiO_2$  (SP) gives higher 1-octene insertion than that of  $SiO_2$  (LP) support due to most of the active is present on the external surface for  $SiO_2$  (SP) leading to decreased steric hindrance. The obtained result is also consistent with Shan et al. [22].

Fig. 5 shows the SEM image of copolymer produced using support. It can be seen that after copolymerization, the support was covered with copolymer. Particles size of polymer is 20  $\mu m$ , which are about 1.5 times larger than supports. Polymer density measured by the densimeter, was about 0.89–0.91 g/cm³ for all polymer produced indicating the typical LLDPE obtained. However, the measured density was slightly lower than the commercial LLDPE ( $\sim\!0.92-0.93$  g/cm³). The lower density is probably due to higher insertion (>10 mol%) of 1-octene comonomer having low crystallinity [23].

**Table 4**<sup>13</sup>C NMR analysis of ethylene/1-octene copolymer.

System	Triad distribution of copolymer						1-Octene insertion (mol%)
EEE	EEE	EEO	EOE	EOO	OEO	000	
Homogeneous	0.467	0.226	0.177	0.078	0.052	0.000	26
SiO <sub>2</sub> (LP)	0.448	0.391	0.097	0.004	0.024	0.000	11
SiO <sub>2</sub> (LP)-Ga-1.0%	0.595	0.241	0.101	0.040	0.021	0.000	14
SiO <sub>2</sub> (SP)	0.472	0.190	0.168	0.096	0.074	0.000	26
SiO <sub>2</sub> (SP)-Ga-1.0%	0.612	0.211	0.094	0.053	0.030	0.000	15

E refers to ethylene monomer and O refers to 1-octene comonomer.

M. Wannaborworn et al./Journal of Industrial and Engineering Chemistry 18 (2012) 373-377

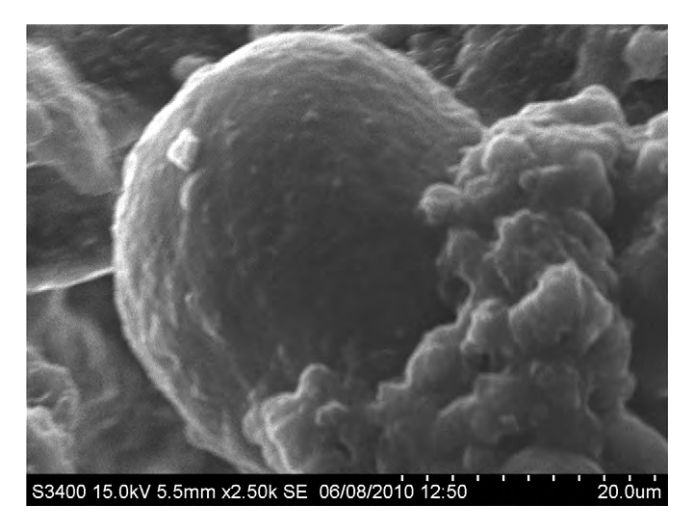


Fig. 5. A typical SEM micrograph of copolymer using Ga-modified silica support.

#### 4. Conclusion

Copolymerization of Ga-modified silica-supported zirconocene/MMAO catalyst via in situ impregnation on different pore sizes of supports was investigated. It revealed that the small-pored silica support exhibited higher polymerization activity than the large-pored silica due to lower content of MMAO present in small pore. However, MMAO remains in external surface, and therefore activity increased. In the part of Ga-modification, it was found that Ga loading improves catalytic activity without any significant change in the polymer microstructure.

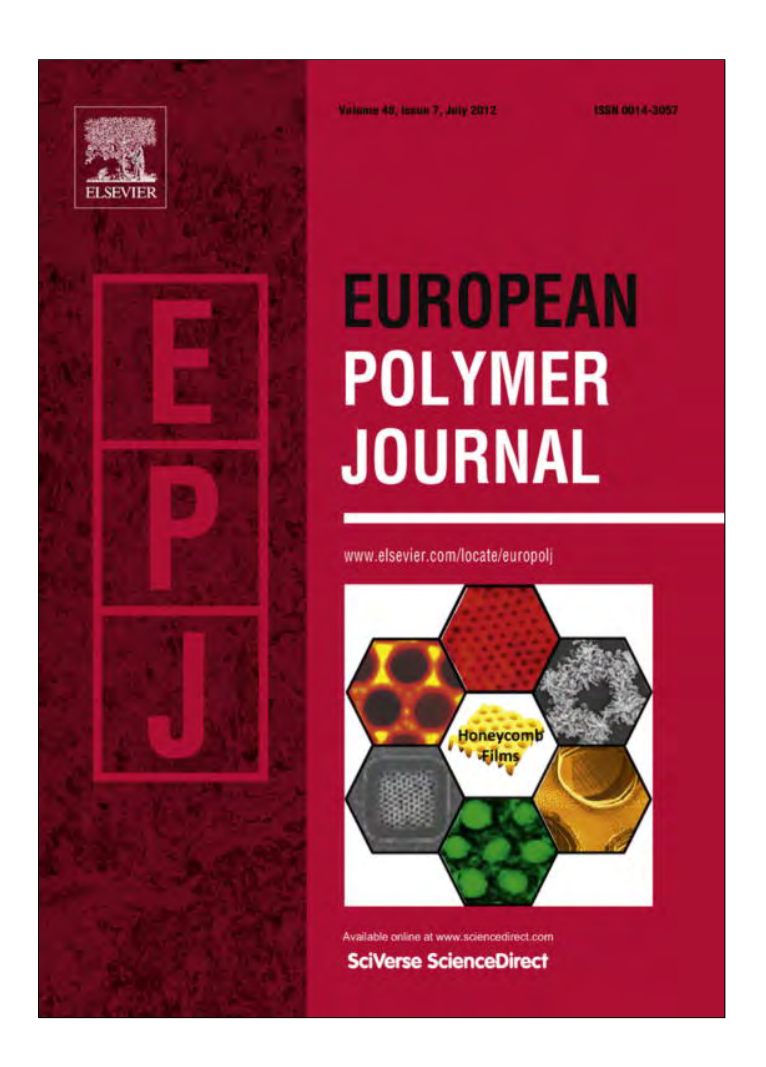
#### Acknowledgements

The authors thank the Thailand Research Fund (TRF), Office of the Higher Education Commission (CHE) and CU-NRU (AM1088A) for the financial support of this project.

#### References

- [1] G.B. Galland, M. Seferin, R. Guimarães, J.A. Rohrmann, F.C. Stedile, J.H.Z. Dos Santos, J. Mol. Catal. A: Chem. 189 (2002) 233.
- H.S. Cho, J.S. Chung, W.Y. Lee, J. Mol. Catal. A: Chem. 159 (2000) 203.
- [3] J. Móczó, B. Pukánszky, J. Ind. Eng. Chem. 14 (2008) 535.
- S.J. Park, K. Li, S.K. Hong, J. Ind. Eng. Chem. 11 (2005) 561.
- [5] S.Y. Lee, J.Y. Jho, W. Huh, J. Ind. Eng. Chem. 4 (1998) 258.
  [6] R. Georetzki, G. Fink, Polym. Sci. 37 (1999) 677.
- G.B. Galland, M. Seferin, R.S. Mauler, J.H.Z. Dos Santos, Polym. Int. 48 (1999) 660.
- B. Jongsomjit, P. Kaewkrajang, P. Praserthdam, Eur. Polym. J. 40 (2004) 2813.
- E. Chaichana, B. Jongsomjit, P. Praserthdam, Chem. Eng. Sci. 62 (2007) 899.
- [10] K. Ikenaga, S. Chen, M. Ohshima, H. Kurokawa, H. Miura, Catal. Commun. 8 (2007) 36.
- [11] B. Jongsomiit, S. Ngamposri, P. Praserthdam, Catal, Lett. 100 (2005) 139.
- [12] H. Rahiala, I. Beurroies, T. Eklund, K. Hakala, R. Gougeon, P. Trens, J.B. Rosenholm, J. Catal. 188 (1999) 14.
- T. Pothirat, B. Jongsomjit, P. Praserthdam, Catal. Commun. 9 (2008) 1426.
- [14] J.M. Campos, M.R. Ribeiro, J.P. Lourenço, A. Fernandes, J. Mol. Catal. A: Chem. 277 (2007)93.
- [15] J.C. Randall, J. Macromol. Sci. Rev. 29 (1989) 201.
- [16] S. Jungling, S. Koltzenburg, R. Mulhaupt, J. Polym. Sci. A: Polym. Chem. 35
- [17] B. Jongsomjit, P. Kaewkrajang, T. Shiono, P. Praserthdam, Ind. Eng. Chem. Res. 43 (2004) 7959.
- [18] B. Jongsomjit, J. Panpranot, M. Okada, T. Shiono, P. Praserthdam, Iran. Polym. J. 15 (2006) 433.
- R. Sakthivel, E. Kemnitz, Indian J. Technol. 15 (2008) 36.
- [20] K.V.R. Chary, G. Kishan, C.P. Kumar, G.V. Sagar, Appl. Catal. A 246 (2003) 330.
- [21] K. Yamamoto, Appl. Catal. A: Gen. 368 (2009) 65.
- C.L.P. Shan, J.B.P. Soares, A. Penlidis, J. Polym. Sci. A: Polym. Chem. 40 (2002) 4426.
- E. Chaichanal, S. Khaubunsongserm, P. Praserthdam, B. Jongsomjit, Express Polym. Lett. 4 (2010) 94.

Provided for non-commercial research and education use. Not for reproduction, distribution or commercial use.



This article appeared in a journal published by Elsevier. The attached copy is furnished to the author for internal non-commercial research and education use, including for instruction at the authors institution and sharing with colleagues.

Other uses, including reproduction and distribution, or selling or licensing copies, or posting to personal, institutional or third party websites are prohibited.

In most cases authors are permitted to post their version of the article (e.g. in Word or Tex form) to their personal website or institutional repository. Authors requiring further information regarding Elsevier's archiving and manuscript policies are encouraged to visit:

http://www.elsevier.com/copyright

### **Author's personal copy**

European Polymer Journal 48 (2012) 1304-1312



Contents lists available at SciVerse ScienceDirect

## European Polymer Journal

journal homepage: www.elsevier.com/locate/europolj



# Effect of Ga- and BCl<sub>3</sub>-modified silica-supported [t-BuNSiMe<sub>2</sub>(2,7-t-Bu<sub>2</sub>Flu)]TiMe<sub>2</sub>/MAO catalyst on ethylene/1-hexene copolymerization

Patcharaporn Kaivalchatchawal <sup>a</sup>, Sutheerawat Samingprai <sup>b</sup>, Takeshi Shiono <sup>c</sup>, Piyasan Praserthdam <sup>a</sup>, Bunjerd Jongsomjit <sup>a,\*</sup>

#### ARTICLE INFO

#### Article history: Received 12 January 2012 Received in revised form 1 March 2012 Accepted 18 April 2012 Available online 27 April 2012

Keywords:
Heterogeneous
Copolymerization
Metallocene catalyst
CGC catalyst
Acidic modification

#### ABSTRACT

In this present study, the copolymerization of ethylene and 1-hexene was conducted over the [t-BuNSiMe<sub>2</sub>(2,7-t-Bu<sub>2</sub>Flu)]TiMe<sub>2</sub> (CGC)/MAO catalyst immobilized on different supports. The effects of Ga and the Lewis acid BCl<sub>3</sub> modification of the silica support on the copolymerization behavior were investigated based on catalytic activity and polymer properties. It was found that the silica support modified with BCl<sub>3</sub> exhibited the highest activity. However, both Ga and BCl<sub>3</sub> modifiers are capable of enhancing the catalytic activity, probably attributed to stronger interaction between the MAO and support together with the acidic sites exerted by the modification which could assist MAO to activate the catalyst during polymerization. Besides, a role of BCl<sub>3</sub> as a spacer to keep apart the catalyst on the silica surface was proposed as another probable reason for activity increased. This led to the more homogeneous-like behavior with less effect of support and also caused the higher comonomer incorporation content. Moreover, the results revealed that narrow polymer molecular weight distribution can be achieved by the supported CGC catalyst, especially for acidic modified supports. On the other hand, there was no noticeable effect with regards to the melting temperature and copolymer microstructure of the Ga and BCl<sub>3</sub> modification. Therefore, based on the study it may be regarded that the efficient supported CGC catalyst can be accomplished through the acidic modification namely Ga and BCl<sub>3</sub>.

#### © 2012 Elsevier Ltd. All rights reserved.

#### 1. Introduction

Based on the volume of material consumed annually worldwide consumption, polyolefins, especially linear low-density polyethylene (LLDPE), are the largest volume polymers in the plastics industry. This is because they exhibit many useful properties, such as low density, high strength, and resistance to chemical attack, as well as being cost-effective. Therefore, much effort in both academic and

\* Corresponding author. Fax: +66 2 2186877. E-mail address: bunjerd.j@chula.ac.th (B. Jongsomjit). industrial research has been directed towards the development of highly active olefin polymerization catalysts for the synthesis of desired copolymers [1–3]. Single site catalysts, namely metallocene catalyst, have been reported to be potentially useful for the copolymerization of ethylene and  $\alpha$ -olefins, such as 1-butene, 1-hexene and 1-octene, to produce LLDPE with short chain branching. Comparable to conventional Ziegler–Natta systems, metallocene catalysts display a high activity and allow rational catalyst design to construct a relationship between catalyst structure and resulting polymer microstructure [4]. They also offer superior product properties in terms of a narrow molecular

<sup>&</sup>lt;sup>a</sup> Center of Excellence on Catalysis and Catalytic Reaction Engineering, Department of Chemical Engineering, Faculty of Engineering, Chulalongkorn University, Bangkok 10330, Thailand

b Innovation & Technology, PTT Global Chemical Public Company Limited, Tambon Map Ta Phut, Amphoe Mueang Rayong, Rayong 21150, Thailand

<sup>&</sup>lt;sup>c</sup> Department of Applied Chemistry, Graduate School of Engineering, Hiroshima University, Higashi-Hiroshima 739-8527, Japan

weight distribution (MWD) and a uniform short chain branching distribution [5].

Even if there are many advantages of homogeneous metallocene catalysts, such as high activity and stereoregularity, there are also some crucial problems for the commercial applications, including the difficulties in controlling the polymer morphology, instabilities for slurry or gas phase processes and the requirement of a large amount of expensive methylaluminoxane (MAO) [6]. To overcome these drawbacks, it is desirable to heterogenize the soluble catalysts on supports such as silica, alumina and titania for their possible industrial applications [7]. It has been reported that silica has been the attractive and the most widely used support for metallocene catalysts [8–10]. Nonetheless, the properties of silica itself probably bring about some dissatisfaction based on activities and quality of polymer produced. Thus, some additives or modifiers are required for modification in order to achieve the better performance [11–13]. Most researchers reviewed that treating the silica surface with hydrophobic functional groups such as aryl, alkyl, and silane can improve the catalytic behavior [14–19]. Some researchers accentuated that the surface acidity properties of solid supports may play the determinant role in the activation of the metallocene catalyst, contributing to the polymerization activity increase [20,21]. The most frequently used pathway to modify the acidic surface property is the incorporation of acidic metal atoms in their frameworks [22-24]. Recently, it has been reported that the exploitation of acidic Ga metal is a promising alternative way to enhance the performance of metallocene catalysts during the ethylene polymerization [25,26].

In previous studies, a unique catalyst type called constrained geometry catalyst (CGC) using half sandwich titanocenes has been found and categorized as one of the metallocene group. This complex provides high catalytic activity and high insertion of  $\alpha$ -olefins into copolymers. According to our previous research, we investigated the influence of the t-butyl and cyclododecyl substitution of ansa-fluorenylamidodimethyltitanium derivatives on ethylene/1-hexene copolymerization in the homogenous system. We revealed that the 2,7 t-butyl group led the [t-BuNSiMe<sub>2</sub>(2,7-t-Bu<sub>2</sub>Flu)]TiMe<sub>2</sub> to achieve the highest activity [27].

The main objective of this present study was to investigate how the Ga and the Lewis acid BCl $_3$  modification of the silica support would impact on the ethylene/1-hexene copolymerization in terms of catalytic activity and polymer properties. The CGC complex of [t-BuNSiMe $_2$ (2,7-t-Bu $_2$ Flu)]TiMe $_2$  was used to be further developed for the heterogeneous system and to generate the more efficient supported CGC catalyst in the near future.

#### 2. Experimental

#### 2.1. Materials

All operations were performed under an argon atmosphere using Schlenk techniques and glove box. All solvents were dried over dehydrated CaCl<sub>2</sub> and distilled over sodium/benzophenone before use. MAO was donated from

Tosoh-Finechem Co. Ltd. Ethylene gas (99.96% pure) was donated by the National Petrochemical Co. Ltd., Thailand. 1-Hexene was purchased from Aldrich Chemical Company and purified by distilling over sodium/benzophenone under argon atmosphere before use. Silica gel (SP9-602 from Grace Davison) was calcined at 673 K for 6 h. Ga(NO<sub>3</sub>)<sub>3</sub> and BCl<sub>3</sub> were purchased from Aldrich Chemical Company. [t-BuNSiMe<sub>2</sub>(2,7-t-Bu<sub>2</sub>Flu)]TiMe<sub>2</sub> (CGC complex) was synthesized according to procedures reported previously [28]. The chemical structure of catalyst is shown in Scheme 1.

#### 2.2. Preparation of Ga-modified silica support

The gallium modification on the silica support was prepared by the incipient-wetness impregnation method according to the procedure described previously [26]. Ga(NO<sub>3</sub>)<sub>3</sub> was used as a Ga source. Gallium was impregnated onto silica gel with 0.2 wt.% of Ga. The support was dried in oven at 383 K for 12 h and calcined in air at 773 K for 2 h. The resulting mixture was reffered to SiO<sub>2</sub>–Ga.

#### 2.3. Preparation of BCl<sub>3</sub>-modified silica support

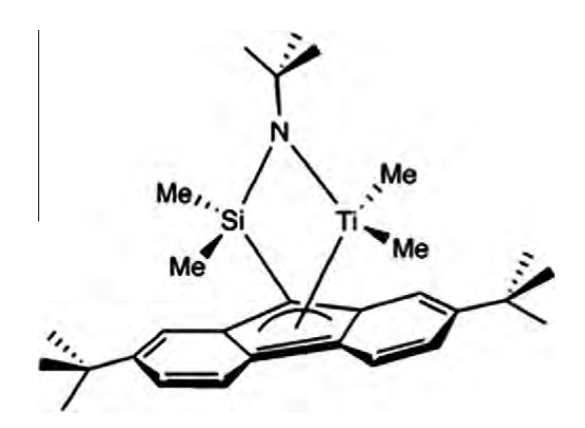
Silica surface was treated with  $BCl_3$  that 14.25 g of silica was added with 150 ml of hexane as diluent, and then 7 ml of  $BCl_3$  were added. The mixture was stirred for 30 min in an oil bath at 313 K, until temperature was raised up to 343 K, followed by drying under vacuum. The resulting mixture was referred to  $SiO_2$ – $BCl_3$ .

#### 2.4. Preparation of supported MAO

One gram of calcined silica or modified silica was reacted with the desired amount of MAO in 20 ml of toluene at room temperature for 30 min. The solid part was separated and washed 3 times with 20 ml of toluene, followed by drying in vacuum at room temperature to obtain the catalyst precursor.

#### 2.5. Polymerization procedure

The ethylene/1-hexene copolymerization reaction was performed in a 100 ml semi-batch stainless steel autoclave reactor equipped with magnetic stirrer. At first the desired



**Scheme 1.** Chemical structure of  $[t-BuNSiMe_2(2,7-t-Bu_2Flu)]TiMe_2$  (CGC complex).

amount of the support/MAO was introduced into the reactor. After that the catalyst was put into the reactor to make the amount of catalyst at 10 µmol, and then toluene was injected to adjust the total volume to 30 ml. Then, the reactor was immersed in liquid nitrogen, followed by addition of the 1-hexene into the frozen reactor. The reactor was heated up to the polymerization temperature at 343 K. Lastly, the reaction was terminated by adding acidic methanol. After filtration, the resulting polymers were washed with methanol and dried at room temperature.

#### 2.6. Supports and supported MAO characterization

#### 2.6.1. N<sub>2</sub> physisorption

BET surface area, average pore diameter and pore size distribution of silica and modified silica were determined by Brunauer–Emmett-Teller (BET) method via nitrogen adsorption. The instrument was an AUTOSORB 1-MP, Quantachrome Instruments. Samples were determined using  $N_2$  adsorption at 77 K and handled to the analysis tubes under nitrogen atmosphere and the surface area measurements were carried out inertly. The temperature of evacuated degassing was 423 K.

#### 2.6.2. X-ray diffraction (XRD)

SIEMENS D-5000 X-ray diffractometer with Cu  $K_{\alpha}$  (l = 1.54439 Å) was conducted to determine the bulk crystalline phases of samples. The spectra were scanned at a rate of  $2.4^{\circ}$  min<sup>-1</sup> in the range of  $2\theta = 20-80^{\circ}$ .

## 2.6.3. Temperature programmed desorption of ammonia $(NH_3-TPD)$

Acidity of the supports was determined by temperature programmed desorption of ammonia using a Micromeritics Chemisorp 2750 system. The samples were activated at 773 K for 1 h in a flow of helium. Subsequently, the samples were loaded with ammonia and thermal desorption was carried out in a dried He stream at a heating rate of 10 K/min.

## 2.6.4. Scanning electron microscope (SEM) and energy dispersive X-ray spectroscopy (EDX)

Scanning electron microscope (SEM), JEOL model JSM-6510 LV, was employed to investigate the morphology of silica, modified silica and catalyst precursor. EDX was performed using Link Isis series 300 program to observe catalyst precursor elemental distribution.

#### 2.6.5. Thermogravimetric analysis (TGA)

TGA was performed to determine the interaction force of the supported MAO. It was conducted using TGA Instruments TG 209F1 analyzer. The samples of 10 mg and a temperature ramping from 303 to 923 K at 5 K/min were used in operation. The carrier gas was  $N_2$  UHP.

#### 2.7. Polymer characterization

#### 2.7.1. Gel permeation chromatography (GPC)

The average molecular weight and molecular weight distribution of obtained polymer in this study were determined

by GPC Waters 150 CV at 413 K with 1,2,4-trichlorobenzene as the solvent and the feed flow rate is 1.0 ml/min.

#### 2.7.2. Differential scanning calorimetry (DSC)

The melting temperature ( $T_m$ ) of polymer was measured by means of DSC, using DSC 204 F1  $Phoenix^{\otimes}$  operating at a heating rate of 10 K/min from 303 K to 473 K. The heating cycle was run twice. In the first scan, the samples were heated, and then cooled to room temperature. In the second, the samples were reheated at the same rate, but only the results of the second scan were reported because the first scan was influenced by the mechanical and thermal history of samples.

## 2.7.3. <sup>13</sup>Carbon nuclear magnetic resonance spectroscopy (<sup>13</sup>C NMR)

The  $^{13}$ C NMR spectra were recorded at 383 K using JEOL JNM-A500 operating at 125 MHz. Copolymer solutions were prepared using 1,2,4 -trichlorobenzene as solvent and benzene-d<sub>6</sub> for internal lock.

#### 3. Results and discussion

#### 3.1. Characteristics of catalyst support

In this study, three kinds of supports composing of unmodified silica ( $SiO_2$ ), Ga-modified silica ( $SiO_2$ –Ga), and  $BCl_3$ -modified silica ( $SiO_2$ – $BCl_3$ ) were used for supporting the [t-BuNSiMe<sub>2</sub>(2,7-t-Bu<sub>2</sub>Flu)]TiMe<sub>2</sub> (the CGC complex)/MAO catalyst. After modification with Ga and Lewis acid  $BCl_3$ , the silica and modified silica supports were characterized by means of  $N_2$  physisorption,  $NH_3$ -TPD and SEM/EDX. The specific properties of supports determined by  $N_2$  physisorption are shown in Table 1. As seen, the BET surface area, pore volume and pore diameter of all supports were in the same range, indicating that the acidic modification on silica surface did not have significant effect on these structural parameters.

The XRD patterns (not shown) for all supports were similar exhibited only a board peak between 20° and 30°, as seen typically for the conventional amorphous silica. No XRD peaks of Ga or BCl<sub>3</sub> were observed after impregnation due to its homogeneous distribution or at least that the aggregates formed do not have a significant size to be detected by XRD [25].

Temperature-programmed desorption of ammonia was used to estimate the number and the strength of acid sites on modified silica supports based on the fact that the acidic properties of supports may influence the type of interaction with the metallocene complex and its activation process,

**Table 1** Specific properties of various supports obtained from N<sub>2</sub> physisorption.

Support	BET surface area (m²/g)	Pore volume (mL/g)	Pore diameter (Å)
SiO <sub>2</sub>	309	1.53	198
SiO <sub>2</sub> -Ga	300	1.50	199
SiO <sub>2</sub> -BCl <sub>3</sub>	299	1.47	197

P. Kaivalchatchawal et al./European Polymer Journal 48 (2012) 1304-1312

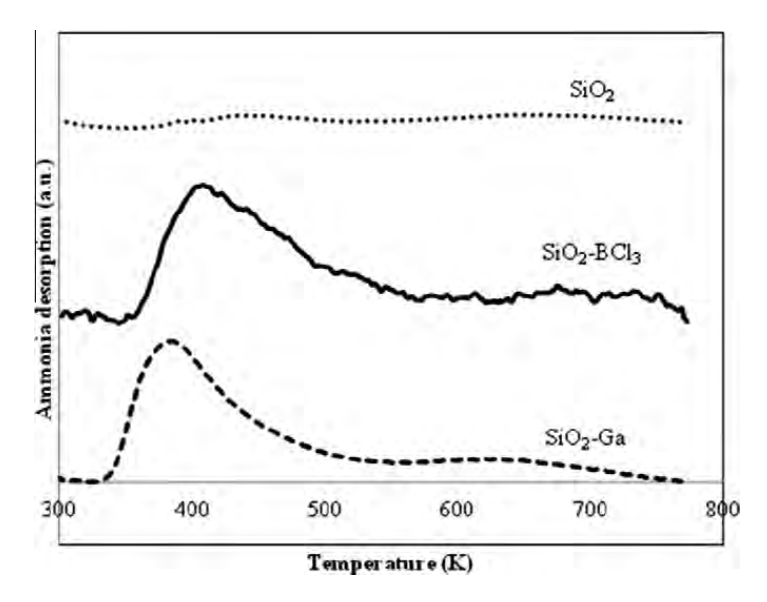


Fig. 1. NH<sub>3</sub>-TPD profiles of SiO<sub>2</sub>, SiO<sub>2</sub>-Ga and SiO<sub>2</sub>-BCl<sub>3</sub> supports.

consequently resulting in overall productivity [22]. The typical NH<sub>3</sub>-TPD profiles for silica support before and after treatment with Ga and BCl<sub>3</sub> can be represented in Fig. 1. The SiO<sub>2</sub> support exhibited no peak, indicating no acidic sites before treatment; on the other hand, both of SiO<sub>2</sub>–Ga and SiO<sub>2</sub>–BCl<sub>3</sub> supports showed two broad peaks at the temperature ranged around 350–550 K and 570–750 K. According to Kosslick et al. [23], these peaks can be ascribed to the NH<sub>3</sub> desorbed from acid sites with low and medium to high strengths. The total acidity concentration of SiO<sub>2</sub>–Ga and SiO<sub>2</sub>–BCl<sub>3</sub> determined by NH<sub>3</sub> temperature program desorption experiments was 283 and 325 μmol NH<sub>3</sub>/g, respectively. Therefore, it is clearly shown that the acidity of silica support can be improved with the modification of Ga and BCl<sub>3</sub>.

The morphologies and elemental distributions of the supports before and after MAO impregnation were investigated by using SEM and EDX, respectively. The SEM images of different supports prior to MAO impregnation are shown in Fig. 2. The similar spherical shape was mainly observed, indicating no change of support morphology with the acidic modification.

After impregnation with MAO, the [Al]<sub>MAO</sub> content on the silica surface was measured using EDX. Table 2 represents the [Al]<sub>MAO</sub> content on various silica supports. It can be seen that the [Al]<sub>MAO</sub> concentration of each support slightly varied probably due to the adsorption ability. Results revealed that the  $SiO_2$ –Ga supported MAO achieved the highest amount of [Al]<sub>MAO</sub>, suggesting that the adsorption ability of MAO on silica support can be enhanced with

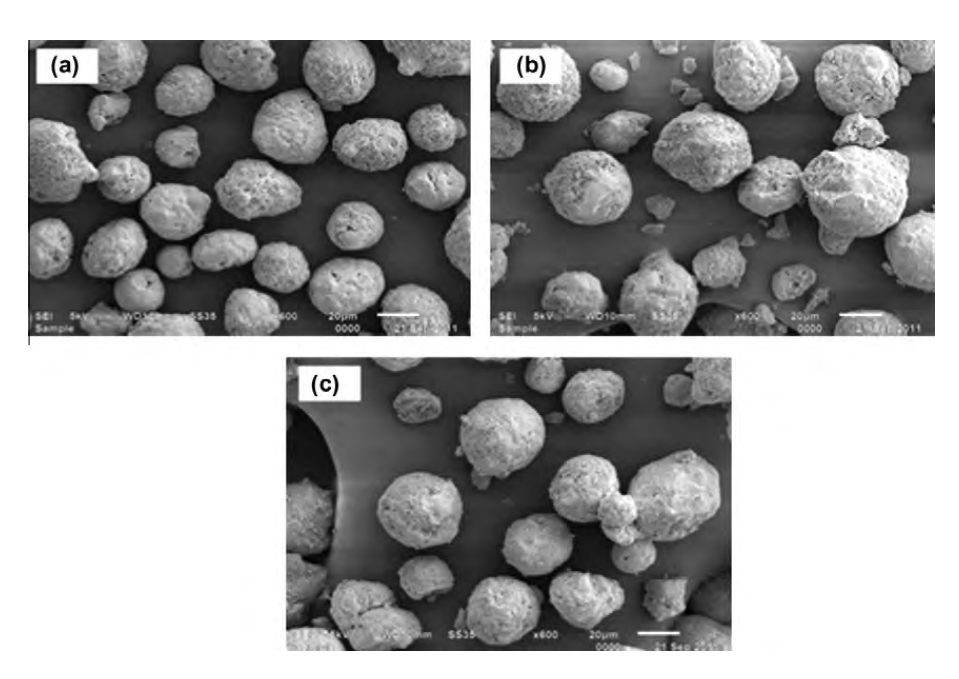


Fig. 2. SEM micrographs of different supports before MAO impregnation: (a) SiO<sub>2</sub>, (b) SiO<sub>2</sub>–Ga and (c) SiO<sub>2</sub>–BCl<sub>3</sub>.

**Table 2**[Al]<sub>MAO</sub> content of the supported MAO from EDX analysis.

Catalyst precursor	[Al] <sub>MAO</sub> (wt.%)
SiO <sub>2</sub> /MAO	13.6
SiO <sub>2</sub> –Ga/MAO	14.5
SiO <sub>2</sub> –BCl <sub>3</sub> /MAO	13.4

the introduction of Ga. However, the modification of silica with  $BCl_3$  caused only a slight decrease of immobilized MAO cocatalyst on silica. In addition to the content of  $[Al]_{MAO}$ , it should consider the distribution of this element through the support. Therefore, EDX mapping of all elements was used for this purpose and represented in Fig. 3. It can be observed that the distribution for all elements, especially for  $[Al]_{MAO}$  was well dispersed all over the catalyst granule without any changes in morphology. Then, the different supports with and without acidic modification having MAO impregnation were employed for ethylene and 1-hexene copolymerization.

#### 3.2. Catalytic activity

Copolymerization of ethylene and 1-hexene via various SiO<sub>2</sub>-supported MAO with the CGC catalyst was performed so as to determine the catalytic activities influenced by different acidic modification of support. The polymerization activities of homogeneous system and a variety of supports are summarized in Table 3. Regarding to Table 3, the catalytic activities were in the order of SiO<sub>2</sub>–BCl<sub>3</sub> > homogeneous > SiO<sub>2</sub>–Ga > SiO<sub>2</sub>. It can be apparently seen that the supported system (except SiO<sub>2</sub>–BCl<sub>3</sub>) exhibited lower activities compared to the homogeneous one, particularly for the unmodified silica. This can be explained taking into

account that in the supported catalyst preparation, different adsorption might take place, contributing to some inactive species for polymerization [29]. Another possible reason for this observation is the depression of the polymerization rate as a result of mass transfer limitation in heterogeneous system. Nonetheless, considering only the supported system, the modification of silica support, like Ga and BCl<sub>3</sub>, was able to increase the polymerization activities. Generally, increased activities can be owing to the increased amount of [Al]<sub>MAO</sub> presented on the support and the interaction between support and MAO [30,31]. However, in this work the former factor can be neglected by using the same ratio of  $[Al]_{MAO}/[Ti]_{cat} = 400$  and adjusting the required amount of the supported MAO in each experiment. Thus, the latter factor should be considered as the probable cause for this increased activity. Based on this study, MAO was dispersed over the silica supports by impregnation prior to polymerization. The degree of interaction between the [Al]<sub>MAO</sub> and the support can be investigated by the TGA measurement. According to Severn et al. [32], the connection of the support and the cocatalyst occurred via the O<sub>support</sub>-Al<sub>cocatalyst</sub> linkage. The TGA can provide the beneficial information on the degree of the interaction for MAO bound to silica in terms of weight loss and removal temperature [26,30,31]. In fact, too strong interaction leads to more difficult for [Al]<sub>MAO</sub> bound to the support to react with the metallocene catalyst during activation step and thus low polymerization activity. On the contrary, the leaching of MAO can be occurred due to weak interaction between support and MAO. Therefore, the optimum degree of interaction should be required in order to achieve the high activity. Fig. 4 represents TGA profiles of various supports. It was observed that the weight loss of [Al]<sub>MAO</sub> presented on the supports was in

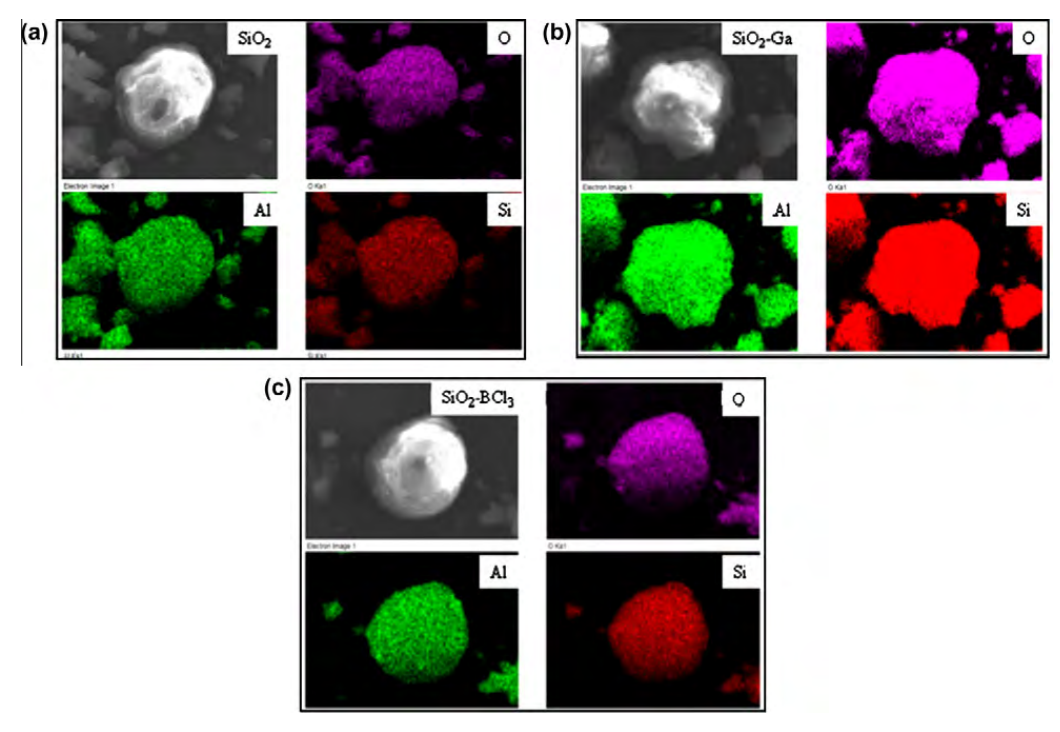


Fig. 3. EDX mapping of (a) SiO<sub>2</sub> supported MAO (b) SiO<sub>2</sub>–Ga supported MAO (c) SiO<sub>2</sub>–BCl<sub>3</sub> supported MAO.

**Table 3**Summary of ethylene/1-hexene copolymerization catalytic activities.

System	Time (s)	Weight (g)	Activity <sup>a</sup> (kg polymer/mol Ti.h)
Homogeneous	85.8	1.04	4377
SiO <sub>2</sub>	99.2	0.97	3519
SiO <sub>2</sub> -Ga	92.4	1.00	3901
SiO <sub>2</sub> -BCl <sub>3</sub>	78	0.96	4454

 $<sup>^</sup>a$  Polymerization condition: [Ti] = 10  $\mu mol,~MAO$  as cocatalyst, [Al]/[Ti] = 400, liquid volume (toluene) = 30 mL, temperature = 343 K, ethylene pressure = 349 kPa (50 psi).

the order of  $SiO_2$ – $BCl_3$  (25.2%) <  $SiO_2$ –Ga (25.6%) <  $SiO_2$  (26.2%). This indicated the strongest interaction of the  $SiO_2$ – $BCl_3$  supported MAO, demonstrating the highest activity compared to other supports. Thus, for this supported CGC system, it should be mentioned that the stronger interaction between cocatalyst and support is favorable in order to prevent the leaching of the cocatalyst.

Besides the interaction, one should concern on the acidic property of the silica support after modification with Ga and BCl<sub>3</sub>. As a matter of fact, the literature reviewed that the surface acidity properties of supports have the important role in the activation of metallocene catalyst and accordingly on the activity enhancement. Moreover, Campos et al. [25] constructed a correlation between polymerization activity and support acidity and revealed that the activities increased with an increase of acidic sites. In this work, the incorporation of Ga and BCl<sub>3</sub> generated the acid sites in the silica supports (as confirmed by NH<sub>3</sub>-TPD) and these sites are able to assist MAO that performed as a main activating agent to activate the CGC catalyst during the polymerization. As a consequence, this should be an explanation for an obvious rise of polymerization activities in modified supports compared to the conventional silica support. Furthermore, a higher degree of activity increase for BCl3-modified silica system can be mainly attributed to the higher acidity than the Ga-modified one.

With regard to the result in Table 3, it is worth nothing that the catalytic activity obtained from BCl<sub>3</sub>-modified

support was the highest and can be comparable to the homogeneous one, suggesting the homogeneous-like behavior of this system. It was presumably on account of the role of BCl<sub>3</sub> as a spacer group on the surface of silica. Investigation of a spacer such as  $TiO_2$ , silane and zirconia in copolymerization of ethylene and  $\alpha$ -olefins was studied as well [15–17]. In order to gain a better understanding, a conceptual model for BCl<sub>3</sub> effect is illustrated in Scheme 2. As seen, after immobilization MAO or active sites can be anchored on the modified silica through the BCl molecule, which acted as a spacer and hence less steric hindrance between them. Consequently, a monomer during polymerization can insert more easily into this structure, and thus enhancing activity.

#### 3.3. Characteristics of polymer

The various obtained copolymers were further characterized by means of GPC, DSC and <sup>13</sup>C NMR. Table 4 is constructed to summarize the properties yielded from homogeneous and various supported systems. The GPC was performed to measure  $M_w$  and MWD of polymers. It should be mentioned that all polymers exhibited rather low molecular weights. However, these results were in the same range (20-40 kg/mol) with other metallocene or CGC catalysts under similar conditions [6,16,33-35]. This is probably due to the nature of metallocene catalyst that is usually relatively sensitive to chain transfer reaction despite no apparent chain termination reagent. Nevertheless, in order to improve or control the molecular weight, this constrained geometry catalyst system should be further investigated in living polymerization. Comparing to the homogeneous system, it was apparently observed that the molecular weight for other heterogeneous systems increased drastically (more than 3 times). This should be because of an obstruction of bimolecular reaction between two catalytic sites by immobilization of MAO on the support surface. Therefore, a β-hydrogen transfer might be lessened, and then enables longer growth of the polymer chain, leading to higher molecular weight of polymers

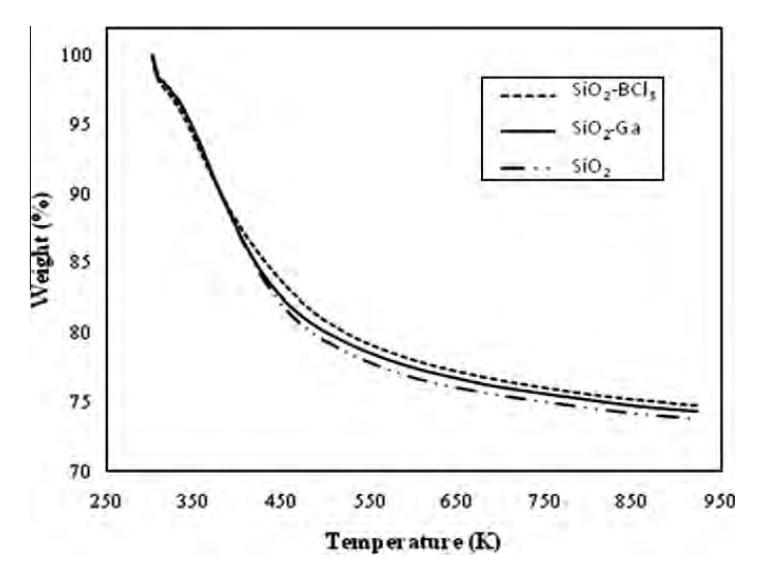
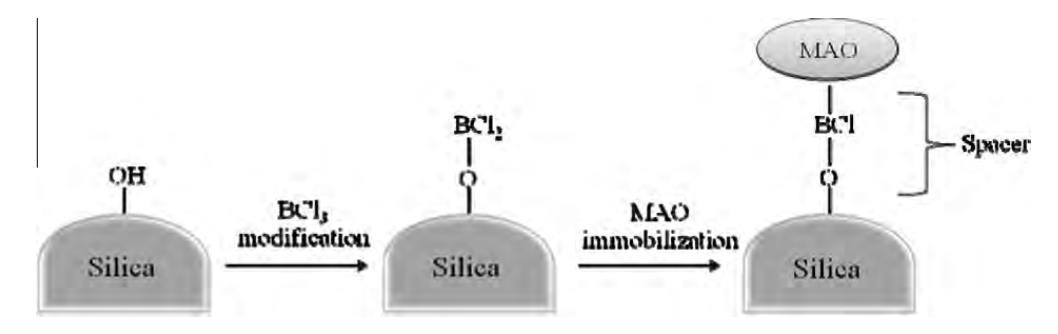


Fig. 4. TGA profiles of supported MAO on various supports.

P. Kaivalchatchawal et al./European Polymer Journal 48 (2012) 1304-1312



**Scheme 2.** Conceptual model for BCl<sub>3</sub> effect as a spacer.

**Table 4**Properties of the resulted copolymers from homogeneous and supported system.

System	Melting point <sup>a</sup> $(T_m)$ (K)	Molecular weight <sup>b</sup> ( <i>M<sub>w</sub></i> ) (kg/mol)	$MWD^{\rm b} \ (M_w/M_n)$	Insertion% <sup>c</sup>
Homogeneous	378	9	3.26	13.6
SiO <sub>2</sub>	391	35	2.81	9.3
SiO <sub>2</sub> -Ga	390	28	2.61	11.3
SiO <sub>2</sub> -BCl <sub>3</sub>	382	27	2.40	15.0

- <sup>a</sup> Determined by DSC.
- <sup>b</sup> Determined by GPC.
- <sup>c</sup> 1-hexene insertion in copolymer determined by <sup>13</sup>C NMR.

[32]. Fig. 5 shows the GPC curves for all polymers, indicating the unimodal molecular weight distribution. In addition, it was found that the molecular weight distribution of the copolymer resulted from the heterogeneous system became narrower, especially after modification with Ga and BCl<sub>3</sub>. This indicated that the more uniform catalytic sites can be achieved through the acidic modification.

Considering only the supported systems, a slight reduction in molecular weight was observed for the modified support. The cause of this is based on the fact that a rise of 1-hexene insertion compared to unmodified support promotes chain transfer reactions, consequently contributing to lower molecular weight copolymers [29]. The melting temperature  $(T_m)$  of copolymers evaluated by DSC is also shown in Table 4. It revealed that  $T_m$  was in the range between 378 and 391 K. However,  $T_m$  tended to slightly decrease with Ga and BCl<sub>3</sub> modification generally attributed to the increased degree of 1-hexene insertion.

The quantitative analysis of triad distribution for all copolymers was conducted on the basis assignment of the <sup>13</sup>C NMR spectra of ethylene/1-hexene copolymer [36]. The triad distributions and 1-hexene contents, which were calculated according to the Randall method [36] are presented in Table 5. Ethylene incorporation in all systems gave copolymers with similar triad distribution regardless of acidic modification. Only random copolymers can be produced with this system. On the other hand, it is shown that the unmodified silica support presented a noticeable

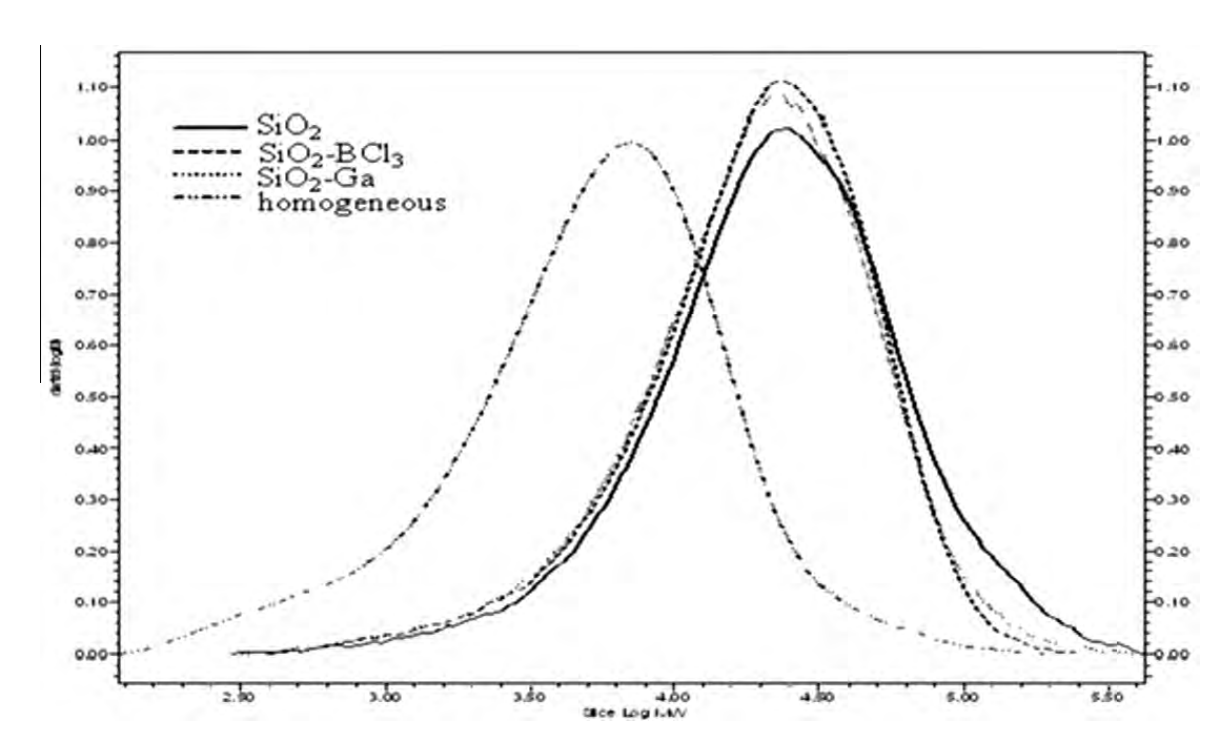


Fig. 5. GPC curves of copolymers obtained from various supports.

**Table 5**Triad distribution of copolymers obtain from <sup>13</sup>C NMR.

System	[ННН]	[EHH]	[EHE]	[EEE]	[HEH]	[HEE]	[H] (%)
Homogeneous	0.000	0.000	0.129	0.630	0.000	0.241	12.9
SiO <sub>2</sub>	0.000	0.000	0.090	0.738	0.000	0.172	9.0
SiO <sub>2</sub> -Ga	0.000	0.000	0.094	0.761	0.000	0.145	9.4
SiO <sub>2</sub> -BCl <sub>3</sub>	0.000	0.000	0.138	0.646	0.031	0.186	13.8

decrease of 1-hexene insertion compared to the homogeneous one. The lower comonomer incorporation can be by reason of a steric effect inserted by silica surface, preventing one of the CGC catalyst faces, therefore reducing the accessibility of the comonomer onto the active sites [29]. This steric effect is able to be relieved with the silica modification like BCl<sub>3</sub> which can act as a spacer group to keep apart active sites from the silica surface, thus being apt to enhance the 1-hexene extent.

#### 4. Conclusion

The activities of ethylene/1-hexene copolymerization with silica-supported CGC/MAO catalyst can be improved with the Ga and BCl<sub>3</sub> acidic modification on the silica support. Increased activity was due to the stronger interaction between support and cocatalyst coupled with a formation of acidic sites derived from the modification. Additionally, BCl<sub>3</sub> is able to be a spacer on the silica support leading to the highest activity and the highest 1-hexene incorporation. The supported catalytic system resulted in polymers with significantly higher molecular weight (almost 4 times) and narrower molecular weight distribution, especially after acidic modification. However, the Ga and BCl<sub>3</sub> modifications seem not to greatly influence on the melting temperature and the microstructure of copolymers.

#### Acknowledgements

The authors gratefully thank the Dusadeepipat scholarship (Chulalongkorn University Fund), Graduate school of Chulalongkorn University and Innovation & Technology of PTT Global Chemical Public Company Limited for the financial support of this work. The authors also extend the thankful for the Thailand Research Fund (TRF) and Office of the Higher Education Commission (CHE).

#### References

- [1] Chum P, Swogger K. Olefin polymer technologies-history and recent progress at the Dow Chemical Company. Prog Polym Sci 2008;33:797–819.
- [2] Mitani M, Saito J, Ishii S, Nakayama Y, Maiko H. FI catalysts: new olefin polymerization catalysts for the creation of value-added polymers. Chem Rec 2004;4(3):137–58.
- [3] Gromadaa J, Carpentier J, Mortreux A. Group 3 metal catalysts for ethylene and olefin polymerization. Coordin Chem Rev 2004; 248:397–410.
- [4] Matsui S, Fujita T. FI catalysts: super active new ethylene polymerization catalysts. Catal Today 2001;66:63–73.
- [5] Braunschweig H, Breitling F. Constrained geometry complexes synthesis and applications. Coordin Chem Rev 2006;250:2691–720.
- [6] Lee K, Oh C, Yim J, Ihm S. Characteristics of zirconocene catalysts supported on Al-MCM-41 for ethylene polymerization. J Mol Catal A: Chem 2000;159:301–8.

- [7] Ketloy C, Jongsomjit B, Praserthdam P. Characteristics and catalytic properties of [t-BuNSiMe<sub>2</sub>Flu]TiMe<sub>2</sub>/dMMAO catalyst dispersed on various supports towards ethylene/1-octene copolymerization. Appl Catal A 2007;327:270–7.
- [8] Hlatky G. Metallocene catalysts for olefin polymerization. Coordin Chem Rev 1999;181:243–96.
- [9] Babushkin DE, Panchenko VN, Timofeeva MN, Zakharov VA, Brintzinger HH. Novel zirconocene hydride complexes in homogeneous and in SiO<sub>2</sub>-supported olefin polymerization catalysts modified with diisobutylaluminum hydride or triisobutylaluminum. Macromol Chem Phys 2008;209(12):1210–9.
- [10] Marques MFV, Conte A. The influence of the preparing conditions of SiO<sub>2</sub> supported Cp<sub>2</sub>ZrCl<sub>2</sub> catalyst on ethylene polymerization. J Appl Polym Sci 2002;86(8):2054–61.
- [11] Jongsomjit B, Ngamposri S, Praserthdam P. Catalytic activity during copolymerization of ethylene and 1-hexene via mixed TiO2/SiO2supported MAO with rac-Et[Ind]<sub>2</sub>ZrCl<sub>2</sub> metallocene catalysts. Molecules 2005;10:672–8.
- [12] Ciardelli F, Altomare A, Michelotti M. From homogeneous to supported metallocene catalysts. Catal Today 1998;41:149–57.
- [13] Dorcier A, Merle N, Taoufik M, Bayard F, Lucas C, Mallmann A, et al. Preparation of a well-defined silica-supported nickel-diimine alkyl complex – application for the gas-phase polymerization of ethylene. Organometallics 2009;28(7):2173–8.
- [14] Alonso C, Antiñolo A, Carrillo-Hermosilla F, Carrión P, Otero A, Sancho J, et al. Modified silicas as supports for single-site zirconocene catalysts. J Mol Catal A: Chem 2004;220(2):285–95.
- [15] Jongsomjit B, Kaewkrajang P, Wanke S, Praserthdam P. Catal Lett 2004:94:205.
- [16] Jongsomjit B, Kaewkrajang P, Praserthdam P. Effect of silanemodified silica/MAO-supported Et[Ind]<sub>2</sub>ZrCl<sub>2</sub> metallocene catalyst on copolymerization of ethylene. Eur Polym J 2004;40:2813–7.
- [17] Lee D, Yoon K. Polymerization of ethylene by using zirconocene catalyst anchored on silica with trisiloxane and pentamethylene spacers. Macromol Rapid Commun 1997;18:427–31.
- [18] Soga K, Shiono T, Ki HJ. Activation of SiO₂-supported zirconocene catalysts by common trialkylaluminums. Macromol Chem 1993;194(12):3499–504.
- [19] Chao C, Pratchayawutthirat W, Praserthdam P, Shiono T, Rempel GL. Copolymerization of ethylene and propylene using silicon tetrachloride-modified silica/MAO with Et[Ind]<sub>2</sub>ZrCl<sub>2</sub> metallocene catalyst. Macromol Rapid Commun 2002;23(12):672–5.
- [20] Coperet C, Chabanas M, Saint-Arroman RP, Basset JM. Homogeneous and heterogeneous catalysis: bridging the gap through surface organometallic chemistry. Angew Chem Int Ed 2003;42(2):156–81.
- [21] Jezequel M, Dufaud V, Ruiz-Garcia MJ, Carrillo-Hermosilla F, Neugebauer U, Niccolai GP, et al. Supported metallocene catalysts by surface organometallic chemistry. Am Chem Soc 2001;123:3520–40.
- [22] Campos M, Ribeiro MR, Lourenc JP, Fernandes A. Ethylene polymerisation with zirconocene supported in Al-modified MCM-41: catalytic behaviour and polymer properties. J Mol Catal A: Chem 2007;277:93–101.
- [23] Kosslick H, Lischke G, Walther G, Storek W, Martin A, Fricke R. Physico-chemical and catalytic properties of Al-, Ga- and Fesubstituted mesoporous materials related to MCM-4. Micropor Mater 1997:9:13–33.
- [24] Rahiala H, Beurroies I, Eklund T, Hakala K, Gougeon R, Trens P, et al. Preparation and characterization of MCM-41 supported metallocene catalysts for olefin polymerization. J Catal 1999;188(1):14–23.
- [25] Campos JM, Lourenc JP, Fernandes A, Rego AM, Ribeiro MR. Mesoporous Ga-MCM-41 as support for metallocene catalysts: acidity-activity relationship. J Mol Catal A: Chem 2009;310:1–8.
- [26] Wannaborworn M, Jongsomjit B. Ethylene/1-octene copolymerization over Ga-modified SiO2-supported zirconocene/ MMAO catalyst using in situ and ex situ impregnation methods. Iran Polym J 2009;18:969–79.

- [27] Kaivalchatchawal P, Praserthdam P, Sogo Y, Cai Z, Shiono T, Jongsomjit B. The influence of t-butyl and cyclododecyl substitution on ethylene/1-hexene copolymerization using ansa-fluorenylamidodimethyltitanium derivatives. Molecules 2011;16:4122–30.
- [28] Cai Z, Ikeda T, Akita M, Shiono T. Substituent effects of tert-butyl groups on fluorenyl ligand in syndiospecific living polymerization of propylene with ansa fluorenylamidodimethyltitanium complex. Macromolecules 2005;38(20):8135–9.
- [29] Galland G, Seferin M, Mauler RS, Santos JHZ. Linear low-density polyethylene synthesis promoted by homogeneous and supported catalysts. Polym Int 1999;48(8):660–4.
- [30] Pothirat T, Jongsomjit B, Praserthdam P. A comparative study of SiO<sub>2</sub>- and ZrO<sub>2</sub>-supported zirconocene/MAO catalysts on ethylene/1-olefin copolymerization. Catal Commun 2008;9:1426–31.
- [31] Wongwaiwattanakul P, Jongsomjit B. Copolymerization of ethylene/ 1-octene via different pore sized silica-based-supported zirconocene/dMMAO catalysts. Catal Commun 2008;10:118–22.

- [32] Severn JR, Chadwick JC, Duchateau R, Friderichs N. Bound but not gagged, immobilizing single-Site-olefin polymerization catalysts. Chem Rev 2005;105:4073–147.
- [33] Fereres M, Koch T, Hawkins E, Eisen M. Synthesis and olefin polymerization using supported and non-supported geometry constrained titanium complexes. J Organomet Chem 1999;580:145–55.
- [34] Chaichana E, Khaubunsongserm S, Praserthdam P, Jongsomjit B. Effect of Ga modification on different pore size silicas in synthesis of LLDPE by copolymerization of ethylene and 1-hexene with [t-BuNSiMe<sub>2</sub>Flu]TiMe<sub>2</sub>/MMAO catalyst. Polym Bull 2011;48:1301–12.
- [35] Desharun C, Jongsomjit B, Praserthdam P. Study of LLDPE/alumina nanocomposites synthesized by in situ polymerization with zirconocene/d-MMAO catalyst. Catal Commun 2008;9:522–8.
- [36] Eric T, Randall C. Monomer sequence distributions in ethylene-1-hexene copolymers. Macromolecules 1986;15:1402–11.

## ARTICLE IN PRESS

Journal of Industrial and Engineering Chemistry xxx (2012) xxx-xxx



Contents lists available at SciVerse ScienceDirect

## Journal of Industrial and Engineering Chemistry

journal homepage: www.elsevier.com/locate/jiec



## Observation on inhibition of Ti<sup>3+</sup> reduction by fumed silica addition in Ziegler-Natta catalyst with *in situ* ESR

Jirawat Pinyocheep <sup>a</sup>, Sirachaya Kunjara Na Ayudhya <sup>b</sup>, Bunjerd Jongsomjit <sup>a,\*</sup>, Piyasan Praserthdam <sup>a</sup>

#### ARTICLE INFO

Article history: Received 9 March 2012 Accepted 24 April 2012 Available online xxx

Keywords: Ziegler-Natta Polyethylene Fumed silica Molecular weight Oxidation state

#### ABSTRACT

This study focused on elucidation of effect of fumed silica added in the commercial Ziegler-Natta catalysts by physical solid-solid stirring. The added fumed silica seemed to cover around the catalyst revealed by SEM-EDX and apparently resulted in decreased activity of ethylene polymerization, but increased molecular weight of polyethylene as measured by GPC. Based on the *in situ* ESR measurement, it can be concluded that fumed silica can inhibit the reduction of Ti<sup>3+</sup> by triethylaluminum (TEA). It is suggested that the delay reduction of Ti<sup>3+</sup> may be beneficial for propylene polymerization.

© 2012 The Korean Society of Industrial and Engineering Chemistry. Published by Elsevier B.V. All rights

#### 1. Introduction

More than fifty years, many researchers have enormously considered on the Ziegler-Natta catalysts both in academic and industrial viewpoints. Polyethylene has been used widely in many applications such as high strength fabricated structure. Each application has to be produced with particular catalysts and conditions. Silica is known as a support material that provides an advantage on the polymer morphology, but it causes to lose in the catalytic activity [1-5] due to silanol groups (i.e. SiOH) on the silica surface [3-7]. In order to remove the OH group on the surface, silica has usually been calcined at different temperatures between 110 and 820 °C [1-9]. Although the silanol groups of the silica have been exerted with high calcination temperature, the experimental evidences showed that the high calcination temperature still cannot get rid of all the OH groups [4,6,8,10,11]. Another method is to functionalize it with some substance such as alkyl silyl, alkyl silyl halide or alkyl aluminum to change the silanol groups into the other forms [1-4,6,7,10,12]. Although the activity has lost, the catalyst produced from mixed supports with silica (i.e. magnesium-silica bisupport) tends to affect not only on morphology, but also on the properties of the polymer such as rheological properties afforded by functional groups on the silica surface [1,2].

As in the industrial field of production of high density polyethylene, the commercial Ziegler-Natta catalyst produced from the adduct method with anhydrous magnesium chloride support gives an excellent catalytic activity in the acceptable variation of polymer properties of specific grades for end-use applications. Synthesis of a new catalyst such as bi-supported catalyst may lead to a huge investment due to the need of many manufacturing units. To utilize the advantage and benefit of the commercial catalyst, fumed silica has been considered to be the solid substance interacted at the commercial catalyst surface to control the polymer properties. Fumed silica was able to provide extreme amounts of contact surface bound to another material due to its high surface area.

In this study, fumed silica was used as a hypothetical catalytic controllable material to change the catalytic properties of the commercial Ziegler-Natta catalyst. The effect of fumed silica, which was added physically by solid-solid stirring, on the properties of polyethylene obtained was also investigated. Moreover, to elucidate the role of fumed silica on the reduction of Ti<sup>4+</sup>, the *in situ* electron spin resonance (ESR) was performed successfully. More details are further discussed.

#### 2. Experimental

#### 2.1. Materials

Purified argon gas (99.999%), commercial polymerization grade ethylene gas and hydrogen gas were purchased from Thai

<sup>&</sup>lt;sup>a</sup> Center of Excellence on Catalysis and Catalytic Reaction Engineering, Department of Chemical Engineering, Faculty of Engineering, Chulalongkorn University, Bangkok 10330, Thailand

<sup>&</sup>lt;sup>b</sup> SCG Chemicals Co., Ltd., Bangkok 10800, Thailand

<sup>\*</sup> Corresponding author. Fax: +66 2 2186877. E-mail address: bunjerd.j@chula.ac.th (B. Jongsomjit).

## ARTICLE IN PRESS

J. Pinyocheep et al./Journal of Industrial and Engineering Chemistry xxx (2012) xxx-xxx

Industrial Gas Co., Ltd. The commercial catalyst was a Ziegler-Natta titanium-magnesium based catalyst for ethylene polymerization. Fumed silica purchased from Sigma was non-porous type with surface area of  $390 \pm 40 \text{ m}^2/\text{g}$  and its primary particle size was 7 nm as reported by Cabot Corporation. Hexane, triethylaluminum (TEA) and fumed silica were operated under an argon atmosphere via a glove box, glove bags and Schlenk techniques.

#### 2.2. Silica calcination

In order to keep the original OH group on surface, fumed silica was calcined at  $150\,^{\circ}\text{C}$  for intend to only remove physical adsorbed water from the surface. The calcination was performed under argon atmosphere.

#### 2.3. Polymerization

The ethylene polymerization was carried out with 2 l autoclave reactor connected with the lines available for argon, hydrogen and ethylene gases and also the hexane feed line. The reactor and all connected feed lines were cleared humid and oxygen by evacuation, and then followed by purging with the argon many times. First, 1 l of hexane was filled and heated to 80 °C. The desired amount of catalyst was stirred with 0, 10, 20, and 60 wt% with fumed silica in hexane solvent for 15 min. Then, TEA of 1 mmol was injected into the reactor subsequence by the stirred catalyst with 0.003 mmolTi. In the condition with the presence of hydrogen, the reactor was pressurized with 1 bar of argon followed by pressurizing with hydrogen gas to 3.5 bars and finally pressurizing with ethylene gas to 8 bars. In addition, the partial pressure of the gases is 1, 2.5 and 4.5 bars. The catalysts were named as ZNOOS, ZN10S, ZN20S, and ZN60S for stirring with 0, 10, 20, and 60% of fumed silica, respectively.

#### 2.4. Characterization

The catalysts were characterized with different techniques to investigate the reasonable model. Electron spin resonance (ESR) was performed to measure changes of Ti oxidation state after activation by TEA. The molecular weights (Mw) and molecular weight distribution (MWD) of polymer were measured by gel permeation chromatography (GPC). Details are as follows;

#### 2.4.1. In situ ESR

The extent of Ti<sup>3+</sup> content of the catalyst stirred with various amounts of fumed silica was observed by the *in situ* ESR technique. The ESR equipment used is JEOL model JES-RE2X filled with argon atmosphere. DPPH standard was used for *g*-factor calibration. First, the catalyst was stirred with fumed silica in hexane for 15 min in glove box. After activation by TEA, the sample was measured by ESR starting at room temperature (25 °C). In order to evaluate the extent of Ti<sup>3+</sup> at the polymerization temperature (80 °C), the catalyst sample was heated to 80 °C and held for 90 min for ESR measurement. The ESR spectrum was collected every 15 min from the beginning until 90 min.

#### 2.4.2. GPC

A high temperature GPC (Waters 150-C) equipped with a viscometric detector was used to determine the molecular weight and molecular weight distribution of the polymers. 1, 2, 4-trichlorobenzene was used as a solvent and the temperature was performed at  $140\,^{\circ}$ C.

#### 2.4.3. SEM-EDX

The external surface of the catalysts and their morphologies were obviously revealed by scanning electron microscopy

 Table 1

 Activities of catalyst and molecular weight of polymer.

Sample	Activity (kgPE/molTi/h)	Mn (kg/mol)	Mw (kg/mol)	MWD
ZN00S	25,043	24	122	5.1
ZN10S	21,335	28	175	6.2
ZN20S	16,120	29	170	5.9
ZN60S	13,230	31	155	5.0

technique with a JEOL model S-3400 and the elemental distributions were also observed by energy dispersive X-ray spectroscopy by EDAX device. The polymer samples for SEM analysis were coated with platinum particles by ion sputtering device to provide electrical contact to the specimen. The samples were performed with overflowing of argon gas to reduce oxygen and moisture toward the catalysts.

#### 3. Results and discussion

Activities of the catalysts stirred with various amounts of fumed silica along with Mw, MWD obtained from GPC are shown in Table 1. The results show that when the amount of fumed silica increased the activities decreased. The molecular weight of polymer tended to increased with fumed silica addition, whereas only slight change in MWD was observed.

In addition, the GPC profiles are also shown in Fig. 1 indicating that they shift to a higher molecular weight position with fumed silica addition along with slightly broader MWD up to ZN20S.

It is well known that the change in activities of ZN catalysts must be related to the Ti oxidation state during polymerization. Based on the results as mentioned above, the addition of fumed silica apparently decreased the catalytic activity during polymerization. Thus, the addition of fumed silica may alter the Ti oxidation state during polymerization. In order to elucidate the effect of fumed silica, the in situ ESR measurement was performed. ESR is one of the most powerful techniques used to measure the oxidation of Ti<sup>3+</sup>, especially upon the in situ condition [13]. In this measurement, the catalyst samples having different amounts of fumed silica added were activated by TEA based on polymerization condition. Then, the extent of the Ti<sup>3+</sup> extent during reduction by TEA for each sample was observed. The ESR results for ZN00S, ZN20S, and ZN60S samples are shown in Fig. 2. For all samples, there are three peaks located at g values equal to 1.985, 1.97, and 1.94 in each spectrum. The different g values refers to the various types of Ti<sup>3+</sup> coordination. For instance, the g values of 1.97 and 1.985 are assigned to the tetrahedral coordination of Ti<sup>3+</sup> [14– 16] and the g value of 1.94 refers to the six-coordinated Ti<sup>3+</sup> dissolved in MgCl<sub>2</sub> [14] or to isolated octahedral coordinated Ti<sup>3+</sup> [15]. It is evident that peak areas between the g values of 1.985 and

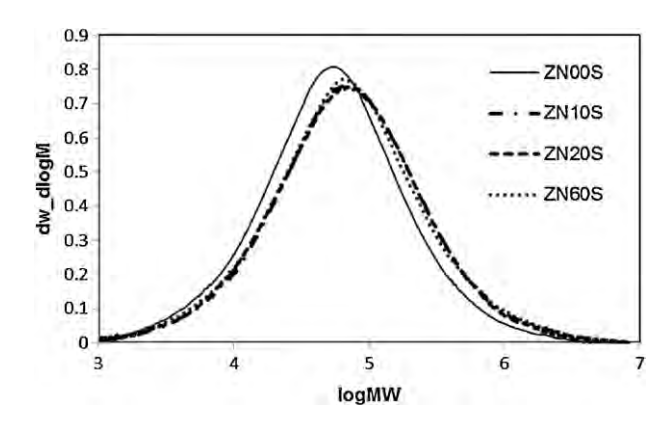


Fig. 1. The GPC profiles of polymers obtained from different catalysts.

Please cite this article in press as: J. Pinyocheep, et al., J. Ind. Eng. Chem. (2012), http://dx.doi.org/10.1016/j.jiec.2012.04.018

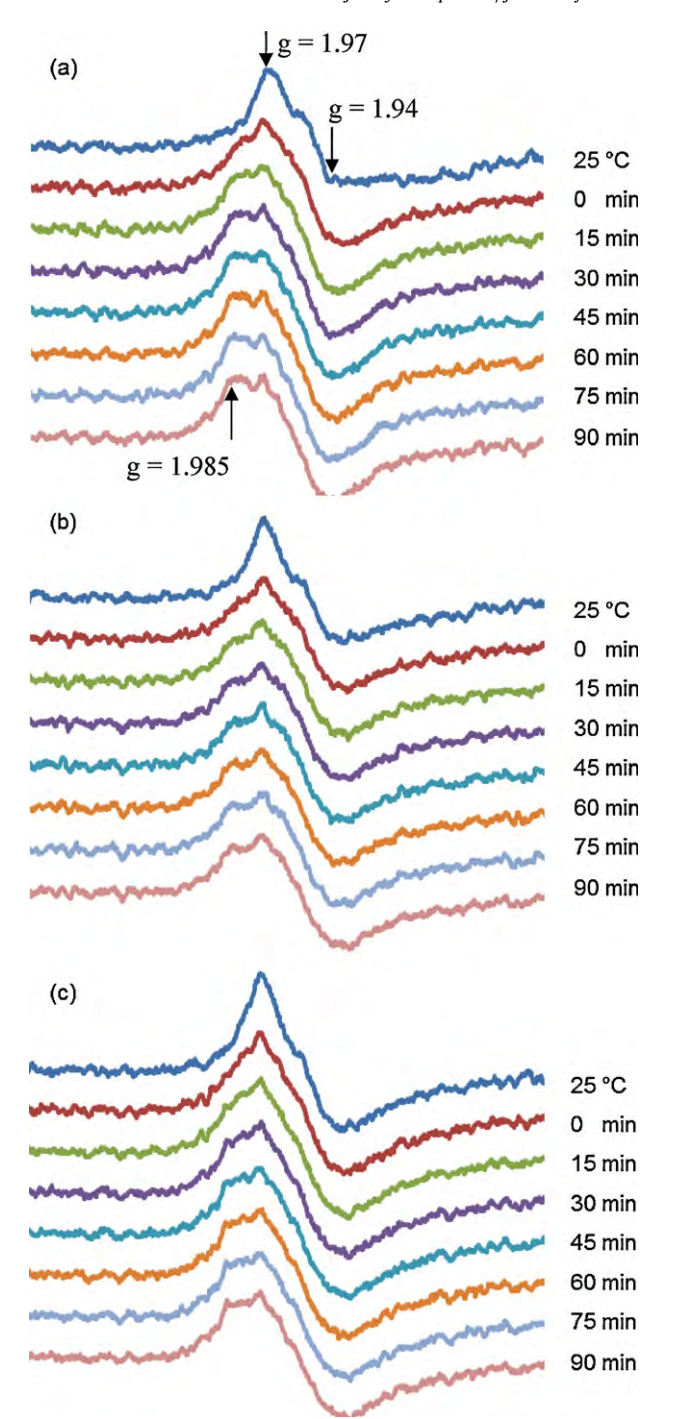


Fig. 2. The ESR spectra of the catalyst; (a) ZN00S, (b) ZN20S and (c) ZN60S.

1.97 are altered by different amounts of fumed silica added. On the other hand, intensity of the peakes at g values of 1.985, 1.94 increased with addition of fumed silica.

From the ESR spectra, it revealed that the catalyst stirred with fumed silica contributed to the inhibition of change in  ${\rm Ti}^{3+}$  extent. The spectra were taken double integration in order to measure the amounts of  ${\rm Ti}^{3+}$  absorbance upon each interval time. The integrated areas are plotted in terms of relative area related to the beginning of 80 °C as shown in Fig. 3.

As seen in Fig. 3, the relative areas for catalyst having fumed silica up to 20% apparently resulted in the less change of  ${\rm Ti}^{3+}$  amounts. This indicates that fumed silica may act as a buffer which inhibits the reducing power of TEA to reduce  ${\rm Ti}^{4+}$  to  ${\rm Ti}^{3+}$ , and  ${\rm Ti}^{3+}$  to

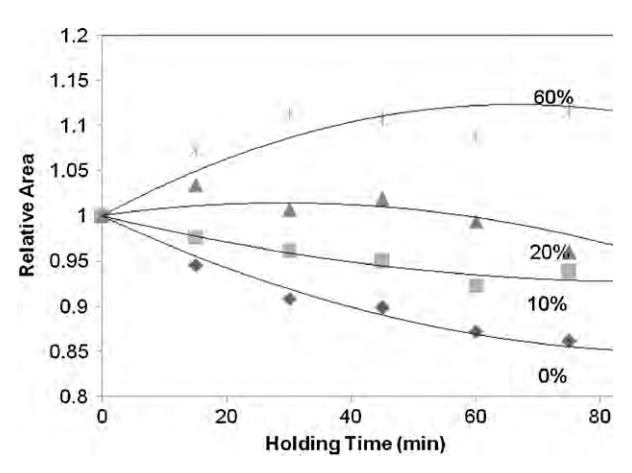
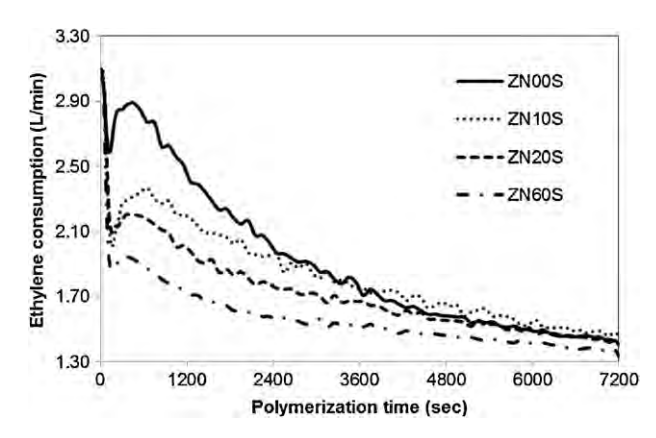


Fig. 3. The relative amount of Ti<sup>3+</sup> at 80 °C.

Ti<sup>2+</sup>. Thus, the amounts of Ti<sup>3+</sup> decreased with time. For such the phenomenon, the slope of 0% of fumed silica added exhibits the highest rate of decreased Ti<sup>3+</sup> upon time, while the addition of 10% and 20% of fumed silica lowers the rate of decreased Ti<sup>3+</sup> upon time. It should be noted that with 60% of fumed silica added, Ti<sup>3+</sup> increased due to the reduction of Ti<sup>4+</sup> to Ti<sup>3+</sup> (not Ti<sup>3+</sup> to Ti<sup>2+</sup> as mentioned before). It is suggested that fumed silica can be adsorbed on the catalyst particles and inhibit the reduction of Ti<sup>3+</sup> by TEA. As the result, the activity of ethylene polymerization decreased with silica addition as seen in Fig. 4 due to Ti<sup>3+</sup> is less active than Ti<sup>2+</sup> for ethylene polymerization [17]. It should be mentioned that the catalysts with silica showed much lower rate



**Fig. 4.** Ethylene consumption profiles of the catalyst stirred with various amounts of fumed silica.

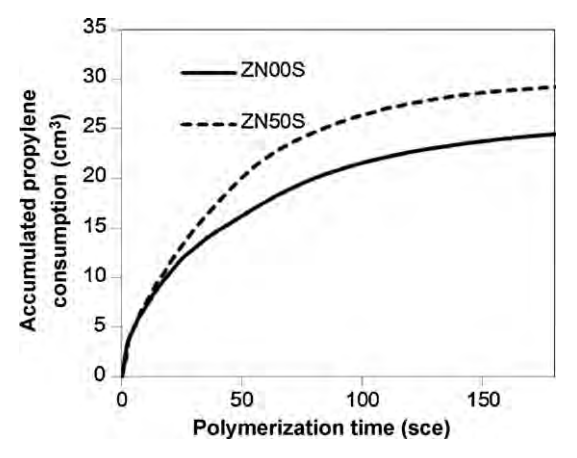


Fig. 5. Effect of fumed silica added on propylene polymerization.

J. Pinyocheep et al./Journal of Industrial and Engineering Chemistry xxx (2012) xxx-xxx

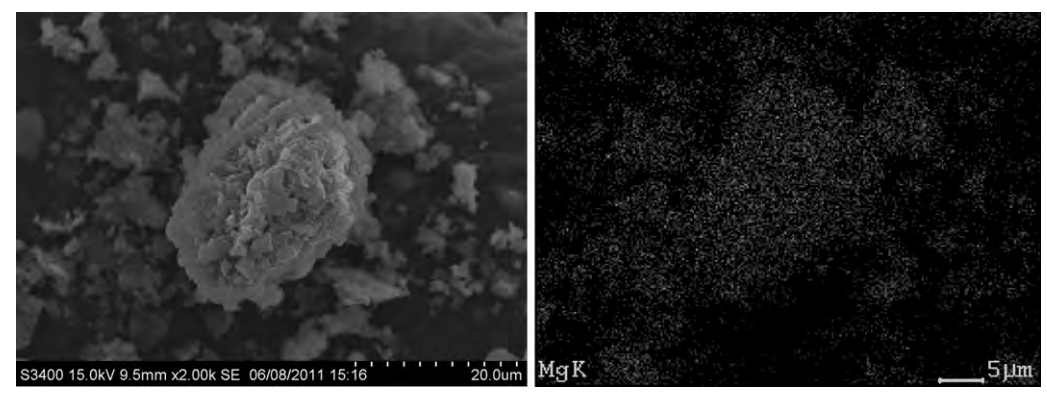


Fig. 6. SEM/EDX of the original commercial catalyst.

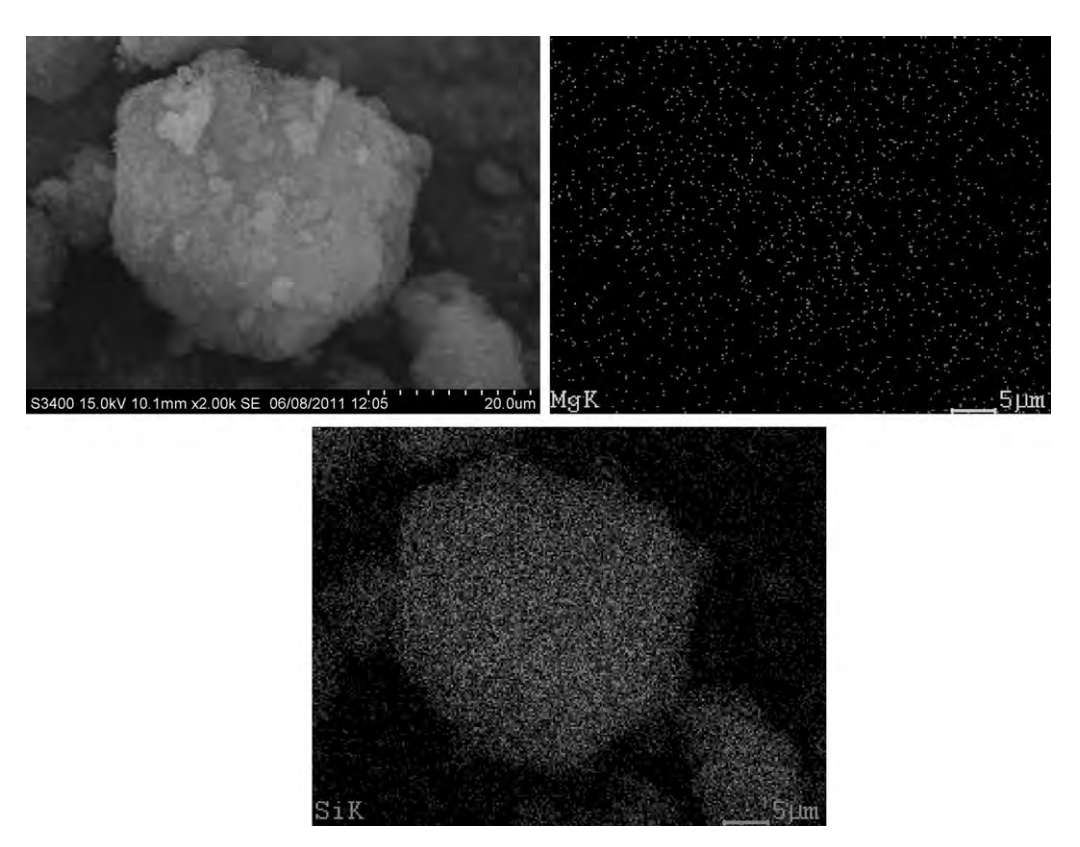


Fig. 7. SEM/EDX of the commercial catalyst stirred with fumed silica.

than the original catalyst in the first hour of reaction, but the rates in the second hour are almost the same for all the catalysts. This phenomenon may reflect the different stability of active centers from Ti<sup>2+</sup> and Ti<sup>3+</sup> species as also seen from the ESR results. The slower interaction between catalyst and cocatalyst also contributed to the decrease in polymer chain termination reactions by cocatalyst [18] which results in higher molecular weight polymer.

The other way to trace the increased amounts of Ti<sup>3+</sup> is to perform propylene polymerization. It is well known that propylene polymerization is only active with Ti<sup>3+</sup> [19,20]. Thus, propylene polymerization was also performed using ZN00S and ZN50S samples as shown in Fig. 5. It can be observed that activity of propylene polymerization increased (*ca.* 19%) with fumed silica added indicating more amounts of Ti<sup>3+</sup> present.

The elemental distributions on the catalyst surface were performed by SEM/EDX. The results revealed that the catalyst was covered by fumed silica which made most of magnesium

element disappeared from the catalyst surface as shown in Figs. 6 and 7.

#### 4. Conclusions

The main objective of this research is to use fumed silica for improvement of the commercial Ziegler-Natta catalyst. It was found that the fumed silica added to the catalyst by physical stirring affected on the catalyst covered around by fumed silica resulted in decreased activity for ethylene polymerization, but increased molecular weight and only slightly increased MWD. The significant finding is to elucidate the effect of fumed silica using the *in situ* ESR measurement. It is evident that fumed silica can inhibit the reduction of Ti<sup>3+</sup> to Ti<sup>2+</sup> resulting in decreased ethylene polymerization activity. In contrast, the activity of propylene polymerization remarkably increased.

## ARTICLE IN PRESS

J. Pinyocheep et al./Journal of Industrial and Engineering Chemistry xxx (2012) xxx-xxx

Acknowledgments

The authors thank the Thailand Research Fund (TRF), Office of the Higher Education Commission (CHE) and SCG Chemicals Co., Ltd. for the financial support of this project.

#### References

- [1] L.L. Bohm, Angewandte Chemie International Edition 42 (2003) 5010.
- [2] N. Senso, B. Jongsomjit, P. Praserthdam, Molecules 16 (2011) 1323.
- [3] T.J. Pullukat, R.E. Hoff, Catalysis Review 41 (1999) 389.
- [4] M. Vakili, H. Arabi, H.S. Mobarakeh, M. Ghafelebashi, Journal of Applied Polymer Science 118 (2010) 2216.
- [5] M.A. Apecetche, P.A. Cao, M.D. Awe, A.M. Schoeb-Wolters, R.W. Impelman, US 0265402 A1 (2007).
- [6] T. Garoff, M. Vaananen, A. Root, M. Stalhammar, K. Pesonen, European Polymer Journal 43 (2007) 5055.

- [7] H. Luo, R. Tang, K. Gao, Journal of Catalysis 210 (2002) 328.
- [8] S. Haukka, E. Lakomaa, A. Root, Journal of Physical Chemistry 97 (1993) 5085.
- [9] S. Haukk, E. Lakomaa, O. Jylha, J. Vilhunen, S. Hornytzkyj, Langmuir 9 (1993) 3497.
   [10] K. Schrijnemakers, P. Van Der Voort, E.F. Vansant, Physical Chemistry Chemical Physics 1 (1999) 2569.
- [11] E. Van Grieken, A. Carrero, I. Suarez, B. Paredes, European Polymer Journal 43 (2007) 1267.
- [12] V.N. Panchenko, V.A. Pozimenko, E.A. Paukshtis, V.A. Zakharov, Russian Journal of Inorganic Chemistry 54 (2009) 1798.
- [13] K. Tangjituabun, B. Jongsomjit, P. Praserthdam, Catalysis Letters 109 (2006) 147.
- [14] P. Brant, A.N. Speca, Macromolecules 20 (1987) 2740.
- [15] V.A. Poluboyarov, V.F. Anufrienko, V.A. Zakharov, S.A. Sergeev, S.I. Makhtarulin, G.D. Bukatov, Reaction Kinetics and Catalysis Letters 26 (1984) 347.
- [16] K. Chu, H. Chang, S. Ihm, European Polymer Journal 30 (1994) 1467.
- [17] D.B. Ludlum, A.W. Anderson, C.E. Ashby, Journal of the American Chemical Society 80 (1957) 1380.
- [18] U. Zucchini, G. Cecchin, Advances in Polymer Science 51 (1983) 101.
- [19] N. Kashiwa, J. Yoshitake, Macromolecular Chemistry and Physics 85 (1984) 1133.
- [20] K. Soga, M. Terano, Polymer Bulletin 4 (1981) 39.

5

## **AUTHOR'S PROOF**

Korean J. Chem. Eng. DOI: 10.1007/s11814-012-0094-0

## Effect of nanocrystallite size of TiO<sub>2</sub> in Co/TiO<sub>2</sub> and Co/TiO<sub>2</sub>-Ru catalysts on methanation

Kitima Pinkaew, Piyasan Praserthdam, and Bunjerd Jongsomjit<sup>†</sup>

Center of Excellence on Catalysis and Catalytic Reaction Engineering, Department of Chemical Engineering, Faculty of Engineering, Chulalongkorn University, Bangkok 10330, Thailand (Received 27 October 2011 • accepted 18 June 2012)

**Abstract**—We studied the effect of crystallite size of nanocrystalline  $TiO_2$  derived from the sol-gel method on the properties of  $Co/TiO_2$  catalysts. First, nanocrystalline  $TiO_2$  supports having different crystallite sizes were prepared via the sol-gel method by varying the water:alkoxide ratios from 4 to 165. Then, they were used as support for the cobalt catalyst. After calcination, the crystallite size of  $Co_3O_4$  was dependent on the size of  $TiO_2$  support. CO hydrogenation under methanation was performed to determine the activity and selectivity of  $Co/TiO_2$  catalysts. It revealed that the catalyst with smaller size of  $TiO_2$  crystallite exhibited higher catalytic activity due to higher Co dispersion without significant change in product selectivity. In addition, the Ru modification on the  $TiO_2$  support was also investigated. The Ru modification resulted in increased activity regardless of the size of  $TiO_2$  crystallite.

Key words: Nanocrystalline TiO2, Sol-gel, Cobalt Catalyst, Methanation, CO Hydrogenation

#### INTRODUCTION

Fischer-Tropsch (FT) synthesis has been successfully used for future alternative resources instead of coal or crude oil. There are many active metals, such as Ru, Fe, Co, and Pd that can be used for hydrogenation of carbon monoxide (CO) to petroleum wax. For example, cobalt and iron are used for hydrocarbon synthesis. Even though the cobalt catalysts are more expensive, they are more resistant to deactivation than iron metals [1]. Supported cobalt catalysts have been extensively investigated with many inorganic supports for years, such as  $SiO_2$  [2],  $Al_2O_3$  [3],  $TiO_2$  [4]. They have been the most popular FT catalysts for years due to their high catalytic activity and selectivity [5,6]. CO and H<sub>2</sub> (syngas) have been converted to paraffinic or long chain hydrocarbon through hydrogenation reaction. In fact, the interaction between cobalt oxide species and supports plays an important role in dispersion of cobalt oxide species [7]. The addition of small amount of noble metals apparently improves the catalytic properties [7-9]. For instance, the promotion with Ru in the supported cobalt catalysts also enhances the turnover rate and Co site density during reaction, as reported by Iglesia et al. [10].

Due to the significant developments in nanoscience and nanotechnology over recent years, many inorganic nanomaterials have been captivating the research in heterogeneous catalysis area. These inorganic nanomaterials can be potentially used as catalysts in some specified reactions, as supports for the catalytic phase, and also as nanofillers in composite materials. This can be attributed to their unique properties, great thermal and mechanical stability. In the present work, nanocrystalline TiO<sub>2</sub> having different crystallite sizes was prepared via the sol-gel method and used as the support for Co catalysts. In fact, the crystallite size of TiO<sub>2</sub> can be controlled by varying the water: alkoxide ratios during sol-gel synthesis. Thus, the effect

of crystallite size of the TiO<sub>2</sub> support on the properties of Co catalysts can be elucidated. The characteristics of different supports and catalysts were determined by means of several techniques, such as XRD, SEM/EDX, TEM, TPR, CO chemisorption, and XPS. The activity and product selectivity of catalysts were measured via CO hydrogenation under methanation condition to minimize the catalyst deactivation.

#### **EXPERIMENTAL**

#### 1. Preparation of Nanocrystalline TiO<sub>2</sub>

 ${
m TiO_2}$  was prepared by the sol-gel method [11,12]. First, the titania precursor [titanium (IV) isopropoxide] was dissolved in ethanol and then mixed with the solution of water:alkoxide, having molar ratios between 4 to 165 in order to obtain different crystallite sizes of  ${
m TiO_2}$ . The mixture was added dropwise to the aqueous solution with ultrasonic stirring at room temperature for 2 h. The obtained amorphous precipitates was centrifuged and redispersed in ethanol five times prior to filtration. After that, the sample was dried and calcined at  $450\,{}^{\circ}{\rm C}$  in air flow for 2 h.

#### 2. Preparation of Ru-modified Nanocrystalline TiO,

The Ru-modified TiO<sub>2</sub> support was prepared by the incipient wetness impregnation having 0.03 wt% of Ru. The desired amount of ruthenium (III) nitrosyl nitrate [Ru(NO(NO<sub>3</sub>)<sub>3</sub>)] was dissolved in deionized water, and then was dropped slowly to the TiO<sub>2</sub> support. The modified support was dried at 110 °C for 12 h and calcined in air at 500 °C for 4 h.

#### 3. Preparation of Cobalt Catalysts

A 20 wt% of Co metal was impregnated onto the  $TiO_2$  supports according to sections 1 and 2 using cobalt nitrate  $[Co(NO_3)_2 \cdot 6H_2O]$  as the precursor. The sample was dried at  $110\,^{\circ}C$  for  $12\,h$  and calcined in air at  $500\,^{\circ}C$  for 4 h to convert all cobalt nitrate precursors into Co oxide species [13].

The nomenclature used for the catalyst samples in this study is

<sup>&</sup>lt;sup>†</sup>To whom correspondence should be addressed. E-mail: bunjerd.j@chula.ac.th

2 K. Pinkaew et al.

as follows:

- Co/TiO<sub>2</sub>\_xx nm
- Co/TiO<sub>2</sub>\_xx nm\_Ru

 $\text{Co/TiO}_2$ \_xx nm refers to  $\text{Co/TiO}_2$  catalyst with  $\text{TiO}_2$  having the crystallite size of xx nm.

Co/TiO<sub>2</sub>\_xx nm\_Ru refers to the Co/TiO<sub>2</sub> catalyst with TiO<sub>2</sub> having the crystallite size of xx nm with Ru modification on TiO<sub>2</sub> as mentioned in section 2.

#### 4. Methanation

CO hydrogenation ( $H_2/CO=10/1$ ) under methanation condition was performed to determine the overall activity of the samples. Hydrogenation of CO was carried out at 220 °C and 1 atm. A flow rate of  $H_2/CO/Ar=20/2/8$  cm³/min in a fixed-bed flow reactor was used. A relatively high  $H_2/CO$  ratio was used to minimize deactivation due to carbon deposition during reaction. Typically, 10 mg of a sample was reduced *in situ* in flowing  $H_2$  (30 cm³/min) at 350 °C for 10 h prior to the reaction. Reactor effluent samples were taken at 30-min intervals and analyzed by GC. Thermal conductivity detector (TCD) with molecular sieve 5A was used to detect the CO. A flame ionization detector (FID) with a VZ-10 column was used to detect the light hydrocarbons, such as  $C_1$ - $C_4$  hydrocarbons. In all cases, steady-state was reached within 5 h.

#### 5. Characterization of Supports and Catalysts

#### 5-1. N<sub>2</sub> Physisorption

The surface area was determined by physisorption of nitrogen  $(N_2)$  using a Micromeritics Pulse Chemisorb 2700 system. It was calculated based on nitrogen uptake at liquid-nitrogen temperature (77 K) using the Brunauer-Emmett-Teller (BET) equation by the single point method.

#### 5-2. X-ray Diffraction

XRD was performed to determine the bulk crystalline phases of the sample. It was conducted using a SIEMENS D-5000 X-ray diffractometer with Cu  $K_{\alpha}$  ( $\lambda$ =1.54439 Å). The spectra were scanned at a rate of 2.4°/min in the range  $2\theta$ =20-80°.

5-3. Scanning Electron Microscopy and Energy Dispersive X-ray Spectroscopy

SEM and EDX were used to determine the catalyst morphologies and elemental distribution throughout the sample granules, respectively. SEM involved a JEOLmodel JSM-5800LV. EDX was performed using Link Isis series 300 program.

#### 5-4. Transmission Electron Microscopy

TEM was used to determine the dispersion of cobalt oxide species using JEOL-TEM 200CX transmission electron spectroscopy operated at  $100\,\mathrm{kV}$  with  $50\,\mathrm{k}$  magnification. The sample was dispersed in ethanol to obtain the uniform dispersion of sample prior to the measurement.

#### 5-5. Temperature-programmed Reduction

TPR was used to determine the reduction behaviors of the samples. It was carried out using 50 mg of a sample and a temperature ramp from 35 to 800  $^{\circ}$ C at 5  $^{\circ}$ C/min. The carrier gas was 10%  $H_2$  in Ar. A cold trap was placed before the detector to remove water produced during the reaction.

#### 5-6. X-ray Photoelectron Spectroscopy

XPS was used to examine the binding energy and the surface composition of the catalysts by using an AMICUS spectrometer with X-ray source of Mg  $K_{\alpha}$  radiation operated at voltage of 20 kV, current of 10 mA using the AMICUS "VISION2" software.

#### 5-7. CO Chemisorption

The active sites and the relative percentages dispersion of cobalt catalyst were determined by CO-pulse chemisorption technique using Micromeritics ChemiSorb 2750 (pulse chemisorption system) and ASAP 2101C V.3.00 software. 20 mg of a sample was used and reduced in  $\rm H_2$  flow rate at 50 ml/min with heating from room temperature to 350 °C at rate 10 °C/min and held at this temperature for 3 h after being cooled to room temperature in He flow. Gas volumetric chemisorption at 100 °C was performed. Desorbed CO was measured with a thermal conductivity detector. Pulsing was continued until no further carbon monoxide adsorption was observed.

#### RESULTS AND DISCUSSION

#### 1. Characteristics

First, the crystallite size of the sol-gel derived  $\text{TiO}_2$  was varied by changing the water:alkoxide molar ratios (3 values from 4, 40, and 165) during the synthesis. In this sol-gel process, the reaction between the alkoxide precursor and the desired amount of water occurred in an anhydrous alcohol medium. The hydrolysis and condensation reactions can be summarized as follows [14]:

Hydrolysis: 
$$Ti(OC_3H_7)_4+4H_2O \rightarrow Ti(OH)_4+4C_3H_7OH$$
 (1)

Condensation: 
$$Ti(OH)_4 \rightarrow TiO_2 + 2H_2O$$
 (2)

Net reaction: 
$$Ti(OC_3H_7)_4+2H_2O \rightarrow TiO_2+4C_3H_7OH$$
 (3)

As seen from the net reaction (3), the nucleation rate of TiO<sub>2</sub> increases with increasing the water:alkoxide ratios. As a result, the crystallite size and nanoparticle size should decrease with increasing the water:alkoxide ratios [15]. After calcination, the obtained TiO<sub>2</sub> supports were characterized using XRD and N<sub>2</sub> physisorption. All samples exhibited similar XRD patterns (not shown) at 26° (major), 37°, 48°, 55°, 56°, 62°, 69°, 71°, and 75° assigned to TiO<sub>2</sub> in the anatase phase. The crystallite sizes of TiO2 were calculated based on the XRD line broadening using the Scherrer equation [16]. The crystallite sizes of TiO<sub>2</sub> were in the range of 11, 13 and 16 nm corresponding to the water:alkoxide ratios of 165, 40 and 4, respectively. It appeared that increased water:alkoxide molar ratio apparently resulted in decreased crystallite size of TiO<sub>2</sub> [14,15]. The BET surface areas of samples were found to be 71, 63 and 48 m<sup>2</sup>/g for TiO<sub>2</sub>\_11 nm, TiO<sub>2</sub>\_13 nm, and TiO<sub>2</sub>\_16 nm, respectively, which is usual for anatase TiO<sub>2</sub> obtained from the sol-gel method. After Ru modification of the TiO<sub>2</sub> supports, it showed only a slight decrease in surface area. No XRD peaks of Ru were detected due to its highly dispersed form.

After impregnation of Co onto the different TiO<sub>2</sub> supports as mentioned above, the catalysts were calcined and characterized using various techniques. The XRD patterns for the calcined catalyst samples without Ru modification are shown in Fig. 1. Besides the appearance of XRD patterns of the anatase TiO<sub>2</sub> as mentioned above, all calcined samples exhibited XRD peaks at 31° (weak), 36° (strong), 46° (weak), and 65° (weak), which were assigned to the presence of Co<sub>3</sub>O<sub>4</sub>. Contrarily to Co/TiO<sub>2</sub>\_16 nm, XRD patterns of Co/TiO<sub>2</sub>\_11 nm and Co/TiO<sub>2</sub>\_13 nm both present a huge background. Such a background may originate from a larger water content that would be linked to the higher water:alkoxide ratio used for these catalysts or more probably from the poor crystallinity of TiO<sub>2</sub>. However, no

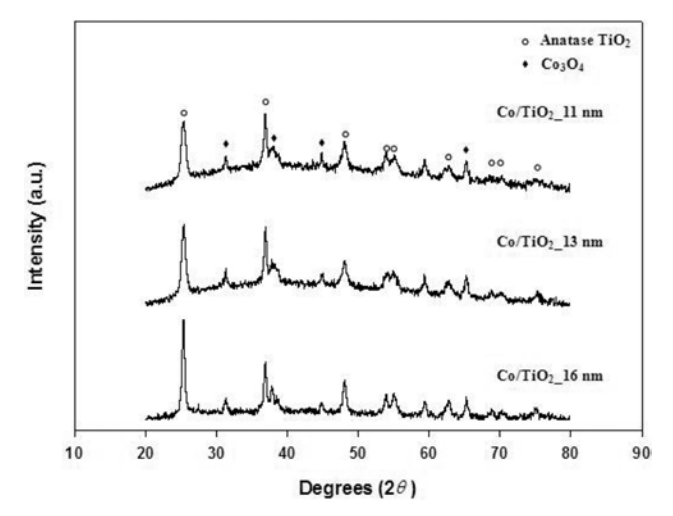


Fig. 1. XRD patterns for Co catalysts with different crystallite sizes of TiO<sub>2</sub> supports.

other forms of Co oxide species can be detected by XRD measurement. The XRD patterns for the calcined catalyst samples with Ru modification (not shown) were similar to those without Ru modification. The surface areas of the catalysts with and without Ru modification are shown in Table 1. They slightly decreased with Ru modification. It should be noted that high surface area could result in better distribution of Co, but somehow does not guarantee good dispersion as shown in our previous work [17]. The crystallite sizes of  $\text{Co}_3\text{O}_4$  are also shown in Table 1. It indicated that the Ru modification can result in decreased crystallite size of  $\text{Co}_3\text{O}_4$  on  $\text{TiO}_2$  supports. To determine the Co dispersion and active sites, CO chemisorption was performed as also listed in Table 1. Apparently, the Co dispersion increased with Ru modification on the support. This phenomenon was in agreement with our previous work [6] when Ru was co-impregnated with cobalt onto the alumina support.

The morphologies and elemental distribution of the catalyst samples were determined by using SEM and EDX, respectively. The SEM micrographs for all catalyst samples are illustrated in Fig. 2. It can be seen that the larger crystallite sizes of TiO<sub>2</sub> support can result in more agglomeration of catalyst particles. The EDX mapping for all samples (not shown) also revealed good distribution of cobalt on the support granules. To determine the dispersion of cobalt oxide species on the different TiO<sub>2</sub> supports, a more powerful technique such as TEM was applied for all samples. The TEM micro-

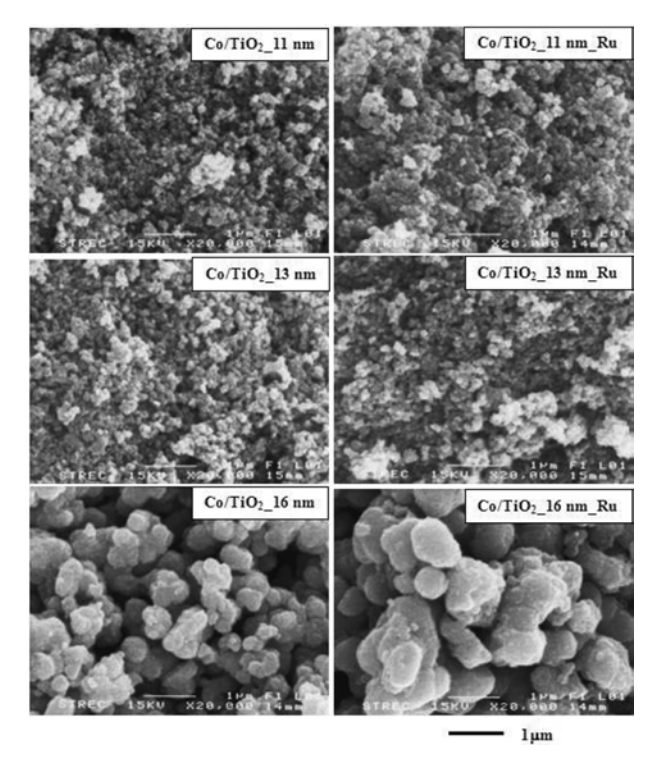


Fig. 2. SEM micrographs of Co catalysts with different crystallite sizes of TiO<sub>2</sub> supports with and without Ru modification.

graphs of all catalysts are shown in Fig. 3. The dark spots represent cobalt oxide species dispersed on the different TiO<sub>2</sub> supports. Based on TEM micrographs, the catalyst present on smaller size of TiO<sub>2</sub> crystallite exhibits better dispersion (seen as smaller patches) than the larger one. It is suggested that the dispersion of cobalt oxide species could be altered by size of the support, as mentioned in our previous work [18]. The Ru modification on TiO<sub>2</sub> supports shows a similar appearance to those without Ru modification. In addition, with the presence of the highly dispersed form of cobalt oxide species as seen for the smaller size of TiO<sub>2</sub> crystallite, the interaction of the cobalt oxides and support should be considered. Therefore, temperature-programmed reduction (TPR) on the calcined catalyst samples was performed to gain a better understanding according to such a reduction behavior.

The TPR profiles for all catalyst samples are shown in Fig. 4. The reduction of cobalt oxides to cobalt metal (Co<sup>0</sup>) was observed

Table 1. Characteristics of catalyst samples

Comples	Surface area	Crystallite size of	CO chemisorption	1
Samples	$(m^2/g)$	$\text{Co}_3\text{O}_4(\text{nm})^a$	CO chemisorption (µmole CO/g cat)	Co <sup>0</sup> dispersion <sup>b</sup> (%)
Co/TiO <sub>2</sub> _11 nm	52	11	23.1	3.5
Co/TiO <sub>2</sub> _11 nm_Ru	47	8.7	31.1	4.6
Co/TiO <sub>2</sub> _13 nm	40	14.9	21.4	3.3
Co/TiO <sub>2</sub> _13 nm_Ru	36	13.9	24.3	3.6
Co/TiO <sub>2</sub> _16 nm	11	19.5	6.7	1.0
Co/TiO <sub>2</sub> _16 nm_Ru	10	15.8	11.7	1.8

<sup>&</sup>lt;sup>a</sup>Calculated based on XRD line broadening using Scherrer Equation

<sup>&</sup>lt;sup>b</sup>Calculated based on fraction of Co<sup>0</sup> detected from CO chemisorption per Co<sup>0</sup> loading ×100

4 K. Pinkaew et al.

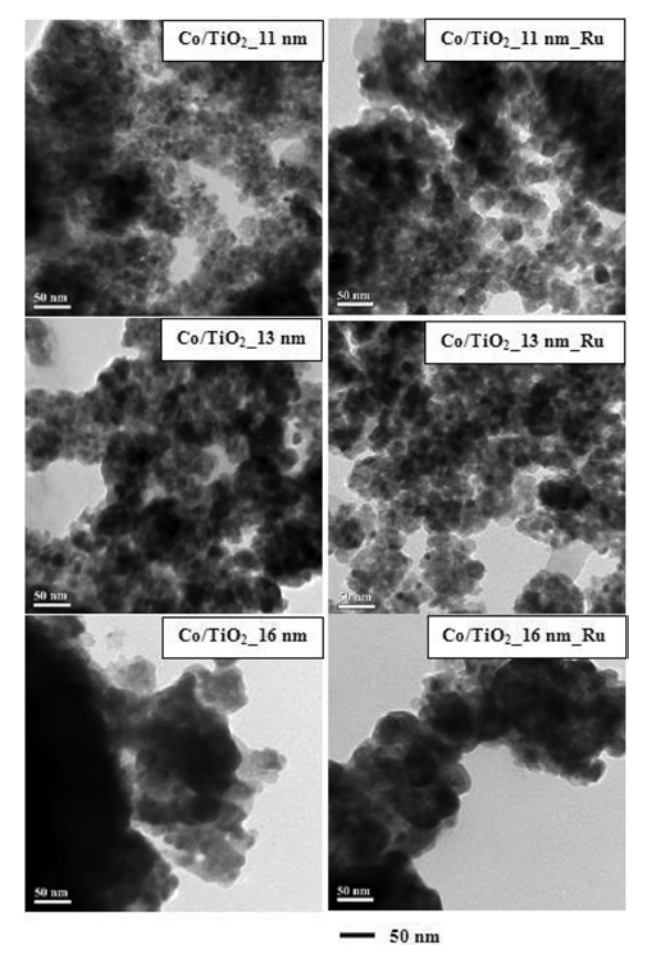


Fig. 3. TEM micrographs of Co catalysts with different crystallite sizes of TiO<sub>2</sub> supports with and without Ru modification.

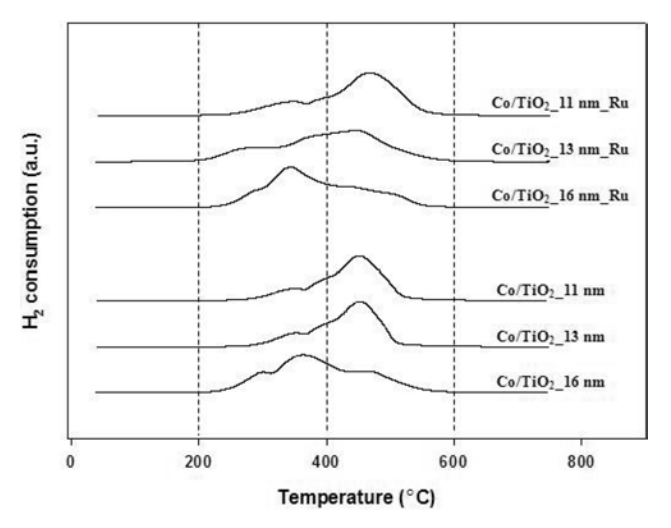


Fig. 4. TPR profiles of Co catalysts with different crystallite sizes of TiO<sub>2</sub> supports with and without Ru modification.

for all catalyst samples that occurred in a shoulder and one major peak. The lower reduction temperature shoulder peak of the unmodified catalysts was located at the 300 °C (for Co/TiO $_2$ 16 nm) and 350 °C (for Co/TiO $_2$ 11 and 13 nm). The broad peak was related to a two-step reduction of Co $_3$ O $_4$  to CoO, and then to Co metal [5,

13,18]. The Co/TiO<sub>2</sub>\_16 nm sample exhibits broader TPR peaks compared to the others. This may be due to the presence of more various Co<sub>x</sub>O<sub>y</sub> species. With Ru modification, there is also one shoulder and one major peak for the catalysts with Ru modification located at 260 and between 350 and 460 °C. It appears that the broad peak is shifted to lower temperature with Ru modification. However, this phenomenon is not clearly seen for the Co/TiO<sub>2</sub> 11 nm sample, suggesting that the Ru modification has less pronounced effect on the smaller crystallites. This indicates that Ru modification facilitates the reduction of Co catalysts. In some particular cases, the peak of the decomposition of the cobalt nitrates, as a cobalt precursor can be observed between 200 and 300 °C, especially on silica and alumina supports [6]. Prolonged calcination or reduction and recalcination resulted in complete decomposition of any cobalt nitrates present [6]. In addition, it has been often found that, due to interactions between Co<sub>3</sub>O<sub>4</sub> and support materials, such as silica or alumina, the highest temperature peak represented the incomplete reduction of Co<sub>x</sub>O<sub>y</sub> support. The TPR of supported Co<sub>3</sub>O<sub>4</sub> can also manifest a separation of the two reduction steps [6,18-20]. A lower temperature shoulder between 200 and 350 °C peaks was observed due to some possible decomposition of residual Co nitrate. The reduction of Co<sub>3</sub>O<sub>4</sub> to CoO and Co<sup>0</sup> occurred between 300 and 550 °C and can be assigned to the reduction of metal oxides on the support [6, 18-20]. The strong interaction between Co metal and support depends on the size of cobalt oxide species and nature of supports [6]. This suggested that the Ru may possibly help in the reduction of Co oxides and the support to make small crystallite size, which would decrease the Co<sup>0</sup> crystallite size. These results were in accordance with those reported by Hosseini et al. [21]. It was suggested that the use of Ru modified-TiO<sub>2</sub>\_11 nm and 13 nm supports can result in higher reduction temperature of Co oxides with larger amount of reducible cobalt oxide species.

XPS analysis was used to examine the binding energy and surface concentrations of species on the catalysts. The catalyst samples were analyzed in the Co 2p, Ti 2p, O 1s, Ru 3d with regards to the binding energy regions (not shown). The peaks of Ru 3d would be detected around 280 eV [22,23], but there was no observation of the Ru 3d due to very small amount of Ru loading. The binding energy values corresponding to Co 2p and Ti 2p were not affected by the small amount of Ru modification with the values of ca. 780 eV and 459.1 eV, respectively. These results are in accordance with those reported by Infantes-Molina et al. [22] and Reinikainen et al. [23].

#### 2. Reaction Study

The reaction study was carried out via CO hydrogenation under methanation condition in order to minimize the catalyst deactivation due to carbon deposition. The conversion, reaction rate and product selectivity for all samples are shown in Table 2. The CO conversion ranged between 32 and 91% upon different crystallite sizes of TiO<sub>2</sub> supports. Based on the reaction rates, it is obvious that the activities of catalysts decreased with increasing the size of TiO<sub>2</sub> crystallite from 11 to 16 nm due to the decrease of Co dispersion. In addition, Ru modification apparently resulted in increased activity for all different crystallite sizes of TiO<sub>2</sub> supports. However, the Ru modification had more pronounced effect on the larger crystallite size support where the conversion increased about two times. This can be attributed to the promotion of cobalt dispersion by Ru because it can facilitate the reduction of cobalt oxide species [6]. It

Table 2. Reaction study

Samples	Conversion (%)	SS rate (×10 <sup>2</sup> gCH <sub>2</sub> /	Product selectivity (%)	
	(%)	g cat·h)	$C_1$	C <sub>2</sub> -C <sub>4</sub>
Co/TiO <sub>2</sub> _11 nm	77	28.9	97	3
Co/TiO <sub>2</sub> _11 nm_Ru	91	34.1	97	3
Co/TiO <sub>2</sub> _13 nm	49	18.4	94	6
Co/TiO <sub>2</sub> _13 nm_Ru	89	33.4	99	1
Co/TiO <sub>2</sub> _16 nm	32	12.0	94	6
Co/TiO <sub>2</sub> _16 nm_Ru	77	28.9	99	1

is worth noting that Ru can be added into the Co catalyst as a promoter by coimpregnation with the cobalt precursor, such as cobalt nitrate. As a promoter for  $\text{Co/Al}_2\text{O}_3$  catalysts [6], Ru increased both overall activity and reducibility. It was suggested that the Ru promoter not only facilitates the reduction of cobalt oxide at lower temperature, but also decreases the formation of Co strongly interacting with the alumina  $(\text{Co}_x\text{O}_y\text{-Al}_2\text{O}_3)$  and nonreducible Co aluminate by minimizing the impact of water vapor on this formation. However, for Ru promotion in  $\text{Co/TiO}_2$  catalysts [24], it revealed that Ru promotion can only facilitate the reduction of cobalt oxide species, but has no effect on water vapor produced during reaction. Based on this study, it can be observed that the effects of Ru modification of  $\text{TiO}_2$  supports are similar with those of Ru promotion as mentioned earlier. It is worth noting that with Ru modification, the effect of size of  $\text{TiO}_2$  crystallite on  $\text{Co/TiO}_2$  catalysts is less pronounced.

Considering the product selectivity, in all cases methane was present as a majority product, which is typical for CO hydrogenation under methanation. Without Ru modification, the catalysts having larger crystallite size of TiO<sub>2</sub> trended to give greater amounts of longer chain hydrocarbons (C<sub>2</sub>-C<sub>4</sub>). However, the C<sub>1</sub>-C<sub>4</sub> decreased with the Ru promotion. It is known that CO hydrogenation is a kind of polymerization reaction where insertion of the -CH<sub>2</sub>- (methylene group) occurs through the active centers [25], rate of propagation, and rate of termination. Obviously, a termination of chain growth occurs and is recognized as the chain growth probability. Based on product selectivity as found here, it can be concluded that the Ru modification in TiO<sub>2</sub> supports slightly inhibited the chain growth probability. As a matter of fact, it resulted in the observation of higher methane selectivity with Ru modification.

#### **CONCLUSIONS**

Based on this study, the effect of different crystallite sizes of  $\text{TiO}_2$  supports on the catalytic properties of  $\text{Co/TiO}_2$  catalysts can be elucidated. The smaller crystallite size of  $\text{TiO}_2$  support exhibited higher catalytic activity due to higher Co dispersion. The crystallite sizes of cobalt oxide species were replicated by those of the  $\text{TiO}_2$  support. It also revealed that the Ru modification on the support apparently increased the activity of catalysts as seen when Ru was used as a promoter by coimpregnation with the cobalt precursor. However, with the Ru modification, the effect of size of  $\text{TiO}_2$  crystallite on  $\text{Co/TiO}_2$  catalyst was less pronounced. The Ru promotion can result in slightly decreased  $\text{C}_2\text{-C}_4$  hydrocarbons during methanation.

#### ACKNOWLEDGEMENT

The authors thank the Thailand Research Fund (TRF) and Office of the Higher Education Commission (CHE) for the financial support of this project.

#### REFERENCES

- A. Y. Khodakov, W. Chu and P. Fongarland, *Chem. Rev.*, **107**, 1692 (2007).
- K. Okabe, X. Li, M. Wei and H. Arakawa, *Catal. Today*, 89, 431 (2004).
- 3. A. Kogelbauer, J. G. Goodwin, Jr. and R. Oukaci, *J. Catal.*, **160**, 125 (1996)
- 4. S. J. Tauster, S. C. Fung and R. L. Garten, *J. Am. Chem. Soc.*, **100**, 170 (1978).
- 5. B. Jongsomjit and J. G. Goodwin, Jr., Catal. Today, 77, 191 (2002).
- B. Jongsomjit, J. Panpranot and J. G Goodwin Jr., *J. Catal.*, 204, 98 (2001).
- 7. S. L. Soleda, E. Iglesia, R. A. Fiatoa, J. E. Baumgartnera, H. Vromana and S. Miseoa, *Topics Catal.*, **26**, 101 (2003).
- 8. N. Tsubaki, S. Sun and K. Fujimoto, J. Catal., 199, 236 (2001).
- G Jacobs, T. K. Das, Y. Zhang, J. Li, G Racoillet and B. H. Davis, *Appl. Catal. A: Gen.*, 233, 263 (2002).
- E. Iglesia, S. L. Soled, R. A. Fiato and G. H. Via, *J. Catal.*, **143**, 345 (1993).
- K. Suriye, P. Praserthdam and B. Jongsomjit, Appl. Surf. Sci., 253, 3849 (2007).
- K. Suriye, P. Praserthdam and B. Jongsomjit, *Ind. Eng. Chem. Res.*, 44, 6599 (2005).
- 13. B. Jongsomjit, C. Sakdamnuson, J. G. Goodwin Jr. and P. Praserthdam, *Catal. Lett.*, **94**, 209 (2004).
- S. Shukla, S. Seal and R. Vanfleet, *J. Sol-Gel Sci. Technol.*, 27, 119 (2003).
- K. V. Baiju, S. Shukla, K. S. Sandhya, J. James and K. G. K. Warrier, *J. Phys. Chem. C*, **111**, 7612 (2007).
- 16. L. E. Alexander, *X-ray diffraction procedures for polycrystalline amorphous*, 2<sup>nd</sup> Ed., Wiley & Sons, New York (1974).
- 17. B. Jongsomjit, T. Wongsalee and P. Praserthdam, *Mater. Chem. Phys.*, **97**, 343 (2006).
- S. Kittiruangrayab, T. Burakorn, B. Jongsomjit and P. Praserthdam, Catal. Lett., 124, 376 (2008).
- A. Kogelbauer, J. G. Goodwin, Jr. and R. Oukaci, *J. Catal.*, **160**, 125 (1996).
- 20. J. Li, G Jacobs, Y. Zhang, T. Das and B. H. Davis, *Appl. Catal. A: Gen.*, **223**, 195 (2002).
- 21. S. A. Hosseini, A. Taeb, F. Feyzi and F. Yaripour, *Catal. Commun.*, 5, 137 (2004).
- 22. A. Infantes-Molina, J. M. Rida-Robles, E. R. Guez-Castello, J. L. G. Fierro and A. J. Nez-Lopez, *Appl. Catal. A: Gen.*, **341**, 35 (2008).
- 23. M. Reinikainen, M. K. Niemela, N. Kakuta and S. Suhonen, *Appl. Catal. A: Gen.*, **174**, 61 (1998).
- 24. B. Jongsomjit, C. Sakdamnuson, J. Panpranot and P. Praserthdam, *React. Kinet. Catal. Lett.*, **88**, 65 (2006).
- B. Jongsomjit S. Kittiruangrayub and P. Praserthdam, *Mater. Chem. Phys.*, 105, 14 (2007).

## ARTICLE IN PRESS

CHEMICAL ENGINEERING RESEARCH AND DESIGN XXX (2012) XXX-XXX



Contents lists available at SciVerse ScienceDirect

## Chemical Engineering Research and Design



journal homepage: www.elsevier.com/locate/cherd

## Integrated methane decomposition and solid oxide fuel cell for efficient electrical power generation and carbon capture

Narisra Triphob<sup>a</sup>, Suwimol Wongsakulphasatch<sup>b</sup>, Worapon Kiatkittipong<sup>b</sup>, Tawatchai Charinpanitkul<sup>c</sup>, Piyasan Praserthdam<sup>a</sup>, Suttichai Assabumrungrat<sup>a,\*</sup>

- <sup>a</sup> Center of Excellence in Catalysis and Catalytic Reaction Engineering, Department of Chemical Engineering, Faculty of Engineering, Chulalongkorn University, Bangkok 10330, Thailand
- <sup>b</sup> Department of Chemical Engineering, Faculty of Engineering and Industrial Technology, Silpakorn University, Nakhon Pathom 73000, Thailand
- <sup>c</sup> Center of Excellence in Particle Technology, Department of Chemical Engineering, Faculty of Engineering, Chulalongkorn University, Bangkok 10330, Thailand

#### ABSTRACT

This work proposes the application of methane decomposition (MD) as a fuel processor to replace methane steam reforming (MSR) for hydrogen production for a methane-fuelled solid oxide fuel cell (SOFC) system. In this work, comparison between the MD–SOFC and the MSR–SOFC was performed in terms of SOFC performances and economic analysis to demonstrate a benefit of using MD as a fuel processor. Energy analysis of SOFC system was evaluated based on thermally self-sufficient condition where no external energy is required for the system. Although the MD–SOFC system offers lower electrical efficiency than that of the MSR–SOFC as solid carbon is generated without being further combusted to generate energy; however, the MD–SOFC stack can be operated at higher power density due to high purity of hydrogen supplied to the fuel cell, resulting in smaller size of the system when compared to the MSR–SOFC. Moreover, the MD–SOFC system is less complicated than that of the MSR–SOFC as the CCS facility is not necessary to be included to reduce CO<sub>2</sub> emission. Economic analysis demonstrated that the SOFC system with MD is more competitive than the conventional system with MSR when considering the valuable by-products of solid carbon even with the low-valued carbon black. It is suggested that the success of this proposed SOFC system with MD relies on the technology development on cogeneration of hydrogen and valuable carbon products.

© 2012 The Institution of Chemical Engineers. Published by Elsevier B.V. All rights reserved.

Keywords: Solid oxide fuel cell; Hydrogen production; Methane decomposition; Energy self-sufficient operation

#### 1. Introduction

Over the past decades, the continuous growth of world economy has caused a number of problems such as shortage of energy resources, environmental problems and climate changes. Based on traditional technologies, combustion of fossil fuels has emitted a large amount of greenhouse gases to environment (Simbeck, 2004; Suelves et al., 2005; Naser and Timothy, 2007; Edwards et al., 2008; Ahmed et al., 2009). Therefore, many researchers have focused on the development of alternative energy with high-efficiency as well as environmental friendly power generation technologies (Karl and Gunter, 1995; Dicks, 1996; Coutelieris et al., 2003; Edwards et al., 2008).

Solid oxide fuel cell (SOFC) is one of promising technologies that directly transforms chemical energy of a fuel into electrical energy with high efficiency and reduced environmental burden (Karl and Gunter, 1995; Poirer and Sapundzhiev, 1997; Martin and Ralph, 2003; Ahmad Hajimolana et al., 2012; Laguna-Bercero, 2012). A variety of fuels (e.g., alcohol, natural gas, coal and petroleum based substance) can be used in SOFC systems due to their high operating temperature range (873–1273 K) (Stambouli and Traversa, 2002; Assabumrungrat et al., 2005; Hernadez-Pacheco et al., 2005; Hussain et al., 2006; Naser and Timothy, 2007; Douvartzides et al., 2003; Sangtongkitcharoen et al., 2008; Piroonlerkgul et al., 2008, 2009a,b,c; Arpornwichanop et al., 2010; Patcharavorachot et al.,

Received 13 January 2011; Received in revised form 10 May 2012; Accepted 20 May 2012

0263-8762/\$ – see front matter © 2012 The Institution of Chemical Engineers. Published by Elsevier B.V. All rights reserved. http://dx.doi.org/10.1016/j.cherd.2012.05.014

<sup>\*</sup> Corresponding author. Tel.: +66 2 2186868; fax: +66 2 2186877. E-mail address: Suttichai.A@chula.ac.th (S. Assabumrungrat).

2

#### Nomenclature

A<sub>single cell</sub> active area of SOFC single cell (m<sup>2</sup>)  $A_{total}$ total active area of SOFC (m<sup>2</sup>)  $C_{\text{cell}}$ capital cost of SOFC single cell (\$) C<sub>compressor</sub> capital cost of compressor (\$) capital cost of SOFC stack (\$)  $C_{\text{stack}}$ 

effective diffusion coefficient of electrode m  $D_{m(eff)}$ 

 $(cm^2 s^{-1})$ 

Ε theoretical open-circuit voltage of the cell (V) E<sup>0</sup> theoretical open-circuit voltage of the cell at

standard pressure (V) activation energy (kJ  $mol^{-1}$ ) Eact

Faraday constant  $(9.6495 \times 10^4)$  (C mol<sup>-1</sup>) F

Gibb's free energy (kJ mol<sup>-1</sup>)  $\Delta H^{\circ}$ heat of reaction (kJ  $mol^{-1}$ )

HP power consumption in compressor (HP)

current density (A cm<sup>-2</sup>) i

exchange current density of electrode m  $i_{o,m}$ 

 $(A cm^{-2})$ 

 $K_i$ equilibrium constant of reactions j (various

units)

 $l_m$ thickness of electrode m (µm) L thickness of electrolyte (µm) mole of component i (mol) ni  $N_{\text{cell}}$ number of SOFC single cell  $N_{\text{stack}}$ number of SOFC stack

pressure (Pa)

partial pressure of component i (Pa)  $p_i$ inlet pressure of component i (Pa)  $p_i^I$ 

difference between heat demand and heat gen-Qnet

eration in SOFC system (kW)

thermal energy supplied from fuel cell stack Q<sub>stack</sub>

gas constant  $(8.3145 \,\mathrm{J}\,\mathrm{mol}^{-1}\,\mathrm{K}^{-1})$ R

Т temperature (K)  $U_f$ fuel utilization cell voltage (V)

W<sub>sep,min</sub> minimum electricity work consumed in CO<sub>2</sub>

number of electron participating in the electroz

chemical reaction

#### Greek letters

charge transfer coefficient (dimensionless)  $\alpha$ electrode tortuosity (dimensionless) ξ

 $\delta_{\text{O}_2}$ coefficient used in concentration overpotential

(dimensionless) total loss (V)  $\eta_{loss}$ 

activation loss (V)  $\eta_{act}$ concentration loss (V)  $\eta_{conc}$ 

ohmic loss (V)  $\eta_{
m ohm}$ 

pre-exponential factor for electrode exchange

#### Subscripts

anode а cathode C

reference condition ref methane decomposition MD MSR methane steam reforming WGS water-gas shift reaction

RWGS reverse water-gas shift reaction

CCS carbon capture storage SOFC solid oxide fuel cell TER thermal to electrical ratio

2010). Typically, an SOFC system consists of 2 main parts; (1) a fuel processor for hydrogen generation and (2) a SOFC unit, which generates electricity from hydrogen and recovers useful heat from spent fuel for utilization in the system.

Methane is considered as a suitable and convenient fuel for the SOFC system due to its availability, highest hydrogen to carbon ratio in hydrocarbon substances and low cost (Ermakova et al., 2000; Vivanpatarakij et al., 2007; Serrano et al., 2010). There are several reaction routes for generating hydrogen from methane such as methane steam reforming (MSR), partial oxidation, dry reforming, autothermal reforming, and methane decomposition (MD) (Edwards and Maitra, 1995; Laosiripojana et al., 2005; Suelves et al., 2005; Bonura et al., 2006; Vivanpatarakij et al., 2007; Li et al., 2008; Wang et al., 2009). Nowadays, the MSR (Eq. (1)) is probably the most well-established technology and widely used as the fuel processor in the conventional SOFC system. Although, it offers the highest hydrogen production but the MSR demands the highest energy and has impurities such as carbon oxide or steam, in the reformed gas.

$$CH_4 + H_2O \rightarrow 3H_2 + CO_2 \qquad \Delta H^{\circ} = +206.9 \text{ kJ mol}^{-1}$$
 (1)

A number of researches have been focused on improving efficiency and performances of the methane-fuelled SOFC systems. Due to the impurities in the reformed gas from the conventional SOFC system, membrane reactor technology (a combination of membrane and steam reforming reactor) (Damen et al., 2006a,b; Powell and Qiao, 2006) is the promising pre-carbon capture technology in power generation. Palladium type has been widely applied as a selective hydrogen, installing in the fuel processor, to purify hydrogen and to increase methane conversion (Basile et al., 2003; Gallucci et al., 2004; Fernandes and Soares, 2006; Patel and Sunol, 2007). Vivanpatarakij et al. (2009) presented an upgraded SOFC system with the application of various operation modes in membrane reactor such as the combination of compressor and vacuum pump. However, this system is difficult to apply in real system due to high cost of membrane material. Another technique that is developed to purify hydrogen before feeding to the SOFC is the use of CaO-CO2 acceptor after the fuel processor; however, this technique has a disadvantage of which CO<sub>2</sub> is produced afterburner (Iordanidisa et al., 2006; Vivanpatarakij et al., 2009; Piroonlerkgul et al., 2010). Consequently, the conventional SOFC system needs to be equipped with a carbon capture and storage (CCS) after the afterburner. The CCS, as shown in Fig. 1, is composed of three main steps; CO<sub>2</sub> separation, CO<sub>2</sub> compression to the liquid form for transport purpose, and CO<sub>2</sub> sequestration (or storage) (Abu-khader, 2006; Damen et al., 2006a,b; House et al., 2009). However, this system is still under developed and is not applied extensively in large scale production due to high capital cost with complex system and high energy demand (Meyer, 2009; Piroonlerkgul et al., 2008, 2009a,b,c; Farhad et al., 2010).

MD (Eq. (2)) is therefore an interesting alternative reaction for hydrogen production as it requires lower energy consumption than the conventional MSR. Moreover, the gas product

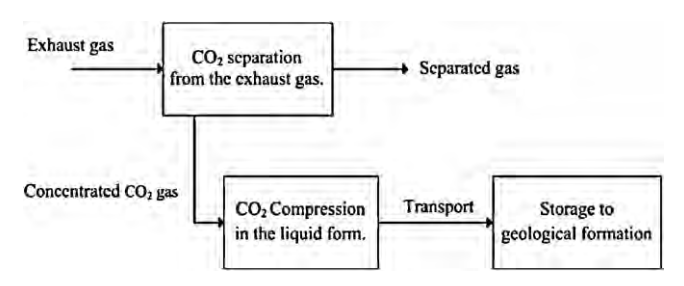


Fig. 1 - Carbon capture and storage facility (CCS).

contains  $CO_x$ -free due to the absence of oxidant substances (i.e., steam or oxygen).

$$CH_4 \rightarrow 2H_2 + C$$
  $\Delta H^{\circ} = +75.6 \text{ kJ mol}^{-1}$  (2)

It should be noted that although the hydrogen generated from MD is less than that from MSR, the pure hydrogen generated by MD offers potential benefits on improved performance of the SOFC when compared with that achieved in the conventional MSR-SOFC (Baron et al., 2004; Damen et al., 2006a,b; Suwanwarangkul et al., 2006; Piroonlerkgul et al., 2009a,b,c; Yusuke et al., 2009). With the consideration of their by-products, MD produces a separated phase by-product, solid carbon, in different valuable forms. So that no carbon oxides is supplied to SOFC, resulting in a long operation life time of the SOFC stack (Takenaka et al., 2001; Coutelieris et al., 2003; Villacampa et al., 2003; Sangtongkitcharoen et al., 2005). Furthermore, such solid carbon can be used as a commodity product in various fields e.g., sorbent material, membrane, catalyst, electrical devices, and fuel cell or sequestered (or stored) for future use (Muradov, 2001; Meyer, 2009; Muradov et al., 2010). As a consequence, the CCS facility required in the MSR-SOFC is not necessary when MD is applied, resulting in lower cost and energy consumption (Bonura et al., 2006; Abbas and Wan Daud, 2009; Ahmed et al., 2009; Yusuke et al., 2009).

This study is aimed to evaluate and compare performances between the two fuel processors, MD and MSR with and without CCS facility. Our SOFC system operations are performed under an energy self-sufficient condition ( $Q_{\rm net}$  = 0), where no external heat is required to supply to the reactor (Sangtongkitcharoen et al., 2005; Palazzi et al., 2007; Piroonlerkgul et al., 2008, 2009a,b,c; Vivanpatarakij et al., 2009). Furthermore, the economic analysis is carried out to determine the appropriate fuel processor for the SOFC at the optimal operating condition (operating voltage and fuel utilization) for the same net electrical power of 1 MW.

#### 2. Process description of SOFC systems

Figs. 2 and 3 show schematic diagrams of the SOFC systems with MSR with/without CCS, and the SOFC system with MD, respectively. The major components in the system include feed pre-heaters, a fuel processor, an SOFC stack, and an afterburner. For the conventional SOFC system with MSR (Fig. 2), steam is generated in a pre-heater and mixed with the heated methane. Then the gas mixture is fed into the fuel processor where the steam methane reforming and water–gas shift reaction take place to generate H<sub>2</sub>-rich gas. After that the reformed gas and air are introduced into the SOFC stack. The exhaust gases are then combusted in the afterburner to generate heat for utilizing in the system. In case of the MSR–SOFC system with the addition of CCS, the CCS is placed after the

afterburner for  $CO_2$  capture. For our proposed SOFC system with MD (Fig. 3), the operation is less complicated as there is no steam input to the reactor and no additional CCS. It should be noted that because solid carbon is also generated as a byproduct of the MD, there is a concern of carried-over carbon in hydrogen gas because it could damage the SOFCs.

#### 3. SOFC system modeling

#### 3.1. Fuel processor

For the MSR process, hydrogen production from methane can be obtained via methane steam reforming reaction (Eq. (1)) and water–gas shift reaction (WGS) (Eq. (3)). These reactions usually take place in series, resulting in an overall reaction as shown in Eq. (4).

$$CO + H_2O \leftrightarrow H_2 + CO_2 \qquad \Delta H^{\circ} = -41.2 \text{ kJ mol}^{-1}$$
 (3)

$$CH_4 + 2H_2O \leftrightarrow 4H_2 + CO_2 \qquad \Delta H^\circ = +165.7 \text{ kJ mol}^{-1}$$
 (4)

Several works have reported a suitable amount of steam to provide long activity and reduce carbon formation, basis industrial methane steam reforming reaction is usually run under a steam to carbon molar ratio of 1.4 or higher (Dicks, 1996). With the equilibrium consideration of the side reaction (WGS), the steam to carbon molar ratio is suggested to be 2 or higher (Renner and Marschner, 1985; Palsson et al., 2000; Sangtongkitcharoen et al., 2005; Vivanpatarakij et al., 2009; Arpornwichanop et al., 2010). However, it is noted that using high excess of water in the system has some disadvantages; (1) excess steam dilutes the hydrogen concentration in the reformed gas, (2) higher thermal energy is required in the SOFC system, and (3) power density and performance of the SOFC can be lower as reported by Piroonlerkgul et al. (2009a,b,c) and Dokmaingam et al. (2010). In this work, we selected the steam to carbon ratio of 2.5 as the carbon activity at this value tends to approach zero (Renner and Marschner, 1985; Palsson et al., 2000; Sangtongkitcharoen et al., 2005; Zhang et al., 2005). For the MD system, methane is directly decomposed to pure hydrogen and carbon follows Eq. (2) without any side reactions.

To simplify the calculations for the fuel processors, thermodynamic chemical equilibrium is assumed to identify the product compositions under the isothermal operation. The equilibrium constant of the related reactions  $(K_j)$  is shown in Eqs. (5)–(7):

Conventional MSR;

$$K_{MSR} = \frac{p_{H_2}^3 p_{CO}}{p_{CH_4} p_{H_2O}} \tag{5}$$

$$K_{WGS} = \frac{p_{H_2} p_{CO_2}}{p_{H_2} o p_{CO}} \tag{6}$$

MD:

$$K_{\rm MD} = \frac{p_{\rm H_2}^2}{p_{\rm CH_4}} \tag{7}$$

#### 3.2. SOFC stack model

The modeling of SOFC stack in this work is based on our previous work (Piroonlerkgul et al., 2009a,b,c). The SOFC

4

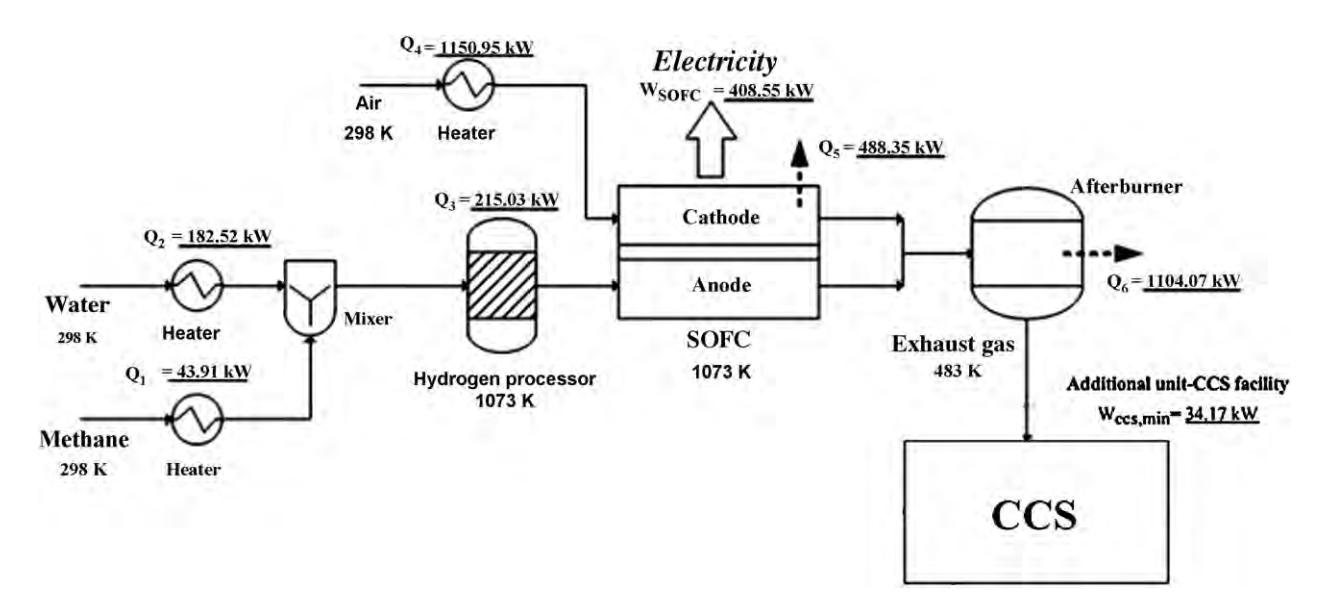


Fig. 2 - The conventional SOFC system configurations with MSR as hydrogen processor with/without CCS facility.

anode, electrolyte, and cathode are made of Ni–YSZ, YSZ, and LSM–YSZ, respectively. It is assumed that only  $\rm H_2$  contributes to the electrochemical reaction and the anode gas in the stack is at its chemical equilibrium compositions due to high operating temperature of SOFC and fast reaction rates. It was reported that the electro-oxidation of  $\rm H_2$  is much faster than that of CO (Khaleel et al., 2004), and the reaction rate of WGS is fast at high temperatures (Blom et al., 1994; Swaan et al., 1994; Bradford and Vannice, 1996).

Open circuit voltage or theoretical voltage (E) can be calculated from the Nernst equation, where the value depends upon the reversible potential (E<sup>0</sup>), temperature, and gas compositions. Such open circuit voltage can be obtained by:

$$E = E^{0} + \frac{RT}{2F} \ln \left( \frac{p_{H_{2}} p_{O_{2}}^{1/2}}{p_{H_{2}O}} \right)$$
 (8)

Actual cell potential (V) as expressed in Eq. (9) is always less than the open-circuit voltage (E) due to overpotentials. Three major overpotentials are involved in the system, ohmic

overpotential ( $\eta_{\rm ohm}$ ), activation overpotential ( $\eta_{\rm act}$ ), and concentration overpotential ( $\eta_{\rm conc}$ ).

$$V = E - \sum \eta_{loss} = E - \eta_{act} - \eta_{ohm} - \eta_{conc}$$
 (9)

The ohmic overpotential  $(\eta_{\rm ohm})$  involves the resistance to flow of electrons through the electrodes and the interconnectors and to flow of ions through the electrolyte. Due to the high electronic conductivity of the electrodes and the interconnectors compared to the ionic conductivity of the electrolyte, only the ohmic overpotential of the electrolyte (Eq. (10)) is considered (Ferguson et al., 1996).

$$\eta_{\text{ohm}} = 2.99 \times 10^{-11} \text{iL} \exp\left(\frac{10,300}{T}\right)$$
(10)

The activation overpotential ( $\eta_{act}$ ) is controlled by the kinetics of electrochemical reaction at the electrode surface. High temperature operation in SOFC promotes fast reaction rate, leading to a reduction of this loss. In this work, the Butler-Volmer equation is performed to compute the activation.

$$i = i_0 \left[ \exp\left(\frac{\alpha z F \eta_{act}}{RT}\right) - \exp\left(\frac{(\alpha - 1)z F \eta_{act}}{RT}\right) \right]$$
 (11)

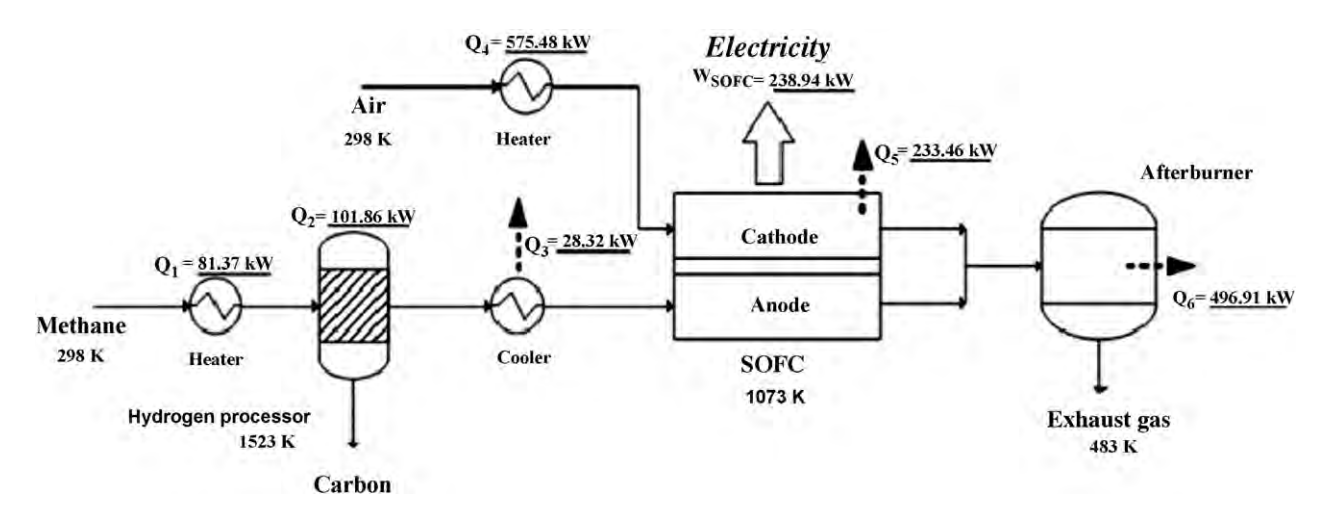


Fig. 3 - The proposed SOFC system configuration with MD as hydrogen processor.

m-1-1 - 4	6 1 - 1	parameters.
Tanle I –	7 OT MOGEL	narameters
IUDIC I	OI IIIOGCI	parameters.

Parameters	Values	
Hydrogen processor		
P	1 atm	
T <sub>MD</sub>	1523 K	
T <sub>MSR</sub>	1073 K	
SOFC stack (Piroonlerkgul et al., 2009a,	b,c)	
n	0.48	
ξ	5.4	
$\gamma_{a}$	$1.344\times 10^{10}~A~m^{-2}$	
$\gamma_{c}$	$2.051 \times 10^9 \ A \ m^{-2}$	
E <sub>act,a</sub>	$1 \times 10^5  \text{J mol}^{-1}$	
E <sub>act,c</sub>	$1.2 \times 10^5  J  mol^{-1}$	
la	750 µm	
$l_c$	50 μm	
L	50 µm	
P	1 atm	
$T_{SOFC}$	1073 K	

In case of SOFC,  $\alpha$  and z are set to be 0.5 and 2 according to Chan et al. (2001). Consequently, the activation potential at each electrode is simplified as:

$$\eta_{\text{act},j} = \frac{RT}{F} \sinh^{-1} \left( \frac{i}{2i_{0,j}} \right), \quad j = a, c$$
(12)

The exchange current density (i<sub>0</sub>) in each electrode is related to partial pressure and operating temperature. The expression for the anode and cathode electrodes can be computed from the following equations (Fleig, 2003):

$$i_{0,\alpha} = \gamma_a \left(\frac{p_{H_2}}{P_{ref}}\right) \left(\frac{p_{H_2O}}{P_{ref}}\right) \exp\left(-\frac{E_{act,a}}{RT}\right) \tag{13}$$

$$i_{0,c} = \gamma_c \left(\frac{p_{O_2}}{P_{rof}}\right)^{0.25} \exp\left(-\frac{E_{act,c}}{RT}\right)$$
(14)

The concentration overpotential ( $\eta_{conc}$ ) is a loss occurring from a slow mass transfer. While the electrochemical reaction takes place over the stack, the reactant gases diffuse to the pore of catalyst, resulting in the difference in concentration of gas between the bulk and the reaction site. Therefore, this loss can be computed by the relation between gas diffusion coefficients and operating temperature as shown in Eqs. (15) and (16) (Chan et al., 2001):

$$\eta_{\rm conc,a} = \frac{RT}{2F} \ln \left[ \frac{(1 + (RT/2F)(l_a/D_{a(eff)}p_{\rm H_2O}^I)i)}{(1 - (RT/2F)(l_a/D_{a(eff)}p_{\rm H_2}^I)i)} \right]$$
(15)

$$\eta_{\rm conc,c} = \frac{RT}{4F} \ln \left[ \frac{p_{\rm O_2}^{\rm I}}{(P_{\rm c} - \delta_{\rm O_2}) - ((P_{\rm c} - \delta_{\rm O_2}) - p_{\rm O_2}^{\rm I}) \exp \left[ (RT/4F)(\delta_{\rm O_2} l_{\rm c}/D_{\rm c(eff)} P_{\rm c}) i \right]} \right]$$
The parameters of the SOFC stock performance are sum.

The parameters of the SOFC stack performance are summarized in Table 1.

#### 3.3. Heat exchanger

Heat requirement for each unit can be determined using conventional energy balance by calculating changes in enthalpy of the inlet and outlet streams. It is assumed that the heat exchangers in the SOFC system are operated under adiabatic condition (no heat loss).

#### 3.4. Afterburner

The anode and cathode exhaust gases are fed to the afterburner unit, where the residual fuels are completely combusted, to generate heat for supplying to all energy-demanding units in the SOFC system. It is assumed that the heat can be extracted from the combusted gas without heat loss and the final exhaust gas emits to the environment at 483 K which is enough to supply heat for steam generation and air preheating.

#### 3.5. CCS facility

For the SOFC system with MSR, an additional CCS facility is installed after the afterburner in order to prevent  $CO_2$  emission to the environment (Simbeck, 2004; Abu-khader, 2006; Damen et al., 2006a,b). The operation of CCS employs the power generation of the SOFC to utilize in its steps. The energy requirement is calculated as follows:

CO<sub>2</sub> separation from the exhaust gas
 The work required for CO<sub>2</sub> separation from the exhaust gas equals the change in Gibbs free energy before and after separation

$$W_{\text{sep,min}} = -dG = \Delta G_{\text{sep}} = \sum_{i} \left( \frac{\partial G_{i}}{\partial n_{i}} \right)$$
 (17)

The calculations follow the procedure suggested by House et al. (2009). The ideal gas was assumed as the separation takes place near atmospheric and  $N_2$  and  $CO_2$  do not chemically interact. It is further assumed that the separation process takes place under isothermal and isobaric, and therefore, the calculated values represent the minimum required work.

- CO<sub>2</sub> compression and transportation
   After CO<sub>2</sub> is separated out of the exhaust gas, it is compressed to liquid phase and transported to a geological reservoir (Abu-khader, 2006). Minimum work required in this stage is obtained by the reversible isothermal compression condition; a typical value is about 13 kJ mol<sup>-1</sup> CO<sub>2</sub> (House et al., 2009).
- CO<sub>2</sub> storage into the geological reservoir
   Liquid CO<sub>2</sub> is compressed to emplace at depth, displacing denser ground water upward. Pressure of this step is around the hydrostatic pressure of ground water at the well head. This step is assumed to overcome the physical barriers which are gravity and surface tension. Minimum work is about the power from the change of pressure and concerned

on the injection lifetime due to an increasing of reservoir pressure (Damen et al., 2006a,b). A typical value of the minimum work over the life time of injection is approximately  $2 \, \text{kJ} \, \text{mol}^{-1} \, \text{CO}_2$  (House et al., 2009).

(16)

#### 3.6. Operation at thermally self-sufficient condition

The SOFC systems in this study are focused on an operation at the thermally self-sufficient condition. At this condition, the value of  $Q_{\rm net}$  is equal to zero, indicating that the total generated thermal energy from the SOFC system is performed

6

CHEMICAL ENGINEERING RESEARCH AND DESIGN XXX (2012) XXX-XXX

to supply the overall heat-demanding units without external heat input. From the system configuration in Figs. 2 and 3, there are main units which play an important role in releasing thermal energy namely; SOFCs (Q5) and afterburner (Q6). But the MD requires a further cooler due to its high temperature in hydrogen processor. Therefore, this proposed system with MD consists of three generated thermal energy units,  $Q_3$ ,  $Q_5$ , and Q6. In term of thermal energy demand, this value consists of the energy consumption in heaters and fuel processors. The Q<sub>net</sub> in the thermally self-sufficient operation is calculated by: SOFC system with MSR;

$$Q_{\text{net}} = (Q_1 + Q_2 + Q_3 + Q_4) - (Q_5 + Q_6)$$
(18)

SOFC system with MD;

$$Q_{\text{net}} = (Q_1 + Q_2 + Q_4) - (Q_3 + Q_5 + Q_6)$$
(19)

Note that the calculations of Qi are based on enthalpy changes of the input and output streams of the units.

The thermally self-sufficient condition can be achieved by tuning of fuel utilization ( $U_f$ ) at various operating voltages. The fuel utilization (Zhang et al., 2005) and electrical efficiency (Piroonlerkgul et al., 2009a,b,c) in the SOFC system are estimated from Eqs. (20) and (21), and overall electrical efficiency is calculated by Eq. (22):

Fuel utilization (%)

$$= \frac{H_{2,equivalent} \text{ consumption in SOFC stack}}{H_{2,equivalent} \text{fed to the SOFC system}} \times 100 \tag{20}$$

Stack cell electrical efficiency (%)

$$= \frac{\text{Net electrical power generated}}{\text{(LHV of fuel} \times \text{fuel feed rate)}_{\text{at anode side}}} \times 100$$
 (21)

Overall electrical efficiency (%)

$$= \frac{\text{Net electrical power generated}}{\text{LHV of methane} \times \text{methane feed rate}} \times 100$$
 (22)

#### Results and discussion 4.

#### 41 Thermodynamics of reactions in fuel processors

Thermodynamic chemical equilibrium between two main reactions of methane steam reforming (MSR) and methane decomposition (MD) is firstly investigated in term of product distribution basis on 1 mol of pure methane feed. The steam to carbon molar ratio input of MSR is fixed to higher basis requirement at the value of 2.5 as mentioned earlier. The system is operated under the atmospheric pressure to minimize cost of operation and to obtain higher yield follow the Le Chaterlier's principle at different temperatures, ranging from 273 K to 2000 K.

Product distribution depicted in Fig. 4 shows the endothermic nature of both MD and MSR reactions as the amount of CH<sub>4</sub> was increasingly consumed to produce hydrogen fuel when the operating temperature is raised. It is noted that H<sub>2</sub> can be generated higher in the MSR process due to the

presence of water reagent and higher stoichiometric coefficient in the reactions (Eqs. (2) and (4)) (Dokmaingam et al., 2010; Halabi et al., 2010). At temperature higher than 1100 K, the endothermic reverse water gas shift reaction (RWGS) (reverse of Eq. (3)), in turn, plays an important role in the MSR process, resulting in the declination of H<sub>2</sub> production. Although, the MSR provides higher methane conversion and hydrogen yield but other unwanted-by-products are also produced from this process especially COx, which significantly reduces the purity of hydrogen fuel and affects the performance and stability of SOFC stack.

The MD, on the other hand, produces H2 without any side reactions and hence large amount of purified H2 can be obtained at high temperature (Poirer and Sapundzhiev, 1997; Muradov, 2001; Liu et al., 2010). The results reveal that almost 100% of hydrogen and carbon production from the MD process can be achieved at temperature over 1373 K. It is noted that the presence of small amount of CH4 in gas stream from the fuel processor, resulting from unconverted feed, does not affect the electrochemical reaction in the SOFC, in turn, it provides the internal reforming with H2O to produce H2 again in SOFC stack (Piroonlerkgul et al., 2008). The reduction of H<sub>2</sub>O in the anode chamber promotes the diffusion of H2 to generate the electrical power as reported by Patcharavorachot et al. (2010). Further, small amount of H2O at anode side can enhance forward electrochemical reaction so that stack cell efficiency of the MD-SOFC becomes higher than that of the MSR-SOFC as will be discussed later.

Although, the MSR process shows a better performance in producing much larger amount of H2 over the MD process but to apply the fuel processor with SOFC, the performance of the entire process, MSR-SOFC and MD-SOFC, is needed to be considered. In this study, the performance of the fuel processor with SOFC is determined in terms of maximum power density, electrical efficiency, and the effect of hydrogen purity (which is considered as the overpotential). Finally, economic analysis is taken into account in order to determine a suitable fuel processor for operating with SOFC.

#### Comparison of methane-fuelled SOFC systems performance with different fuel processors

For both MD-SOFC and MSR-SOFC, the systems are operated under the thermally self-sufficient condition ( $Q_{net} = 0$ ) at fuel cell temperature of 1073 K, which is previously reported as a suitable SOFC operating temperature (Vivanpatarakij et al., 2007; Piroonlerkgul et al., 2009a,b,c). To find the optimal condition at thermally self-sufficient condition, the total heat consumption is calculated via a trial-and-error method by tuning the fuel utilization (U<sub>f</sub>) at a fixed operating voltage of SOFC stack to where the total heat consumption is equal to the total heat generation from the system. It is noted that the fuel utilization (Uf) can be defined as the equivalent of hydrogen consumption in the SOFC stack divided by overall the equivalent of hydrogen fed to the SOFC. As shown in Fig. 5 (MSR-SOFC) and Fig. 6 (MD-SOFC), Qnet can be either positive or negative value. A positive value of Qnet means external heat source is required to supply for the thermal energy consumption unit and the negative value indicates that there is some heat release from the overall process. The  $Q_{\text{net}}$  can be zero when the optimal fuel utilization is elected at varying operating voltage. In addition, the value of produced thermal to electrical ratio (TER), which is defined as the portion of fuel needed to utilize as a thermal energy to obtain an equal

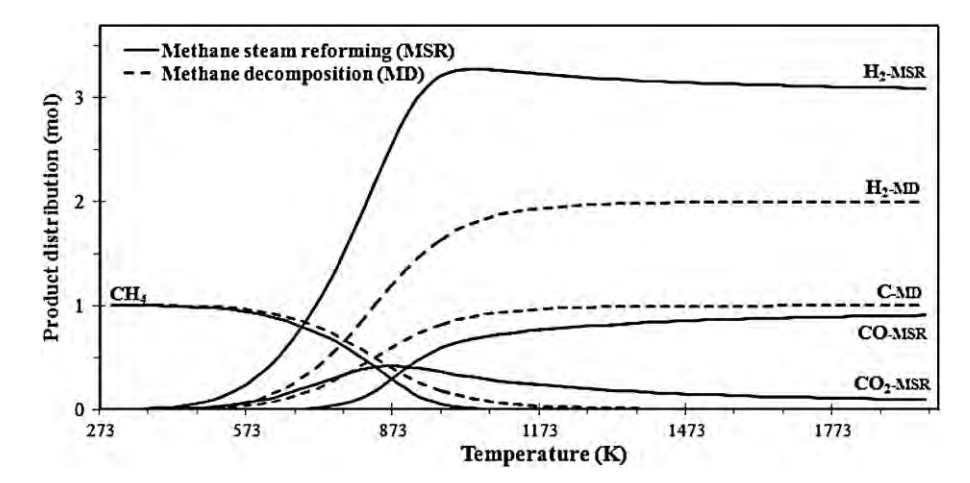


Fig. 4 – Product distribution of methane decomposition (dash line) and of conventional methane steam reforming  $(H_2O:CH_4=2.5)$  (solid line) at atmospheric pressure and varying temperature (basis on 1 mol of pure methane for both processes).

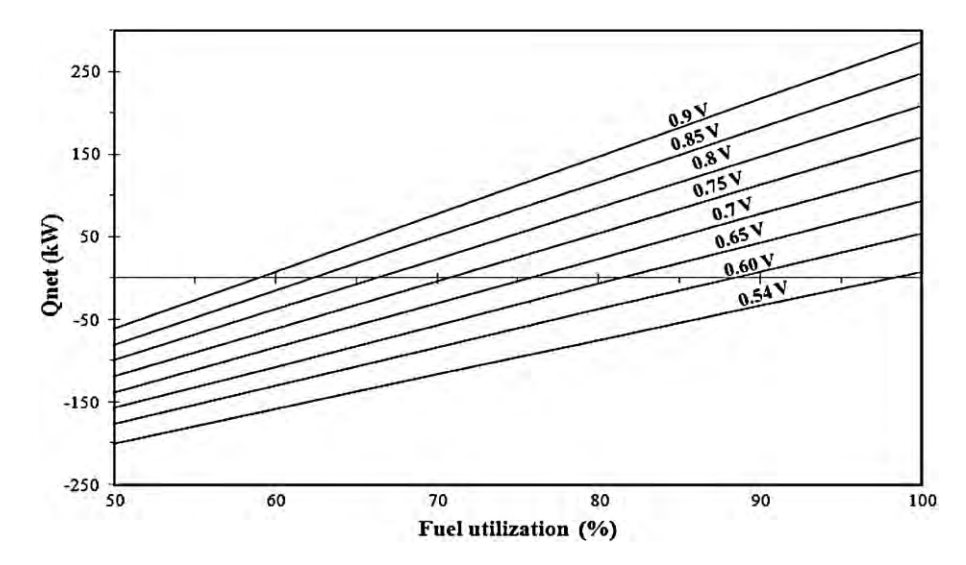


Fig. 5 –  $Q_{net}$  at different fuel utilization and operating voltage at 1073 K in conventional SOFC system with MSR, basis on 1 mol of pure methane ( $H_2O:CH_4=2.5$ ).

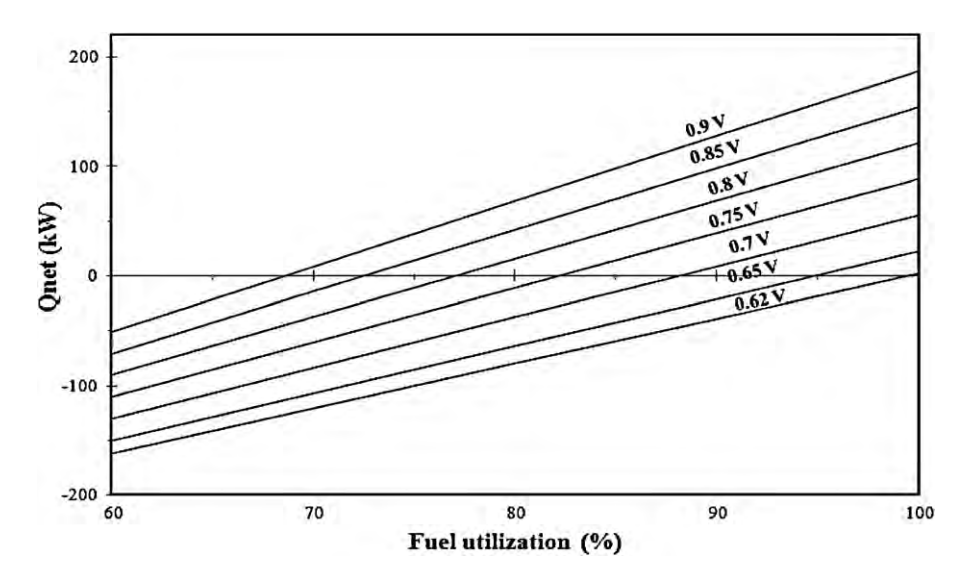


Fig. 6 –  $Q_{net}$  at different fuel utilization and operating voltage at 1073 K in proposed SOFC system with MD, basis on 1 mol of pure methane.

## ARTICLE IN PRESS

CHEMICAL ENGINEERING RESEARCH AND DESIGN XXX (2012) XXX-XXX

electricity production (Farhad et al., 2010), is found to be 3.90 for the MSR–SOFC, and 2.66 for the MD–SOFC system at the thermally self-sufficient point ( $Q_{net} = 0$ ). The higher value of TER observed in the MSR–SOFC system is because the MSR is more endothermic than the MD.

The relationship between the operating voltage and power density at the energy self-sufficient operation is shown in Fig. 7. The optimum operating voltage which offers the maximum power density for the MSR-SOFC system is at 0.60 V and for the MD-SOFC is at 0.65 V. Moreover, higher power density is observed in the case of the MD–SOFC since the MD produces purer H<sub>2</sub> than the MSR-SOFC as will be evidenced later in Fig. 8 showing operating voltage and polarization at various fuel utilizations. The larger the fuel utilization, the more depletion of fuel at the anode is, leading to an increase in polarization. Moreover, because the impurity in hydrogen fuel in case of the MSR is higher than that of the MD, the polarizations in SOFC system in case of the MSR are therefore higher than that of the MD at similar fuel utilization. This result is in good agreement with those reported by Eguchi et al. (2002) and Baron et al. (2004), of which polarizations in SOFC system, such as activation and concentration polarization, are occurred due to CO impurity in hydrogen fuel, leading to lower SOFC performance.

Based on similar 1MW of net electricity production, the stack cell efficiency of the MSR-SOFC was found to be 45.9%, lower than that of the MD-SOFC of which is 53.5% (Table 3). However, overall electrical efficiency of the MSR-SOFC system, either with or without the CCS, is much higher than that of the MD-SOFC. This is because the flue gas in the MSR-SOFC is combusted and generates thermal energy whereas the byproduct, solid carbon, is not further combusted; hence the energy in case of the MD-SOFC is stored in the system. In case of the MSR-SOFC with CCS, the additional CCS has no effect from either external energy or electrical input due to the operation under energy self-sufficient condition, therefore only the electrical power produced from the SOFC has an effect. Slightly higher feed rate of methane is required to produce a surplus of electricity for CCS. The CCS needs the electrical power from the SOFC system to separate out CO<sub>2</sub> ca. 19.2 kW, to compress, transport, and storage approximately 15 kW. Consequently, the addition of CCS reduces the net electrical efficiency ca. 3.9%.

Fig. 9 depicts the influence of feed processor to generating thermal energy from SOFC stack per area and area of the stack under the thermally self-sufficient operation at 1 MW of net electrical power production. For lower operating voltage, the difference between the theoretical voltage and the actual one is larger hence the thermal energy supplied from fuel cell stack ( $Q_{\rm stack}/a{\rm rea}$ ) is larger and, in turn, the area of the cell stack becomes smaller to obtain thermally self-sufficient operation. It is noted that the trend of  $Q_{\rm stack}/a{\rm rea}$  as a function of operating voltage is similar to that of the power density (Fig. 7). This phenomenon proves that not only MD gives the highest performance (power density and electrical efficiency) but it also has lower SOFC stack area compared to the MSR–SOFC and the MSR–SOFC-CCS.

#### 4.3. Economic analysis

After comparing the optimal operating conditions between two main fuel processors, it is necessary to further consider the benefit in term of economic in order to apply in large-scale industrial operation. In this paper, economic analysis is based on 1 MW of electrical power generation. Three parameters are

## Table 2 – Costing models and economic parameters used in the economic analysis.

#### Costing model

SOFC (Piroonlerkgul et al., 2009a,b,c)

 $\begin{array}{ll} \text{Cell cost (US\$)} & C_{\text{cell}} = A_{\text{single cell}} \times 0.1442^{a} \\ \text{Number of cells} & N_{\text{cell}} = A_{\text{total}}/A_{\text{single cell}} \\ \text{Number of stacks} & N_{\text{stack}} = N_{\text{cell}}/100 \\ \text{Fuel cell stacks cost (US\$)} & C_{\text{stack}} = 2.7 \times \left[ (C_{\text{cell}} \times N_{\text{cell}}) \right] \\ \end{array}$ 

+ (2 ×  $N_{\text{stack}}$  ×  $A_{\text{single cell}}$  × 0.46425)]

Capture capital cost 42.33 (Herzog, 1999)

(US\$/tonne)

**Economic parameters** 

Fuel feed cost (US\$/1000 ft³) 9.36 (IEA Natural Gas, 2010)
Carbon selling cost (US\$/lb) 0.5 (http://www.icispricing.com)

Project life time (year) 5

<sup>a</sup> A single cell area is fixed at 200 cm<sup>2</sup>.

used to justify the economic benefits: capital cost, cost of raw materials, and return profit from by-products. Table 2 summarizes the costing model and economic parameters used in our analysis. For the capital cost, only the SOFC stack and the CCS facility are considered due to their high costs. The difference in costs of the other units such as heat exchangers, reactor and afterburner for the MSR–SOFC and the MD–SOFC are assumed to be small and therefore not considered in the economic analysis.

Economical profiles under thermally self-sufficient operation are summarized in Table 3. At the optimal condition, the MD–SOFC system can reduce the SOFC stack size 1.89% comparing to the conventional MSR–SOFC, whereas the stack size in case of the MSR–SOFC-CCS is larger than that of the MSR–SOFC 9.13% as it has to produce higher electrical power for CCS facility. In addition, the MD–SOFC can improve the power density 1.93% comparing to the conventional MSR–SOFC. This is why the SOFC stack area of the MD–SOFC is smaller than that of the MSR–SOFC (approximately 4.8 m²). As a consequence, using the MD–SOFC can save the total capital cost approximately \$19,000.

Considering the reactants used and products obtained from different fuel processors. At the similar net electrical power production, the fuel feed cost of the MD-SOFC system is higher than that of the MSR-SOFC or the MSR-SOFC-CCS. This result is because the MD-SOFC requires higher number of methane to produce the same amount of H2 for the SOFC. It is noted that although the fuel feed cost of the MSR-SOFC-CCS is more expensive than that of the MSR-SOFC system due to the need of more electrical power but it is still a lot lower than the case of MD-SOFC system. With a consideration only of the fuel feed cost, the MD-SOFC might not be a good alternative fuel processor supplying to the SOFC system. However, it is worthy to note that the MD system can remarkably return some precious benefit as the valuable by-product, solid carbon, can be obtained. Many types of solid carbon can be formed depend upon the decomposition conditions such as graphite, carbon black, activated carbon, carbon nanotube, or carbon filaments, of which each has different selling prices (http://www.timesnano.com/price.asp; http://www.helixmaterial.com/Ordering.html). In this study, we chose to examine the return profit for the cheapest solid carbon, carbon black, along 5 years operation. The evaluation results in Table 3 show that the return profit is around 11 million dollars leads to the net cost saving ca. 9 million dollars.

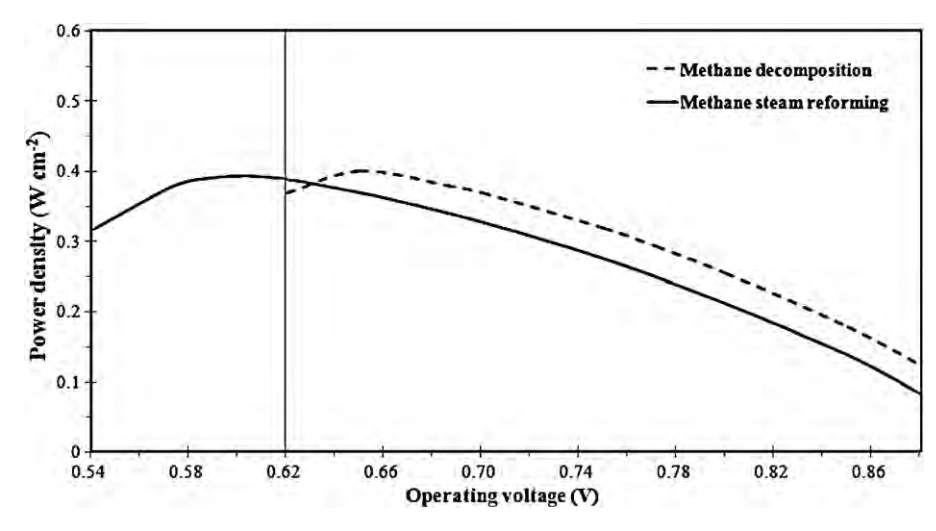


Fig. 7 - Power density at various operating voltages under the energy self-sufficient operation (Qnet = 0) in SOFC system.

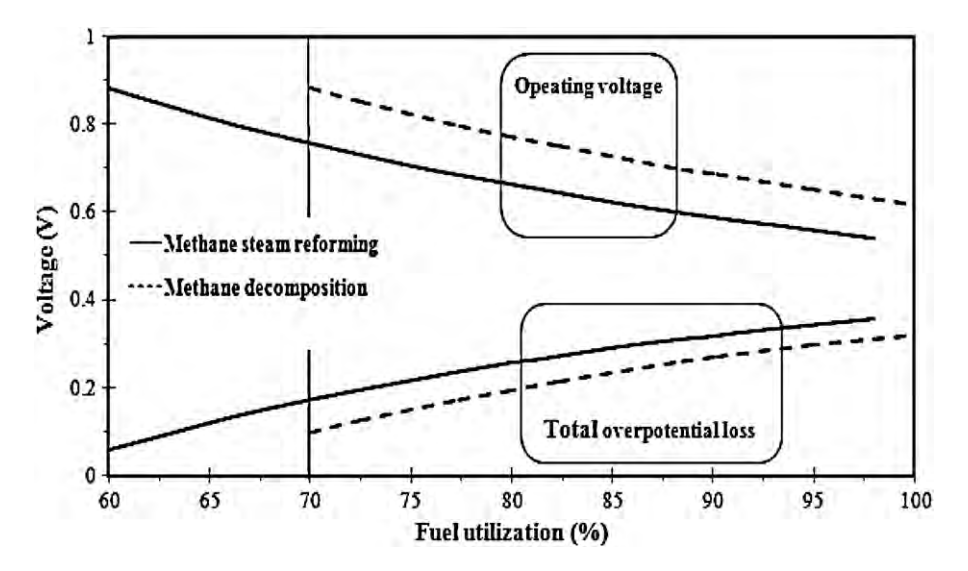


Fig. 8 - Operating voltage and polarization at various fuel utilizations under the energy self-sufficient operation ( $Q_{net} = 0$ ) in SOFC system.

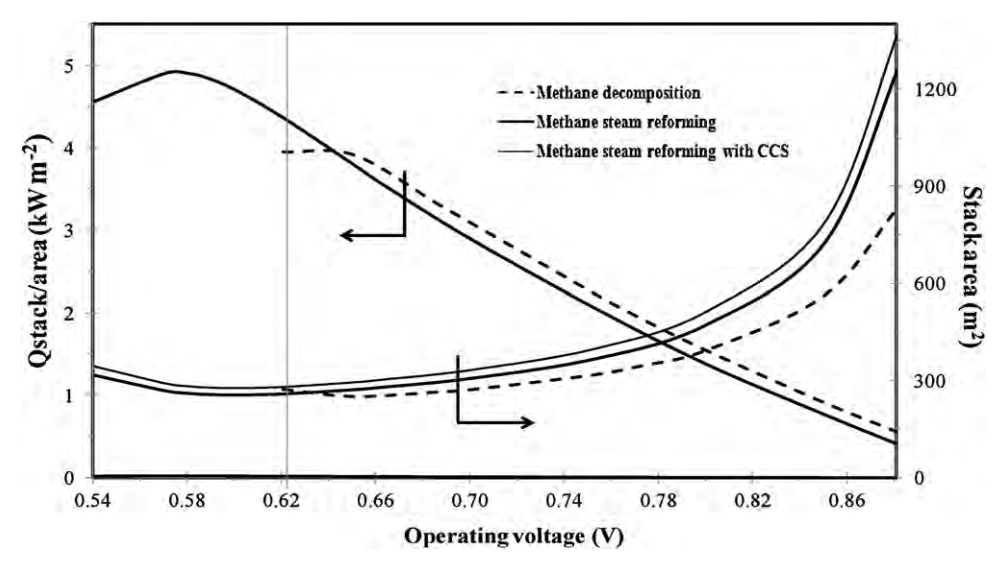


Fig. 9 - Q<sub>stack</sub>/area and stack area for different SOFC systems at the energy self-sufficient operation (Q<sub>net</sub> = 0).

	Steam methane reforming		Methane decomposition
	Conventional unit	With CCS technology	
Net electricity produced (MW)	1	1	1
Methane feed rate (mol/s)	2.45	2.67	4.19
Operating voltage (V)	0.60	0.60	0.65
% Fuel utilization	88.2	88.2	94.9
Power density (W/cm <sup>2</sup> )	0.39	0.39	0.40
Improvement of power density (%)	-	_	1.93
Electricity produced in SOFC (MW)	1	1.09	1
Stack cell efficiency (%)	45.9	42.0	53.5
Overall electrical efficiency (%)	45.9	42.0	26.8
SOFC active area (m <sup>2</sup> )	254	278	250
Improvement in SOFC area (%)		-9.12	1.89
Capital cost of SOFC (US\$)	997,578	1,088,642	978,719
Capital cost of CCS (US\$)	-	810,246	_
Fuel feed cost (US\$)	3,124,930	3,410,188	5,343,206
Carbon by-product selling cost (US\$)	-	_	11,606,897
Saving capital cost (US\$)	-	-901,309	18,858
Saving of raw material (US\$)	-	-285,259	-2,218,276
Return profit from by product (US\$)	-	_	11,606,897
Net cost saving (US\$)	_	-1,186,568	9,407,480

#### 5. Conclusion

Performances of two fuel processors, conventional methane steam reforming (MSR) and methane decomposition (MD), were investigated in the methane-fuelled SOFC system under thermally self-sufficient condition ( $Q_{net} = 0$ ). At this condition, the system is operated with no external energy requirement. The results demonstrated that high performances and high electrical efficiency can be obtained when the system was operated at the self-sufficient condition. The MD-SOFC performs more advantages over the MSR-SOFC as high purity of H<sub>2</sub> feed is obtained, giving a lower polarization and thus higher in power density and cell stack efficiency. As a result, lower cell stack area can be used in the case of MD-SOFC. Moreover, the MD yields valuable by-products, solid carbon, rather than undesired-by-products such as CO<sub>x</sub> as observed in the MSR. In addition, when CCS is applied to MSR-SOFC, of course the system become more complex with an increase in the capital cost and operating cost of surplus electricity for CCS unit. As a consequence, the MD is more environmental friendly and can gain the return profit from such by-product. Economic analysis reveals that the MD-SOFC has the gratifying result with larger net saving cost (ca. 9 million dollars for 1 MW with 5 years of project life). As such, applying the MD processor with SOFC system is proved to be an attractive method for power generation.

#### Acknowledgement

This work is financially supported by the Thailand Research Fund and Office of the Higher Education Commission.

#### References

- Abbas, H.F., Wan Daud, W.M.A., 2009. Hydrogen production by methane decomposition: a review. Int. J. Hydrogen Energy, 1–31.
- Abu-khader, 2006. Recent progress in  $CO_2$  capture/sequestration: a review. Energy Sources Part A 28, 1261–1279.
- Ahmad Hajimolana, S., Azlan Hussain, M., Ashri Wan Daud, W.M., Soroush, M., Shamiri, A., 2012. Mathematical modeling

- of solid oxide fuel cells: a review. Renew. Sustain. Energy Rev. 15, 1893–1917.
- Ahmed, S., Aitani, A., Rahman, F., Al-Dawood, Ali, Al-Muhaish, F., 2009. Decomposition of hydrocarbons to hydrogen and carbon. Appl. Catal. A: Gen. 359, 1–24.
- Arpornwichanop, A., Patcharavorachot, Y., Assabumrungrat, S., 2010. Analysis of a proton-conducting SOFC with direct internal reforming. Chem. Eng. Sci. 65, 581–589.
- Assabumrungrat, S., Laosiripojana, N., Pavarajarn, V., Sangtongkitcharoen, W., Tangjitmatee, A., Praserthdam, P., 2005. Thermodynamic analysis of carbon formation in solid oxide fuel cells with a direct internal reformer fueled by methanol. J. Power Sources 139, 55–60.
- Baron, S., Brandon, N., Atkinson, A., Steele, B., Rudkin, R., 2004. The impact of wood-derived gasification gases on Ni-CGO anodes in intermediate temperature solid oxide fuel cells. J. Power Sources 126, 58–66.
- Basile, A., Paturzo, L., Gallucci, F., 2003. Co-current and counter-current modes for water gas shift membrane reactor. Catal. Today 82 (1–4), 275–281.
- Blom, R., Dahl, I.M., Slagtem, A., Sortland, B.A., Spjelkavik, E., 1994. Tangstad, Carbon dioxide reforming of methane over lanthanum-modified catalysts in a fluidized-bed reactor. Catal. Today 21, 535–543.
- Bonura, G., Di Blasi, O., Spadaro, L., Arena, F., Frusteri, F., 2006. A basic assessment of the reactivity of Ni catalysts in the decomposition of methane for the production of  $CO_x$ -free hydrogen for fuel cells application. Catal. Today 116, 298–303.
- Bradford, M.C.J., Vannice, M.A., 1996. Catalytic reforming of methane with carbon dioxide over nickel catalysts. II: reaction kinetics. Appl. Catal. A: Gen. 142, 97–122.
- Chan, S.H., Khor, K.A., Xia, Z.T., 2001. A complete polarization model of a solid oxide fuel cell and its sensitivity to the change of cell component thickness. J. Power Sources 93, 130–140.
- Coutelieris, F.A., Douvartzides, S., Tsiakaras, P., 2003. The importance of the fuel choice on the efficiency of a solid oxide fuel cell system. J. Power Sources 123, 200–205.
- Damen, K., Troost, M.V., Faaij, A., Turkenburg, W., 2006a. A comparison of electricity and hydrogen production systems with CO<sub>2</sub> capture and storage. Part A: review and selection of promising conversion and capture technologies. Prog. Energy Combust. Sci. 32, 215–246.
- Damen, K., Troost, M.V., Faaij, A., Turkenburg, W., 2006b. A comparison of electricity and hydrogen production systems with  $\rm CO_2$  capture and storage. Part B: Chain analysis of

- promising CCS options. Prog. Energy Combust. Sci. 32, 215–246.
- Dicks, A.L., 1996. Hydrogen generation from natural gas for the fuel cell systems of tomorrow. J. Power Sources 61, 113–124.
- Dokmaingam, P., Assabumrungrat, S., Soottitantawat, A., Laosiripojanab, N., 2010. Modeling of tubular-designed solid oxide fuel cell with indirect internal reforming operation fed by different primary fuels. J. Power Sources 195, 69–78.
- Douvartzides, S.L., Coutelieris, F.A., Demin, K., Tsiakaras, P.E., 2003. Fuel options for solid oxide fuel cells: a thermodynamic analysis. AIChE J. 49, 248–257.
- Edwards, J.H., Maitra, A.M., 1995. The chemistry of methane reforming with carbon dioxide and its current and potential applications. Fuel Process. Technol. 42, 269–289.
- Edwards, P.P., Kuznetsov, V.L., David, W.I.F., Brandon, N.P., 2008. Hydrogen and fuel cells: towards a sustainable energy future. Energy Policy 36, 4356–4362.
- Eguchi, K., Kojo, H., Takeguchi, T., Kikuchi, R., Sasaki, K., 2002. Fuel flexibility in power generation by solid oxide fuel cells. Solid State Ionics 411 (6), 152–153.
- Energy Information Administration (IEA), 2010. Natural Gas Monthly September. Office of Oil and Gas, U.S. Department of Energy, Washington DC, EIA0130.
- Ermakova, M.A., Ermakov, D.Yu., Kuvshinov, G.G., 2000. Effective catalysts for direct cracking of methane to produce. Appl. Catal. A: Gen. 201. 61–70.
- Farhad, S., Hamdullahpur, F., Yoo, Y., 2010. Performance evaluation of different configurations of biogas-fuelled SOFC micro-CHP systems for residential applications. Int. J. Hydrogen Energy 35, 3758–3768.
- Ferguson, J.R., Fiard, J.M., Herbin, R., 1996. Three-dimensional numerical simulation for various geometries of solid oxide fuel cells. J. Power Sources 58, 109–122.
- Fernandes, F.A.N., Soares Jr., A.B., 2006. Methane steam reforming modeling in a palladium membrane reactor. Fuel 85,
- Fleig, J., 2003. Solid oxide fuel cell cathodes: polarization mechanisms and modeling of the electrochemical performance. Annu. Rev. Mater. Res. 33, 361–382.
- Gallucci, F., Paturzo, L., Basile, A., 2004. A simulation study of the steam reforming of methane in a dense tubular membrane reactor. Int. J. Hydrogen Energy 29 (6), 611–617.
- Halabi, M.H., DeCroon, M.H.J.M., Van der Schaaf, J., Cobden, P.D., Schouten, J.C., 2010. Low temperature catalytic methane steam reforming over ceria-zirconia supported rhodium. Appl. Catal. A: Gen. 389, 68-79.
- Hernadez-Pacheco, E., Mann, M.D., Hutton, P.N., Singh, D., artin, K.E., 2005. A cell level model for a solid oxide fuel cell operated with syngas from a gasification process. Int. J. Hydrogen Energy 138, 1221–1233.
- Herzog, H., 1999. The Economics of  $CO_2$  Capture Greenhouse Gas Control Technologies. Elsevier Science Ltd., Oxford, pp. 101–106.
- House, K.Z., Harvey, C.F., Michael, J.A., Daniel, P.S., 2009. The energy penalty of post-combustion  $CO_2$  capture & storage and its implications for retrofitting the U.S. installed base. Energy Environ. Sci. 2 (2), 193–205.
- Hussain, M.M., Li, X., Dincer, I., 2006. Mathematical modeling of planar solid oxide fuel cells. J. Power Sources 161, 1012–1022.
- Iordanidisa, A.A., Kechagiopoulosb, P.N., Voutetakisa, S.S., Lemonidoub, A.A., Vasalosb, I.A., 2006. Autothermal sorption-enhanced steam reforming of bio-oil/biogas mixture and energy generation by fuel cells: concept analysis and process simulation. Int. J. Hydrogen Energy 31, 1058–1065.
- Karl, V.K., Gunter, R.S., 1995. Environmental impact of fuel cell technology. Chem. Rev. 95, 191–207.
- Khaleel, M.A., Lin, Z., Singh, P., Surdoval, W., Collin, D., 2004. A finite element analysis modeling tool for solid oxide fuel cell development: coupled electrochemistry, thermal and flow analysis. J. Power Sources 130, 136–148.
- Laguna-Bercero, M.A., 2012. Recent advances in high temperature electrolysis using solid oxide fuel cells: a review. J. Power Sources 203, 4–16.

- Laosiripojana, N., Sutthisripok, W., Assabumrungrat, S., 2005. Synthesis gas production from dry reforming of methane over CeO<sub>2</sub> doped Ni/Al<sub>2</sub>O<sub>3</sub>: influence of the doping ceria on the resistance toward carbon formation. Chem. Eng. J. 112, 13–22
- Li, W., Wang, H., Ren, Z., Wang, G., Bai, J., 2008. Co-production of hydrogen and multi-wall carbon nanotubes from ethanol decomposition over Fe/Al<sub>2</sub>O<sub>3</sub> catalysts. Appl. Catal. B: Environ. 84, 433–439.
- Liu, Q., Tian, Y., Li, H., Jia, L., Xia, C., Thompson, L.T., Li, Y., 2010. High efficiency chemical energy conversion system based on a methane catalytic decomposition reaction and two fuel cells. Part II. Energy analysis. J. Power Sources 195, 6539– 6548.
- Martin, W., Ralph, J.B., 2003. What are batteries, fuel cells, and supercapacitors? Chem. Rev. 104, 4245–4269.
- Meyer, S., 2009. Application of the natural gas direct carbon fuel cell (NGDCFC) to a gas filling station for hydrogen and electricity supply. Energy Procedia 1, 1427–1434.
- Muradov, N., 2001. Hydrogen via methane decomposition: an application for decarbonization of fossil fuels. Int. J. Hydrogen Energy 26, 1165–1175.
- Muradov, N., Choi, P., Smith, F., Bokerman, G., 2010. Integration of direct carbon and hydrogen fuel cells for highly efficient power generation from hydrocarbon fuels. J. Power sources 195, 1112–1121.
- Naser, A.O., Timothy, T.C., 2007. Life cycle GHG assessment of fossil fuel power plants with carbon capture and storage. Energy Policy 36, 367–380.
- Palazzi, F., Autissier, N., Marechal, F.M.A., Favrat, D., 2007. A methodology for thermo-economic modeling and optimization of solid oxide fuel cell systems. Appl. Thermal Eng. 27, 2703–2712.
- Palsson, J., Selimovie, A., Sjunnesson, L., 2000. Combined solid oxide fuel cell and gas turbine systems for efficient power and heat generation. J. Power Sources 860, 442–448.
- Patel, K.S., Sunol, A.K., 2007. Modeling and simulation of methane steam reforming in a thermally coupled membrane reactor. Int. J. Hydrogen Energy 32 (13), 2344–2358.
- Patcharavorachot, Y., Paengjuntuek, W., Assabumrungrat, S., Arpornwichanop, A., 2010. Performance evaluation of combined solid oxide fuel cells with different electrolytes. Int. J. Hydrogen Energy 35, 4301–4310.
- Piroonlerkgul, P., Assabumrungrat, S., Laosiripojana, N., Adesina, A.A., 2008. Selection of appropriate fuel processor for biogas-fuelled SOFC system. Chem. Eng. J. 140, 341–351.
- Piroonlerkgul, P., Soottitantawat, A., Kiatkittipong, W., Laosiripojana, N., Arpornwichanop, A., Assabumrungrat, S., 2009a. Operation viability and performance of solid oxide fuel cell fuelled by different feeds. Chem. Eng. J. 155, 411–418.
- Piroonlerkgul, P., Laosiripojana, N., Adesina, A.A., Assabumrungrat, S., 2009b. Performance of biogas-fed solid oxide fuel cell systems integrated with membrane module for CO<sub>2</sub> removal. Chem. Eng. Process. 48, 672–682.
- Piroonlerkgul, P., Kiatkittipong, W., Arpornwichanop, A., Soottitantawat, A., Wiyarat, W., Laosiripojana, N., Adesina, A.A., Assabumrungrat, S., 2009c. Integration of solid oxide fuel cell and palladium membrane reactor: technical and economic analysis. Int. J. Hydrogen Energy 34, 3894–3907.
- Piroonlerkgul, P., Kiatkittipong, W., Arpornwichanop, A., Soottitantawat, A., Wiyarat, W., Laosiripojana, N., Adesina, A.A., Assabumrungrat, S., 2010. Technical and economic study of integrated system of solid oxide fuel cell, palladium membrane reactor, and CO<sub>2</sub> sorption enhancement unit. Chem. Eng. Process. 49, 1006–1016.
- Poirer, M.G., Sapundzhiev, C., 1997. Catalytic decomposition of natural gas hydrogen for fuel cell applications. Int. J. Hydrogen Energy 22 (4), 429–433.
- Powell, C.E., Qiao, G.G., 2006. Polymeric  $CO_2/N_2$  gas separation membranes for the capture of carbon dioxide from power plant flue gases. J. Membrane Sci. 279, 1–49.
- Renner, H.J., Marschner, R., 1985. Catalytic reforming of natural gas and other hydrocarbon. Ullmann's Encyclopedia of

- Industrial Chemistry, vol. A2., fifth ed. VCH Verlagsgesellschaft, Weinheim, Germany, pp. 186–204.
- Sangtongkitcharoen, W., Assabumrungrat, S., Pavarajarn, V., Laosiripojana, N., Praserthdam, P., 2005. Comparison of carbon formation boundary in different modes of solid oxide fuel cells fueled by methane. J. Power Sources 142, 75–80.
- Sangtongkitcharoen, W., Vivanpatarakij, S., Laosiripojana, N., Arpornwichanop, A., Assabumrungrat, S., 2008. Performance analysis of methanol-fueled solid oxide fuel cell system incorporated with palladium membrane reactor. Chem. Eng. J. 138, 436–441.
- Serrano, D.P., Botas, J.A., Fierro, J.L.G., Guil-Lopez, R., Pizarro, P., Gomez, G., 2010. Hydrogen production by methane decomposition: origin of the catalytic activity of carbon materials. Fuel 89, 1241–1248.
- Simbeck, D.R., 2004. CO<sub>2</sub> capture and storage: the essential bridge to the hydrogen economy. Energy 29, 1633–1641.
- Stambouli, A.B., Traversa, E., 2002. Solid oxide fuel cells (SOFCs): a review of an environmentally clean and efficient source of energy. Renew. Sust. Energy Rev. 6, 433–455.
- Suelves, I., Lazaro, M.J., Moliner, R., Corbella, B.M., Palacios, J.M., 2005. Hydrogen production by thermo catalytic decomposition of methane on Ni-based catalysts: influence of operating conditions on catalyst deactivation and carbon characteristics. Int. J. Hydrogen Energy 30 (4), 1555–1567.
- Suwanwarangkul, R., Croiset, E., Entchev, E., Charojrochkul, S., Pritzker, M.D., Fowler, M.W., Douglas, P.L., Chewathanakup, S., Mahaudom, H., 2006. Experimental and modeling study of solid oxide fuel cell operating with syngas fuel. J. Power Sources 161, 308–322.
- Swaan, H.M., Kroll, V.C.H., Martin, G.A., Mirodatos, C., 1994. Deactivation of supported nickel catalysts during the

- reforming of methane by carbon dioxide. Catal. Today 21, 571–578.
- Takenaka, S., Ogihara, H., Yamanaka, I., Otsuka, K., 2001.

  Decomposition of methane over supported-Ni catalysts:
  effects of the supports on the catalytic lifetime. Appl. Catal. A:
  Gen. 217, 101–110.
- Villacampa, J.I., Royo, C., Romeo, E., Montoya, J.A., Del Angel, P., Monzón, A., 2003. Catalytic decomposition of methane over  $Ni-Al_2O_3$  coprecipitated catalysts. Reaction and regeneration studies. Appl. Catal. A: Gen. 252, 363–383.
- Vivanpatarakij, S., Laosiripojana, N., Arpornwichanop, A., Assabumrungrat, S., 2009. Performance improvement of solid oxide fuel cell system using palladium membrane reactor with different operation modes. Chem. Eng. J. 146 (1), 112–119.
- Vivanpatarakij, S., Assabumrungrat, S., Laosiripojanab, N., 2007. Improvement of solid oxide fuel cell performance by using non-uniform potential operation. J. Power Sources 167, 139–144.
- Wang, G., Wang, H., Tang, Z., Li, W., Bai, J., 2009. Simultaneous production of hydrogen and multi-walled carbon nanotubes by ethanol decomposition over  $Ni/Al_2O_3$  catalysts. Appl. Catal. B: Environ. 88, 142–151.
- Yusuke, A., Koki, U., Daisuke, N., Tsutomu, I., Hirofumi, K., Tomonori, O., Masako, Y., Iijima, S., Katsumi, K., 2009. Efficient production of H<sub>2</sub> and carbon nanotube from CH<sub>4</sub> over single wall carbon nanohorn. Chem. Phys. Lett. 482, 269–273.
- Zhang, W., Croiset, E., Douglas, P.L., Fowler, M.W., 2005.
  Simulation of a tubular solid oxide fuel cell stack using
  AspenPlus™ unit operation models. Energy Convers. Manage.
  46. 181–196.



# JOURNAL OF NATURAL GAS CHEMISTRY 天然气化学

Editors-in-Chief:

Xinhe BAO Alexis T. BELL

Vol.21 No.2 March 2012



#### **CONTENTS**

#### Communications

105 Metathesis of 1-butene and 2-butene to propene over  $Re_2O_7$  supported on macro-mesoporous  $\gamma$ -alumina prepared via a dual template method

Lei Sang, Sheng-Li Chen, Guimei Yuan, Min Zheng, Ju You, Aicheng Chen, Rui Li, Lanjing Chen

109 CF<sub>4</sub> decomposition over solid ternary mixture NaF-Si-MO (MO = La<sub>2</sub>O<sub>3</sub>, CeO<sub>2</sub>, Pr<sub>6</sub>O<sub>11</sub>, Nd<sub>2</sub>O<sub>3</sub>, Y<sub>2</sub>O<sub>3</sub>) Yanfei Pan, Xianjun Niu, Yanan Wang, Xiufeng Xu

#### Articles

113 Preparation of LaFe<sub>0.95</sub>Pd<sub>0.05</sub>O<sub>3</sub> perovskites and their catalytic performances in methane combustion Xiaojing Zhang, Yong Li, Huaju Li, Wenjie Shen

119 Methane hydrate stability in the presence of watersoluble hydroxyalkyl cellulose

M. Mohammad-Taheri, A. Zarringhalam Moghaddam, K. Nazari, N. Gholipour Zanjani

126 Kinetic hydrate inhibitor performance of new copolymer poly(N-vinyl-2-pyrrolidone-co-2-vinyl pyridine)s with TBAB

Jun Hu, Sijia Li, Yanhong Wang, Xuemei Lang, Qingping Li, Shuanshi Fan

132 Decomposition of methylamine on Mo(100) surface:
A DFT study

Jianhong Liu, Cunqin Lü, Dongli Du, Yong Guo

138 Effects of Zr/Ti molar ratio in SO<sub>4</sub><sup>2</sup>/ZrO<sub>2</sub>-TiO<sub>2</sub> calcined at different temperatures on its surface properties and glucose reactivity in near-critical methanol

Lincai Peng, Junping Zhuang, Lu Lin

148 Mathematical modeling of a slurry reactor for DME direct synthesis from syngas

Sadegh Papari, Mohammad Kazemeini, Moslem Fattahi

158 Role of support nature  $(\gamma-Al_2O_3)$  and  $SiO_2-Al_2O_3$  on the performances of rhenium oxide catalysts in the metathesis of ethylene and 2-pentene

Weena Phongsawat, Benjamas Netiworaruksa, Kongkiat Suriye, Siraprapha Dokjampa Piyasan Praserthdam, Joongjai Panpranot 165 Effect of Bi promoter on the performances of selective oxidation of isobutane to methacrolein over MoVO/AlPO<sub>4</sub> catalysts

Xitao Wang, Mei Li, Fen Wang, Shunhe Zhong, Shi Jiang, Sihe Wang

170 Ni/Al<sub>2</sub>O<sub>3</sub> catalysts for syngas methanation: Effect of Mn promoter

Anmin Zhao, Weiyong Ying, Haitao Zhang, Hongfang Ma, Dingye Fang

178 Dry reforming reaction over nickel catalysts supported on nanocrystalline calcium aluminates with different CaO/Al<sub>2</sub>O<sub>3</sub> ratios

Atiyeh Ranjbar, Mehran Rezaei

184 An accurate empirical correlation for predicting natural gas compressibility factors

Ehsan Sanjari, Ebrahim Nemati Lay

189 Comparative study between gas phase and liquid phase for the production of DMC from methanol and

Ahmed Aouissi, Salem S. Al-Deyab

194 Weakening internal diffusion effect in selective hydrodesulfurization of FCC gasoline by novel designed eggshell CoMoS/Al<sub>2</sub>O<sub>3</sub> catalysts

Bin Liu, Yongming Chai, Yajing Wang, Yunqi Liu, Chenguang Liu

200 CO<sub>2</sub> reforming of methane over nickel catalysts supported on nanocrystalline MgAl<sub>2</sub>O<sub>4</sub> with high surface area

Narges Hadian, Mehran Rezaei, Zeinab Mosayebi, Fereshteh Meshkani

207 Effect of aluminum modification on catalytic properties of PtSn-based catalysts supported on SBA-15 for propane dehydrogenation

Yongzheng Duan, Yuming Zhou, Yiwei Zhang, Xiaoli Sheng, Shijian Zhou, Zewu Zhang

www.jngc.org www.elsevier.com/locate/jngc

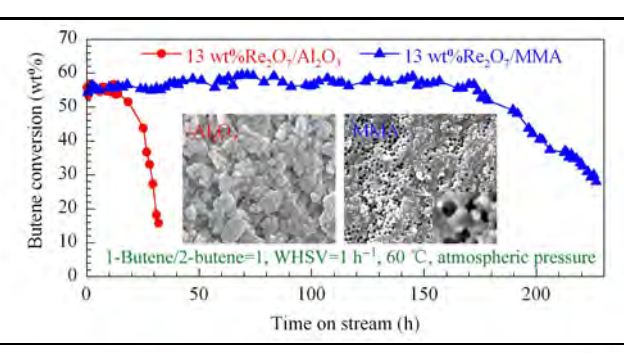
#### **CONTENTS**

#### **Communications**

105

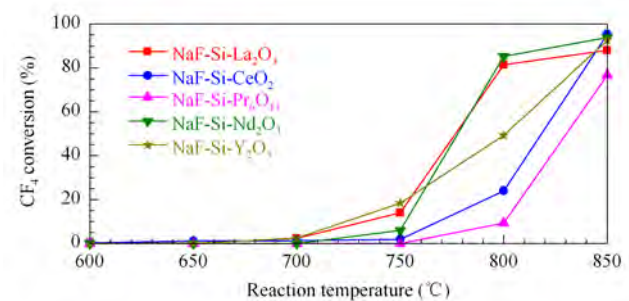
Metathesis of 1-butene and 2-butene to propene over  $Re_2O_7$  supported on macro-mesoporous  $\gamma$ -alumina prepared via a dual template method

Lei Sang, Sheng-Li Chen, Guimei Yuan, Min Zheng, Ju You, Aicheng Chen, Rui Li, Lanjing Chen



109

CF<sub>4</sub> decomposition over solid ternary mixture NaF-Si-MO (MO = La<sub>2</sub>O<sub>3</sub>, CeO<sub>2</sub>, Pr<sub>6</sub>O<sub>11</sub>, Nd<sub>2</sub>O<sub>3</sub>, Y<sub>2</sub>O<sub>3</sub>)

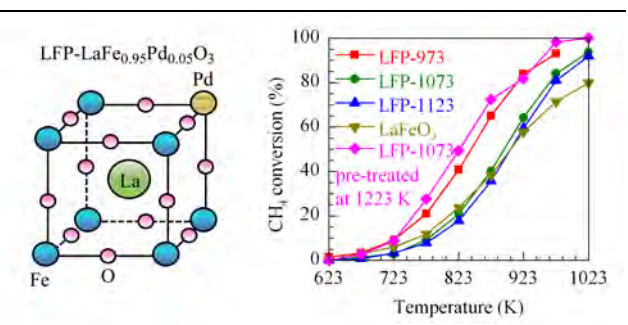


Yanfei Pan, Xianjun Niu, Yanan Wang, Xiufeng Xu

#### **Articles**

113

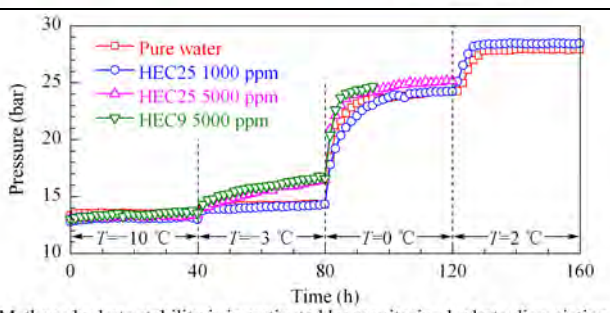
Preparation of LaFe<sub>0.95</sub>Pd<sub>0.05</sub>O<sub>3</sub> perovskites and their catalytic performances in methane combustion



Xiaojing Zhang, Yong Li, Huaju Li, Wenjie Shen

119

Methane hydrate stability in the presence of watersoluble hydroxyalkyl cellulose

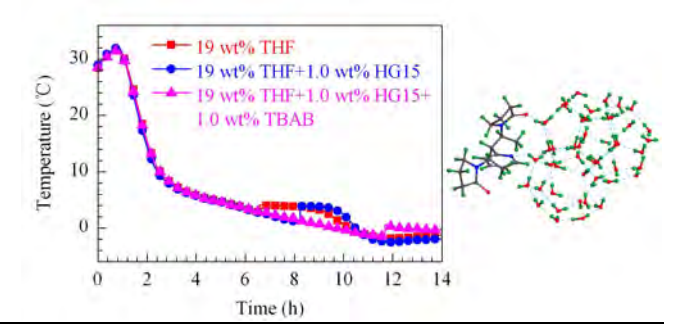


M. Mohammad-Taheri, A. Zarringhalam Moghaddam, K. Nazari, N. Gholipour Zanjani

Methane hydrate stability is investigated by monitoring hydrate dissociation.

126

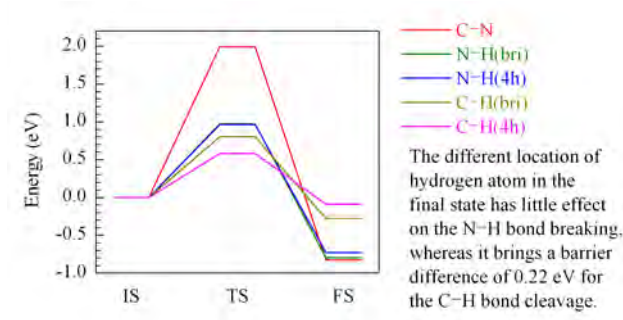
Kinetic hydrate inhibitor performance of new copolymer poly(N-vinyl-2-pyrrolidone-co-2-vinyl pyridine)s with TBAB



Jun Hu, Sijia Li, Yanhong Wang, Xuemei Lang, Qingping Li, Shuanshi Fan

#### 132

Decomposition of methylamine on Mo(100) surface: A DFT study



N-H(4h) C-H(bri) C-H(4h) The different location of hydrogen atom in the final state has little effect

whereas it brings a barrier

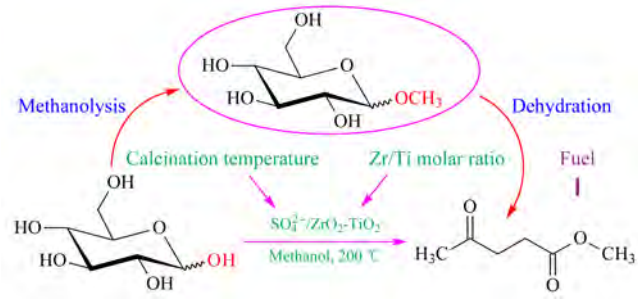
C-N

N-H(bri)

Jianhong Liu, Cunqin Lü, Dongli Du, Yong Guo

#### 138

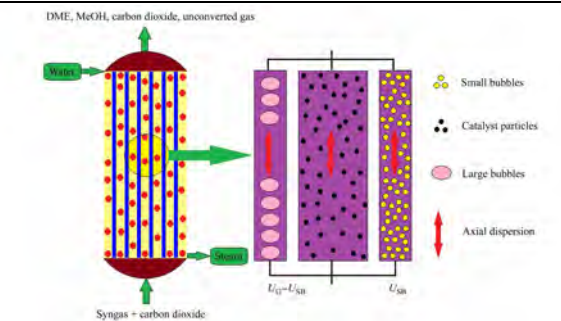
Effects of Zr/Ti molar ratio in SO<sub>4</sub><sup>2</sup>/ZrO<sub>2</sub>-TiO<sub>2</sub> calcined at different temperatures on its surface properties and glucose reactivity in near-critical methanol



Lincai Peng, Junping Zhuang, Lu Lin

#### 148

Mathematical modeling of a slurry reactor for DME direct synthesis from syngas

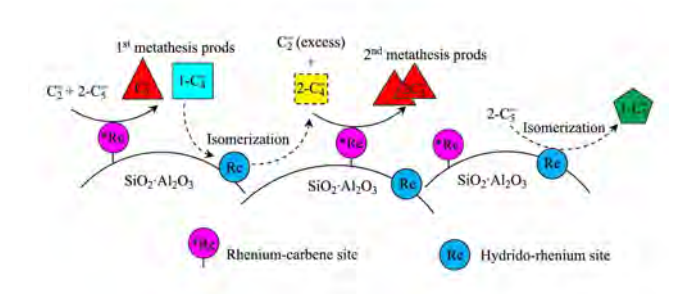


Sadegh Papari, Mohammad Kazemeini, Moslem Fattahi

#### 158

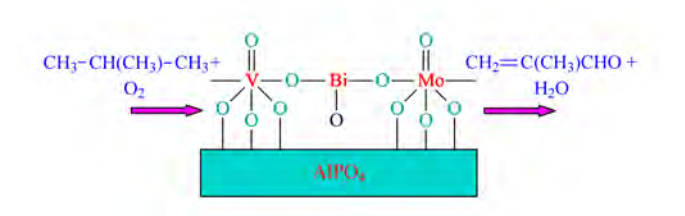
Role of support nature ( $\gamma$ -Al<sub>2</sub>O<sub>3</sub> and SiO<sub>2</sub>-Al<sub>2</sub>O<sub>3</sub>) on the performances of rhenium oxide catalysts in the metathesis of ethylene and 2-pentene

Weena Neti-Phongsawat, Benjamas woraruksa, Kongkiat Suriye, Siraprapha Dokjampa Piyasan Praserthdam, Joongjai Panpranot



#### 165

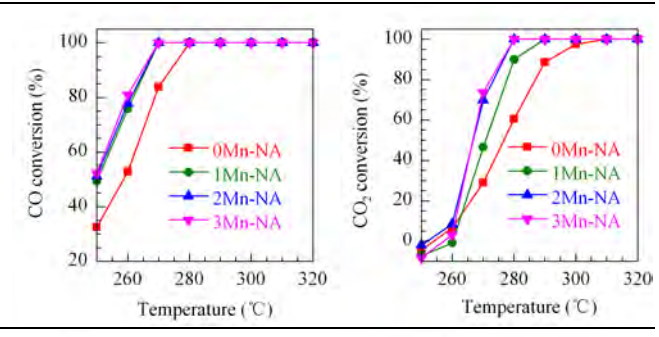
Effect of Bi promoter on the performances of selective oxidation of isobutane to methacrolein over MoVO/AlPO<sub>4</sub> catalysts



Xitao Wang, Mei Li, Fen Wang, Shunhe Zhong, Shi Jiang, Sihe Wang

#### 170

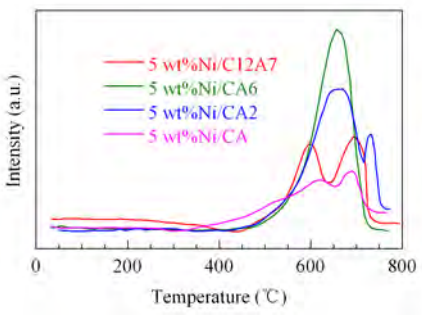
 $Ni/Al_2O_3$  catalysts for syngas methanation: Effect of Mn promoter



Anmin Zhao, Weiyong Ying, Haitao Zhang, Hongfang Ma, Dingye Fang

#### 178

Dry reforming reaction over nickel catalysts supported on nanocrystalline calcium aluminates with different  $CaO/Al_2O_3$  ratios

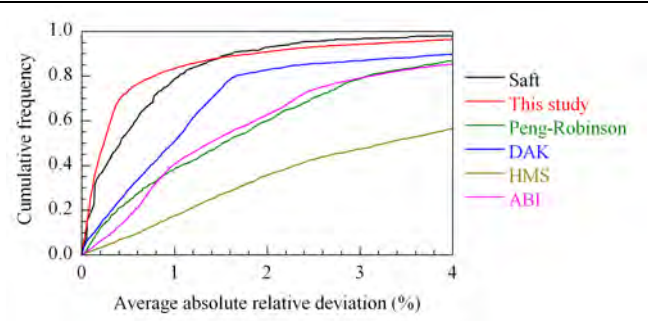


Increasing in CaO content decreased the amount of deposited carbon

Atiyeh Ranjbar, Mehran Rezaei

#### 184

An accurate empirical correlation for predicting natural gas compressibility factors



Ehsan Sanjari, Ebrahim Nemati Lay

#### 189

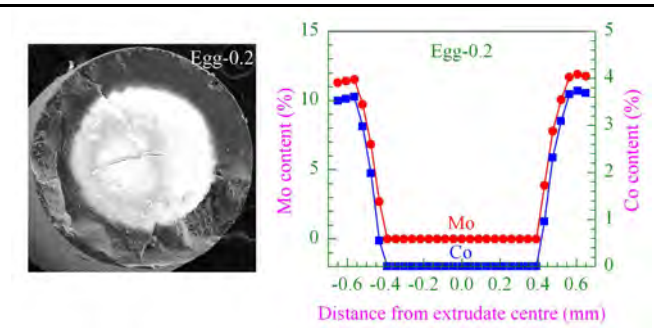
Comparative study between gas phase and liquid phase for the production of DMC from methanol and  ${\rm CO}_2$ 



Ahmed Aouissi, Salem S. Al-Deyab

194

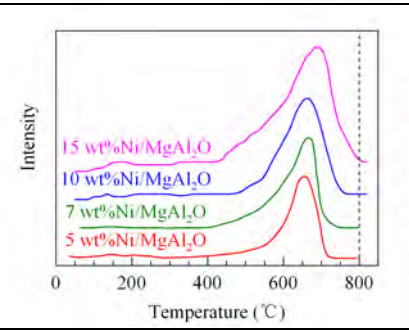
Weakening internal diffusion effect in selective hydrodesulfurization of FCC gasoline by novel designed eggshell CoMoS/Al $_2$ O $_3$  catalysts



Bin Liu, Yongming Chai, Yajing Wang, Yunqi Liu, Chenguang Liu

#### 200

 $\rm CO_2$  reforming of methane over nickel catalysts supported on nanocrystalline  $\rm MgAl_2O_4$  with high surface

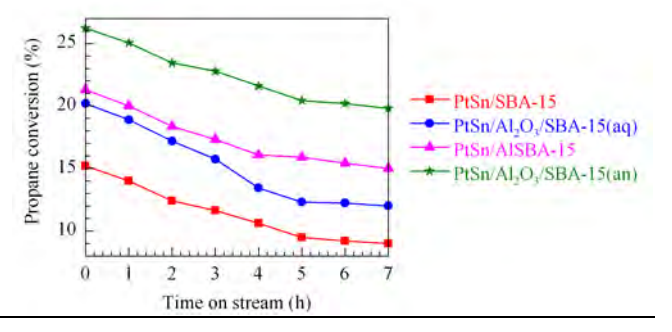


The results of TPO analysis showed that with increasing in Ni loading the amount of deposited carbon increased.

Narges Hadian, Mehran Rezaei, Zeinab Mosayebi, Fereshteh Meshkani

#### 207

Effect of aluminum modification on catalytic properties of PtSn-based catalysts supported on SBA-15 for propane dehydrogenation



Yongzheng Duan, Yuming Zhou, Yiwei Zhang, Xiaoli Sheng, Shijian Zhou, Zewu Zhang



Journal of Natural Gas Chemistry

Journal of Natural Gas Chemistry 21(2012)158-164

### Role of support nature ( $\gamma$ -Al<sub>2</sub>O<sub>3</sub> and SiO<sub>2</sub>-Al<sub>2</sub>O<sub>3</sub>) on the performances of rhenium oxide catalysts in the metathesis of ethylene and 2-pentene

Weena Phongsawat<sup>1</sup>, Benjamas Netiworaruksa<sup>1</sup>, Kongkiat Suriye<sup>2</sup>, Siraprapha Dokjampa<sup>2</sup>, Piyasan Praserthdam<sup>1</sup>, Joongjai Panpranot<sup>1\*</sup>

 Center of Excellence on Catalysis and Catalytic Reaction Engineering, Department of Chemical Engineering, Faculty of Engineering, Chulalongkorn University, Bangkok 10330, Thailand;
 SCG Chemicals CO., Ltd. 1 Siam Cement Rd., Bangsue, Bangkok 10800, Thailand

[ Manuscript received August 19, 2011; revised November 2, 2011 ]

#### Abstract

The metathesis of ethylene and 2-pentene was studied as an alternative route for propylene production over  $Re_2O_7/\gamma$ - $Al_2O_3$  and  $Re_2O_7/SiO_2$ - $Al_2O_3$  catalysts. Both NH<sub>3</sub> temperature-programmed desorption (NH<sub>3</sub>-TPD) and H<sub>2</sub> temperature-programmed reduction (H<sub>2</sub>-TPR) results showed that  $Re_2O_7/SiO_2$ - $Al_2O_3$  exhibited stronger acidity and weaker metal-support interaction than  $Re_2O_7/\gamma$ - $Al_2O_3$ . At 35–60 °C, isomerization free metathesis was observed only over  $Re_2O_7/\gamma$ - $Al_2O_3$ , suggesting that the formation of metal-carbene metathesis active sites required only weak acidity. Our results suggest that on the  $Re_2O_7/SiO_2$ - $Al_2O_3$ , hydrido-rhenium species ([Re]-H) were formed in addition to the metathesis active sites, resulting in the isomerization of the initial 1-butene product into 2-butenes. A subsequent secondary metathesis reaction between these 2-butenes and the excess ethylene could explain the enhanced yields of propylene observed. The results demonstrate the potential for high yield of propylene from alternative feedstocks.

#### Key words

metathesis; isomerization; propylene production; 2-pentene; rhenium

#### 1. Introduction

The growth in propylene production is driven by the industry demand for polypropylene, which is used in everyday products such as packaging and clothing. The majority of propylene worldwide is supplied as a by-product of steam crackers and fluid catalytic cracking units. Because the future propylene demand is expected to grow faster than the supply, the on-purpose technologies for propylene production such as propane dehydrogenation, metathesis, and methanol-to-olefins conversion have received much attention recently [1]. Among them, the cross-metathesis of ethylene and 2-butenes has already been commercialized as an economical means to produce propylene [2–3].

For industrial applications, heterogeneous catalysts are typically preferred due to the ease of catalyst recovery and separation. The most widely studied heterogeneous catalysts for olefin metathesis are based on WO<sub>3</sub>/SiO<sub>2</sub>, MoO<sub>3</sub>/Al<sub>2</sub>O<sub>3</sub>, and Re<sub>2</sub>O<sub>7</sub>/Al<sub>2</sub>O<sub>3</sub> [1,4–8]. The rhenium-based catalysts are of particular interest because they show high activity and selectivity for olefin metathesis at low reaction temperatures

(25–100 °C) [3,9,10] and high tolerance of catalyst poisons such as alkoxycarbonyl and alkoxy groups [9]. Transition  $\gamma$ -Al<sub>2</sub>O<sub>3</sub> is the commonly used support because of its suitable textural and acid-base properties for dispersion of the ReO<sub>4</sub> active species. Other inorganic supports that have shown to produce high activity of supported Re<sub>2</sub>O<sub>7</sub> catalysts include silica-alumina [11,12], alumina-boria [13,14], phosphated alumina [15], and borated silica-alumina [11]. A certain acidity level appears to be necessary for the formation of the metathesis active sites [14,16–20]. Recently, it has been reported that Re<sub>2</sub>O<sub>7</sub> supported on mesostructured aluminas exhibited superior catalytic performances in several metathesis reactions comparing to the conventional Re<sub>2</sub>O<sub>7</sub>/ $\gamma$ -Al<sub>2</sub>O<sub>3</sub> [21–25].

Although the process of the metathesis of ethylene and 2-butenes has been established, it presents some drawbacks such as the increasing price and demand of butenes as an industrial feedstock [9,26]. A recent study from our group showed that high propylene yield (88%) can be obtained via an unconventional metathesis of ethylene and 2-pentene over  $\rm Re_2O_7/SiO_2-Al_2O_3$  catalysts under mild conditions [27]. The main products from this reaction are propylene and 1-butene. 1-butene

 $<sup>*\</sup> Corresponding\ author.\ Tel:\ +66-2218-6869;\ Fax:\ +66-2218-6877;\ E-mail:\ joongjai.p@chula.ac.th$ 

is also an important petrochemical feedstock for organic syntheses, and also used as a monomer and comonomer for oligo/polymeric and co-oligo/polymeric products [28].

In the present work, detailed characterization of the  $Re_2O_7/SiO_2$ - $Al_2O_3$  catalysts before and after metathesis of ethylene and 2-pentene is reported. For comparison purposes,  $Re_2O_7/\gamma$ - $Al_2O_3$  was also prepared and studied under similar reaction conditions (35 and 60 °C). The catalysts were characterized by  $N_2$  physisorption, inductively coupled plasma optical emission spectrometer (ICP-OES), scanning electron spectroscopy (SEM), X-ray diffraction (XRD), temperature-programmed desorption of  $NH_3$  ( $NH_3$ -TPD),  $H_2$  temperature-programmed reduction ( $H_2$ -TPR), and X-ray photoelectron spectroscopy (XPS).

#### 2. Experimental

#### 2.1. Catalyst preparation

The catalysts were prepared by an incipient wetness impregnation method using an aqueous solution of ammonium perrhenate (NH<sub>4</sub>ReO<sub>4</sub>, 99.999%, Aldrich) as the rhenium precursor with the desired amount of 8 wt% Re metal loading. When the quantity of the solution of desired Re-metal is greater than pore volume of the supports, the impregnation was repeated several times with drying (6 h, 110 °C) between each cycle to eliminate excess solvent. The number of times of impregnation varied depending on the support pore volume. The SiO<sub>2</sub>-Al<sub>2</sub>O<sub>3</sub> (99.9% grade135, Aldrich) and both types of γ-Al<sub>2</sub>O<sub>3</sub> (chromatography grade of Fluka and KNH-3 grade of Sumitomo) were obtained commercially and employed as the catalyst supports. After impregnation, the catalysts were dried overnight at 110 °C in air and then calcined at 550 °C for 8 h under oxygen flow with a heating rate of 10 °C/min. Hereafter,  $Re_2O_7/SiO_2-Al_2O_3$ ,  $Re_2O_7/\gamma-Al_2O_3$ -(A), and  $Re_2O_7/\gamma$ -Al<sub>2</sub>O<sub>3</sub>-(B) are referred to the Re<sub>2</sub>O<sub>7</sub> catalysts supported on  $SiO_2-Al_2O_3$ , chromatographic grade  $\gamma$ -Al<sub>2</sub>O<sub>3</sub>, and KNH-3  $\gamma$ -Al<sub>2</sub>O<sub>3</sub>, respectively.

#### 2.2. Catalyst characterization

The specific surface area, pore volume, average pore diameter and pore size distribution of the supports and catalysts were measured by N<sub>2</sub>-physisorption performed on a Micromeritics model ASAP 2000. The alumina composition of supports and Re mass percentages for each catalyst were measured by ICP-OES on a Perkin Elmer Optima 2100DV. The sample preparation was performed by digestion of each catalyst with a mixture of hydrofluoric and nitric acids at 60 °C. SEM images were recorded on a JEOL JSM 5500LV scanning electron microscope. The XRD patterns of the supports and catalysts were measured in a range of  $2\theta$  value between 20° and 80° at a rate of 0.02°/s using a SIEMENS D5000 X-ray diffractometer and Cu  $K_{\alpha}$  radiation with a Ni filter. The PCPDFWIN database was used to identify the crystalline phases. The H<sub>2</sub>-TPR measurements were carried out in a quartz U-tube reactor. Prior to these measurements, all the catalyst samples were pretreated with a N<sub>2</sub> flow (25 mL/min, 2 h, 200 °C). The TPR profiles were obtained by passing carrier gas (10% H<sub>2</sub> in argon) through the catalyst samples (25 mL/min, ramping from 30 to 500 °C at 10 °C/min). The NH<sub>3</sub>-TPD measurements were also carried out in a quartz U-tube reactor. Firstly, the catalyst samples were pretreated in a helium flow (25 mL/min) at 200 °C for 2 h prior to measurement. Subsequently they were cooled to 25 °C before 30% NH<sub>3</sub> in He passed over the samples (25 mL/min, 1 h) to ensure thorough adsorption on the acid sites. After ammonia adsorption on catalyst surface was complete, excess ammonia was eradicated by a helium flow (25 mL/min, 1 h, 25 °C). Finally, samples were heated (linearly rise of 10 °C/min) and the TPR and TPD profiles were recorded by a TCD detector and analyzed with a Micromeritics Chemisorb 2750 automated system (ChemiSoft TPx software). The XPS measurement was carried out using an AMICUS photoelectron spectrometer equipped with an Mg  $K_{\alpha}$  X-ray as a primary excitation and KRATOS VISION2 software. XPS elemental spectra were acquired with 0.1 eV energy step at a pass energy of 75 eV. All the binding energies were referenced to the C 1s peak at 285 eV of the surface adventitious carbon.

#### 2.3. Metathesis of ethylene and 2-pentene

Gas-phase metathesis reactions between ethylene and 2-pentene were carried out in a fixed-bed tabular flow reactor (stainless steel  $ID_{tube} = 0.7$  cm) at atmospheric pressure. The gas hourly space velocity (GHSV) was 2000 h<sup>-1</sup>, using a feed gas ratio (ethylene/2-pentene) of 3. In each experiment, the catalyst sample was placed in the middle of the reactor. A temperature sensor-type K thermocouple was mounted into the reactor at the middle. Firstly, the catalyst was pretreated under a nitrogen flow (500 °C, 1 h) and then cooled to the desired operating temperature under the same gas. An on-line gas chromatograph (Agilent GC 7820A), equipped with a capillary GS-Gaspro113-4362 column (60 m×0.32 mm), monitored both reactant and product levels every 30 min, starting 35 min after commencement of each reaction. GC signals were recorded using an EZChrom Elite integrated peak program integrator.

#### 3. Results and discussion

#### 3.1. Characterization results

The  $N_2$  physisorption results of the supports and the supported  $Re_2O_7$  are shown in Table 1. Both of the  $\gamma$ -Al $_2O_3$  samples comprised 100 wt% alumina powder whereas the SiO $_2$ -Al $_2O_3$  contained only 13 wt% of alumina. After impregnation of rhenium, the BET surface area and pore volume decreased proportionately, indicating that some of the metal had become lodged inside the pores of the alumina supports. The pore size distribution plots (Figure 1) showed that the impregnation, drying, and calcination processes did not significantly alter the pore size distribution or the average pore diameter of the supports.

Re2O7/SiO2-Al2O3

C + 1 +	$Al_2O_3$	$S_{ m BET}{}^{ m a}$	$V_{ m Pore}{}^{ m b}$	$d_{ m Pore}{}^{ m c}$	Total (weak/strong) acidity <sup>d</sup>
Catalyst	(wt%)	$(m^2 \cdot g^{-1})$	$(\text{cm}^3 \cdot \text{g}^{-1})$	(nm)	$(10^3  \mu \text{mol}_{\text{NH}_3} \cdot \text{g}^{-1})$
$Re_2O_7/\gamma$ - $Al_2O_3$ - $(A)$	100	131 (145)	0.21 (0.25)	4.68 (5.09)	4.942/0.133
$Re_2O_7/\gamma$ - $Al_2O_3$ -(B)	100	191 (247)	0.47 (0.59)	7.68 (6.92)	7.794/0.243

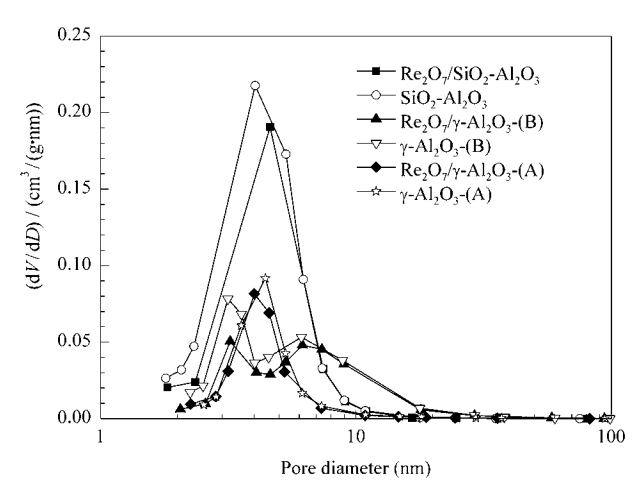
0.60 (0.79)

5.89 (5.57)

Table 1. Characteristics of the supports and supported Re<sub>2</sub>O<sub>7</sub> catalysts

The numbers in parenthesis indicate the surface area, pore volume, and average pore diameter of the bare supports; <sup>a</sup> Surface area was determined by the BET method; <sup>b</sup> Pore volume was determined by the BJH desorption method; <sup>c</sup> Average pore size was determined by BJH desorption method; <sup>d</sup> Total surface acidity of the catalysts was probed by the NH<sub>3</sub>-TPD

396 (548)



13

Figure 1. Pore size distribution of the supports and supported  $Re_2O_7$  catalysts

Figure 2 shows the SEM images of the supports and the supported rhenium catalysts in the calcined state.

 $\gamma$ -Al<sub>2</sub>O<sub>3</sub>-(B) (Figure 2c), which displayed a higher BET surface area and higher pore volume than γ-Al<sub>2</sub>O<sub>3</sub>-(A) (Figure 2a) (as obtained by Table 1), was predominantly made up of smaller and rather fluffy particles, while the  $\gamma$ -Al<sub>2</sub>O<sub>3</sub>-(A) was composed of denser, plate-like agglomerates. SEM micrographs (Figure 2e) reveal the morphology of SiO<sub>2</sub>-Al<sub>2</sub>O<sub>3</sub> support was rather spherical with rough surfaces. These morphologies remained apparent after impregnation and calcination of the supported Re<sub>2</sub>O<sub>7</sub> catalysts. XRD patterns (Figure 3) show the exhibiting peaks of alumina supports  $\gamma$ -Al<sub>2</sub>O<sub>3</sub>-(A) and  $\gamma$ -Al<sub>2</sub>O<sub>3</sub>-(B), characteristic of  $\gamma$ -alumina phase at  $2\theta = 32^{\circ}$ ,  $37^{\circ}$ ,  $46^{\circ}$ ,  $61^{\circ}$  and  $67^{\circ}$ , according to the PCPDFWIN database. For the silica-alumina support, a broad peak was seen at  $2\theta = 20^{\circ} - 25^{\circ}$ , indicating a typical amorphous solid. No peaks assignable to the crystalline phase of Re<sub>2</sub>O<sub>7</sub> were observed for any of the catalysts. According to previous studies [3,21,29,30] involving relatively high rhenium loadings, most of the metal remaining adhered to the surface exists in the form of ReO<sub>4</sub><sup>-</sup>, simply because crystalline Re<sub>2</sub>O<sub>7</sub> is volatile above calcination temperature of 300 °C.

7.428/6.910

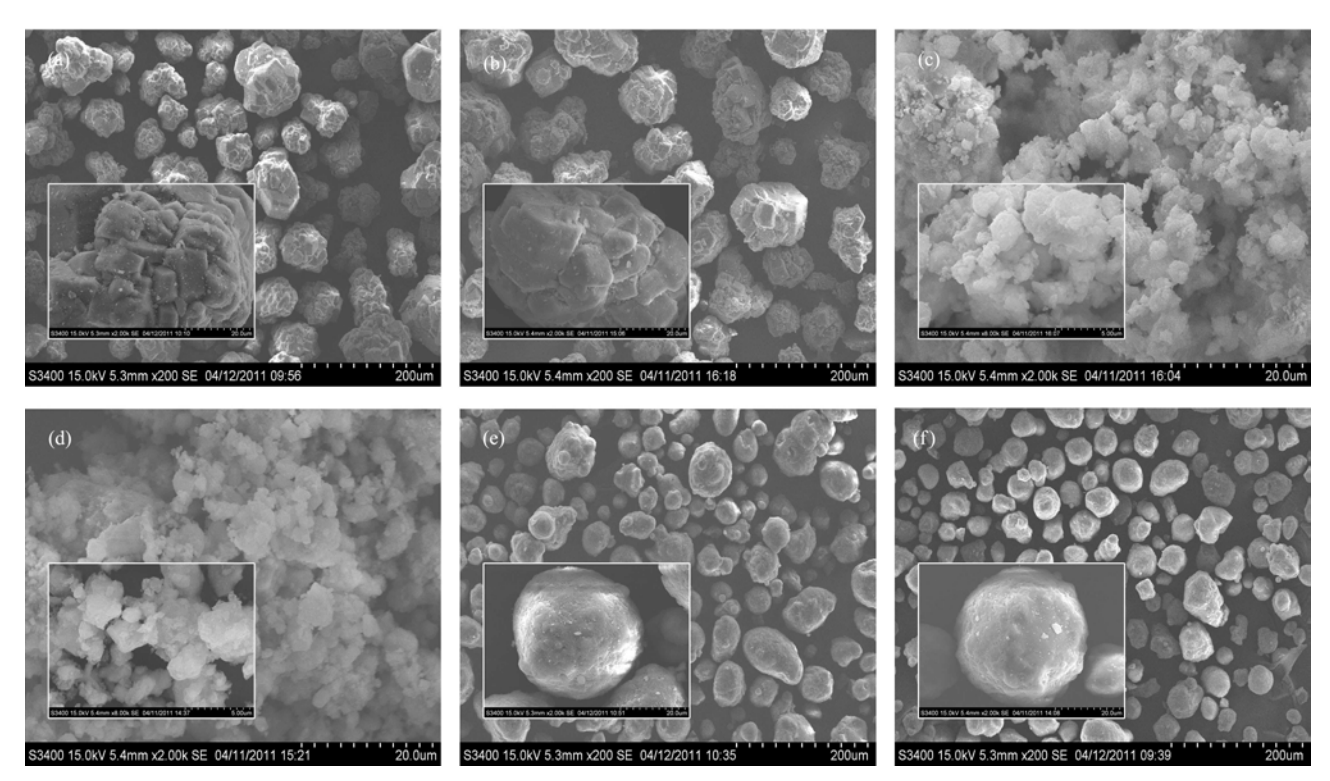


Figure 2. SEM images of (a)  $\gamma$ -Al<sub>2</sub>O<sub>3</sub>-(A), (b) Re<sub>2</sub>O<sub>7</sub>/ $\gamma$ -Al<sub>2</sub>O<sub>3</sub>-(A), (c)  $\gamma$ -Al<sub>2</sub>O<sub>3</sub>-(B), (d) Re<sub>2</sub>O<sub>7</sub>/ $\gamma$ -Al<sub>2</sub>O<sub>3</sub>-(B), (e) SiO<sub>2</sub>-Al<sub>2</sub>O<sub>3</sub> and (f) Re<sub>2</sub>O<sub>7</sub>/SiO<sub>2</sub>-Al<sub>2</sub>O<sub>3</sub> catalysts

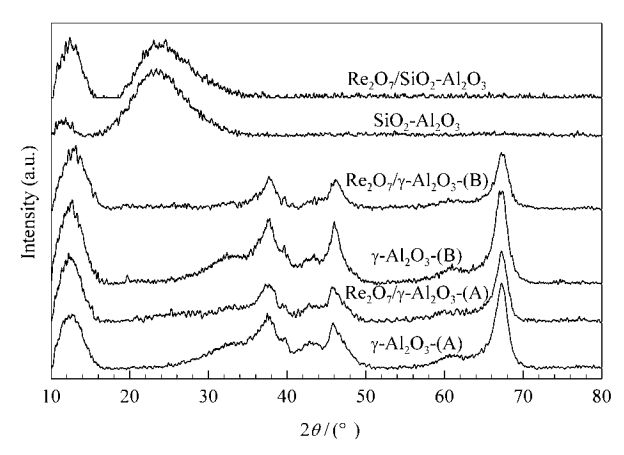


Figure 3. XRD patterns of the supports and supported  $Re_2O_7$  catalysts

Although alkene metathesis is not commonly regarded as an acid-catalyzed reaction, acidity often affects the performance of this reaction [3,14,17,31,32]. The surface acidity of the Re<sub>2</sub>O<sub>7</sub> catalysts was determined by NH<sub>3</sub>-TPD and the results are shown in Figure 4. As expected, the Re<sub>2</sub>O<sub>7</sub>/SiO<sub>2</sub>-Al<sub>2</sub>O<sub>3</sub> (Figure 4) exhibited not only greater acidity overall but also possessed a significantly higher proportion of stronger acidic sites than the Re<sub>2</sub>O<sub>7</sub>/ $\gamma$ -Al<sub>2</sub>O<sub>3</sub>. The desorption peak at around 50–200 °C corresponded to the weak acid sites of alumina [33]. It is typical that silica-alumina supported metathesis catalysts are more acidic than alumina supported catalysts [3,34–36]. The amounts of total surface acidity in terms of mol NH<sub>3</sub> per gram of catalysts are given in Table 1.

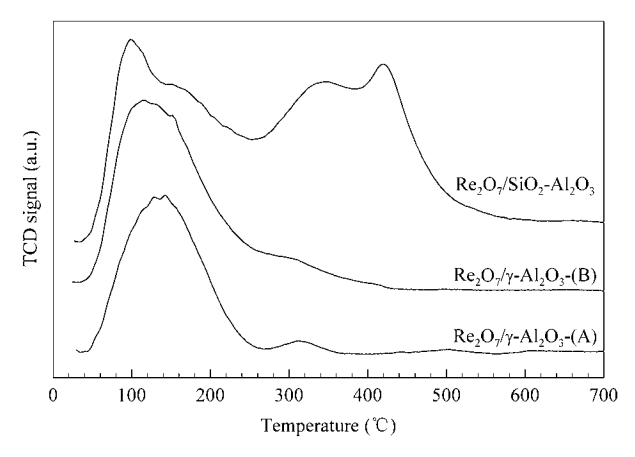


Figure 4. NH<sub>3</sub>-TPD profiles of different catalysts

The reducibility of rhenium oxide catalysts is another important parameter affecting their performance. Partial reduction of rhenium oxides, which affords metal species in a stable lower oxidation state, is a necessary step to generate the metal-carbene metathesis active sites [13,17,37,38]. An over-reduction of rhenium oxide usually results in the formation of inactive rhenium species and rapid catalyst deactivation, especially at high temperature [3,35,39,40]. Figure 5 shows the  $\rm H_2$ -TPR results of various  $\rm Re_2O_7/\gamma$ -Al $_2O_3$  and the  $\rm Re_2O_7/SiO_2$ -Al $_2O_3$  catalysts. Typically, the reduction of the

Re<sub>2</sub>O<sub>7</sub> supported catalysts from +7 oxidation state to zero (Re metal) is very fast and often appears as a single sharp reduction peak [30,38]. In the present study, the reduction temperatures for Re<sub>2</sub>O<sub>7</sub>/SiO<sub>2</sub>-Al<sub>2</sub>O<sub>3</sub> and Re<sub>2</sub>O<sub>7</sub>/ $\gamma$ -Al<sub>2</sub>O<sub>3</sub> were determined to be ca. 280 °C and 340 °C, respectively. It is suggested that the rhenium oxide on the silica-alumina was easier to reduce while bounded to silica-alumina than to the pure  $\gamma$ -Al<sub>2</sub>O<sub>3</sub> support. Moreover, the TPR profiles of the Re<sub>2</sub>O<sub>7</sub>/SiO<sub>2</sub>-Al<sub>2</sub>O<sub>3</sub> catalysts showed a very sharp main reduction peak with a shoulder at higher temperature, inferring the presence of a different rhenium oxide species. Typically, a strong metal-support interaction can diminish sintering of the Re-active sites and sublimation during calcination and/or pretreatment. The metal-support interaction seemed to be weaker on the  $Re_2O_7/SiO_2-Al_2O_3$  than on the  $Re_2O_7/\gamma-Al_2O_3$ . The actual amounts of Re metal loading, as determined by the ICP-OES, were ca. 8.3 and 5.8 wt%, respectively (see Table 2) for the calcined  $Re_2O_7/\gamma$ - $Al_2O_3$  and the  $Re_2O_7/SiO_2$ -Al<sub>2</sub>O<sub>3</sub>. The lower amount of the actual Re metal loading on the Re<sub>2</sub>O<sub>7</sub>/SiO<sub>2</sub>-Al<sub>2</sub>O<sub>3</sub> also corresponded to the weaker metal-support interaction. However, there was no significant decrease in the amount of rhenium after the reaction.

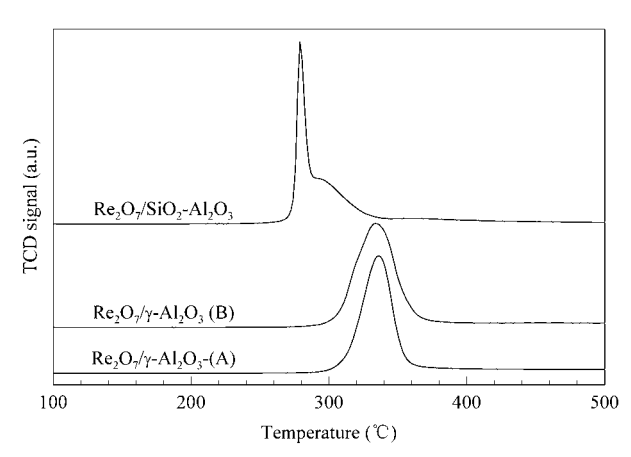


Figure 5. H<sub>2</sub>-TPR profiles of different catalysts

Table 2. Actual amount of Re metal (wt%) from the ICP-OES results

	Actual amount of Re metal (wt%)				
Catalyst samples	Before	After reaction <sup>b</sup>			
	reaction <sup>a</sup>	T = 35 °C	T = 60 °C		
$Re_2O_7/\gamma$ - $Al_2O_3$ - $(A)$	8.23	8.34	8.17		
$Re_2O_7/\gamma$ - $Al_2O_3$ - $(B)$	8.40	8.57	8.38		
Re <sub>2</sub> O <sub>7</sub> /SiO <sub>2</sub> -Al <sub>2</sub> O <sub>3</sub>	5.83	5.69	5.78		

<sup>&</sup>lt;sup>a</sup> After calcination and N<sub>2</sub>-pretreatment; <sup>b</sup> After metathesis reaction at the conditions of p = 0.1 MPa, mole ratio of ethylene/2-pentene = 3/1, GHSV = 2000 h<sup>-1</sup>, and time on stream = 455 min

The deconvoluted XPS spectra of Re 4f of all the catalysts after calcination and  $N_2$  pretreatment are shown in Figure 6. The component of rhenium species on the catalyst surface is summarized in Table 3. It was found that rhenium oxide existed in the oxidation state of +7 for both  $Re_2O_7/\gamma$ -Al<sub>2</sub>O<sub>3</sub>-(A) and  $Re_2O_7/\gamma$ -Al<sub>2</sub>O<sub>3</sub>-(B) [41–43]. For

the  $Re_2O_7/SiO_2$ - $Al_2O_3$ , 85% of rhenium component was assigned to rhenium oxide existed in the oxidation state between +6 and +7 with only 15% in the oxidation state of +7. The two

different Re oxidation states observed on the  $Re_2O_7/SiO_2$ -  $Al_2O_3$  were in good agreement with the  $H_2$ -TPR results showing additional peak shoulder.

Table 3. T	he fraction of	f different	Re oxidation	states of	f fresh catalysts
------------	----------------	-------------	--------------	-----------	-------------------

Catalyat	Fraction of	Re (+7) (%)	Fraction of Re $(+7>x>+6)$ (%)		
Catalyst	Re 4f <sub>5/2</sub> (48.8–49.2 eV)	$4f_{5/2}$ (48.8–49.2 eV) Re $4f_{7/2}$ (46.4–46.8 eV)		Re 4f <sub>7/2</sub> (45.0–45.4 eV)	
$Re_2O_7/\gamma$ - $Al_2O_3$ - $(A)$	6	94	_	_	
$Re_2O_7/\gamma$ - $Al_2O_3$ - $(B)$	6	94	_	_	
Re <sub>2</sub> O <sub>7</sub> /SiO <sub>2</sub> -Al <sub>2</sub> O <sub>3</sub>	15	_	12	73	

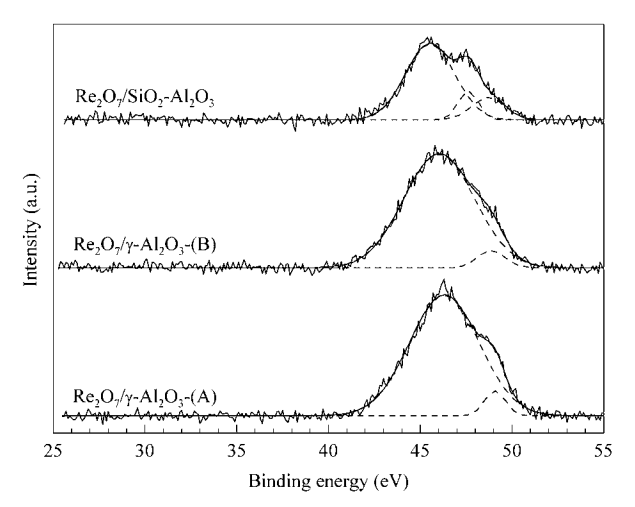
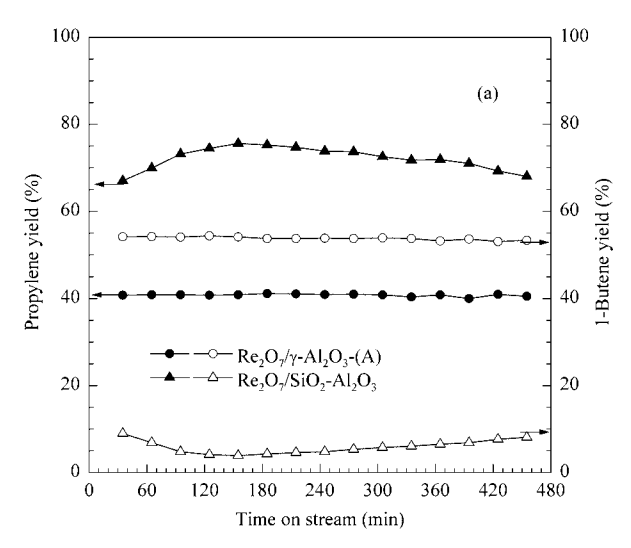


Figure 6. XPS spectra of different catalysts

#### 3.2. Catalyst performances in the metathesis of ethylene and 2-pentene

Figure 7 shows the yields of the dominant products (propylene and 1-butene) from the metathesis of ethylene and 2-pentene over the  $Re_2O_7/SiO_2-Al_2O_3$  and the  $Re_2O_7/\gamma-Al_2O_3-(A)$  catalysts during the 455 min time-on-

stream It was found that under identical operating conditions, Re<sub>2</sub>O<sub>7</sub>/SiO<sub>2</sub>-Al<sub>2</sub>O<sub>3</sub> gave a much higher total yield of propylene than the Re<sub>2</sub>O<sub>7</sub>/ $\gamma$ -Al<sub>2</sub>O<sub>3</sub>-(A). Furthermore, Re<sub>2</sub>O<sub>7</sub>/SiO<sub>2</sub>-Al<sub>2</sub>O<sub>3</sub> generated relatively little 1-butene ( $\sim$ 10 wt%), whereas Re<sub>2</sub>O<sub>7</sub>/ $\gamma$ -Al<sub>2</sub>O<sub>3</sub>-(A) produced about 55 wt% of this product. Based on the desired complete conversion of 2-pentene, the stoichiometric yields for propylene and 1-butene were 43 wt% and 57 wt%, respectively. In fact, the propylene yield obtained over the Re<sub>2</sub>O<sub>7</sub>/SiO<sub>2</sub>-Al<sub>2</sub>O<sub>3</sub> catalyst far exceeded the theoretical stoichiometric value. This additional propylene is likely to be formed via a secondary metathesis of excess ethylene and 2-butene, itself arising from the isomerization of 1-butene. The double-bond isomerization side reaction became more pronounced at 60 °C. However, at this higher temperature the Re<sub>2</sub>O<sub>7</sub>/SiO<sub>2</sub>-Al<sub>2</sub>O<sub>3</sub> exhibited more rapid deactivation than  $Re_2O_7/\gamma$ -Al<sub>2</sub>O<sub>3</sub>-(A). It is assumed that the isomerization side reaction did not occur over  $Re_2O_7/\gamma$ -Al<sub>2</sub>O<sub>3</sub>-(A) even when the temperature was increased to 60 °C, since the propylene yield remained close to its stoichiometric values (ca. 50 mol% or around 43 wt% based on 100% 2-pentene conversion). Although most of the products obtained from the  $Re_2O_7/\gamma$ - $Al_2O_3$ -(A) catalyst were directly derived from the primary metathesis between ethylene and 2-pentene, small amounts of by-products such as 2-butene and 3-hexene were produced via a self metathesis of 2-pentene as illustrated in Figure 8.



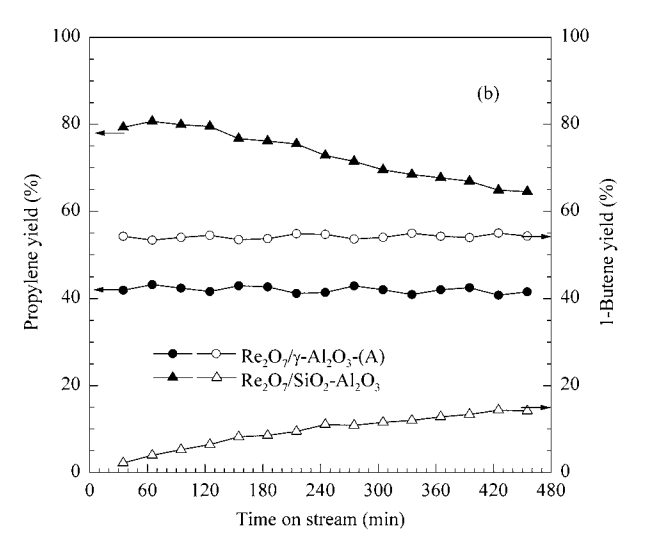
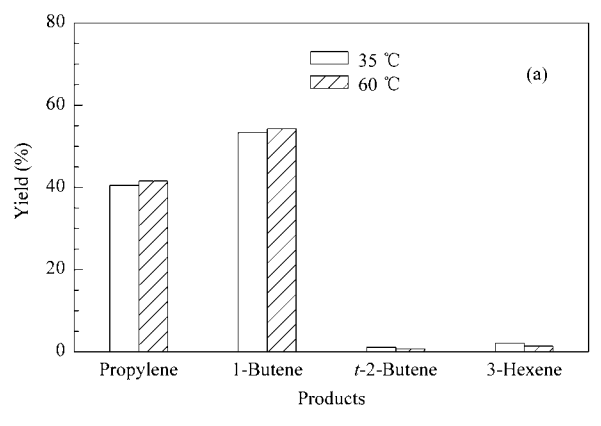


Figure 7. The comparison in the yields of the primary metathesis products (propylene and 1-butene) at reaction temperature of (a) 35 °C and (b) 60 °C (Reaction conditions: p = 0.1 MPa, mole ratio of ethylene/2-pentene = 3/1, GHSV = 2000 h<sup>-1</sup>)



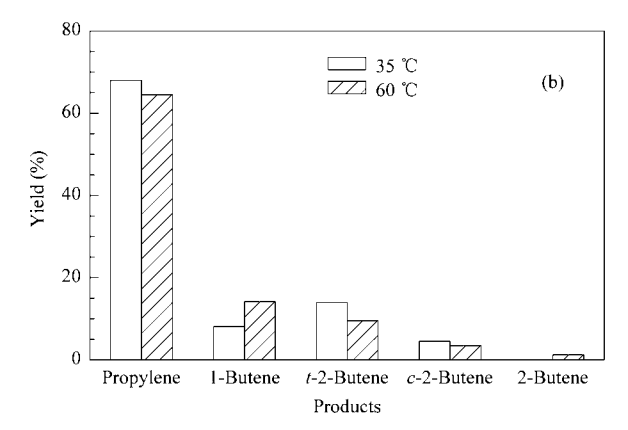


Figure 8. Comparison in total product distribution between  $Re_2O_7/\gamma-Al_2O_3-(A)$  (a) and  $Re_2O_7/SiO_2-Al_2O_3$  (b) catalysts (Reaction conditions: time on stream 455 min, 0.1 MPa, mole ratio of ethylene/2-pentene = 3/1, GHSV = 2000 h<sup>-1</sup>)

#### 3.3. Possible reaction schemes

To better elucidate the reaction mechanisms, two types of γ-Al<sub>2</sub>O<sub>3</sub>-supported Re<sub>2</sub>O<sub>7</sub> catalysts were studied under similar reaction conditions. The  $\gamma$ -Al<sub>2</sub>O<sub>3</sub>-(A) possessed lower BET surface area and lower pore volume than the  $\gamma$ -Al<sub>2</sub>O<sub>3</sub>-(B). However, there were no significant differences in terms of 2-pentene conversion and product selectivities between the two types of  $\gamma$ -Al<sub>2</sub>O<sub>3</sub>-supported Re<sub>2</sub>O<sub>7</sub> catalysts (see Table 4). From the NH<sub>3</sub>-TPD results, both the Re<sub>2</sub>O<sub>7</sub>/ $\gamma$ - $Al_2O_3$ -(A) and the  $Re_2O_7/\gamma$ - $Al_2O_3$ -(B) contained only weak acid sites in similar abundance. Therefore, it seems that the weak acidic sites of the Re<sub>2</sub>O<sub>7</sub>/γ-Al<sub>2</sub>O<sub>3</sub> catalysts promoted the metathesis reaction but were unable to catalyze the isomerization of 1-butene. Noticeably, even at room temperature, isomerization of 1-butene (primary metathesis product) occurred instantaneously over the Re<sub>2</sub>O<sub>7</sub>/SiO<sub>2</sub>-Al<sub>2</sub>O<sub>3</sub>. The existence of more abundant Brönsted acid sites on silicaalumina is likely to be responsible for its isomerization activity [12]. This greater acidity and the easier reducibility of the Re<sub>2</sub>O<sub>7</sub>/SiO<sub>2</sub>-Al<sub>2</sub>O<sub>3</sub> catalysts could promote the formation of hydrido-rhenium complexes. Such [Re]-H species, generated from protonation of rhenium centers by Brönsted species (silica-alumina), have been claimed to act as isomerization sites [12,29,44]. In order to confirm the role of metal in the isomerization mechanism, bare silica-alumina support was tested. The negative results obtained with 1-butene at 35-60 °C confirmed the lack of isomerization activity of the catalyst supports. Figure 9 illustrates a possible scheme for the origins of various reactions in the metathesis of ethylene and 2-pentene over the Re<sub>2</sub>O<sub>7</sub>/ $\gamma$ -Al<sub>2</sub>O<sub>3</sub> and the Re<sub>2</sub>O<sub>7</sub>/SiO<sub>2</sub>-Al<sub>2</sub>O<sub>3</sub> catalysts. It is also well known that metal-carbene active species were generated through the interaction between the partial reduction of rhenium metal and the alkene reactant on an acidic support [3,16,19].

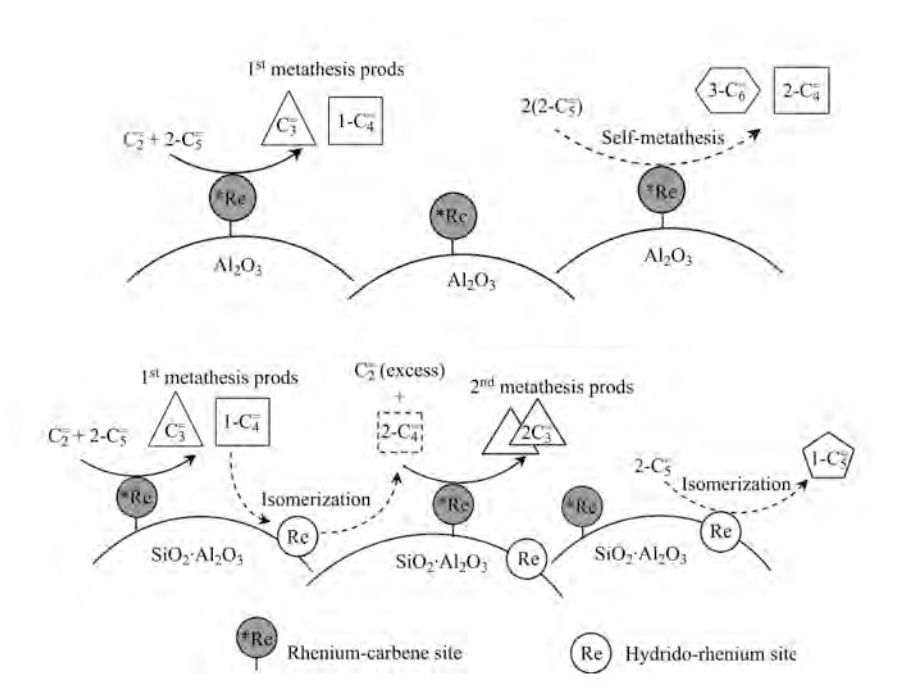


Figure 9. Possible origins of various reactions in the metathesis system of ethylene and 2-pentene over the  $Re_2O_7/\gamma$ - $Al_2O_3$  and the  $Re_2O_7/SiO_2$ - $Al_2O_3$  catalysts

Table 4. Catalytic performances of Re<sub>2</sub>O<sub>7</sub> supported on SiO<sub>2</sub>-Al<sub>2</sub>O<sub>3</sub> and two types of  $\gamma$ -Al<sub>2</sub>O<sub>3</sub> supports

	Selectivity (%) <sup>a</sup>				
	C <sub>3</sub> =	1-C <sub>4</sub>	$2-C_4^=$	1-C <sub>5</sub>	$3-C_6^=$
$T_{\rm Rxn}$ = 35 °C					
$Re_2O_7/\gamma$ - $Al_2O_3$ - $(A)$	42.2	55.9	0.8	_	1.2
$Re_2O_7/\gamma$ - $Al_2O_3$ - $(B)$	42.2	55.6	0.7	_	1.4
Re2O7/SiO2-Al2O3	71.9	8.6	19.5	_	_
$T_{\rm Rxn}$ = 60 $^{\circ}{\rm C}$					
$Re_2O_7/\gamma$ - $Al_2O_3$ - $(A)$	42.4	55.4	0.8	_	1.4
$Re_2O_7/\gamma$ - $Al_2O_3$ - $(B)$	43.9	54.2	0.8	_	1.2
$Re_2O_7/SiO_2$ - $Al_2O_3$	69.4	15.3	14.0	1.3	_

Reaction conditions: P=0.1 MPa, mole ratio of ethylene/2-pentene = 3/1, GHSV =  $2000 \, \mathrm{h^{-1}}$ , time on stream = 455 min; <sup>a</sup> Selectivity (%) on the basis of 100% 2-pentene conversion

#### 4. Conclusions

The nature of the support material in rhenium-based metathesis catalysts appears to significantly affect their catalytic performances in the unconventional metathesis of ethylene and 2-pentene for propylene production. Under the reaction conditions used (35-60 °C), Re<sub>2</sub>O<sub>7</sub>/SiO<sub>2</sub>-Al<sub>2</sub>O<sub>3</sub> exhibited much higher double-bond isomerization activity than  $Re_2O_7/\gamma$ -Al<sub>2</sub>O<sub>3</sub>. However, unlike the conventional metathesis of ethylene and 2-butenes, isomerization here was considered as a useful reaction for the transformation of 1-butene (primary product) to 2-butenes which could instantly react with excess ethylene to form additional propylene. Metathesis reaction over Re<sub>2</sub>O<sub>7</sub>/ $\gamma$ -Al<sub>2</sub>O<sub>3</sub> occurred without isomerization side reactions. It is proposed that both the presence of weak acidic sites and the stabilization of Re-active species on the support were important factors in the formation of the necessary active metal-carbene complexes.

#### Acknowledgements

The financial supports from the Thailand Research Fund (TRF), and the Office of Higher Education Commission are gratefully acknowledged. The authors would like to thank the Royal Golden Jubilee Ph. D. scholarship from TRF and SCG Chemicals for W. P.

#### References

- [1] Stoyanova M, Rodemerck U, Bentrup U, Dingerdissen U, Linke D, Mayer R W, Rotgerink H G J L, Tacke T. Appl Catal A, 2008, 340(2): 242
- [2] Mol J C. J Mol Catal A, 2004, 213(1): 39
- [3] Mol J C. Catal Today, 1999, 51(2): 289
- [4] Fierro J L G, Mol J C. Metathesis of olefins on Metal Oxides. Taylor & Francis Group: CPC Press, 2006. 517
- [5] Mol J C, Buffon R. J Braz Chem Soc, 1998, 9(1): 1
- [6] Moffat A J, Clark A, Johnson M M. J Catal, 1971, 22(3): 379
- [7] Luckner R C, Wills G B. J Catal, 1973, 28(1): 83
- [8] Lojacono M, Hall W K. J Colloid Interface Sci, 1977, 58(1): 76
- [9] Ivin K J, Mol J C. Olefin Metathesis and Metathesis Polymerization. San Diego: Academic Press, 1997
- [10] Edrevakardjieva R M, Andreev A A. J Catal, 1986, 97(2): 321
- [11] Rodella C B, Buffon R. Appl Catal A, 2004, 263(2): 203

- [12] Bakala P C, Briot E, Millot Y, Piquemal J Y, Bregeault J M. J Catal, 2008, 258(1): 61
- [13] Sheu F C, Hong C T, Hwang W L, Shih C J, Wu J C, Yeh C T. Catal Lett, 1992, 14(3-4): 297
- [14] Xu X D, Mol J C, Boelhouwer C. J Chem Soc Faraday Trans, 1986, 82(9): 2707
- [15] Sibeijn M, Spronk R, van Veen J A R, Mol J C. Catal Lett, 1991, 8(2-4): 201
- [16] Commereuc D, Olivier-Bourbigou H, Kruger-Tissot V, Saussine L. J Mol Catal A, 2002, 186(1-2): 215
- [17] Xu X D, Boelhouwer C, Vonk D, Benecke J I, Mol J C. J Mol Catal, 1986, 36(1-2): 47
- [18] Hsu C C. [PhD Dissertation]. Oklahoma: Oklahoma University,
- [19] Buffon R, Auroux A, Lefebvre F, Leconte M, Choplin A, Basset J M, Herrmann W A. J Mol Catal, 1992, 76(1-3): 287
- [20] Schekler-Nahama F, Clause O, Commereuc D, Saussey J. Appl Catal A, 1998, 167(2): 237
- [21] Balcar H, Hamtil R, Zilkova N, Cejka J. Catal Lett, 2004, 97(1-2): 25
- [22] Onaka M, Oikawa T. Chem Lett, 2002, (8): 850
- [23] Oikawa T, Ookoshi T, Tanaka T, Yamamoto T, Onaka M. Microporous Mesoporous Mater, 2004, 74(1-3): 93
- [24] Balcar H, Cejka J. Macromol Symp, 2010, 293(1): 43
- [25] Martin-Aranda R M, Cejka J. Top Catal, 2010, 53(3-4): 141
- [26] Cornil B, Herrmann A W, Schogl R, Wong C. A Concise Encyclopedia Catalysis from A to Z. New York: Wiley-VCH Press, 2000
- [27] Phongsawat W, Netivorruksa B, Suriye K, Dokjampa S, Praserthdam P, Panpranot J. J Nat Gas Chem, 2012, 21(1): 83
- [28] Kotov S V, Kankaeva I N. Chem Technol Fuels Oils, 1994, 30(5-6): 240
- [29] Rodella C B, Cavalcante J A M, Buffon R. Appl Catal A, 2004, 274(1-2): 213
- [30] Mitra B, Gao X T, Wachs I E, Hirt A M, Deo G. Phys Chem Chem Phys, 2001, 3(6): 1144
- [31] Ellison A, Coverdale A K, Dearing P F. J Mol Catal, 1985, 28(1-3): 141
- [32] Xu X D, Boelhouwer C, Vonk D, Benecke J I, Mol J C. J Mol Catal, 1986, 36(1-2): 47
- [33] Chary K V R, Kishan G, Kumar C P, Sagar G V. Appl Catal A, 2003, 246(2): 335
- [34] Sibeijn M, Mol J C. Appl Catal, 1991, 67(2): 279
- [35] Moulijn J A, Mol J C. J Mol Catal, 1988, 46(1-3): 1
- [36] Andreini A, Xu X D, Mol J C. Appl Catal, 1986, 27(1): 31
- [37] Vuurman M A, Stufkens D J, Oskam A, Wachs I E. J Mol Catal, 1992, 76(1-3): 263
- [38] Daniell W, Weingand T, Knozinger H. J Mol Catal A, 2003, 204: 519
- [39] Behr A, Schuller U, Bauer K, Maschmeyer D, Wiese K D, Nierlich F. *Appl Catal A*, 2009, 357(1): 34
- [40] Mol J C, MouQn J A, Anderson J R, Boudart M. Catalysis: Science and Technology. Berlin: Springer-Verlag, 1987
- [41] Wagner C D, Riggs W M, Davis L E, Moulder J F, Muilenberg G E. Handbook of X-ray Photoelectron Spectroscopy. USA: Perkin-Elmer Corporation, 1979. 151
- [42] Balcar H, Zilkova N, Bastl Z, Dedecek J, Hamtil R, Brabec L, Zukal A, Cejka J. *Stud Surf Sci Catal*, 2007, 170: 1145
- [43] Yuan Y Z, Iwasawa Y. J Phys Chem B, 2002, 106(17): 4441
- [44] Bregeault J M. Catalyse Homogene par les Complexes des Metaux de Transition. Paris: Masson Press, 1992. 128

## Effect of SiO<sub>2</sub>-Al<sub>2</sub>O<sub>3</sub> Composition on the Catalytic Performance of the Re<sub>2</sub>O<sub>7</sub>/SiO<sub>2</sub>-Al<sub>2</sub>O<sub>3</sub> Catalysts in the Metathesis of Ethylene and 2-Pentene for Propylene Production

Weena Phongsawat · Benjamas Netiworaruksa · Kongkiat Suriye · Piyasan Praserthdam · Joongjai Panpranot

Received: 21 May 2012/Accepted: 15 July 2012/Published online: 2 August 2012 © Springer Science+Business Media, LLC 2012

**Abstract** The production of propylene via a gas-phase metathesis of ethylene and 2-pentene has been studied over the Re<sub>2</sub>O<sub>7</sub>/SiO<sub>2</sub>-xAl<sub>2</sub>O catalysts containing various SiO<sub>2</sub>- $Al_2O_3$  compositions (13, 25, 50, 75, and 100 wt%  $Al_2O_3$ ). Using ethylene and 2-pentene as the reactants, isomerization of the initial 1-butene product into 2-butenes and a subsequent secondary metathesis reaction between 2-butenes and excess ethylene enhanced the propylene formation so that propylene yield higher than its stoichiometric amount (>50 %) could be obtained. While the pure Al<sub>2</sub>O<sub>3</sub> supported Re<sub>2</sub>O<sub>7</sub> catalyst possessed only the first type of isolated monomeric ReO<sub>4</sub><sup>-</sup> tetrahedra structure with a stronger Re-O-support bond, the second type with a weaker Re-O-support bond was observed on the SiO<sub>2</sub>-Al<sub>2</sub>O<sub>3</sub> supported ones. The double-bond isomerization and the metathesis activities were optimized to produce the highest propylene yield over the Re<sub>2</sub>O<sub>7</sub>/SiO<sub>2</sub>-Al<sub>2</sub>O<sub>3</sub> catalyst containing 50 wt% Al<sub>2</sub>O<sub>3</sub>.

**Keywords** Metathesis · Isomerization · Propylene production · 2-pentene · Silica–alumina

W. Phongsawat  $\cdot$  B. Netiworaruksa  $\cdot$  P. Praserthdam  $\cdot$  J. Panpranot  $(\boxtimes)$ 

Department of Chemical Engineering, Faculty of Engineering, Center of Excellence on Catalysis and Catalytic Reaction Engineering, Chulalongkorn University, Bangkok 10330, Thailand

e-mail: joongjai.p@chula.ac.th

K. Suriye SCG Chemicals Co., Ltd, 1 Siam-cement Rd Bang sue, Bangkok 10800, Thailand

#### 1 Introduction

Olefin metathesis is one of industrial important reactions in olefin conversion that opens up many new routes to produce important petrochemical products. Current commercial technology for producing propylene via metathesis reaction is based on the conversion of ethylene and 2-butene over heterogeneous catalyst systems [1-4]. However, this route has some drawbacks although high propylene yield can be obtained. It needs C4 streams that are free of isobutene and butadiene [5] and both cost and demand of butene industrial feedstock have increased continuously [4, 6, 7]. In our recent work, a cross-metathesis of ethylene and 2-pentene over Re<sub>2</sub>O<sub>7</sub>/Al<sub>2</sub>O<sub>3</sub> catalysts has been studied as an interesting route to produce propylene from cheaper raw materials [8, 9]. The products from this route are not only high valuable propylene but also 1-butene that are increasing in both demand and cost nowadays [6, 7].

The Re<sub>2</sub>O<sub>7</sub>/Al<sub>2</sub>O<sub>3</sub> catalysts have been employed in large scale metathesis of ethylene and 2-butene into propylene [10]. Their catalytic activities can be further improved by the use of mixed metal oxides supports such as SiO<sub>2</sub>–Al<sub>2</sub>O<sub>3</sub> [2, 11–13], phosphated alumina (AIPO) [14] and Al<sub>2</sub>O<sub>3</sub>–B<sub>2</sub>O<sub>3</sub> [15]. In addition, recently mesoporous materials have been studied as supports for Re<sub>2</sub>O<sub>7</sub> catalysts in the metathesis reactions [16–22]. The improved catalytic activity of the mesoporous alumina supported Re<sub>2</sub>O<sub>7</sub> than those supported on conventional alumina was directly correlated to their large pore size and higher specific surface area [16]. However, the synthesis of these mesostructured oxides was more complicated and may not be suitable for industrial application [23].



W. Phongsawat et al.

Among the various mixed oxides used to stabilize the Re species in the favorable oxidation state for the formation of the rhenium carbene active complex, the SiO<sub>2</sub>-Al<sub>2</sub>O<sub>3</sub> receives considerable attention and has shown significant improvement in the metathesis reaction. According to the literature [2, 24, 25], low rhenium-loading Re<sub>2</sub>O<sub>7</sub>/Al<sub>2</sub>O<sub>3</sub> catalysts exhibited poor or negligible activity for the alkene metathesis. However, 2 wt% Re<sub>2</sub>O<sub>7</sub> over SiO<sub>2</sub>-Al<sub>2</sub>O<sub>3</sub> was found to be more active than the 18 wt% Re<sub>2</sub>O<sub>7</sub>/Al<sub>2</sub>O<sub>3</sub> catalysts [26, 27]. In epoxidation of alkenes, the stability of rhenium-based catalysts also depended on the alumina content of mixed silica-alumina supports in which ReO<sub>4</sub> supported on higher alumina content or pure alumina supports showed no metal lost [28] According to Moulijn and Mol [12], the Si-O-Re bonds are very weak comparing to the Al-O-Re bonds.

Acidity of the catalysts plays an important role in alkene metathesis reactions [1, 2, 13, 26, 27, 29, 30]. In general, silica-alumina is more acidic than alumina [31] and it contains both strong Lewis and Brönsted acidic sites [13, 30]. Xiaoding et al. [13, 27] showed the distinct correlation between the Brönsted acidity which was directly proportional to the silica-alumina compositions and the metathesis activity for the Re-based catalyst. A model for the generation of metallacarbenes including the function of partial reduced rhenium species and neighboring Brönsted acid sites has been proposed [27, 32]. The presence of Al in the SiO<sub>2</sub>-Al<sub>2</sub>O<sub>3</sub> supports was found to affect the performance of MoO<sub>3</sub>/SiO<sub>2</sub>-Al<sub>2</sub>O<sub>3</sub> catalysts in various works [33-39]. Debecker et al. [33] suggested that the acidity created by the presence of alumina in silica was beneficial for the better dispersion of active Mo species.

A number of previous studies of Re-based catalysts [27, 28, 30, 40–43] have shown that double-bond isomerization activity of silica-alumina was much higher than that of alumina. The isomerization activity of Re<sub>2</sub>O<sub>7</sub>/ SiO<sub>2</sub>-Al<sub>2</sub>O<sub>3</sub> catalyst was even more higher than the corresponding sole SiO<sub>2</sub>-Al<sub>2</sub>O<sub>3</sub> support [40]. Nevertheless, in our previous studies [8, 9], double-bond isomerization of 1-butene was found to be useful for producing additional propylene formation in the unconventional metathesis of ethylene and 2-pentene. The present work was aimed to further investigate the influence of SiO<sub>2</sub>-Al<sub>2</sub>O<sub>3</sub> composition on the catalytic performances of Re<sub>2</sub>O<sub>7</sub>/SiO<sub>2</sub>-Al<sub>2</sub>O<sub>3</sub> in the metathesis of ethylene and 2-pentene for propylene production. The catalysts were also characterized by inductively coupled plasma optical emission spectroscopy (ICP-OES), N<sub>2</sub>-physisorption (BET and BJH methods), X-ray diffraction (XRD), temperature program desorption of NH<sub>3</sub> (NH<sub>3</sub>-TPD), X-ray photoelectron spectroscopy (XPS), UV-Visible, and FT-Raman spectroscopy.



#### 2 Experimental

#### 2.1 Catalyst Preparation

#### 2.1.1 Synthesis of $SiO_2$ - $Al_2O_3$ Supports

The SiO<sub>2</sub>-xAl<sub>2</sub>O<sub>3</sub> supports containing various amount of alumina (x = 13, 25, 50, 75,and 100 wt%) were prepared by a co-precipitation method according to that of Okada et al. [44]. Aluminium nitrate nonahydrate [ANN; Al(NO<sub>3</sub>)<sub>3</sub>·9H<sub>2</sub>O] and tetraethylorthosilicate [TEOS; Si(OC<sub>2</sub>H<sub>5</sub>)<sub>4</sub>] solution were coprecipitated and adjusted to 1.2 mol l<sup>-1</sup> for all the sample preparation. The distilled water and ethanol was first mixed, then ANN was added and the resulting solution was stirred for 15 min. The amount of H<sub>2</sub>O in the solution was adjusted to give H<sub>2</sub>O/ TEOS = 18/1, this ratio indicating a large excess of  $H_2O$ for hydrolysis of TEOS. An ethanol solution containing a desired amount of TEOS was then added and stirred for 3 h, 25 wt% of ammonia solution was added rapidly to the solution with vigorous stirring. The precipitates were immediately dried over a hot plate at 60 °C for 3 h and subsequently dried overnight at 110 °C in an oven. After drying, they were calcined under oxygen flowing at 300 °C for 4 h with a heating rate of 3 °C/min to obtain the xerogels. These xerogels were then calcined at 550 °C for 4 h under oxygen flowing with a heating rate of 10 °C min<sup>-1</sup> before used as the SiO<sub>2</sub>-Al<sub>2</sub>O<sub>3</sub> supports for preparation of supported rhenium oxide catalysts. The synthesized SiO<sub>2</sub>- $Al_2O_3$  supports were denoted as SixAl where x indicated wt% of Al<sub>2</sub>O<sub>3</sub> in the silica-alumina supports.

#### 2.1.2 Preparation of Supported Rhenium Oxide Catalysts

The catalysts were prepared by incipient wetness impregnation with aqueous solution of ammonium perrhenate (99.999 %, Aldrich). When quantity of the solution of the desired Re-metal loading (8 wt% Re-metal) was greater than pore volume of the supports, the impregnation was performed several times with drying at 110 °C in between to eliminate the solvent for 6 h. After impregnation, these catalysts were dried overnight at 110 °C and then calcined at 550 °C for 8 h under oxygen flow with a heating rate of 10 °C min<sup>-1</sup>. The catalyst nomenclature Re/SixAl is referred to the Re<sub>2</sub>O<sub>7</sub> supported on the SiO<sub>2</sub>–xAl<sub>2</sub>O<sub>3</sub> containing *x* wt% of Al<sub>2</sub>O<sub>3</sub>.

#### 2.2 Catalyst Characterization

The weight percentage of actual Re metal for each catalyst after calcination was measured by ICP-OES on a Perkin Elmer Optima 2100DV. The samples were digested with hydrofluoric and nitric acid at 60 °C. The specific surface

area, pore volume, average pore diameter and pore sizes distribution of the supports and the supported rhenium catalysts were measured by the N<sub>2</sub>-physisorption with using a Micrometritics model ASAP 2000 automated system. The measurements were performed with a degassing at 350 °C (Ramp rate = 10 °C min<sup>-1</sup>) for 4 h prior to N<sub>2</sub> physisorptions at -196 °C. The specific surface area was calculated based on the Brunauer-Emmett-Teller (BET) isotherms and the pore volume and pore size distribution were calculated based on the Barrett-Joyner-Halenda (BJH) desorption branch analysis. The XRD patterns of the supports and the catalysts were measured in a range of  $2\theta$ value between 20° and 80° at a rate of 0.02° s<sup>-1</sup> using a SIEMENS D5000 X-ray diffractometer and Cu K<sub>x</sub> radiation with a Ni filter. The PCPDFWIN database was used as reference to identify the crystalline phases. The NH<sub>3</sub>-TPD measurements were carried out in a quartz U-tube reactor using a Micromeritic Chemisorb 2750 automated system. The catalyst samples were firstly pretreated in a He flow (25 ml min<sup>-1</sup>) at 200 °C for 2 h prior to measurement. Subsequently they were cooled to room temperature around 25 °C then a 30 %NH<sub>3</sub>/He mixed gas was flowed (25 ml min<sup>-1</sup>) over the samples for 1 h to throughout adsorb on the acid sites. After ammonia adsorption on catalyst surface was completed, the excess ammonia was eradicated by the He flowing (25 ml min<sup>-1</sup>) at the room temperature for 1 h. Then, the samples were heated linearly with a rate of 10 °C min<sup>-1</sup>. The TPD profiles were detected by TCD detector and analyzed with a ChemiSoft TPx software. XPS was carried out using an AMICUS photoelectron spectrometer equipped with an Mg K<sub>α</sub> X-ray as a primary excitation and KRATOS VISION2 software. XPS elemental spectra were acquired with 0.1 eV energy step at a pass energy of 75 eV. All the binding energies were referenced to the C 1 s peak at 285 eV. Diffuse reflectance UV-Vis spectra were collected on Lambda 650 UV-Vis spectrometer equipped with a diffuse reflectance attachment and an integrating sphere. The samples were studied in the form of powder carried out in sample holder. The spectra were recorded under air-exposed conditions in the range 200-900 nm and the scan speed was  $1 \text{ nm min}^{-1}$ .

#### 2.3 Catalytic Tests

The catalytic performances were tested in the gas-phase metathesis reaction between ethylene and 2-pentene, which was carried out in a stainless steel ( $\rm ID_{tube}=0.7~cm$ ) fixed-bed tabular flow reactor under atmospheric pressure. The gas-phase of 2-pentene was prepared by dilution a small

amount liquid 2-pentene (≥99 % mixture of isomers, Aldrich) in low pressure N<sub>2</sub> gas (4 vol.% of 2-pentene in 12 bar N<sub>2</sub> balance). The reactants were pre-mixed with high purity ethylene (99.999 %), and high purity N<sub>2</sub> to have the composition of 6.75 vol.% 2-pentene, 2.25 vol.% ethylene in N<sub>2</sub> balance before passing through the reactor. The feed flow rates were adjusted to 70–77.5 cm<sup>3</sup> min<sup>-1</sup> depending on the bed volume of each catalyst. In a typical run, 1 g of the catalyst sample was placed in the middle of the reactor. The reaction temperature, gas hourly space velocity (GHSV), and mole of feed ratio (ethylene/2-pentene) were kept at 35  $\pm$  2 °C, 3,000 h<sup>-1</sup> and 3, respectively. Start up with pretreatment the catalyst sample at 500 °C under N<sub>2</sub> flow for 1 h and then cooled down to the reaction temperature. The analysis of reaction products was started after an initial reaction for 35 min. Both reactants and products of reaction were followed and analyzed every half an hour using an on-line gas chromatograph (Agilent GC 7820A) equipped with a capillary GS-Gaspro113-4362 column (60 m  $\times$  0.32 mm). The GC signals were collected using an EZChrom Elite integrated peak program integrator.

#### 3 Results and Discussion

#### 3.1 Catalytic Performances of the Re/SixAl Catalysts

The catalytic performances of the SiO<sub>2</sub>-xAl<sub>2</sub>O<sub>3</sub> supported rhenium oxide catalysts were evaluated in the gas-phase metathesis reaction of ethylene and 2-pentene at 35 °C, GHSV 3,000  $h^{-1}$ , and ethylene/2-pentene mole ratio = 3. The conversion of 2-pentene, the yield of propylene, 1-butene, and 2-butene as a function of time-on-stream are shown in Fig. 1a-d, respectively. The conversion of 2-pentene in average at 485 min time-on-stream was ranging between 97 and 84 %. However, lower 2-pentene conversion was obtained over the Re/Si13Al and Re/ Si25Al whereas those supported on the SiO<sub>2</sub>-xAl<sub>2</sub>O<sub>3</sub> containing higher amounts of Al<sub>2</sub>O<sub>3</sub> Re/Si50Al, Re/ Si75Al, and Re/100Al exhibited higher 2-pentene conversion at ca. 95–97 %. As shown in Eq. (1), the theoretical stoichiometric value of reactants in the metathesis reaction of ethylene and 2-pentene is equimolar.

$$CH2 = CH2 + CH3CH = CHCH2CH3 \leftrightarrow CH2$$
  
= CH<sub>2</sub>CH<sub>3</sub> + CH<sub>2</sub> = CHCH<sub>2</sub>CH<sub>3</sub> (1)

The conversion of limited 2-pentene reactant and the yield of products were calculated using the following equations:



W. Phongsawat et al.

Conversion of 2-pentene (%) =  $100 \times \frac{\text{amount of } 2\text{-pentene in feed } - \text{amount of } 2\text{-pentene remained in products}}{\text{amount of } 2\text{-pentene in feed}}$ 

Yield of component i (%) = conversion of 2-pentene  $\times \frac{\text{amount of component i in products}}{\text{amount of total products}}$ 

In the present work, the propylene yields for all the Re/SixAl catalysts far exceeded the stoichiometric values (propylene selectivity of 50 mol% or  $\sim 43$  wt%). Only the Re/100Al exhibited propylene yield equal to the stoichiometric value. The highest propylene yield ca. 70 % was achieved over the Re/Si50Al with good stability during the 488 min time-on-stream. Thermodynamically, excess ethylene would shift the reaction (1) from left to right, producing more propylene and 1-butene products. However, as shown in Fig. 1, the yield of 1-butene product was not increased in the same trend as that of propylene for the catalysts exhibiting propylene yield higher than its

stoichiometric amount (i.e., for Re/Si50Al and Re/Si75Al). It has been suggested that the isomerization of 1-butene product from the metathesis of ethylene and 2-pentene to 2-butenes (Eq. 2) can further react with excess ethylene in the feed, resulting in additional propylene formation (Eq. 3) [8, 9].

Isomerization:

$$CH_2 = CHCH_2CH_3 \rightarrow CH_3CH_2 = CH_2CH_3$$
 (2)

Secondary metathesis:

$$CH_2 = CH_2 + CH_3CH_2 = CH_2CH_3 \rightarrow 2(CH_2 = CH_2CH_3)$$
 (3)

The yield of 1-butene was found to be varied from 55 % for the Re/100Al, 30 % for the Re/Si75Al, and <20 % for the other catalysts (Re/Si13Al, Re/Si25Al, and Re/Si50Al). The lowest yield of 1-butene was obtained over the

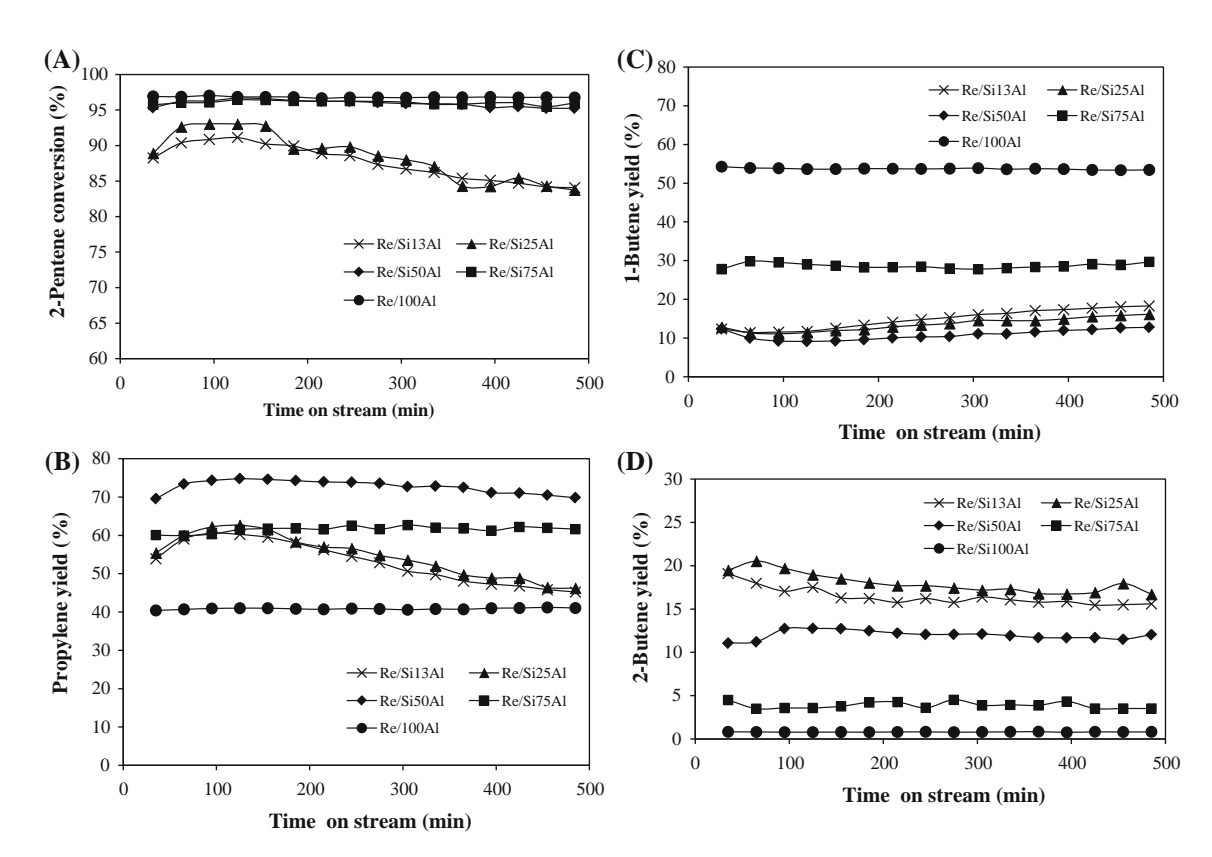


**Fig. 1** Effect of silica–alumina composition ( $SiO_2$ – $xAl_2O_3$ , x=13, 25, 50, 75 and 100 wt%  $Al_2O_3$ ) of  $Re_2O_7/SiO_2$ – $xAl_2O_3$  catalysts on the **a** 2-pentene conversion, **b** propylene yield, **c** 1-butene yield,

d 2-butene yield. (Pressure: 0.1 MPa; E/2P mole ratio: 3; GHSV: 3,000  $h^{-1};$  Temperature: 35  $^{\circ}\text{C})$ 



Re/Si50Al, suggesting that 1-butene was isomerized to 2-butene and further reacted with excess ethylene to form additional propylene product. This view point can also be considered in terms of the yield of 2-butene, higher yields of 2-butene were produced over the Re<sub>2</sub>O<sub>7</sub> catalysts supported on the relatively high silica content supports (Re/Si13Al and Re/Si25Al) whereas moderately high and lower 2-butene yields were obtained over Re/Si50Al and Re/75-100Al catalysts, respectively. Both the isomerization and the cross-metathesis activity strongly depended on the Si/Al composition of the SiO<sub>2</sub>-xAl<sub>2</sub>O<sub>3</sub> supports. Unlike the conventional metathesis of ethylene and 2-butenes that double-bond isomerization was a competing side reaction; it was considered as a useful reaction for the transformation of 1-butene primary product to 2-butenes which could further react with excess ethylene to form additional propylene in the metathesis of ethylene and 2-pentene [8, 9]. The results in this study, however, suggest an optimum composition of the SiO<sub>2</sub>-Al<sub>2</sub>O<sub>3</sub> supports for the Re<sub>2</sub>O<sub>7</sub> catalysts to exhibit high activities for both double-bond isomerization and cross-metathesis reactions so that higher propylene yield (than its stoichiometric amount) was attained with high stability. Besides propylene and 1-butene primary metathesis products, the other by-products including cisand trans-2-butene, 1-pentene, 3-hexene, and C<sub>5+</sub> oligomers can also be produced by various side reactions [8]. However, under the reaction conditions used in the present study, the only C<sub>5+</sub> hydrocarbon found in the products was 3-hexene, which was produced in very small amount (<3 % yield) by self-metathesis of 2-pentene. A relationship between the catalyst physicochemical properties and their catalytic performances was further investigated by catalyst characterization using several techniques.

#### 3.2 Catalyst Characterization

The BET surface area, pore volume, and average pore diameter of the supports and the supported rhenium oxide catalysts are shown in Table 1. It was found that all the SiO<sub>2</sub>-xAl<sub>2</sub>O<sub>3</sub> supports had larger BET surface area and pore volume than that of the pure Al<sub>2</sub>O<sub>3</sub> which is in good agreement with those of Okada et al. [44]. However, considering the changes in BET surface area, pore volume, and pore diameter of the supports after impregnation of rhenium metal and calcination, the Re/Si50Al exhibited the least change in their textural properties. Such results suggest that most of the rhenium was highly dispersed on the surface of the SiO<sub>2</sub>-xAl<sub>2</sub>O<sub>3</sub> support. As revealed by ICP-OES results, the actual Re-metal loadings varied from 4.6 to 8.1 wt%, depending on the supports used. Higher amount of Re-metal (7.8-8.1 wt%) remained on the Al<sub>2</sub>O<sub>3</sub> rich supports (>50 wt% Al<sub>2</sub>O<sub>3</sub>). Because some of the Re<sub>2</sub>O<sub>7</sub> can be volatized during high temperature calcination step especially the inactive rhenium centers of the type  $\equiv$  Si-O-ReO<sub>3</sub> [40], the use of SiO<sub>2</sub>-xAl<sub>2</sub>O<sub>3</sub> supports with relatively higher silica content (i.e., Si13Al and Si25Al) resulted in lower amount of rhenium metal on the catalyst samples. It is quite well known that Re<sub>2</sub>O<sub>7</sub>/SiO<sub>2</sub> catalyst has no activity in olefin metathesis due to poor interaction between silica and rhenium oxide that tends to form inactive rhenium clusters [45].

Although one can notice the differences in the actual Re metal loadings on the various Re<sub>2</sub>O<sub>7</sub>/SiO<sub>2</sub>–*x*Al<sub>2</sub>O<sub>3</sub> catalysts, they seemed to make little influence on the catalytic performances. The amount of 2-pentene converted per gram Re metal was calculated and was found to be even higher on the catalysts with lower Re contents (Re/Si13Al and Re/Si25Al). However, it is quite well known that the number of rhenium active sites were only small fraction of

Table 1 The physicochemical property of the bare silica-alumina supports and the supported rhenium oxide catalysts

Sample	Al <sub>2</sub> O <sub>3</sub> content <sup>a</sup> (wt%)	Surface area <sup>b</sup> (m <sup>2</sup> g <sup>-1</sup> )	Pore volume <sup>c</sup> (cm <sup>2</sup> g <sup>-1</sup> )	Average pore diameter <sup>c</sup> (nm)	Re-metal loading <sup>d</sup> (wt%)	Total acidity <sup>e</sup> (10 <sup>3</sup> μmol NH <sub>3</sub> g <sup>-1</sup> )
Re/Si13Al	13	224 (291)	1.10 (1.07)	13.7 (17.2)	4.7	7.487
Re/Si25Al	25	210 (277)	0.71 (0.58)	8.7 (9.7)	4.6	7.333
Re/Si50Al	50	308 (316)	0.83 (0.79)	8.3 (8.7)	7.5	14.554
Re/Si75Al	75	389 (431)	0.86 (0.77)	6.1 (6.0)	7.8	14.967
Re/100A1	100	213 (233)	0.40 (0.33)	5.1 (4.9)	8.2	7.698

The numbers in parenthesis indicated the values of the bare supports



<sup>&</sup>lt;sup>a</sup> Based on the calculated amounts that were used for synthesis of various SiO<sub>2</sub>-Al<sub>2</sub>O<sub>3</sub> supports

<sup>&</sup>lt;sup>b</sup> Based on the Brunauer-Emmett-Teller (BET) method

<sup>&</sup>lt;sup>c</sup> Based on the Barret-Joyner-Halenda (BJH) desorption method

<sup>&</sup>lt;sup>d</sup> Actual re-metal loading for each catalyst after calcination was measured by ICP-OES

<sup>&</sup>lt;sup>e</sup> Total surface acidity of the catalysts was probed by the NH<sub>3</sub>-TPD

W. Phongsawat et al.

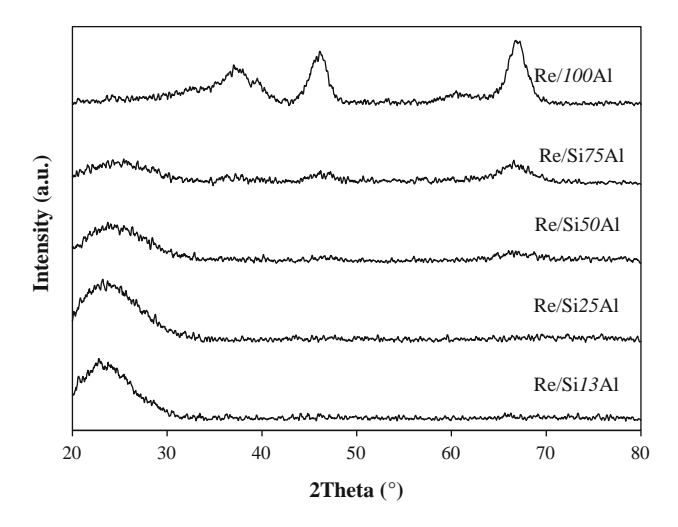


**Fig. 2** The X-ray diffraction (XRD) patterns of the different Re<sub>2</sub>O<sub>7</sub>/SiO<sub>2</sub>–xAl<sub>2</sub>O<sub>3</sub> catalysts (x = 13, 25, 50, 75 and 100 wt% Al<sub>2</sub>O<sub>3</sub>)

the Re atoms presented on supported rhenium oxide catalysts. The rhenium active centers have been quantitatively determined by various techniques including poisoning experiments using NO [4], kinetic studies [46], and chemical counting method [47]. These studies showed the percentage of active Re centers of approximately 1 % of the total actual amount Re loading.

The XRD patterns of the Re/SixAl catalysts are shown in Fig. 2. A broad peak around  $20\text{--}30^\circ$  represents a typical character of amorphous solid of these samples. The XRD characteristic peaks of the  $\gamma$ -phase alumina appeared at  $2\theta = 32$ , 37, 46, 61 and 67° for the samples containing  $\geq 50$  wt% of Al<sub>2</sub>O<sub>3</sub>. The intensity of the  $\gamma$ -phase alumina increased with increasing amount of Al<sub>2</sub>O<sub>3</sub> in the samples. The peaks corresponding to the crystalline Re<sub>2</sub>O<sub>7</sub> were not detected for all the supported Re<sub>2</sub>O<sub>7</sub> catalysts. According to the literature [2, 16, 42, 48], most of the rhenium species formed on the surface is isolated ReO<sub>4</sub><sup>-</sup> form and the crystalline Re<sub>2</sub>O<sub>7</sub> can be volatilized during high temperature calcination at above 300 °C.

Although alkene metathesis reaction does not regard as an acid-catalyzed reaction, surface acidity of the catalysts strongly influences the formation of metathesis active sites [2, 26, 27, 29, 33, 49]. Acidity of the catalysts was probed by the NH<sub>3</sub>-TPD measurements and the results are shown in Fig. 3. The total amounts of acidity was found to be directly related to the specific surface area of the catalysts, in which they were increased with increasing alumina content from 13 to 75 wt% and then markedly declined for the 100 wt% Al<sub>2</sub>O<sub>3</sub> support (Table 1). It is generally accepted that silica–alumina supported metathesis catalysts are more acidic than alumina supported catalysts [2, 11–13]. From the NH<sub>3</sub>-TPD profiles (Fig. 3), the desorption peaks in the temperature range below and above 300 °C were assigned to the weak and the strong acid sites, respectively

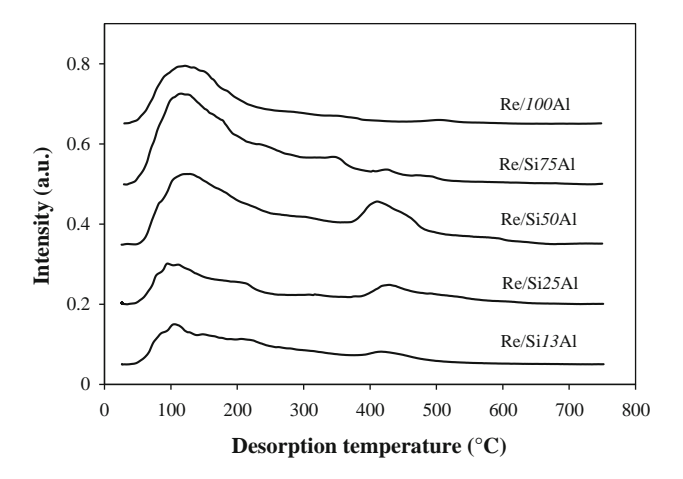


**Fig. 3** Temperature programmed desorption of ammonium (NH<sub>3</sub>-TPD) spectra of the Re<sub>2</sub>O<sub>7</sub>/SiO<sub>2</sub>–xAl<sub>2</sub>O<sub>3</sub> catalysts (x = 13, 25, 50, 75 and 100 wt% Al<sub>2</sub>O<sub>3</sub>)

[8, 9]. In Fig. 4, it was found that the amount of strong acid sites was maximized for the Re/Si50Al. The Re/100Al<sub>2</sub>O<sub>3</sub> shows only the weak acidity characteristic. The acid strength thus strongly influenced both the isomerization and metathesis activity over the supported Re<sub>2</sub>O<sub>7</sub> catalyst. Since the major products of the metathesis of ethylene and 2-pentene obtained over the Re/100Al<sub>2</sub>O<sub>3</sub> catalyst were in accordance with their stoichiometric amounts, it is suggested that the weak acidity of the Re/100Al<sub>2</sub>O<sub>3</sub> was not strong enough for isomerization reaction of the 1-butene product so that the secondary metathesis reaction did not occur.

The oxidation states of rhenium in the various Re<sub>2</sub>O<sub>7</sub>/SiO<sub>2</sub>-Al<sub>2</sub>O<sub>3</sub> catalysts were determined by XPS and the results are shown in Fig. 5. According to the literatures [50–52], the XPS spectra revealed that most of rhenium oxidation state of the fresh catalysts lied in oxidation state

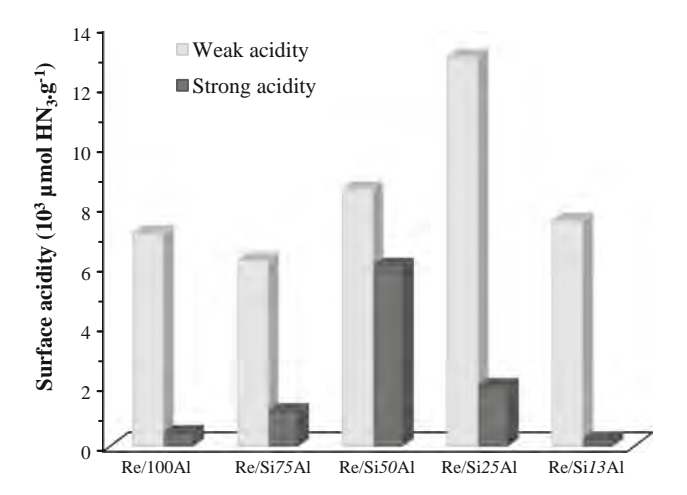


**Fig. 4** The amount of surface acidity of the different  $Re_2O_7/SiO_2$ – $xAl_2O_3$  catalysts in terms of  $\mu$ mol  $NH_3$  per gram of catalysts by classification into weak and strong acidity



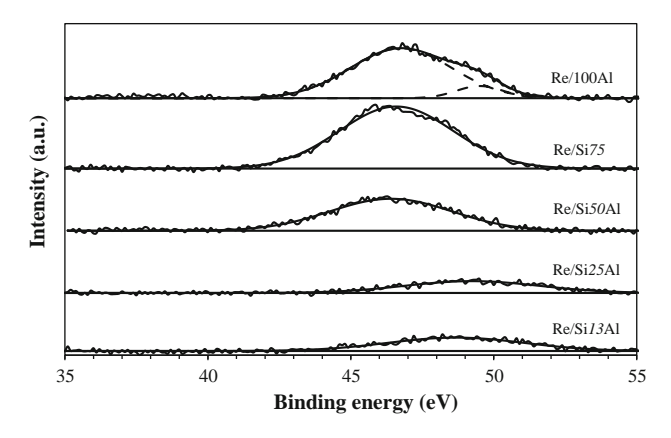


**Fig. 5** XPS spectra of the fresh  $Re_2O_7/SiO_2-xAl_2O_3$  catalysts (x = 13, 25, 50, 75 and  $100 \text{ wt}\% \text{ Al}_2O_3$ )

+(7), however a fraction of rhenium oxidation state +(6-7)was also detected for the Re<sub>2</sub>O<sub>7</sub>/SiO<sub>2</sub>-50Al<sub>2</sub>O<sub>3</sub>, Re<sub>2</sub>O<sub>7</sub>/ SiO<sub>2</sub>-75Al<sub>2</sub>O<sub>3</sub> and Re<sub>2</sub>O<sub>7</sub>/100Al<sub>2</sub>O<sub>3</sub> catalysts. Based on the XPS results, the catalysts in this study can be categorized into three different characters; the first one is the group of low metal-support interaction Re<sub>2</sub>O<sub>7</sub>/SiO<sub>2</sub>-13Al<sub>2</sub>O<sub>3</sub> and Re<sub>2</sub>O<sub>7</sub>/SiO<sub>2</sub>-25Al<sub>2</sub>O<sub>3</sub> catalysts possessing only the rhenium oxidation state +(7). The second one is the group of stronger metal-support interaction Re<sub>2</sub>O<sub>7</sub>/ SiO<sub>2</sub>-50Al<sub>2</sub>O<sub>3</sub> and Re<sub>2</sub>O<sub>7</sub>/SiO<sub>2</sub>-75Al<sub>2</sub>O<sub>3</sub> catalysts that showed lower binding energy of the rhenium oxidation state +(6-7). Both of the rhenium species (Re<sup>7+</sup> and Re<sup>6-7+</sup>) were detected on the surface of the Re<sub>2</sub>O<sub>7</sub>/100Al<sub>2</sub>O<sub>3</sub> catalysts, the third type possessing metal-support interaction strength in between the first two groups. The different characteristics observed may be related to the dispersion degree of rhenium oxide on the surface. Well-dispersion species were found on the SiO<sub>2</sub>-50Al<sub>2</sub>O<sub>3</sub> and the SiO<sub>2</sub>-75Al<sub>2</sub>O<sub>3</sub>. Iwasawa and Yuan [52] also found that the binding energy of rhenium species shifted towards lower binding energy for the catalysts possessing stronger metalsupport interaction.

The structure of transition metal species was investigated by diffuse reflectance UV–Visible spectroscopy. The diffuse reflectance UV–Visible spectra of the various supported Re<sub>2</sub>O<sub>7</sub> catalysts are shown in Fig. 6. Two intense absorption bands centered at ca. 210 and 240 nm were assigned to the undistorted tetrahedral ReO<sub>4</sub><sup>-</sup> ion [53]. The presence of isolated tetrahedral species of rhenium active species was found on the Re<sub>2</sub>O<sub>7</sub>/SiO<sub>2</sub>–xAl<sub>2</sub>O<sub>3</sub> composing of higher alumina content ( $x \ge 50$  wt% Al<sub>2</sub>O<sub>3</sub>). Hence, it would be an evidence for the highly dispersion of rhenium over these suitable support compositions. The isolated tetrahedral structure of rhenium is necessary for the formation of metal–carbene metathesis active sites and better catalyst performance. The Re/100Al<sub>2</sub>O<sub>3</sub> shows additional absorption bands centered at ca. 300 and 330 nm which

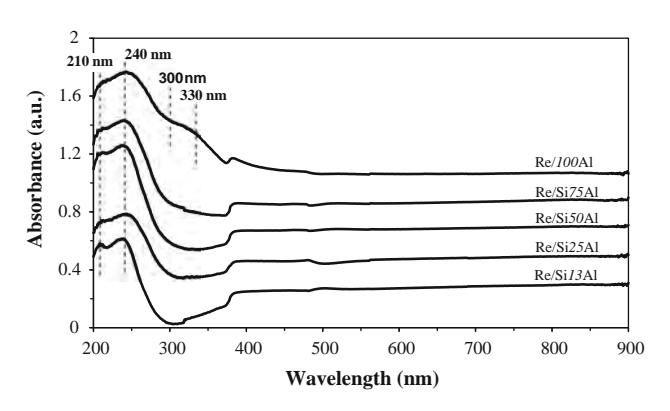


**Fig. 6** Diffuse reflectance UV–Visible spectra of the different  $Re_2O_7/SiO_2$ – $xAl_2O_3$  catalysts (x = 13, 25, 50, 75 and 100 wt%  $Al_2O_3$ )

were attributed to the existence of rhenium in a distorted octahedral species [13, 53].

The surface structures of ReO<sub>x</sub> species on the various supported Re<sub>2</sub>O<sub>7</sub> catalysts were characterized by Raman spectroscopy and the results are shown in Fig. 7. Consistent to the XRD results, the Raman shifts corresponding to the crystalline Re<sub>2</sub>O<sub>7</sub> (at 800, 450, and below 200 cm<sup>-1</sup>) [54, 55] were not detected for all the catalyst samples and only isolated ReO<sub>4</sub><sup>-</sup> species existed. The monomeric tetrahedral ReO<sub>4</sub><sup>-</sup> ions were observed at  $\sim 990-975$  cm<sup>-1</sup> [ $v_s(Re=O)$ , the most intense band],  $\sim 900-930 \text{ cm}^{-1}$ [ $v_{as}(Re=O)$ , weak band], and ~340 cm<sup>-1</sup> [ $\delta_{s,as}(O-Re-O)$ , intense band] [48, 54-57]. For all the SiO<sub>2</sub>-xAl<sub>2</sub>O<sub>3</sub> supported Re<sub>2</sub>O<sub>7</sub> catalysts, two separated peaks of the terminal Re=O bond were observed at 970 and 990 cm<sup>-1</sup>, indicating the existence of two different surface rhenium oxide species. The position of the higher frequency peaks tended to shift to lower frequency when the alumina composition in the SiO<sub>2</sub>-xAl<sub>2</sub>O<sub>3</sub> supports increased and eventually merged into a single peak at 976 cm<sup>-1</sup> for the case of Re/100Al catalyst. The shift of Raman to lower frequency was interpreted as a result of the stronger of the bridging Re-O-support bond strength [58, 59]. The Re/100Al<sub>2</sub>O<sub>3</sub>

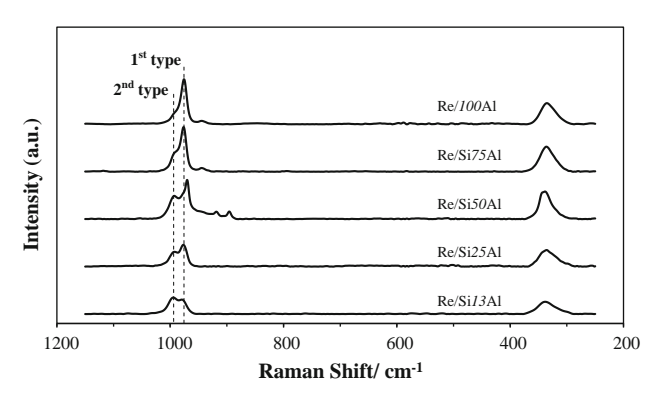


**Fig. 7** Raman spectra of the different  $Re_2O_7/SiO_2-xAl_2O_3$  catalysts  $(x = 13, 25, 50, 75 \text{ and } 100 \text{ wt\% } Al_2O_3)$ 



W. Phongsawat et al.

catalyst showed metathesis activity with negligible isomerization activity. It is likely that the catalyst had only one type of surface rhenium species with rather strong Re-O-support bond (shown as a single Raman shift at 976 cm<sup>-1</sup>). Contrarily, all the Re/SixAl catalysts exhibited double-bond isomerization activity in addition to the metathesis reaction. The second type of surface rhenium species with a weaker Re-O-support bond (additional peak at 990 cm<sup>-1</sup>) could be attributed to the hydrido-rhenium species ([Re]-H) which was claimed to act as isomerization sites [30, 42, 60]. The Raman spectroscopy results strongly support the UV-Vis results that isolated monomeric ReO<sub>4</sub><sup>-</sup> tetrahedra is the rhenium metathesis active structure. It is noted that the hydrolyzed ReO<sub>4</sub><sup>-</sup> or the ReO<sub>4</sub> ion in aqueous solution also resemble in the form of isolated monomeric ReO<sub>4</sub><sup>-</sup> tetrahedral species [54, 57, 61– 64]. A shift in all Raman bands to lower range of frequency is often observed particularly in the measurements that performed under ambient conditions [54]. It appears that an increase in alumina component in the SiO2-xAl2O3 supports could stabilize the surface rhenium species as the first type of isolated monomeric ReO<sub>4</sub><sup>-</sup> tetrahedra metathesis active structure whereas the proportion of the second type decreased. The intensity of Raman bands also increased with increasing amount of surface rhenium oxides as determined by the ICP-OES results. The Re/Si50Al catalyst that exhibited the highest propylene yield and good catalyst stability had the highest proportion of isolated monomeric ReO<sub>4</sub><sup>-</sup> tetrahedral with relatively strong bond strength.

#### 4 Conclusions

The role of silica-alumina composition in the unconventional metathesis of ethylene and 2-pentene has been investigated over the Re<sub>2</sub>O<sub>7</sub>/SiO<sub>2</sub>-Al<sub>2</sub>O<sub>3</sub> catalysts at 35 °C, GHSV  $3{,}000 \text{ h}^{-1}$ , and ethylene/2-pentene mole ratio 3. The SiO<sub>2</sub>-Al<sub>2</sub>O<sub>3</sub> composition has strong influence on the acidity, the metal-support interaction, and the dispersion of Re-active species. Higher amount of Re metal remained on the catalysts was observed in the Al<sub>2</sub>O<sub>3</sub> rich Re<sub>2</sub>O<sub>7</sub>/SiO<sub>2</sub> $xAl_2O_3$  catalysts ( $x \ge 50$  wt%  $Al_2O_3$ ), corresponding to the stronger metal-support interaction. These characters also suggest a well dispersion of Re-active species as a monolayer of the isolated ReO<sub>4</sub><sup>-</sup> species. The second type of the isolated monomeric ReO<sub>4</sub><sup>-</sup> tetrahedral structure with a weaker Re-O-support bond appeared in all the catalysts except the one supported on pure alumina. The optimum amount of alumina in the SiO2-Al2O3 was determined to be 50 wt% Al<sub>2</sub>O<sub>3</sub> in which the highest propylene yield was obtained. The isomerization of the initial 1-butene product into 2-butenes and a subsequent secondary metathesis reaction between these 2-butenes and excess ethylene enhanced the propylene yield over the  $Re_2O_7/SiO_2-Al_2O_3$  catalysts.

Acknowledgments The financial supports from the Thailand Research Fund (TRF), the Office of Higher Education Commission (CHE), and the CU-NRU (AM1088A) are gratefully acknowledged. The authors would like to thank the Royal Golden Jubilee Ph.D. scholarship from TRF and SCG chemicals Co., Ltd for W.P.

#### References

- 1. Mol JC (2004) J Mol Catal A Chem 213:39
- 2. Mol JC (1999) Catal Today 51:289
- 3. Luckner RC, Wills GB (1973) J Catal 28:83
- Ivin KJ, Mol JC (1997) Olefin metathesis and metathesis polymerization. Academic Press, San Diego
- Park YK, Lee CW, Kang NY, Choi WC, Choi S, Oh SH, Park DS (2010) Catal Surv Asia 14:75
- 6. Cornil B, Herrmann AW, Schogl R, Wong C (2000) A concise encyclopedia catalysis from A to Z. Wiley, New York
- Gartside RJ, Stanley SJ (2011) C<sub>5</sub> metathesis for increased propylene, In: AIChE ethylene producers conference proceedings
- Phongsawat W, Netivorruksa B, Suriye K, Dokjampa S, Praserthdam P, Panpranot J (2012) J Nat Gas Chem 21:83
- 9. Phongsawat W, Netivorruksa B, Suriye K, Dokjampa S, Praserthdam P, Panpranot J (2012) J Nat Gas Chem 21:158
- Cosyns J, Chodorge J, Commereuc D, Torck B (1998) Hydrocarbon Process 77:61
- 11. Sibeijn M, Mol JC (1990) Appl Catal 67:279
- 12. Moulijn JA, Mol JC (1988) J Mol Catal 46:1
- 13. Andreini A, Xiaoding X, Mol JC (1986) Appl Catal 27:31
- Sibeijn M, Spronk R, van Veen JAR, Mol JC (1991) Catal Lett 8:201
- Sheu FC, Hong CT, Hwang WL, Shih CJ, Wu JC, Yeh CT (1992) Catal Lett 14:297
- 16. Balcar H, Hamtil R, Zilkova N, Cejka J (2004) Catal Lett 97:25
- 17. Onaka M. Oikawa T (2002) Chem Lett 8: 850
- Oikawa T, Ookoshi T, Tanaka T, Yamamoto T, Onaka M (2004) Microporous Mesoporous Mater 74:93
- 19. Balcar H, Cejka J (2002) Macromol Symp 293:43
- 20. Martin-Aranda RM, Cejka J (2010) Top Catal 53:141
- 21. Zukal A, Siklova H, Cejka J (2008) Langmuir 24:9837
- Gommes CJ, Friedrich H, Wolters M, De Jongh PE, De Jong KP (2009) Chem Mater 21:1311
- 23. Schmidt F (2001) Appl Catal. A 221:15
- 24. Ellison A, Coverdale AK, Dearing PF (1983) Appl Catal 8:109
- Kapteijn F (1980) Catalytic metathesis of unsaturated esters by alumina supported rhenium oxide. PhD thesis, Amsterdam
- Xu X, Boelhouwer C, Vonk D, Benecke JI, Mol JC (1985) J Mol Catal 36:47
- 27. Xiaoding X, Boelhouwer C, Vonk D, Benecke JI, Mol JC (1986) J Mol Catal 36:47
- Mandelli D, Van Vliet MCA, Arnold U, Sheldon RA, Schuchardt U (2001) J Mol Catal A Chem 168:165
- Xiaoding X, Mol JC, Boelhouwer C (1986) J Chem Soc Faraday Trans 1F(82):2707
- 30. Bakala PC, Briot E, Millot Y, Piquemal JY, Bregeault JM (2008) J Catal 258:61
- 31. Andreini A, Mol JC (1985) J Chem Soc Faraday Trans 1F(81):1705
- Bregeault J-M, El Ali B, Martin J, Martin C, Derdar F, Bugli G, Delamar M (1988) J Mol Catal 46:37



- Debecker DP, Hauwaert D, Stoyanova M, Barkschat A, Rodemerck U, Gaigneaux EM (2010) Appl Catal. A 391:78
- 34. Aritani H, Fukuda O, Yamamoto T, Tanaka T, Imamura S (2000) Chem Lett 1:66
- Handzlik J, Ogonowski J, Stoch J, Mikolajczyk M, Michorczyk P (2006) Appl Catal. A 312:213
- Handzlik J, Ogonowski J, Stoch J, Mikolajczyk M (2005) Catal Lett 101:65
- 37. Mol JC (1994) Catal Lett 23:113
- 38. Debecker DP, Bouchmella K, Poleunis C, Eloy P, Bertrand P, Gaigneaux EM, Mutin PH (2009) Chem Mater 21:2817
- 39. Handzlik J, Sautet P (2008) J Catal 256:1
- 40. Mol JC, Andreini A (1988) J Mol Catal 46:151
- 41. Spronk R, Andreini A, Mol JC (1991) J Mol Catal 65:219
- 42. Rodella CB, Cavalcante JAM, Buffon R (2004) Appl Catal A 274:213
- 43. Rost AMJ, Schneider H, Zoller JP, Herrmann WA, Kuhn FE (2005) J Organomet Chem 690:4712
- Okada K, Tomita T, Kameshima Y, Yasumori A, MacKenzie KJD (1999) J Mater Chem 9:1307
- 45. Amigues P, Chauvin Y, Commereuc D, Lai CC, Liu YH, Pan JM (1990) Hydrocarbon Process Int Ed 69:79
- Kapteijn F, Homburg E, Mol JC (1983) J Chem Thermodyn 15:147
- 47. Chauvin Y, Commereuc D (1992) J Chem Soc Chem Commun 462
- 48. Handzlik J, Ogonowski J (1998) Politechnika Krakowska, seria Inzynieria i, eds. Technologia Chemiczna, Kraków

- Wang Y, Chen Q, Yang W, Xie Z, Xu W, Huang D (2003) Appl Catal A 250:25
- Wagner CD, Riggs WM, Davis LE, Moulder JF, Muilenberg GE (1979) Handbook of X-ray photoelectron spectroscopy. Perkin-Elmer Corporation, Eden Prairie
- Balcar H, Zilkova N, Bastl Z, Dedecek J, Hamtil R, Brabec L, Zukal A, CŒejka J (2007) Stud Surf Sci Catal 170:1145
- 52. Yuan Y, Iwasawa Y (2002) J Phys Chem B 106:4441
- Stoyanova M, Rodemerck U, Bentrup U, Dingerdissen U, Linke D, Mayer RW, Lansink Rotgerink HGJ, Tacke T (2008) Appl Catal A 340:242
- 54. Okal J, Baran J (2001) J Catal 203:466
- Edreva-Kardjieva RM, Vuurman MA, Mol JC (1992) J Mol Catal 76:297
- Daniell W, Weingand T, Knozinger H (2003) J Mol Catal A Chem 204–205:519
- Lacheen HS, Cordeiro PJ, Iglesia E (2006) J Am Chem Soc 128:15082
- Vuurman MA, Stufkens DJ, Oskam A, Wachs IE (1992) J Mol Catal 76:263
- 59. Olsthoorn AA, Boelhouwer C (1976) J Catal 44:207
- Bregeault J-M (1992) Catalyse homogene par les complexes des metaux de transition. Masson, Paris
- 61. Wang L, Hall WK (1983) J Catal 82:177
- 62. Williams KPJ, Harrison K (1990) J Chem Soc Faraday Trans 86:1603
- 63. Wachs IE (1996) Catal Today 27:437
- 64. Okal J, Kepinski L, Krajczyk L, Drozd M (1999) J Catal 188:140



#### REVISED II

## Formation of CoAl<sub>2</sub>O<sub>4</sub> nanoparticles via low temperature solid-state reaction of fine gibbsite and cobalt precursor

Natpakan Srisawad<sup>1</sup>, Wasu Chaitree<sup>1</sup>, Okorn Mekasuwandumrong<sup>2</sup>, Piyasan Praserthdam<sup>1</sup>, and Joongjai Panpranot<sup>1,\*</sup>

<sup>1</sup>Center of Excellence on Catalysis and Catalytic Reaction Engineering, Department of Chemical Engineering, Faculty of Engineering Chulalongkorn University, Bangkok, Thailand, 10330

<sup>2</sup> Department of Chemical Engineering, Faculty of Engineering and Industrial Technology, Silpakorn University, Nakorn Pathom 73000, Thailand

E-mail: joongjai.p@chula.ac.th

#### **Abstract**

Nanocrystalline cobalt aluminate (CoAl<sub>2</sub>O<sub>4</sub>) was synthesized by the solid-state reaction method with cobalt chloride hexahydrate (CoCl<sub>2</sub>·6H<sub>2</sub>O) as the source of Co and gibbsite (Al(OH)<sub>3</sub>) as the source of Al, respectively. The effects of particle size of the starting fine gibbsite (0.6 and 13 μm) and calcination temperatures (450, 550, and 650°C) on the properties of CoAl<sub>2</sub>O<sub>4</sub> were investigated by means of X-ray diffraction (XRD), thermogravimetry analysis and differential thermal analysis (TG/DTA), X-ray photoelectron spectroscopy (XPS), UV-visible absorption spectroscopy (UV-Vis), scanning electron microscopy (SEM), and transmission electron microscopy (TEM). Increasing of calcination temperature promoted the insertion amounts of Co<sup>2+</sup> in alumina matrix in CoAl<sub>2</sub>O<sub>4</sub> structure, which resulted in the brighter blue particles and increasing of UV spectra band. The lowest temperature for the formation of nanocrystalline CoAl<sub>2</sub>O<sub>4</sub> particles was 550°C for the solid-state reaction of cobalt chloride and 0.6 μm fine gibbsite.

Keywords: cobalt aluminate, cobalt precursor, gibbsite, solid-state reaction

#### **Conflict of Interests:**

I, Joongjai Panpranot, the corresponding author of the manuscript, confirm that I do not have a direct financial relation with the commercial identity mentioned in the paper submitted that might lead to a conflict of interest for any of the authors.

#### 1. Introduction

Cobalt aluminate is a binary oxide consisting of cobalt and aluminium oxides. It is a thermally and chemically stable pigment of intense blue color and is usually synthesized at high temperature by solid-state reaction between two oxide components [1-2]. In the past decades, it has received attention due to its applications as inorganic ceramic blue pigment which is widely used for coloration of plastics, paint, fiber, paper, rubber, phosphor, glass, cement, glazes, ceramic bodies and porcelain enamels [3,4,5]. Moreover, its uniqueness optical properties leads to its extensive use as color filter for automotive lamps or pigment layer on luminescent materials in optical devices [6,7,8]. The coloring performance of cobalt pigments strongly depends on their thermal stability, chemical reactivity, and coordination of Co<sup>2+</sup> ions [9]. Other applications of cobalt aluminate is an important material for heterogeneous catalysis such as selective catalytic reduction of NO<sub>x</sub> with hydrocarbons [10] and carbon dioxide reforming of methane [11].

Cobalt aluminate can be synthesized by various routes such as polymerized complex [3], molten salt [4], polyol [8], low temperature combustion [9], co-precipitation [7,12], sol–gel [13,14,15], citrate-gel [16], metal–organic chemical vapor deposition (MOCVD) [17], EDTA chelating precursor [18], glycine chelated precursor [19], hydrothermal [20], polymer aerosol pyrolysis [21] and reverse micelle processes [22]. Nonetheless, the selection of preparation method is usually based upon the desired properties of the final materials [3]. The solid-state reaction of a mechanical mixture between gibbsite and cobalt precursor is interested due to three main advantages approach. They (i) are simple, cheaper and convenient; (ii) involve less solvent and reduce contamination; and (iii) give high yields of products [23]. The solid-state reactions involve four steps in a typical proceeding: diffusion, reaction, nucleation, and growth. Any chemical interaction between solids proceeds exclusively on the contact area between the particles [24].

In the present work, cobalt aluminate was synthesized by the solid-state reaction method with cobalt chloride hexahydrate (CoCl<sub>2</sub>·6H<sub>2</sub>O) as the source of Co and gibbsite (Al(OH)<sub>3</sub>) as the source of Al, respectively. The effects of particle size of gibbsite and calcination temperature on the formation of cobalt aluminate and theirs properties were investigated by means of X-ray diffraction (XRD), thermogravimetry analysis and differential thermal analysis (TG/DTA), X-ray photoelectron spectroscopy (XPS), UV-visible absorption spectroscopy (UV-Vis), scanning electron microscopy (SEM), and transmission electron microscopy (TEM).

#### 2. Experimental

#### 2.1 Preparation of CoAl<sub>2</sub>O<sub>4</sub>

Fine gibbsite (Al(OH)<sub>3</sub>, Merck) and cobalt chloride hexahydrate (CoCl<sub>2</sub>·6H<sub>2</sub>O, Fluka) were used as starting materials. The starting fine gibbsite has an average particle size of 13 μm and is denoted as FG-13 μm. After milling of 100 g of fine gibbsite in an attrition mill for 24 h, the particle size of the fine gibbsite was reduced to 0.6 μm and is denoted as FG-0.6 μm [25]. The solid-state reaction between fine gibbsite and cobalt chloride took place at 450, 550, and 650°C with a Co:Al molar ratio 1:6. Firstly, a certain amount of fine gibbsite and cobalt chloride hexahydrate were mixed in an agate mortar. Secondly, the mixed materials were dried in oven at 110°C overnight. Finally, the mixtures were calcined in a tube furnace in an air flow (95 ml/min) by heating to a desired temperature (450, 550, and 650°C) at a rate of 10°C/min and held at that temperature for 5 h. Then, the mixed materials were cooled down to room temperature in N<sub>2</sub> (75 ml/min).

#### 2.2 Characterization

Particle size distribution was measured using a laser diffraction-based size analyzer (Malvern Mastersizer, reflective index 1.57). All the samples were done on deionized water as dispersant. Dispersion and deagglomeration of particles were ensured by ultrasonic treatment before measurement. XRD was performed to determine the bulk phase of particles by SIEMENS D 5000 X-ray diffractometer connected with a computer with Diffract ZT version 3.3 programs for fully control of the XRD analyzer. The experiments were carried out by using Cu K<sub>α</sub> radiation with Ni filter in the 2θ range of 10-80 degrees resolution 0.04°. The crystallite size was estimated from line broadening according to the Scherrer's equation and α-alumina (α-Al<sub>2</sub>O<sub>3</sub>) as an external standard. The decomposition of cobalt chloride and fine gibbsite and CoAl<sub>2</sub>O<sub>4</sub> formation was studied by TG/DTA using an SDT Analyzer Model Q600 from TA Instruments, USA from room temperature to 1000°C at a heating rate of 10°C/min in air. The chemical state of Co and surface elemental composition were determined by XPS analysis using an AMICUS spectrometer equipped with a MgK<sub>α</sub> X-ray radiation. For a typical analysis, the source was operated at voltage of 15 kV and current of 12 mA. The pressure in the analysis chamber was less than 10<sup>-5</sup> Pa. The AMICUS system is computer controlled using the AMICUS "VISION 2" software. The optical properties of CoAl<sub>2</sub>O<sub>4</sub> particles were studied by UV-Vis

analysis using a Perkin Elmer Lambda 650 spectrophotometer. The diffuse absorption spectra were recorded in the wavelength range 200–900 nm with the step size for the scan was 1 nm. BaSO<sub>4</sub> was used as a blank for the measurement. The particles morphology was obtained using a JEOL JSM-35CF SEM operating at 20 kV and JEOL JEM 2010 TEM operating at 200 kV.

#### 3. Results and Discussion

The median particle sizes ( $d_{50}$ ) of fine gibbsite used as starting materials for producing CoAl<sub>2</sub>O<sub>4</sub> in this study were determined by a laser diffraction-based size analyzer to be 0.6 and 13 µm. Figure 1 shows the XRD patterns of fine gibbsite samples with different particle sizes. The intensities of the XRD peaks decreased and the peaks became wider as the average particle size of gibbsite decreased from 13 µm (FG-13) to 0.6 µm (FG-0.6). The XRD patterns of samples obtained from the solid-state reaction of cobalt chloride with FG-13 (Figure 2(A)), and FG-0.6 (Figure 2(B)) at various calcination temperatures are shown in Figure 2. The XRD peaks at 20 degrees = 31.3°, 36.8°, 44.9°, 59.3°, and 65.3° were observed and could be assigned to either CoAl<sub>2</sub>O<sub>4</sub> or Co<sub>3</sub>O<sub>4</sub> because their peak positions are almost identical [26]. CoAl<sub>2</sub>O<sub>4</sub> and Co<sub>3</sub>O<sub>4</sub> have the same spinel cubic (Fd3m) crystallgraphic structure with slightly difference in the lattice constant (a = 8.111 for CoAl<sub>2</sub>O<sub>4</sub> and a = 8.0885 for Co<sub>3</sub>O<sub>4</sub>). Therefore they have a similar peak pattern and the positions of peak are nearly same. The transition alumina phase was also found at  $2\theta = 68^{\circ}$  in some samples. However, the relatively low intensity and broad XRD patterns suggest that crystallinity of the samples was not very good and/or the average crystallite size may be very small. The peak detected at  $2\theta$  = 13° corresponded to an impurity peak. Figure 3 shows the SEM images of CoAl<sub>2</sub>O<sub>4</sub> nanoparticles synthesized via the solid-state reaction between cobalt chloride and FG-13 and FG-0.6 at 650°C. Agglomeration of fine particles forming large irregular particle was observed. However, there is inappreciable change in morphology after calcination at different temperatures.

Figure 4(a) shows the TG/DTA curve of the cobalt chloride which included three endothermic peaks and one exothermic peak. The first and the second endothermic peaks with maxima at 100 and 175°C were accompanied by weight losses of 1.79 and 12.92%, respectively. These peaks corresponded to the loss of water. The exothermic peak at 708°C, which was accompanied by a 48.44% loss in weight,

corresponded to the loss of chloride and the subsequent formation of Co<sub>3</sub>O<sub>4</sub>. Finally, the last endothermic peak at 920°C, which was accompanied by a 50.49% loss in weight, corresponded to a small oxygen loss and the conversion of Co<sub>3</sub>O<sub>4</sub> into CoO [27]. Figure 4(b) and 4(c) illustrate the TG/DTA curves of a mechanical mixture of cobalt chloride and FG-13 and FG-0.6, respectively. The dehydration of a mechanical mixture between cobalt chloride with FG-13 (Figure 4(b)); includes a series of endothermic peaks. The first, second, and third of endothermic peaks were corresponding to the loss of water in the sample. The endothermic peak at around 300°C was the formation of boehmite. In addition, the endothermic peak at around 500°C indicated the formation of cobalt aluminate. It is interesting that the exothermic peak at around 708°C corresponding to chloride elimination disappeared and the formation of CoAl<sub>2</sub>O<sub>4</sub> occurred at much lower temperature. It is suggested that in the presence of gibbsite, cobalt chloride was decomposed easier probably due to the hydrolysis reaction by water dehydrated from gibbsite. Moreover, a decrease of gibbsite particle size from 13 µm to 0.6 µm, the series of endothermic peaks decreased and the endothermic peaks at around 230 and 500°C disappeared (comparing to Figure 3(b) and 3(c)). Such results suggest that the dehydration of a mechanical mixture between gibbsite and cobalt chloride was accelerated when the particle size of gibbsite was decreased. As a consequence, cobalt aluminate was formed at lower calcination temperature. The images of synthesized CoAl<sub>2</sub>O<sub>4</sub> nanoparticles are shown in Figure 5. Bright blue color was clearly observed for the FG-13 and FG-0.6 calcined at 650°C and FG-0.6 calcined at 550°C, indicating the formation of CoAl<sub>2</sub>O<sub>4</sub> structure.

The XPS analyses were carried out to examine surface species on the samples. The samples were analyzed in the Co 2p, Al 2s, and O 1s binding energy regions. The binding energy, the atomic concentration, and the FWHM of Co 2p<sub>3/2</sub> and Al 2s are given in **Table 1**. According to the literature [20, 28], cobalt in an oxide state (Co 2p<sub>3/2</sub> in Co<sub>3</sub>O<sub>4</sub>) exhibited lower binding energy (780.0 eV) than that in CoAl<sub>2</sub>O<sub>4</sub> (781.9 eV). The XPS results confirm that the samples prepared by solid-state reaction between cobalt chloride and FG-13 calcined at 650°C and FG-0.6 calcined at 550°C were CoAl<sub>2</sub>O<sub>4</sub> which were in good agreement with the blue color observed in Figure 5. Moreover, the relative amount of Co<sup>2+</sup> ions in tetrahedral sites was found to increase with increasing calcination temperature. Decreasing the particles size of fine gibbsite probably increased the rate of diffusion step during a solid-state reaction [24], thus the CoAl<sub>2</sub>O<sub>4</sub> was formed at lower calcination temperature for FG-0.6 than FG-13. The average crystallite sizes of synthesized CoAl<sub>2</sub>O<sub>4</sub> were

calculated from the full width at half maximum of the XRD peak at  $2\theta = 36.8^{\circ}$  using the Scherrer's equation and are reported in **Table 1** ( $d_{XRD}$ ). The TEM images of synthesized CoAl<sub>2</sub>O<sub>4</sub> are shown in **Figure 6**. The TEM results clearly show that the synthesized CoAl<sub>2</sub>O<sub>4</sub> consisted of very fine particles with average size below 10 nm which are in good agreement with the average crystallite size calculated from the Scherrer's equation.

UV-Vis spectroscopy was carried out in order to study the correlation between cation distribution and the optical properties of synthesized CoAl<sub>2</sub>O<sub>4</sub> nanoparticles. Figure 7 shows the absorption spectra of the CoAl<sub>2</sub>O<sub>4</sub> particles obtained from the solid-state reaction of cobalt chloride and FG-13 and FG-0.6 at various calcination temperatures. The UV-Vis results were consistent to the XPS analyses. The Co<sup>2+</sup> in a tetrahedral ligand field is responsible for its blue color. It has been reported that the coloration of CoAl<sub>2</sub>O<sub>4</sub> was strongly dependent on the temperature of the heat treatment and on the stoichiometry of Co and Al in the Co3-1Al,O4 sample with the brightest blue coloration was obtained for S = 2.25 [16]. The intense absorption peak at around 600 nm for both of the prepared CoAl<sub>2</sub>O<sub>4</sub> particles are the characteristic of Co<sup>2+</sup> ions in the tetrahedral sites in crystalline materials [9]. From the UV-Vis spectra of the prepared CoAl<sub>2</sub>O<sub>4</sub> particles in Figure 7, a triple band were observed at around 540-630 nm, attributing to the spin-allowed [ ${}^{4}A_{2}(F) \rightarrow {}^{4}T_{1}(P)$ ] transition. This triple band can be attributed to a Jahn-Teller distortion of the tetrahedral structure [29]. It was found that the intensity of this triple band decreased with decreasing particles size of the starting fine gibbsite for a given calcination temperature (i.e., at 650°C). According to the XPS results, the atomic concentration of Co/Al increased with decreasing particles size of the starting fine gibbsite. It has been also reported that the intensity of this triple band decreased as the S value was increased, and might be probably due to the formation of white Al<sub>2</sub>O<sub>3</sub> from excess Al in the samples, lowering the intensity of color although the S values were larger than 2.25 and remained blue [16]. The results in this study also suggest that reduction of particle size of the starting material could have an influence on the band shift. However, further detailed study is necessary to confirm whether the blue shift is because of the reduction of particle size [27-30].

#### 4. Conclusions

Nanocrystalline CoAl<sub>2</sub>O<sub>4</sub> particles were successfully synthesized at low temperature by solid-state reaction using calcination of the mechanical mixture between fine gibbsite and cobalt chloride. The particle sizes of the starting fine gibbsite were 0.6 and 13 µm and the calcination temperature was varied in the range of 450-650°C. The XRD and XPS results revealed that the crystallization of CoAl<sub>2</sub>O<sub>4</sub> from the mixture between cobalt chloride and FG-13 and FG-0.6 occurred at 650°C and 550°C, respectively. The reduction of the starting particle size of fine gibbsite resulted in the lower crystallization temperature of CoAl<sub>2</sub>O<sub>4</sub> formation due to the increasing of contact area between reacting particles. However, increasing of calcination temperature promoted the insertion amounts of Co<sup>2+</sup> in alumina matrix in CoAl<sub>2</sub>O<sub>4</sub> structure, which resulted in the brighter blue particles and increasing of UV spectra band.

#### Acknowledgement

The financial supports from the Thailand Research Fund (TRF), the Office of Higher Commission Education, and the CU-NRU project (AM1088A) are gratefully acknowledged.

 $\textbf{Table 1} \ \text{The crystallite size and XPS results of the } \ \text{CoAl}_2\text{O}_4 \ \text{particles obtained via solid-state reaction of fine gibbsite and cobalt chloride.}$ 

Samples	d <sub>XRD</sub> (nm)	Co(II) 2p <sub>3/2</sub>		A1 2s		Atomic Conc%	
		B.E. (eV)	FWHM	B.E. (eV)	FWHM	Al/O	Co/Al
FG-13-650°C	6	781.9	2.819	119.1	2.828	0.50	0.032
FG-0.6-550°C	6	781.5	3.223	118.6	2.772	0.50	0.050
FG-0.6-650°C	6	782.1	3.385	119.2	2.678	0.48	0.053
$^{a}C_{O3}O_{4}$		$780.0 \pm 0.7$					
<sup>a</sup> CoAl <sub>2</sub> O <sub>4</sub>		$781.9 \pm 0.5$					

a ref [20, 27]

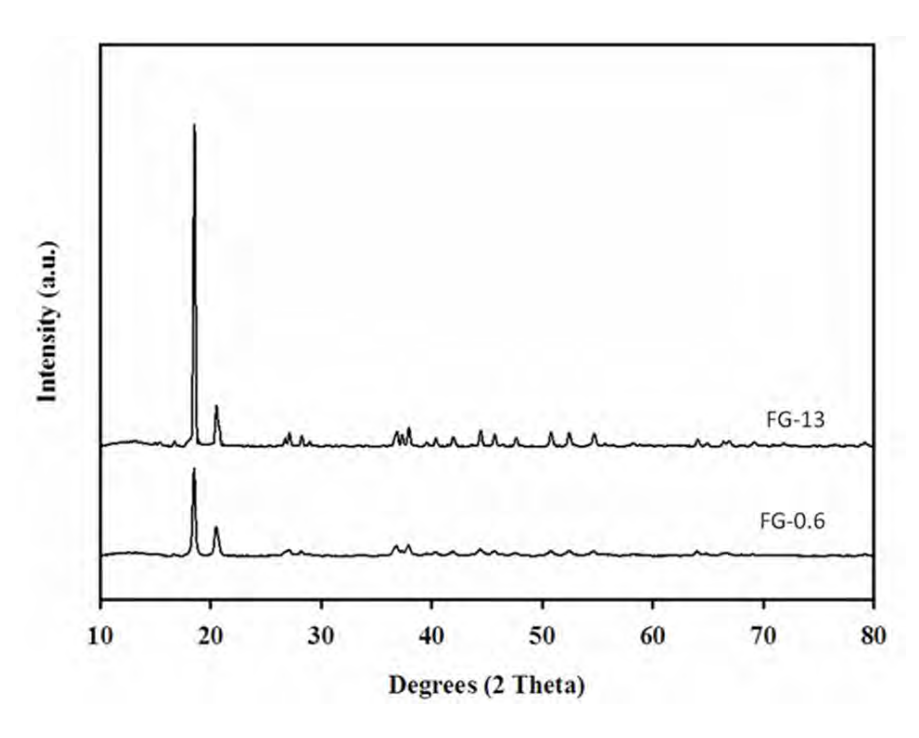


Figure 1 The XRD patterns of fine gibbsite (13  $\mu m$  and 0.6  $\mu m$ ).

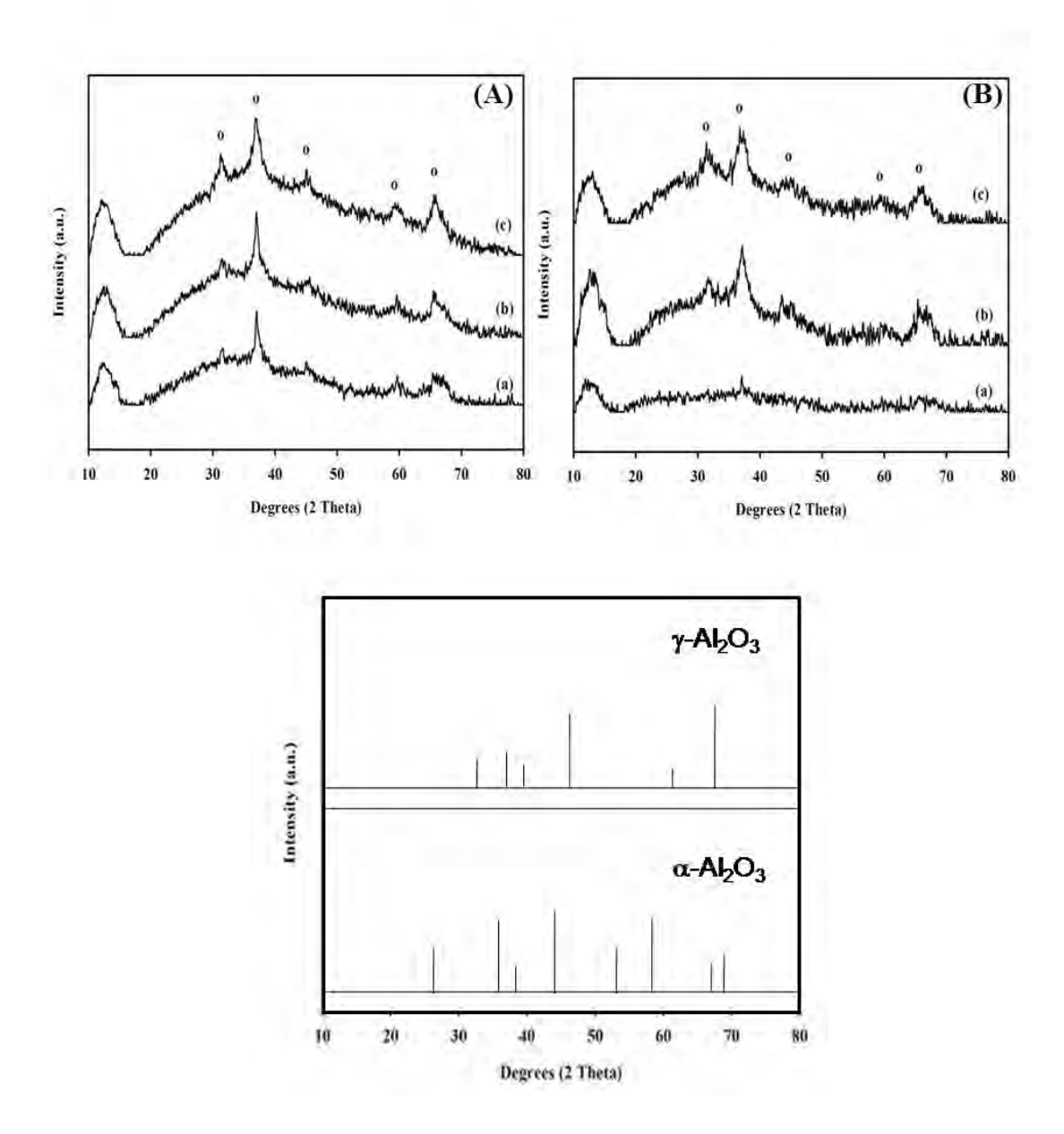
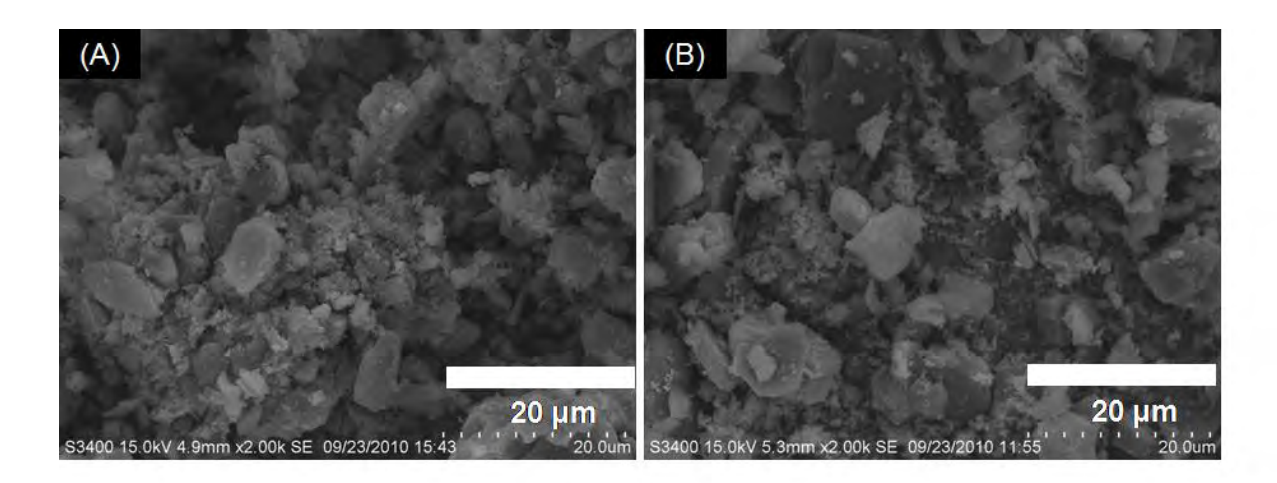
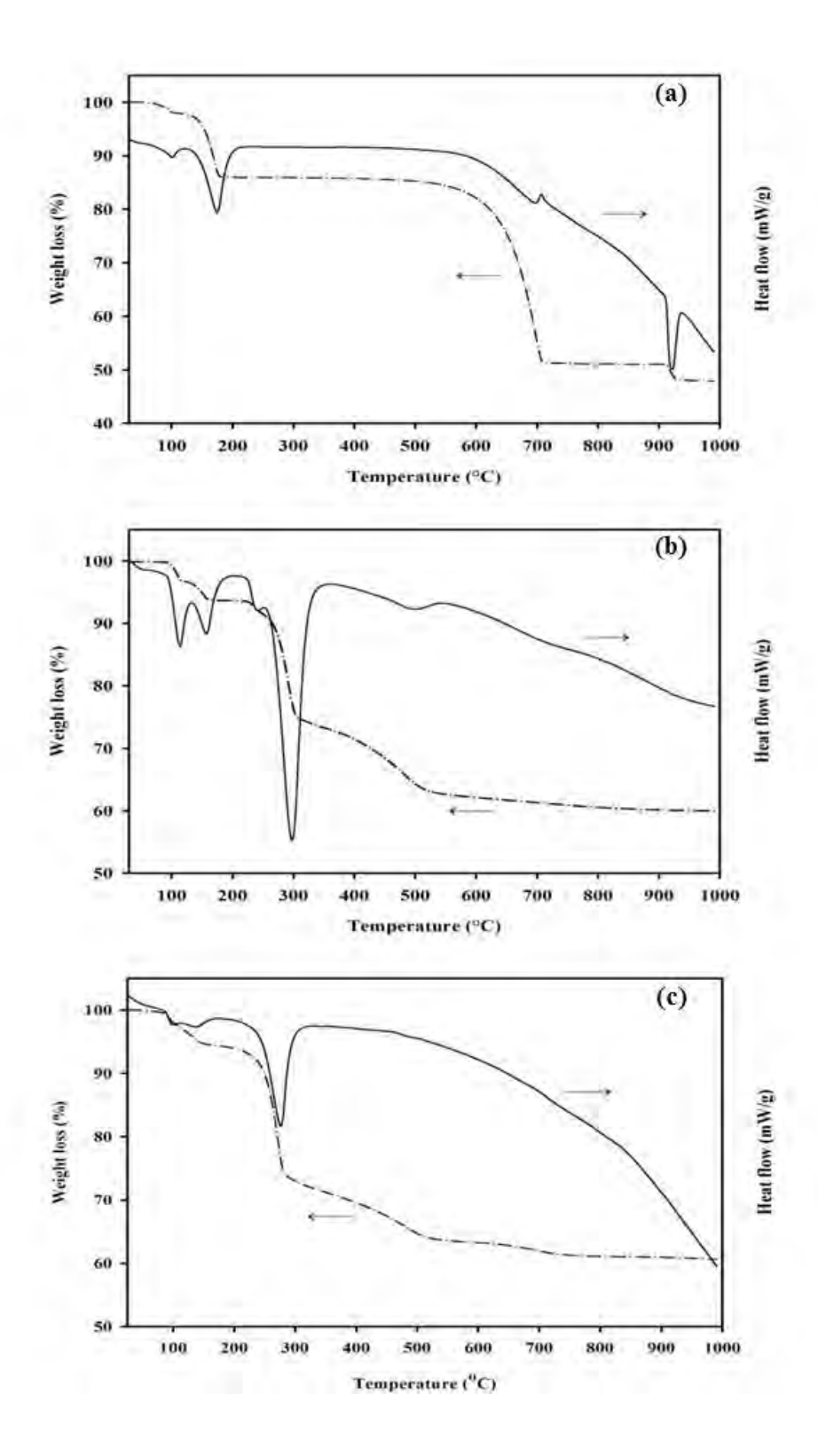


Figure 2 The XRD patterns of the  $CoAl_2O_4$  nanoparticles synthesized via the solid-state reaction between cobalt chloride and FG-13 (A) and FG-0.6 (B), after calcination at various temperatures: 450°C (a), 550°C (b), 650°C (c);  $o = CoAl_2O_4$ .



**Figure 3** SEM images of the CoAl<sub>2</sub>O<sub>4</sub> nanoparticles synthesized via the solid-state reaction between cobalt chloride and FG-13 (A), FG-0.6 (B) at 650°C.



**Figure 4** The TG/DTA curves of samples: bulk cobalt chloride (a), a mechanical mixture of cobalt chloride and FG-13 (b), and a mixture of cobalt chloride and FG-0.6 (c).

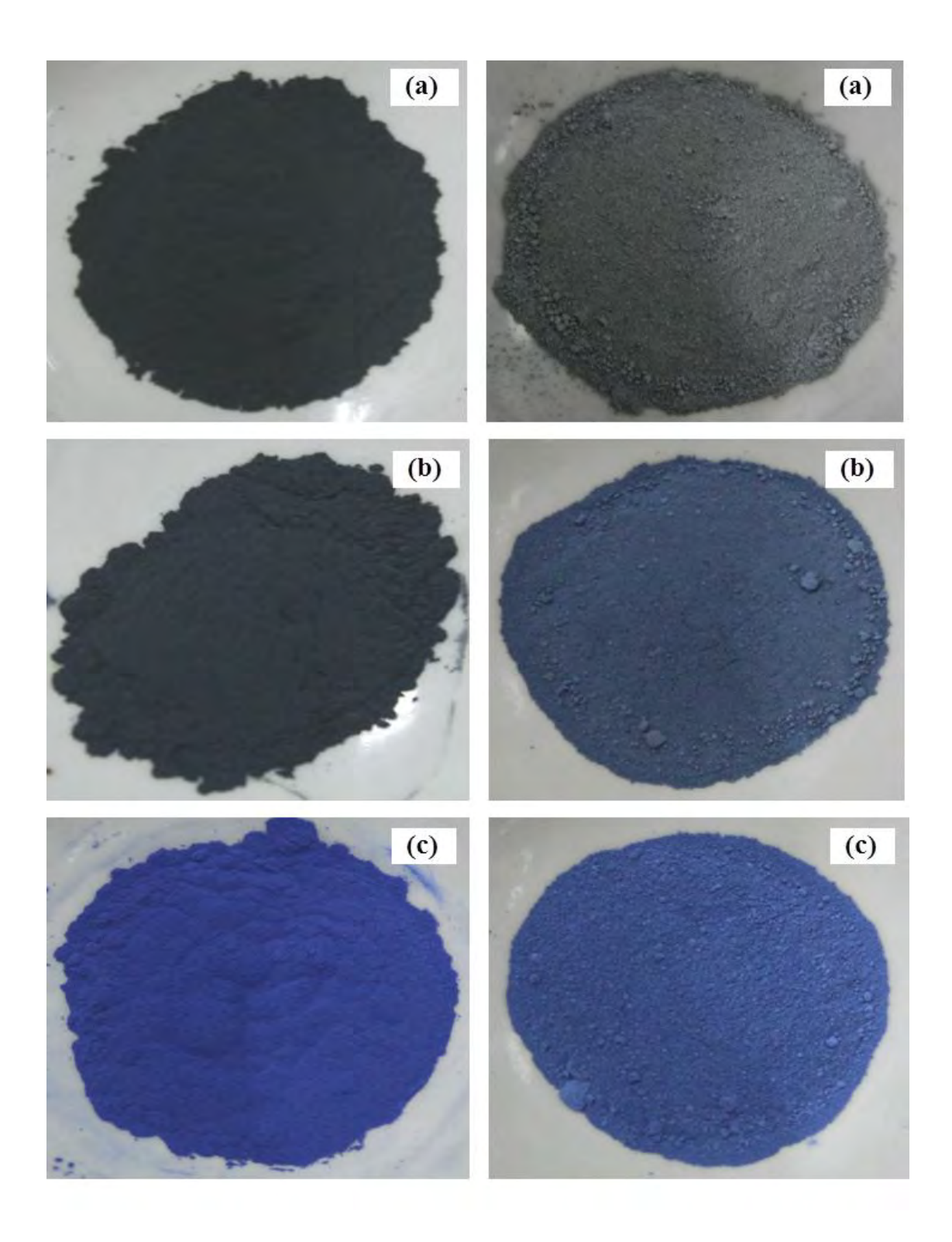


**Figure 5** The images of the CoAl<sub>2</sub>O<sub>4</sub> nanoparticles synthesized via the solid-state reaction between cobalt chloride and FG-13 (left-hand side) and FG-0.6 (right-hand side) after calcination at various temperatures: 450°C (a), 550 °C (b), and 650°C (c).

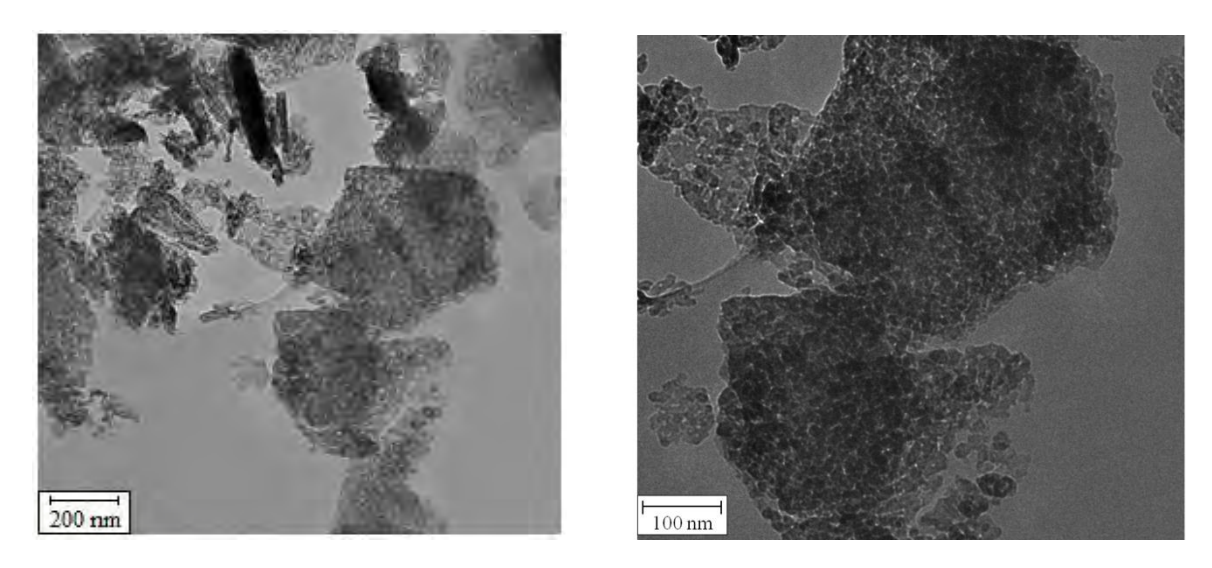


Figure 6 TEM images of the synthesized CoAl<sub>2</sub>O<sub>4</sub> nanoparticles (FG-0.6 calcined at 650°C)

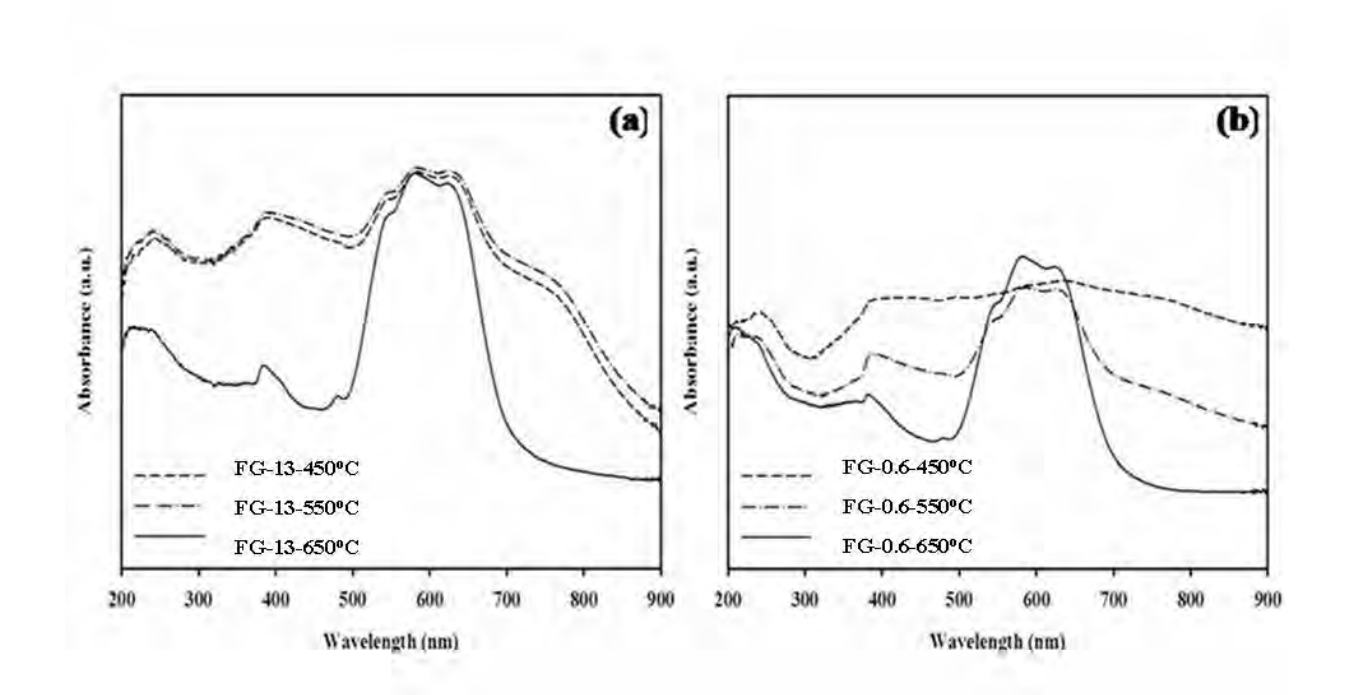


Figure 7 Absorption spectra in the wavelength range 200–900 nm of the CoAl<sub>2</sub>O<sub>4</sub> nanoparticles synthesized via the solid-state reaction between cobalt chloride and FG-13 (a) calcined at various temperatures and (b) the solid-state reaction of cobalt chloride and FG-0.6 calcined at various temperatures.

#### References

- [1] H.P. Bolt, M.P.H.F. Habraken, W.J. Geus, "Formation of nickel, cobalt, copper, and iron aluminates from α- and γ-alumina-supported oxides: A comparative study", *J. Solid-state Chem.*, **1998**, 135, 59-69.
- [2] F.M.J. Colinas, O.C. Areán, "Kinetics of solid-state spinel formation: Effect of cation coordination preference", *J. Solid-state Chem.*, **1994**, 109, 43-46.
- [3] W.S. Cho, M. Kakihana, "Crystallization of ceramic pigment CoAl<sub>2</sub>O<sub>4</sub> nanocrystals from Co-Al metal organic precursor", *J. Alloys and Compounds*, **1999**, 287, 87-90.
- [4] N. Ouahdi, S. Guillemet, B. Durand, R. Elouatib, E.L. Rakhob, R. Moussab, A. Samdi, "Synthesis of CoAl<sub>2</sub>O<sub>4</sub> by double decomposition reaction between LiAlO<sub>2</sub> and molten KCoCl<sub>3</sub>", *J. Eur. Ceram. Soc.*, **2008**, 28, 1987-1994.
- [5] W. Lv, Q. Qiu, F. Wang, S. Wei, B. Liu, Z. Luo, "Sonochemical synthesis of cobalt aluminate nanoparticles under various preparation parameters", *Ultrasonics Sonochem.*, **2010**, 17, 793–801.
- [6] X. Duan, D. Yuan, X. Cheng, Z. Sun, H. Sun, D. Xu, M. Lv, "Spectroscopic properties of Co<sup>2+</sup>: ZnAl<sub>2</sub>O<sub>4</sub> nanocrystals in sol-gel derived glass-ceramics", *J. Phys. Chem. Solids*, **2003**, 64, 1021-1025.
- [7] D.M.A. Melo, J.D. Cunha, J.D.G. Fernandes, M.I. Bernardi, M.A.F. Melo, A.E. Martinelli, "Evaluation of CoAl<sub>2</sub>O<sub>4</sub> as ceramic pigments", *Mater. Res. Bull.*, **2003**, 38, 1559–1564.
- [8] J. Merikhi, O.H. Jungk, C. Feldmann, "Sub-micrometer CoAl<sub>2</sub>O<sub>4</sub> pigment particles Synthesis and preparation of coatings", *J. Mater. Chem.*, **2000**, 10, 1311-1314.
- [9] W. Li, J. Li, J. Guo, "Synthesis and characterization of nanocrystalline CoAl<sub>2</sub>O<sub>4</sub> spinel powder by low temperature combustion", *J. Eur. Ceram. Soc.*, **2003**, 23, 2289–2295.
- [10] B. Jongsomjit, J. Panpranot, J.G. Goodwin Jr., "Co-support compound formation in alumina-supported cobalt catalysts", *J. Catal.*, **2001**, 204, 98–109.

- [11] L. Ji, S. Tang, H.C. Zeng, J. Lin, K.L. Tan, "CO<sub>2</sub> reforming of methane to synthesis gas over sol-gel-made Co/γ-Al<sub>2</sub>O<sub>3</sub> catalysts from organometallic precursors", *Appl. Catal. A*, **2001**, 207, 247-255.
- [12] S. Chokkaram, R. Srinivasan, R.D. Milburn, H.B. Davis, "Conversion of 2-octanol over nickel-alumina, cobalt-alumina, and alumina catalysts", *J. Mol. Catal. A*, **1997**, 121, 157-169.
- [13] S. Chemlal, A. Larbot, M. Persin, J. Sarrazin, M. Sghyar, M. Rafiq, "Cobalt spinel CoAl<sub>2</sub>O<sub>4</sub> via sol-gel process: Elaboration and surface properties", *Mater. Res. Bull.*, **2000**, 35, 2515–2523.
- [14] M. Sales, C. Valentin, J. Alarcon, "Cobalt aluminate spinel-mullite composites synthesized by sol-gel method", J. Eur. Ceram. Soc., 1997, 17, 41-47.
- [15] S. Kurajica, E. Tkalcec, J. Schmauch, "CoAl<sub>2</sub>O<sub>4</sub>-mullite composites prepared by sol-gel processes", *J. Eur. Ceram. Soc.*, **2007**, 27, 951–958.
- [16] M. Zayat, D. Levy, "Blue CoAl<sub>2</sub>O<sub>4</sub> particles prepared by the sol-gel and citrate-gel methods", *Chem. Mater.*, **2000**, 12, 2763-2769.
- [17] G. Carta, M. Casarin, E.N. Habra, M. Natali, G. Rossetto, C. Sada, E. Tondello, P. Zanella, "MOCVD deposition of CoAl<sub>2</sub>O<sub>4</sub> films", *Electrochimica Acta*, **2005**, 50, 4592–4599.
- [18] C. Wang, X. Bai, S. Liu, L. Liu, "Synthesis of cobalt-aluminum spinels via EDTA chelating precursors", *J. Mater. Sci.*, **2004**, 39, 6191–6201.
- [19] C. Wang, S. Liu, L. Liu, X. Bai, "Synthesis of cobalt-aluminate spinels via glycine chelated precursors", *Mater. Chem. Phys.*, **2006**, 96, 361–370.
- [20] Z.Z. Chen, W.E. Shi, J.W. Li, Q.Y. Zheng, Y.J. Zhuang, B. Xiao, A.L. Tang, "Preparation of nanosized cobalt aluminate powders by a hydrothermal method", *Mater. Sci. Eng. B*, **2004**, 107, 217–223.
- [21] H. Guorong, D. Xinrong, C. Yanbing, P. Zhongdong, "Synthesis of spherical CoAl<sub>2</sub>O<sub>4</sub> pigment particles with high reflectivity by polymeric-aerosol pyrolysis", Rare Metals, 2007, 26, 236–241.

- [22] J. Chandradass, M. Balasubramanian, H.K. Kim, "Size effect on the magnetic property of CoAl<sub>2</sub>O<sub>4</sub> nanopowders prepared by reverse micelle processing", *J. Alloys and Compounds*, **2010**, 506, 395–399.
- [23] F. Li, X. Yu, H. Pan, M. Wang, X. Xin, "Syntheses of MO<sub>2</sub> (M= Si, Ce, Sn) nanoparticles by solid-state reactions at ambient temperature", *Solid-state Sci.*, **2000**, 2, 767–772.
- [24] V.V. Boldyrev, "Mechanochemistry and mechanical activation of solids", Russ. Chem. Rev., 2006, 75, 177–189.
- [25] W. Chaitree, S. Jiemsirilers, O. Mekasuwandumrong, P. Praserthdam, T. Charinpanitkul, J. Panpranot "Effect of milling on the formation of nanocrystalline x-Al<sub>2</sub>O<sub>3</sub> from gibbsite" *J. Amer. Ceram. Soc.*, **2010**, 93, 3377-3383.
- [26] L. Ji, J. Lin, C.H. Zeng, "Metal-support interactions in Co/Al<sub>2</sub>O<sub>3</sub> catalysts: A comparative study on reactivity support", *J. Phys. Chem.*, **2000**, 104, 1783-1790.
- [27] K.A. Bhattacharya, A. Hartridge, K.K. Mallick, R.C. Werrett, L.J. Woodhead, "Low-temperature decomposition of hydrated transition metal chlorides on hydrous gel substrates", *J. Mater. Sci.*, **1996**, 31, 4479–4482.
- [28] Z. Zsoldos, L. Guczi, "Structure and catalytic activity of alumina supported platinum-cobalt bimetallic catalysts 3. Effect of treatment on the interface layer", *J. Phys. Chem.*, **1992**, 96, 9393-9400.
- [29] D. Rangappa, S. Ohara, T. Naka, A. Kondo, M. Ishii, T. Adschiri, "Synthesis and organic modification of CoAl<sub>2</sub>O<sub>4</sub> nanocrystals under supercritical water conditions", *J. Mater. Chem.*, **2007**, 17, 4426–4429.
- [30] S.M. Niasari, F.M. Khouzani, F. Davar, "Bright blue pigment CoAl<sub>2</sub>O<sub>4</sub> nanocrystals prepared by modified sol-gel method", *J. Sol-Gel Sci. Tech.*, **2009**, 52, 321–327.

# สถาบันทรัพย์สินทางปัญญาแห่งจุฬาลงกรณ์มหาวิทยาลัย Chulalongkorn University Intellectual Property Institute



เมษายน 2554

เรื่อง ขอผ่อนผันการส่งเอกสารประกอบคำขอรับสิทธิบัตร ครั้งที่ 1

1101000535

เรียน ผู้อำนวยการสำนักสิทธิบัตร

ค้วยสถาบันทรัพย์สินทางปัญญาแห่งจุฬาลงกรณ์มหาวิทยาลัยได้รับมอบหมายจากจุฬาลงกรณ์ มหาวิทยาลัย สำนักงานคณะกรรมการการอุคมศึกษา และสำนักงานกองทุนสนับสนุนการวิจัย ให้คำเนินการยื่น คำขอรับสิทธิบัตร เรื่อง "กรรมวิธีการเตรียมตัวเร่งปฏิกิริยาทั้งสเตนบนตัวรองรับเชอร์โคเนียมไดออกไซค์ที่ปรับปรุง ด้วยออกไซค์ของโลหะทรานสิชันหมู่ IIIB เพื่อนำไปใช้เป็นตัวเร่งปฏิกิริยาในปฏิกิริยาเอสเทอร์ริฟิเคชัน" โดยมี ข้าพเจ้านายมงคล แก้วมหา ตัวแทนสิทธิบัตร เลขที่ 1453 เป็นผู้ดำเนินการ ซึ่งขณะนี้อยู่ระหว่างคำเนินการให้ผู้ที่ เกี่ยวข้องลงนามในสัญญาโอนสิทธิในการขอรับสิทธิบัตร และหนังสือมอบอำนาจ ซึ่งจำเป็นที่จะต้องใช้ระยะเวลา หนึ่งในการคำเนินการ แต่เนื่องจากการประดิษฐ์นี้ ทางผู้ประดิษฐ์มีความประสงค์ที่จะเผยแพร่ผลงานวิจัย ซึ่งหาก มีการนำไปเผยแพร่ผลงานก่อนที่จะได้มีการยื่นคำขอรับสิทธิบัตร ข้าพเจ้าเกรงว่าจะมีผลต่อการพิจารณารับจด ทะเบียนของคำขอรับสิทธิบัตรฉบับนี้ได้

ด้วยเหตุผลดังกล่าวข้างต้น ข้าพเจ้าจึงเรียนมาเพื่อ โปรคพิจารณาอนุมัติผ่อนผันการยื่นเอกสาร ประกอบคำขอรับสิทธิบัตรพร้อมกับคำขอรับสิทธิบัตรด้วย จักขอบพระคุณยิ่ง

ขอแสดงความนับถือ

(นายมงคล แก้วมหา)

MILLETHIN MACH

ผู้รับมอบอำนาจ

ตัวแทนสิทธิบัตร เลขที่ 1453

สำหรับเจ้าหน้าที่





	วันรับคำขอ	น เลขที่คำขอ	
	วันยื่นคำขอ	1101000535	
•••• คำขอรับสิทธิบัตร/อนุสิทธิบัตร	สัญลักษณ์จำแนกการประดิษฐ์ระหว่างประเทศ		
🗹 การประดิษฐ์	ใช้กับแบบผลิตภัณฑ์		
🗖 การออกแบบผลิตภัณฑ์	ประเภทผลิตภัณฑ์		
🗖 อนุสิทธิบัตร	วันประกาศโฆษณา	เลขที่ประกาศโฆษณา	
ข้าพเจ้าผู้ลงลายมือชื่อในคำขอรับสิทธิบัตร/อนุสิทธิบัตรนี้ เอรับสิทธิบัตร/อนุสิทธิบัตร ตามพระราชบัญญัติสิทธิบัตร พ.ศ. 2522	วันออกสิทธิบัตร/อนุสิทธิบัตร	เลขที่สิทธิบัตร/อนุสิทธิบัตร	
ก้ไขเพิ่มเติมโคยพระราชบัญญัติสิทธิบัตร (ฉบับที่ 2) พ.ศ 2535 และ เระราชบัญญัติสิทธิบัตร (ฉบับที่ 3) พ.ศ 2542	ลายมือชื่อเจ้าหน้าที่		
กรรมวิธีการเครียมตัวเร่งปฏิกิริยาทั้งสเตนบนตัวรองรับเซอร์โคเนียม เพื่อนำไปใช้เป็นตัวเร่งปฏิกิริยาในปฏิกิริยาเอสเทอร์ริฟิเคชัน .คำขอรับสิทธิบัตรการออกแบบผลิตภัณฑ์นี้เป็นคำขอสำหรับแบบผลิต ในจำนวน คำขอ ที่ยื่นในคราวเดียวกัน	·	·	
.ผู้ขอรับสิทธิบัตร/อนุสิทธิบัตร และที่อยู่ (เลขที่ ถนน ประเทศ)	3.1 สัญชาติ		
ดูที่หน้า 3	3.2 โทรศัพท์		
	3.3 โทรสาร		
	3.4 อีเมล์		
.สิทธิในการขอรับสิทธิบัตร/อนุสิทธิบัตร  ผู้ประคิษฐ์/ผู้ออกแบบ 🗹 ผู้รับโอน 🔲 ผู้ขอรับสิทธิ์	โคยเหตุอื่น		
.ตัวแทน(ถ้ามี)/ที่อยู่ (เลขที่ ถนน จังหวัค รหัสไปรษณีย์)	5.1 ตัวแทนเลขที่ 1453	5.1 ตัวแทนเลขที่ 1453	
นายมงคล แก้วมหา	5.2 โทรศัพท์ 0-2160-	5.2 โทรศัพท์ 0-2160-5340-2	
สถาบันทรัพย์สินทางปัญญาแห่งจุฬาลงกรณ์มหาวิทยาลัย อาคารจัศุรัสจามจุรี ชั้น 12 ยูนิต 13 ถนนพญาไท แขวงปทุมวัน เขค	5.3 โทรสาร 0-2160- ปทบวับ	5.3 โทรสาร 0-2160-5343	
กรุงเทพฯ 10330	5.4 อีเมล์	5.4 อีเมล์	
.ผู้ประดิษฐ์/ผู้ออกแบบผลิตภัณฑ์ และที่อยู่ ( เลขที่ ถนน ประเทศ )			
ศาสตราจารย์ คร.ปียะสาร ประเสริฐธรรม และ นางสาวเพียงพิศ วะ อยู่ที่ ภาควิชาวิศวกรรมเคมี คณะวิศวกรรมศาสตร์ จุฬาลงกรณ์มหา		ารุงเทพง 10330	
'. คำขอรับสิทธิบัตร/อนุสิทธิบัตรนี้แยกจากหรือเกี่ยวข้องกับคำขอเคิม			
ผู้ขอรับสิทธิบัตร/อนุสิทธิบัตร ขอให้ถือว่าได้ยื่นคำขอรับสิทธิบั	ตร/อนุสิทธิบัตรนี้ ในวันเดียวกับคำ	ขอรับสิทธิบัตร	
ลงที่ วันยื่น เพราะคำขอรับสิทธิบัตร/อนุสิทธิ	บิตรนี้แยกจากหรือเกี่ยวข้องกับคำข	บอเคิมเพราะ	
🔲 คำขอเดิมมีการประดิษฐ์หลายอย่าง 🔲 ถูกคัดค้านเนื่องจากผู้ขย	าไม่มีสิทธิ์ 🔲 ขอเปลี่ยนแปลงปร	ระเภทของสิทธิ	

หมายเหตุ ในกรณีที่ไม่อาจระบุรายละเอียดได้ครบถ้วน ให้จัดทำเป็นเอกสารแนบท้ายแบบพิมพ์นี้โดยระบุหมายเลขกำกับข้อและหัวข้อที่แสดงรายละเอียด เพิ่มเติมดังกล่าวด้วย

8.การยื่นคำขอนอกราชอาณาจักร						
วันยื่นคำขอ	เลขที่คำขอ	ประเทศ	สัญลักษณ์จำแนกการ ประดิษฐ์ระหว่างประเทศ	สถานะคำขอ		
8.1						
8.2						
8.3	***************************************					
8.4 🗖 ผู้ขอรับสิทธิบัตร/อนุสิ	8.4 🗖 ผู้ขอรับสิทธิบัตร/อนุสิทธิบัตรขอสิทธิให้ถือว่าได้ยื่นคำขอนี้ในวันที่ได้ยื่นคำขอรับสิทธิบัตร/อนุสิทธิบัตรในต่างประเทศเป็นครั้งแรกโดย					
🗖 ได้ยื่นเอกสารหลักฐาน	เพร้อมคำขอนี้ 🛮 ขอยื่	นเอกสารหลักฐานหลังจาก	วันยื่นคำขอนี้			
9.การแสดงการประคิษฐ์ หรือก	ารออกแบบผลิตภัณฑ์ ผู้ขอ	รับสิทธิบัตร/อนุสิทธิบัตร	ใค้แสดงการประดิษฐ์ที่หน่วยงานขอ	องรัฐเป็นผู้จัด		
วันแสดง 27 มีนาคม 2551	วันเปิดงานแสดง	27 มีนาคม 2551	ผู้จัด สำนักงานกองทุนสนับสนุ	นการวิจัย		
10.การประคิษฐ์เกี่ยวกับจุลซีพ						
10.1 เลขทะเบียนฝากเก็บ	10.2 วันร์	าี่ฝากเก็บ	10.3 สถาบันฝากเก็บ/ร	ประเทศ		
				y .		
			นี้ และจะจัดยื่นคำขอรับสิทธิบัตร/	อนุสิทธิบัตรนีที่จัดทำ		
เป็นภาษาไทยภายใน 90 วัน นัก						
🗌 อังกฤษ 🔲 ฝรั่งเศ		0				
-		ษณาคำขอรับสิทธิบัตร หรื	เอรับจดทะเบียน และประกาศโฆษเ	ณาอนุสิทธิบัตรนี้		
หลังจากวันที่	เดือน	พ.ศ	٠			
🗖 ผู้ขอรับสิทธิบัตร/อนุสิทธิบัตรขอให้ใช้รูปเขียนหมายเลข ในการประกาศโฆษณา						
13.คำขอรับสิทธิบัตร/อนุสิทธิบัตรนี้ประกอบด้วย			14.เอกสารประกอบคำขอ			
ก. แบบพิมพ์คำขอ	3 หน้า					
	พ. รายละเอียคการประดิษฐ์ 🔲 หนังสือรับรองการแสดงการประดิษฐ์/การออกแบบ หรือคำพรรณนาแบบผลิตภัณฑ์ 7 หน้า ผลิตภัณฑ์		การออกแบบ			
กรอกเพรานน แบบพฤต ค. ข้อถือสิทธิ์ 3	มณฑ / กนา หน้า	ผลิตภัณฑ์ หนังสือมอบอำนาจ				
า. รูปเขียน รู1			<ul> <li>ทนงถอมอบอานาง</li> <li>เอกสารรายละเอียดเกี่ยวกับจุลชีพ</li> </ul>			
ง. รูปเบอน จ. ภาพแสดงแบบผลิตภัณฑ์			<ul> <li>□ เอกสารการขอนับวันยื่นคำขอในต่างประเทศเป็นวันยื่น</li> </ul>			
🔲 รูปเขียน รูป			คำขอในประเทศไทย			
ี			🗖 เอกสารขอเปลี่ยนแปลงประเภทของสิทธิ			
ฉ. บทสรุปการประดิษฐ์	! หน้า	🔲 เอก	🔲 เอกสารอื่น ๆ			
15. ข้าพเจ้าขอรับรองว่า						
🗹 การประดิษฐ์นี้ไม่เคยยื่นขอรับสิทธิบัตร/ อนุสิทธิบัตรมาก่อน						
🗖 การประดิษฐ์นี้ใด้พัฒนาปรับปรุงมาจาก						
16 a 1 g 1 a 2 a 2 a 2 a 2 a 2 a 2 a 2 a 2 a 2 a	ทริกัตร / อาเสินธิกัดร โ	71 ตัวแรง \	VIALUE III			
16.ลายมือชื่อ ( ロ ผู้ขอรับสิทธิบัตร / อนุสิทธิบัตร: 図 ตัวแทน ) นายมงคล แก้วมหา みりのん ほがみび						
In ION ALLEE WELL WILL DE	N VEVINA 11/19CV	Λ				

หมายเหตุ บุคคลใดขึ้นขอรับสิทธิบัตรการประดิษฐ์หรือการออกแบบผลิตภัณฑ์ หรืออนุสิทธิบัตร โดยการแสดงข้อความอันเป็นเท็จแก่พนักงานเจ้าหน้าที่ เพื่อให้ ได้ไปซึ่งสิทธิบัตรหรืออนุสิทธิบัตร ต้องระวางโทษจำคุกไม่เกินหกเดือน หรือปรับไม่เกินห้าพันบาท หรือทั้งจำทั้งปรับ 3. ผู้ขอรับสิทธิบัตร/อนุสิทธิบัตร และที่อยู่ (เลขที่ ถนน ประเทศ)
 จุฬาลงกรณ์มหาวิทยาลัย
 อยู่ที่ เลขที่ 254 ถนนพญาไท แขวงวังใหม่ เขตปทุมวัน กรุงเทพฯ 10330

 3.1 สัญชาติ ใทย 3.2 โทรศัพท์ 0-2160-5340-2 3.3 โทรสาร 0-2160-5343

สำนักงานคณะกรรมการการอุดมศึกษา อยู่ที่ เลขที่ 328 ถนนศรีอยุธยา เขตราชเทวี กรุงเทพฯ 10400 3.1 สัญชาติ ไทย 3.2 โทรศัพท์ 0-2610-5200 3.3 โทรสาร 0-2354-5524

สำนักงานกองทุนสนับสนุนการวิจัย อยู่ที่ ชั้น 14 อาคาร เอส เอ็ม ทาวเวอร์ เลขที่ 979/17-21 ถนนพหลโยธิน แขวงสามเสนใน เขตพญาไท กรุงเทพฯ 10400 3.1 สัญชาติ ไทย 3.2 โทรศัพท์ 0-2278-8200 3.3 โทรสาร 0-2298-0476

#### หน้า 1 ของจำนวน 7 หน้า

#### รายละเอียดการประดิษฐ์

# ชื่อที่แสดงถึงการประดิษฐ์

5

10

15

20

กรรมวิธีการเตรียมตัวเร่งปฏิกิริยาทั้งสเตนบนตัวรองรับเซอร์โคเนียมใดออกใชด์ ที่ปรับปรุงด้วยออกใชด์ของโลหะทรานสิชันหมู่ IIIB เพื่อนำไปใช้เป็นตัวเร่งปฏิกิริยาในปฏิกิริยา เอสเทอร์ริฟิเคชัน

## ลักษณะและความมุ่งหมายของการประดิษฐ์

การประดิษฐ์นี้เกี่ยวข้องกับกรรมวิธีการเตรียมตัวเร่งปฏิกิริยาเพื่อใช้ในปฏิกิริยาเอสเทอร์ ริฟิเลชัน โดยใช้เซอร์โลเนียมไดออกไซด์ที่ปรับปรุงด้วยออกไซด์ของโลหะทรานสิชันหมู่ IIIB เป็น ตัวรองรับของตัวเร่งปฏิกิริยาทั้งสเตน ซึ่งมีขั้นตอนการเตรียมดังนี้

- การปรับปรุงตัวรองรับเซอร์โกเนียมใดออกใชด์ ซึ่งทำโดยวิธีการใดวิธีการหนึ่ง ดังต่อไปนี้คือ
- (1) โดยการเติมสารละลายของสารประกอบของโลหะทรานสิชันหมู่ IIIB ในขั้นตอน การเตรียมตัวรองรับเซอร์โคเนียมใดออกไซด์ หรือ
- (2) โดยการเติมสารละลายของสารประกอบของโลหะทรานลิชันหมู่ IIIB ลงบน เซอร์โคเนียมใดออกใชค์
- การเตรียมตัวเร่งปฏิกิริยาทั้งสเตนบนตัวรองรับเซอร์ โคเนียมใดออกใชด์ที่ปรับปรุง ด้วยออกใชด์ของโลหะทรานสิชันหมู่ IIIB ทำโดยการเติมสารละลายของสารประกอบโลหะทั้งสเตน บนตัวรองรับเซอร์ โคเนียมใดออกใชด์ที่ปรับปรุงด้วยออกใชด์ของโลหะทรานสิชันหมู่ IIIB จากนั้น ตั้งทิ้งไว้ที่อุณหภูมิห้อง แล้วนำไปอบให้แห้ง หลังจากนั้นนำตะกอนที่แห้งสนิทไปผ่านขั้นตอนการ เผาที่อุณหภูมิสูง

กวามมุ่งหมายของการประดิษฐ์นี้ เพื่อพัฒนาตัวเร่งปฏิกิริยาที่นำมาใช้ในปฏิกิริยา เอสเทอร์ริฟิเคชันที่ให้ประสิทธิภาพสูงกว่าหรือดีกว่าตัวเร่งปฏิกิริยาที่ใช้อยู่ในปัจจุบัน

# สาขาวิทยาการที่เกี่ยวข้องกับการประดิษฐ์

วิศวกรรมเคมีในส่วนที่เกี่ยวข้องกับกรรมวิธีการเตรียมตัวเร่งปฏิกิริยา

## 25 ภูมิหลังของคิดปะหรือวิทยาการที่เกี่ยวข้อง

ปัจจุบัน ตัวเร่งปฏิกิริยาในเชิงการค้าที่ใช้ในปฏิกิริยาเอสเทอร์ริฟิเคชัน คือ ทั้งสเตนบนตัว รองรับเซอร์โคเนียมไดออกไซด์ ซึ่งมีประสิทธิภาพต่ำ ทั้งนี้ จากการตรวจสอบเอกสารสิทธิบัตร พบว่า ยังไม่มีสิทธิบัตรใดที่อ้างถึงการปรับปรุงตัวรองรับเซอร์โคเนียมไดออกไซด์ด้วยโลหะ

#### หน้า 2 ของจำนวน 7 หน้า

ทรานสิชันหมู่ IIIB แต่อย่างใด การปรับปรุงตัวรองรับด้วยโลหะทรานสิชันหมู่ IIIB ทำให้ตัวเร่ง ปฏิกิริยาตามการประดิษฐ์นี้มีความว่องไวสูงกว่าตัวเร่งปฏิกิริยาที่ใช้ในปัจจุบัน

## การเปิดเผยการประดิษฐ์โดยสมบูรณ์

5

10

15

20

25

การประดิษฐ์นี้เกี่ยวข้องกับกรรมวิธีการเตรียมตัวเร่งปฏิกิริยาเพื่อใช้ในปฏิกิริยาเอสเทอร์ ริฟิเคชัน โดยใช้เซอร์โคเนียมไดออกไซด์ที่ปรับปรุงด้วยออกไซด์ของโลหะทรานสิชันหมู่ IIIB เป็น ตัวรองรับของตัวเร่งปฏิกิริยาทั้งสเตน ซึ่งมีขั้นตอนการเตรียมดังนี้

- การปรับปรุงตัวรองรับเซอร์โคเนียมใดออกใซค์ ซึ่งทำโคยวิธีการใดวิธีการหนึ่ง ดังต่อไปนี้คือ
- (1) โดยการเติมสารละลายของสารประกอบของโลหะทรานสิชันหมู่ IIIB ในขั้นตอน การเตรียมตัวรองรับเซอร์โคเนียมไดออกไซด์ หลังจากการทำให้เกิดเป็นตะกอนแล้วจะทำการล้าง ตะกอนโดยการหมุนเหวี่ยง และนำตะกอนไปอบให้แห้ง ในบางกรณีอาจจะนำตะกอนที่แห้งแล้ว ไปเผาที่อุณหภูมิสูงเพื่อให้เกิดเป็นเซอร์โคเนียมไดออกไซด์ที่มืออกไซด์ของโลหะทรานซิชันหมู่ IIIB ปนอยู่ หรือ
  - (2) โดยการเติมสารละลายของสารประกอบของโลหะทรานลิชันหมู่ IIIB ลงบน เซอร์โคเนียมไดออกไซค์ จากนั้นอบให้แห้ง แล้วนำไปเผาที่อุณหภูมิสูง
  - การเตรียมตัวเร่งปฏิกิริยาทั้งสเตนบนตัวรองรับเซอร์โคเนียมใดออกใชด์ที่ปรับปรุง ด้วยออกใชด์ของโถหะทรานสิชันหมู่ IIIB ทำโดยการเติมสารละลายของสารประกอบโถหะทั้งสเตน บนตัวรองรับเซอร์โคเนียมใดออกใชด์ที่ปรับปรุงด้วยออกใชด์ของโถหะทรานสิชันหมู่ IIIB จากนั้น ตั้งทิ้งไว้ที่อุณหภูมิห้อง เป็นเวลา 1-10 ชั่วโมง แต่ที่เหมาะสมคือ 5 ชั่วโมง แล้วนำไปอบให้แห้ง หลังจากนั้นนำตะกอนที่แห้งสนิทไปผ่านขั้นตอนการเผาที่อุณหภูมิสูง

โลหะทรานสิชันหมู่ IIIB ตามการประดิษฐ์นี้ ใด้แก่ โลหะสแกนเดียม โลหะอิตเทรียม โลหะแลนทานัม และ โลหะแอกทีเนียม แต่ที่ควรใช้ ได้แก่ โลหะอิตเทรียม และ โลหะแลนทานัม

สารประกอบของโลหะเซอร์โคเนียมตามการประดิษฐ์นี้ ได้แก่ เซอร์โคเนียมในเตรด เซอร์โคเนียมคลอไรด์ เซอร์โคเนียมแอซิเตค เซอร์โคเนียมโพรพอกไซด์ เซอร์โคเนียมไอโซโพรพอก ใชด์ และ เซอร์โคเนียมนอมัลบิวทอกไซด์ แต่ที่ควรใช้ คือ เซอร์โคเนียมนอมัลบิวทอกไซด์

สารประกอบของโลหะแลนทานัมตามการประดิษฐ์นี้ ได้แก่ แลนทานัมกลอไรด์ แลนทานัมในเตรต แลนทานัมแอซิเตด และ แลนทานัมอะซิติลอะซิโตเนต แต่ที่ควรใช้ คือ แลนทานัมในเตรต

#### หน้า 3 ของจำนวน 7 หน้า

สารประกอบของโลหะอิตเทรียมตามการประคิษฐ์นี้ ได้แก่ อิตเทรียมคลอไรด์ อิตเทรียม ในเตรต อิตเทรียมแอซิเตด อิตเทรียมอะซิติลอะซิโตเนต และ อิตเทรียมอะซิเตรต แต่ที่ควรใช้ คือ อิตเทรียมในเตรต

สารประกอบของโลหะทั้งสเตนตามการประดิษฐ์นี้ ได้แก่ แอมโมเนียมเมทาทั้งสเตน แอมโมเนียมพาราทั้งสเตน ทั้งสเตนเฮกซะคลอไรด์ ทั้งสเตนเฮกซะคาร์บอนิล และ ทั้งสเตนเพนตะ ออกไซด์ แต่ที่ควรใช้ คือ ทั้งสเตนเฮกซะคลอไรด์

ในขั้นตอนการถ้างโดยวิธีหมุนเหวี่ยง จำนวนครั้งที่เหมาะสมในการถ้างอยู่ในช่วง 3-10 ครั้ง แต่ที่เหมาะสมที่สุดคือ 5 ครั้ง สำหรับความเร็วรอบที่เหมาะสมสำหรับการหมุนเหวี่ยงอยู่ในช่วง 1,000-5,000 รอบต่อนาที แต่ที่เหมาะสมที่สุดคือ 3,000 รอบต่อนาที และสำหรับเวลาที่เหมาะสมในการหมุนเหวี่ยงเพื่อเหวี่ยงแยกตะกอนอยู่ในช่วง 10-30 นาที แต่ที่เหมาะสมที่สุดคือ 15 นาที

ในขั้นตอนการเผาที่อุณหภูมิสูง ช่วงอุณหภูมิที่เหมาะสมอยู่ในช่วง 300-800 องศา เซลเซียส แต่ที่เหมะสมที่สุดคือ 500 องศาเซลเซียส ส่วนช่วงเวลาที่เหมาะสมอยู่ในช่วง 2-6 ชั่วโมง แต่ที่เหมาะสมที่สุดคือ 3 ชั่วโมง

ในขั้นตอนการอบให้แห้ง ช่วงอุณหภูมิที่เหมาะสมอยู่ในช่วง 100-200 องศาเซลเซียส แต่ที่เหมาะสมที่สุดคือ 110 องศาเซลเซียส ส่วนช่วงเวลาที่เหมาะสมอยู่ในช่วง 6-30 ชั่วโมง แต่ที่ เหมาะสมที่สุดคือ 20 ชั่วโมง

สำหรับตัวอย่างการเตรียมตัวเร่งปฏิกิริยาทั้งสเตนบนตัวรองรับเซอร์โคเนียมใดออกใชด์ และการทดสอบในปฏิกิริยาเอสเทอร์ริฟิเคชัน แสดงในตัวอย่างข้างล่างนี้ แต่ตัวอย่างเหล่านี้มิได้ มีวัตถุประสงค์ที่จะจำกัดขอบเขตของการประดิษฐ์นี้แต่อย่างใด

## ตัวอย่างที่ 1

5

10

15

20

25

การเตรียมเซอร์โคเนียมใดออกไซด์ที่ปรับปรุงด้วยแลนทานัม ร้อยละ 0.1 โดยโมล ทำโดยเติมสารประกอบแลนทานัมในเตรต จำนวน 2.8 กรัม ลงในสารเซอร์โคเนียมนอมัลบิวทอก ไซด์ (ร้อยละ 80 โดยน้ำหนักในสารละลายบิวทานอล ) จำนวน 25 กรัม ละลายในสารละลาย 1.4-บิวเทนใดออล (ร้อยละ 90 โดยน้ำหนัก) จำนวน 100 มิลลิลิตร กวนให้สารละลายเป็นเนื้อเดียวกัน นำไปใส่ในเครื่องปฏิกรณ์ความดันสูง โดยเติมสารละลาย 1,4-บิวเทนใดออล จำนวน 30 มิลลิลิตร ในช่องว่างเครื่องปฏิกรณ์เพื่อทำปฏิกิริยาภายใต้ความดันของสารละลาย 1,4-บิวเทนใดออล ให้ความ ร้อนที่อุณหภูมิ 300 องสาเซลเซียส เป็นเวลา 2 ชั่วโมง เมื่ออุณหภูมิลดลงเท่ากับอุณหภูมิห้อง นำตะกอนที่ได้มาล้างโดยวิธีหมุนเหวี่ยงด้วยเมทานอล ล้างจำนวน 5 ครั้ง หมุนเหวี่ยงด้วยความเร็ว

#### หน้า 4 ของจำนวน 7 หน้า

รอบ 3,000 รอบต่อนาที เป็นเวลา 15 นาที นำตะกอนไปอบที่อุณหภูมิ 110 องศาเซลเซียส เป็นเวลา 12 ชั่วโมง จะได้ตัวรองรับเซอร์โคเนียมใดออกใชด์ที่ถูกปรับปรุงด้วยออกใชด์ของโลหะแลนทานัม ร้อยละ 0.1

การเตรียมตัวเร่งปฏิกิริยาทั้งสเตนร้อยละ 15 โดยน้ำหนักบนตัวรองรับเซอร์โคเนียม ใดออกใชด์ที่ถูกปรับปรุงด้วยออกใชด์ของโลหะแลนทานัม ร้อยละ 0.1 โดยการละลายสารทั้งสเตน เฮกซะคลอไรด์จำนวน 0.76 กรัม ด้วยน้ำบริสุทธิ์ และค่อยๆ หยดสารละลายทั้งสเตนเฮกซะคลอไรด์ บนผงเซอร์โคเนียมใดออกใชด์ที่ถูกปรับปรุงจำนวน 2 กรัม ตั้งไว้ที่อุณหภูมิห้อง เป็นเวลา 6 ชั่วโมง หลังจากนั้นนำไปอบที่อุณหภูมิ 110 องศาเซลเซียส เป็นเวลา 12 ชั่วโมง ขั้นตอนสุดท้ายนำไปเผา ภายใต้บรรยากาศของอากาศด้วยอัตราการใหล 100 ลูกบาศก์เซนติเมตรต่อนาที อุณหภูมิ 500 องศา เซลเซียสค้วยอัตรา 10 องศาเซลเซียสต่อนาที เป็นเวลา 3 ชั่วโมง จะได้ตัวเร่งปฏิกิริยาทั้งสเตนบนตัว รองรับเซอร์โคเนียมใดออกใชด์ที่ถูกปรับปรุงด้วยออกใชด์ของโลหะแลนทานัม ร้อยละ 0.1

การนำตัวเร่งปฏิกิริยาทั้งสเตนบนตัวรองรับเซอร์ โคเนียมใดออกใซด์ที่ถูกปรับปรุง มาทคสอบด้วยปฏิกิริยาเอสเทอร์ริฟิเคชัน ระหว่างกรดอะซิติกและเมทานอลเกินพอในอัตราส่วน 1 ต่อ 3 โดยโมล โดยชั่งกรดอะซิติก 20 กรัม ลงในขวดสามคอขนาด 250 ลูกบาสก์เซนติเมตร เติม ตัวเร่งปฏิกิริยาทั้งสเตนเซอร์ โคเนียมใดออกใซด์ที่ถูกปรับปรุง 0.4 กรัม ให้ความร้อนคงที่ที่ 60 องศา เซลเซียสพร้อมกวนอย่างต่อเนื่อง เมื่อได้อุณหภูมิที่ต้องการเติมเมทานอลจำนวน 32.5 กรัม ทำปฏิกิริยาอย่างต่อเนื่องเป็นเวลา 6 ชั่วโมง ผลที่ได้แสดงดังตารางที่ 1

## ตัวอย่างที่ 2

5

10

15

20

25

30

การเตรียมเซอร์โคเนียมใดออกใชด์ที่ปรับปรุงด้วยแลนทานัม ร้อยละ 0.2 โดยโมล ทำเหมือนตัวอย่างที่ 1 แต่ทำการเติมสารประกอบแลนทานัมในเตรต จำนวน 5.6 กรัม ลงในสาร เซอร์โคเนียมนอมัลบิวทอกใชด์ จะได้ตัวรองรับเซอร์โคเนียมใดออกไซด์ที่ถูกปรับปรุงด้วยออกใชด์ ของโลหะแลนทานัม ร้อยละ 0.2

การเตรียมตัวเร่งปฏิกิริยาทั้งสเตนร้อยละ 15 โดยน้ำหนักบนตัวรองรับเซอร์โคเนียม ใดออกใชด์ที่ถูกปรับปรุงด้วยออกใชด์ของโลหะแลนทานัม ร้อยละ 0.2 และการทดสอบตัวเร่ง ปฏิกิริยาทำเหมือนตัวอย่างที่ เ ผลการทดสอบที่ได้แสดงดังตารางที่ 1

## <u>ตัวอย่างที่ 3</u>

การเตรียมเซอร์โกเนียมใดออกใชด์ที่ปรับปรุงด้วยแลนทานัม ร้อยละ 0.3 โดยโมล ทำเหมือนตัวอย่างที่ 1 แต่ทำการเติมสารประกอบแลนทานัมในเตรต จำนวน 8.5 กรัม ลงในสาร เซอร์โกเนียมนอมัลบิวทอกใชด์ จะได้ตัวรองรับเซอร์โกเนียมใดออกใชด์ที่ถูกปรับปรุงด้วยออกใชด์ ของโลหะแลนทานัม ร้อยละ 0.3

#### หน้า 5 ของจำนวน 7 หน้า

การเตรียมตัวเร่งปฏิกิริยาทั้งสเตนร้อยละ 15 โคยน้ำหนักบนตัวรองรับเซอร์โคเนียม ใคออกใชด์ที่ถูกปรับปรุงด้วยออกใชด์ของโลหะแลนทานัม ร้อยละ 0.3 และการทดสอบตัวเร่ง ปฏิกิริยาทำเหมือนตัวอย่างที่ 1 ผลการทดสอบที่ได้แสดงดังตารางที่ 1

## ตัวอย่างที่ 4

5

10

15

20

25

การเตรียมเซอร์โคเนียมใดออกใชด์ที่ปรับปรุงด้วยอิตเทรียม ร้อยละ 0.1 โดยโมล ทำเหมือนตัวอย่างที่ 1 แต่ทำการเติมสารประกอบอิตเทรียมในเตรต จำนวน 2.5 กรัม ลงในสาร เซอร์โคเนียมนอมัลบิวทอกใชด์ ก่อนละลายด้วยสารละลาย 1,4-บิวเทนใดออล จะได้ตัวรองรับ เซอร์โคเนียมใดออกใชด์ที่ถูกปรับปรุงด้วยออกใชด์ของโลหะอิตเทรียม ร้อยละ 0.1

การเตรียมตัวเร่งปฏิกิริยาทั้งสเตนร้อยละ 15 โดยน้ำหนักบนตัวรองรับเซอร์โคเนียม ใดออกไซด์ที่ถูกปรับปรุงด้วยออกไซด์ของโลหะอิตเทรียม ร้อยละ 0.1 และการทดสอบตัวเร่ง ปฏิกิริยาทำเหมือนตัวอย่างที่ 1 ผลการทดสอบที่ได้แสดงดังตารางที่ 1

### ตัวอย่างที่ 5

การเตรียมเซอร์โคเนียมใคออกใชค์ที่ปรับปรุงด้วยอิตเทรียม ร้อยละ 0.2 โดยโมล ทำเหมือนตัวอย่างที่ 4 แต่ทำการเติมสารประกอบอิตเทรียมในเตรต จำนวน 4.9 กรัม ลงในสาร เซอร์โคเนียมนอมัลบิวทอกใชค์ จะได้ตัวรองรับเซอร์โคเนียมใดออกใชค์ที่ถูกปรับปรุงด้วยออกใชค์ ของโลหะอิตเทรียมร้อยละ 0.2

การเตรียมตัวเร่งปฏิกิริยาทั้งสเตนร้อยละ 15 โดยน้ำหนักบนตัวรองรับเซอร์โกเนียม ใดออกไซด์ที่ถูกปรับปรุงด้วยออกไซด์ของโลหะอิตเทรียมร้อยละ 0.2 และการทดสอบตัวเร่ง ปฏิกิริยาทำเหมือนตัวอย่างที่ 1 ผลการทดสอบที่ได้แสดงดังตารางที่ 1

## ตัวอย่างที่ 6

การเตรียมเซอร์โคเนียมใดออกใชด์ที่ปรับปรุงด้วยอิตเทรียม ร้อยละ 0.3 โดยโมล ทำเหมือนตัวอย่างที่ 4 แต่ทำการเติมสารประกอบอิตเทรียมในเตรต จำนวน 5.9 กรัม ลงในสาร เซอร์โคเนียมนอมัลบิวทอกใชด์ จะได้ตัวรองรับเซอร์โคเนียมใดออกใชด์ที่ถูกปรับปรุงด้วยออกใชด์ ของโลหะอิตเทรียมร้อยละ 0.3

การเตรียมตัวเร่งปฏิกิริยาทั้งสเตนร้อยละ 15 โดยน้ำหนักบนตัวรองรับเซอร์โคเนียม ใคออกไซด์ที่ถูกปรับปรุงด้วยออกไซด์ของโลหะอิตเทรียมร้อยละ 0.3 และการทดสอบตัวเร่ง ปฏิกิริยาทำเหมือนตัวอย่างที่ 1 ผลการทดสอบที่ได้แสดงดังตารางที่ 1

#### หน้า 6 ของจำนวน 7 หน้า

# <u>ตัวอย่างเปรียบเทียบที่ 1</u>

การเตรียมตัวรองรับเซอร์โคเนียมไดออกไซด์ที่ไม่ได้ปรับปรุง ทำเหมือนตัวอย่างที่ 1 ยกเว้นการเติมสารประกอบแลนทานัมในเตรต จะได้เซอร์โคเนียมไดออกไซด์ลักษณะผงละเอียด สีขาว

การเตรียมตัวเร่งปฏิกิริยาทั้งสเตนร้อยละ 15 โดยน้ำหนักบนตัวรองรับเซอร์ โคเนียม ใคออกใชด์ และการทคสอบตัวเร่งปฏิกิริยาทำเหมือนตัวอย่างที่ 1 ผลการทคสอบที่ได้แสดงดังตาราง ที่ 1

# ตารางที่ 1

5

ประเภท	ตัวเร่งปฏิกิริยา	ปริมาณ H <sup>+</sup>	ร้อยละการเกิดปฏิกิริยา
		(µmol/g catalyst)¹	ที่เวลา 6 ชั่วโมง
ตัวอย่างที่ 1	ร้อยละ 15 โดยน้ำหนัก	373	73
	ทั้งสเตนบนตัวรองรับ		
	เซอร์โคเนียมใดออกใชด์		
	ที่ปรับปรุงด้วยออกไซค์ของ		
	แลนทานัม ร้อยละ 0.1		
ตัวอย่างที่ 2	ร้อยละ 15 โดยน้ำหนัก	418	75
	ทั้งสเตนบนตัวรองรับ		
	เซอร์โคเนียมใดออกใซค์		
	ที่ปรับปรุงด้วยออกใชด์ของ		
	แลนทานัม ร้อยละ 0.2		
ตัวอย่างที่ 3	ร้อยละ 15 โดยน้ำหนัก	358	69
	ทั้งสเตนบนตัวรองรับ		
	เซอร์โคเนียมใดออกใชค์		
	ที่ปรับปรุงด้วยออกไซด์ของ		
	แลนทานัม ร้อยละ 0.3		
ตัวอย่างที่ 4	ร้อยละ 15 โดยน้ำหนัก	251	67
	ทั้งสเตนบนตัวรองรับ		
	เซอร์โคเนียมใดออกใชด์		
	ที่ปรับปรุงด้วยออกใซด์ของ		
	อิตเทรียม ร้อยละ 0.1		

#### หน้า 7 ของจำนวน 7 หน้า

ประเภท	ตัวเร่งปฏิกิริยา	ปริมาณ H⁺	ร้อยละการเกิดปฏิกิริยา
		(µmol/g catalyst)	ที่เวลา 6 ชั่วโมง
ตัวอย่างที่ <i>5</i>	ร้อยละ 15 โดยน้ำหนัก	298	69
	ทั้งสเตนบนตัวรองรับ		
	เซอร์โคเนียมใดออกใชด์		
	ที่ปรับปรุงด้วยออกไซด์ของ		
	อิตเทรียม ร้อยละ 0.2		
ตัวอย่างที่ 6	ร้อยละ 15 โดยน้ำหนัก	368	71
	ทั้งสเตนบนตัวรองรับ		
	เซอร์โคเนียมใดออกใชค์		
	ที่ปรับปรุงด้วยออกใซค์ของ		
	อิตเทรียม ร้อยละ 0.3		
ตัวอย่าง	ร้อยละ 15 โดยน้ำหนัก	112	55
เปรียบเทียบ	ทั้งสเตนบนตัวรองรับ		
ที่ 1	เซอร์โคเนียมใดออกใชค์		
	ที่ไม่ได้ปรับปรุง		

<sup>์</sup> ทดสอบปริมาณ H๋ ด้วยการไตเตรตโดยใช้เทคนิกการแลกเปลี่ยนไอออนกรค-เบส

ดังแสดงในตารางที่ 1 ปฏิกิริยาเอสเทอร์ริฟิเคชันระหว่างกรดอะซิติกกับเมทานอล โดย ตัวเร่งปฏิกิริยาที่ประดิษฐ์ขึ้นดังตัวอย่างที่ 1 ถึง ตัวอย่างที่ 6 มีความเป็นกรดและให้ผลการทดสอบ ที่ดีกว่าใช้ตัวเร่งปฏิกิริยาทั้งเสตนบนตัวรองรับเซอร์โคเนียมใดออกใชด์ที่ไม่ได้รับการปรับปรุง ดังตัวอย่างเปรียบเทียบที่ 1

# วิธีการในการประดิษฐ์ที่ดีที่สุด

5

เหมือนกับที่ได้กล่าวมาแล้วในหัวข้อการเปิดเผยการประดิษฐ์โดยสมบูรณ์

#### หน้า 1 ของจำนวน 3 หน้า

#### ข้อถือสิทธิ

5

10

15

20

25

- 1. กรรมวิธีการเตรียมตัวเร่งปฏิกิริยาทั้งสเตนบนตัวรองรับเซอร์โคเนียมใดออกใชด์ที่ปรับปรุง ด้วยออกใชด์ของโลหะทรานสิชันหมู่ IIIB เพื่อนำไปใช้เป็นตัวเร่งปฏิกิริยาในปฏิกิริยาเอสเทอร์ริฟิเค ชัน ซึ่งมีขั้นตอนการเตรียมดังนี้
- การปรับปรุงตัวรองรับเซอร์โคเนียมใดออกใซด์ ซึ่งทำโดยวิธีการใดวิธีการหนึ่ง ดังต่อไปนี้คือ
- (1) โดยการเติมสารละลายของสารประกอบของโลหะทรานสิชันหมู่ IIIB ในขั้นตอนการเตรียมตัวรองรับเซอร์โคเนียมไดออกไซด์ หลังจากการทำให้เกิดเป็นตะกอนแล้วจะทำ การล้างตะกอนโดยการหมุนเหวี่ยง และนำตะกอนไปอบให้แห้ง
- (2) โดยการเติมสารละลายของสารประกอบของโลหะทรานลิชันหมู่ IIIB ลงบน เซอร์โคเนียมใดออกใชด์ จากนั้นอบให้แห้ง แล้วนำไปเผา
- การเตรียมตัวเร่งปฏิกิริยาทั้งสเตนบนตัวรองรับเซอร์โคเนียมใดออกไซด์
  ที่ปรับปรุงค้วยออกไซด์ของโลหะทรานสิชันหมู่ IIIB ทำโดยการเติมสารละลายของสารประกอบ
  โลหะทั้งสเตนบนตัวรองรับเซอร์โคเนียมใดออกไซด์ที่ปรับปรุงด้วยออกไซด์ของโลหะทรานสิชัน
  หมู่ IIIB จากนั้นตั้งทิ้งไว้ที่อุณหภูมิห้อง แล้วนำไปอบให้แห้ง หลังจากนั้นนำตะกอนที่แห้งไปผ่าน
  ขั้นตอนการเผา
- 2. กรรมวิธีตามข้อถือสิทธิ 1 ที่ซึ่งโลหะทรานซิชันหมู่ IIIB ตามที่กล่าวแล้ว ได้แก่ โลหะ สแคนเดียม โลหะอิตเทรียม โลหะแลนทานัม และ โลหะแอกทีเนียม
- 3. กรรมวิธีตามข้อถือสิทธิ 1 ที่ซึ่งโลหะทรานซิชันหมู่ IIIB ตามที่กล่าวแล้ว ได้แก่ โลหะ แลนทานัม และ โลหะอิตเทรียม
- 4. กรรมวิธีตามข้อถือสิทธิ 2 หรือ 3 ที่ซึ่งสารประกอบของโลหะแลนทานัมตามที่กล่าวแล้ว เลือกจากกลุ่มที่ประกอบด้วย แลนทานัมคลอไรค์ แลนทานัมในเตรต แลนทานัมแอซิเตค และ แลนทานัมอะซิติลอะซิโตเนต
- 5. กรรมวิธีตามข้อถือสิทธิ 2 หรือ 3 ที่ซึ่งสารประกอบของโลหะแลนทานัมตามที่กล่าวแล้ว เลือกจาก แลนทานัมในเตรต
- 6. กรรมวิธีตามข้อถือสิทธิ 2 หรือ 3 ที่ซึ่งสารประกอบของโลหะอิตเทรียมตามที่กล่าวแล้ว เลือกจากกลุ่มที่ประกอบด้วย อิตเทรียมคลอไรด์ อิตเทรียมในเตรต อิตเทรียมแอซิเตด และ อิตเทรียมอะซิติลอะซิโตเนต
- 7. กรรมวิธีตามข้อถือสิทธิ 2 หรือ 3 ที่ซึ่งสารประกอบของโลหะอิตเทรียมตามที่กล่าวแล้ว 30 เลือกจากอิตเทรียมในเตรต

#### หน้า 2 ของจำนวน 3 หน้า

- 8. กรรมวิธีตามข้อถือสิทธิ 1 ที่ซึ่งสารประกอบของโลหะเซอร์โกเนียมตามที่กล่าวแล้วเลือกจาก กลุ่มที่ประกอบด้วย เซอร์โคเนียมในเตรด เซอร์โคเนียมกลอไรด์ เซอร์โคเนียมแอซิเตด เซอร์โคเนียม โพรพอกไซด์ เซอร์โคเนียมไอโซโพรพอกไซด์ และ เซอร์โคเนียมนอมัลบิวทอกไซด์
- 9. กรรมวิธีตามข้อถือสิทธิ 1 ที่ซึ่งสารประกอบของโลหะเซอร์โคเนียมตามที่กล่าวแล้วเลือกจาก เซอร์โคเนียมนอมัลบิวทอกไซด์

5

10

30

- 10. กรรมวิธีตามข้อถือสิทธิ 1 ที่ซึ่งสารประกอบของโลหะทั้งสเตนตามที่กล่าวแล้วเลือกจากกลุ่ม ที่ประกอบด้วย แอมโมเนียมเมทาทั้งสเตน แอมโมเนียมพาราทั้งสเตน ทั้งสเตนเฮกซะคลอไรด์ ทั้งสเตนเฮกซะคาร์บอนิล และ ทั้งสเตนเพนตะกอกไซด์
- กรรมวิธีตามข้อถือสิทธิ 1 ที่ซึ่งสารประกอบของโลหะทั้งสเตนตามที่กล่าวแล้วเลือกจาก ทั้งสเตนเฮกซะกลอไรด์
  - 12. กรรมวิธีตามข้อถือสิทธิ 1 ที่ซึ่งจำนวนครั้งในการถ้างตะกอนโดยวิธีหมุนเหวี่ยง คือ 3-10 ครั้ง
  - 13. กรรมวิธีตามข้อถือสิทธิ 1 ที่ซึ่งจำนวนครั้งในการถ้างตะกอนโดยวิธีหมุนเหวี่ยง คือ 5 ครั้ง
  - 14. กรรมวิธีตามข้อถือสิทธิ 1 ที่ซึ่งความเร็วรอบสำหรับการหมุนเหวี่ยงอยู่ในช่วง 1,000-5,000 รอบต่อนาที
- 15 15. กรรมวิธีตามข้อถือสิทธิ 1 ที่ซึ่งความเร็วรอบสำหรับการหมุนเหวี่ยง คือ 3,000 รอบต่อนาที
  - 16. กรรมวิธีตามข้อถือสิทธิ 1 ที่ซึ่งระยะเวลาในการหมุนเหวี่ยงอยู่ในช่วง 10-30 นาที
  - 17. กรรมวิธีตามข้อถือสิทธิ 1 ที่ซึ่งระยะเวลาในการหมุนเหวี่ยง คือ 15 นาที
  - 18. กรรมวิธีตามข้อถือสิทธิ 1 ที่ซึ่งอุณหภูมิที่ใช้ในการเผาตะกอน คือ 300-800 องศาเซลเซียส
  - 19. กรรมวิธีตามข้อถือสิทธิ 1 ที่ซึ่งอุณหภูมิที่ใช้ในการเผาตะกอน คือ 500 องศาเซลเซียส
- 20 20. กรรมวิธีตามข้อถือสิทธิ 1 ที่ซึ่งระยะเวลาที่ใช้ในการเผาตะกอน คือ 2-6 ชั่วโมง
  - 21. กรรมวิธีตามข้อถือสิทธิ 1 ที่ซึ่งระยะเวลาที่ใช้ในการเผาตะกอน คือ 3 ชั่วโมง
  - 22. กรรมวิธีตามข้อถือสิทธิ 1 ที่ซึ่งอุณหภูมิที่ใช้ในการอบตะกอนให้แห้ง คือ 100-200 องศา เซลเซียส
  - 23. กรรมวิธีตามข้อถือสิทธิ 1 ที่ซึ่งอุณหภูมิที่ใช้ในการอบตะกอนให้แห้ง คือ 110 องศาเซลเซียส
- 25 24. กรรมวิธีตามข้อถือสิทธิ 1 ที่ซึ่งระยะเวลาที่ใช้ในการอบตะกอนให้แห้ง คือ 6-30 ชั่วโมง
  - 25. กรรมวิธีตามข้อถือสิทธิ 1 ที่ซึ่งระยะเวลาที่ใช้ในการอบตะกอนให้แห้ง คือ 20 ชั่วโมง
  - 26. กรรมวิธีตามข้อถือสิทธิ 1 ที่ซึ่งระยะเวลาที่ใช้ในการตั้งทิ้งไว้ที่อุณหภูมิห้อง คือ 1-10 ชั่วโมง
  - 27. กรรมวิธีตามข้อถือสิทธิ 1 ที่ซึ่งระยะเวลาที่ใช้ในการตั้งทิ้งไว้ที่อุณหภูมิห้อง คือ 5 ชั่วโมง
  - 28. กรรมวิธีตามข้อถือสิทธิ 1 ที่ซึ่งขั้นตอนการปรับปรุงตัวรองรับเซอร์โคเนียมใดออกใชด์โดยวิธี ที่ 1 ยังประกอบด้วย ขั้นตอนการเผาตะกอนที่แห้ง
    - 29. กรรมวิธีตามข้อถือสิทธิ 28 ที่ซึ่งอุณหภูมิที่ใช้ในการเผาตะกอน คือ 300-800 องศาเซลเซียส
  - 30. กรรมวิธีตามข้อถือสิทธิ 28 ที่ซึ่งอุณหภูมิที่ใช้ในการเผาตะกอน คือ 500 องศาเซลเซียส

## หน้า 3 ของจำนวน 3 หน้า

- 31. กรรมวิธีตามข้อถือสิทธิ 28 ที่ซึ่งระยะเวลาที่ใช้ในการเผาตะกอน คือ 2-6 ชั่วโมง
- 32. กรรมวิธีตามข้อถือสิทธิ 28 ที่ซึ่งระยะเวลาที่ใช้ในการเผาตะกอน คือ 3 ชั่วโมง

#### หน้า 1 ของจำนวน 1 หน้า

#### บทสรุปการประดิษฐ์

5

10

15

การประดิษฐ์นี้เกี่ยวข้องกับกรรมวิธีการเตรียมตัวเร่งปฏิกิริยาเพื่อใช้ในปฏิกิริยาเอสเทอร์ ริฟิเคชัน โดยใช้เซอร์โคเนียมไดออกไซด์ที่ปรับปรุงด้วยออกไซด์ของโถหะทรานสิชันหมู่ IIIB เป็น ตัวรองรับของตัวเร่งปฏิกิริยาทั้งสเตน ซึ่งมีขั้นตอนการเตรียมดังนี้

- การปรับปรุงตัวรองรับเซอร์โคเนียมใดออกใชด์ ซึ่งทำโดยวิธีการใดวิธีการหนึ่ง ดังต่อไปนี้คือ
- (1) โดยการเติมสารละลายของสารประกอบของโลหะทรานสิชันหมู่ IIIB ในขั้นตอน การเตรียมตัวรองรับเซอร์โคเนียมใดออกใชด์ หรือ
- (2) โดยการเติมสารละลายของสารประกอบของโลหะทรานลิชันหมู่ IIIB ลงบน เซอร์โคเนียมใดออกใชด์
  - การเตรียมตัวเร่งปฏิกิริยาทั้งสเตนบนตัวรองรับเซอร์ โคเนียมใดออกไซด์ที่ปรับปรุง ด้วยออกไซด์ของโลหะทรานสิชันหมู่ IIIB ทำโดยการเติมสารละลายของสารประกอบโลหะทั้งสเตน บนตัวรองรับเซอร์ โคเนียมใดออกไซด์ที่ปรับปรุงด้วยออกไซด์ของโลหะทรานสิชันหมู่ IIIB จากนั้น ตั้งทิ้งไว้ที่อุณหภูมิห้อง แล้วนำไปอบให้แห้ง หลังจากนั้นนำตะกอนที่แห้งสนิทไปผ่านขั้นตอนการ เผาที่อุณหภูมิสูง